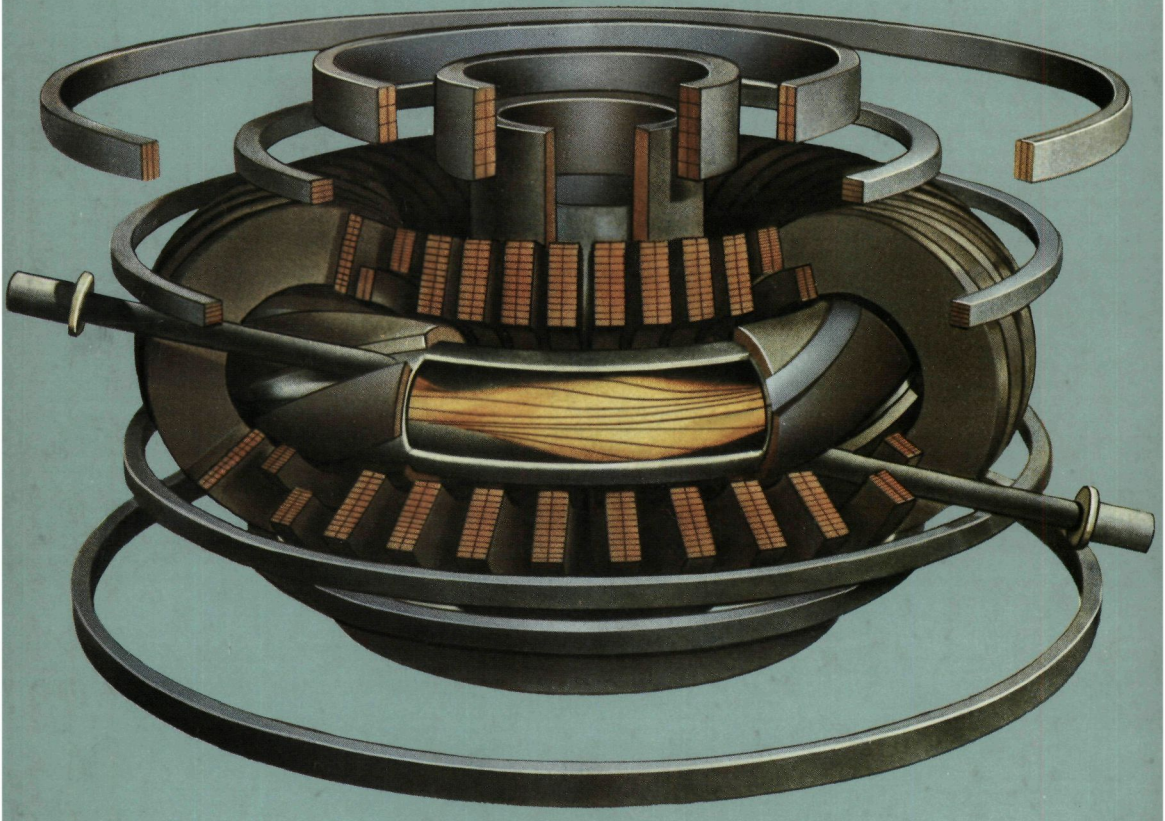
PLASMA PHYSICS AND CONTROLLED NUCLEAR FUSION RESEARCH 1976

VOL. III

Sixth Conference Proceedings, Berchtesgaden, 6-13 October 1976

NUCLEAR FUSION, SUPPLEMENT 1977



INTERNATIONAL ATOMIC ENERGY AGENCY, VIENNA, 1977

PLASMA PHYSICS
AND CONTROLLED
NUCLEAR FUSION RESEARCH
1976

The following States are Members of the International Atomic Energy Agency:

AFGHANISTAN
ALBANIA
ALGERIA
ARGENTINA
AUSTRALIA
AUSTRIA
BANGLADESH
BELGIUM
BOLIVIA
BRAZIL
BULGARIA
BURMA
BYELORUSSIAN SOVIET SOCIALIST REPUBLIC
CANADA
CHILE
COLOMBIA
COSTA RICA
CUBA
CYPRUS
CZECHOSLOVAKIA
DEMOCRATIC KAMPUCHEA
DEMOCRATIC PEOPLE'S REPUBLIC OF KOREA
DENMARK
DOMINICAN REPUBLIC
ECUADOR
EGYPT
EL SALVADOR
ETHIOPIA
FINLAND
FRANCE
GABON
GERMAN DEMOCRATIC REPUBLIC
GERMANY, FEDERAL REPUBLIC OF
GHANA
GREECE
GUATEMALA
HAITI
HOLY SEE
HUNGARY
ICELAND
INDIA
INDONESIA
IRAN
IRAQ
IRELAND
ISRAEL
ITALY
IVORY COAST
JAMAICA
JAPAN
JORDAN
KENYA
KOREA, REPUBLIC OF
KUWAIT
LEBANON
LIBERIA
LIBYAN ARAB JAMAHIRIYA
LIECHTENSTEIN
LUXEMBOURG
MADAGASCAR
MALAYSIA
MALI
MAURITIUS
MEXICO
MONACO
MONGOLIA
MOROCCO
NETHERLANDS
NEW ZEALAND
NICARAGUA
NIGER
NIGERIA
NORWAY
PAKISTAN
PANAMA
PARAGUAY
PERU
PHILIPPINES
POLAND
PORTUGAL
QATAR
ROMANIA
SAUDI ARABIA
SENEGAL
SIERRA LEONE
SINGAPORE
SOCIALIST REPUBLIC OF VIET NAM
SOUTH AFRICA
SPAIN
SRI LANKA
SUDAN
SWEDEN
SWITZERLAND
SYRIAN ARAB REPUBLIC
THAILAND
TUNISIA
TURKEY
UGANDA
UKRAINIAN SOVIET SOCIALIST REPUBLIC
UNION OF SOVIET SOCIALIST REPUBLICS
UNITED ARAB EMIRATES
UNITED KINGDOM OF GREAT BRITAIN AND NORTHERN IRELAND
UNITED REPUBLIC OF CAMEROON
UNITED REPUBLIC OF TANZANIA
UNITED STATES OF AMERICA
URUGUAY
VENEZUELA
YUGOSLAVIA
ZAIRE
ZAMBIA

The Agency's Statute was approved on 23 October 1956 by the Conference on the Statute of the IAEA held at United Nations Headquarters, New York; it entered into force on 29 July 1957. The Headquarters of the Agency are situated in Vienna. Its principal objective is "to accelerate and enlarge the contribution of atomic energy to peace, health and prosperity throughout the world".

Printed by the IAEA in Austria
May 1977

NUCLEAR FUSION · SUPPLEMENT 1977

PLASMA PHYSICS AND CONTROLLED NUCLEAR FUSION RESEARCH 1976

PROCEEDINGS OF THE
SIXTH INTERNATIONAL CONFERENCE ON PLASMA PHYSICS
AND CONTROLLED NUCLEAR FUSION RESEARCH
HELD BY THE
INTERNATIONAL ATOMIC ENERGY AGENCY
AT BERCHTESGADEN, 6–13 OCTOBER 1976

In three volumes

VOL.III

INTERNATIONAL ATOMIC ENERGY AGENCY
VIENNA, 1977

PLASMA PHYSICS AND CONTROLLED NUCLEAR FUSION RESEARCH
1976
IAEA, VIENNA, 1977
STI/PUB/439
ISBN 92–0–130277–0

FOREWORD

The IAEA Conferences on Plasma Physics and Controlled Nuclear Fusion Research are becoming one of the major forums for physicists and engineers involved in this field of research. On the recommendation of the International Fusion Research Council the time between Conferences has been reduced from the earlier three years to two years in order to keep pace with the rapid progress being made. The last Conference was held in Tokyo in 1974.

The 6th Conference in this series, held in Berchtesgaden from 6 to 13 October 1976, was organized by the Agency in cooperation with the Government of the Federal Republic of Germany with the assistance of the Max-Planck-Institut für Plasmaphysik (Garching). Nearly 450 participants from 30 countries and four international organizations attended. A total of 149 papers were presented on the various physics and engineering aspects of nuclear fusion.

The Proceedings of the Conference are here published in English in three volumes as a supplement to the IAEA journal Nuclear Fusion.

The Agency promotes the close international collaboration among plasma physicists of all countries by regularly organizing conferences on controlled nuclear fusion and by holding seminars and specialists' meetings in selected topics. These activities will, it is hoped, contribute to the rapid use of this new source of energy to meet the future world's energy requirements.

EDITORIAL NOTE

The papers and discussions have been edited by the editorial staff of the International Atomic Energy Agency to the extent considered necessary for the reader's assistance. The views expressed and the general style adopted remain, however, the responsibility of the named authors or participants. In addition, the views are not necessarily those of the governments of the nominating Member States or of the nominating organizations.

Where papers have been incorporated into these Proceedings without resetting by the Agency, this has been done with the knowledge of the authors and their government authorities, and their cooperation is gratefully acknowledged. The Proceedings have been printed by composition typing and photo-offset lithography. Within the limitations imposed by this method, every effort has been made to maintain a high editorial standard, in particular to achieve, wherever practicable, consistency of units and symbols and conformity to the standards recommended by competent international bodies.

The use in these Proceedings of particular designations of countries or territories does not imply any judgement by the publisher, the IAEA, as to the legal status of such countries or territories, of their authorities and institutions or of the delimitation of their boundaries.

The mention of specific companies or of their products or brand names does not imply any endorsement or recommendation on the part of the IAEA.

Authors are themselves responsible for obtaining the necessary permission to reproduce copyright material from other sources.

CONTENTS OF VOLUME III

HEATING (Session XVIII)

Rapid further heating of tokamak plasma by fast-rising magnetic pulse (IAEA-CN-35/G5-1) 3
N. Inoue, H. Nihei, K. Yamazaki, M. Ichimura, J. Morikawa, K. Hoshino, T. Uchida

Turbulent heating of a toroidal plasma through a skin layer (IAEA-CN-35/G5-2) 11
Y. Amagishi, A. Hirose, H.P. Piekaar, H.M. Skarsgard

A new method of collisionless heating for toroidal plasmas involving low-frequency axisymmetric pumping (IAEA-CN-35/G6) 19
E. Canobbio

Discussion on paper IAEA-CN-35/G6 29

Plasma heating in a toroidal system by a helical quadrupole RF field with $\omega < \omega_{Bi}$ (IAEA-CN-35/G7) 31
R.A. Demirkhanov, A.G. Kirov, S.N. Lozovskij, F.M. Nekrasov, A.G. Elfimov, S.E. Il'inskij, V.V. Onishchenko

Discussion on paper IAEA-CN-35/G7 37

Magnetosonic wave generation and damping in the TFR tokamak near the ion cyclotron frequencies (IAEA-CN-35/G8) 39
Equipe TFR

Discussion on paper IAEA-CN-35/G8 47

Experiments at the lower hybrid frequency in the Wega tokamak (IAEA-CN-35/G9) 49
P. Blanc, W. Hess, G. Ichtchenko, P. Javel, P. Lallia, C. Mahn, T.K. Nguyen, W. Ohlendorf, G.W. Pacher, H.D. Pacher, S. Takamura, G. Tonon, J.G. Wegrowe

Discussion on paper IAEA-CN-35/G9 59

Magnetoacoustic-heating experiments in tokamak T-4 plasma (IAEA-CN-35/G10) 61
V.V. Buzankin, V.A. Vershkov, N.V. Ivanov, I.A. Kovan, V.A. Krupin, I.A. Popov, I.B. Semenov, Yu.A. Sokolov

Discussion on paper IAEA-CN-35/G10 75

HIGH BETA IV (Session XIX)

Limits in the production of a low compressed high-beta plasma in the linear theta pinch Isar II (IAEA-CN-35/E13-1) 79
W. Köppendörfer, M. Münich, J. Sommer

Shock heating of collisionless plasmas in toroidal geometry (IAEA-CN-35/E13-2) 89
F. Söldner, K.-H. Steuer

Discussion on papers IAEA-CN-35/E13-1, E13-2 101

Experimental study of a two-stage ion-heating plasma injection and compression experiment (IAEA-CN-35/E14) 103
H. Itô, S. Gotô, T. Uyana, N. Satomi, K. Watanabe

Discussion on paper IAEA-CN-35/E14 111

Kinetic and numerical studies of microstability properties and anomalous transport in theta pinches (IAEA-CN-35/E15) 113
R.C. Davidson, N.T. Gladd, J. Huba, B.H. Hui, P.C. Liewer, C.S. Liu, J.P. Mondt, J.M. Ogden, C.S. Wu, S. Hamasaki, N.A. Krall, C.E. Wagner
Discussion on paper IAEA-CN-35/E15 121
Kinetic behaviour of high-beta plasmas (IAEA-CN-35/E16) 123
J.P. Freidberg, R.A. Gerwin, D.W. Hewett, H.R. Lewis, C.W. Nielson, A.G. Sgro, L. Turner, D. Winske
Discussion on paper IAEA-CN-35/E16 131

OPEN TRAPS (Session XX)

2XIIB plasma confinement experiments (IAEA-CN-35/C1) 135
F.H. Coensgen, J.F. Clauser, D.L. Correll, W.F. Cummins, C. Gormezano, B.G. Logan, A.W. Molvik, W.E. Nexsen, T.C. Simonen, B.W. Stallard, W.C. Turner
Discussion on paper IAEA-CN-35/C1 145
Theoretical explanation of present mirror experiments and linear stability of larger scaled machines (IAEA-CN-35/C2) 147
H.L. Berk, D.E. Baldwin, T.A. Cutler, L.L. Lodestro, N. Maron, L.D. Pearlstein, T.D. Rognlien, J.J. Stewart, D.C. Watson
Discussion on paper IAEA-CN-35/C2 159
Theory of mirror machines at high beta (IAEA-CN-35/C3) 161
B. McNamara, D.V. Anderson, J.K. Boyd, J.A. Byers, R. Cohen, T.A. Cutler, L.S. Hall, R.F. Post, M. Rensink
Discussion on paper IAEA-CN-35/C3 175
Open trap with ambipolar mirrors (IAEA-CN-35/C4) 177
G.I. Dimov, V.V. Zakajdakov, M.E. Kishinevskij
Discussion on paper IAEA-CN-35/C4 189

REACTOR DESIGN I (Session XXI)

Reactor costs and maintenance, with reference to the Culham Mark II conceptual tokamak reactor design (IAEA-CN-35/I1-1) 193
R. Hancox, J.T.D. Mitchell
A high-performance non-circular tokamak power reactor design study – UWMAK-III (IAEA-CN-35/I1-2) 203
R.W. Conn, G.L. Kulcinski, C.W. Maynard, R. Aronstein, R.W. Boom, A. Bowles, R.G. Clemmer, J. Davis, G.A. Emmert, S. Ghose, Y. Gohar, J. Kesner, S. Kuo, E. Larsen, J. Scharer, I. Sviatoslavsky, D.K. Sze, W.F. Vogelsang, T.F. Yang, W.D. Young
Discussion on papers IAEA-CN-35/I1-1, I1-2 221
Mirror reactor studies (IAEA-CN-35/I2) 223
R.W. Moir, W.L. Barr, D.J. Bender, R.J. Burleigh, G.A. Carlson, R.S. Devoto, J.N. Doggett, J.H. Fink, G.W. Hamilton, J.D. Lee, M.E. Rensink, C.E. Taylor, R.W. Werner, K.R. Schultz
Discussion on paper IAEA-CN-35/I2 237

Preliminary design of a tokamak experimental fusion reactor (IAEA-CN-35/I3-1) 239
K. Sako, T. Tone, Y. Seki, H. Iida, S. Matsuda, H. Yamato, N. Asami, F. Eto, T. Ide, T. Suzuki, K. Maki, K. Ioki
Tokamak experimental power reactor studies (IAEA-CN-35/I3-2) 255
W.M. Stacey, Jr., C.C. Baker, M. Roberts
Discussion on papers IAEA-CN-35/I3-1, I3-2 279
Pure-fusion and fusion-fission reactor applications of high-density linear confinement systems (IAEA-CN-35/I4) 281
R.A. Krakowski, R.L. Miller, R.L. Hagenson, L.C. Steinhauer, G.C. Vlases, R.T. Taussig, P.H. Rose, A.L. Hoffman, D.C. Quimby, G.L. Woodruff, H.J. Willenberg

REACTOR DESIGN II (Session XXII)

Neutral beam injector research and development work in the USA (IAEA-CN-35/I5) 293
L.D. Stewart, G.C. Barber, W.K. Dagenhart, R.C. Davis, L.R. Grisham, H.H. Haselton, J. Kim, N.S. Ponte, P.M. Ryan, D.E. Schechter, G. Schilling, W.L. Stirling, C.C. Tsai, J.H. Whealton, R.E. Wright, W.R. Baker, K.H. Berkner, W.S. Cooper, K.W. Ehlers, J.M. Haughian, D.B. Hopkins, W.B. Kunkel, B.A. Pritchard, R.V. Pyle, H.M. Owren, J.W. Stearns, O.A. Anderson, D.H. Birdsall, D.L. Correll, E.B. Hooper, Jr., L.C. Pittenger, D.S. Prono, K. Prelec, T. Sluyters, H. Halama
Discussion on paper IAEA-CN-35/I5 301
Development of fast neutral beam injectors at Fontenay-aux-Roses (IAEA-CN-35/I6) 303
A. Bariaud, R. Becherer, J.F. Bonnal, J. Druaux, M. Fumelli, R. Oberson, P.A. Raimbault, F.P.G. Valckx
Discussion on paper IAEA-CN-35/I6 315
Pulsed energy storage in fusion devices (IAEA-CN-35/I7) 317
K.I. Thomassen, J.D. Rogers, F.L. Ribe, D.M. Weldon, C.E. Swannack, H.F. Vogel, H.G. Rylander, W.F. Weldon, K.M. Tolk, M.D. Driga, W.L. Bird, Jr., H.H. Woodson, C.J. Mole, R.E. Stillwagon
Discussion on paper IAEA-CN-35/I7 325
Removal of foreign atoms from a metal surface bombarded with fast atomic particles (IAEA-CN-35/I8) 327
S.K. Dolotov, S.A. Evstigneev, S.Yu. Luk'yanov, Yu.V. Martynenko, V.M. Chicherov
Discussion on paper IAEA-CN-35/I8 335
Dynamic characteristics of alpha-particle heating based upon the Fokker-Planck equation in D-T fusion reactor core plasmas (IAEA-CN-35/I9-1) 337
H. Saito, M. Katsurai, H. Tsuji, T. Sekiguchi
Thermal thermonuclear instability in a tokamak reactor (IAEA-CN-35/I9-2) 347
Ya.I. Kolesnichenko, S.N. Reznik
Stationary temperature profile in a tokamak reactor operated in the neoclassical regime (IAEA-CN-35/I9-3) 359
T.F. Volkov, Yu.L. Igitkhanov, M.Z. Tokar'
Discussion on papers IAEA-CN-35/I9-1, I9-2, I9-3 367

MISCELLANEOUS (Session XXIII)

Energy principles for non-ideal MHD (IAEA-CN-35/H1) 371
H. Tasso
Discussion on paper IAEA-CN-35/H1 383
Experimental studies on generation and behaviour of field-reversing E- and P-layers (IAEA-CN-35/H2-1) 385
H.A. Davis, H.H. Fleischmann, S.C. Luckhardt, R.A. Meger
Formation of a high-current relativistic-electron-beam ring for plasma confinement (IAEA-CN-35/H2-2) 395
A. Mohri, M. Masuzaki, K. Narihara, T. Tsuzuki, K. Yamanaka, K. Ikuta
Discussion on papers IAEA-CN-35/H2-1, H2-2 403
Macroparticle acceleration by laser-induced ablation pressure (IAEA-CN-35/H3) 405
M.D.J. Burgess, H. Motz, P.T. Rumsby, M. Michaelis
Generation of intense ion beams and their application to controlled fusion research (IAEA-CN-35/H4) 415
P. Dreike, R.L. Ferch, A. Friedman, S. Humphries, R.V. Lovelace, G. Ludwig, R.N. Sudan, D.L. Book, G. Cooperstein, A.T. Drobot, J. Golden, S.A. Goldstein, C.A. Kapetanakos, R. Lee, W. Manheimer, S.J. Marsh, D. Mosher, E. Ott, S.J. Stephanakis, P.J. Turchi
Plasma confinement in a cusp field with RF plugging (IAEA-CN-35/H5) 427
S. Hiroe, T. Sato, T. Watari, S. Hidekuma, R. Kumazawa, K. Adati, T. Shoji, S. Kawasaki, T. Hatori, H. Obayashi, T. Watanabe, N. Watanabe, S. Miyake, A. Miyahara, K. Takayama

FOCUS, LINER, WALL CONTAINMENT (Session XXIV)

Neutron production in the dense plasma focus (IAEA-CN-35/E18-1(a)) 437
H.J. Kaeppeler
Dynamics of 120 and 20 kV plasma focus devices with respect to density and current distribution, and neutron and X-ray emission (IAEA-CN-35/E18-1(b)) 441
G. Decker, B. Nahrath, T. Oppenländer, G. Pross, B. Rückle, H. Schmidt, M. Shakhatre, M. Trunk
Preliminary results of the 1-MJ plasma focus experiment (IAEA-CN-35/E18-2) 447
C. Maisonnier, J.P. Rager, C. Gourlan, M. Galanti, P.D. Morgan
Dynamics of a non-cylindrical Z-pinch and the particle acceleration mechanism (IAEA-CN-35/E18-3) 455
V.V. Vikhrev, K.G. Gureev, S.K. Zhdanov, V.M. Korzhavin, B.A. Trubnikov
Structure of current sheath and fast-particle beams in the focus experiment (IAEA-CN-35/E18-4) 471
A. Bernard, A. Coudeville, J.P. Garçonnet, A. Jolas, J. De Mascureau, C. Nazet
Experimental verification of a theory of the current sheath in the plasma focus (IAEA-CN-35/E18-5(a)) 483
M. Vargas, F. Gratton, J. Gratton, H. Bruzzone, H. Kelly
Magnetic tension and thickness in the current sheath dynamics (IAEA-CN-35/E18-5(b)) ... 489
F. Gratton, M. Vargas

Some properties of the neutron yield in a low-energy plasma focus (IAEA-CN-35/E18-5(c)) 491
H. Bruzzone, R. Delellis, R. Gratton, H. Kelly, M. Milanese, J. Pouzo
Discussion on papers IAEA-CN-35/E18-1, E18-2, E18-3, E18-4, E18-5 495
Space-time structure of neutron and X-ray sources in a plasma focus (IAEA-CN-35/PD2) 497
W.H. Bostick, V. Nardi, W. Prior
Stabilized imploding liner fusion systems (IAEA-CN-35/E19-1) 507
D.L. Book, A.L. Cooper, R. Ford, K.A. Gerber, D.A. Hammer, D.J. Jenkins, A.E. Robson, P.J. Turchi
Investigation of model thermonuclear systems with liners (IAEA-CN-35/E19-2) 517
S.G. Alikhanov, V.P. Bakhtin, V.M. Brusnikin, I.S. Glushkov, R.Kh. Kurtmullaev, A.L. Lunin, A.D. Muzychenko, V.P. Novikov, V.V. Pichugin, V.N. Semenov, G.E. Smolkin, E.G. Utyugov, I.Ya. Shipuk
Energetic aspects of fast-fusion reactors with dense liners of medium velocities (10 to 100 km · s^{-1}) (IAEA-CN-35/E20) 527
C. Rioux
Theory and calculations of non-magnetic dense-plasma confinement (IAEA-CN-35/E21) 535
G.E. Vekshtejn, V.V. Mirnov, D.D. Ryutov, P.Z. Chebotaev
Discussion on paper IAEA-CN-35/E21 545

SUMMARY OF THE CONFERENCE (Session XXV)

Summary of magnetic confinement (experiments) (IAEA-CN-35/S1) 549
R.S. Pease
Summary of magnetic confinement (theory) (IAEA-CN-35/S2) 555
M.N. Rosenbluth
Summary of inertial confinement (IAEA-CN-35/S3) 563
O.N. Krokhin
Summary of reactor systems (IAEA-CN-35/S4) 571
K.-H. Schmitter

Chairmen of Sessions 575
Secretariat of the Conference 576
List of Participants 577
Author Index 603

Session XVIII

HEATING

Chairman

K. Takayama
Japan

Papers G 5-1 and G 5-2 were presented
by T. Uchida as Rapporteur

RAPID FURTHER HEATING OF TOKAMAK PLASMA BY FAST-RISING MAGNETIC PULSE

N. INOUE, H. NIHEI, K. YAMAZAKI, M. ICHIMURA,
J. MORIKAWA, K. HOSHINO, T. UCHIDA
Department of Nuclear Engineering,
University of Tokyo,
Tokyo, Japan

Abstract

RAPID FURTHER HEATING OF TOKAMAK PLASMA BY FAST-RISING MAGNETIC PULSE.

The object of the experiment was to study the rapid further heating of a tokamak plasma and its influence on confinement. For this purpose, a high-voltage theta-pinch pulse was applied to a tokamak plasma and production of a high-temperature (keV) plasma was ensured within a microsecond. The magnetic pulse is applied at the plasma current maximum parallel or antiparallel to the steady toroidal field. In either case, the pulsed field quickly penetrates the plasma and the plasma resistivity estimated from the penetration time is about 100 times larger than the classical. A burst of energetic neutrals of ~ 1 μs duration was observed and the energy distribution had two components of the order of 1 keV and 0.1 keV in the antiparallel case. Doppler broadening measurement shows heating of ions to a temperature higher than 200 eV; however, the line profile is not always Maxwellian distribution. The X-rays disappear at the moment of applying the magnetic pulse and reappear about 100 μs later with an intensive burst, while both energy levels are the same ($\sim$ 100 keV).

1. INTRODUCTION

As is well known, in tokamak plasmas keV temperatures can easily be achieved by toroidal-plasma-current Ohmic heating. However, further heating should be applied by some other means when plasma of much higher temperature is desired. On the other hand, the theta-pinch phenomenon is used to produce a high-temperature and high-beta plasma within several microseconds [1, 2]. The object of the present experiment was to study rapid further heating of a tokamak plasma and its influence on confinement, by applying a high-voltage theta-pinch pulse to the tokamak plasma.

The ordinary theta pinch results in some reduction of the cylindrical plasma column radius, but the reduction is unfavourable to the stability and confinement of tokamak plasma. To avoid this disadvantage, an ultra-fast theta pinch with Blumlein lines may be considered [3, 4] because the duration of the magnetic pulse is so short, say less than 1 μs, that the plasma column radius could remain almost unchanged after the pulse application.

By pulse application, it has been demonstrated that a keV high-temperature plasma is produced in the tokamak within a microsecond [3]. A burst of energetic neutral atoms is observed and the energy distribution shows two components with temperatures of 1.2 keV and 0.12 keV as typical data. Ions are heated as a result of repeated reflection by a moving sheath region due to the magnetic pulse, where the radial electric field is induced.

At the moment of applying the magnetic pulse, the X-rays disappear and re-appear about 100 μs later with an intensive burst. The disappearance might be due to the expansion of drift surfaces of runaway electrons.

2. EXPERIMENTAL SET-UP

The experiment was carried out with the Pinch Tokamak-II (PT-II). Figure 1 gives a schematic diagram of the machine, which consists of two components, as tokamak and as theta pinch. The

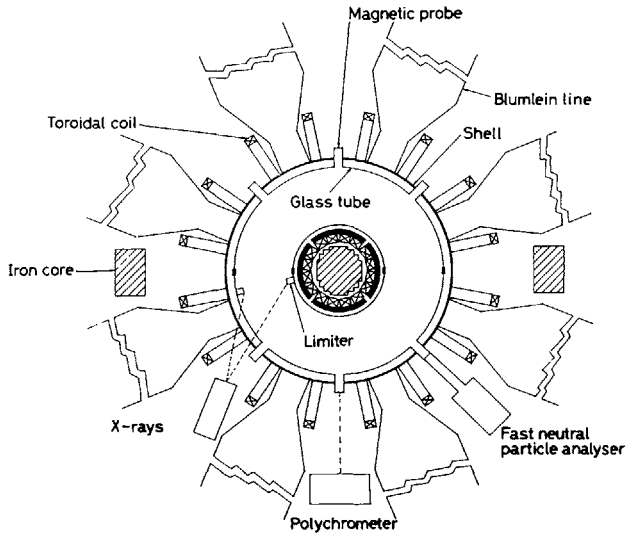


FIG. 1. Schematic diagram of experimental device.

TABLE I. MACHINE PARAMETERS OF TOKAMAK AND HIGH-VOLTAGE THETA PINCH

major radius	25 cm
minor radius of plasma	8 cm
of glass tube	10 cm
of shell (coil)	12 cm
maximum toroidal magnetic field	7 kG
maximum toroidal current (safety factor = 3)	30 kA
maximum duration of current flow	5 ms
self-inductance of the theta-pinch coil	40 nH
characteristic impedance of a Blumlein line	1 Ω
maximum charging voltage of Blumlein line	100 kV
electric field to be induced azimuthally along the plasma surface	0.44 kV/cm
increasing rate of pulsed magnetic field	1.1×10^7 kG/s
maximum amplitude of pulsed magnetic field	2.1 kG
duration of pulsed magnetic field	750 ns

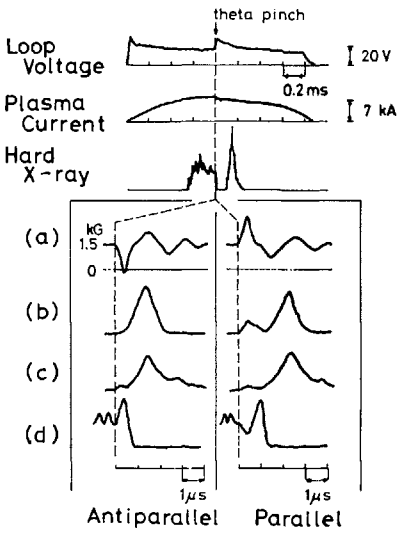


FIG.2. Oscillograms obtained with the antiparallel and parallel magnetic pulse.
(a) Toroidal magnetic field.
(b) Flux of charge-exchange atoms emitted from the plasma.
(c) Intensity of carbon line C-II (4267 Å).
(d) Hard X-ray intensity.

tokamak shell has two functions: a plasma stabilizer and a single-turn coil to which a high-voltage pulse is fed from eight sets of charged Blumlein lines connected parallel to the shell. To apply the theta pinch, the discharge tube is made of Pyrex glass which is evacuated to 1×10^{-6} torr. The parameters of PT-II are listed in Table I.

Before the tokamak plasma is produced, the theta pinch is triggered at an arbitrary phase of the toroidal plasma current. A large-amplitude, fast-rising and short-width magnetic pulse generated by the theta pinch is superposed on the steady toroidal magnetic field. The pulsed field can be applied either parallel or antiparallel to the toroidal field. The reflection of the high-voltage pulse in the Blumlein transmission lines causes a series of damping pulses to appear, which alternate sign during about 4 μs (see Fig.2(a)). This period is much shorter than the duration of the toroidal plasma current (several ms). Further details of the device are described in Ref.[4].

Tools for plasma diagnostics are a multi-channel monochromator, hard and soft X-ray detectors, electric and magnetic probes, a neutral particle energy analyser, and a beam probe system [5].

3. EXPERIMENTAL RESULTS

3.1. Initial tokamak plasma

The working gas mainly used throughout the experiment is hydrogen. For the spectroscopic measurement, helium gas is also used. The tokamak was operated with a low toroidal field of 0.5 – 3.5 kG, to investigate the plasma behaviour when the toroidal field alters in a wide range by the application of the pulse field to 2.1 kG (Table I).

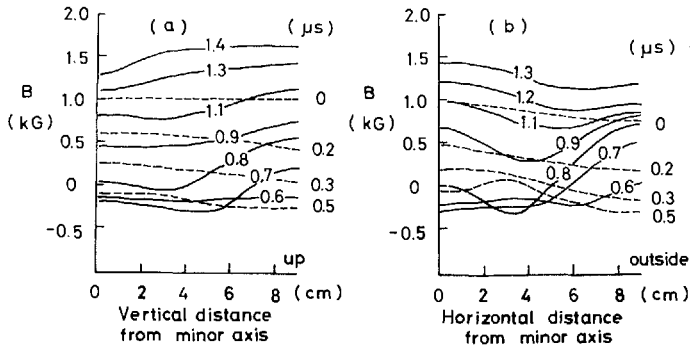


FIG.3. Time variations of radial distribution of magnetic field for the antiparallel case, where the steady toroidal field is 1 kG.
(a) Vertical distributions; (b) horizontal distributions.

The tokamak plasma parameters at the application of the high-voltage theta pinch are as follows. The plasma current and the loop voltage are typically 7 kA and 20 V, respectively, for the toroidal field of 2 kG. The ion density on the axis measured with the beam probe system, assuming a parabolic distribution, is $2.5-5\times10^{13}\,\mathrm{cm}^{-3}$ when the fill pressure is $5-8\times10^{-4}$ torr. A highly ionized plasma is obtained. The dependence of the ion density on the toroidal field is small.

The electron temperature as calculated from the plasma conductivity, on the assumption that the effective charge number is 3, amounts to 15 eV, while the temperature measured by a double probe is 12 eV. Doppler broadening of the H_β line gives the hydrogen atom temperature of ~3 eV. For the initial tokamak plasma, we have not detected the emission of charge-exchange neutrals with the sensitivity of the present apparatus.

The duration of the toroidal plasma current varies between 1 ms and 5 ms depending on the operating condition. Typical values of the energy confinement time is ~ 50 μs.

Emission of hard X-rays due to runaway electrons occurs at lower fill pressure of the working gas. Observation of the maximum intensity of the runaway X-rays is ensured in the case when the detecting area is collimated to the molybdenum aperture limiter.

3.2. Results on high-voltage theta-pinch application

The high-voltage theta pinch was applied at the maximum of the toroidal plasma current. When the steady toroidal field of the tokamak is smaller than the antiparallel magnetic pulse, the toroidal magnetic field is reversed.

Time variations of the radial distribution of the toroidal magnetic field is shown in Fig.3 for the case when the toroidal field is reversed. At the decreasing phase of the toroidal field (from 0 to 0.5 μs), the pulsed field penetrates the plasma very quickly; the penetration speed is several times that of the Alfvén velocity. The plasma conductivity derived from this penetration speed is two orders of magnitude lower than the classical. At the increasing phase (0.5 − 1.4 μs), the radial gradient of the toroidal field appears, showing the generation of the current sheath. In this phase the electrons are magnetized and the ions are unmagnetized due to the comparatively small toroidal field. This phenomenon has also been observed in the linear high-voltage theta-pinch experiment. The formation of the sheath is always observed in the phase when the toroidal field increases even in the parallel case. Due to the toroidal geometry, the vertical distribution of the magnetic field differs from the horizontal; the radial gradient of the latter is larger than that of the former.

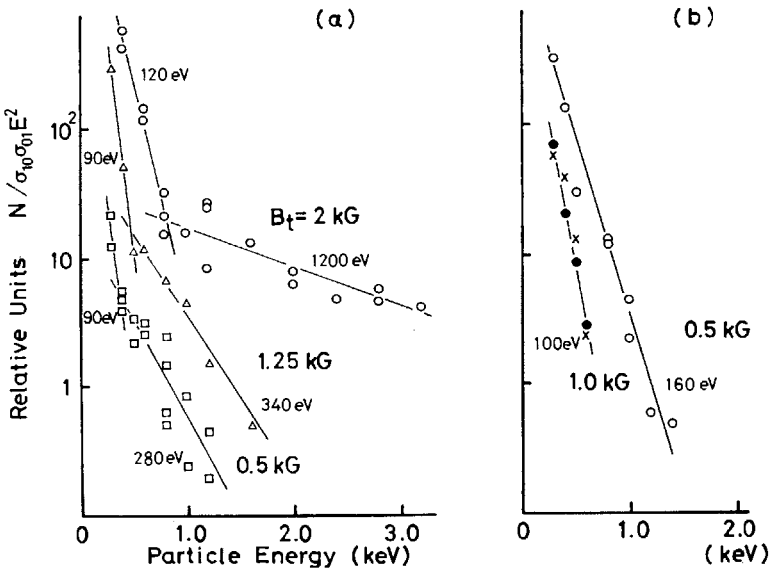


FIG.4. Energy distributions of charge-exchange hydrogen atoms when the pulsed magnetic field with a maximum amplitude of 1.6 kG is applied. Here, σ_{10} and σ_{01} are the charge-exchange cross-section between proton and atomic hydrogen and the stripping cross-section of atomic hydrogen in the hydrogen gas, respectively; E is the energy of hydrogen atoms emitted from the plasma and N is the flux of hydrogen atoms.
(a) Antiparallel case.
(b) Parallel case; X: first burst, ●: second burst.

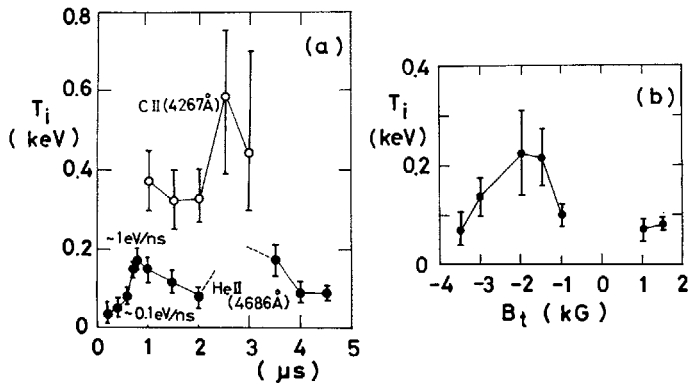


FIG.5. (a) Time variations of ion temperature measured by Doppler broadening of C-II (4267 Å) from the hydrogen plasma and He-II (4686 Å) from the helium plasma.
(b) Dependence of Doppler ion temperature (He-II) on the steady toroidal field. Negative B_t and positive B_t correspond to the antiparallel and the parallel case, respectively.

Figure 2 shows several oscillograms obtained with parallel and antiparallel magnetic pulse. In the lower part of the figure, the enlarged time scale is used. At the moment of pulse application, the loop voltage increases stepwise and the plasma current decreases slightly. These changes are small compared with those observed when the tokamak is operated at the unstable parameter regime.

At the first decreasing phase of the toroidal field, a small increment of hard X-rays is observed. After that, hard X-rays vanish during about 100 μs and reappear as a burst. The average energy of the burst X-rays is 100 keV and is the same as that of X-rays emitted before vanishing. The electrons gain this energy when they are accelerated by the toroidal electric field during about 100 μs. Observations imply that: (a) runaway electrons are confined until they gain the energy of about 100 keV; (b) runaway electrons produced before the application of the magnetic pulse are lost from the plasma because of the expansion of their drift surfaces; and (c) application of the magnetic pulse produces favourable conditions for part of the electrons to run away yet again.

At the increasing phase of the toroidal field, bursts of charge-exchange atoms and impurity lines are observed. Figure 4 shows the energy distribution of charge-exchange atoms as a function of the steady toroidal magnetic field B_t. Lines are isotropic Maxwellian distributions with the indicated temperature. Two bursts are observed in the parallel case (see Fig.2(b)) and the energy distribution has a single component on both bursts with the same temperature. The temperature decreases as the steady toroidal field increases. In the antiparallel case, only one burst is recognized; however, two components of ion temperature are determined. In contrast to the parallel case, the temperature increases as the steady toroidal field increases. With a toroidal field higher than 3 kG, the detectable atom flux diminishes. The emission of fast hydrogen atoms lasts about 60 μs, but the level of the flux is two orders of magnitude smaller than that of the burst. This implies that some of the hot particles are still confined in the tokamak.

Figure 5(a) shows the time variations of the ion temperature estimated by Doppler broadening of C-II (4267 Å) radiated from the hydrogen plasma and He-II (4686 Å) from the helium plasma for the antiparallel case with the toroidal field of 1.5 kG. The maximum heating rate of 1 eV$\cdot$ ns^{-1} is obtained in the first rising phase of the toroidal field when the radial gradient of the toroidal field exists. Ion heating to $\sim$ 1 keV is expected during the pulse duration $\sim$ 1 μs ($\equiv 10^3$ ns). In the second rising phase (from 2 to 3.5 μs) the line profile of He-II has two or three peaks and differs from the Gaussian distribution. Figure 5(b) shows the dependence of the ion temperature of the helium plasma on the steady toroidal field. The maximum temperature is seen at 2 kG, which is almost equal to the pulse field amplitude.

Increase of the electron temperature has not been observed by soft X-ray measurement.

4. DISCUSSION AND CONCLUSIONS

Although the application of high-voltage theta pinch causes a large disturbance on the magnetic field of the tokamak configuration, serious disruption of the plasma has not been observed. In the limiting case of a current-carrying plasma without parallel magnetic field, the growing time of the macroscopic instability is nearly equal to the propagation time of sound across the plasma radius. The duration of the magnetic pulse is, in the present experiment, much shorter than the growing time of the limiting case referred to above.

Theoretical and experimental work on the high-voltage theta pinch has shown that in the case of weak bias magnetic field the ion heating can be explained by the fluid-particle model [2, 6]. In this model, ions are considered as unmagnetized particles and electrons as magnetized fluid. Ions are heated as a result of repeated reflections by the moving sheath region where the radial electric field is produced. The results of the present experiment are consistent with the model, except the first burst of the charge-exchange atoms emitted during the first rising phase in the parallel case (see Fig.2(b)), in which the toroidal field is high enough to magnetize ions, and no

formation of a distinct sheath is observed. In addition to the sheath reflection, heating mechanisms such as turbulent heating may also occur in the present experiment.

In conclusion, by applying high-voltage theta pinch to tokamak plasma, the rapid production of hot ions and the sudden alteration of the condition of electron runaway are demonstrated without any disruption of the current ring. This technique may be applicable to the further heating of tokamak plasma and may be useful in studying transport phenomena in tokamak plasmas.

ACKNOWLEDGEMENT

The authors gratefully acknowledge the assistance of T. Matsuda, M. Kikuchi and Y. Ogawa in performing the experiment.

REFERENCES

[1] OKTAY, E., DESILVA, A.W., LIEWER, P.C., CHEN, Y.G., GRIEM, H.R., HESS, R., KRALL, N.A., "A turbulently heated high-voltage theta pinch", Plasma Physics and Controlled Nuclear Fusion Research 1974 (Proc. 5th Int. Conf. Tokyo, 1974) **3**, IAEA, Vienna (1975) 365.

[2] CHODURA, R., DUM, C.T., KEILHACKER, M., KORNHERR, M., NIEDERMEYER, H., PROTZ, R., SÖLDNER, F., STEUER, K.-H., "Numerical and experimental results on the production of weakly compressed thermonuclear plasmas in the Garching high-voltage theta and belt pinch", idem, 397.

[3] INOUE, N., et al., Proc. 3rd Top. Conf. Pulsed High-Beta Plasmas, Culham, 1975, Paper A3.5.

[4] INOUE, N., et al., Rev. Sci. Instrum. **47** (1976) 735.

[5] INOUE, N., J. Phys. Soc. Jpn. **32** (1972) 1095.

[6] CHODURA, R., Nucl. Fusion **15** (1975) 55.

TURBULENT HEATING OF A TOROIDAL PLASMA THROUGH A SKIN LAYER*

Y. AMAGISHI**, A. HIROSE, H.W. PIEKAAR†,
H.M. SKARSGARD
University of Saskatchewan,
Saskatoon, Saskatchewan,
Canada

Abstract

TURBULENT HEATING OF A TOROIDAL PLASMA THROUGH A SKIN LAYER.

In the first part of the paper methods are considered by which turbulent heating might be used as supplementary heating for an eventual toroidal reactor. Single pulse heating may not be adequate; with the total heating current limited by requirements for MHD stability, and a skin depth increasing with time, the permissible electron drift velocity decreases during the pulse, eventually falling below the threshold for wave instability. An alternating-current version of multiple pulse heating is proposed in which the toroidal skin current alternates in time and with azimuth around the minor circumference. Some features of the scheme, as worked out with reference to a system like the Princeton Fusion Power Plant design are: a.c. frequency $\omega = 2\pi \cdot s^{-1}$; spatial period = $2\pi a/3$; skin depth $\delta \cong 0.2$ m; heating time $t_H = 1.8$ s; amplitude of the induced electric field (loop voltage) = 0.6 $V \cdot m^{-1}$ (300 V). The second part of the paper presents results of experiments related to the proposed a.c. scheme, although carried out in a small torus (R/a = 19 cm/2.5 cm; toroidal field $\leqslant 1.0$ T). The heating current flows in opposite toroidal directions in the outer (larger major radius) and inner portions of the pre-formed argon plasma. In the first experiment (rf field with f = 1.8 MHz; $E \leqslant 500$ $V \cdot m^{-1}$) rapid heat conduction is observed from the periphery to the interior where Joule heating is negligible. Preliminary results from a second experiment (f = 60 kHz; $E \sim 3$ $kV \cdot m^{-1}$ of similar E-field configuration indicate $T_e \sim$ several keV at $n \sim 10^{19}$ m^{-3}; $T_i \leqslant 0.1$ keV for the Ar^+ ions.

Conventional turbulent heating - by means of a strong, unidirectional electric field E applied parallel to the confining magnetic field - has yielded high plasma temperatures without inducing gross instabilities. The toroidal experiments carried out by different workers are similar with respect to the time scale ($\sim$ 1 μs) and the thermal energy density achieved ($\sim 10^{22}$-10^{23} eV/m^3). The plasma electrons are commonly heated to keV temperatures, as a result of the turbulent resistivity, which in different experiments has been attributed to the ion acoustic instability [1,2], the electron-ion two-stream instability [3] and a trapped electron instability [4]. Observed ion temperatures are somewhat lower, and are generally attributed to heating by ion acoustic turbulence. The experiments are sufficiently small that the current penetrates quickly and flows throughout the plasma cross-section.

In this paper we consider ways in which turbulent heating might be used on a large toroidal plasma, as supplementary heating for example in an eventual toroidal reactor. Scaling problems are first considered and possible heating schemes examined. These include the use of a single pulse of current flowing in a thin skin layer, and an a.c. scheme in which the toroidal skin current alternates in time and with position around the minor circumference of the plasma. In Section 2 some experiments related to this proposal are reported; the heating current flows in opposite (toroidal) directions in different regions of the plasma.

---

* Research supported by the Atomic Energy Control Board of Canada.

** On leave from Shizuoka University, Shizuoka, Japan.

† On leave from FOM-Instituut Voor Plasmafysica, Jutphaas, The Netherlands.

1. SCALING PROBLEMS AND HEATING SCHEMES

In a large torus the turbulent heating current will be limited to a skin layer of thickness $\delta << a$, the minor radius. Although this poses a problem for heating the interior of the plasma it is also beneficial in making it possible for a limited turbulent heating current to provide the large current densities needed to drive wave instabilities such as the ion acoustic instability.

1.1. Single heating pulse

In work reported separately [5] we have considered the possibility of heating a large toroidal plasma by a single pulse of current $I = ne\gamma c_s \delta\ 2\pi a$, where n is the electron concentration, $\gamma = u/c_s$, u is the electron drift velocity and $c_s = \sqrt{KT_e/m_i}$ is the ion sound speed. The skin current I is superimposed on an ohmic heating or tokamak current, I_{OH}, of parabolic form. For $I \leq I_{OH}$ the safety factor q does not fall below its value q_o near the center of the plasma. Previous experimental results showing an apparent limit, $\beta_p \sim 1$, for the beta factor associated with the poloidal field of the skin current, and results on energy transport form the basis for the heating model used. Account is taken of the variation of skin depth, δ, with time in the heating pulse. For certain values of γ and α, the fraction of the thermal energy deposited in the skin layer which is transported to the interior, it is found that the total energy supplied to the plasma in the pulse is greater than W_{ig}, the energy required for ignition, in some large machine designs. Since these parameters are difficult to predict, single-pulse heating seems to be somewhat marginal. The basic difficulty is that with a limited heating current I for MHD stability, and a skin depth δ growing during the pulse, the electron drift velocity eventually falls below the threshold for ion acoustic instability and the heating terminates. Thus some form of multiple pulsing may have to be used.

1.2. Alternating-current heating scheme

De Kluiver and Piekaar [6] have proposed a succession of unidirectional current pulses for turbulent heating of JET. An a.c. scheme as illustrated in Fig. 1 may be advantageous since it does not alter the rotational transform, or q, but simply modulates (spatially and temporally) the pitch of the lines of force. To be practical the scheme must satisfy the constraints: (i) $T_e \geq 10$ keV in the skin layer at peak current; (ii) $ne\gamma c_s\delta < I_{OH}/2\pi a$ so the poloidal field of a reverse skin current does not locally cancel out that due to the tokamak current; (iii) $W \geq W_{ig}$ within a heating time $t_H \lesssim \tau_E$, the energy containment time; (iv) $R_\ell >> (R_{p\ell}^2 + X_{p\ell}^2)^{1/2}$, $\tau_\ell << 2\pi/\omega$, where R_ℓ, $R_{p\ell}$, $X_{p\ell}$ are the liner resistance, plasma resistance and reactance respectively, τ_ℓ is the time for the heating fields to penetrate through the liner, W is the energy supplied to the plasma and $W_{ig} = 6\pi^2 Ra^2 \bar{n} KT_{ig}$ is the energy required for ignition; R is the major radius, $\bar{n}$ is the average density over the cross section. Taking $T_{ig} = 5$ keV, at which temperature alpha particle heating [7] leads to "n-squared ignition"; we then require $T_e \geq 10$ keV, assuming the half-period of the a.c., π/ω, is shorter than the temperature equipartition time ($\tau_{ei} \sim 1$ s) between the hotter electrons and the ions. The liner or first wall is considered to be a continuous conductor, which must not short out the heating voltage.

For a skin depth $\delta = (2\eta/\mu_o\omega)^{1/2}$, constraint (ii) leads to

$$c_s(\eta/\omega)^{1/2} < \mu_o^{1/2} I_{OH}(2^{3/2}\pi ane\gamma)^{-1} \qquad (1)$$

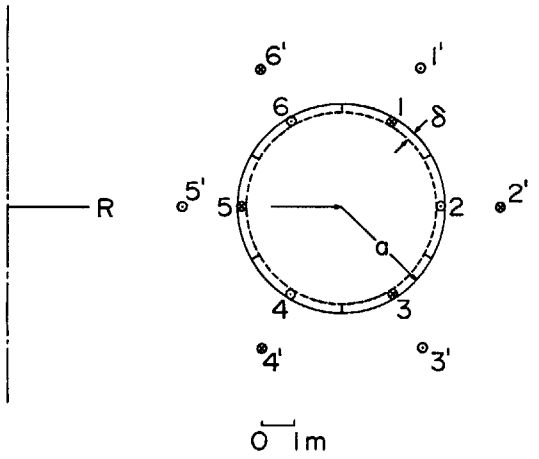


FIG.1. Alternating current scheme. 1 to 6: skin currents, driven by primary currents centered at locations 1' to 6'. Scale based on FPP design.

and the heating time, assuming that energy deposited in the skin layer is transported to the interior, is

$$t_H = \pi^{-2}(\mu_o\omega/2\eta^3)^{1/2}W_{ig}/(n^2e^2\gamma^2c_s^2aR) \qquad (2)$$

Several tokamak and stellarator experiments, operating with $\gamma > 1$, have indicated an anomalous resistance satisfying $\eta/\eta_{c\ell} \propto E/E_{ra}$ where $\eta_{c\ell}$ is the classical resistivity and E_{ra} the critical runaway field [8]. This is consistent with γ equal to a constant in the identity $j = nec_s\gamma = E/\eta$. Taking $\gamma = 2$, $T_e = 10$ keV and with reference to FPP [7], the Princeton Fusion Power Plant design ($R = 10.5$ m; $a = 3.25$ m; $\bar{n} = 5 \times 10^{19}$ m^{-3} = 3 n; $I_{OH} = 14.6$ MA are assumed) we find from (1) $\eta/\omega < 2.9 \times 10^{-8}$ Ω m·s. Choosing a frequency $\omega = 2\pi$ s^{-1} and the limiting value in (1) then gives $\eta = 1.8 \times 10^{-7}$ Ω·m, $E = 0.6$ V·m^{-1}, $\delta = 0.21$ m and $t_H = 1.8$ s, compared with $\tau_E = 4$ s for the FPP design. The current amplitude in one segment of the skin layer is $I_s = 2^{-1/2}ne\gamma c_s\delta\, 2\pi a/\ell = 2.3 \times 10^6$ A where $\ell = 6$ (Fig. 1) is the number of segments.

The low loop voltage, $V_s = 2\pi RE(X_{p\ell}^2 + R_{p\ell}^2)^{1/2}/R_{p\ell} \simeq 300$ V, is technically attractive. The heating time can be shortened by increasing ω, at the expense of a larger loop voltage. The a.c. skin current is generated in this scheme with primary conductors located outside the blanket, as shown in Fig. 1 which is based on an approximation (circular cross-section) to the FPP design. Approximate inductance calculations show that $NI_p = 6 \times 10^6$ A-turns, $V_p = 1.0 \times 10^3$N·V (peak) are required at each primary location. The total stored energy is $W_p = 3 \times 10^9$ J, compared with $W_{ig} = 2.6 \times 10^8$ J. Part of the excess stored energy may be needed to provide for losses from the plasma and dissipation in the liner but, if necessary, the primary conductors could be placed within the blanket material, closer to the plasma, to improve the coupling and the energy economy. The first wall in the FPP design consists of a 1-cm thickness, approximately, of a nickel-based alloy ($\eta_\ell = 1.0 \times 10^{-6}$ Ω·m) giving $R_\ell \simeq 15(R_{p\ell}^2 + X_{p\ell}^2)^{1/2}$, $\tau_\ell \simeq 10^{-4}$ s to satisfy constraint (iv).

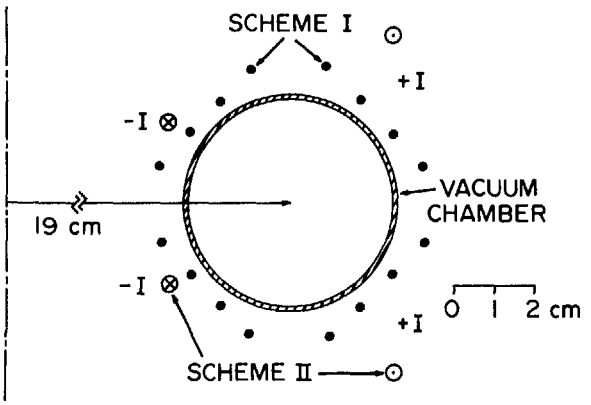


FIG.2. Toroidal device used in the experiments (R = 19 cm; a = 2.5 cm) and the locations of two sets of heating windings.

2. PLASMA HEATING BY A DIPOLE FIELD

The simplest form of alternating current scheme is obtained by applying a time-varying dipole magnetic field perpendicular to a toroidal magnetic field. This induces a nonuniform toroidal electric field which passes through zero and changes direction at the center of the chamber. Two dipole field schemes are tested on a toroidal device shown in Fig. 2. The first scheme uses a high-frequency (1.8 MHz), low-intensity field ($|E| \lesssim 500$ V/m), and the second uses a low-frequency (60 kHz) strong field (3 kV/m).

The experiments are performed using argon plasmas prepared by an rf preionizer alone or with additional preheating. The toroidal magnetic field is varied in the range 0.3-1.0 T. The diagnostic methods include electrostatic probes, diamagnetic measurements, spectroscopic determination of the ion temperature, microwave interferometers for the electron density, magnetic probes, and a Rogowsky probe for local current density measurements.

2.1. High-frequency dipole field

Preliminary results reported previously [4] showed rapid heating of electrons and ions with maximum temperatures $T_e \simeq 0.2$ keV and $T_i = 30$ eV(Ar^+) at $n \simeq 10^{18}$ m^{-3}. The most striking result obtained in the experiment is that the energy deposited at the periphery of the plasma is rapidly transferred toward the plasma center where the energy input is negligibly small. Figure 3 shows the temporal evolution of the electron density n, and temperature T_e, and the input power density calculated from the measured plasma current density and electric field. (The local electron density and temperature are measured by a double probe, and checked by the microwave interferometer and diamagnetic measurements. The results of these independent methods agree within 30%. The plasma current density J and the electric field E are determined by magnetic probes which measure two magnetic field components perpendicular to the toroidal magnetic field.) It can be seen that the electron temperature profile becomes flattened within several microseconds, indicating the presence of rapid

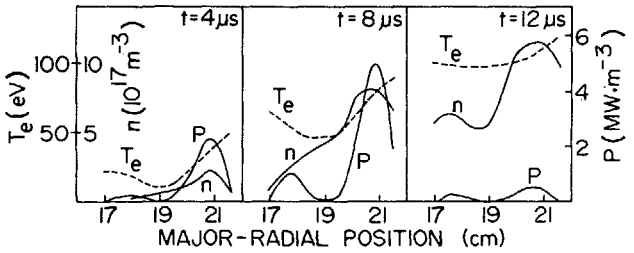


FIG.3. Electron density (n), temperature (T_e) and input power density (P) profiles (scheme I). $B_\phi = 0.27$ T, $|E| \leqslant 400$ V·m^{-1}.

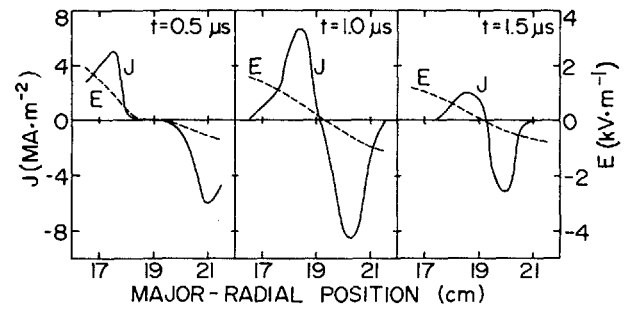


FIG.4. Profiles of plasma current density (solid lines) and electric field (broken lines). $B_\phi = 0.4$ T; V_c (condenser voltage) = 10 kV.

thermal conduction from the outer regions toward the plasma center. That the temperature flattening is due to thermal conduction, not particle convection or diffusion, is manifest since the electron density profile stays nonuniform, having its minimum at the center of the plasma. Furthermore, spectroscopic measurements fail to reveal convective motion which would be easily resolvable if the thermal transport were caused by convection (instrument half-width 0.14Å).

The thermal conductivity estimated from Fig. 3 is of the order of 10^{20} m^2/s·m^3, which is approximately 10^5 times larger than the classical value, $nr_{ce}^2\nu_{ee}$, where r_{ce} is the electron cyclotron radius and ν_{ee} is the collision frequency. There are several possible mechanisms responsible for the anomalous thermal conduction. One of them is the presence of high frequency (~ 100 MHz, correlation time $\tau \approx 50$ ns) fluctuations observed in the experiment. The fluctuations are localized at the outer regions of the plasma, and the propagation is perpendicular to the toroidal magnetic field, with a correlation length Δx of the order of 1 mm. As described earlier, the experiment is characterized by a strong nonuniformity in the toroidal electric field across the plasma and the electron drift velocity consequently has a strong shear. It is known [9] that such a nonuniform drift velocity profile is unstable against the high-frequency, pure electron

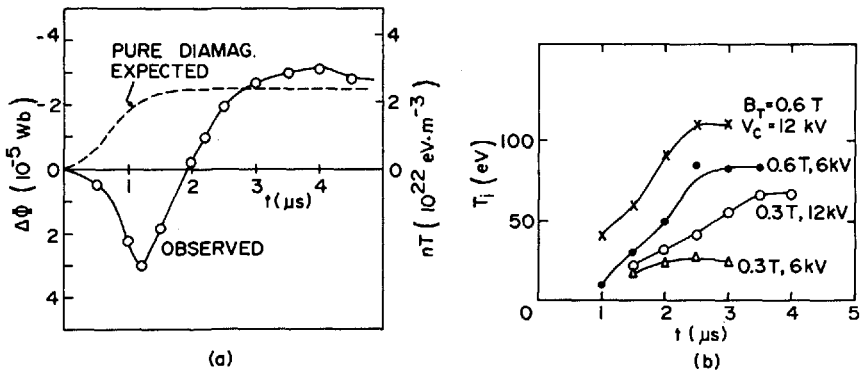


FIG. 5. (a) Observed diamagnetic signal (solid line) and that expected from the Joule energy input (broken line). Paramagnetic effects can be seen at earlier times. $B_\phi = 0.4$ T; $V_c = 10$ kV.
(b) Ar^+ ion temperature at different toroidal magnetic fields and condenser voltages.

instability and the available information about the fluctuations is consistent with the theoretical predictions. If we estimate the thermal conductivity from $n(\Delta x)^2/\tau$, we obtain $\kappa_\perp \simeq 2 \times 10^{20}$ m^2/s·m^3 which is of the same order as the observed value. A more detailed discussion of the possible role of the fluctuations will be reported separately.

2.2. Low-frequency dipole field

The experiment is performed in the same toroidal device but with a different set of windings (Fig. 2) from that used in the high-frequency scheme. The system inductance is reduced to 1.2 μH, and a 5-μF, 20-kV condenser is discharged through the windings. All measurements are carried out within the first quarter period (4 μs). A preheater is used before applying the main heating pulse and the electron density during the first quarter period is typically 1.0×10^{19} m^{-3}.

The plasma current density profile is measured by a Rogowsky probe (major radius 4 mm, minor radius 0.5 mm) directly inserted into the plasma. The Rogowsky probe data can be independently checked by a magnetic probe. The agreement is within 20%. The magnetic probe data also provides the local electric field intensity.

Figure 4 shows the observed current density and electric field profiles on the midplane. The momentum transfer collision frequency of the electrons is of the order of 10^8/s. The current density peaks move progressively inward. This is apparently not due to plasma compression which we fail to observe with the microwave interferometer and the spectrometer, but is caused by the vertical magnetic field produced by the heating windings. Indeed, it is found that the addition of a slow bias magnetic field has pronounced effects on the current profiles and its duration.

The diamagnetic effects are measured using the flux conservation principle. A Rogowsky coil measures the change of the total current induced in the circuit providing the toroidal magnetic field. Results are shown in Fig. 5(a). The maximum energy density is 3×10^{22} eV/m^3, and an average electron temperature of several keV is achieved. It is possible that the electron temperature is spatially nonuniform, as in the case of the high-frequency scheme. Spatially resolved temperature profiles will be the subject of future studies.

The Ar^+ ion temperature is measured spectroscopically. Both radial and tangential components are measured and they agree within 30%. Figure 5(b) shows the temporal evolution of the ion temperature under various experimental conditions. In all cases, the ion temperature rapidly increases and then saturates. Strong dependence on the toroidal magnetic field is evident. The maximum ion temperature achieved so far is close to 0.1 keV at the toroidal field of 0.6 T.

In conclusion, an a.c. turbulent heating scheme has been proposed, whose feasibility depends on energy transport from a thin skin layer to the interior of the large, toroidal plasma. There are some indications, from experiments reported here and elsewhere [10], that such transport can occur effectively.

REFERENCES

[1] ZAVOJSKIĬ, E.K., *et al.*, in Plasma Physics and Controlled Nuclear Fusion Research (Proc. 4th Int. Conf. Madison, 1971) 2, IAEA, Vienna (1971) 3.

[2] KALFSBEEK, H.W., de GROOT, B., WINKEL, T.G.A., deKLUIVER, H., PIEKAAR, H.W., Proc. 7th European Conference on Controlled Fusion and Plasma Physics, Lausanne (1975) p. 163.

[3] HAMBERGER, S.M., JANCARIK, J., Phys. Fluids 15 (1972) 825.

[4] HIROSE, A., AMAGISHI, Y., SHUBALY, M.R., SKARSGARD, H.M., WHITE, B.F., in Plasma Physics and Controlled Nuclear Fusion Research (Proc. 5th Int. Conf. Tokyo, 1974) 3, IAEA, Vienna (1975) 299.

[5] HIROSE, A., PIEKAAR, H.W., SKARSGARD, H.M. (to be published).

[6] PIEKAAR, H.W., deKLUIVER, H., Workshop on Additional Heating for JET, Culham Laboratory, 1974, EUR-JET-R6, p. 12.

[7] MILLS, R.G. (Ed.), A Fusion Power Plant, MATT-1050, Princeton University Plasma Physics Laboratory Report (1974).

[8] COPPI, B., MIT Quarterly Progress Report No. 98 (July 15, 1970) p. 57; Burchenko, P. Ya., *et al.*, in Plasma Physics and Controlled Nuclear Fusion Research (Proc. 4th Int. Conf. Madison, 1971) 3, IAEA, Vienna (1971) 119.

[9] HIROSE, A., ALEXEFF, I., Phys. Rev. Lett. 26 (1971) 949; Phys. Fluids 16 (1973) 1087.

[10] ARANCHUK, L.E., ZAVOISKII, E.K., LIN, D.N., RUDAKOV, L.I., Zh. Eksp. Teor. Fiz. Pis'ma Red. 15 (1972) 33.

A NEW METHOD OF COLLISIONLESS HEATING FOR TOROIDAL PLASMAS INVOLVING LOW-FREQUENCY AXISYMMETRIC PUMPING

E. CANOBBIO
Association Euratom-CEA,
Département de physique du plasma et de la fusion contrôlée,
Service IGn – Centre d'études nucléaires,
Grenoble

Abstract

A NEW METHOD OF COLLISIONLESS HEATING FOR TOROIDAL PLASMAS INVOLVING LOW-FREQUENCY AXISYMMETRIC PUMPING.

A new axisymmetric method for low-β toroidal plasma heating is proposed which uses such a low frequency, $\omega/2\pi \cong 1$ kHz that the r.f.-coils may be located outside the liner. It involves the work of a travelling vertical $\vec{E}$-field component, $E_z(\omega t - kz)$, on the toroidal drift velocity of the ions, $V_z = (v_\perp^2/2 + v_\parallel^2)/\omega_c R$. Phase mixing is provided by perpendicular Landau damping near $\omega = kV_z \gg \nu_i$, the ion collision frequency. Field E_z can be produced by modulating the current flowing in a number of horizontal coils. Both in present- and next-generation devices, efficient heating may be achieved with modulation rates which are one order of magnitude smaller than those required by any proposed variant of axisymmetric gyrorelaxation pumping. Such r.f.-field amplitudes are well below the threshold for excitation of parametric instabilities which are deleterious to plasma confinement, as is shown by two TTMP experiments on small stellarators.

1. COLLISIONLESS HEATING AND ADIABATIC INVARIANTS

Most of the r.f.-heating methods considered for toroidal plasmas involve a collisionless linear wave-particle resonance. The frequency ω is much higher than the ion collision frequency ν_i which, in turn, is sufficient to bring about Fokker-Planck scattering of the resonant particles before wave trapping occurs.

As a rule, at least one of the adiabatic invariants of particle motion is destroyed by the pump wave. When the magnetic moment μ is not conserved (ICRH, LHRH, etc.), the perpendicular energy of the resonant particles is increased directly. Then, because of the presence of a loss disc in velocity space, toroidal confinement may be affected adversely. An interesting case is ICRH at the first harmonic $\omega = 2\omega_{cD}$ (ω_{cD} is the deuterium gyro-frequency) in a deuterium plasma which also contains a small amount of hydrogen (density ratio $n_H/n_D \ll 1$). Since $\omega_{cH} = 2\omega_{cD}$, the ratio P_H/P_D of the mean power absorbed by the H-component to the mean power absorbed by the D-component is (see, e.g. Ref. [1])

$$P_H/P_D \cong (n_H/n_D)/\beta_D \qquad (1)$$

where β_D is the ratio of deuterium pressure to magnetic pressure. Usually, the r.f.-power has to be chosen such as to heat deuterium at a rate which is not too small compared with ν_i. As a result, the H-impurity ions, which are accelerated $10^2 - 10^3$ times faster, run away and hit the wall surrounding the plasma. This effect, which has already been observed [2], might well jeopardize the thermonuclear use of this scheme of ICRH.

Transit Time Magnetic Pumping (TTMP) leaves μ constant (apart from collisions) and directly increases the parallel energy of the resonant particles. Here, the longitudinal invariant $J^{\uparrow}$ is still

destroyed. Although lack of axisymmetry, both in static and r.f.-configurations, produces some additional neoclassical diffusion effects [3], these cannot account for the pump-out observed experimentally [4]. Both the order of magnitude and the parameter dependence of this pump-out point to the existence of low-frequency flute-like drift waves which are parametrically driven unstable [5] by $\vec{E}_{\perp 1}$, the electrostatic component of the TTMP field perpendicular to $\vec{B}_0$, when

$$E_{\perp 1}^2/8\pi \gtrsim (v_A/c)^2 \; n\,(T_e + T_i)$$

(v_A is Alfven speed) or

$$E_{\perp 1\,(V\cdot cm^{-1})} \gtrsim 1.4 \times 10^{-2}\, B_{0(G)} \sqrt{(T_e + T_i)_{(eV)}\, m_H/m_i} \qquad (2)$$

Condition (2) was easily satisfied in the experiments quoted, while, fortunately, it can definitely be violated in larger devices.

The remaining trouble with TTMP is the necessity of having r.f.-coils in facing the plasma as ω is still too high to allow r.f.-field penetration through the metallic wall of a vacuum chamber.

In this paper, we propose a new r.f.-method which uses such a low frequency ($\omega/2\pi \cong 1$ kHz) that the r.f.-coils may be located outside the liner. The r.f.-configuration is axisymmetric, leaves both μ and J constant, while destroying only the third adiabatic invariant [6]: the flux of $\vec{B}$ enclosed by the drift trajectories in the toroidal equilibrium configuration. The r.f.-field amplitudes required for efficient heating in present and future low-β devices will be always much below the threshold (2) for the appearance of parametric instabilities.

2. THE NEW HEATING METHOD

This heating method involves: a) the work of a vertical $\vec{E}$ field component

$$E_{1z}\,(t, R, z) = E_1(R)\, \exp\,[i\,(\omega t - kz)] \qquad (3)$$

(we assume cylindrical co-ordinates, Fig.1) on the toroidal drift velocity of the ions $V_z = (v_\perp^2/2 + v_\parallel^2)/R\,\omega_{ci}$, and b) a Landau-like phase mixing perpendicular to $\vec{B}_0$ near $\omega = k\, V_z\,(v_\perp^2, v_\parallel^2)$. The interesting point here is that the resonance involves only the unidirectional vertical drift velocity which is a small fraction of the actual z-velocity of the particles. As a matter of fact, the particles involved in the resonance have

$$v_\perp^2/2 + v_\parallel^2 = v_t^2\,(\omega/kV) \gtrsim v_t^2 \qquad (4)$$

where

$$V \equiv v_t^2/R\,\omega_{ci}, \qquad v_t^2 = 2T_i/m_i$$

even though the phase velocity of the wave is much smaller: $\omega/k \cong 0(V) \ll v_t$.

The field (3) can be produced by modulation with an appropriate de-phasing of the current flowing in a number of horizontal coils (schematically shown in Fig.1), some of which can even be those which produce the vertical field B_v necessary to tokamak plasma equilibrium.

Landau-like damping can occur when the wave frequency $\omega \equiv \alpha k V \cong 4$ kV (see Section 3) is much larger than ν_{Ei}, the relevant collision frequency (for energy exchange) of the resonant ions which have $v^2 \cong 3\alpha\, v_t^2/2$. Assuming $k = \pi/b$ where b is the vertical minor radius of the plasma, we have for a deuterium plasma and for $\alpha > 3$

$$\alpha\pi V \Big/ b\nu_{ED} \gtrsim 25\, \alpha^{5/2}\, T^{5/2}_{(keV)} \Big/ b_{(m)} R_{0(m)} B_{0(T)} n_{0(10^{13}\ cm^{-3})} \gg 1 \qquad (5)$$

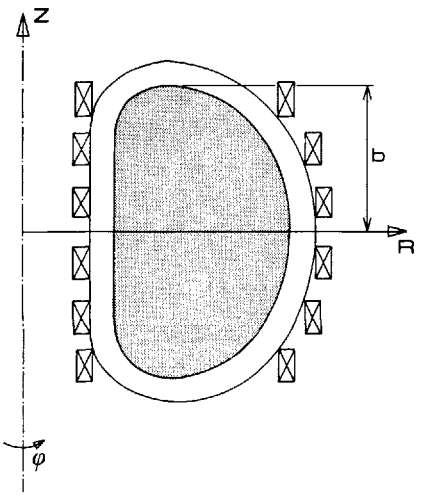


FIG.1. Co-ordinate system and meridian cross-section of plasma and r.f.-coils.

As will be shown later, the magnetic perturbation within the plasma is negligible. Moreover, in contrast to TTMP, also the perpendicular energy of the resonant particles is increased:

$$d(v_\perp^2/2)/dt = (v_\perp^2/2B)dB/dt \cong (v_\perp^2/2B)\ \vec{V}_1 \cdot \text{grad}\ B_0 = (v_\perp^2/2B)c\ E_{1z}/R \tag{6}$$

On the other hand, the energy equation gives

$$d\epsilon/dt = e\vec{V}\cdot\vec{E} + \mu\partial B/\partial t \cong m((v_\perp^2 + 2v_\parallel^2)/2B)cE_{1z}/R \tag{7}$$

Thus we easily see that the quantity $(v_\perp/v)^2$ is decreased by our pump since

$$d(v_\perp/v)^2/dt = -(v_\perp v_\parallel/v^2)^2\ cE_{1z}/RB \tag{8}$$

To calculate power absorption as a function of the external currents without unnecessary complications, we first consider the ideal model of a uniform Maxwellian plasma with two cylindrical free surfaces $R = R_1$ and $R = R_2$ (see Fig.2) embedded in a purely toroidal $\vec{B}_0$ field. The real case of a toroidal system will be considered in Section 5.

3. THE CYLINDRICAL MODEL

The mean power density absorbed by the ions is

$$P_i = \frac{1}{2}\ \text{Re}\{\int d^3\vec{v} f_{1i}\ (d\epsilon/dt)^*\} \tag{9}$$

where $(d\epsilon/dt)^*$ is the complex conjugate of Eq.(7) and f_{1i} is the solution of the guiding-centre Vlasov equation

$$(\partial/\partial t + V_z\ \partial/\partial z)f_{1i} + eV_z\ (E_{1z} - \partial\phi/\partial z)df_m/d\epsilon = 0 \tag{10}$$

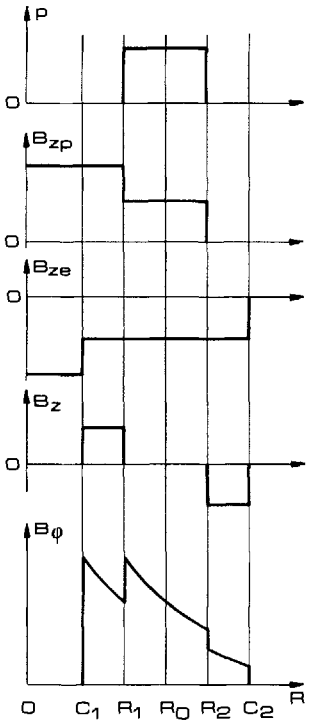


FIG.2. Radial profiles of pressure, vertical and toroidal magnetic field components in the cylindrical model.

where f_m is the Maxwellian. The electrostatic field gradient, grad ϕ, is necessary to ensure plasma neutrality in spite of the preferential action of the externally induced E_{1z} component on the plasma ions. Since ω is much lower than any characteristic electronic frequency, including ν_e, the electrons behave as a non-viscous fluid with finite pressure but negligible inertia. Assuming that T_e remains essentially unchanged on the time scale ω^{-1}, and using the MHD Ohm's law, $\vec{E}_1 + \vec{v} \times \vec{B}_0/c = 0$, the equation of electron motion becomes

$$0 \cong -\text{grad } p_e - n_0 e\,(\vec{E}_1 - \text{grad } \phi + \vec{v}_e \times \vec{B}_0/c)$$

$$\cong -T_e \text{ grad } n_{e1} + n_0 e \text{ grad } \phi \qquad (11)$$

Thus, the equation which gives ϕ in terms of $\vec{E}_1$ is obtained by calculating the ion density perturbation $n_{1i}(\phi, E_{1z})$ and setting

$$n_{1i}(\phi, E_{1z}) = n_0 e\phi/T_e \qquad (12)$$

(ion-sound eigenmodes are excluded by the condition $\omega/k \ll v_t$). With ansatz (4), we find

$$n_{1i} = -(\phi + E/ik)\,(A(\alpha) + iB(\alpha))\, n_0 e/T_i \qquad (13)$$

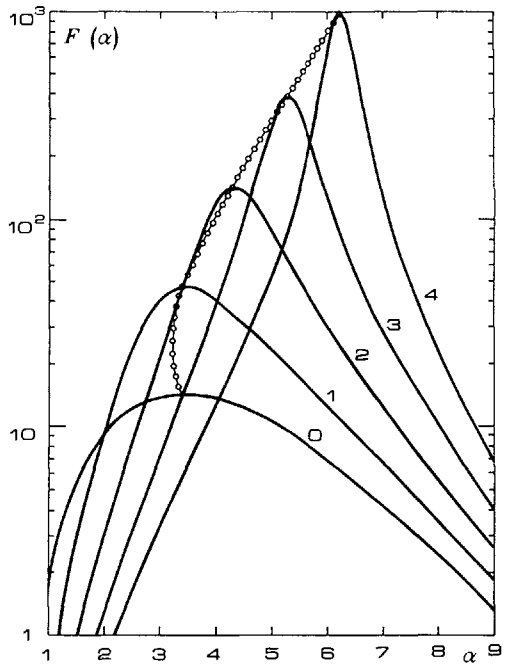


FIG.3. Function $F(\alpha, T_e/T_i)$ (Eq.(17)) versus $\alpha = \omega/kV$ for different values of T_e/T_i.

where

$$a \equiv \omega/kV$$

$$A(\alpha) = 1 + \pi\alpha e^{-2\alpha} + 4\alpha e^{-2\alpha} \int_0^{\sqrt{\alpha}} dt\ e^{2t^2} \mathrm{Re}\{Z(t)\}$$

$$B(\alpha) = 2\sqrt{\pi\alpha}\, e^{-\alpha}\, \mathrm{Re}\{Z(-\sqrt{\alpha})\}$$

and Z(t) is the Fried-Conte function.
Thus

$$(E_{1z} + ik\phi) = E_{1z}\,(1 + (A + iB)\,T_e/T_i)^{-1} \tag{14}$$

It is useful to express E_{1z} in terms of the radial MHD displacement

$\xi \equiv \xi_R$ ($\vec{\xi} = \vec{v}$; $\vec{E} + \vec{\xi} \times \vec{B}_0/c = 0$)

$$E_{1z} = -\frac{i\omega}{c} B_{0\phi}\, R\,(\xi/R) \tag{15}$$

Then P_i can be found to be

$$P_i = \frac{3}{2}\, nT_i\, kV\, |\xi/R|^2\, F(\alpha, T_e/T_i) \tag{16}$$

where

$$F(\alpha, T_e/T_i) = \frac{8}{3}\sqrt{\pi}\, \frac{\alpha^4 e^{-\alpha}\, \mathrm{Re}\{Z(-\sqrt{\alpha})\}}{(1 + AT_e/T_i)^2 + (BT_e/T_i)^2} \tag{17}$$

The function $F(\alpha, T_e/T_i)$ is plotted in Fig.3 for $T_e/T_i = 0; 1; 2; 3; 4$. The chain of small circles gives $F_{(max)}$ and $\alpha_{(max)}$ for intermediate T_e/T_i values.

It is worthwhile to comment on the numerical values of $F(\alpha)$ as compared to the corresponding functions in the Torsional and Compressional TTMP cases [7,8], called $F_T(x)$ and $F_C(x)$ here, where $x = \omega/k_{\|}v_t$. The energy equation for torsional TTMP is similar to ours (vanishing betatron term), while compressional TTMP is based on the betatron effect. This explains why both $F_{(max)}(\alpha)$ and $F_{T(max)}(\alpha)$ are, at least, one order of magnitude larger than in the compressional case. The fact that $F_{(max)}(\alpha)$ is, at least, three times larger than in the torsional TTMP case is due to phase mixing: in our case, the resonant surface in velocity space (Eq.(4)) is much closer to the equidensity surfaces $v_\perp^2 + v_{\|}^2 = \text{const}$, than in the TTMP cases, where the resonant surface is $v_{\|} = \omega/k$. The large value of $F_{(max)}(\alpha)$ allows us to use reasonably small $|\xi/R|$ values in order to heat toroidal systems, where the invoked resonance can occur only in a fraction of the whole plasma volume (see Section 5).

4. THE FIELD CONFIGURATION

We have now to calculate $|\xi/R|$ in terms of the external r.f.-currents. For the equilibrium, we assume the step model of Fig.2. At the plasma edges there are toroidal and vertical surface currents. The former produce a vertical field B_{zp} which is superposed on the external field $B_{ze} = 4\pi j_{02}^{\#}/c$ produced by a sheet current at $R = C_2$. The latter produce a toroidal $\vec{B}$-component, $B_{\phi p}\, R_1/R$, within the plasma, in addition to the external main field $B_0 R_0/R$. Although $|B_{\phi p}/B_0| \ll 1$, $B_{\phi p}$ has to be retained in order that correct jump conditions for the r.f.-perturbations can be formulated (see below).

Assuming that, within the plasma,

$$B_{zp} + B_{ze} = 0 \tag{18}$$

from $\mathrm{grad}(8\pi p + B^2) = 2(\vec{B}\cdot\mathrm{grad})\vec{B}$, we find

$$2\, B_0 B_{\phi p} R_0/R_1 = (B_{ze} R_2/R_1)^2\, (1 - \beta_p) \tag{19}$$

where

$\beta_p = 8\pi p/B_{ze}^2$, and for $C_1 < R < R_1$

$$B_z = -(B_{ze} R_2/R_1)\, (1 - \beta_p\, (1 - R_1^2/R_2^2))^{1/2}$$

The relevant jump conditions for the r.f.-field at the perturbed plasma-vacuum interfaces are

$$\vec{n}\cdot\langle\vec{B}\rangle = 0; \quad \langle 8\pi p + B^2\rangle = 0 \tag{20}$$

where $\langle B \rangle$ denotes the increment in B across the boundary in the direction $\vec{n}$. Since

$$\vec{n} = \vec{e}_R + \vec{e}_R \, \partial\xi/\partial R - \text{grad}\, \xi$$

($\vec{e}_R$ is the unit vector in the R-direction), conditions (20) become

$$\langle B_{1R} \rangle + ik\xi \langle B_{0z} \rangle = 0 \tag{21}$$

and

$$8\pi p_1 + \vec{\xi} \cdot \langle \text{grad}(8\pi p_0 + B_0^2) \rangle + 2 \langle \vec{B}_1 \cdot \vec{B}_0 \rangle = 0 \tag{22}$$

where $p_1 \cong -(5/3) p_0 \, \text{div}\, \vec{\xi}$.

We now derive the external and the internal r.f.-fields to be used in Eqs (21) and (22).

In vacuum, the non-vanishing r.f.-components are:

$$\begin{aligned} B_{1R} &= -(kc/\omega) E_{1\phi}; \; B_{1z} = i(c/\omega) \{\partial E_{1\phi}/\partial R + E_{1\phi}/R\} \\ E_{1\phi} &= a I_1(kR) + b K_1(kR) \end{aligned} \tag{23}$$

where a and b are constants determined by the boundary conditions, and I_1 and K_1 are Bessel functions of imaginary argument. As $kR \cong \pi R/b \gtrsim 10$, asymptotic expansions may be used.

Within the plasma, the non-vanishing r.f.-components are $B_{1\phi}$, E_{1R}, and E_{1z}. Since $\omega/k \ll v_t \ll v_A \ll c$, the r.f.-plasma current is essentially the polarization current [9], so that the Ampère law, $v_A^2 \, \text{rot}\, \vec{B}_1 = c\vec{E}_1$, and Faraday law give

$$\begin{aligned} \frac{i\omega}{c} B_{1\phi} &\cong -(\omega/kv_A)^2 \, \partial E_{1z}/\partial R \\ ik E_{1R} &\cong -\partial E_{1z}/\partial R \end{aligned} \tag{24}$$

and

$$\partial^2 E_{1z}/\partial R^2 + 3 \, \partial E_{1z}/R\partial R - k^2 E_{1z} = 0$$

Thus

$$RE_{1z}, \xi \to a_p I_1(kR) + b_p K_1(kR) \tag{25}$$

Equations (24) prove that the betatron term in Eq.(7) is indeed negligible. Thus, with respect to the r.f.-field, the plasma behaves essentially as a piezo-electric superconducting fluid. Notice, moreover, that, in contrast to the Cartesian case where $\text{div}\, \vec{v} = \text{rot}\, \vec{v} = B_{1\|} = \text{div}\, \vec{E}_1 = 0$, here, owing to the toroidal $\vec{B}_0$ field, compressibility and vorticity do not vanish, and $\text{div}\, \vec{E}_1$, $\text{rot}\, \vec{E}_1 \neq 0$.

A lengthy calculation based on Eqs (19–25) in the limit $kR \gg 1$ allows us to write down the following simple expressions of $k\xi$ at $R = R_1, R_2$ in terms of the modulation rate of the external current sheets at $R = C_1, C_2$:

$$\begin{aligned} k\xi &\cong (j^{\#}_{\text{r.f.}}/j^{\#}_0)_1 \; \exp k(C_1 - R_1), (R = R_1) \\ k\xi &\cong (j^{\#}_{\text{r.f.}}/j^{\#}_0)_2 \; \exp k(R_2 - C_2), R = R_2) \end{aligned} \tag{26}$$

where we disregarded terms of the order β_p/kR.

Expressions (26) have the remarkable property of being independent of the plasma parameters which have a step structure in our model; thus they have, in fact, a much larger domain of applicability.

5. THE TOROIDAL MODEL

In a toroidal system, the z-component of the particle guiding-centre velocity is the superposition of the unidirectional, essentially constant, vertical drift V_z and of the z-component of the parallel velocity $v_{\|} \vec{B}_0/B_0$, which oscillates in time around the value $-V_z$. Since in the plasma the pump $\vec{E}$-field is essentially perpendicular to $\vec{B}_0$, its work on $\vec{v}$ is again $\cong eV_zE_z$ (this effect is reminiscent of the basic mechanism of active bird flight).

Let us now consider the wave particle resonance condition. This is not affected by $v_{\|z}$ only in the thin – almost cylindrical – plasma zone where

$$|v_{\|} B_{0z}/B_0| < (v_{\perp}^2/2 + v_{\|}^2)/\omega_{ci}R$$

This corresponds to a radial width $2|\Delta R|$ which is readily estimated by writing $B_{0z}/B_0 \cong B_\theta(r)\,\Delta R/rB_0$, where r and θ refer to the usual poloidal co-ordinate system (where $R = R_0 + r\cos\theta$):

$$2|\Delta R| \cong 2\alpha^{3/4}\, b\, \rho_{i\theta}/R_0 \tag{27}$$

where $\rho_{i\theta}$ is the poloidal ion Larmor-radius at the plasma edge. This corresponds to the fraction

$$\alpha^{3/4}\, \rho_{i\theta}\, 4b/\pi a R_0 \gtrsim \alpha^{3/4}/50 \tag{28}$$

of the entire volume. Outside zone (27), power absorption is no longer given by Eq.(16) since now the resonance involves particles for which

$$v_{\|}\, B_{0z}(r,\theta)/B_0 = \omega/k \cong v_t^2/R\,\omega_{ci} \tag{29}$$

i.e. $v_{\|} \cong v_t\, \rho_{i\theta}/R \ll v_t$. These are trapped particles for which the drift due to the centrifugal force is negligible. Then, the power they absorb is comparable to that of compressional TTMP [8], once $(\omega/k_{\|} v_t)$ is substituted by $(\omega B_0/kv_t B_\theta) \ll 1$. Per particle this is, at least, two orders of magnitude smaller than within zone (27). Neglecting this contribution we have for the *space* average of the mean power density absorbed by plasma ions:

$$\langle P_i \rangle \cong \frac{3}{2}\, nT_i\, kV(4\alpha^{3/4}\, b\rho_{i\theta}/\pi a R_0)|\xi/R|^2 F(\alpha, T_e/T_i) \tag{30}$$

To estimate the required modulation rate, note that, for $1 \lesssim T_e/T_i \lesssim 2$

$$f_{(max)\,(kHz)} \cong 2v_t^2/b\omega_{ci} R_0 \cong \frac{4T_{i\,(keV)}}{b_{(m)} R_{0(m)} B_{0(T)}} \tag{31}$$

With JET-like parameters, $T_i = B_0 = R = 3$; $b = 1.3$; $b/a = 1.6$, we have $f_{(max)} \cong 1$ kHz. Then, to have average heating times of, say, 3×10^{-1} s, we must have $|\xi/R| \cong 1.5 \times 10^{-2}$, which corresponds to $j^{\#}_{r.f.}/j^{\#}_0 \cong 1.5 \times 10^{-1}$. These are reasonably low values, at least one order of magnitude smaller than those required to heat the same plasma by either axisymmetric variant, [10] and [11], of the tokamak gyrorelaxation pumping.

It remains to examine briefly the validity condition of the collisionless linear derivation of Eqs (16) and (30). As is discussed in Refs [8,12], Fokker-Planck scattering prevents wave trapping of the resonant particles if

$$\nu_i > \nu_{crit} \cong \left| \frac{2}{\Delta v_z} \frac{dv_z}{dt} \left(\frac{\Delta v_z}{v_t} \right)^2 \right| \tag{32}$$

where, by order of magnitude,

$$\frac{dv_z}{dt} \cong (\omega_{ci} R)^{-1} \, dv^2/dt \cong 2V \, d(\gamma \xi / R)/dt$$

$$\gamma \equiv |1 + (T_e/T_i)(A + iB)|^{-1} \quad \text{(see Eq. (13))} \tag{33}$$

and

$$\Delta v_z \cong 2V(\gamma \xi / R)^{1/2}$$

Δv_z, the maximum of the oscillation of $(v_z - \omega/K)$ due to the finite amplitude of the wave, characterizes the velocity range of the possible distortion of $f(\vec{v})$ with respect to f_m. We find

$$\nu_{crit} \cong 2\omega(\rho_i/R)^2 \, |2\gamma\xi/R|^{3/2}$$

$$\cong \nu_H (\rho_i^2/R^2) \sqrt{2\gamma\xi/R} \ll \nu_H \lesssim \nu_i \tag{34}$$

where ρ_i is the Larmor radius, and ν_H the ion heating rate defined by Eq. (30). We conclude that there is no serious practical lower limit to $(n_0 T_i^{-3/2})$ for efficient heating by the proposed r.f.-method.

ACKNOWLEDGEMENTS

I should like to express my appreciation to Drs O. De Barbieri, M. Brambilla, T. Consoli and P. Javel for helpful discussions.

REFERENCES

[1] ADAM, J., SAMAIN, A., Report EUR-CEA-FC 579 (1971).
[2] VDOVIN, V.L., SHAPOTKOVSKII, N.V., RUSANOV, V.D., in Plasma Heating (Proc. 3rd Conf. Grenoble) 2 (1976).
[3] BRAMBILLA, M., in Toroidal Plasma Confinement (Proc. 3rd Symp. Garching, 1973); STRINGER, T.E., in Toroidal Plasma Heating (Proc. Symp. Varenna, 1974).
[4] MILLAR, W., Report CLM-R-144 (1975); PACHER, H.D., MAHN, C., CATTANEI, G., Bull. Am. Phys. Soc. 18 (1973) 1353.
[5] CANOBBIO, E., Symposium on Toroidal Plasma Heating, Varenna (1976).
[6] NORTHROP, T.G., TELLER, E., Phys. Rev. 117 (1960) 215.
[7] KOECHLIN, F., SAMAIN, A., Phys. Rev. Lett. 26 (1971) 490.
[8] CANOBBIO, E., in Plasma Physics and Controlled Nuclear Fusion Research (Proc. 4th Int. Conf. Madison, 1971) 3, IAEA, Vienna (1971) 491.
[9] LONGMIRE, C.L., Elementary Plasma Physics, Interscience Publishers, New-York, 1963.
[10] ARTSIMOVICH, L.A., Nucl. Fusion 12 (1972) 215.
[11] FURTH, H.P., ELLIS, R.A., Plasma Phys. 15 (1973) 719.
[12] CANOBBIO, E., Report EUR-5064-e, Varenna Course (1971).

DISCUSSION

ON PAPER IAEA-CN-35/G 6

F. WERKOFF: At the Tokyo Conference (Proc. 5th Int. Conf. Tokyo, 1974, 3, Vienna, 1975, 333) you presented a new class of parametric instabilities induced by transit time magnetic pumping and ion cyclotron heating, and you indicated that these instabilities could strongly affect the confinement. My question is whether you think that your new method of heating should give better confinement than transit time magnetic pumping.

E. CANOBBIO: Yes, as a result of the much lower frequency used, and for several reasons indicated at the end of Section 1 and in Ref. [5] of my paper.

PLASMA HEATING IN A TOROIDAL SYSTEM BY A HELICAL QUADRUPOLE RF FIELD WITH $\omega < \omega_{Bi}$

R.A. DEMIRKHANOV, A.G. KIROV, S.N. LOZOVSKIJ,
F.M. NEKRASOV, A.G. ELFIMOV, S.E. IL'INSKIJ,
V.V. ONISHCHENKO
Physico-Technical Institute of the USSR State Committee for Utilization of Atomic Energy,
Sukhumi, Union of Soviet Socialist Republics

Presented by V.A. Suprunenko

Abstract

PLASMA HEATING IN A TOROIDAL SYSTEM BY A HELICAL QUADRUPOLE RF FIELD WITH $\omega < \omega_{Bi}$.

Experimental results from investigations of resonance heating on the circular two-turn stellarator R-02 over a wide range of densities ($n_e = 1 - 5 \times 10^{13}$ cm^{-3}), constant magnetic fields ($H_0 = 6 - 15$ kG) and RF field strengths ($\tilde{B}_\varphi \cong 0 - 150$ G) by means of a helical quadrupole RF magnetic field at frequencies of $\omega < \omega_{Bi}$ are presented in the present paper. A theoretical interpretation which assumes that this phenomenon is a two-stage mechanism is given. This involves the linear resonance excitation of slightly damped natural MHD helical modes followed by the non-linear (parametric) excitation of natural volume oscillations of the plasma column. At the linear stage it is possible for the so-called "helical resonance" to exist. This is found when the external RF field is at the same frequency as the natural helical oscillations of the plasma column (stable "Shafranov modes"). Another possible mechanism is the so-called "quasi-Alfvén resonance" when Alfvén-type waves are excited inside the plasma. It is assumed that RF energy is dissipated at the non-linear stage when slow magneto-acoustic waves are excited in the plasma as a result of parametric resonance and these effectively heat the ions as a result of ion-ion collisions or collisionless damping.

1. RF heating of a plasma at relatively low frequencies is a very interesting proposition for the toroidal programme. This is mainly because most of the technology necessary to meet the requirements of a closed thermonuclear reactor is already available at the present time for the given range of frequencies. It is, therefore, interesting to examine the possible physical mechanisms for the excitation and dissipation of RF waves at $\omega < \omega_{Bi}$ in a magneto-active plasma.

Additional experimental results obtained for a wider range of parameters (n_e, B_0) are also presented in the present paper, as are the results of measuring the RF field structure in the plasma under heating conditions, and the main experimental results obtained to date are summarized. Particular attention is paid to the possible theoretical interpretations of these experimental results and to the construction of a more or less closed model of this phenomenon.

2. The experimental results obtained on the circular stellarator R-02 with Ohmic heating[1] ($d = 8$ cm, $D = 130$ cm, $B_0 \lesssim 15$ kG, $i \leqslant 1.5\ \pi$, and $\bar{J}_p \cong 2$ kA) are briefly summarized as follows:

(a) When a helical rotating quadrupole RF field ($\tilde{B}_\varphi^{(0)} \cong 150$ G, $f = 1.2$ MHz) is applied to a stellarator plasma with $n_e \approx 2 - 5 \times 10^{13}$ cm^{-3} and $T_e \cong 10 - 20$ eV and a certain relationship is satisfied between the plasma density, the ion mass, the constant magnetic field strength and the parameters of the RF field (its period along the discharge chamber λ and its

[1] The device and the main methods used are descrived in Ref.[1]. A functional diagram of the device is given in Fig.1.

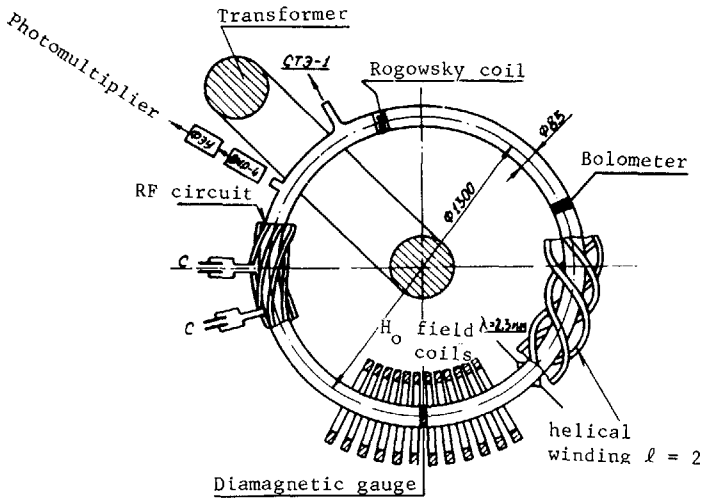


FIG.1. Functional diagram of R-02 device.

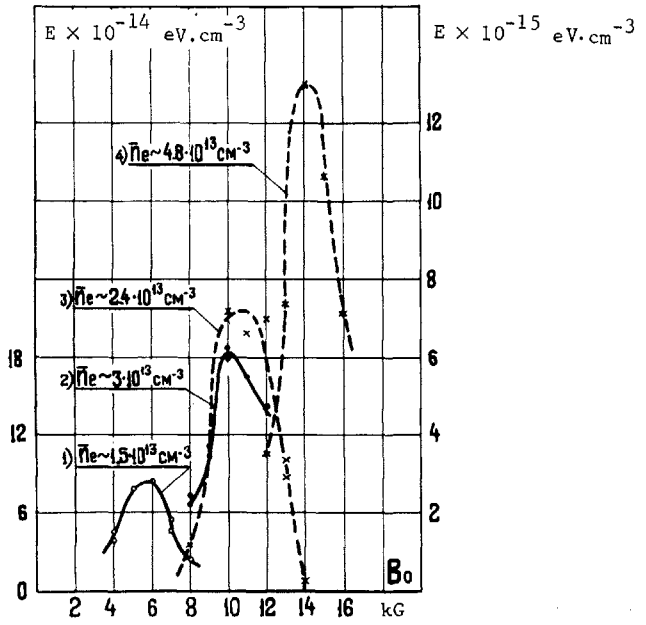


FIG.2. Specific plasma energy as a function of B_0 for different densities. ---- right-hand ordinate; —— left-hand ordinate. For curves 1, 3, 4: $B_\varphi \cong 56$ G; for curve 2: $B_\varphi \cong 47$ G.

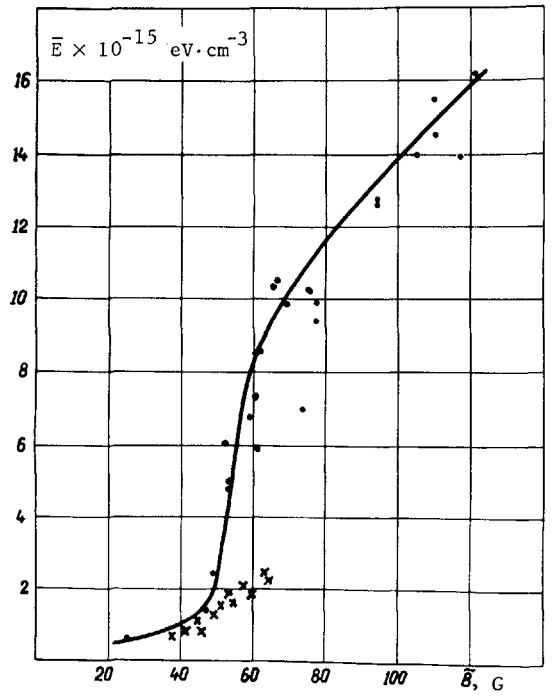


FIG.3. Specific plasma energy as a function of the external RF field amplitude. • – B_0 = 11 kG; × – B_0 = 5 kG.

frequency f), efficient interaction between the RF field and the plasma is observed and intense heating of the plasma takes place. For the given plasma density and type of gas this phenomenon assumed the form of a relatively narrow resonance on the scale of the constant magnetic field. When the plasma density and ion mass varied, the resonance value $B_{0,res}$ also varied $\sim\sqrt{n_e m_i}$ (Fig.2).

By analysing the experimental results obtained on the R-02 and R-0 (which had different values of λ and f) devices, it is possible to construct an empirical formula for $B_{0,res}$:

$$B_{0,res} = \alpha \sqrt{4\pi\rho}\, \lambda f$$

where α is a coefficient ≈ 1 – 2.5.

(b) The dependence of the heating $(n_e(T_e + T_i))$ on the RF field strength was found to be non-linear. A threshold RF field strength was found to exist for each resonance and when this threshold value was exceeded, intense heating of the plasma was initiated (Fig.3). The threshold RF field strength at which intense heating begins is virtually independent of the plasma density n_e and the constant field strength B_0 (Fig.3).

(c) Magnetic probe measurements have shown that at the instant when heating is initiated, when the diamagnetism of the plasma begins to increase rapidly, an RF field several times stronger than the vacuum RF field corresponding to the same RF currents in the circuit is built up in the plasma. The resonance build-up of quadrupole RF waves takes place throughout the plasma.

(d) Throughout the whole range of B_0 values investigated the RF field frequency at which heating took place was substantially lower than the ion cyclotron frequency for hydrogen and helium which were used as the working gases.

(e) In peak regimes a diamagnetic temperature, i.e. the value $(T_e + T_i)$ averaged over the plasma cross-section, of the order of 500 eV, was obtained. Spectroscopic measurements from the Doppler broadening of the impurity lines averaged over the cross-section and over the discharge time give $T_i \cong 250$ eV. The electron temperature T_e measured from the conductivitiy did not exceed $\cong 50$ eV. Calculations on the average ion temperature over the cross-section give $T_i \cong 400$ eV.

(f) In RF heating regimes an increase in the macroscopic stability of the plasma was observed as the familiar dynamic stabilization effect appeared simultaneously [2]. The plasma energy life-time was $\cong 30\ \mu$s which is fairly high compared with the empirical formulas for existing stellarators and tokamaks.

3. The complexity of experimental results obtained enables an attempt to be made to explain the ion heating effect which is observed. As this effect has a clearly defined resonance character, a certain resonance mechanism pumping the energy of the external RF field into the plasma must clearly exist in the system. These resonance mechanisms may give rise to noticeable absorption of RF power even at the linear stage as a result of collisional or collisionless mechanisms. With a view to determining the linear resonance mechanisms, calculations were made on the RF fields excited by the external helical currents

$$\tilde{J}_\varphi, \tilde{J}_z \sim \exp i(\Omega t - m\varphi - k_\parallel z)$$

where

$$\Omega = 2\pi f$$

is the frequency prescribed by the RF generator,

$$k_\parallel = 2\pi/\lambda_\parallel$$

($\lambda_\parallel$ is the wavelength in the winding for the RF circuit, and m is the multipolarity) in a plasma column with a density n_e and radius a located in a constant helical magnetic field

$$\vec{B}(0, B_{0\varphi}, B_0),\ B_0 \gg B_{0\varphi}$$

($B_{0\varphi}$ is generated by the longitudinal quasi-constant current flowing through the plasma). It is assumed that

$$\Omega \ll \omega_{Bi} (\omega_{Bi} = eB_0/m_i c),\ \lambda_\parallel \gg 2\pi a$$

In the general case of a collisionless cold plasma model, the RF field comprises two types of waves superposed on each other. One of these types of waves (designated by us as the second type of wave) is the fast magnetoacoustic wave and the other type (the first type or "quasi-Alfvén" wave) continues the Alfvén branch of the oscillations in the region of high refractive indices. Provided that

$$B_0 = \frac{B_{cr}}{\sqrt{2F(Q)}}$$

or

$$\Omega = \sqrt{2F(Q)}k_{\parallel}c_A, \quad F(Q) = 1 - \frac{1}{Q} + \frac{m-1}{2mQ^2} \tag{1}$$

where

$$Q = -\frac{k_{\parallel}a}{m}\frac{B_0}{B_{0\varphi}} = -\frac{n}{m}q, \quad q = \frac{a}{R}\frac{B_0}{B_{0\varphi}}$$

(q is the "safety factor", n is the number of waves along the major circumference of the torus,

$$c_A^2 = B_0^2/4\pi n_e m_i,$$

and a is the radius of the plasma column) resonance is produced (described by us as "helical") due to the excitation of natural helical oscillations of the plasma column by the external RF field. Oscillations of this type which were investigated by V.D. Shafranov et al. [3] are responsible for the Kruskal-Shafranov instability in tokamaks. When $B_{0\varphi} = 0$ in particular (i.e. a longitudinal current is absent), the value of B_0 corresponding to resonance is $B_{0,res} = \beta_{cr}/\sqrt{2}$ where the "critical" value of the magnetic field $B_{cr} = \sqrt{4\pi n_e m_i} f\lambda_{\parallel}$ is determined from the condition $C_A = f\lambda_{\parallel}$.

The physical nature of helical resonance is as follows: when the resonance condition (1) is fulfilled, the volume RF currents due to the magnetoacoustic waves can be closed by the skin currents due to the first type of waves and this ensures that natural oscillations exist in the plasma with the amplitude of these oscillations possible exceeding the amplitude of the vacuum fields by a substantial margin.

Another linear mechanism for pumping of RF power in a plasma takes place when $B_0 \gtrsim B_{0,cr}$, when waves of the first type penetrate deep into the plasma column. At certain values of the ratio $\lambda_{\perp}/a$ (where $\lambda_{\perp}$ is the wavelength in the radial direction) these waves may be noticeably amplified ("quasi-Alfvén resonance"). The way in which the first waves propagate means that it is apparently possible, in principle, to use them to heat the plasma although calculations show that this heating mechanism is not very efficient and the version whereby RF field energy is pumped into the plasma and the plasma is efficiently heated at helical resonance is the most probable.

4. The linear resonance mechanism can clearly only result in heating of the plasma electron component. To explain the preferential heating of the ions, it should be borne in mind that parametric instabilities can develop in the plasma at a certain RF field level. When the resonance conditions $\Omega = \omega_1 + \omega_2$; $k_0 = k_1 + k_2$ are satisfied, the initial pumping wave decays into two short-wave modes, for example, into two ion-acoustic branches or into an ion-acoustic and an Alfvén branch. This assumption is supported in particular by the threshold nature of the heating which was observed experimentally. As a result of the non-linear wave interaction processes, energy is pumped over the spectrum in the region of efficient ion absorption as a result of Landau damping (at the phase resonance when $v_{Ti} \cong v_{\varphi}$) or as a result of Coulomb collisions. If, moreover, the wavelength of the short-wave mode is found to be shorter than the ion Larmor radius the ions will be non-magnetoactive with respect to this wave, and, as a result, the conditions of phase resonance can also be achieved in the transverse direction.

Decay processes were investigated in detail in the magnetohydrodynamic approximation [4] ($\nu_{ei} > \Omega$). In this region where the growth rate is extremely high, decay into Alfvén and

slow magnetoacoustic waves is observed. In the region near the threshold value, the instability growth rate assumes the following form:

$$\gamma = \frac{\gamma_{max}^2 - \nu_s \nu_A}{\nu_s + \nu_A} \; ; \quad \gamma_{max} = \frac{1}{4} \frac{B_{0\varphi}}{B_0} \frac{\Omega}{\sqrt[4]{\beta}} \tag{2}$$

where $\beta = c_s^2/c_A^2 \ll 1$ is the ratio of the ion-acoustic and Alfvén velocities, and ν_A, ν_s describe the collisional damping of slow magnetoacoustic waves and Alfvén waves. The maximum instability development time is $\tau_{instab} = 1/\gamma \cong 10^{-5}$ s and the threshold amplitude

$$B_{thres,\varphi}^{(0)} = B_0 \sqrt[4]{\beta} \sqrt{\frac{k^4 c^2 v_{Ti}^2 \tau_i}{4\sigma\Omega^2}}$$

for the experimental conditions gives 20–40 oersted. These values agree qualitatively with the threshold amplitude of 46 Oe determined from the diamagnetic signal and with the plasma heating time of $\cong 0.5 \times 10^{-5}$ s. In this case, slow magnetoacoustic waves are dissipated as a result of the ion viscosity. This dissipation may explain the heating which takes place in the range of several tens of eV. At high temperatures the MHD approximation is violated and a collisionless mechanism of preferential ion heating should be sought. A mechanism of this type which is currently under investigation and appears to be fairly plausible is as follows. Ion-acoustic oscillations which are highly damped by ions and have a damping decrement of the order of the frequency exist in a collisionless plasma with $T_i \gtrsim T_e$. When an RF field is present, these oscillations can be excited as a result of the decay instability of Alfvén and ion-acoustic waves and the threshold for the build-up of these oscillations is usually determined by the relationship $\gamma_{max} = \nu_s \nu_A$. If this equation is approximated to the process under consideration and a value of the order of the frequency ($\nu_s \cong \omega_s$) is taken as the damping decrement of the ion-acoustic waves, the instability threshold does not increase significantly compared with that given previously. The excitation of these ion-acoustic oscillations naturally results in preferential heating of the plasma ion component.

The authors are grateful to V.P. Sidorov, A.M. Abzianidze, N.I. Malykh, V.B. Majburov and I.Ya. Kadysh for assistance with this work and useful discussions.

REFERENCES

[1] DEMIRKHANOV, R.A., KIROV, A.G., et al., in Plasma Physics and Controlled Nuclear Fusion Research (Proc. 7th Europ. Conf. Lausanne, 1975) 317.
[2] DEMIRKHANOV, R.A., et al., Pis'ma Zh. Ehksp. Teor. Fiz. 8 (1973) 17.
[3] SHAFRANOV, V.D., At. Ehnerg. 5 (1956) 38.
[4] ELFIMOV, A.G., NEKRASOV, F.M., Nucl. Fusion 12 (1972) 201; 13 (1973) 653.

DISCUSSION

ON PAPER IAEA-CN-35/G7

M. PORKOLAB: Could you say a few words about (i) the type of heating obtained – i.e. whether the perpendicular or parallel component of the ion temperature was involved, (ii) how the temperature was measured, and (iii) how long the heated ions were confined?

V.A. SUPRUNENKO: We assume that there is a process of successive transformation of long-wave oscillations into ion-acoustic oscillations as a result of the parametric instability, and that these are well absorbed by the plasma. The perpendicular component of the ion temperature was measured from the diamagnetic signal, the electron temperature (measured from the conductivity) being subtracted from the signal. The energy life-time of the ions was 30 μs – twice the value given by neoclassical theory for the plateau.

MAGNETOSONIC WAVE GENERATION AND DAMPING IN THE TFR TOKAMAK NEAR THE ION CYCLOTRON FREQUENCIES

EQUIPE TFR
Association Euratom-CEA sur la fusion,
Département de physique du plasma
et de la fusion contrôlée,
Centre d'etudes nucléaires,
Fontenay-aux-Roses,
France

Abstract

MAGNETOSONIC WAVE GENERATION AND DAMPING IN THE TFR TOKAMAK NEAR THE ION CYCLOTRON FREQUENCIES.

A low-power experimental investigation of wave generation and damping at frequencies between ω_{ci} and $2\omega_{ci}$ is reported. As already observed in other tokamaks, high-Q toroidal eigenmodes are generated in the absence of resonant layer in the plasma. However, the Q measured in this case are substantially lower than the values estimated on the basis of current theories, indicating the existence of unexpected damping mechanisms. While high-Q modes also exist if $\omega = 2\omega_{cH}$ in a H-plasma, strong damping is observed if $\omega = 2\omega_{cD}$ in a D-plasma and if $\omega \leqslant \omega_{cH}$ in a H-plasma. This effect is interpreted as due to the presence of H^+ ions, even in a D-plasma, and to the possible occurrence of a singular layer where the fast wave is converted into a slow mode if $\omega \leqslant \omega_{cH}$.
A mode-tracking system has been tested successfully, allowing a significant increase in the duration of the resonance conditions for an eigenmode: a resonant peak lasting normally for about 0.2 ms is extended by this method to more than 5 ms.

Fast magnetosonic wave generation in the ion cyclotron range appears an attractive way of transferring large additional power to a Tokamak plasma [1] [2] [3].

At frequencies above ω_{ci} ($\Omega_i > 1$), the expected damping mechanisms are weak but this results in large amplification of the RF field by cavity resonance [4], strong coupling of the launching structure and uniform deposition of the energy in the body of the plasma. If $\Omega_i = 1$ in the plasma, conditions for efficient cyclotron damping can be met in a two-component plasma containing a fraction of resonant ions [2] [3]. In this case, however, the possibility also exists for the magnetosonic wave to be locally converted into a slow mode [5] [6] and the results presented here underline the importance of this effect on the wave damping.

The experimental investigation reported in this paper was undertaken to gain the necessary information on the relative importance of the damping mechanisms of the magnetosonic waves and to test the efficiency of power transfer using a coil as the launching structure. It will be followed by a high-power heating experiment in the next version of this machine, TFR 600.

I. DISPERSION RELATION AND LAUNCHING COIL IMPEDANCE

The cold plasma dispersion relation of the fast mode in TFR has been computed assuming cylindrical geometry, uniform toroidal field and plasma current, parabolic density profile and $\Omega > 1$. The results shown in Fig.1 for $\Omega = 2$, $m = 0$ and $|m| = 1$ indicate that, for densities above a few

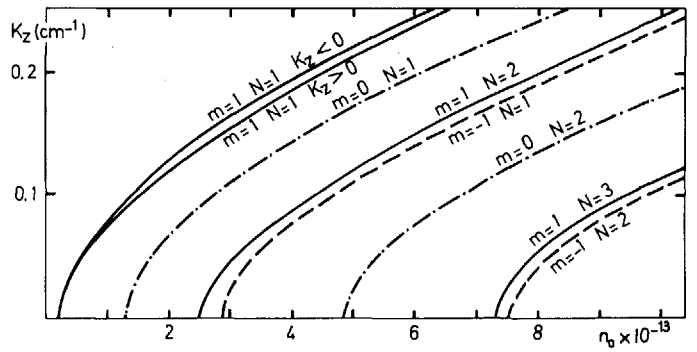


FIG.1. Dispersion relation for m = 0 and m = 1 modes at $\Omega_D = 2$. The curves for m = 1 are computed with a plasma current of 150 kA.

times 10^{13} cm^{-3}, a wide variety of modes can be generated. The poloidal field leads to a discrimination between the positive and negative toroidal directions [7]. This results in splitting each m ≠ 0 curve, as indicated in Fig.1 for the fundamental m = 1 mode.

The impedance Z of a coil located around the plasma at a radius r_o and the wave field in the plasma can be easily evaluated in the low-frequency approximation where the RF current is assumed constant along the coil.

For a given m mode, one finds :

$$Z_m = i\omega \mathcal{L} + 2\,(\pi r_o)^2 / \left[\beta |G_m|^2 (1 - i\gamma)\right] \qquad (1)$$

$$|E_{\theta m}|_{r_0} = \pi r_0 I / \left[\beta |G_m| (1 + \gamma^2)^{1/2}\right] \qquad (2)$$

where $\mathcal{L}$ is the coil inductance and G_m the ratio of the RF current I to its m-th Fourier component,

$\beta = 2S\,[\sinh(\alpha L) + \alpha/K.\sin(KL)] / [\cosh(\alpha L) + \cos(KL)]$

$\gamma = \sin(KL)/\sinh(\alpha L)$

S is the power carried by the wave for $(E_\theta)_{r_0} = 1$, $\alpha^{-1} = \lambda_i$ the damping length, $L = 2\pi R_o$ and $K = K_{//}$.

Z_m and $E_\theta(r)$ have been computed for different modes, at $\Omega = 2$, taking into account wall resistivity, damping due to cyclotron heating [2] and Landau and transit time electron absorption [3].

For current values of the TFR plasma parameters, one reaches the following principal conclusions :

a) For the m = 1 modes (N = 1 and N = 2), the damping length is between 3×10^4 cm and 3×10^5 cm. This leads to very high Q resonant peaks and large values of the coil resistance.

b) Harmonic cyclotron damping (HCD) reduces λ_i to a few times L for m = 0, N = 2 and m = -1, N = 1. Fig.2 shows the wave field E_θ ($r = r_o$) vs. density for m = 0, N = 2. The width at half height of the resonant peaks is in this case $\Delta n/n \simeq 5\times10^{-3}$, corresponding to a Q factor of 700. The corresponding resistance of a coil of poloidal length $r_o\theta$ = 30 cm is 4Ω.

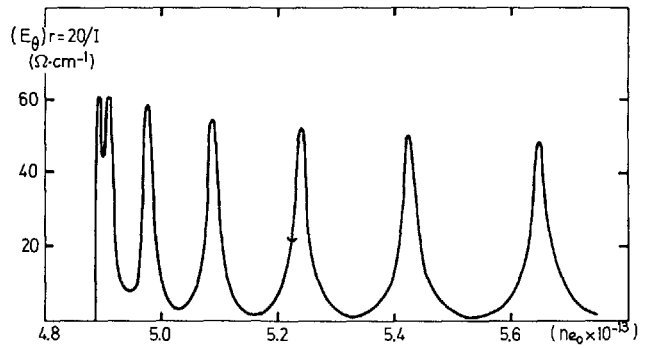


FIG. 2. Amplitude of the E_θ field for the mode m = 0, N = 2 computed at r = 20 cm for a coil surrounding the plasma at the same radius ($\Omega_D = 2$).

c) Electron damping plays a minor role at $\Omega_i = 2$ and does not decrease λ_i to less than 3×10^4 cm.

II. EXPERIMENTAL EQUIPMENT

Two types of coils have been successively used in one of the large ports of TFR (Fig.3).

In coil I, the RF current flows in a V-shaped conductor(A)(40 cm long, 6 cm wide) supplied by a coaxial transmission line. The conductor is protected from direct view of the plasma by an alumina case(B). This case is covered by an array of stainless steel strips(C) preventing metallic deposit on the alumina and acting as a Faraday shield.

Coil II has a total length of 98 cm. The volume between the conductors is a solid block of alumina reducing the characteristic impedance to 25Ω. No connection exists between the central and return conductors, each half coil acting as an open transmission line. The two coils can be supplied in phase or out of phase, allowing selective excitation of m = 1 or m = 0 modes.

The coils were supplied by a RF amplifier capable of delivering up to 1kW at frequencies between 50 and 90 MHz. Between the generator and the coil, a two-stub matching network transforms the loading impedance into a value close to 50Ω.

Both coils could be moved in and out in the horizontal plane, allowing large plasma radii to be used for other experiments. Coil I was used with a plasma radius of 19 cm, coil II with a radius of 17 cm.

The signals from 10 magnetic probes located in different ports in the shadow of the limiter were chopped at a frequency of 200 kHz and recorded in phase and amplitude by the central data acquisition system.

III. EXPERIMENTS WITH NO RESONANT LAYER INSIDE THE PLASMA

3.1. Toroidal eigenmodes

If the $\Omega_D = 2$ layer is outside a D-plasma or if Ω_H is larger than 1 in a H-plasma, the probe signals observed during the periods of rise and fall of the plasma density appear as a sequence of sharp resolvable peaks.

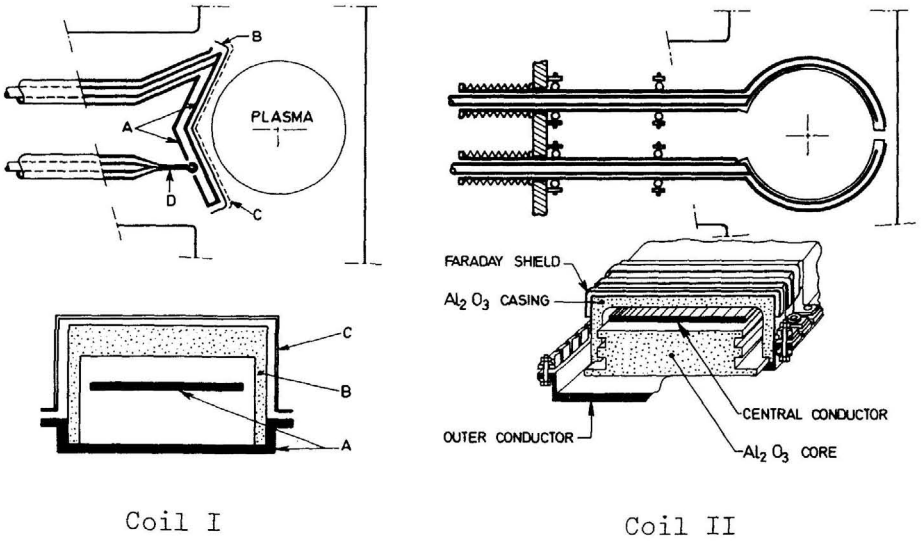


FIG.3. Sketches of the launching coils.

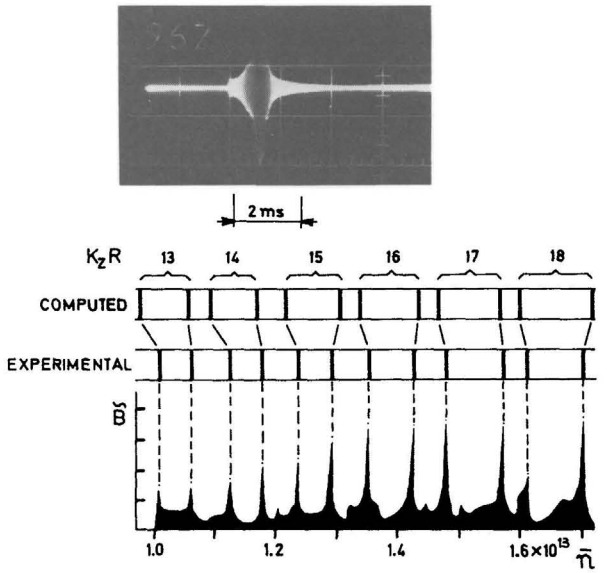


FIG.4. Probe signal versus density compared with the spectrum of m = 1 mode.

This has been noticed earlier [7] [8], and no doubt remains that such peaks occur whenever the density value matches the conditions required for an eigenmode of the magnetosonic wave in the Tokamak cavity.

Since a wide variety of modes can be generated in TFR, the signal appears frequently as a dense spectrum in which the different "lines" can hardly be identified unambiguously.

A comparison between theoretical and experimental dispersion relation can be attempted, however, when the density is low enough: Fig.4 shows an example of these resonant peaks on an expanded time scale and compares the probe signal observed between average densities of 1.0 and 1.7×10^{13} cm^{-3} with the spectrum predicted by integration of the wave equation for the fundamental m = 1 mode. The effect of the poloidal magnetic field ($q_a = 4$) has been taken into account in the calculation and results in the doublet structure of the theoretical spectrum.

While cold cylindrical theory probably accounts fairly well for the occurrence of discrete peaks in the probe signal, the actual Q are quite generally smaller than the values derived on the basis of conventional damping mechanisms (see § 1) : experimental values are always smaller than 10^3 while values up to 10^5 should be expected for m = 1 modes.

Two explanations can be suggested: interaction of the wave with the turbulence of the plasma [9] and damping near the edge where $\omega \simeq \omega_{pi}$ [10]. But whatever the additional damping mechanism is, one must expect it to compete with harmonic cyclotron heating occurring when $\Omega_i = 2$, overwhelming it completely for low-density modes (especially the fundamental m = 1) and being of comparable importance for higher order modes.

As mentioned above, the two halves of coil II can be supplied either in phase or out of phase. Phase analysis of the signals from 2 probes 180° apart along θ in the same port actually shows that even or odd m modes can be preferentially excited depending on the mode of operation.

The loading resistance of coil I, defined as $R_S = 2P/I^2$ (where P is the power absorbed by the plasma and I the RF current) is $\leq 1\Omega$ at the maximum of the peaks. With coil II (defining now I as the peak RF current in the transmission line), values between 4 and 8Ω are commonly found. These figures, usually smaller by a factor of ~ 4 than the values expected from Eq.(1) (assuming the experimental damping efficiency) demonstrate the essential role of the coil length in the coupling efficiency.

3.2. Mode tracking

Neutral gas injection allows the density in TFR to stay constant within a few % for several tens of ms during the current plateau, and eigenmodes lasting for 20 ms are currently observed.

However, some mode tracking technique is probably required in a high-power experiment to compensate an eventual density increase during the RF pulse [7] and the fast oscillations of the density profile related to the internal "sawtooth" disruptions which lead to a strong modulation of the resonant peak amplitude [11]. The possibility of compensating the density variations by a change in frequency has been first demonstrated in TFR by imposing a linear change of the frequency. This resulted in broadening a peak from 0.1 to 2 ms [12].

A more refined circuit, tested recently, is sketched in Fig.5: a large resonant peak in a probe signal triggers the opening of a gate allowing the phase between another probe signal and a reference to sweep the pilot oscillator in frequency. This equipment is still in a test phase. As shown in Fig.5, however, it already allows the broadening of a resonant peak from 0.2 to 5 ms.

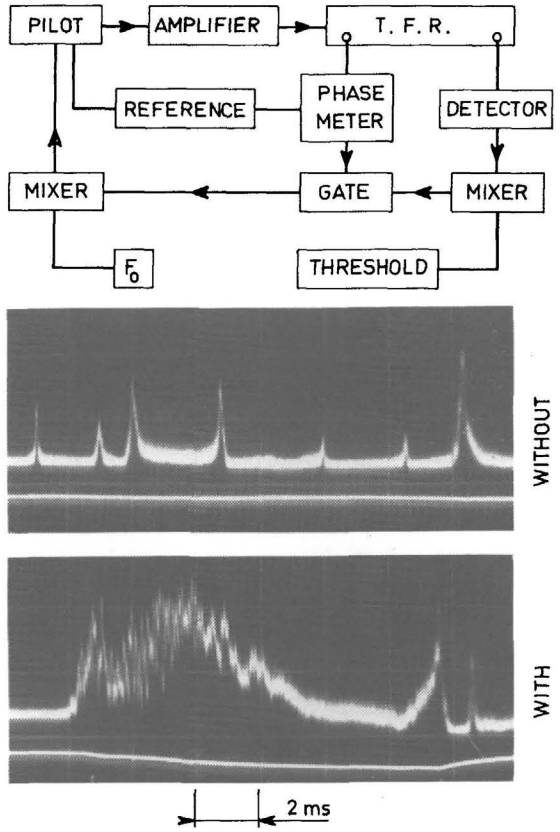


FIG.5. Sketch of the feedback circuit; example of peak broadening.

IV. EXPERIMENTS WITH RESONANT LAYERS INSIDE THE PLASMA

4.1. Hydrogen plasma, $\Omega_H = 2$

Measurements were made in a H plasma at 86 MHz and fields between 35 and 25 kG. The location of the $\Omega_H = 2$ layer varied accordingly between major radii of 87 cm up to 122 cm. No basic differences in the wave signals were noticed although the maximum amplitude of the resonant peaks were generally smaller (by 20 to 40%) when the $\Omega_H = 2$ layer was inside the plasma (Fig.6a). The difference is compatible with the expected effect of harmonic cyclotron damping (HCD). However, the smallness of the effect underlines the fact that damping mechanisms other than the ones considered in current theories limit the maximum Q and compete with HCD when the latter is not very strong.

4.2. Hydrogen plasma, $\Omega_H = 1$

A clear change in the wave signals is noticed when the $\Omega_H = 1$ layer is introduced in the plasma from the high B_φ side (Fig.6b). A spectrum of

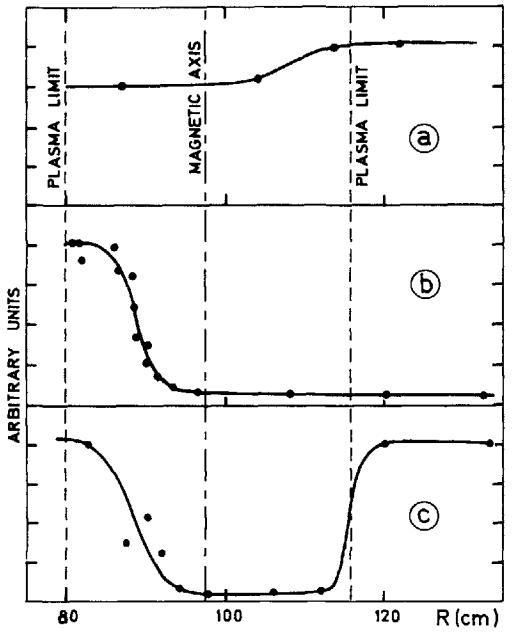


FIG.6. Maximum amplitude of wave field versus position of (a) $\Omega_H = 2$ (H-plasma); (b) $\Omega_H = 1$ (H-plasma); (c) $\Omega_H = 1$ (D-plasma).

sharp peaks is preserved as long as the radius R_{H1} (where $\Omega_H = 1$) is smaller than 86 cm. For higher B_φ, the resonant peaks gradually damp out and between $R_{H1} = 98$ and 132 cm no resonant structure is noticed, the maximum power transferred to the plasma being accordingly severely reduced.

4.3. Deuterium plasma, $\Omega_D = 2$ ($\Omega_H = 1$)

In this case also, high-Q resonant peaks occurring if R_{H1} (where $\Omega_H = 1$) is smaller than 86 cm are gradually damped if B_φ is increased (Fig.6c). However, in contrast with the situation in a H plasma (§ 4.2), the resonant peaks recover high Q values for $R_{H1} > 118$ cm ($\Omega_H = 1$ outside the plasma).

4.4. Discussion

A major difference is thus noticed between the 3 cases considered above. A priori, no difference is expected between the cases where $\Omega_D = 2$ and $\Omega_H = 2$ inside the plasma and the only plausible explanation for that difference is that the D plasma contains some amount of H. No measurement of H^+ density is available during the pulse. However, mass analysis of the residual gas after the discharge indicates (by comparison of masses 3 and 4) a ratio of 15 to 20% between H and D populations.

An analysis of these three series of experiments suggests strongly that the damping observed in the $\Omega_H \simeq 1$ range must be related to the possible occurrence in the plasma of a resonant layer defined by

$$n_\eta^2 - S = 0 \qquad (3)$$

where

$$n_\eta = K_\eta c/\omega$$

and

$$S = 1 - \sum_i \left[\omega_{pi}^2 \ / (\omega^2 - \omega^2{}_{ci}) \right]$$

Such a resonance, several times rediscovered by theorists [6] [13] [14] [15], is characterizedby a mode conversion process of the fast wave into a slow mode which can be ultimately absorbed by linear or non-linear mechanisms.

In pure hydrogen, and provided $\Omega_H = 1$ in the plasma, condition (3) can obviously be satisfied for any value of $n_{//}$. This, however, remains true for all $n_{//}$ values compatible with the fast wave dispersion relation, if $\Omega_H < 1$ in the plasma.

In a mixed H + D plasma, the situation is different. Due to the large negative term in S corresponding to deuterium, Eq.3 can be satisfied only by a sufficiently large positive term due to hydrogen. If the H content is small this is possible only if $\Omega_H = 1$ inside the plasma limits.

This crude model thus explains fairly well the principal differences between the three situations presented in Fig.6.

Mass analysis of the charge-exchange neutrals will be possible in TFR 600 and will allow more refined investigation of this effect.

The same mechanism is probably responsible for the heating effects observed in other Tokamaks [16] [17], and should be carefully taken into account in RF heating schemes considering two component plasmas [2] [3].

REFERENCES

[1] ADAM, J., SAMAIN, A., Rep. EUR-CEA-FC-579 (1971).
[2] ADAM, J., Rep. EUR-CEA-FC-711 (1973).
[3] STIX, T., Nucl. Fusion **15** (1975) 737.
[4] MESSIAEN, A., VANDENPLAS, P., Plasma Phys. **15** (1973) 505.
[5] KLIMA, R., LONGINOV, A., STEPANOV, K., Nucl. Fusion **15** (1975) 1157.
[6] SWANSON, D., Phys. Fluids **18** (1975) 1269.
[7] ADAM, J., et al. "Wave generation and heating in the ST-tokamak at the fundamental and harmonic ion cyclotron frequencies", Plasma Physics and Controlled Nuclear Fusion Research 1974 (Proc. 5th Int. Conf. Tokyo, 1974) **1**, IAEA, Vienna (1975) 65.
[8] VDOVIN, V., et al., JETP Lett. **14** (1971) 149.
[9] SAMAIN, A., in Proc. Symposium on Plasma Heating, Varenna, 1974.
[10] LALLIA, P., Nucl. Fusion **15** (1975) 1190.
[11] TFR Group, Rep. EUR-CEA-FC-838 (1976).
[12] TFR Group, in Proc. Theoretical and Experimental Aspects of Heating of Toroidal Plasma, Grenoble, 1976.
[13] STIX, T., The Theory of Plasma Waves, Ch. 3, McGraw Hill, New York (1962).
[14] ADAM, J., ALVAREZ de TOLEDO, F., REBUT, P., TOROSSIAN, A., Plasma Phys. **11** (1969) 297.
[15] GROSSMAN, W., TATARONIS, J., Z. Phys. **261** (1973) 203.
[16] PERKINS, F., in Proc. Theoretical and Experimental Aspects of Heating of Toroidal Plasma, Grenoble, 1976.
[17] VDOVIN, V., ibid.

DISCUSSION

ON PAPER IAEA-CN-35/G8

A. GIBSON: Are you suggesting that, while large amounts of hydrogen contamination are unacceptable, a small amount of hydrogen contamination might be beneficial for heating a deuterium plasma?

J. ADAM: As was shown in our paper presented at the Symposium on Plasma Heating (Varenna 1976), the conversion layer in a plasma containing a dominant fraction of hydrogen (with $\omega = \omega_{CH}$ in the plasma) occurs near the wall. In a deuterium plasma contaminated by a small fraction of hydrogen, the same layer occurs near the $\omega = \omega_{CH}$ layer, deep inside the plasma. In that sense, if the conversion layer is responsible for the damping, the second situation might be more favourable.

M. KRISTIANSEN: What limited the bandwidth of the RF system used in the feedback experiment, and what was the RF system bandwidth? Secondly, how did you track the eigenmodes, i.e. what was your sensing device?

J. ADAM: The bandwidth of the RF amplifier was 7 MHz. However, only about half of this band could be used because, owing to the time-varying conditions of the plasma, the circuits are never correctly matched. The feedback was monitored by comparing the phase of magnetic probe measuring the wave field near the wall with a reference signal.

EXPERIMENTS AT THE LOWER HYBRID FREQUENCY IN THE WEGA TOKAMAK

P. BLANC*, W. HESS*, G. ICHTCHENKO*, P. JAVEL**,
P. LALLIA*, C. MAHN**, T.K. NGUYEN*, W. OHLENDORF**,
G.W. PACHER**, H.D. PACHER**, S. TAKAMURA†,
G. TONON*, J.G. WEGROWE**

Abstract

EXPERIMENTS AT THE LOWER HYBRID FREQUENCY IN THE WEGA TOKAMAK.

Application of HF-power near the lower hybrid frequency to the Wega tokamak plasma results in typical bulk ion temperature increases of 20 to 30%, (80 kW). As no indication of electron heating or the production of superthermal electrons by the HF is found, it is probable that a large portion of the energy goes into the observed fast ions, produced at the edge and lost before thermalizing. Under not yet reproduced conditions, an increase by a factor 2 in the perpendicular ion temperature measured only by charge exchange has been found.

1 - INTRODUCTION.

Wega is a joint experiment at Grenoble of the Commissariat à l'Energie Atomique, Grenoble, France, and the Max-Planck-Institut für Plasmaphysik, Garching, Federal Republic of Germany, performed under the auspices of EURATOM and with the participation of the Ecole Royale Militaire, Bruxelles, Belgium. Conceived as a Stellarator [1] ,the device is presently run as a tokamak. It is characterized by the following parameters : major radius 72 cm, minor radii 22 cm (vacuum vessel), 16 cm (guard limiter) and usually 13 cm (horizontal rail limiter) ; and magnetic field 1.4 Tesla. A more detailed description of the device as well as first results are found elsewhere [2] . This paper discusses the effect on the tokamak plasma of the application of HF power near the lower hybrid frequency.

R.F. power at 500 MHz is applied in pulses up to 15 msec at power levels up to 80 kW. The power is coupled by means of two closed loops (Fig. 1), which are fed in phase but whose fields are out of phase due to their geometrical arrangement. From their separation, the parallel refractive index is around 2, so that the accessibility condition [3] is satisfied ($N_{\parallel} > 1.4$). In order that the lower hybrid resonant surface and the

* Association Euratom-CEA, Département de physique du plasma et de la fusion contrôlée, Service IGn., Centre d'études nucléaires, Grenoble, France.

** Max-Planck-Institut für Plasmaphysik, Garching, Federal Republic of Germany.

† Visitor from Nagoya University, Japan.

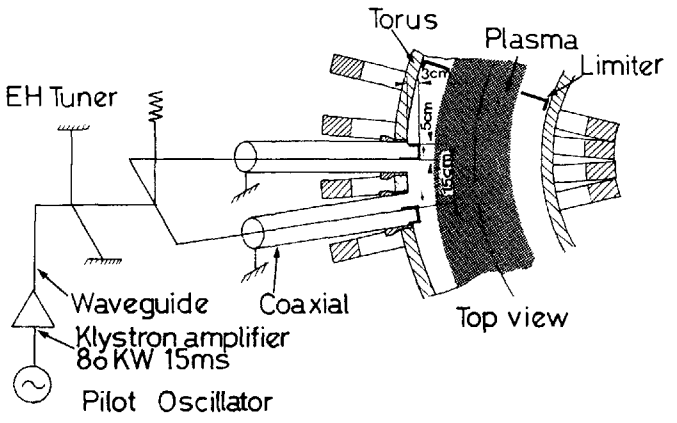


FIG.1. Schematic view of HF system including two-loop coupling structure.

turning point [4] be well inside the plasma, the central density, as deduced from the measured line electron density, is adjusted to be 3.10^{13} cm^{-3}, in the case of deuterium. As the electron density in WEGA, after an initial peak roughly proportional to the filling pressure, always drops to values below 5.10^{12} in the first 20 msec of the discharge, a fast gas valve (maximum throughput 1.5 torr-ℓ/sec) is programmed for the entire discharge duration to obtain and maintain the desired density.

2 - BASIC PLASMA PARAMETERS

For the "standard series" with HF, the time evolution of the discharge is represented in Fig. 2. The plasma current drops slowly from a peak value of 50 kA, the loop voltage is around 3 V, and rises slightly during the HF over that observed without HF. The radial plasma position is controlled by a feedback system (no copper shell). While catastrophic radial displacements were observed during and just after the HF in earlier series, no effect on the radial position is now observable due to an improved feedback system [5] . With the improved radial stabilization and intensive discharge cleaning, the originally observed line density increase of 20 to 30 % during the HF is no longer found systematically. During the HF, no increase in D_α emission near the limiter is observed.

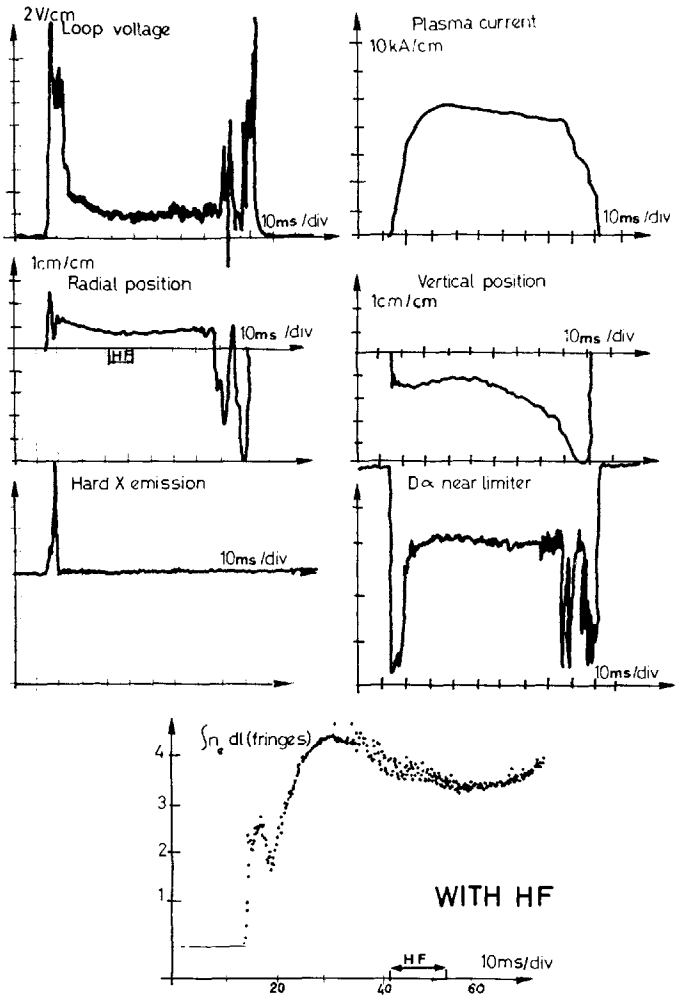


FIG. 2. Standard series: Evolution of basic plasma parameters with time. HF power of 80 kW is applied from t = 42 to t = 52 ms.

3 - ELECTRON MEASUREMENTS

As measured by a soft-X-ray detector using the multi-absorber technique and corroborated by Thomson scattering, the electron temperature at the center of the discharge (700-800 eV) does not change significantly when the HF is applied (Fig. 3).

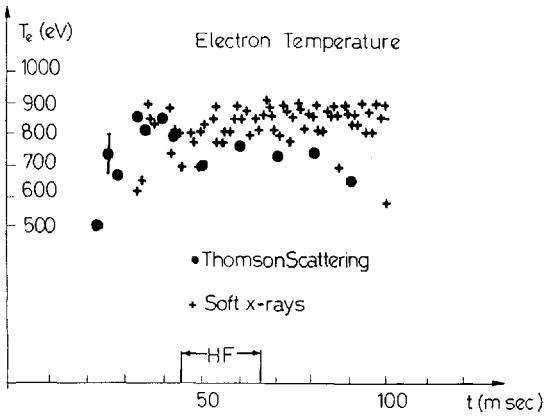


FIG.3. Electron temperature with HF measured by Thomson scattering and soft-X-ray emission as a function of time.

Some shots seem to indicate that the electron temperature may even drop by 10 % during the HF. No evidence exists for the production of significant numbers of superthermal electrons by the HF, as shown by the following observations : A radiometer tuned to twice the electron cyclotron frequency in the outer third of the discharge shows no increase in synchrotron emission. No increase in hard X-emission for energies above 50 keV is observed. While each of the soft X-ray signals, representing an integral over a portion of the energy spectrum, increases during the HF, the shape of the deduced spectrum up to 20 keV remains the same.

4 - ION MEASUREMENTS

The analysis of charge-exchanged neutrals always indicates the presence of a high-energy tail of the ion distribution during the HF, a tail which appears to be Maxwellian with temperatures around 1 keV (Fig. 4). The flux of charge-exchanged neutrals varies exponentially with the applied HF power up to 25 kW (Fig. 5). The particles observed have $v_{\parallel} / v_{\perp} = 0.1$ to 0.2 (angle of sight) and are therefore in banana orbits which are not blocked by the local magnetic mirrors [6] . The lifetime of the fast ions is observed to be around 100 microseconds, which corresponds to the bounce time. As the time for charge exchange collisions at the edge is also of the same order, it seems likely that the fast ions are lost by charge exchange at the edge during one

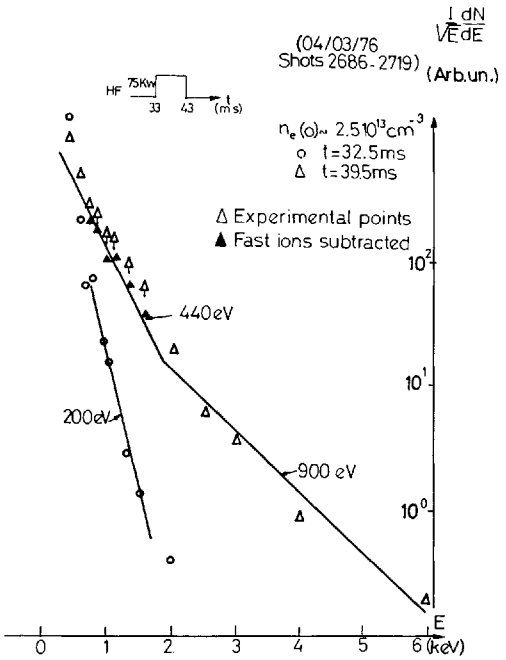


FIG. 4. Spectrum of charge-exchanged neutrals on line of sight passing through plasma centre versus energy, with and without HF. Result from, as yet, unreproduced early series.

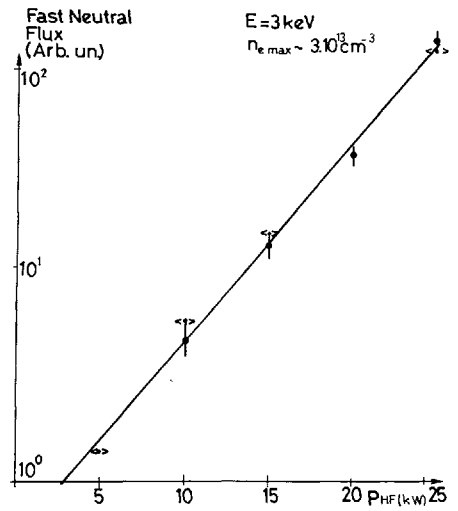


FIG. 5. Charge-exchange flux at 3 keV as a function of HF power.

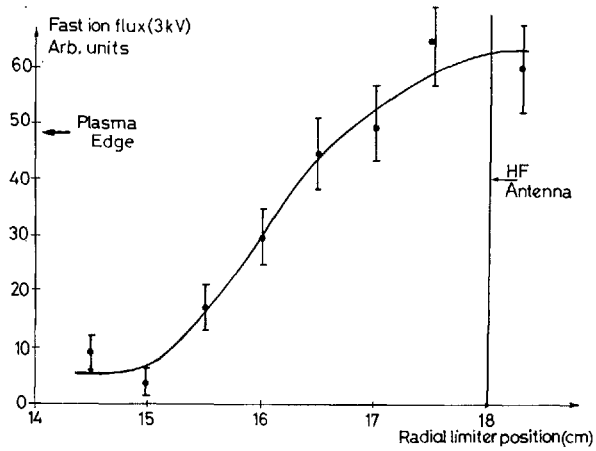


FIG.6. Flux of fast ions at 3 keV as position of a radial limiter is varied in region exterior to the main plasma.

banana orbit before being thermalized ($\tau_{DD} \sim$ 8 msec). The fact that they are Maxwellian can therefore not be explained by collisions during their lifetime. That they exist at the edge is further corroborated by an experiment in which a radial limiter was placed at various positions between the antenna and the edge of the plasma (r=14 cm) : the flux of fast ions decreases by an order of magnitude before the limiter reaches the plasma edge (Fig. 6).

The bulk ion temperature is obtained from the charge exchange measurement by subtracting the fast-ion Maxwellian from the measured points and fitting another Maxwellian to the corrected points (Fig. 4). In one particular case, obtained in an earlier series before good radial stabilization and without corroboration by other diagnostics, an increase in the peak ion temperature from 200 to 400 eV was observed (Fig. 7).

In the more recent series with reduced plasma radius, an increase of 20 to 30 % for HT input power of 80 kW is observed (Fig. 8). In these series, the ion temperature is obtained simultaneously from the measurement of the Doppler broadening of the O VII line (1623 Å) emission. Since this measurement reflects the main ion temperature one-half the plasma radius, it is lower than the peak ion temperature measured by charge exchange, but also shows about 20 % increase for the shots with HF as compared to the shots without (Fig. 8). For both measurements, the ion temperature increase decays with a time constant of several milliseconds.

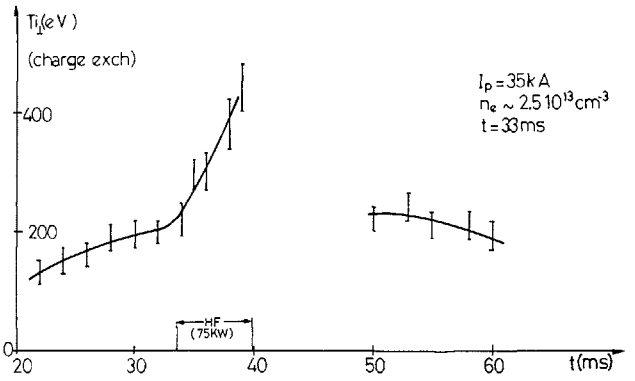


FIG. 7. Time evolution of ion temperature measured by charge exchange. Result from the same series as Fig.4, in which measurement after the HF was impossible owing to then occurring large radial displacement.

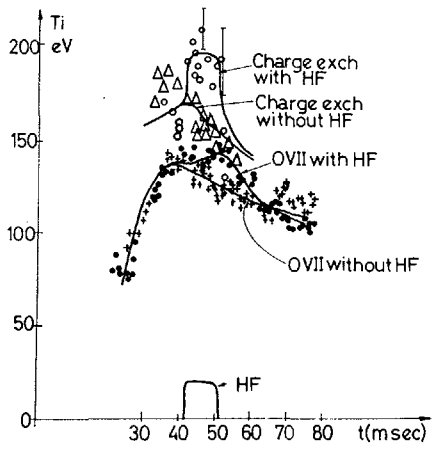


FIG. 8. Standard series: Evolution of ion temperature with and without HF from charge exchange (r = 0 cm) and Doppler broadening of O VII (r ~ 6 cm) measurements.

5 - HF MEASUREMENTS

HF spectra are observed with pickup loops placed at various positions around the torus. Sidebands are observed only below the pump frequency. The amplitude of this lower sideband decreases away from the pump, presenting maxima, the first of which corresponds to the ion cyclotron frequency

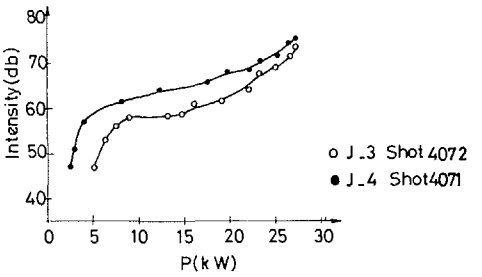


FIG.9. HF emission at second peak of lower sideband ($f - f_{pump} = 20$ MHz) as a function of applied HF power during slowly rising HF pulse.

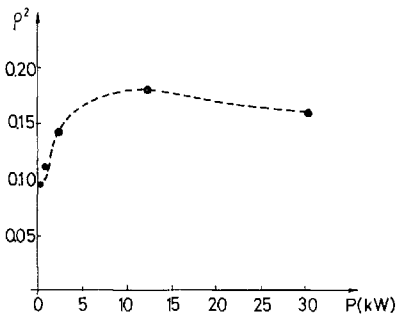


FIG.10. Power reflection coefficient as a function of HF power during slowly rising HF pulse.

at the low magnetic field side of the plasma periphery. The next maxima correspond to even harmonics of a slightly larger frequency. To each of these maxima corresponds a low-frequency maximum at the difference frequency to the pump. From the observation of the sideband intensity during a slowly rising HF pulse (Fig. 9), a threshold lies below 5 kW.

The plasma impedance as seen from the generator changes as a function of the input HF power, indicating the presence of nonlinear processes. The power reflection coefficient varies strongly with power level (Fig.10).

6 - DISCUSSION

The ion temperature increase on the application of 80 kW HF for 10 msec in the standard case was 20 to 30 %. Since the power transferred from the electrons to the ions by collisions is 10 to 15 kW (ohmic heating power 150 kW), and the ion temperature is in good agreement with the Artsimovich scaling [7] , the power transferred to the ions by the HF is estimated to be less than 10 kW. Under these conditions, the major part of the HF power is not absorbed by the bulk ions.

There is no evidence that this HF power is absorbed by the electrons. The electron temperature does not change significantly, and the hard X-ray, soft X-ray, and synchrotron emission measurements do not indicate that significant numbers of superthermal electrons are produced. However, there are indications that the impurity content increases during the HF : the soft X-ray emission and the O VII line emission both increase.

The existence of a plasma outside the limiter radius, measured by Langmuir probes to be of the order of 10^{11} cm^{-3} near the HF antennas just before the HF pulse, modifies the energy coupling to the bulk plasma. The fast ions, which are produced at the edge, are lost before completing a banana orbit and may easily carry away the rest of the power.

7 - CONCLUSION

Although in one particular case, under not yet reproduced conditions, an increase in the perpendicular ion temperature by a factor 2 has been observed, more typical results show an increase in the bulk ion temperature of 20 to 30 % on the application of HF power near the lower hybrid frequency, decaying in several milliseconds.

Further experiments will concentrate on study and modification of the coupling conditions.

8 – ACKNOWLEDGEMENTS

The authors wish to express their appreciation to the engineering and technical staff of WEGA for their many efforts.

Fruitful discussions on Thomson scattering with Dr. Desopere (University of Ghent, ERM Brussels) during his stay at Grenoble are acknowledged.

REFERENCES

[1] R. FRITSCH, M. LIPA, W. OHLENDORF, G.W. PACHER, H.D. PACHER, J.G. WEGROWE, 9th Symposium on Fusion Technology, paper C2-4, Garmisch Partenkirchen, (1976).

[2] P. BLANC et al.,3 rd International Meeting on Theoretical and Experimental Aspects of Heating of Toroidal Plasmas, Vol. II, Grenoble, (1976).

[3] V.E. GOLANT, Sov. Phys. Techn. Phys., 16, 12, (1972), 1980.

[4] P. LALLIA, Report Association EURATOM-CEA, DPh-PFC-SIG, EUR-CEA-FC 774, (1975).

[5] G.W. PACHER, H.D. PACHER, to be published.

[6] P. LALLIA et al., Symposium on Plasma Heating in Toroidal Devices, Varenna, (1976).

[7] L.A. ARTSIMOVICH, Nuclear Fusion 12, (1972) 215.

DISCUSSION

ON PAPER IAEA-CN-35/G9

A. GIBSON: Can you expand upon your remark that you have indications that better heating efficiency may be possible?

G.W. PACHER: As I indicated in my presentation, we have seen appreciably greater ion heating, with the same power level, than in the series discussed here in detail. Likewise, we have seen approximately equal or slightly greater heating at lower power levels. However, these other series are not well documented diagnostically, and it would be premature to say more at this time.

T. TAMANO: Could you elaborate on the mechanism of the improved coupling you plan to use in future?

G.W. PACHER: Basically, we shall still use loop coupling because of the port size. However, we can and shall use other loop shapes to give geometrical spectra with power concentrated at other values of the parallel refractive index. Also, the coupling will be changed by varying the density of the discharge, thus varying the region of the lower hybrid resonant layer and the conditions in the region between loop and plasma.

R.J. COLCHIN: Is there any increase in the amount of impurity radiation when high-frequency heating is applied, as would be the case if heated fast ions were reaching the wall?

G.W. PACHER: There are two indications that impurities might increase slightly, one being an increase in the intensity of the O VII line, the other an increase in the soft-X-radiation when the HF is applied. However, the resistivity does not change appreciably.

MAGNETOACOUSTIC-HEATING EXPERIMENTS IN TOKAMAK T-4 PLASMA

V.V. BUZANKIN, V.A. VERSHKOV, N.V. IVANOV,
I.A. KOVAN, V.A. KRUPIN, I.A. POPOV,
I.B. SEMENOV, Yu.A. SOKOLOV
I.V. Kurchatov Institute of Atomic Energy,
Moscow, Union of Soviet Socialist Republics

Presented by V.S. Strelkov

Abstract

MAGNETOACOUSTIC-HEATING EXPERIMENTS IN TOKAMAK T-4 PLASMA.

Results of experiments with plasma high-frequency heating in the T-4 in the frequency range $\omega_i \leqslant \omega \leqslant 3\omega_i$ are presented. A 23-MHz fixed-frequency HF oscillator with rated power of approximately 1 MW is used to excite magnetoacoustic oscillations in the plasma. The exciter is designed as a loop uninsulated from the plasma by a dielectric which encloses the pinch and is protected by auxiliary molybdenum diaphragms on both sides. Experiments demonstrate the high electrical strength of this injection design in the absence of plasma as well as in the discharge pulse of the tokamak. The experiments are conducted in deuterium plasma containing a small admixture of hydrogen, in the density range of 5×10^{12} to 5×10^{13} cm^{-3}, with a magnetic field strength of from 10 to 35 kOe. They show that the excitation range of magnetoacoustic oscillations agrees well with the theoretical range obtained for a parabolic profile of radial plasma density distribution. When a high-frequency power of about 50 kW is injected into the plasma at the second harmonic of the deuterium ion cyclotron frequency, effective heating of the small hydrogen admixture takes place; this heating results in enriching the high-energy "tail" of the distribution function of the charge-exchange neutrals. This effect is explained by the cyclotron acceleration of the hydrogen ions in the magnctoacoustic wave field with elliptic polarization. When the HF power injected into the plasma is increased, a stripping instability develops in the form of an increase in the plasma magnetohydrodynamic activity and in the form of characteristic negative "peaks" in the discharge voltage. It is established that this instability is not the result of local action of the HF exciter and takes place only in exciting the natural magnetoacoustic oscillations of the pinch. Its occurrence is apparently not associated with the appearance of a high-energy "tail" in the plasma vessel on the ion distribution function.

This paper contains the results of studies on magnetoacoustic heating of plasma in the tokamak T-4. The following problems were accorded our principal attention in the experiments:

The first problem was associated with finding a high-frequency exciter design promising for use in large installations. In experiments [1,2], exciters insulated from the plasma by a dielectric were used to inject HF power into the plasma. It was necessary to insulate the exciter because the plasma density in the diaphragm shadow, where the exciting loop was located, was high enough to cause the capacitive currents and conductance currents to bypass the exciter. The use of exciters with dielectric insulation on existing small installations makes it possible to overcome this difficulty. However, the use of the design in larger-scale installations designed to produce pure hot plasma is not promising. Therefore, an exciter design with an uncovered metal loop protected from the plasma by diaphragms [3,4] or inserted into a special recess in the chamber wall [5] is more promising. The efficiency of this design under sufficiently charged conditions with regard to the large scale tokamak T-4 is checked in this work.

The second problem involves an experimental check of the results of calculations of the excitation conditions of natural magnetoacoustic oscillations of the pinch [6].

The outlook for creating a two-component tokamak reactor is being widely discussed at the present time in the literature [7–12]. The method of neutral-atom injection as well as the method of magnetoacoustic heating at the ion cyclotron frequency in plasma consisting of two

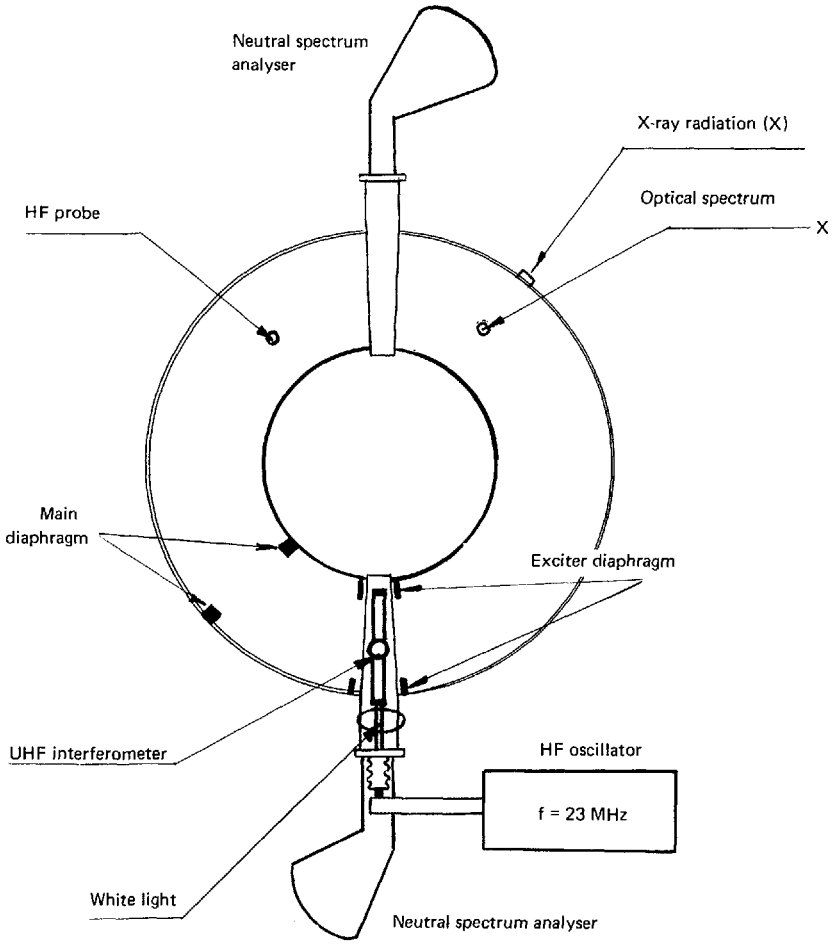


FIG.1. Diagnostic equipment.

types of ions can be used to produce a plasma with two ion components [12]. The third point of this paper involves a study of the magnetoacoustic method of obtaining a two-component plasma.

As is noted in Ref.[2], the injection of too much HF power into the tokamak plasma at the second harmonic of the ion cyclotron frequency resulted in the development of a stripping instability. Excitation of this instability was observed in our experiments on T-4, as well. Therefore, a great deal of attention is given the explanation of its causes in this work. For this reason, both changes in the plasma state which take place when the HF power level is below the instability excitation threshold and the dynamics of instability development when the HF power level exceeds this critical value were studied.

Deuterium with a small admixture of hydrogen, amounting to several percent, was used as the working gas in experiments. The strength of the toroidal magnetic field varied within 10 to 35 kOe. The following methods were used to study the plasma parameters: optical measurements of spectral-line intensity and the overall radiation intensity in the visible range, diamagnetic measurements, spectral analysis of charge-exchange atoms being emitted from the plasma at right angles to the direction of the toroidal magnetic field, intensity measurement and spectral analysis of soft-X-ray radiation, probe measurements of the pinch position, magnetohydrodynamic activity and HF field amplitude of the magnetoacoustic oscillations near the chamber wall, measurements of plasma concentration and basic electronic measurements. The basic diagram for the arrangement of the construction parts of tokamak T-4 diagnostic instruments and the HF exciter is shown in Fig.1.

The exciter was introduced into the unit chamber through a lateral branch pipe; it was a stainless-steel loop uninsulated from the plasma by a dielectric which encircled the pinch and which was located in the diaphragm shadow. The excitation loop was further protected from the plasma by two molybdenum diaphragms at a distance of several centimetres from each side of the loop.

In accordance with our concepts, the operation of an excitation loop uninsulated from the plasma by a dielectric was based on the vacuum insulation effect which should occur when the amplitude of the HF electric field exceeds the level of the secondary electron resonance discharge. Under these conditions, the electron multiplication mechanisms are absent in the interelectrode gap and its electrical strength should be extremely high. In this case, apparently, spontaneous removal of plasma entering this interelectrode gap from the outside is possible. Spontaneous removal should occur because of the action of the high-intensity HF electric field which, by preventing the penetration of secondary electrons into the interelectrode gap, creates an area of constant positive potential there and accelerates plasma flow to the electrodes along the lines of force of a constant magnetic field. The spontaneous removal process requires the expenditure of some HF power and is amplified by plasma turbulence and heating in the interelectrode gap by the HF electrical field. These phenomena can occur, of course, only when the electrode surfaces are sufficiently clean and especially when there are no oil or other dielectric films on them.

No basic differences in HF exciter behaviour from an exciter of similar design used earlier on tokamak T0-1 [3,4] were observed in our experiments. With relatively great HF voltage amplitudes exceeding 3–4 kV, the current through the excitation loop was proportional to the voltage and depended little on plasma occurrence. In doing this, the HF oscillator was subjected to a residual load even when natural magnetoacoustic oscillations were not excited in the plasma, and capacitive action on the plasma was absent. The HF power consumed in doing this was expended, apparently, on heating the plasma entering the gap between the loop and the protective diaphragms, and in spontaneous removal of plasma from this gap; the nature of the dependency of this power on the amplitude of the applied HF voltage is shown in Fig.2. It can be seen from the drawing that the power introduced there increases considerably more slowly than the square root of the amplitudes of the applied HF voltage (broken curve). This fact indicates the non-linear nature of the applied load and that part of the HF power being wasted in the area of the excitation loop is removed as the voltage amplitude increases. It should be noted that this parasitic load depends to a great extent on the discharge mode of the tokamak, and, in particular, it drops rapidly when the strength of the toroidal magnetic field is increased. When the stripping instability develops, parasitic charging increases sharply.

It is well known that resonance conditions must be fulfilled to excite the natural magneto-acoustic oscillations of a pinch:

$$\omega = \frac{\mu}{b} \frac{H_z}{\sqrt{4\pi M n}} \qquad (1)$$

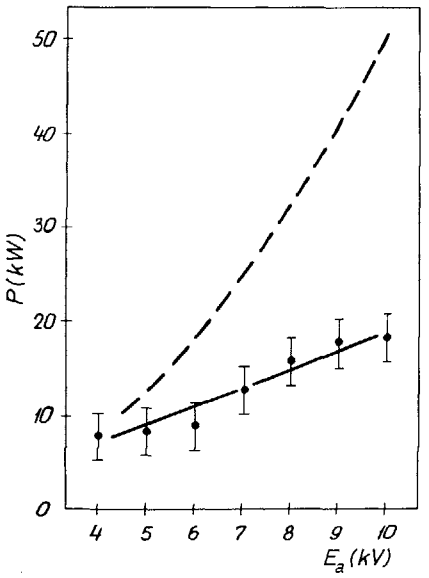


FIG.2. HF oscillator power as a function of the anode voltage amplitude in the absence of natural magnetoacoustic oscillations in the plasma volume.

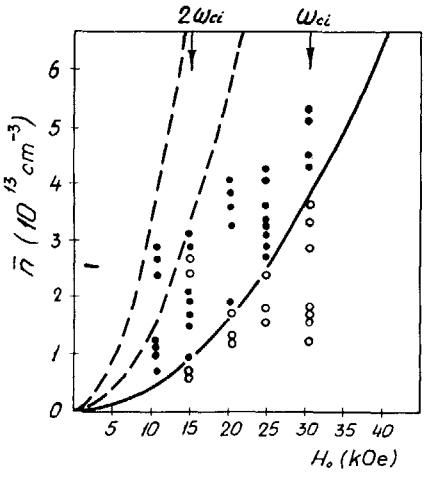


FIG.3. Excitation region of the natural magnetoacoustic oscillations. Solid curve: boundary of existence of lowest radial types. Dotted lines: that of the first and second radial harmonics. ● oscillations excited; ○ oscillations unexcited.

where ω is the cyclic frequency of the oscillations, b the small radius of the tokamak chamber, H_z the strength of the constant linear magnetic field, M the ion mass, $\bar{n}$ the plasma density, and μ are eigenvalues depending on the type of oscillations and shape of the radial distribution of the plasma density in the pinch cross-section.

If the eigenvalue μ corresponding to the lowest type of oscillations which can be excited in this system is substituted in formula (1), this formula shows the boundary of the discharge parameter variation range and where the magnetic sound can be excited. The result of this substitution, in which experimental values $\omega = 2\pi \times 23$ MHz; B = 20 cm, $M = 3.4 \times 10^{-24}$ g were used, is shown in Fig.3. A value of $\mu = 4.6$ corresponding to the lowest type of axisymmetric oscillations in the pinch with a parabolic profile of the plasma density distribution n, was chosen as the eigenvalue. The experimental points entered on this drawing are in good agreement with the results of calculations.

The change in the shape of the natural oscillation spectrum when the strength of the toroidal magnetic field changes is shown in Fig.4. Here the tokamak discharge mode is maintained in such a manner that the plasma concentration is kept at one level which reaches a maximum of 10^{13} cm^{-3} from discharge to discharge. The appearance and gradual crowding of the natural oscillation spectrum when the toroidal magnetic field is weakened can be seen from the oscillograms submitted. In addition, broadening of spectral lines near $H_z = 15$ kOe, corresponding to the conditions of ion cyclotron resonance in the hydrogen, can be noted on the oscillograms.

The development of plasma magnetohydrodynamic activity recorded by low-frequency magnetic probes which measured the poloidal component of the variable magnetic field was accompanied by the occurrence of considerable amplitude modulation of the signals from the high-frequency magnetic probes which measured the linear component of the magnetoacoustic wave field. This effect, which is illustrated by the oscillograms in Fig.5, is apparently explained by the periodic change in the HF magnetic probe connection to the plasma volume when the excited pinch is rotated.

The magnetoacoustic method of obtaining plasma with two energy components is based on the nature of the dependency of magnetoacoustic wave polarization on the ratio between the oscillation frequency and the ion cyclotron frequency. In a plasma consisting of one type of ion, the magnetoacoustic wave has cyclic polarization at a frequency $\omega = \omega_i$, while the electric field vector rotates in the direction opposite to the ion Larmor rotation. In this case, cyclotron absorption is weak and only due to finite spatial dispersion.

In a plasma consisting of two types of ions, the magnetoacoustic wave propagating at one of the two cyclotron frequencies has elliptical polarization and should be effectively absorbed by transferring its energy to the resonance ions [12,13]. Under these conditions, the plasma quality, based on Ref.[12], is expressed by the formula

$$Q = 2\frac{n_{iD}b}{n_{iH}R}\left[1 + \left(\frac{3}{4}\frac{n_{iH}R}{n_{iD}\rho_{iH}\ell}\right)^2\right] \qquad (2)$$

while maximum absorption should be observed when the fraction of resonance ions in the plasma is several percent. In this formula n_{iH}, n_{i0} are the hydrogen and deuterium ion densities, respectively, ρ_{iH} is proton Larmor radius, R is the large radius of the torus, and ℓ the number of waves around torus.

The energy distribution analyser for the charge-exchange neutrals being emitted from the plasma at right angles to the direction of the toroidal magnetic field which was used in our experiments made it possible to study hydrogen and deuterium distribution separately. The analyser was mounted in two ways: in the chamber cross-section, where the HF exciter was located, and in the diametrically opposed cross-section.

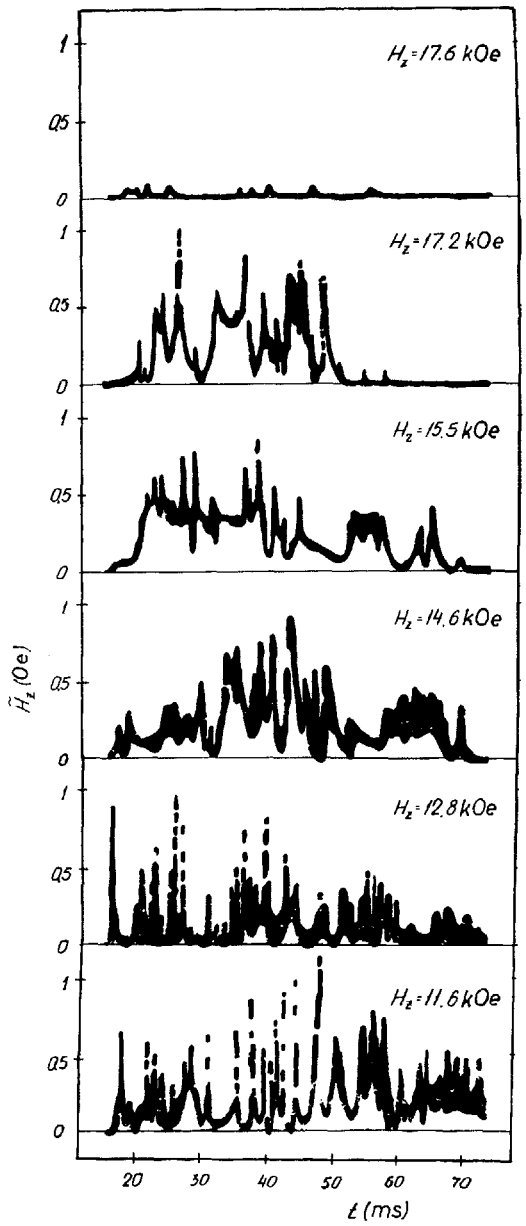


FIG.4. Temporal change signal detected with magnetic probe as a function of toroidal magnetic field strength.

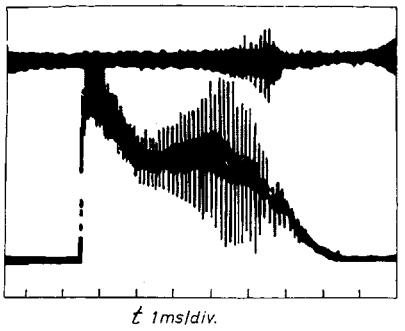


FIG.5. Amplitude modulation of signal from the high-frequency probe, as a function of plasma magneto-hydrodynamic activity.

The experiments were conducted in two tokamak discharge modes which differed in the strength of the toroid magnetic field, H_z = 15 kOe and H_z = 21 kOe. In these two modes, the plasma density at the instant the HF oscillator was engaged was kept the same, equal to $\bar{n} = 10^{13}$ cm^{-3}. In the H_z = 15 kOe mode, at which the oscillation frequency matched the cyclotron ion frequency for hydrogen and its second harmonic that for deuterium, engagement of the HF oscillator resulted in excitation of the natural magnetoacoustic oscillations of the pinch and was accompanied by a strong change in the hydrogen distribution function (see Fig.6a). In doing this the plasma quality measured from the shape of the resonance curves [14] was $Q = 3 \times 10^2$; this is in good agreement with the quality estimation from formula (2), and the level of the HF power injected into the plasma does not exceed 50 kV. It should be noted that, in accordance with estimations, under these conditions absorption in pure deuterium plasma would be $Q = 3 \times 10^3$, and the quality calculated from absorption in the chamber walls would be $Q = (2 - 5) \times 10^3$.

It can be seen from Fig.7a that HF heating leads to a considerable increase in the energy content of the small hydrogen admixture, especially in the "tail" of its distribution function. This effect is not observed in the H_z = 21 kOe mode, when the cyclotron resonance condition is not fulfilled and natural magnetoacoustic oscillations in the plasma are not excited as a result of the limits being exceeded (see Fig.6b).

When the neutral analyser is placed in one section of the chamber with the HF exciter, along with heating of the hydrogen admixture, which takes place only when the cyclotron resonance condition is fulfilled, a measurement of the hydrogen and deuterium distribution functions was observed which did not depend on the fulfillment of the resonance conditions (see Fig.7). This change was due to local heating of the plasma by the HF fields of the excitation loop. This assumption is confirmed by data concerning the life-time of particles of various types of energy, which are demonstrated in Fig.8.

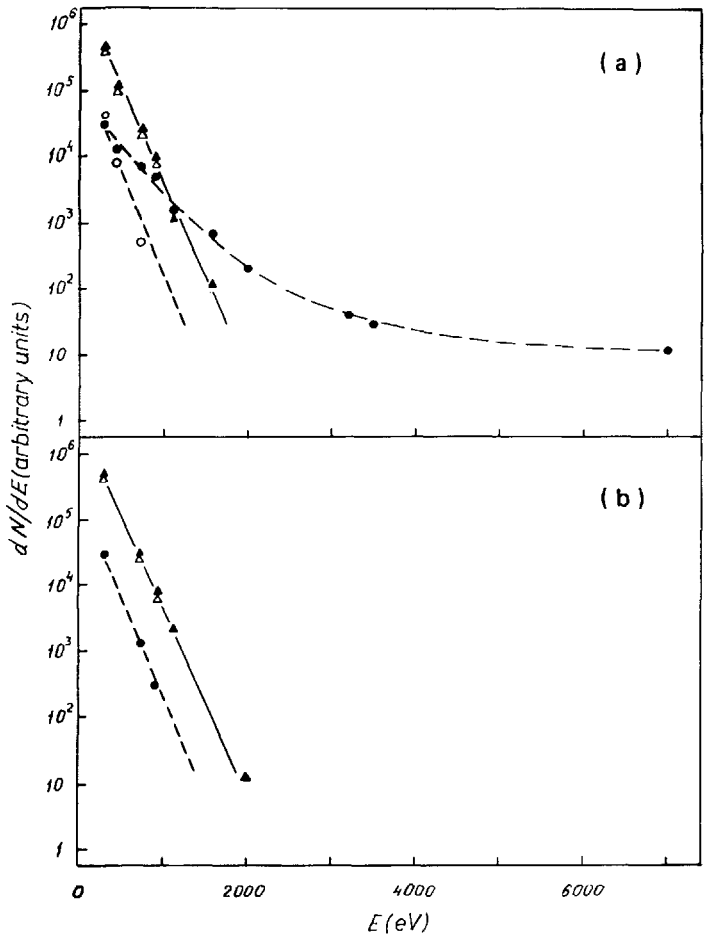


FIG.6. Energy spectra of charge-exchange atoms of hydrogen (dotted curves) and deuterium (solid curves) in a 15 kOe field (a) and in a 21 kOe field (b). Symbols: ○ hydrogen; △ deuterium in the absence of HF heating; ● hydrogen; ▲ deuterium during HF heating.– The analyser was located in the opposite cross-section of the exciter.

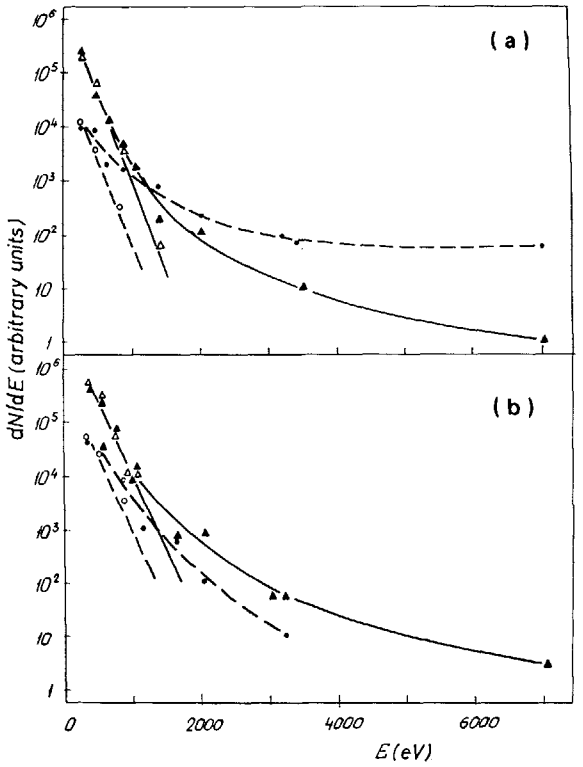


FIG.7. Energy spectra of charge-exchange atoms in a 15 kOe field (a) and in a 21 kOe field (b) in the HF exciter cross-section. The symbols are the same as those for Fig.6.

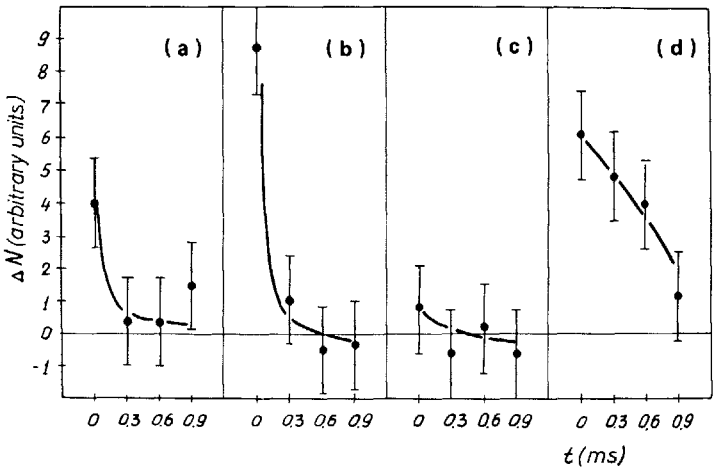


FIG.8. Temporal change of intensity of charge-exchange atomic current of deuterium with an energy of 500 eV (a) and 1080 eV (b) and of hydrogen with an energy of 500 eV (c) and 920 eV (d). The intensity level in the atoms of HF heating is assumed for the beginning of the calculation. The analyser was located in the exciter cross-section.

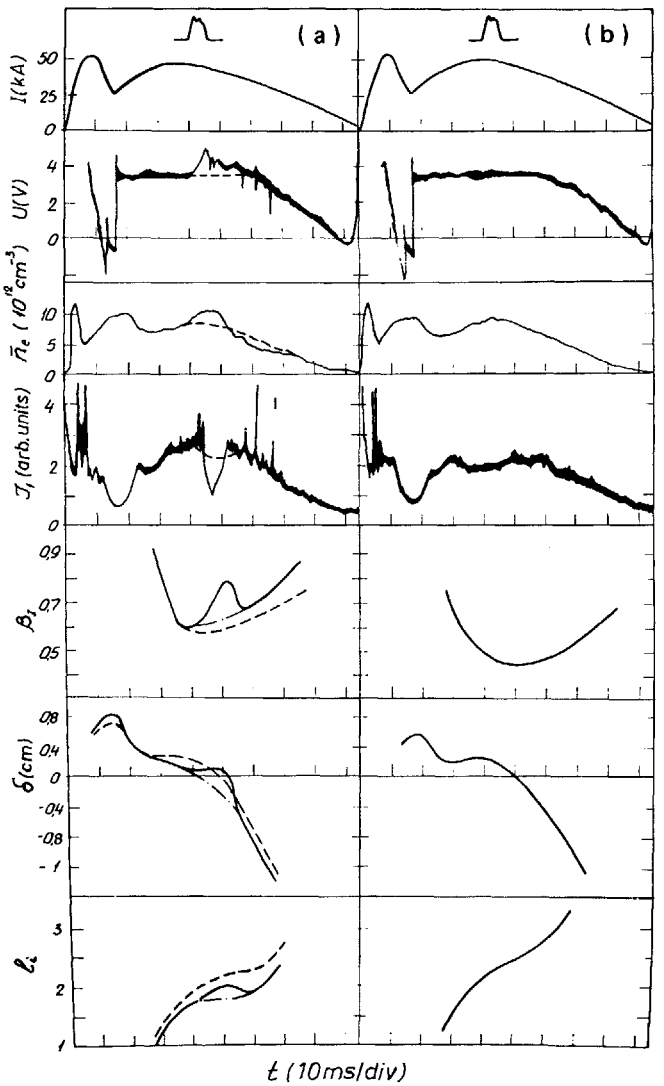


FIG.9. Temporal change of current I, discharge voltage U, plasma density $\bar{n}_e$, radiation intensity in the visible range J_1, the value of β_1, bias δ, and internal inductance ℓ_i of the pinch in a 15 kOe field (a) and in a 21 kOe field (b). The instant the HF oscillator was engaged is shown at the top of the drawing. The behaviour of the signals in the absence of a HF pulse is shown by the dotted line.

Together with the change in the proton energy distribution function, engagement of the HF oscillator affects a host of other plasma parameters. This effect, which is demonstrated together in Figs 9, 10, 11, was observed only when the resonance conditions were fulfilled and the natural magnetoacoustic oscillations were excited in the plasma. Excitation of the oscillations resulted in an increase in plasma density and energy content, displacement of the pinch outwards and an increase in its internal inductance. In this case, the radiation intensity in the visible

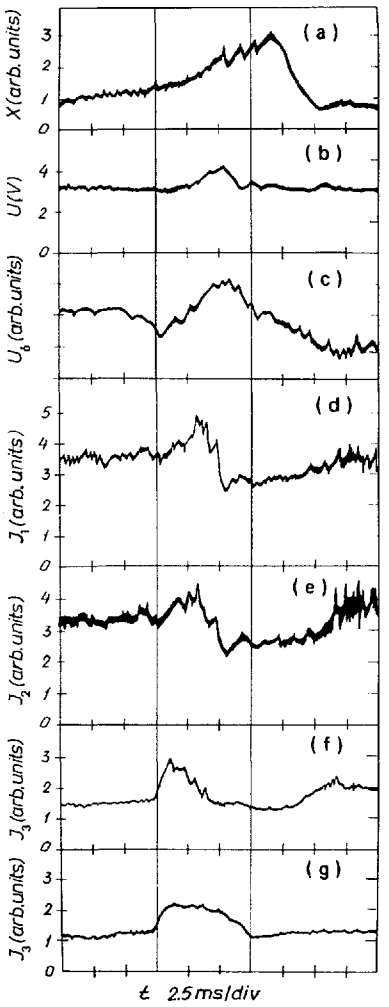


FIG.10. Temporal change of intensity of soft-X-ray radiation (a), discharge voltage (b), difference signal of magnetic bias probes (c), radiation intensity in the visible range from the diaphragm (d) in the opposite cross-section (e), and in the exciter cross-section (f) in a 15 kOe field. The HF oscillator was engaged for 40 ms of the discharge, the pulse duration is shown by the vertical lines. The intensity signal J_3 in the 21 kOe field is shown (g).

range of the spectrum first increased, then decreased during the HF pulse. These changes in visible radiation occurred simultaneously along the entire length of the pinch, including the cross-section where the main diaphragm and HF exciter were placed; the increase in light intensity was primarily determined by the contribution of low-ionized impurity lines. At the same time, an increase in soft-X-ray radiation intensity from the central region of the plasma was observed which was accompanied by saw-toothed oscillations during the HF pulse [15].

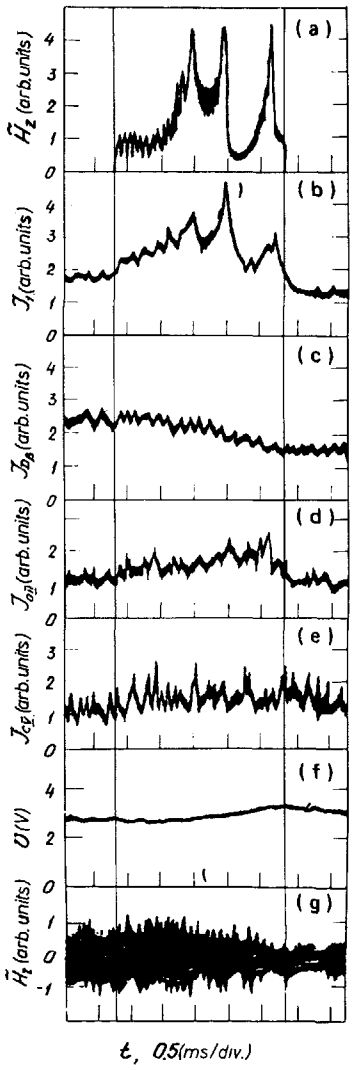


FIG.11. Temporal change of signal amplitude detected with magnetic probe 4(a), radiation intensity in the visible range (b), line intensity of deuterium (c), oxygen (d), carbon (e), discharge voltage (f) and plasma magnetohydrodynamic activity (g) in a short scan. The duration of the HF pulse is shown by the vertical lines.

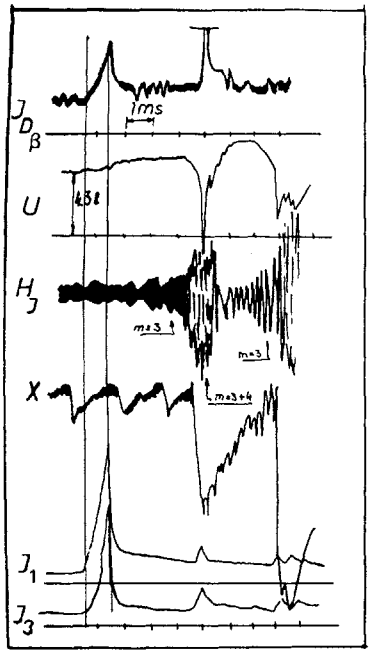


FIG.12. Temporal change of line intensity D_β, discharge voltage U, signal of low-frequency magnetic probe $\tilde{H}_J$, intensity of soft-X-ray radiation X, radiation intensity in the visible range of the spectrum J_1 and at a distance J_3 below the exciter. The duration of the HF pulse is shown by the vertical lines.

The nature of the change in the X-ray signal, together with data concerning the increase in internal inductivity of the pinch, indicates a sharp fall in the profile of the radial discharge current distribution. The drop in magnetohydrodynamic activity of the plasma is apparently explained by this drop.

When the HF power injected is increased in this mode, a stripping instability is observed. It may be assumed that it is due to intense cooling of the pinch periphery as a result of the introduction of impurities from the chamber and diaphragm walls. Is this introduction associated with the appearance of high-energy ions in the plasma vessel? Our results on the excitation of magnetic sound at the ion cyclotron frequency of deuterium are inconsistent with this explanation.

The change in time of several discharge characteristics in a field $H_z = 30$ kOe is shown in Fig.12. The HF oscillator was engaged near the maximum of the discharge current with plasma densities of $\bar{n}_e \cong 4 \times 10^{13}$ cm^{-3}. It can be seen from the drawing that 3 ms after the HF pulse is completed, instability accompanied by increasing magnetohydrodynamic activity of the plasma and a powerful change in the X-ray signal in the central region of the pinch occurs in the plasma. In this case, in accordance with the readings on the neutral analyser, no changes in the charge-exchange atom spectrum are observed during the HF pulse. It should also be noted that in this case absorption of magnetoacoustic oscillations in the plasma at a frequency $\omega = \omega_i$ is negligibly small in comparison to absorption in the chamber walls. The observed powerful build-up of HF fields in the plasma is associated with this.

The following basic conclusions can be drawn from these results:

A HF exciter uninsulated from the plasma with a dielectric demonstrated its high electrical strength and the possibility of using it in charged modes with regard to large-scale Tokamak T-4.

The range of tokamak discharge parameters in which natural magnetoacoustic oscillations of the pinch are excited is in good agreement with the results of calculations.

It is shown that in deuterium plasma containing a small hydrogen admixture, the excitation of magnetoacoustic oscillations at the ion cyclotron frequency of the protons results in effective absorption of oscillation energy by these resonance ions, in their preferred heating and the occurrence of a plasma ion state with two energy components.

It was established that the stripping instability which develops when injecting a large HF power into the plasma is not the result of local action of the HF exciter, and, apparently, is not associated with the appearance of a high-energy "tail" in the ion distribution function in the plasma.

REFERENCES

[1] VDOVIN, V.L., ZINOV'EV, O.A., IVANOV, A.A., KOZOROVITSKIJ, L.L., KROTOV, M.F., PARAIL, V.V., RAKHIMBABAEV, Ya.R., RUSANOV, V.D., SHAPOTKOVSKIJ, N.V., Pis'ma Zh. Ehksp. Teor. Fiz. **17** (1973) 2.

[2] ADAM, G., CHANCE, M., EUBANK, H., GETTY, W., HINNOV, E., HOOKE, W.M., HOSEA, J., JOBES, F., PERKINS, F., SINCLAIR, R., SPERLING, J., TAKAHASHI, H., in Plasma Physics and Controlled Nuclear Fusion Research (Proc. 5th Int. Conf. Tokyo 1974) **1**, IAEA, Vienna (1975) 65.

[3] IVANOV, N.V., KOVAN, I.A., KOZLOV, P.I., LOS', E.V., SVISHCHEV, V.S., SHVINDT, N.N., Pis'ma Zh. Ehksp. Teor. Fiz. **16** (1972) 88.

[4] IVANOV, N.V., KOVAN, I.A., in Plasma Physics and Controlled Nuclear Fusion Research (Proc. 5th Int. Conf. Tokyo, 1974) **1**, IAEA, Vienna (1975) 255.

[5] IVANOV, N.V., KOVAN, I.A., At. Ehnerg. **40** (1976) 241.

[6] IVANOV, N.V., KOVAN, I.A., At. Ehnerg. **40** (1976) 240.

[7] DAWSON, I.M., FURTH, M.P., TENNY, F.M., Phys. Rev. Lett., **26** (1971) 1156.

[8] DEMIRKHANOV, R.A., KURSANOV, Yu.V., SKRIPAL', L.B., At. Ehnerg. **34** (1973) 490.

[9] PISTUNOVICH, V.I., At. Ehnerg. **35** (1973) 11.

[10] GOLOVIN, I.N., PISTUNOVICH, V.I., SHATALOV, G.E., I.V. Kurchatov Institute of Atomic Energy Preprint, Moscow, 1973.

[11] FURTH, H.P., YASSBY, D.L., Phys. Rev. Lett. **32** (1974) 1176.

[12] STIX, T.H., Nucl. Fusion **15** (1975) 737.

[13] KLIMA, R., LONGINOV, A.V., STEPANOV, K.N., Zh. Tekh. Fiz. **46** (1976) 704.

[14] IVANOV, N.V., KOVAN, I.A., At. Ehnerg. **38** (1975) 229.

[15] VON GOELER, S., STODIEK, W., SAUTHOFF, N., Phys. Rev. Lett. 33 (1974) 1201.

DISCUSSION

ON PAPER IAEA-CN-35/G10

T. CONSOLI: RF heating results are to some extent similar to those obtained with neutral beam heating. With neutral beam heating about 20% of the applied power goes to the ions. In the Wega experiment, too, more than 20% was transferred to the ions at the lower hybrid frequency without destroying the equilibria and the stability of the discharge. In neither case was the electron temperature increased. A disadvantage of RF heating, for the time being at least, is the production of fast ions in a region where they are not desired. The main problem, then, is to understand and control the exact mechanism of their production.

J. ADAM: In a similar experiment performed in the ST tokamak in 1974 it was observed that (i) the maximum RF power the plasma is able to stand without disruption depends on the cleanness of the wall, and that (ii) disruptions may occur after the RF pulse. This indicates that the occurrence of disruptions is not directly related to the presence of the wave field, but only indirectly through enhancement of wall outgassing.

Session XIX

HIGH BETA IV

Chairman

F. Hintz
FRG

Papers E 13-1 and E 13-2 were presented
by K.-H. Steuer as Rapporteur

LIMITS IN THE PRODUCTION OF A LOW COMPRESSED HIGH-BETA PLASMA IN THE LINEAR THETA PINCH ISAR II

W. KÖPPENDÖRFER, M. MÜNICH, J. SOMMER
Max-Planck-Institut für Plasmaphysik,
Garching,
Federal Republic of Germany

Abstract

LIMITS IN THE PRODUCTION OF A LOW COMPRESSED HIGH-BETA PLASMA IN THE LINEAR THETA PINCH ISAR II.

The production of a shock-heated low compressed plasma was investigated in the linear experiment Isar II in preparation for a toroidal high-beta stellarator experiment. Compression ratios between 2.75 and 3 could be obtained at ion temperatures of 600 eV, electron temperatures of 70 eV, and electron densities of 2×10^{21} m^{-3} on axis. To achieve this, a special magnetic field pulse and a filling pressure of 4 mtorr was necessary. This filling density turned out to be the low limit at which ignition and preheating is still possible without contaminating the plasma too much and at which preheating and sufficient sweep-up of plasma in the main discharge is still possible. The neutron emission in series of discharges in deuterium and hydrogen, the measurement of hydrogen, deuterium and oxygen concentration and the investigation of quartz samples exposed to the discharges, revealed that the plasma interacts strongly with the vessel walls during its production. The walls were found to store 2×10^{20} particles per m^{-2} and about half the gas filling is exchanged by the wall surface in every discharge. The equilibrium radial density profile acquired a smooth Gaussian-like shape at 4 mtorr filling pressure. It starts to develop during the implosion phase and becomes strongly influenced by flute-type azimuthal modes of about 1.6 cm wavelength. The electron temperature stays at $T_e \approx 70$ eV smaller than the ion temperature. If circular cylindric symmetry is assumed, the current sheath and the electron energy equation yield an effective collision frequency of $\nu_{eff} = 0.3\ \omega_{pi}$ well in agreement with other experiments. If, however, the current is assumed to flow on the flute distorted surface, a considerably smaller collision frequency can explain the observed electron temperature. The increased current drift velocity could in this case suffice to drive ion sound instabilities.

1. Introduction

The toroidal high-beta stellarator, HBS II, presently under construction in Garching, requires a shock-heated high-beta plasma of small compression ratio in order to enable wall stabilization of $m = 1$ long-wave modes. The plasma parameters envisaged for HBS II are $n_e \approx 10^{21}$ m^{-3}, $T_i \approx 0.5 - 1$ keV, $T_e < T_i$, $0.6 \lesssim \beta \lesssim 0.8$ and a compression ratio of $\kappa = R_{coil}/R_{pl} \approx 2 - 2.5$. The initial plasma density of 2.5×10^{20} m^{-3} corresponds to a filling pressure of 4 mTorr deuterium or hydrogen. For the 20-cm diameter pinch coil, a field rise of 1.2×10^6 T s^{-1} is required over 0.5 microseconds. Thereafter, the magnetic field should stay constant at about 0.6 T.

These parameters and values resulted from applying the following conditions:

- sufficient high filling density to enable ionization and preheating in the microsecond time scale;
- sufficient high filling density such that neutrals can be ionized and effectively swept up by the shock in order to minimize charge exchange losses in the equilibrium state;
- high ion- and electron temperatures produced by the shock for achieving a low compression ratio and for reducing radiation losses. This requires a low filling density and a fast magnetic field rise.

In provision of the HBS II project, the linear theta-pinch experiment Isar II was used for investigating the shock and the plasma equilibrium in the low compressed state. Results of this experiment have been described in [1, 2]. Most discharges were carried out at 4 mTorr deuterium or hydrogen filling pressure, some at 2.2 mTorr and 11.5 mTorr. In this regime, a collisionless shock implosion occurs comparable to several other experiments, e.g. [3, 4, 5, 6, 7]. The high Mach number shock, initially without applied fields, produces hot ions whereas the electron temperature stays low in the shack area, as in [3], in contrast to experiments at still lower filling densities [4, 5, 6]. A filling pressure of 4 mTorr deuterium was found to be about the low limit at which reproducible discharges were still possible, especially if full ionization is required by the preheating discharges.

Two problems essentially arise at low densities which will be discussed in the following. Firstly, the quartz vessel walls get involved when collisions get rare in the gas volume. This brings about that a considerable amount of gas can be stored and released by the walls. Also as a consequence of wall contact, the impurity concentration in the plasma rises and a larger fraction of the plasma energy may be lost by radiation on a long time scale.
Secondly, Rayleigh Taylor-like flute instabilities of large amplitude appear at low densities which lead to a smooth radial density distribution in equilibrium. It does not seem possible to produce a "flat top" high-beta plasma profile at densities $n \leq 10^{21}\,m^{-3}$ and at radii $R_p \leq 5$ cm.
Measurements and experimental results are presented in Section II. In Section III, the influence of the vessel walls is discussed. The properties of the imploding plasma from the experimentalist point of view are discussed in Section IV and compared with other experiments.

II. Measurement and Experimental Results

Two axial discharges of 80 kV and 120 kV charging voltage preceded the theta-pinch discharge, the first serving for breakdown and the second for preheating the plasma. The reproducibility of the discharges could be considerably improved by filling up the tube to 11 mTorr filling pressure first and then pumping the gas off through a throttle valve with a decay time of 1.5 seconds. The moment the desired pressure was reached, the discharges were successively triggered. By this method, it was possible to operate down to 2.2 mTorr but with less reliable reproducibility at this low pressure limit.

The plasma was observed by an image converter and streak camera, the diamagnetic flux measured by loops. For measuring the electron density, an axial interferometer with a rotating mirror operating at 3.3 micron in the infrared and at 0.7 micron wavelength in the visible was used. In addition, moment pictures of the radial density profile were taken by holographic interferometry. Neutron rates were obtained from a scintillation counter. The electron temperature was measured in the midplane at R = 0 and R = 3 cm by help of 90° laser scattering. Spectral lines were observed in the visible side-on and end-on by monochromators. For separating the hydrogen and deuterium H_α and D_α lines, a light pipe multichannel slit assembly was used.

Full ionization with respect to the filling density could only be obtained with a ringing preheating discharge of 50 kA maximum current and 13 microseconds decay time. At the moment when the electron density started to fall below the filling density value, the theta pinch was triggered. In the beginning of the experiments and whenever the quartz tube had been flushed with air, the vacuum walls were usually cleaned by

Table I

Oxygen impurity concentration in per cent in discharges with 4 mTorr deuterium filling pressure

Case 1:	preheating discharge, ringing I_{max} = 50 kA		
	preheater:	1. half wave	0.5 %
		2. half wave	3.8 %
	main discharge:		4.6 %
Case 2:	preheating discharge, damped I_{max} = 15 kA		
	preheater:		0.3 %
	main discharge		1.4 %

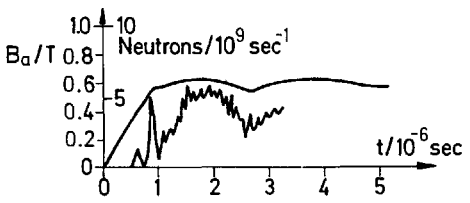


FIG.1. Magnetic field and neutron emission.

30 ringing theta-pinch discharges until all indications of an increased impurity content had vanished. In Table I, the oxygen impurity content of "clean" discharges is given. It increases with every plasma wall contact and reaches a maximum in the theta-pinch discharge. It can be lowered by damping the preheating current, but as a consequence, the degree of ionization falls below 50 percent.

The time development of the magnetic field together with a typical neutron emission pulse is shown in Fig. 1. In paper /2/, the experimental finding was described such that the neutron pulse does not vanish if the deuterium is replaced by a hydrogen filling. The characteristic features found were, if series of discharges in deuterium are followed by those in hydrogen and vice versa:

- the number of neutrons per discharge jumps when the filling gas is changed;
- after the jump, it decays exponentially over typically 15 to 25 discharges in hydrogen and rises somewhat faster if deuterium discharges follow those in hydrogen.

These observations could be quantitatively described by a model assuming that only a fraction of the filling gas enters the discharge volume directly. The other fraction enters a reservoir which releases about the same amount of gas with the composition of its momentary content, to the discharge volume.

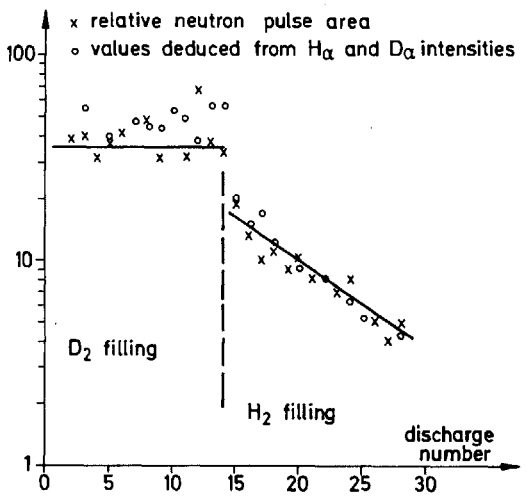


FIG.2. Comparison of hydrogen and deuterium concentration evaluated from emitted neutrons and from H_α and D_α intensities.

Two additional measurements for testing the model and assumptions were carried out. Firstly, the composition of the plasma, as deduced from the neutron emission model, was confirmed by evaluating the hydrogen and deuterium concentration from the measured H_α and D_α emission line intensity. In Fig. 2, the number of neutrons (crosses) emitted per discharge is compared with the corresponding hydrogen and deuterium concentration by plotting also (circles) the expression $C \cdot \left(1 + I_{H\alpha}/I_{D\alpha}\right)^{-2}$ $I_{H\alpha}$ and $I_{D\alpha}$ are the Balmer line intensities measured in the main discharge and C is a normalizing constant. The assumption of the quartz vessel walls being the reservoir was confirmed by exposing two small samples of quartz glass to 110 discharges. They were analysed by Dr. Behrisch and Dr. Scherzer from the surface physics department of the Max-Planck-Institut für Plasmaphysik under 750 keV He^3 ion bombardment. The deuterium content of these quartz surfaces could be deduced from counting the 3 MeV α-particles produced by the $He^3(d,p)He^4$ reaction. This confirmed that about 2×10^{20} m^{-2} deuterons are stored in the quartz tube walls in full agreement with the value obtained from the reservoir model. Discharges with higher filling density (11.5 mTorr) showed considerably smaller plasma wall interaction.

The plasma parameters and dimensions of the equilibrated theta-pinch plasma have been already described in /1/. A typical density profile 1.6 microsecond after initiation of the theta-pinch discharge is shown in Fig. 3. The ion temperature obtained from the neutron emission amounts to 650 eV. This is in agreement with values from pressure balance for $\beta = 1$ on axis and $T_e = 70$ eV as measured by laser scattering (Fig. 4). The density profile can be approximated within the limits of error by $n_e = 10^{21} \ (1 + \cos \pi/2 \ R/R_H)$, for $R \leq 2 R_H$, with R_H being the half density radius. In the case of Fig. 3, $R_H = 3.5$ cm is obtained by yielding a compression ratio $\kappa = R_{coil}/R_{pl} = 2.8$.

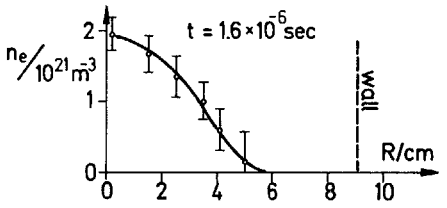


FIG.3. Equilibrium electron density profile measured by end-on interferometry.

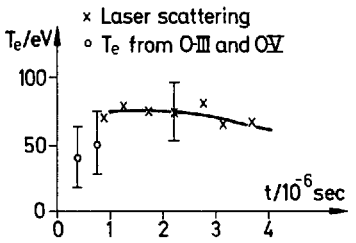


FIG.4. Electron temperature measured by laser scattering on axis and side-on from impurity radiation.

The circular symmetry of the profile at this time could be shown by a holographic interferogram. The ion temperature and the time behaviour of the diamagnetic flux agree essentially with results from a free-particle model [1]. The electron temperature of about 70 eV in the stationary phase can be quantitatively explained by equilibrating collisional energy transfer from the hot ions and axial energy loss by classical heat conduction [8].

The fact that only diffuse density and pressure profiles can be produced at this low filling pressure is less satisfactory. Instabilities appearing during implosion cause the diffuse profile. Axial image converter camera pictures and a side-on smear camera picture shown in Fig. 5 reveal short wavelength $\lambda = 1.6$ cm flute instabilities exactly parallel to the field lines. Similar instabilities were observed in other experiments, e.g. [6] and [7]. McKenna and co-workers [7] could show that perturbations in luminosity correspond indeed to strong density perturbations. In contrast to the Los Alamos experiment, one luminous ring and a simple peaked radial density profile appear during implosion in the present experiment. A possible explanation for this is seen in the fact that full ionization is provided in the Garching experiment whereas preionization produces a 15 per cent ionized plasma at 10 mTorr filling pressure in the Los Alamos experiment. The idealized slope of the magnetic field B^*, as shown in Fig. 6, was evaluated from the diamagnetic flux signal under the

[1] According to the initial temperature of $T_e = T_i = 5$ eV, the Mach number of the shock amounts to about $M = 8$.

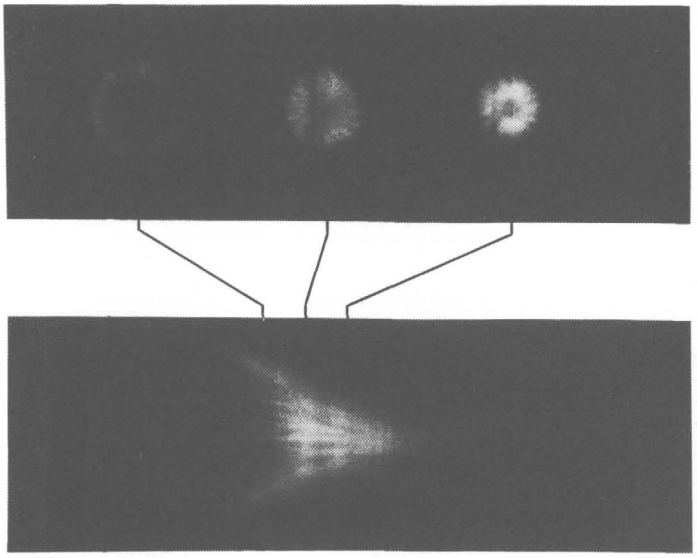


FIG.5. Flute instabilities during implosion observed end-on (upper part of photograph) by an image convertor camera and side-on by a smear camera.

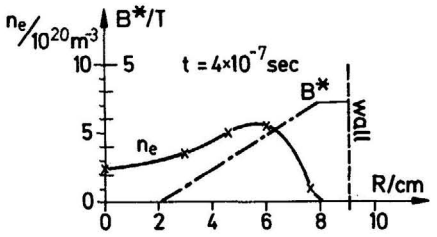


FIG.6. Electron density profile during implosion and magnetic field profile approximated from diamagnetic flux measurements.

assumption of a constant gradient. Magnetic probes could not be used because they were destroyed in the preheating discharges. The electron temperature, Fig. 4, was measured from 0.8 microseconds on at the positions R = 0 and R = 3 cm. Earlier in the discharge, it was deduced from the rise and decay of OIII and OV. In any case, the electron temperature stayed below 100 eV. Up to about 2 microseconds, the laser scattering results gave slightly higher temperatures in the current sheaths than on axis: T_e (R = 3 cm, t = 1 μsec) = 90 eV and T_e (R = 0, t = 1 μsec) = 75 eV.
It should be mentioned that in case of a damped preheating discharge leading to insufficient ionization, $\alpha_i < 50\%$, the electron temperature rose to a value of T_e = 150 eV early in the theta-pinch discharge, probably due to the smaller electron density.

III. Discussion of the Plasma-Wall Interaction Observations

Different independent measurements of the plasma composition and the amount of deuterium stored in the quartz vessel walls have confirmed that the deuterium concentration $c_D = n_D/(n_D + n_H)$ decays during a number z of hydrogen discharges which follow a large number of deuterium discharges according to:

$$c_D = (1-\alpha)\exp[-(1-\alpha) N_0 R_G z/2 N_F] \quad (1)$$

α denotes the fraction of the filling gas which does not enter the discharge volume directly but is exchanged with gas in a reservoir, the walls. N_0 is the filling density, in m^{-3}, N_F the density of gas stored in the walls per m^{-2} and R_G the tube radius in m. In the other case if deuterium discharges follow a large number of discharges in hydrogen, the deuterium concentration rises like

$$c_D = \alpha + (1-\alpha)(1 - \exp[-(1-\alpha) N_0 R_G z/N_F]) \quad (2)$$

Relation (1) and (2) allowed the measurements at 4 mTorr to be interpreted satisfactorily with $0.4 \lesssim \alpha \lesssim 0.5$ and $N_F \approx 2\times10^{20}$ m^{-2}. At 2.2 mTorr, the reproducibility of the discharges did not suffice to evaluate data. At 11 mTorr, the more sudden change of neutron yield with the filling gas gave evidence that, at higher filling density, the walls are of minor importance.

Since these results were obtained from the theta-pinch plasma, the essential plasma wall interaction occurs in the breakdown and preheating discharges. The successive increase of oxygen impurity in the sequence breakdown-, preheating- and theta pinch discharge as well as the x-ray emission, give evidence that particles of quite different energies impinge against the walls during the build-up of the plasma. Surprisingly, the assumption of stationarity of a sequence of discharges required to derive relation (1) and (2) is not contradicted by the experimental results. This requires that the number of particles being trapped in the quartz walls per discharge expel approximately the same number out of the walls. For achieving stationary conditions, however, wall cleaning by many ringing theta-pinch discharges was necessary. At 2.2 mTorr filling pressure, reproducibility could not be obtained in this respect.

IV. Discussion of the Implosion Phase

According to the measured plasma data, the shock can be classified as a collisionless high Mach number $M \approx 8$ shock with $T_e < T_i$. In the latter respect, it is similar to the shock reported by Keilhacker et al. [3]. Usually diffusion and electron heating is described by an effective collision frequency ν_{eff}. For estimation, the energy equation of the electrons can be approximated by a collisional heating term and a heat conduction term assuming a temperature-independent effective collision frequency:

$$\frac{dT_e}{dt} = \frac{m_e \nu_{eff}}{k e^2 n_e^2} j^2 - \frac{k T_e^2}{m_e \nu_{eff} L^2} \quad (3)$$

Adiabatic heating and collisional energy transfer from hot ions were neglected. j is the current density and L essentially the length of the theta pinch. For constant j and ν_{eff}, Eq. (3) can be simply integrated. If, for $\nu_{eff} = 0.3\ \omega_{pi}$ is set according to the findings of several authors [3, 5, 6], the electron temperature becomes

$$T_e = 1.08 \cdot 10^{11}\, j\, n_e^{-1/2}\, \frac{1 - e^{-\tau}}{1 + e^{-\tau}} \quad {}^{\circ}K \qquad (4)$$

in practical units with τ being

$$\tau = 1.7\, v_D/L \cdot t \qquad (5)$$

and v_D being the electron current drift velocity. For the data of Fig. 6, $j = 5 \times 10^6$ A/m^2; $n_e = 4 \times 10^{20}$ m^{-3}; L = 1 m and t = 4×10^{-7} s, an electron temperature of $T_e = 7.2 \times 10^5$ °K or $T_e = 63$ eV is obtained. Surprisingly, Eq. (4) yields also about correct electron temperatures for all shock experiments referred to [3, 4, 5, 6], regardless whether $T_e/T_i < 1$ or $T_e/T_i > 1$ and whether, according to theory, ion sound or Bunemann type or lower hybrid drift instabilities may be excited [9, 10].

This, however, can be only a phenomenological interpretation, not a physical one, because the plasma lacks circular cylindrical symmetry during the shock implosion. The plasma surface shows strong corrugations over the azimuth; in the described experiment in average 24 wavetrains. Their amplitude is usually larger than their wavelength. The accelleration dependence and the fact that they vanish after first implosion hint at accelleration-dependent instabilities. The growthrate of Rayleigh Taylor instabilities $\gamma = 10^7$ sec for 1.6 cm wavelength is well in the range of experimental observation. A collision frequency of $\nu_{eff} = 10^9$ sec^{-1} would provide the necessary resistance to limit the shortest, most unstable wavelength to the observed 1.6 cm, a value by a factor of ten below $0.3\ \omega_{pi}$.

The current density on the corrugated surface, however, differs largely from the value of $j = 5 \times 10^6$ A/m^2 of Fig. 6. If a current sheath thickness of $\lambda/4$ is assumed, a ten times larger current density of $j = 5 \times 10^7$ A/m^2 results. In this case, a collision frequency of only $\nu_{eff} = 5.5 \times 10^7$ sec^{-1} is required to explain the electron temperature of 60 eV from relation (4) if ν_{eff} is retained and not replaced by $0.3\ \omega_{pi}$. The electron drift velocity would furthermore exceed the ion sound velocity and ion sound instabilities could develop.
This example gives evidence that the nature of the instability heating the electrons cannot be clearly determined without knowing the current density distribution. A two-dimensional nonlinearized theory only could help us understand the described observations.

Acknowledgement. The authors are gratefully indebted to Dr. R. Behrisch and Dr. B. Scherzer for analysing the quartz samples.

References

1 Braun, W., Correa, D., Engelhardt, W., Fünfer, E., Gruber, J., Herrnegger, F., Kaufmann, M., Köppendörfer, W., Lortz, D., Lotz, W., Münich, M., Neuhauser, J., Schneider, W., Schramm, G., Seidel, U., Sommer, J., in Plasma Physics and Controlled Nucl. Fusion Research (Proc. 5th Int. Conf. Tokyo 1974), 3, IAEA, Vienna (1975) 25.

2 Engelhardt, W., Köppendörfer, W., Münich, M., Sommer, J., Proc. 7th Eur. Conf. on Controlled Fusion and Plasma Physics, Vol. I, 50 Lausanne (1975).

3 Keilhacker, M., Kornherr, M., Niedermeyer, H., Steuer, K.-H., Chodura, R., in Plasma Physics and Controlled Nuclear Fusion Research, (Proc. 4th Int. Conf. Madison, 1971) 3, IAEA, Vienna (1971) 265.

4 Oktay, E., Desilva, A.W., Liewer, P.C., Chen, Y.G., Griem, H.R., Hess, R., Krall, N.Y. in Plasma Physics and Controlled Fusion Research (Proc. 5th Int. Conf. Tokyo 1974) 3, IAEA, Vienna (1975) 365.

5 Höthker, K., Nucl. Fusion 16 2 (1976) 253.

6 Chodura, R., Dum, C.T., Keilhacker, M., Kornherr, M., Niedermeyer, H., Protz, R., Söldner, F., Steuer, K.-H., in Plasma Physics and Contr. Nuclear Fusion Research (Proc. 5th Int. Conf. Tokyo 1974) 3 IAEA, Vienna (1975) 397.

7 McKenna, K.F., Kristall, R., Zimmermann, E.L., Phys. Fluids, 18 (1975) 1371.

8 Gula, W.P., Morse, R.L., Proc. 2nd Topical Conf. on Pulsed High Beta Plasmas, IPP-Garching Rep. 1/127 (1972)115.

9 Biskamp, D., Nucl. Fusion 13 (1973) 719.

10 Krall, N.A., Liewer, P.C., Phys. Fluids 15 (1972) 1166.

SHOCK HEATING OF COLLISIONLESS PLASMAS IN TOROIDAL GEOMETRY

F. SÖLDNER, K.-H. STEUER
Max-Planck-Institut für Plasmaphysik,
Garching,
Euratom Association,
Federal Republic of Germany

Abstract

SHOCK HEATING OF COLLISIONLESS PLASMAS IN TOROIDAL GEOMETRY.

Toroidal high-β plasmas with keV temperatures and small compression ratios are produced by fast magnetic compression in the High Voltage Belt Pinch. Two typical cases with different plasma behaviour are investigated: at an initial density of $n_{e0} = 3 \times 10^{13}$ cm^{-3} the magnetic field diffuses into the whole plasma and a mean β value of 0.4 is obtained. The electrons are heated up to 3 keV in the piston region. The ions swept up in the magnetic sheath receive an energy of 0.7 keV. 30% of the ions are reflected from the piston acquiring an energy of 2.5 keV. For an initial density of $n_{e0} = 7 \times 10^{13}$ cm^{-3}, a central plasma region with $\beta = 1$ is formed. The electron temperature reaches 1 keV in the sheath.The mean energy of the ions trapped by the magnetic piston amounts to 0.4 keV. 60% of the ions are reflected. In both cases, the electrons are heated by current-driven ion acoustic turbulence ($T_e > T_i$) with an effective collision frequency $\nu_{eff} \approx 0.6\ \omega_{pi}$. The same effective collision frequency determines the electron heat conduction perpendicular to the magnetic field in the turbulent region. The experimental results are in agreement with numerical calculations done with a fluid-particle hybrid code using transport coefficients for ion acoustic turbulence.

1. INTRODUCTION

Fast shock compression as a method of producing weakly compressed thermonuclear plasmas has been studied over many years in linear theta pinches. However, all these experiments are considerably affected by end losses. The electrons are cooled down by heat conduction parallel to the magnetic field lines already during the implosion stage. In toroidal experiments much higher electron temperatures are expected from numerical calculations suppressing electron heat conduction losses [1]. This may change the shock dynamics, e.g. the sheat formation, the onset of instabilities and the transport coefficients. In this paper, we report the first results of fast shock heating of low-density toroidal plasmas. The experiments are performed in a belt pinch with highly elongated plasma cross-section. This configuration has proved MHD-stability at low temperatures [2]. The confinement behaviour at keV temperatures will be investigated later on by crowbarring the shock bank.

2. EXPERIMENTAL SET-UP

2.1. The high voltage belt pinch

The coil system consists of two concentric coils (h = 118 cm, ϕ_i = 37 cm, ϕ_a = 85 cm) (Fig.1). They consist of helical windings which provide the current components producing simultaneously the compressing toroidal main field and the toroidal plasma current necessary for equilibrium. The coil is doubly fed in from Blumlein-type transmission lines, thereby inducing a poloidal electric field strength of 700 V·cm^{-1}. The toroidal magnetic field rises to a maximum

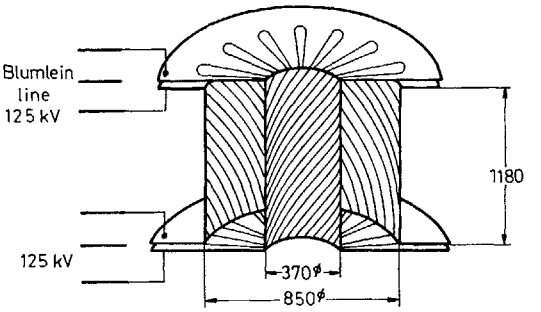


FIG.1. Coil system of High Voltage Belt Binch. Lengths are in millimetres.

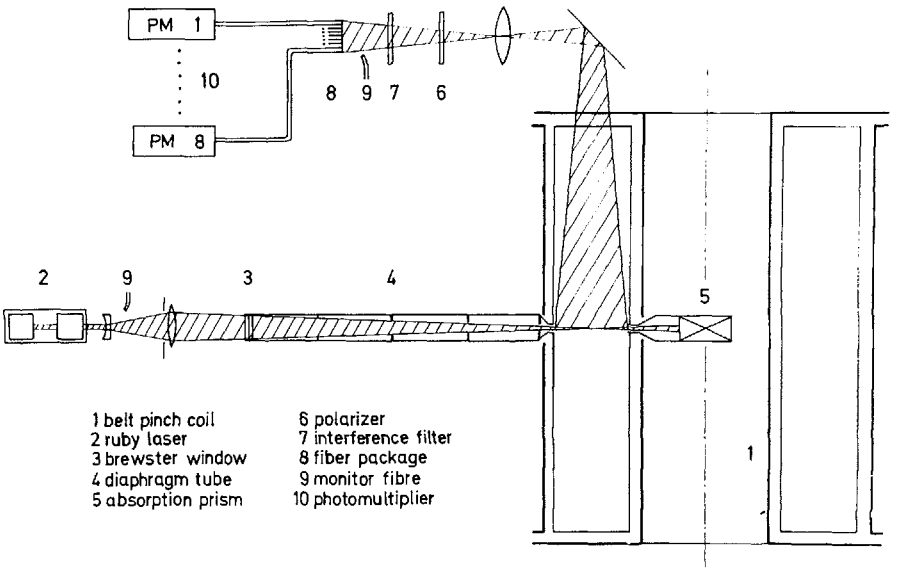


FIG.2. 90° laser light scattering system for measuring radial density and temperature profiles with a multichannel detecting optics.

of 3 kG within 0.5 μs. The initial plasma is generated in two steps: a capacitively coupled r.f. pulse is used to ignite a toroidal pre-discharge which produces radially homogenous plasmas with a degree of ionization of about 50% at 1–2 mtorr filling pressure.

2.2. Diagnostics

Complete radial electron density and temperature profiles are measured by means of a multichannel laser light scattering system (Fig.2). The temporal variation of the magnetic field profiles is measured with multiple probes. The ion temperature is obtained from spectroscopic measurements of the D_α-line profile and from the neutron yield detected by a plastic scintillator. Smear pictures taken with image converter cameras show the radial and axial plasma motions.

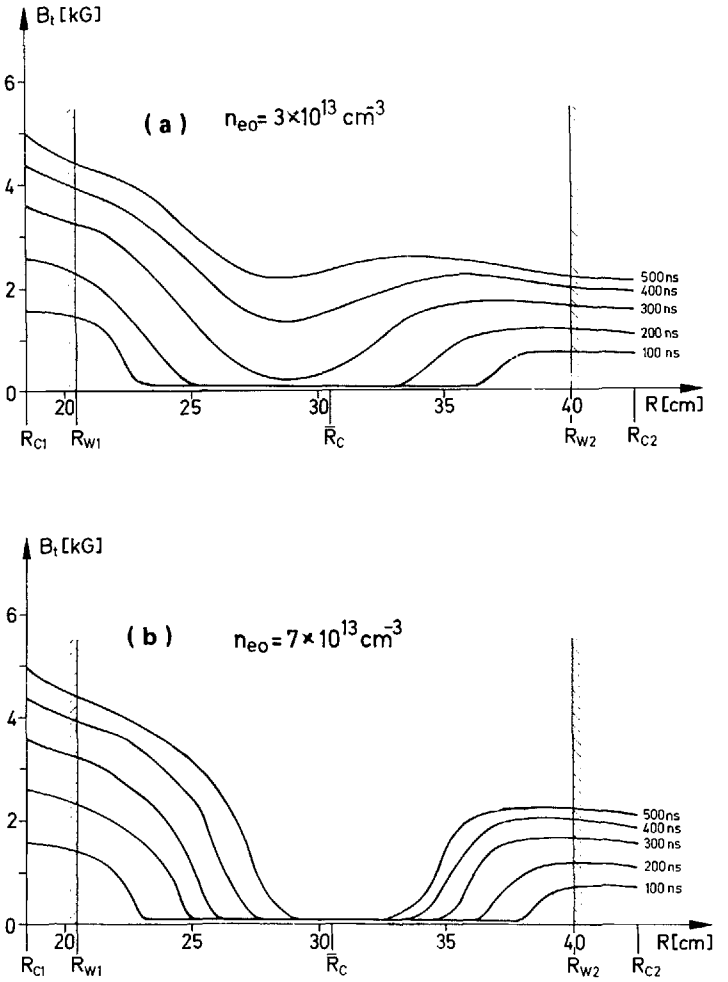


FIG.3. Time development of the radial profile of the toroidal magnetic field. R_{C1}, R_{C2}: coil radii, R_{W1}, R_{W2}: radii of vacuum vessel, a) for deuterium of the initial density $n_{e0} = 3 \times 10^{13}$ cm^{-3}; b) for deuterium of the initial density $n_{e0} = 7 \times 10^{13}$ cm^{-3}.

3. EXPERIMENTAL RESULTS

3.1. Piston formation

The fast magnetic compression has been investigated for deuterium with initial densities of $n_{e0} = 2\text{–}8 \times 10^{13}$ cm^{-3}. A transition was observed from a more diffuse compression at lower densities to a clear separation between the compressed plasma and the driving magnetic piston at higher densities. Two typical cases for $n_{e0} = 3 \times 10^{13}$ cm^{-3} and $n_{e0} = 7 \times 10^{13}$ cm^{-3} are studied in detail.

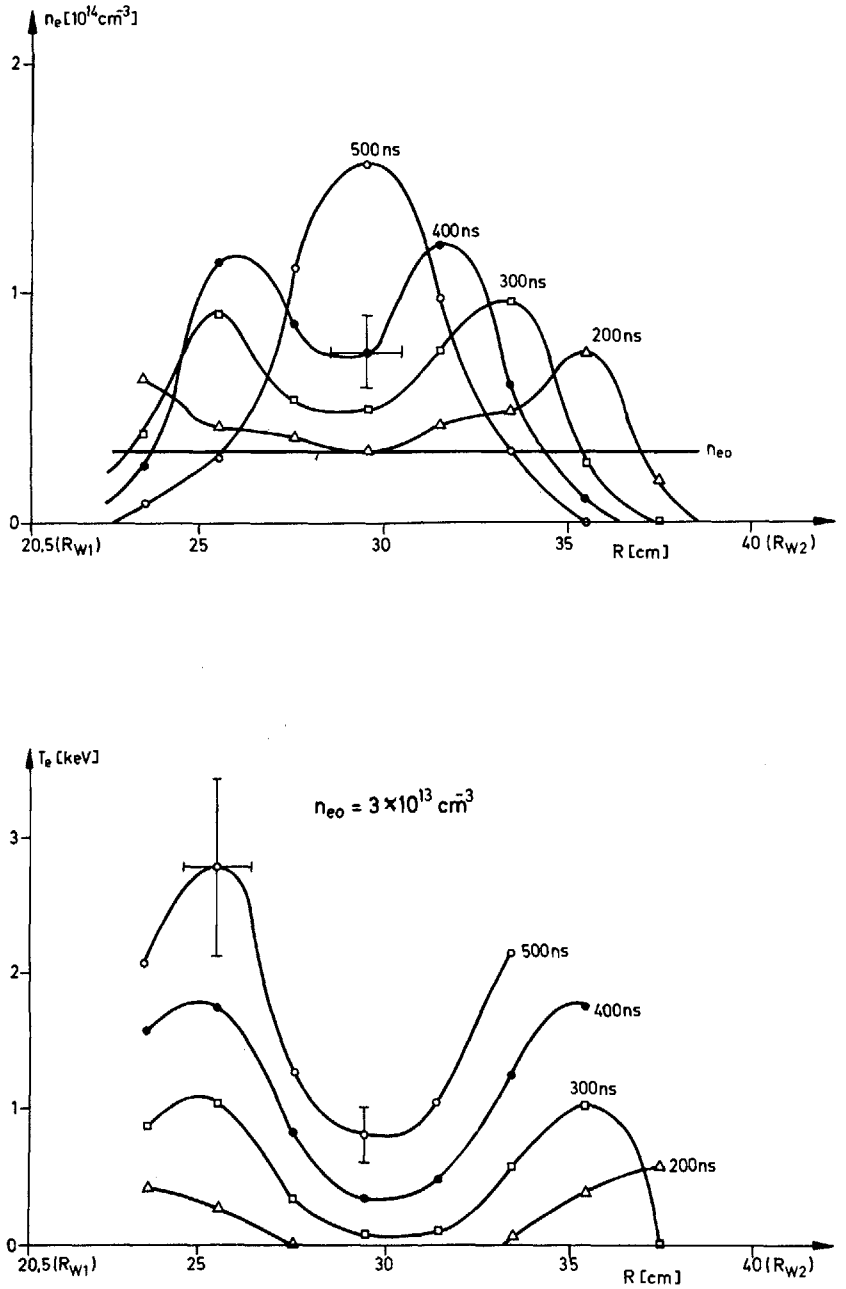


FIG. 4. Time development of the radial electron density and temperature profiles for an initial density $n_{e0} = 3 \times 10^{13}$ *cm*$^{-3}$.

At an initial density of $n_{e0} = 3 \times 10^{13}$ cm^{-3} a broad magnetic piston is formed (Fig.3a). The sheath width increases during the compression and the magnetic field diffuses into the whole plasma. A mean β value of 0.4 and a compression ratio $\kappa = 3.5$ (κ = coil diameter/pressure half width) are obtained after implosion. The velocity of the magnetic piston and the velocity of the luminosity front on smear pictures correspond to an energy of 0.7 keV for the ions collected in the piston according to the snow-plough model. At higher initial densities ($n_{e0} = 7 \times 10^{13}$ cm^{-3}) the plasma and the driving magnetic piston stay well separated during the compression (Fig.3b).

The magnetic piston is decelerated by the pressure of the compressed plasma and is stopped after a compression time of 500 ns at about a third of the initial plasma diameter. The central plasma region stays magnetic-field-free. A mean β value of 0.8 is obtained and the compression ratio amounts to about 2. The piston velocity corresponds to a mean ion energy of 0.4 keV. In both cases, magnetic-field gradients deviating from the vacuum field exist behind the piston. They indicate an outer current-carrying layer surrounding the compressed plasma. A similar behaviour was observed in linear shock compression experiments where the halo plasma was presumably caused by flute instabilities [3].

3.2. Electron density and temperature

The time development of the electron density and temperature profiles during implosion is shown in Fig.4 $n_{e0} = 3 \times 10^{13}$ cm^{-3}. The electron temperature rises up to 3 keV in the piston region. On axis, the electron temperature begins to rise with the incoming magnetic field to about 1 keV. A maximum electron density of 1.5×10^{14} cm^{-3} is reached in the centre of the plasma. For the higher initial density, the electron temperature rises up to 1 keV in the piston region and stays low in the central plasma region ($T_e \lesssim 50$ eV) (Fig.5). In this case, the magnetic piston does not reach the axis.

Steep temperature gradients are maintained during compression in both cases. The radial heat conduction is limited by the magnetic field. A small bias field from the pre-ionization ($B_0 \approx 100$ G) prevents electron heat conduction perpendicular to the magnetic field since $\omega_{ge,0} \gg \nu$. So the heat cannot be carried out of the piston region by electrons.

The electron line density increases during the implosion owing to ionization. From integration over the measured density profiles, a mean electron density $\bar{n}_e = 5 \times 10^{13}$ cm^{-3} is obtained after compression for the initial density $n_{e0} = 3 \times 10^{13}$ cm^{-3}. In the higher-density case, the mean electron density increases up to $\bar{n}_e = 1.1 \times 10^{14}$ cm^{-3} ($n_{e0} = 7 \times 10^{13}$ cm^{-3}).

A density rise in front of the magnetic piston is measured in both cases. This indicates reflection of ions from the potential jump in the shock layer.

3.3. Ion dynamics and heating

Ion reflection can be observed if the sheat thickness is smaller than half of the total compression length and if the transit time of the ions through the piston is shorter than the compression time. Both conditions are fulfilled for the lower and for the higher density case. From the density profiles, a degree of reflection of 30% after compression is obtained for $n_{e0} = 3 \times 10^{13}$ cm^{-3} and 60% of the compressed ions are reflected for $n_{e0} = 7 \times 10^{13}$ cm^{-3}.

The reflected ions produce a rise of the neutron flux at a time when the magnetic piston has travelled half the compression length and the piston ions are not yet colliding (Fig.6 for $n_{e0} = 3 \times 10^{13}$ cm^{-3}). The first maximum of the neutron flux is observed when the reflected ions hit the piston again. The following drop of the neutron flux is due to a decrease of reflected ions colliding with piston ions. A second bouncing of the ions from the potential jump causes another increase of the neutron flux. From the neutron yield, a mean energy of 2.5 keV is calculated for the reflected ions. In the higher-density case, no reaction neutrons could be detected because of the lower ion temperatures.

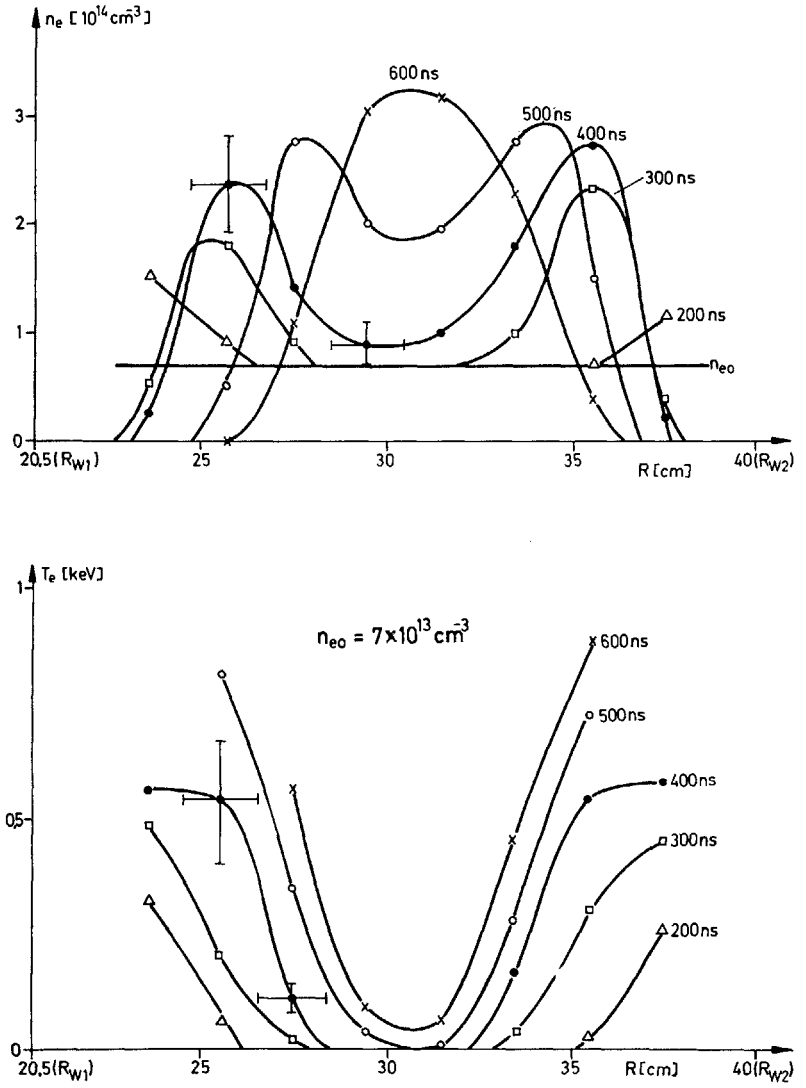


FIG.5. Time development of the radial electron density and temperature profiles for the initial density $n_{e0} = 7 \times 10^{13}\ cm^{-3}$.

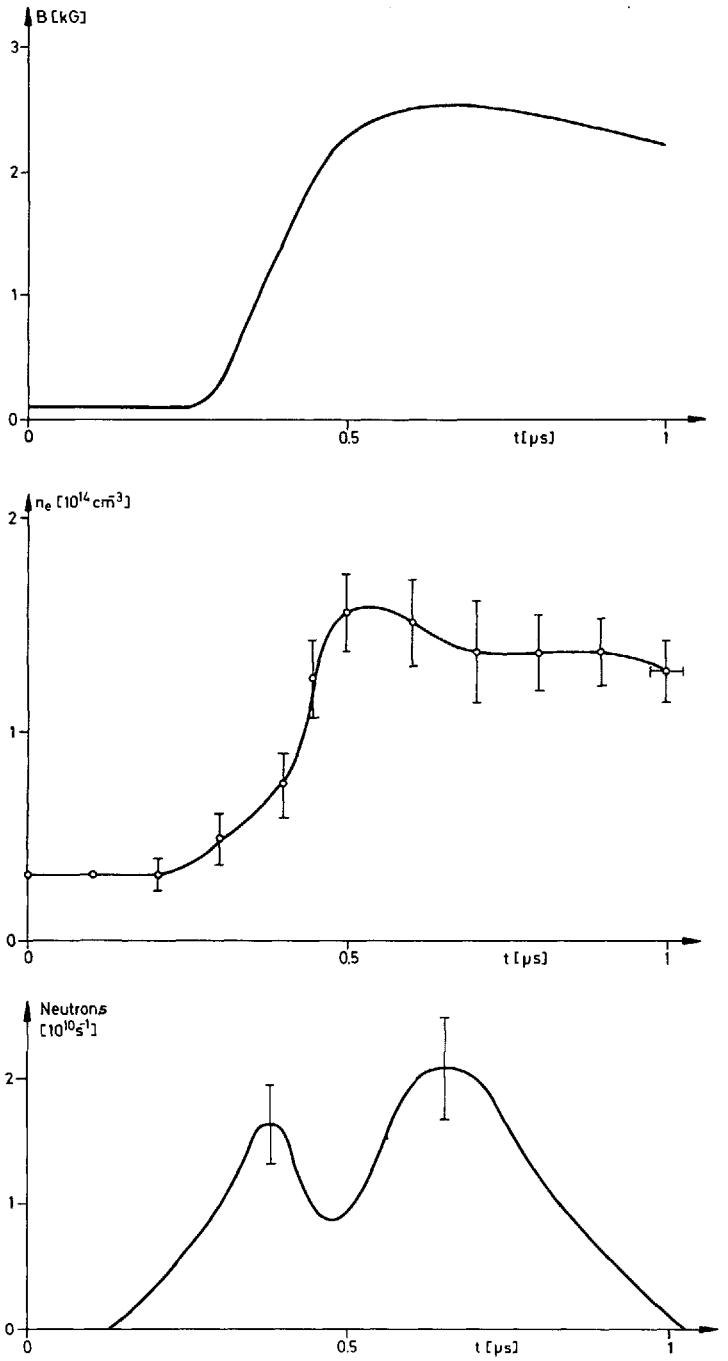


FIG. 6. Toroidal magnetic field B(t) and electron density $n_e(t)$ measured at coil centre and temporal variation of neutron flux at initial density $n_{e0} = 3 \times 10^{13}$ cm^{-3}.

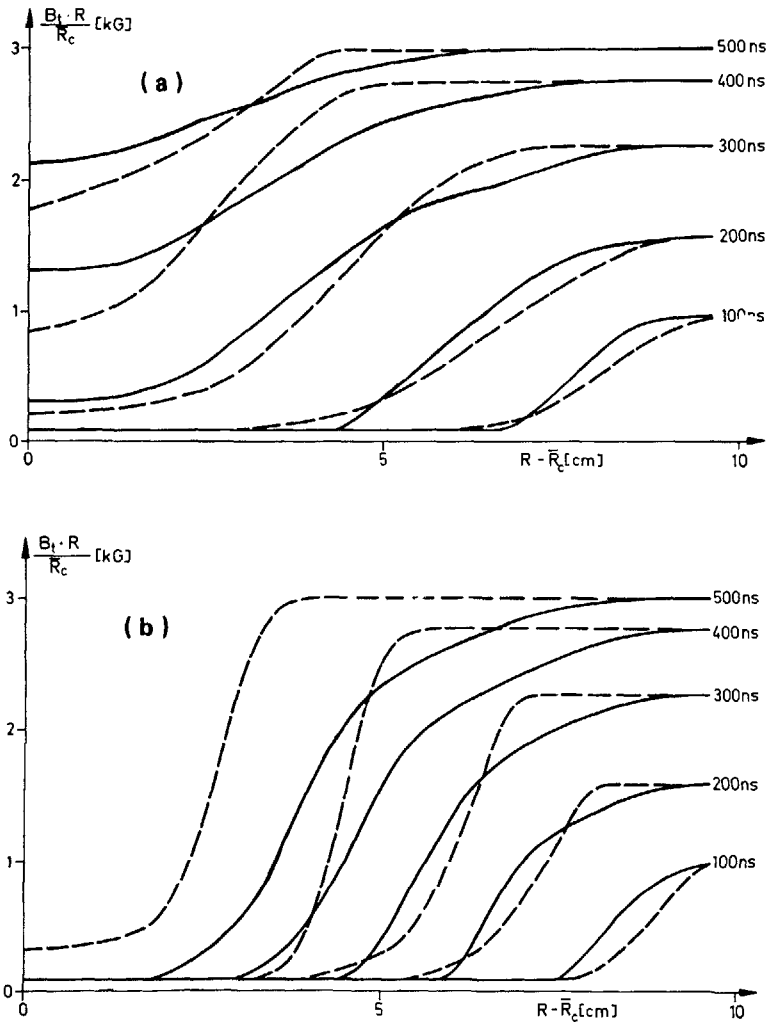


FIG. 7. Measured (solid lines) and numerically calculated (dashed lines) radial profiles of the toroidal magnetic field during shock compression. The 1/R dependence is eliminated by transforming to linear geometry. The mean coil radius is taken as origin of the frame.
a) initial density $n_{e0} = 3 \times 10^{13}$ *cm*$^{-3}$
b) initial density $n_{e0} = 7 \times 10^{13}$ *cm*$^{-3}$

The reflected ions are also seen from radial spectroscopic measurements of the D_α-line emission. Two bumps in the profile correspond to Doppler shifts with piston velocity and with double piston velocity.

In the direction of the diamagnetic current, perpendicular to the direction of the shock front motion, Doppler broadening of the D_α-line is observed which corresponds to ion temperatures of $T_i \approx 200$ eV for $n_{e0} = 3 \times 10^{13}$ cm^{-3} and $T_i \approx 150$ eV for $n_{e0} = 7 \times 10^{13}$ cm^{-3}.

3.4. Electron drift and instabilities

From the sheath thickness ($\Delta \approx 0.5\ c/\omega_{pi}$ in both cases), an effective collision frequency $\nu_{eff} \approx 0.6\ \omega_{pi}$ is calculated which exceeds the binary collision frequencies by about two orders of magnitude. This indicates enhanced resistivity due to current-driven instabilities.

The onset of the instabilities is mainly determined by the magnitude of the electron-ion drift velocity v_d and by the ratio of the electron to the ion temperature T_e/T_i. Lower hybrid drift instability can be excluded because of $T_e > T_i$ and high initial β. The ion acoustic instability can develop if $T_e > T_i$ and $v_d > v_s$ where v_s is the ion sound velocity. In strong shocks, the drift velocity responsible for the growth of the instability is given not only by the net macroscopic drift velocity $v_{d,j}$ derived from the magnetic field gradient, but contributions from the large density and temperature gradients have to be taken into account, as well. These gradients result in a distortion of the electron distribution function and lead to an "effective" drift velocity v_d governing the growth of the ion acoustic instability. v_d can be written in the form $v_d = v_{d,j} + C_1 v_{\nabla n_e} + C_2 v_{\nabla T_e}$ where $v_{\nabla n_e}$ and $v_{\nabla T_e}$ are given mainly by the electron density and the electron temperature gradient, respectively. The coefficients C_1 and C_2 are calculated from the electron distribution function in the quasi-linear theory [4].

The resulting "effective" drift velocity v_d is larger than the ion sound velocity v_s during the compression, and ion sound waves can grow unstable. The macroscopic drift velocity $v_{d,j}$, however, is smaller than v_s.

The quasi-linear theory [5] predicts saturation of the ion sound instability by linear Landau damping on the ions. In this saturated state, the drift velocity should approach a critical velocity $v_{crit} \approx v_s\ (m_i/m_e)^{1/4}\ T_i/T_e$. The drift velocity in the experiment agrees well with the theoretically predicted value.

4. NUMERICAL CALCULATIONS

4.1. Comparison with experiment

Plasma simulation calculations were carried out with the data of the experiment using a plane 1-d fluid-particle hybrid code [6]. Best agreement between the experimental and the numerical results was obtained by taking the same effective collision frequency $\nu_{eff} = 0.6\ \omega_{pi}$ for turbulent electron heating and for radial electron heat conduction perpendicular to the magnetic field in the piston. This can be explained by the large angular spread of the ion acoustic waves [7]. The measured and the calculated radial profiles of the toroidal magnetic field are compared in Fig.7. The 1/R dependence is eliminated and the mean coil radius is taken as the origin of the frame. The differences are presumably due to the halo plasma in the experiment not described in 1d-calculations. Good agreement is obtained also between the calculated and the measured electron temperature profiles. Time behaviour and the value of the ion reflection degree are the same in experiment and calculation.

4.2. Density scaling of shock heating

The good agreement of experimental and numerical results allows a study into the scaling of shock heating in a wider density regime. Hubid-code calculations were carried out for initial densities $n_{e0} = 5 \times 10^{12} - 10^{14}\ cm^{-3}$ with the data of the High Voltage Belt Pinch.

The sheath width increases for lower densities and reaches a value of half the compression length at $n_{e0,c} = 9 \times 10^{12}\ cm^{-3}$. At this critical density, the ion reflection degree drops to zero because the transit time of the ions through the magnetic piston is equal to the implosion time. With increasing density, the ion reflection degree increases up to a value of 65% at $n_{e0} = 10^{14}\ cm^{-3}$.

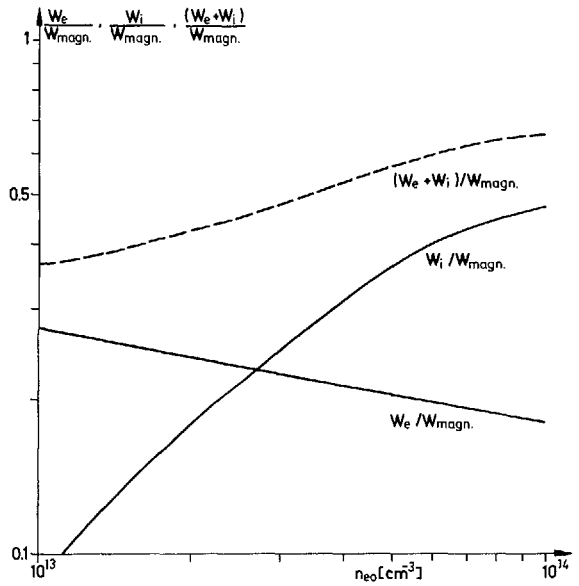


FIG. 8. Electron and ion energies after shock compression from simulation calculations for various initial densities.
$W_e/W_{magn.}$ = total electron energy/total magnetic field energy in the coil;
$W_i/W_{magn.}$ = total ion energy/total magnetic field energy in the coil.

For higher initial densities, the shock heating becomes more effective because of strong ion reflection as is shown in Fig.8. The ratio of the total plasma energy to the total magnetic field energy in the coil increases with increasing initial density.

5. SUMMARY

The results of the High Voltage Belt Pinch show that high-β plasmas with keV temperatures and low compression ratios can be produced by fast magnetic compression avoiding any adiabatic heating. In the piston region, the electrons are heated to keV temperatures by ion acoustic turbulence. Much higher electron temperatures are obtained in the toroidal configuration than in linear theta pinch experiments. Electron heating as well as electron heat conduction perpendicular to the magnetic field are governed by the same effective collision frequency.

At lower densities, most of the ions are trapped in the magnetic sheath which diffuses into the whole plasma. The ion reflection increases with increasing initial density, providing effective non-diabatic ion heating in agreement with the results of a hybrid particle code.

ACKNOWLEDGEMENT

The authors wish to thank Drs R. Chodura and C.T. Dum for many helpful discussions and R. Chodura for supplying his hybrid code for the parameter studies in this paper.

REFERENCES

[1] CHODURA, R., DUM, C.T., KEILHACKER, M., KORNHERR, M., NIEDERMEYER, H., PROTZ, R., SÖLDNER, F., STEUER, K.-H., in Plasma Physics and Controlled Nuclear Fusion Research (Proc. 5th Int. Conf. Tokyo, 1974) **3**, IAEA, Vienna (1975) 397.
[2] GRUBER, O., WILHELM, R., Nucl. Fusion **16** (1976) 243.
[3] KEILHACKER, M., KORNHERR, M., NIEDERMEYER, H., SÖLDNER, F., STEUER, K.-H., Phys. Rev. Lett. **32** (1974) 1044.
[4] DUM, C.T., to be published.
[5] DUM, C.T., CHODURA, R., BISKAMP, D., Phys. Rev. Lett. **32** (1974) 1231.
[6] CHODURA, R., Nucl. Fusion **15** (1975) 55.
[7] BISKAMP, D., CHODURA, R., DUM, C.T., Phys. Rev. Lett. **34** (1975) 131.

DISCUSSION

ON PAPERS IAEA-CN-35/E 13-1, 13-2

H.R. GRIEM: Plasma production by implosion techniques such as you discussed necessarily implies anomalous transport. Will the corresponding microinstabilities *all* damp out sufficiently fast, or will they lead to a loss of the magnetic configuration by diffusion in the planned containment experiments? Recent measurements (COMMISSO, R.J., GRIEM, H.R., Phys. Fluids, in press). in a reverse-field theta pinch yield post-implosion resistivities about one hundred times the classical for conditions intermediate between those of your two experiments.

K-H. STEUER: This may be a problem in the high-β confinement experiments that are being planned. However, I do not think that the experimental results up to now are clear enough to give evidence of enhanced post-implosion resistivity for the envisaged parameter range.

R.C. DAVIDSON: It seems highly unlikely that the phenomenological collision frequency $\nu_{eff} = 0.6\ \omega_{pi}$ is correct throughout the entire sheath region. It appears to be much better (for scaling purposes) to use the self-consistent transport model described by us (IAEA-CN-35/E 15).

Have you correlated the observed flutes with the theoretical predictions of Batchelor and Davidson based on the lower-hybrid-drift instability? This work gives good agreement with the flutes observed in Scylla 1-B.

K-H. STEUER: The wavelengths of the observed flutes in Isar II ($\lambda = 1.6$ cm) are about one order of magnitude larger than the predictions of the lower-hybrid-drift theory.

For a wide range of theta and z-pinch experiments at Garching and Los Alamos (SGRO, A.G., NIELSON, C.W., Phys. Fluids 19 (1976) 126.), the absolute value and the scaling of ν_{eff} with $n^{1/2}$ independent of B have been confirmed. This scaling was also found in PIC calculations on anomalous resistivity by ion acoustic turbulence (DUM, C.T., CHODURA, R., BISKAMP, D., Phys. Rev. Lett. 32 (1974) 1231).

W. KÖPPENDÖRFER: It is quite possible that in the initial phase of the implosion the lower hybrid drift instability provides an anomalous resistance which limits the Rayleigh-Taylor instability to the observed wavelength. During the implosion the question has to be answered whether the current flows on the heavily corrugated surface or is smoothly distributed over the shock layer. In the first case the electron drift velocity would exceed the ion sound velocity and ion-sound instabilities could be excited, whereas in the second case other instabilities like LHD would prevail.

EXPERIMENTAL STUDY OF A TWO-STAGE ION-HEATING PLASMA INJECTION AND COMPRESSION EXPERIMENT

H. ITÔ, S. GOTÔ, T. UYANA, N. SATOMI, K. WATANABE
Plasma Physics Laboratory,
Faculty of Engineering,
Osaka University,
Yamada-Kami, Suita, Osaka,
Japan

Abstract

EXPERIMENTAL STUDY OF A TWO-STAGE ION-HEATING PLASMA INJECTION AND COMPRESSION EXPERIMENT.

A high-β plasma with an ion temperature above 3 keV and a density of $2-3 \times 10^{15}$ cm^{-3} is obtained by theta-compression heating of a counter-streaming plasma. The ion heating process is divided into two stages: phase I with an ion heating rate of $1-2$ eV·ns^{-1} and II with that of ~ 10 eV·ns^{-1}. According to measurements of B_z, E_r, E_θ and the density, the behaviour of these quantities also shows remarkable differences before and after the transition time of these phases. Fast ions created in the early stage of phase I by E_θ near the wall give rise to pronouncedly paramagnetic behaviour near the axis, which moderates the penetration of the magnetic field with the aid of a diamagnetic current existing in the initial plasma. For these reasons, a sharp and increasing magnetic piston is formed after phase I and the plasma pre-heated up to 500 eV at the end of phase I is heated efficiently in phase II.

1. INTRODUCTION

As was reported in previous papers [1, 2], it was found that a plasma obtained by the collision of two counter-streaming flows ejected from two plasma guns could be heated up to a high ion temperature of more than 3 keV, with neutron emission due to rapid theta compression. The process of this ion heating turned out to have two stages: phase I with the ion heating rate of $1-2$ eV · ns^{-1} up to 240 ns and phase II with that of $10-20$ eV·ns^{-1} thereafter. In our experiment, the parameters of the initial plasma can be controlled to some extent by changing the delay time between the onset of the main compression and the instant at which the gun is fired. For a wide change of the delay time, the transition time from phases I to II seems to be unchanged. According to measurements of B_z and E_r in spatial and temporal resolution, the behaviour of these quantities shows remarkably different changes from phase I to phase II. It is supposed that the heating process is strongly influenced by the structure of the initial plasma obtained by the encounter of two plasma streams.

In this paper, experimental data are presented for which the delay time between the ignition of the main compression coil and the gun firing time is fixed to be 13 μs. Under this condition, the behaviour of the magnetic and electric fields are rather modified compared to that obtained by other initial conditions with longer delay times. The temporal and spatial profiles of the density and the electron temperature measured by Thomson scattering method are compared with those of the fields. The heating mechanism and the behaviour of the plasma are considered in connection with the structure of the initial plasma.

2. EXPERIMENTAL RESULTS

2.1. Experimental procedure

Details of the experimental apparatus "PIACE" are presented in the other papers [1, 2]. A simple explanation of the experiment using this machine is the following. A straight discharge tube of 2.5 m length and of 8.4 cm inner diameter has two theta-pinch guns at both ends. Deuterium plasma streams ejected from both guns at the same time are introduced through guiding fields into the region surrounded by the main cylindrical compression coil of 1 m length and 10 cm diameter. In the stage of the encounter of plasma streams, the main coil is used to produce a uniform field of 1 kG. For the compression of the encounter plasma, the coil excited by a main capacitor bank of 65 kJ at 50 kV produces a uniform field with a maximum strength of 25 kG within 1.4 μs. Nearly all measurements were done in the midplane of the main coil.

The flow velocity of the top of the one-sided stream of the density $\sim 5 \times 10^{14}$ cm^{-3} is 1×10^{7} cm$\cdot$s^{-1} in the midplane, while internal energies of ions and electrons are a few electron volts on the axis. After two streams with the same structure make the encounter, the parameters of the plasma made by this process change as time goes on [1, 3]. As stated before, the beginning time of the compression is fixed at a time 13 μs delayed from the synchronized switching time of the guns. The ion temperature measured at the midplane changes as the relation

$$(1/2)mv^2 = (3/2)kT_i \qquad (1)$$

where m is the deuteron mass and v is the flow velocity of the one-sided streams [4]. The ion temperature of the plasma at 13 μs is 100 eV according to Doppler measurements. Initial distributions of the density, the electron temperature and the guiding field are shown in Fig.1. By exciting the main compression coil, such an initial plasma is compressed by a rapidly increasing magnetic field with the same direction as that of the guiding field.

2.2. Measurements of B_z, E_r and E_θ

During the process of the compression heating, temporal and spatial changes of field quantities B_z, E_r and E_θ were measured by specially designed fine magnetic and electric probes. Some of the experimental results on the behaviour of B_z and E_r have already been presented [5]. Several profiles of B_z and E_r which are necessary for discussions in this paper are given in Figs 2 and 3, respectively. The time-resolved radial distributions of E_θ shown in Fig.4 are derived from measurements of B_z under the assumption of the axial symmetry. The direction of E_θ oriented oppositely to the coil current is defined to be positive. As can be seen from these figures, the front of E_θ reaches the axis at 160 ns as does that of B_z, while the value of E_θ near the wall assumes its maximum (~ 1 kV$\cdot$cm^{-1}) at this time. At $t = 200 - 210$ ns, the profile of E_θ denotes a local maximum around $r = 1$ cm and then suddenly becomes zero inside the range $r < 2$ cm at 220 ns. Subsequently, it becomes entirely negative up to $r = 2.5$ cm at 240 ns. B_z near the axis as shown in Fig.2 displays a remarkably strong paramagnetic behaviour during the same time interval. The value of B_z at the axis becomes maximum at 240 ns, and it takes a rather long time ($\sim$300 ns) for the paramagnetic behaviour to vanish completely. The trace of the steepest point of the magnetic field profiles (= magnetic piston) appearing in Fig.2 shows some discontinuity before and after the time point 240 ns [5]. The peak of the radial electric field E_r, which proceeds inwards with a velocity of 1.2×10^{7} cm$\cdot$s^{-1}, stops at nearly $r = 2$ cm. It seems to recede to the wall at $t = 240$ ns and the peak is formed again at $r = 2.5$ cm.

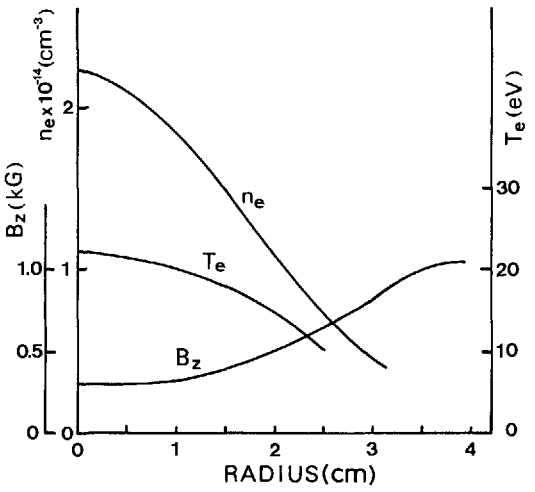


FIG.1. Radial distribution of bias magnetic field and initial-plasma electron density, n_e, and temperature, T_e.

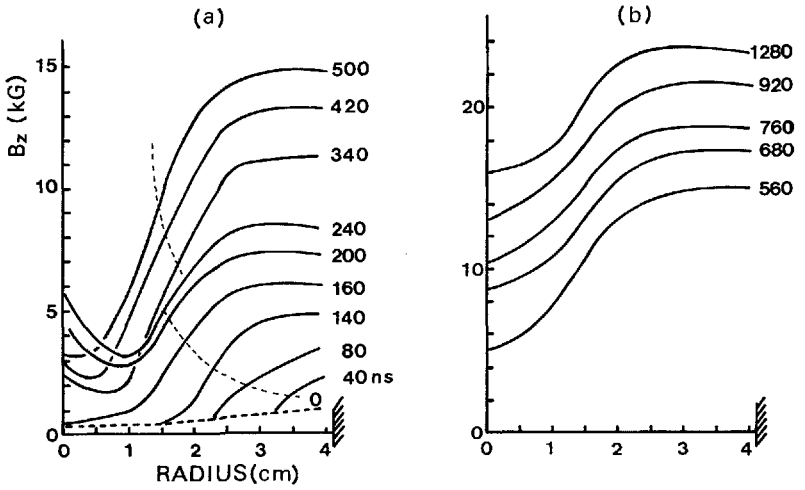


FIG.2. Temporal evolution of magnetic field profile, $B_z(r,t)$; (a) $t \leqslant 500$ ns and (b) $t > 500$ ns.

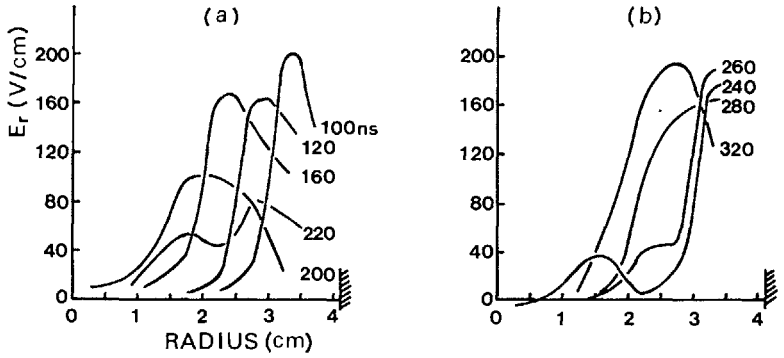


FIG.3. Temporal evolution of radial electric field, $E_r(r,t)$; (a) for phase I ($t < 240$ ns) and (b) for early phase II.

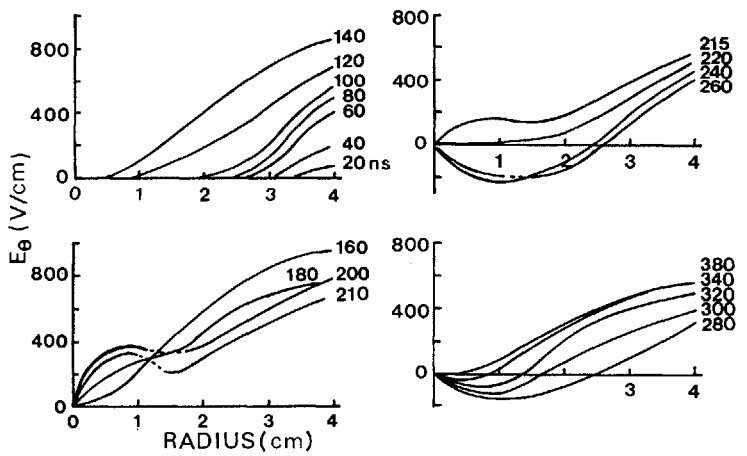


FIG.4. Temporal evolution of azimuthal electric field profile, $E_\theta(r,t)$ (see text on the sign allotted to sense of orientation).

2.3. Measurements of electron density and temperature

To study the behaviour of the plasma column, we carried out measurements of ruby laser light by Thomson scattering. The experimental results are shown in Figs 5 and 6. Before 120 ns, a density hump is seen to propagate inwards together with the magnetic piston. After 160 ns, the peak of the density is completely separated from the magnetic piston and seems to move with the bottom of the B_z profile, which is apart from the axis because of the presence of the paramagnetic field. At 220 ns, the density peak shifts towards the centre although it again leaves the axis at 250 ns. It is noted that no strong laser scattering light is observed outside a region limited by r = 2.5 cm, in spite of the apparently violent behaviour of the plasma column. According to electron temperature measurements, the peak of T_e seems to change its position as that of the induced strong current does. In an early stage of the heating process, T_e is highest around the point r = 2.5 cm. Then another peak produced around the magnetic piston increases rapidly and finally T_e becomes highest around r = 1.5 cm.

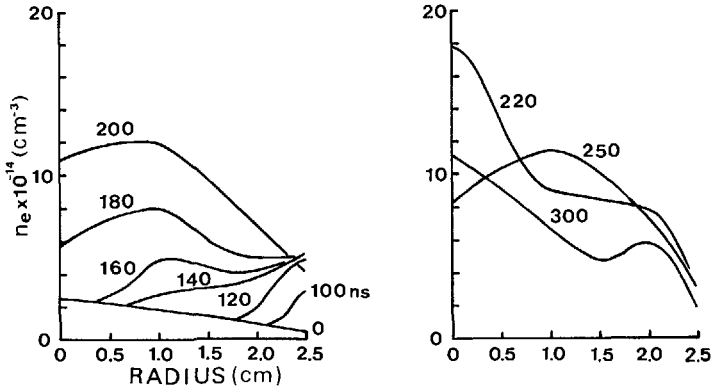


FIG.5. Temporal evolution of density profile, n(r,t), measured by Thomson scattering of ruby laser light.

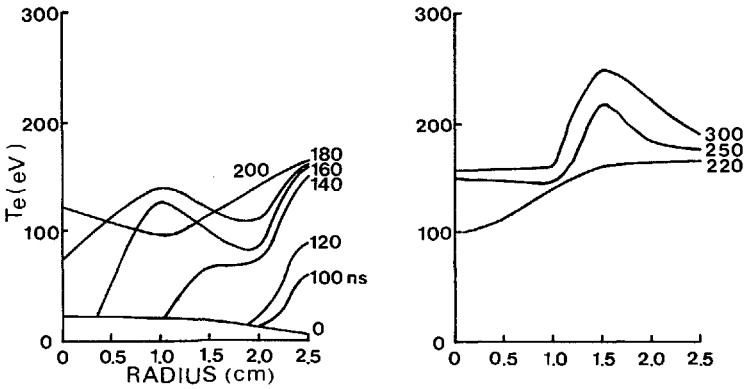


FIG.6. Temporal evolution of electron temperature, $T_e(r,t)$, measured by Thomson scattering.

2.4. Measurement of ion temperature

The ion temperature in the heating phase is estimated from Doppler profiles of He II line (4686 Å) emitted from a small quantity of helium gas added to the deuterium. The ion temperature derived from this measurement is given in Fig.7. T_i becomes 490 eV at 230 ns and decreases rapidly to 340 eV at 240 ns. After this time, the profiles take two-temperature distributions up to 500 ns and thereafter become Gaussian again. The ion heating rate is 1–2 eV·ns^{-1} in phase I while it is ~10 eV·ns^{-1} for the high-temperature component from 250 ns to 500 ns. It begins to be observed for neutrons after 800 ns and the ion temperature estimated from the neutron yield is 3–4 keV at 1200 ns.

2.5. Behaviour of plasma column

The structure of the initial plasma produced by the collision of two counter-streaming plasmas seems to have a strong influence on the behaviour of the heated plasma or the heating mechanism,

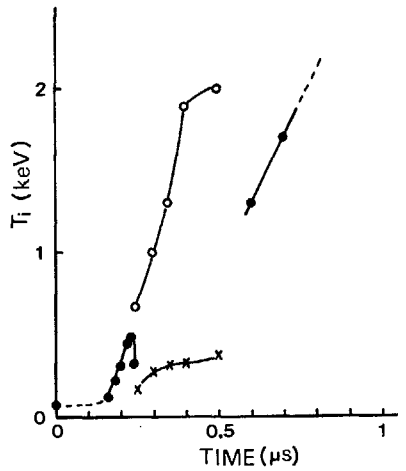


FIG. 7. Temporal variation of ion temperature, $T_i(t)$, estimated by Doppler profiles of He II line (4686 Å) emitted from 5% helium gas added to the deuterium: curves between 250 ns and 500 ns show temperatures of high- and low-temperature components, respectively.

especially in phase I. By comparing the output signals from electric probes inserted into the one-sided stream and the counter-stream, respectively, we obtained the following information on the encounter plasma. Two plasma z-flows pass through each other inside the region limited by r = 2.5 cm, while there are strong outward flows outside. The apparently strange experimental relation (1) is partially understood by this consideration of the encounter process.

The diamagnetic current, which, to a certain extent, exists on a cylindrical shell of 2.5 cm in radius in the encounter process, is considered to be intensified by the external electric field and to play the role of an inner conductor in the heating process. As is seen in Figs 2 and 4, penetration of the magnetic and electric fields is suppressed considerably by this current layer. Then, the intensity of the magnetic field becomes very high, especially in the region surrounded by the wall and the current layer so that each profile of B_z has a sharp gradient, especially in phase II. In the region mentioned above where E_θ is strong, outward flowing ions can be accelerated by E_θ and returned into the central region over the magnetic piston. The paramagnetic behaviour near the axis appearing in the early phase is considered to be due to the collective motion of such high-speed ions ($v \cong 2 \times 10^7$ cm·s^{-1}); their existence can be also predicted by other considerations.

From changes in E_θ and the electron density, the following behaviour of the plasma in the heating process is also discussed. In the relation

$$E_\theta = \eta j_\theta - u_r B_z$$

the first term on the right-hand side of Eq.(2), $\eta j_\theta \cong (dT_e/dt)/j_\theta$, can be negelected compared to the second term in Eq.(2) since the rate of increase of T_e in phase I is relatively small, as is shown in Fig.6. While the inward motion continues as is shown in Fig.5, E_θ is entirely positive as can be seen from Fig.4. At the instance of peak density on the axis, E_θ is nearly zero up to r = 1.5 cm. After this time, E_θ becomes practically everywhere negative so that the plasma tends to move outwards. Comparing the peak density at 220 ns with the density values before and after that time, we conclude that no compression of the plasma as, e.g. a pinch, occurs since neither T_i nor T_e undergoes any remarkable change during this time. In other words, the inward plasma flow away from the piston goes through the centre and interacts with the approaching magnetic piston rather than with the plasma flow from the opposite direction.

3. SUMMARY

Our two-stage ion heating exactly corresponds to changes in the behaviour of electric and magnetic fields as presented in this paper. Furthermore, these changes are due to the special structure of the initial plasma obtained by the encounter of two plasma streams. As far as the mechanism of our ion heating is concerned, the strong E_θ existing near the wall seems to contribute to the production of fast ions, especially in phase I. According to the profiles of B_z, the position of the magnetic piston existing around r = 2 cm does not change effectively owing to the para-magnetic behaviour during the period from 240 ns to 300 ns. Within this time, the ion temperature increases up to 500 eV. Therefore, even if the plasma is compressed by a sufficiently large magnetic field (>10 kG) in phase II, it is considered that a fat high-temperature plasma can be obtained by a small compression ratio.

REFERENCES

[1] KISHIMOTO, H., GOTÔ, S., ITÔ, H., Phys. Rev. Lett. **31** (1973) 1120.
[2] ITÔ, H., GOTÔ, S., KISHIMOTO, H., SATOMI, N., USHIO, M., UYAMA, T., in Plasma Physics and Controlled Nuclear Fusion Research (Proc. 5th Int. Conf. Tokyo 1974), **3**, IAEA, Vienna (1975) 389.
[3] KISHIMOTO, H., ITÔ, H., J. Phys. Soc. Jpn. **40** (1976) 846.
[4] ITÔ, H., "KAKUYUGO-KENKYO", circular in Japanese **32** (1974) 144.
[5] GOTÔ, S., UYAMA, T., SATOMI, N., ITÔ, H., in Controlled Fusion and Plasma Physics (Proc. 7th Europ. Conf. Lausanne) **1** (1975) 30.

DISCUSSION

ON PAPER IAEA-CN-35/E 14

W. BOSTICK: Professor Wells at the University of Miami has observed that his conical-theta-pinch guns produce toroidal plasma structures containing a B toroidal as well as a B poloidal. Do you see any evidence of such structures being produced by your plasma guns?

H. ITÔ: In our experiments the guns are completely separate from the main coil where the compression takes place. We did, of course, measure the current carried by the plasma streams; it is similar to that found in the Miami experiment and disappears before the entrance to the main coil. The current around the plasma stream observed in our experiment is produced by the interaction between the wall and the plasma, as I mentioned.

H.R. GRIEM: As you pointed out, there is a short delay before your plasma streams interact strongly on a time scale too short for ion-ion collisions to occur. Is the observed delay of the order of the ion-cyclotron period, in which case an ion-cyclotron instability might provide the heating mechanism? Such a mechanism seems to explain certain recent measurements of ours (COMMISSO, R.J., GRIEM, H.R., Phys. Rev. Lett. (1976)) on ion heating and thermalization in a reverse-field theta pinch.

H. ITÔ: Measurements of the change in the magnetic field indicate that the inner field increases rapidly around 500 ns. It is after this time that the neutron yield begins – very likely some mechanism of thermalization comes into play around this time. Whether the ion-cyclotron instability occurs or not is a possibility that has not been examined yet.

KINETIC AND NUMERICAL STUDIES OF MICROSTABILITY PROPERTIES AND ANOMALOUS TRANSPORT IN THETA PINCHES*

R.C. DAVIDSON, N.T. GLADD, J. HUBA, B.H. HUI,
P.C. LIEWER, C.S. LIU, J.P. MONDT, J.M. OGDEN, C.S. WU
University of Maryland,
College Park, Maryland

S. HAMASAKI, N.A. KRALL, C.E. WAGNER
Science Applications Inc.,
La Jolla, California,
United States of America

Abstract

KINETIC AND NUMERICAL STUDIES OF MICROSTABILITY PROPERTIES AND ANOMALOUS TRANSPORT IN THETA PINCHES.

This paper summarizes several recent analytic and numerical studies of microstability properties, anomalous transport, and implosion and post-implosion dynamics in theta-pinch plasmas.

1. Finite-Beta Effects on Cross-Field Microinstabilities

Linear and nonlinear theories of current-driven microinstabilities in high-density pinches are usually based on the electrostatic approximation. In this paper we investigate the influence of finite plasma beta on the lower-hybrid-drift instability, which has recently received considerable attention as a mechanism for post-implosion anomalous transport [1], flute perturbations during implosion [2], as well as an anomalous transport mechanism during the implosion [3,4]. The analysis includes the finite-beta effects associated with both (a) transverse electromagnetic perturbations ($\delta\underset{\sim}{B}\neq 0$), and (b) resonant ∇B_0 electron orbit modifications. Linear stability properties are studied assuming flute-like perturbations with $\underset{\sim}{k}\cdot\underset{\sim}{B}_0=0$, $\delta\underset{\sim}{B} \parallel \underset{\sim}{B}_0=B_0(x)\hat{\underset{\sim}{e}}_z$, and $\delta\underset{\sim}{E} \perp \underset{\sim}{B}_0$. The analysis is carried out in slab geometry with $\underset{\sim}{k}=k_y\hat{\underset{\sim}{e}}_y$ (the cross-field current direction), and inhomogeneities in density $N(x)$ and magnetic field $B_0(x)$ in the x-direction. The analysis, valid for arbitrary T_i/T_e and V_E/v_i (here V_E is the cross-field electron $\underset{\sim}{E}\times\underset{\sim}{B}$ velocity, and v_i is the ion thermal velocity), leads to a transcendental integral equation [5] for the complex eigenfrequency $\omega=\omega_r+i\gamma$

$$\left[1+\frac{2\omega_{pi}^2}{k_y^2 v_i^2}\left(1+\xi_i Z(\xi_i)\right)+\frac{2\omega_{pe}^2}{k_y^2 v_e^2}\left(1-\Phi_3\right)\right]\left(1+\frac{2\omega_{pe}^2}{k_y^2 c^2}\Phi_1\right)=-\frac{2\omega_{pe}^2}{c^2 k_y^2}\frac{2\omega_{pe}^2}{k_y^2 v_e^2}\Phi_2^2 \qquad (1)$$

* Research supported by USERDA.

where $v_j=(2T_j/m_j)^{1/2}$, $\xi_j=\omega/k_y v_j$, $Z(\xi)=\pi^{-1/2}\int_{-\infty}^{+\infty} dx\ (x-\xi)^{-1}\exp(-x^2)$ is the plasma dispersion function, and Φ_1, Φ_2 and Φ_3 are defined by

$$\Phi_j = \int_0^\infty d\hat{v}^2\ \frac{\psi_j \exp(-\hat{v}^2)\Lambda}{\omega - k_y V_E - k_y \bar{V}_B \hat{v}^2} \tag{2}$$

with $\hat{v}=v_i/v_e$, $\psi_1=\hat{v}^2[J_0'(\mu)]^2$, $\psi_2=\hat{v}J_0(\mu)J_0'(\mu)$, $\psi_3=[J_0(\mu)]^2$, and $\Lambda=\omega-k_yV_E-k_yV_{de}$. Here $\mu=(k_y v_e/\omega_{ce})\hat{v}$, $\omega_{cj}=|e_j|B_0/m_j c$, $\bar{V}_B=-(T_e/m_e\omega_{ce})(\partial \ell nB_0/\partial x)$, $V_{de}=-(T_e/m_e\omega_{ce})(\partial \ell nN/\partial x)$, and $\partial T_j/\partial x=0$ is assumed. For stationary ions ($V_{yi}=0$), equilibrium force balance on an ion fluid element can be expressed as $NeE_x^0=T_i\partial N/\partial x$, so that $V_E=-cE_x^0/B_0$ is related to the ion diamagnetic drift velocity $V_{di}=(T_i/m_i\omega_{ci})(\partial \ell nN/\partial x)$ by $V_E=-V_{di}$, or equivalently

$$\frac{V_E}{v_i} = -\frac{V_{di}}{v_i} = -\frac{1}{2}\left(\frac{r_{Li}}{N}\frac{\partial N}{\partial x}\right) = \frac{r_{Li}}{2\Delta L_N} \tag{3}$$

where $\Delta L_N=-(\partial \ell nN/\partial x)^{-1}$, and $r_{Li}=v_i/\omega_{ci}$. Moreover, equilibrium pressure balance gives $\Delta L_N=(\beta_e+\beta_i)\Delta L_B/2$, where $\Delta L_B=(\partial \ell nB_0/\partial x)^{-1}$, and $\beta_j=8\pi NT_j/B_0^2$ is the local beta for species j.

Equation (1) has been solved numerically, and the parametric dependence of maximum growth rate on T_i/T_e, β_i and V_E/v_i investigated. The general tendency is for finite-beta effects to reduce the growth rate relative to previous electrostatic analyses. For example, in the limiting case where $T_i \gg T_e$ and $V_E/v_i \lesssim 1$, the maximum growth rate (which can be calculated analytically in this regime) is given by

$$\gamma_M = \frac{\hat{\gamma}_M}{(1+\beta_i/2)^{1/2}} \tag{4}$$

where $\hat{\gamma}_M=(2\pi)^{1/2}(V_E/v_i)^2\Omega_{LH}/8$ is the maximum growth rate based on an electrostatic stability analysis [1] with $\omega_{pe}^2/c^2k_y^2 \to 0$ and $\nabla B_0 \to 0$, and $\Omega_{LH}=\omega_{pi}/(1+\omega_{pe}^2/\omega_{ce}^2)^{1/2}$ is the lower hybrid frequency.

For $T_i \gg T_e$, finite-beta effects give a modest decrease in growth rate [Eq. (4)]. On the other hand, for $T_i \gtrsim T_e$ the growth rate can be substantially reduced by finite-beta effects. This is illustrated in Fig. 1 where the maximum growth rate (maximized with respect to k_y), measured in units of $\omega_{LH}=(\omega_{ce}\omega_{ci})^{1/2}$, is plotted versus V_E/v_i for $T_e/T_i=1$, $m_e/m_i=1/1836$, $T_i=1.02$ keV, and $(\beta_i, \omega_{pe}^2/\omega_{ce}^2)=(0.1,25)$, $(0.25, 62.5)$, $(0.50, 125)$ and $(0.75, 187.5)$. Indeed, for $T_i \gtrsim T_e$ it is found [5] that there is a critical value of local plasma beta (β_{cr}) such that the lower-hybrid-drift instability is completely stabilized ($\gamma<0$) for $\beta>\beta_{cr}$. Thus, when $T_i \lesssim T_e$, a very important conclusion can be drawn for post-implosion theta pinches, where the local beta increases with decreasing r. If the magnetic field depression is sufficiently large that $\beta(r)>\beta_{cr}$ for $r<r_{cr}$, where $\beta_{cr}=\beta(r_{cr})$, then the exterior region of the pinch ($r>r_{cr}$) will be unstable to the lower-hybrid-drift instability, whereas the interior region ($r<r_{cr}$) will be stable.

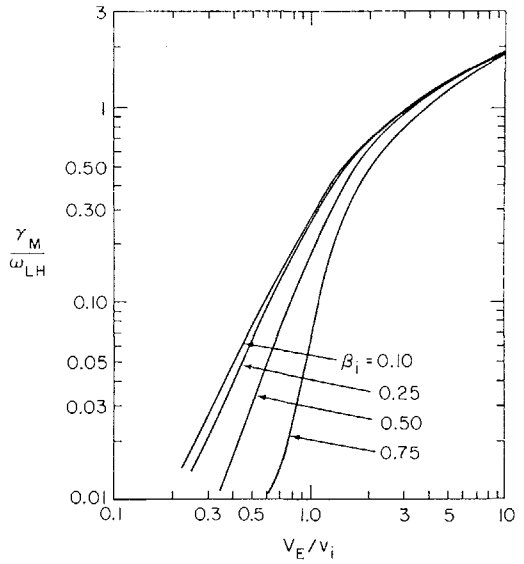


FIG.1. Plot of γ_M/ω_{LH} versus V_E/v_i obtained numerically from Eq. (1) [5].

Finally, we emphasize that the stability studies presented here are no longer valid when the cross-field current velocity relaxes to a sufficiently low value that the unmagnetized ion assumption [$|\omega_r+i\gamma| >> \omega_{ci}$] breaks down, i.e. whenever $|V_{di}/v_i|$ falls below the critical value [6]

$$\left|\frac{V_{di}}{v_i}\right|_{cr} = \left(\frac{r_{Li}}{2\Delta L_N}\right)_{cr} \gtrsim \sqrt{2}\,\frac{\omega_{ci}}{\Omega_{LH}}$$

2. Post-Implosion Anomalous Transport

The collisionless fluid-numerical model of Liewer and Krall [3] has been extended [7] to include the long-time transport effects associated with the lower-hybrid-drift instability [1] in post-implosion theta-pinches with $T_i >> T_e$. The system is initialized close to a two-fluid equilibrium with $r_{Li}/\Delta L_N < 1$, where r_{Li} is the ion Larmor radius and ΔL_N is the density gradient length scale. Resistivity due to the instability causes a decrease in cross-field current, and a corresponding broadening of the sheath and interpenetration of plasma and magnetic field. For a wide range of parameters, numerical results [7] show that the diffusion speed scales with the simple diffusion velocity $V_D=(\eta_{AN}c^2/4\pi)\partial \ell nB_0/\partial x=-(\eta_{AN}c^2\beta/8\pi)\partial \ell nN/\partial x$, where

$$\eta_{AN} = 2\pi\sqrt{\frac{\pi}{2}}\,\frac{\Omega_{LH}^{-1}}{(1+\omega_{pe}^2/\omega_{ce}^2)}\,\frac{\mathscr{E}_w}{NT_i} \qquad (5)$$

is the cross-field anomalous resistivity associated with the lower-hybrid-drift instability for $V_E/v_i \lesssim 1$ and $T_e \ll T_i$. In Eq. (5), $\mathscr{E}_w = 2(1+\omega_{pe}^2/\omega_{ce}^2)\langle(\delta E)^2\rangle/8\pi$ is the wave energy at maximum growth, and the finite-beta effects discussed in Sec. 1 have been neglected. The increase in sheath thickness obtained numerically [7] agrees well with the theoretical estimate

$$\left(\frac{\Delta L_N}{\Delta L_0}\right)^4 = 1 + 4\,\frac{V_D(t=0)\,t}{\Delta L_0} \tag{6}$$

where $V_D(t=0) = \eta_{AN} c^2 \beta/8\pi\Delta L_0$ is the characteristic diffusion velocity in the sheath, and $\Delta L_0 = \Delta L_N(t=0)$ is the initial sheath width.

To estimate the anomalous resistivity η_{AN}, we assume an upper bound on the wave energy $\mathscr{E}_w$ equal to the total directed kinetic energy $Nm_eV_E^2/2$, i.e.

$$[\mathscr{E}_w]_{MAX} = \frac{1}{2}\,Nm_eV_E^2 = NT_i\,\frac{m_e}{m_i}\left(\frac{V_E}{v_i}\right)^2 \tag{7}$$

Making use of Eqs (3), (5) and (7) gives the resistivity bound [7,8]

$$\eta_{AN} \simeq \left(\frac{\pi}{2}\right)^{3/2} \frac{\Omega_{LH}^{-1}}{1+\omega_{pe}^2/\omega_{ce}^2}\,\frac{m_e}{m_i}\left(\frac{r_{Li}}{N}\,\frac{\partial N}{\partial x}\right)^2 \tag{8}$$

The anomalous resistivity estimate in Eq. (8) can be orders of magnitude larger [7] than the classical cross-field resistivity [9]. Indeed, in recent experimental studies by Commisso and Griem [10] the post-implosion resistivity in the Maryland 40-kV theta pinch, the measured resistivity in the sheath region ($r_{Li}/\Delta L_N \sim 1/3$) is about fifty times the classical value, and in reasonably good agreement (approximately a factor of five larger) than the theoretical estimate in Eq. (8).

To compare the size of the anomalous and classical resistivities, we form the ratio η_{AN}/η_{cl}, where η_{cl} is the cross-field classical resistivity [9]. Assuming a gaussian density profile, $N(x) = N_0\exp(-x^2/\sigma^2)$, with $B_0(x=0)=0$ and $B_0(x \gg \sigma) = B_w$, we find [7]

$$\frac{\eta_{AN}}{\eta_{cl}} \simeq 2.1 \times 10^3\,\frac{T_e^{3/2}(T_e+T_i)}{A^{1/2}\,B_w}\left(\frac{r_{Li}}{\sigma}\right)^2 \tag{9}$$

where A is the ion mass number, T_e and T_i are in keV, and B_w in kilogauss.

It is clear from the estimate in Eq. (9) that $\eta_{an} > \eta_{cl}$ unless the electrons are sufficiently cold and/or the confining field B_w is sufficiently large. For example, if $T_e = 1.3$ keV, $T_i = 10$ keV, $B_w = 10$ kG, A=2 (deuterium) and $r_{Li}/\sigma = 0.25$, then $\eta_{AN}/\eta_{cl} \simeq 10^2$ follows from Eq. (9). In Fig. 2, η_{AN}/η_{cl} is plotted versus T_e, for A=2, $B_w = 60$ kG, $T_i = 10$ keV and various values of r_{Li}/σ [7]. Note that $\eta_{AN} < \eta_{cl}$ only for extremely low values of T_e and r_{Li}/σ. For example, if $r_{Li}/\sigma = 0.1$, then $\eta_{AN} < \eta_{cl}$ only for $T_e \lesssim 400$ eV.

The late-time resistivity measurements in the Culham 8-meter experiment [11] are often quoted as general evidence that post-implosion transport in theta pinches is classical. In this regard, we emphasize that the plasma was sufficiently cold ($\lesssim$150 eV) in the Culham experiment that the late-time transport was collision-dominated. Indeed, for the Culham parameters [11], it can be shown [7] that $\eta_{cl} \gtrsim 7\,\eta_{AN}$ in the sheath region, where η_{AN} is the anomalous resistivity estimate in Eq. (8). For high-temperature theta-pinch parameters of fusion interest, however, the condition $\eta_{AN} \gg \eta_{cl}$ is easily satisfied [7], at least during the immediate post-implosion phase

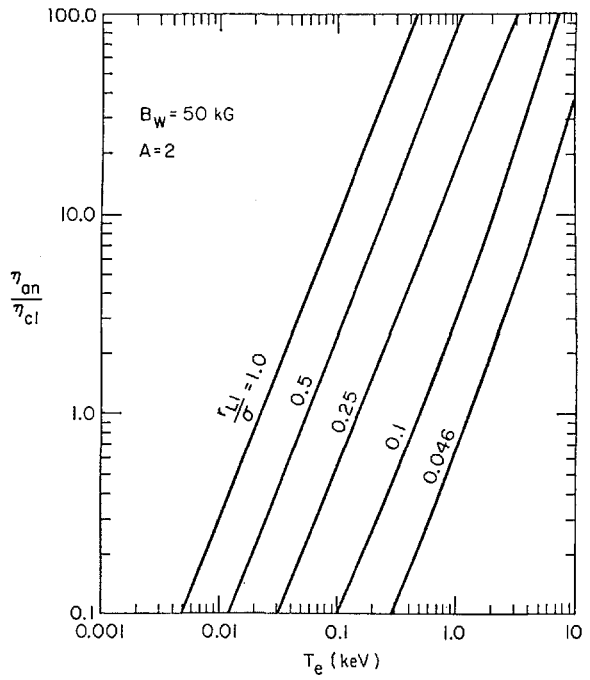


FIG.2. Plot of η_{AN}/η_{cl} versus T_e (Eq. (9)).

where $r_{Li}/\Delta L_n \lesssim 1$. As mentioned earlier, the measured post-implosion resistivity in the Maryland experiment [10] is about fifty times the classical value.

As the plasma-magnetic field interface broadens in response to the diffusion induced by the lower-hybrid-drift instability, the growth rate for this mode also drops, since the maximum growth rate $\hat{\gamma}_M$ scales as $\hat{\gamma}_M \sim (r_{Li}/\Delta L_n)^2$. However, as this occurs, other instabilities might be expected to grow, continuing to tap the free energy in the confined plasma. It can be shown [8] that in the limit $\Delta L_n >> r_{Li}$ the widely studied [12] low-frequency drift waves and universal instabilities have ample time to grow and affect the late-time transport.

3. Hybrid-Numerical Modeling of Theta-Pinch Implosions

A code, HYBRID, has been developed which calculates plasma implosions on the Alfvén wave time scale, appropriate for modeling cylindrical pinch experiments. The code [13] incorporates fluid electrons, particle ions, cylindrical geometry and self-consistent plasma turbulence effects on both the electrical resistivity and the ion and electron heating. The unique feature of this model is the inclusion of self-consistent turbulent ion heating, which is essential for a correct description of the reflected

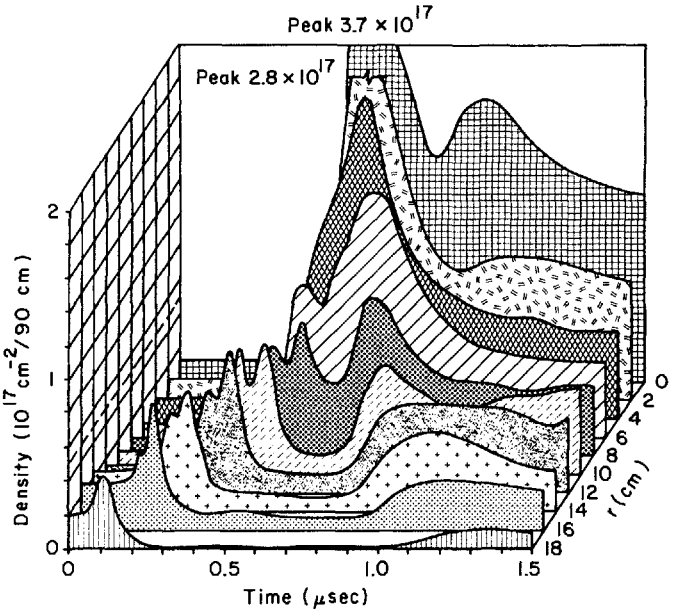


FIG.3. Density profile evolution in Los Alamos IHX experiment [18].

ion motion, especially in cylindrical geometry where the azimuthal velocity acquired in the heating regions can substantially reduce the number of ions which pass near the center of the cylinder.

In this code, the ion equations of motion are taken to be

$$m_i \frac{d\underset{\sim}{W}_i}{dt} = e\left(\underset{\sim}{E} + \frac{\underset{\sim}{W}_i \times \underset{\sim}{B}}{c}\right) + m_i \frac{\Delta \underset{\sim}{V}_i}{\Delta t} \tag{10}$$

where the last term in Eq. (10) includes both the anomalous resistive drag and also the change in velocity obtained by distributing the anomalous ion heating among the particles. The heating is calculated by dividing the anomalous heating into r, θ and z components in the ratio predicted by the quasilinear theory of each instability included in the calculation [13],

$$\Delta T_{ri} = \left[Q_r + (T_e - T_{ri})/\tau_{ei} - (T_{ri} - T_{zi})\left(\frac{1}{\tau_r} + \frac{1}{\tau_{ii}}\right)\right]$$

$$\Delta T_{\theta i} = \left[Q_r + (T_e - T_{\theta i})/\tau_{ei} - (T_{\theta i} - T_{zi})\left(\frac{1}{\tau_r} + \frac{1}{\tau_{ii}}\right)\right] \tag{11}$$

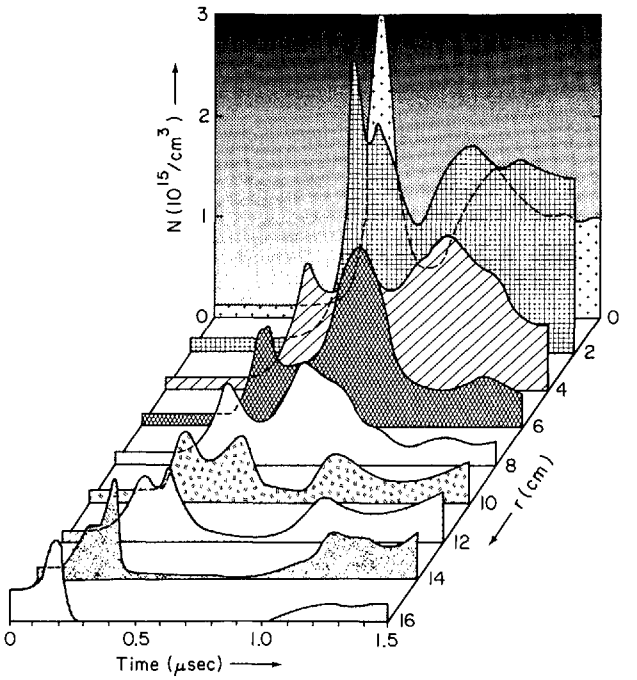


FIG.4. Hybrid-numerical simulation [16] of IHX experiment.

This model grew out of the fluid-turbulent model discussed in [3,14] and the heating rates and drag terms are deduced from ion acoustic, lower-hybrid and Buneman instabilities. Note that the model includes electron-ion equilibration on a time scale τ_{ei} and isotropization on a time scale τ_{ii} and τ_r. The latter scale is the relaxation time of $T_{i\parallel}$ and $T_{i\perp}$ due to electromagnetic ion cyclotron instabilities [15].

Using this code, we have simulated the Los Alamos Implosion Heating Experiment (IHX). The computer simulation [16] shows very strikingly the mechanisms involved in the experimentally observed plasma motion. As the magnetic piston drives in, the reflected ions move ahead of the piston giving a two-hump density distribution, one hump due to the reflected ions, the other due to the particles trapped near the piston. As the bulk of the reflected ions approach the cylindrical center a large density peak appears near the center. Then, as they return to larger radii, a later density rise is observed at the outer radii which pushes the magnetic field toward the wall. Meanwhile, as the magnetic piston slows down, the ions initially trapped at the piston move inward freely due to their inertia. This causes a second density peak to appear near the center. The agreement of our numerical model and the experiment is qualitatively and quantitatively excellent, and confirms the usefulness of the model also in aiding design of experiments [Figs 3 and 4].

Because of the importance of plasma radius on wall stabilization in toroidal versions of the theta pinch, experiments are now beginning which attempt to tailor the plasma size. We have therefore used HYBRID to model [17] various Staged Theta-Pinch Experiments (STP), in which the magnetic pulse contains a programmed mix of implosion and adiabatic compression fields. We predict the effect of full, partial or no staging on the location and temperature of the resultant theta pinch plasma. The numerical results confirm the notion that the tailoring of the wall magnetic field can have a dramatic effect on the trade-off of plasma temperature and radius. With a staged pinch the plasma can be caught before it hits the wall, though a transitory density peak near the wall will result. STP experiments are now beginning at Los Alamos, and our code results can be used to suggest the effect of various current pulses.

Staging helps to increase substantially the plasma radius and the ultimate plasma temperature as expected. The numerical model gives the final plasma radius, r_f=0.4 R and the final plasma temperature, T_f= 0.072 $B_s^2/8\pi n_0$ for the simple implosion, while r_f=0.6 R and T_f=0.15 $B_s^2/8\pi n_0$ for the fully staged implosion, where R and n_0 are the initial plasma radius and density (average), B_s is the driving magnetic field strength (maximum). The results of the numerical calculation show that the final magnetic field and the plasma density have very diffuse profiles; neither the bounce model nor the snow-plow model can reproduce this phenomenon.

REFERENCES

[1] DAVIDSON, R.C., GLADD, N.T., Phys. Fluids 18 (1975) 1327.
[2] BATCHELOR, D.B., DAVIDSON, R.C., Phys. Fluids 19 (1976); WINSKE, D., HEWETT, D.W., Phys. Rev. Lett. 35 (1975) 937.
[3] LIEWER, P.C., KRALL, N.A., Phys. Fluids 16 (1973) 1953.
[4] KRALL, N.A., LIEWER, P.C., Phys. Rev. A4 (1971) 2094.
[5] DAVIDSON, R.C., GLADD, N.T., HUBA, J.D., WU, C.S., "Effects of Finite Plasma Beta on the Lower-Hybrid-Drift Instability", submitted for publication (1976).
[6] FREIDBERG, J.P., GERWIN, R., private communication.
[7] LIEWER, P.C., DAVIDSON, R.C., "Analytic and Numerical Studies of Sheath Broadening by the Lower-Hybrid-Drift Instability in Post-Implosion Theta Pinches", submitted for publication (1976).
[8] DAVIDSON, R.C., KRALL, N.A., Anomalous Transport in High-Temperature Plasmas, submitted to Nuclear Fusion.
[9] SPITZER, L., Physics of Fully Ionized Gases, Wiley, New York (1967).
[10] COMMISSO, R., GRIEM, H.R., Phys. Rev. Lett. 36 (1976) 1038.
[11] BODIN, H.A.B., McCARTAN, J., NEWTON, A.A., WOLF, G.H., "Diffusion and stability of high-β plasma in an 8-metre theta pinch", Plasma Physics and Controlled Nuclear Fusion Research (Proc. 3rd Int. Conf. Novosibirsk, 1968) 2, IAEA, Vienna (1969) 533.
[12] KRALL, N.A., in Advances in Plasma Physics (Eds. A. Simon and W. B. Thompson), Wiley, New York (1968), Vol. 1, p. 153, and references therein.
[13] HAMASAKI, S., KRALL, N.A., WAGNER, C.E., BYRNE, R.N., "Effect of Turbulence on Theta-Pinch Modeling by Hybrid Codes", Phys. Fluids, in press.
[14] HUI, B.H., HAMASAKI, S., DAVIDSON, R.C., Nuclear Fusion 16 (1976) 73.
[15] DAVIDSON, R.C., OGDEN, J., Phys. Fluids 18 (1975) 1045.
[16] HAMASAKI, S., KRALL, N.A., "Numerical Modeling of the IHX Experiment", Phys. Fluids, in press.
[17] HAMASAKI, S., KRALL, N.A., "Theoretical Modeling of the Staged Theta Pinch", Phys. Fluids, in press.
[18] SHERWOOD, A., private communication.

DISCUSSION

ON PAPER IAEA-CN-35/E 15

K. HÖTHKER: I would like to call attention to recent experimental results (HÖTHKER, K., Nucl. Fusion 16 (1976) 253) on microturbulence in a plasma trapped in the imploding magnetic piston of a theta pinch. All measurements indicate that the turbulence is dominated by ion sound turbulence, although – considering only the velocities – one would expect the lower hybrid drift velocities also to contribute to the microturbulence. An explanation seems to be that the lower-hybrid-drift modes are stable because of the high local β ($\beta \approx 2$), with $T_e > T_i$.

M. KAUFMANN: Your paper compares calculated and experimental results. In experiments one would expect the neutral background and cooling of the electrons by heat losses at the ends to have a strong effect on the plasma parameters. Are these effects included in the code?

R.C. DAVIDSON: The SAI hybrid results presented here included the effects of neutral particle ionization but did not include electron cooling by axial heat loss. This latter effect can, however, be incorporated in the model in a straightforward way.

W. KÖPPENDÖRFER: The anomalous resistance of the lower-hybrid-drift instability is evidently anisotropic and exists only perpendicular to the magnetic field. Would one have to assume classical resistivity along the field lines?

R.C. DAVIDSON: The modified-two-stream instability is a natural continuation of the lower-hybrid-drift instability for $k_\parallel \neq 0$, and can contribute to anomalous transport effects along the field lines.

G.H. WOLF: Have you applied your criteria to the question how the life-time of the required profiles might be affected by anomalous relaxation in theta-pinch-type reactor plasmas subject to MHD wall-stabilization?

R.C. DAVIDSON: No detailed parameter studies have been carried out for reactor plasmas. However, with sufficiently strong inhomogeneities it can still be expected that the anomalous transport will be many times classical, until the profiles become sufficiently diffuse.

K.V. ROBERTS: Do you have any information on the effect of shear on the cross-field diffusion produced by the lower-hybrid instability, because this might be important in governing the rate of disappearance of the trapped B_z-field in a reversed-field-pinch experiment?

R.C. DAVIDSON: Theoretical studies by the Maryland and SAI groups indicate that shear can in fact have a stabilizing influence on the lower-hybrid-drift instability for Maxwellian ions. The local growth rate (including shear) remains to be calculated for this instability for typical reversed-field-pinch profiles and parameters.

KINETIC BEHAVIOUR OF HIGH-BETA PLASMAS*

J.P. FREIDBERG, R.A. GERWIN, D.W. HEWETT, H.R. LEWIS,
C.W. NIELSON, A.G. SGRO, L. TURNER, D. WINSKE
Los Alamos Scientific Laboratory,
University of California,
Los Alamos, New Mexico,
United States of America

Abstract

KINETIC BEHAVIOUR OF HIGH-BETA PLASMAS.

The study of the kinetic behaviour of high-beta plasmas has centred round two main problem areas. The first is the investigation of anomalous transport during the fast implosion phase and slow postimplosion phase of high-beta pinches. The second concerns the calculation of finite ion gyroradius effects on unstable MHD modes in diffuse high-beta pinches. The results of these studies are summarized.

1. TRANSPORT IN PINCHES

A detailed understanding of the macroscopic effects of microturbulence requires a lengthy and involved series of several different types of calculations. The first is the identification and isolation of the important microinstabilities by the use of linear Vlasov theory. The second is the investigation of the nonlinear evolution of the instability and its consequences and is usually accomplished by particle simulation techniques. The third step is to incorporate the microtheory into some appropriate form of transport coefficients to be used in hybrid simulation codes, capable of following plasma behavior on macroscopic time scales.

Linear perturbation theory previously indicated that the lower-hybrid drift instability (LHDI) might constitute a danger for magnetically confined post-implosion plasmas, because of its large growth rate $\sim (\omega_{ce}\omega_{ci})^{\frac{1}{2}}$, its minimal requirement on the perpendicular-current drift velocity ($V_{drift} \sim v_{thi}$), its insensitivity to the temperature ratio T_e/T_i, and its lack of dependence upon gyro-resonance (not subject to a low saturation level due to turbulence-induced resonance-broadening). However, the question of the actual threshold drift velocity remained unresolved until now, because its investigation was precluded by the assumption of straight-line zero-order ion orbits.[1]

We have rederived the linear properties of the LHDI both numerically and analytically including the effect of the zero-order magnetic field upon the ions. One might expect this effect to become important when $Re(\omega) \leq \omega_{ci}$. This condition can be translated into $v_{drift}/v_{thi} = o(m_e/m_i)^{\frac{1}{2}}$, and it is verified by our detailed analytical and numerical studies.

In cases of interest to controlled fusion, quasi-neutrality holds for this instability, and the electrostatic dispersion relation may be represented by approximate equality of the species perturbation densities, $n_{i1} \sim n_{e1}$. The n_1's are usually obtained from velocity-space integration of the orbit-integral solutions of the linearized Vlasov equations for each

* Work performed under the auspices of USERDA.

species. In the present instance, we find it numerically convenient to interchange the orders of integration, which, for the flute mode being considered, effectively allows complete summation of the infinite series of gyro-resonant Bessel-function terms for each species. Analytically, the dispersion relation in the very low drift velocity regime is represented by taking a single gyro-resonant contribution for n_{il} and only the $\ell = 0$ Bessel-function term for n_{el} (strongly magnetized electrons).

The two approaches yield good agreement for the threshold drift velocity and growth rates in this regime. For $T_e = T_i$, the threshold velocity is given approximately by

$$v_{drift} \sim 4(m_e/m_i)^{\frac{1}{2}} v_{thi} = v^o_{drift}$$

In the Reference Theta Pinch Reactor[2] with $\beta = 0.9$, $r_o = 15$ cm, $T_e = T_i = 10$ keV, $B_{external} = 10^5$ Gauss, with an assumed density profile $n = n_o \exp[-(r/r_o)^2]$, we find $v_{drift} < v^o_{drift}$ over essentially the entire profile, $n \geq 0.02\, n_o$. Thus, the LHDI can be harmless for important cases of interest.

In situations where the perpendicular-current drift velocity exceeds threshold, one can estimate the anomalous resistivity associated with the LHDI in the following way. By ensemble-averaging the nonlinear ion Vlasov equation over the spatial fluctuations of the LHDI, and then taking the first velocity moment, Davidson and Gladd[1] have derived the following representation of the anomalous resistivity:

$$\eta^* = 4k(\omega_{pi}^2/k^2v_{thi}^2)\ \mathrm{Im}[(\omega/kv_{thi})Z(\omega/kv_{thi})](E_f/(n^2e^2v_{dr})$$

where unmagnetized ions (straight-line orbits) have been assumed. Here Z is the plasma dispersion function and $E_f = E^2/8\pi$ is the energy density of the perturbation electric field. A theory of Manheimer[3] that applies to nearly dispersionless waves such as drift waves would predict that the LHDI instability saturates when the bounce frequency of ions trapped in the wave potential roughly equals the linear growth rate, $\omega_{bounce} \sim \gamma$. From this relation, the fluctuation field energy density can be estimated and used in the above η^* expression to be evaluated at the (ω,γ,k) values corresponding to the fastest-growing mode. The result reads, in the hot-ion regime $v_{drift} \ll v_{thi}$,

$$\eta^* = (\pi^3/2^9)(\pi/2)^{\frac{1}{2}}(v_{dr}/v_{thi})^8(\omega_{ce}^2/\omega_{pe}^2)(1/\omega_{LH})$$

where the simplifying assumption $T_e \ll T_i$ has been invoked. Although it is, strictly speaking, inconsistent to invoke nonlinear ion-trapping in a quasi-linear theory that uses straight-line ion orbits, it is nevertheless a reasonable way to get a rough estimate of η^* since the transition between the linear and saturated regimes, in reality, is probably smeared out. (Our simulations are, thus far, limited to the regime $v_{drift} > v_{thi}$.)

As a concrete example, we consider the Los Alamos Scyllac full torus experiment with $\beta \sim 0.8$, $n \sim 1 \times 10^{16}\mathrm{cm}^{-3}$, $T_i \sim 1$ keV, $T_e \sim 500$ eV, $B_{external} \sim 5 \times 10^4$ Gauss, and a pinch radius $r_o \sim 1$ cm. Assuming a density profile $n = n_o \exp[-(r/r_o)^2]$, we find the radial dependence for η^*:

r/r_o	0.5	0.7	0.9	1.1	1.3	1.5
η^*(sec)	4.7×10^{-21}	2.9×10^{-20}	1.3×10^{-19}	5.4×10^{-19}	2.2×10^{-18}	9.6×10^{-18}

Note that $v_{drift} = 0.29v_{thi}$ at $r/r_o = 1.9$ and always increases with r. The classical resistivity at this T_e is $\eta_{class} \sim 1 \times 10^{-17}$ s. Thus, throughout most of the radial profile, classical resistivity would seem to have been dominant in that experiment.

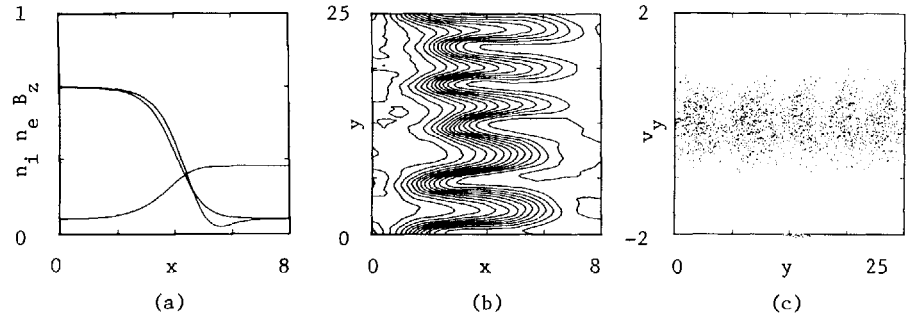


FIG.1. (a) Equilibrium profiles; (b) contour plot of B_z showing the instability; (c) ion phase space at saturation.

In the high drift velocity regime ($v_{dr}/v_{thi} > 1$) two-dimensional particle simulation studies of sheath stability have been carried out in strongly inhomogeneous plasma and magnetic field environments.[4] The simulations were performed using a nonradiative electromagnetic particle code initialized with inhomogeneous self-consistent Vlasov equilibria that represent the sheath region of imploding pinches.[5] An example of such an equilibrium is shown in Fig. 1a. The electron density is slightly larger than the ion density inside the sheath and slightly smaller outside in order to produce the electric field needed to contain the ions. In this case the ions are ten times hotter than the electrons, and at the point where the densities are equal the value of β_i is 0.33 and v_{dr}/v_{thi} is 6.7. The particles (64000 electrons and 64000 ions of mass 100 m_e) were given initial positions and random velocities such that the equilibrium profiles were reproduced. The equilibrium magnetic field B_z is perpendicular to the plane of the simulation.

Typically, a strong flute instability develops. Figure 1b shows the contour plot of B_z at the time the instability has saturated ($T = 200\ \omega_{pe}^{-1} \sim 7\ \omega_{LH}^{-1}$). A similar structure appears in contour plots of the potential and the densities. In the case shown here, one finds $k_y = 1.02\ c\omega_{pe}^{-1} = 0.41\ \rho_e^{-1}$ and $\omega = 1.78 + i0.59\ \omega_{LH}$. The real part of the frequency and wavenumber agree fairly well with the finite-β analysis of Gladd,[6] while the growth rate is too small by a factor of two. The discrepancies are attributed to nonlocal effects. During the stage of rapid linear growth dominated by a single wave the measured values of the heating rates and anomalous resistivity are in good agreement with quasilinear theory.[1] Saturation of the instability is due to ion trapping. The ion phase space at saturation, shown in Fig. 1c, exhibits the usual vortex structure. The phase velocity of the wave is roughly at v_{thi}. A comparison of many runs shows that the saturation potential ϕ_s scales as $e\phi_s/m_i\ (\omega_r/k_y)^2 \sim 0.16$ for $v_{dr}/v_{thi} > 4$ and $e\phi_s/T_i \sim 0.32$ for $v_{dr}/v_{thi} < 4$.

In high-voltage pinch experiments, the time for the ions (electrons) to relax to a Maxwellian is much greater (less) than the implosion time. A useful theoretical model for such experiments is a hybrid model, which assumes collisionless kinetic ions and fluid electrons. Assuming charge neutrality and massless electrons eliminates the microscopic length and time scales of λ_D and ω_{pe}^{-1}. These phenomena, as well as microturbulence due to a non-Maxwellian distribution in the electron phase space, are included on the average by specification of anomalous transport coefficients.

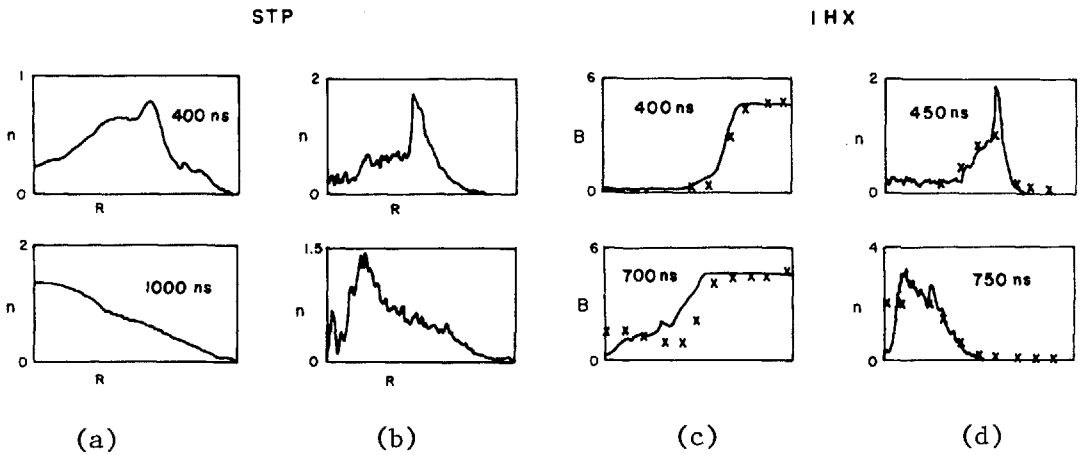


FIG. 2. Comparison of hybrid simulations with experiment.

We have developed such a model[7] in one dimension (cylindrical or planar) which includes a four-dimensional ion phase space (w_r, w_θ, w_z, r) and all nontrivial field components ($E_r, E_\theta, E_z, H_\theta, H_z$) and have applied it to theta pinches, screw pinches and high-β tokamaks. The resistivity used,

$$\nu_{a\,\parallel,\perp} = \omega_{pe}[1-\exp(Vd_{\parallel,\perp}/(3c_s)]$$

$$\nu_{\parallel,\perp} = \max(\nu_{a\,\parallel,\perp}), \nu_{clas}), \quad \eta_{\parallel,\perp} = m_e \nu_{\parallel,\perp}/(ne^2)$$

is a generalization of one suggested by Chodura.[8] Ionization has been included in the model to allow calculation of experiments in which the fill gas has been incompletely preionized, and radiation from impurity atoms has been included in an approximate manner by assuming the state of ionization of these atoms to be that calculated from the assumption of coronal equilibrium at the local electron temperature.

We present our calculations of two LASL theta pinches. Figures 2c and 2d compare experimentally determined (indicated by x) and computed (indicated by the continuous curve) magnetic field and density profiles at various times for the IHX, while Fig. 2b presents the theoretically derived and Fig. 2a the experimentally determined density profiles for the STP. The agreement between experiment and theory is good. Note that the ordinates of Figs 2a and 2b have different scales. In both experiments, before the imploding plasma reaches the center (i.e. for $t <$ 500 ns) the density profile consists of, at successively greater distances from the origin, the preshocked plasma, the region of the reflected ion beam, indicated by a rise from the preshocked level followed by a plateau of approximately constant density, and finally the region of the magnetic sheath, indicated by a rise from the plateau density to a maximum and then to zero. The density peak in the sheath region does not appear clearly in the IHX data because of the coarse spatial resolution. However, it does appear in the data when one looks at plots of density at a given position versus time. Since the data are taken by laser interferometry at given radii, these last mentioned plots are continuous curves. By 600 ns the reflected ion beams have reached the center, and we present one comparison for each experiment after this occurs.

Due to the finite conductivity, the magnetic sheath is not perfectly sharp and diffuses somewhat into the plasma. Both theory and experiment indicate a sheath thickness of $\sim$ 1-2 cm during the implosion. The reflected ions are influenced by this field during and just after the reflection process, and θ velocities comparable to the r velocities result from the ions turning in this field. The large θ velocities cause many of the reflected ions to miss the center by a large distance and to consequently turn around, move to larger radii, and hit the magnetic piston before they would had the θ velocity been zero, as predicted by the perfect conductivity bounce model.

2. STABILITY FOR $m \geq 2$

It has long been known as an experimental fact that $m \geq 2$ modes which are theoretically predicted to be MHD unstable are not observed experimentally. The explanation for this is usually associated with finite ion gyroradii effects. Since the scaling of future large experiments depends fairly sensitively on the finite ion gyroradius criterion, considerable effort has been applied to accurately determine the stability condition. The work has followed along two main lines: one, a general

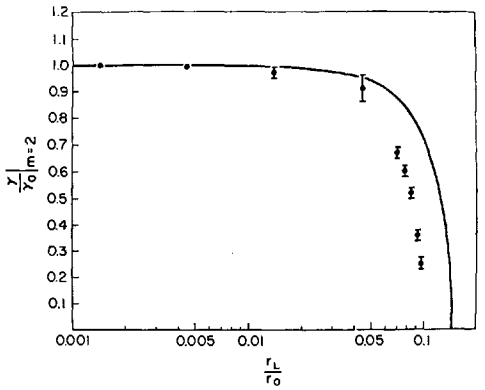


FIG. 3. Growth rate versus ion gyroradius.

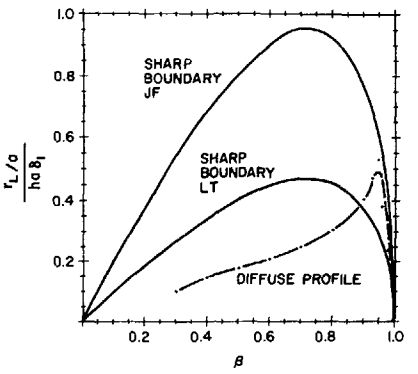


FIG. 4. Normalized gyroradius versus beta for marginal stability.

approach to solving the linear inhomogeneous Vlasov-fluid equations with initial emphasis on the surface current model to test the method; and second, a trial function approach which enables us to obtain good estimates in the short term for diffuse systems.

The equations of the Vlasov-fluid model[9] have been solved analytically for a straight sharp-boundary screw-pinch configuration, keeping the leading order FLR effects of ions due to their motion transverse to the magnetic field.[10,11] The ion motion parallel to the magnetic field leads to a frequency-dependent compressibility function different from that determined by the adiabatic equation of state used in ideal MHD. As a result, many of the equations of the Vlasov-fluid model are, in this order, structurally identical to those of ideal MHD, except for a different compressibility function and the presence of a magnetoviscosity term. The magnetoviscosity term can lead to FLR stabilization of $m \geq 2$ long-wavelength (near-θ-pinch type) modes and, when $\beta|\omega/kv_{th}| \gg 1$ and $|\omega/kv_{th}| \ll 1$, to FLR stabilization of $m \geq 2$ short-wavelength (stabilized Z-pinch type) modes. Even in the absence of FLR effects, the difference between the compressibility functions results in a decreasing value for the ratio of the growth rates γ_{VF}/γ_{MHD} with decreasing wavelength or with decreasing $|\gamma_{MHD}/kv_{th}|$. This ratio is approximately equal to unity only for modes with long wavelengths. In the cases studied, we have verified Freidberg's theorem[9] that the marginal stability limits of the Vlasov-fluid model and of ideal MHD are identical. Our analysis may help to explain the apparent stability of the Kurchatov reversed-field experiment.[12]

In a parallel computation,[13] we have studied numerically the eigenfrequencies of the normal modes of the perturbed, sharp-boundary Vlasov-fluid screw pinch. For the parameters used, appropriate to a near-θ-pinch, we find that the $m = 2$ mode is FLR-stabilized for sufficiently large ion temperature (see Fig. 3); the $m = 1$ mode is unaffected by FLR effects. However, the critical value of the ratio of ion Larmor radius to plasma radius r_L/r_o above which the $m = 2$ mode is stabilized is lower than was predicted by Freidberg[9] by a factor of about 2.5, in good agreement with data obtained from experiments at Garching[14]

and Los Alamos[15], as well as with our analytical treatment.[10] Our treatment gives the following Vlasov-fluid dispersion relation for the long-wavelength unstable modes:

$$\tilde{\omega}^2 - \frac{1}{2}\left(\frac{r_L}{r_o}\right)^2 m(m-1)\,\tilde{\omega} + \tilde{\gamma}_o^2 = 0$$

where $\tilde{\omega} = \omega/\omega_c$, $\tilde{\gamma}_o = \gamma_o/\omega_c$, ω_c = ion gyrofrequency, and γ_o = ideal MHD growth rate. This dispersion relation predicts a critical ratio of r_L/r_o for FLR stabilization of an m = 2 mode that is one-half the value predicted by Freidberg.[9] The smaller critical ratio enhances the possibility of simultaneous wall stabilization of the m = 1 mode and FLR stabilization of the m = 2 mode in near-θ-pinch machines such as Scyllac. We are extending our calculations to diffuse profiles.

The second calculation of finite gyroradii effects utilizes a trial function approach in the Vlasov-fluid model. A diffuse equilibrium is constructed by assuming the ion distribution is a simple function of the total energy of a single particle. The linear stability of such equilibria in this model can be described in terms of a single displacement vector $\vec{\xi}_\perp$. Assuming $\vec{\xi}_\perp(r,t) = \exp(-i\omega t)\vec{\xi}_\perp(r)$, a complex energy relation may be obtained which takes the form

$$-\delta W = \mathrm{Re}\left[|\omega|^2 \int d\vec{r}d\vec{v}\ \frac{\partial f_o}{\partial \varepsilon}|\hat{s}_1|^2\right]$$

$$\mathrm{Im}\left[i\omega_e \int d\vec{r}d\vec{v}\ \vec{\xi}_\perp \cdot (\vec{E}_o + \vec{v} \times \vec{B}_o)\ \frac{\partial f_o}{\partial \varepsilon}\ \hat{s}_1\right] = 0$$

δW is identical to the potential energy of ideal MHD for incompressible displacements. The orbit integral, s_1, has the form

$$\hat{s}_1 = -m_i \int_{-\infty}^{t} \vec{v}' \cdot \frac{d\vec{\xi}_\perp}{dt'}\, dt'$$

where the primes indicate evaluation along particle trajectories.

Because of the close connection between the Vlasov-fluid model and ideal MHD, the MHD eigenfunctions of the equilibrium are used as trial functions in the above equations. FLR expansion leads to the conclusion that δW to lowest order is the ideal MHD energy principle. Consequently, it follows that $\omega_r^2 + \omega_i^2 \leq \gamma_{MHD}^2$. Using the MHD eigenmode as a trial function corresponds to equality in this relation.

To calculate the reduction in MHD growth rate with increasing ion FLR, the imaginary part can be solved iteratively for complex ω as the temperature of the assumed thermal ion distribution is progressively increased. Numerical simulation techniques are used to evaluate $\hat{s}_1$ by choosing a set of particles which represent the ion distribution at time t and stepping each particle backwards in time to obtain its integral contribution. The numerical problem is made tractable by exploiting particle trajectory periodicity in axisymmetric fields so that any given particle need be followed only for one period.

Figure 4 shows typical values of ion FLR required to stabilize the m = 2 mode. Sharp boundary theories of Freidberg[9] and Turner[10] are shown for comparison. Diffuse m = 2 MHD modes are stabilized for much lower temperatures for moderate values of β than would be indicated by either sharp boundary theory.

REFERENCES

1. R. C. Davidson and N. T. Gladd, Phys. Fluids 18, 1327 (1975).
2. F. L. Ribe, Reviews of Modern Phys. 47, 7 (1975).
3. W. M. Manheimer, Phys. Fluids 14, 579 (1971).
4. D. Winske and D. W. Hewett, Phys. Rev. Lett. 35, 937 (1975).
5. D. W. Hewett, C. W. Nielson and D. Winske, Phys. Fluids 19, 433 (1976).
6. R. C. Davidson, N. T. Gladd, C. S. Wu, and J. D. Huba, submitted to Phys. Fluids.
7. A. G. Sgro and C. W. Nielson, Phys. Fluids 19, 126 (1976).
8. R. Chodura, Nucl. Fusion 15, 55 (1975).
9. J. P. Freidberg, Phys. Fluids 15, 1102, (1972).
10. L. Turner, LASL Report LA-UR-76-397 to be published.
11. L. Turner, LASL Report LA-UR-76-1655 to be published.
12. A. G. Es'kov et al., 7th European Conference on Controlled Fusion and Plasma Physics, Lausanne (1975).
13. H. R. Lewis and L. Turner, LASL Report LA-UR-76-1332 to be published.
14. M. Kaufman, Bull. Am. Phys. Soc. 20, 1338 (1975).
15. E. L. Cantrell et al., Third Topical Conference on Pulsed High-Beta Plasmas, Culham Laboratories, England (1975).

DISCUSSION

ON PAPER IAEA-CN-35/E 16

H.R. GRIEM: With regard to the theoretical estimates of saturation levels for the lower hybrid instability, I would just like to point out that measured fluctuation levels in the post-implosion phase of a reversed-field theta pinch are consistent with the Fowler bound (COMMISSO, R.J., GRIEM, H.R., Phys. Fluids, in press).

R.C. DAVIDSON: Your saturation estimate for the lower-hybrid-drift instability based on $\nu \sim \omega_B$ should be correct for $V_d > v_i$ (diamagnetic drift velocity > ion thermal velocity). However, in the post-implosion regime ($V_d < v_i \rightarrow r_{\perp i} < L_N$) resonant ion effects are important in limiting the instability. The Maryland calculations, which include quasilinear stabilization, current relaxation and so on, indicate $\eta_{AN} \propto V_d^2$, which is considerably larger than the LASL scaling with $\eta_{AN} \propto V_d^8$, and give estimates of η_{AN} consistent with the experimental measurements by Commisso and Griem.

D. WINSKE: The initial saturation estimate was obtained from our first simulation results, which all had large values of $v_{\text{electron drift}}/v_{\text{ion thermal}}$. Since then, we have done a number of runs with $v_{\text{electron drift}}/v_{\text{ion thermal}}$ as low as 1.5. Paulette Liewer and I are collaborating on a theory which will give a more realistic value for the resistivity and be in agreement with the simulation results.

M.G. HAINES: First a comment. For many years we at Imperial College have studied finite-ion-Larmor-radius, finite-β effects in θ pinches (1968, 1971) and recently in the diffuse or screw pinch (1976) starting from the Vlasov equation. We have also included anisotropic pressure, rotation, sheared axial flow and axial heat flow and azimuthal heat flow due to radial temperature gradients, as we have an arbitrary distribution function. We have studied the effect of FLR on the Suydam modes. Have you obtained a similar decoupling of fluid and resonance modes by choosing an appropriate ordering procedure?

D. WINSKE: Yes. For a near-theta-pinch configuration, with a long wavelength, low-frequency ordering is assumed. To study short-wavelength modes in a stabilized z-pinch, another ordering is used.

F. SÖLDNER: Have you compared the results of your simulation calculations on implosion heating with those of Krall's code, and, if so, what are the main differences?

D. WINSKE: No, the codes have not been compared directly with each other, only with the experiments. The main difference between the codes lies in the resistivity model used.

F. HERRNEGGER: For stabilization of the m = 2 mode, the dependence of the critical Larmor radius r_L on β should be rather weak in the range $\beta = 0.3$–0.7, as you just showed (this is the range in which the high-β stellarator experiments at Garching are operating). However, it is rather surprising to me that for β values of about 0.9 the critical values of r_L obtained from the diffuse pressure model calculations should be larger than those obtained from the surface current model.

Have you done numerical calculations of finite-Larmor-radius stabilization of m = 2 modes in a two-dimensional helical configuration with a diffuse pressure profile?

D. WINSKE: No. The equilibria used are one-dimensional; a small-δ ordering is assumed.

M.G. HAINES: With regard to the last question, we at Imperial College find that increasing β normally always leads to increased stability. There are two effects of finite β on FLR: first is the increase in diamagnetism ($\sim \text{curl}_\perp(P_{i\perp}/\Omega_i)$) with $\partial B_z/\partial r$ and second is the effect of negative $\partial T_i/\partial r$ in conjunction with positive $\partial B_z/\partial r$. Both increase stability.

Session XX

OPEN TRAPS

Chairman

R.F. Post
USA

2XIIB PLASMA CONFINEMENT EXPERIMENTS*

F.H. COENSGEN, J.F. CLAUSER, D.L. CORRELL, W.F. CUMMINS,
C. GORMEZANO†, B.G. LOGAN, A.W. MOLVIK, W.E. NEXSEN,
T.C. SIMONEN, B.W. STALLARD, W.C. TURNER
Lawrence Livermore Laboratory, University of California
Livermore, California,
United States of America

Abstract

2XIIB PLASMA CONFINEMENT EXPERIMENTS.

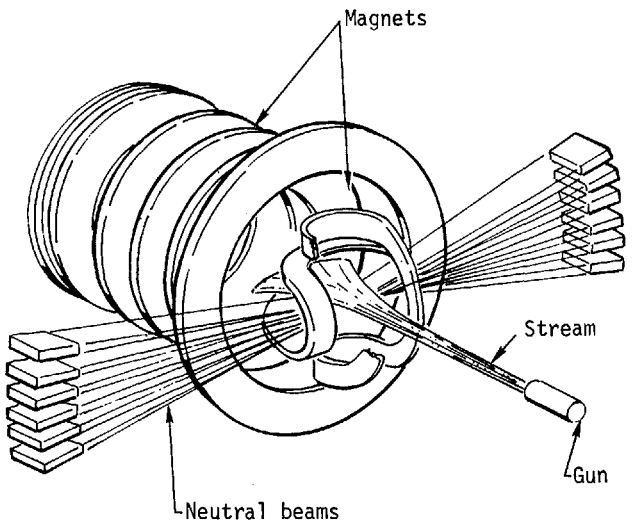
This paper reports results of 2XIIB neutral-beam injection experiments with plasma-stream stabilization. The plasma stream is provided either by a pulsed plasma generator located on the field lines outside the plasma region or by ionization of neutral gas introduced at the mirror throat. In the latter case, the gas is ionized by the normal particle flux through the magnetic mirror. A method of plasma start-up and sustenance in a steady-state magnetic field is reported in which the plasma stream from the pulsed plasma generator serves as the initial target for the neutral beams. After an energetic plasma of sufficient density is established, the plasma generator stream is replaced by the gas-fed stream. Life-times of the stabilized plasma increase with plasma temperature in agreement with the plasma stabilization of the drift-cyclotron loss-cone mode. The following plasma parameters are attained by using the pulsed plasma generator for stabilization: $\hat{n} \approx 5 \times 10^{13}$ cm^{-3}, $\overline{W}_i \approx 13$ keV, $T_e = 85$ eV, and $n\tau_p \approx 7 \times 10^{10}$ cm^{-3}·s. With the gas feed, the mean deuterium ion energy is 9 keV and the peak density $\hat{n} \approx 10^{14}$ cm^{-3}. In the latter case, the energy confinement parameter reaches $\hat{n}\tau_E = 6.2 \times 10^{10}$ cm^{-3}·s, and the particle confinement parameter reaches $n\tau_p = 1.2 \times 10^{11}$ cm^{-3}·s.

1. INTRODUCTION

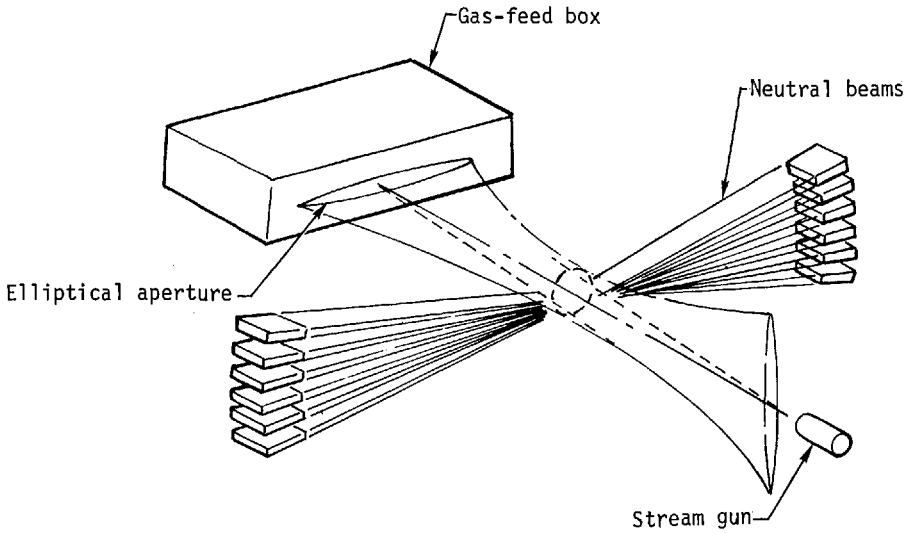
Several results from the 2XIIB magnetic-mirror confinement experiment are reported in this paper. In these experiments using injected neutral beams, it is necessary to stream warm plasma along the magnetic field lines [1] to obtain improved ion confinement and to produce high plasma betas. The stream reduces the amplitude of ion-cyclotron fluctuations and, consequently, the turbulent diffusion loss of ions. The experimental results are described in considerable detail by the quasilinear theory [2,3] for the drift-cyclotron loss-cone (DCLC) mode [4]. Earlier experimental results [5,6] are also explained by this theory. According to this theory, the ion velocity distribution evolves to a marginally stable state as turbulent diffusion from either the hot-ion population or from an external stream fills in the ambipolar hole. In the latter case, the hot-ion confinement is improved.

The 2XIIB magnet is a minimum-B, Yin-Yang set with a 0.67-T central field, a 2:1 mirror ratio, and 150-cm mirror-to-mirror length. The size of the magnet is similar to that of the 2XII magnet but differs in that it has considerably larger openings for neutral-beam injection. The 2XIIB neutral-beam system consists of 12 injectors [7] operating with extraction energies between 15 and 20 keV. Up to 4.8 MW of neutral deuterium atoms with an equivalent current of 370 A have been injected. This current is divided between full-, half-, and one-third-energy components. The stream is supplied either by a deuterium-loaded-titanium washer gun [8] or by ionization of gas injected at the mirror throat as shown in Fig. 1.

* This work was performed under the auspices of the USERDA and under contract No. W-7405-Eng-48.
† On leave from Association Euratom-CEA, Grenoble, France.



(a)



(b)

FIG.1. Schematic diagrams illustrating (a) injection of plasma stream and (b) injection of gas at mirror throat.

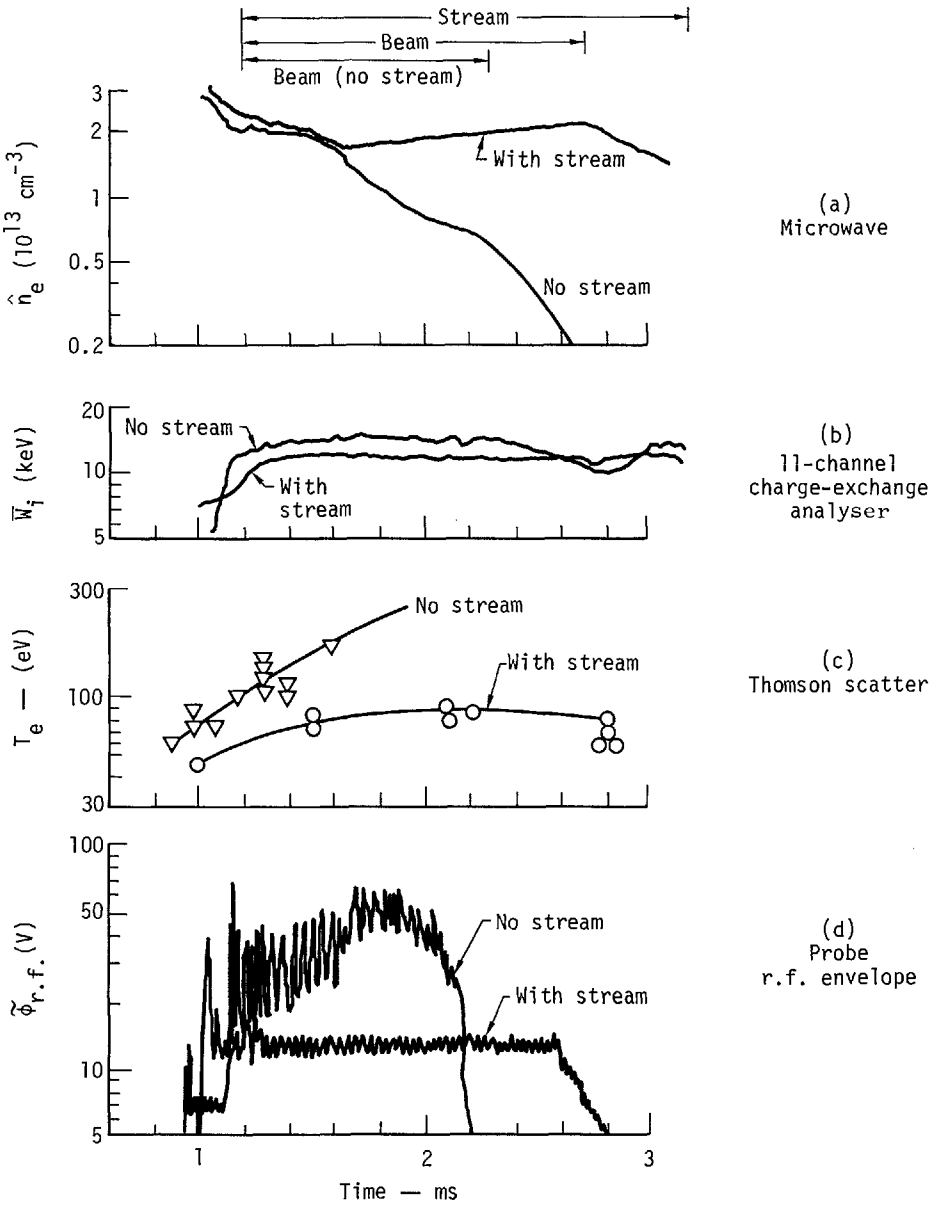


FIG.2. Plasma parameters versus time, showing that the plasma stream (a) permits density build-up, (b) results in small decrease in average ion energy, (c) cools electrons, and (d) reduces ion-cyclotron fluctuations.

We discuss two modes of operation of the 2XIIB device. In the first, described in Section 2, the target plasma is formed by trapping and adiabatically compressing a plasma injected along a magnetic field in the manner of the previous 2XII experiments [6]. In this mode, the target plasma has a density $n_e \approx 4 \times 10^{13}$ cm^3, mean ion energy $\overline{W}_i \approx 3$ keV, and electron temperature $T_e \approx 60$ eV. Approximately 50% of the neutral beam injected into this target is trapped by charge exchange and ionization; the mean ion energy of the contained plasma is raised to 13 keV within a few hundred microseconds. In the second mode of operation, described in Section 3, plasma and beam injection begin after the magnetic field has reached its maximum. In this mode, beam trapping and exponentiation are initiated on the colder and lower-density plasma stream in a quasisteady-state magnetic field.

2. STREAM STABILIZATION AND ENERGY SCALING

The data in Fig. 2, taken with a plasma target trapped and heated by magnetic compression, show the effect of the stabilizing plasma stream. Neutral-beam injection begins at the peak of compression (1.1 ms). With the plasma stream, the neutral-beam current and duration are 200 A and 1.6 ms; without the plasma stream, they are 200 A and 1.2 ms.

Figure 2(a) shows the central plasma electron density $\bar{n}_e$ versus time. These data were obtained by dividing microwave interferometer measurements of line density by the measured (14-cm) mean plasma diameter [9]. The plasma target densities are comparable with and without streaming plasma. With no stream, the neutral beam maintains the density for a brief 0.3 ms. Afterwards, the beam input rate cannot overcome the plasma losses due to the increasing amplitude of the ion-cyclotron fluctuations. By contrast, the density with a plasma stream continues to build up until the neutral beams are shut off.

The mean deuteron ion energy is shown in Fig. 2(b). Without the stream, the mean ion energy increases rapidly. With the streaming plasma, the mean ion energy rises more slowly to 12 keV within 0.3 ms of beam turn-on. The 12-keV mean ion energy has been verified by absolute measurements of fast-atom charge-exchange flux, plasma diamagnetism, and absolute measurements of neutron production [10].

Electron temperature versus time measurements were made by Thomson scattering. In Fig. 2(c), the electron temperature with no stream rises rapidly to 150 eV. With the stream, the electron temperature increases from 45 eV to about 85 eV in 0.5 ms, and then remains relatively constant.

Ion-cyclotron fluctuations are detected with electrostatic probes [11] located beyond the mirrors and with microwave beams [12] at the center of the plasma. Figure 2(d) illustrates that the stream lowers the ion-cyclotron fluctuation amplitude by a factor between 2 and 4. Increasing the streaming-plasma input further reduces the fluctuation amplitude. The large decrease in fluctuation amplitude at 2.2 ms with no stream occurs when the hot-plasma density drops to a low enough level that the plasma is stabilized by background cold gas, much the same as in partially gettered operation [5,6]. The dominant fluctuation frequency is centered near the ion-cyclotron frequency [13], corrected for finite beta. Experimental observations of turbulent ion energy diffusion are obtained from measurements of charge-exchange flux at 12 discrete energies from 0.5 to 38.9 keV. The observed diffusion is reproduced theoretically by the quasilinear theory [14].

Longitudinal density measurements [9] with a movable microwave interferometer indicate that the axial plasma length is $\sim$40 cm. Inverting this density profile [15] determines an ion-angular distribution peaked nearly perpendicular to magnetic field lines. This distribution indicates that the ions, injected near 90°, diffuse primarily in the perpendicular velocity

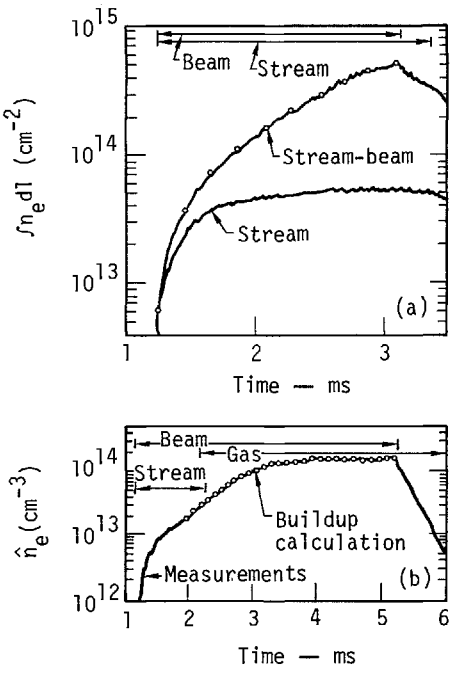


FIG.3. Density build-up history on streaming plasma target, showing (a) $\int n_e dl$ without gas feed and (b) $\hat{n}_e$ with 8000-Å hydrogen gas-feed.

direction by electron drag and wave turbulence, rather than in pitch angle, in agreement with the quasilinear theory.

The scaling of the plasma confinement parameter $n\tau_p$ with mean ion energy has been determined from 3 to 13 keV by varying the neutral-beam extraction voltage. Particle lifetime τ_p is obtained from the density decay rate after the neutral beams are turned off [1,16]. Such measurements indicate that particle confinement increases with ion energy, from $\hat{n}\tau_p$ = 1.5 to 2.0 × 10^{10} cm^{-3}·s at 3 keV up to $\hat{n}\tau_p$ = 7 × 10^{10} cm^{-3}·s at 13 keV. The beam current required to sustain the plasma at 10^{13} cm^{-3} density decreases with mean ion energy, indicating improved energy confinement at higher ion energies.

Energy confinement time τ_E is calculated from energy balance once steady state is achieved. Quantitative determination of τ_E is not available because the power input from the streaming gun is not well known. However, with gas-feed stabilization and with all power being supplied by the neutral beams, $\hat{n}\tau_E$ = 6.2 × 10^{10} cm^{-3}·s.

Electron temperature measurements using Thomson scattering are available for a limited number of shots and indicate a slow increase in electron temperature with ion energy. The hot-ion cooling rate depends on the electron temperature and follows the Spitzer [17] drag $T_e^{3/2}$ dependence over a range of electron temperatures 20 < T_e < 85 eV, where $n\tau$ is orbit averaged over the density profile.

3. HIGH-BETA BUILDUP IN A STEADY MAGNETIC FIELD

We have found that the streaming plasma used for stabilization can be injected into a quasi steady-state magnetic field to form a suitable target

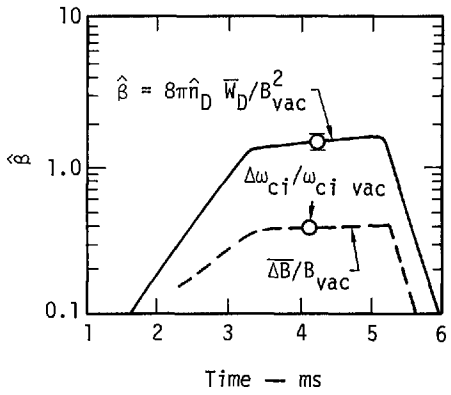


FIG.4. Central values of beta, diamagnetic flux, and ion-cyclotron frequency shift versus time.

plasma [18]. With an injected beam current of 260 A, the data in Fig. 3(a) show that the density of the hot plasma increases exponentially, reaching densities and energies similar to those achieved previously with target plasmas that were trapped by pulsed magnetic fields. The points are computed from a density buildup code [19]. This procedure offers a simple solution to the important technical problem of plasma startup in d.c. magnetic-mirror machines.

Using a single deuterium-loaded-titanium washer gun to provide startup and stabilizing plasma stream, a maximum beam-injected plasma beta of 0.4 is reached. Here beta is defined by $\beta \equiv 8\pi\ \hat{n}_i\ W_i/B^2_{vac}$, where $\hat{n}_i$ is the central hot-ion density, W_i is the average ion energy, and B_{vac} is the applied central field. The beta is limited by end losses associated with periodic bursts of ion-cyclotron fluctuations and not by the available neutral-beam current. Increasing the amount of stabilizing plasma stream with three guns raises the beta to 0.6, but β is again limited by the same phenomenon.

To further increase the plasma stream, a gas-feed system [20] was installed as shown in Fig. 1(b). A ceramic box, with elliptical apertures conforming to the flux tube passing through a 12-cm-diam circle at the central midplane, is located just beyond one mirror throat of the minimum-B field. Hydrogen or deuterium gas is injected at a controlled rate into the box above and below the plasma fan by four pulsed gas valves. Gas neutrals are ionized in the box by electrons ($T_e \approx 60$ eV) conducted along the field from the central plasma. Because the mean free path of gas neutrals is short compared to the thickness of the plasma fan, few neutrals leak out of the box. Measurements of charge-exchange flux from the center of the machine indicate a charge-exchange lifetime on background gas greater than 5 ms. This loss rate was negligible compared to other losses of the hot ions.

To start ionization of injected gas, a hot plasma is initially created as described above. Figure 3(b) shows buildup with 225-A of beam injection. The guns are turned off, and gas injection begins with 8000-A atom equivalent of hydrogen gas. The central density reaches 1.5×10^{14} cm^3 and is sustained for the duration of beam injection. No strong bursts of ion-cyclotron fluctuations are observed, indicating that the stabilizing plasma is not limited with the gas feed. Similar results were obtained with deuterium.

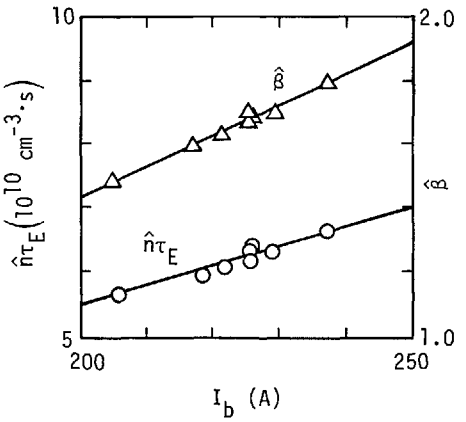


FIG.5. Energy confinement $\hat{n}\tau_e$ and $\hat{\beta}$ increase with neutral-beam current I_b.

The dots shown in Fig. 3(b) are obtained by fitting the observed time dependence of the plasma density to the rate equation

$$\frac{dn}{dt} = a(1 - e^{-bn}) - \frac{n^2}{\langle n\tau_p \rangle} . \qquad (1)$$

The coefficient a is the beam current trapped per unit volume calculated for Gaussian plasma and beam density profiles and taking into account reionization of charge-exchange neutrals. The parameter $b = \langle\sigma v\rangle(2\bar{r}_p)/v_b$ is an attenuation factor averaged over the energy components of the neutral beam. Here, $\langle n\tau\rangle$ is a density-independent loss parameter, appropriate for particle loss by ion-ion scattering and electron drag. For a constant 10% fraction of cold plasma, the best fit of Eq. (1) to the measured density buildup gives a plasma volume V = 4.5 litres (defined by $\hat{n}V$ = total number of particles), and $\langle n\tau_p\rangle = 1.2 \times 10^{11}\ cm^{-3}\cdot s$.

Hydrogen was used in the gas feed with deuterium neutral-beam injection so that hot beam-injected ions could be distinguished from warm ions trapped from the streaming plasma by the mass-selective neutral analyser. At the high-density saturation, after correcting for reionization of charge-exchange neutrals the mean ion energy was calculated to be 9 keV. The maximum fraction of cold ions, hydrogen, and impurities is estimated to be less than 20%.

The dashed line in Fig. 4 shows the average plasma diamagnetism $\overline{\Delta B}/B_{vac}$ measured by a compensated diamagnetic loop around the vacuum chamber. The excluded flux of the plasma is normalized to the total flux excluded by a field-free metal object ($\Delta B = B_{vac}$) of the same volume as the plasma, placed at the position of the plasma for calibration. For constant plasma dimensions, the measured diamagnetic flux will be proportional to the average field reduction $\overline{\Delta B}/B_{vac}$ within the plasma. Because of the substantial reduction in field, the mean ion gyroradius is comparable to the plasma radius. Accordingly, the frequency of ion-cyclotron fluctuations decreases with $\overline{\Delta B}/B_{vac}$, as indicated by the point labeled $(\Delta\omega_{ci}/\omega_{ci\ vac})$ in Fig. 4.

The solid line in Fig. 4 gives the peak value $\hat{\beta}$ obtained from the measured central density $\hat{n}_D$ and average ion energy $\overline{W}_D$. The central beta reaches a value well above unity. The error bar shows the uncertainty in peak density and cold plasma fraction. Because of the short axial length of the plasma ($L_p/r_p \approx 3$) and the high plasma pressure, the field lines are

likely to have substantial curvature; therefore, a central beta value of roughly 2 is required to depress the on-axis field to zero.

Figure 5 shows how the energy confinement parameter $\hat{n}\tau_E$ scales with neutral-beam current I_b for constant average beam energy $\bar{E}_b$. The average plasma energy lifetime in steady state is calculated from

$$\tau_E = (\hat{n}_D V)\bar{W}_D/(fI_b\bar{E}_b) \quad . \tag{2}$$

In Eq. (2), the numerator is the energy content of a total number of ions ($\hat{n}_D V$) at average energy $\bar{W}_D$ = 9 keV, and the denominator is the fraction f of incident beam power that is absorbed in the plasma. This fraction varies with density, but it reaches 0.63. At I_b = 225 A, $\hat{n}\tau_E = 6.8 \times 10^{10}$ cm^{-3}·s. Averaging the Gaussian profiles over the plasma volume rather than taking the central density gives $\langle n\tau_E \rangle \approx 2.4 \times 10^{10}$cm^{-3}·s. At I_b = 225 A, a Thomson scattering measurement of the central electron temperature T_e = 60 ± 15 eV gives a confinement parameter of $n\tau_d = 2.0 \times 10^{10}$ cm^{-3}·s ± 30% due to electron drag. Thus, ion losses are largely accounted for by classical electron drag, consistent with the quasilinear theory for marginal stability [2]. Figure 5 shows that the central beta increases with beam current (at constant beam energy), with no apparent saturation. No evidence is found of a beta limit due to the mirror mode, the Alfvén ion-cyclotron mode, or nonadiabatic effects. Comparison of diamagnetic measurements with density measurements indicates that the energy of the plasma ions remains approximately constant with increasing beta. The energy containment time τ_E is found to be nearly constant over the range of beam current shown in Fig. 5. The product $n\tau_E$ in Fig. 5 increases proportionally to beta (density) as the beam power is increased. Preparations are underway to pursue this favorable scaling of $n\tau_E$ to higher neutral-beam power.

4. CONCLUSIONS

In summary, the principal results of the 2XIIB experiments are:
Demonstration that stabilization is provided by a small fraction of warm plasma.
Demonstration of plasma heating and sustenance by neutral-beam injection.
Demonstration that the plasma confinement parameters $n\tau_p$ and $n\tau_E$ increase with ion energy.
Achievement of startup in a steady-state magnetic field.
Attainment of central plasma beta greater than unity.

Two fundamental properties of mirror systems are shown: the increase in $n\tau$ with ion energy and the ability to contain high-beta plasmas. The energy sealing and the satisfactory theoretical interpretation of these data establish a basis for the design of future open-geometry experiments. The high-beta result has particular significance for mirror fusion reactor design, since high-beta operation enhances the fusion energy balance.

REFERENCES

[1] COENSGEN, F.H., CUMMINS, W.F., LOGAN, B.G., MOLVIK, A.W., NEXSEN, W.E., SIMONEN, T.C., Phys. Rev. Lett. 35 (1975) 1501.
[2] BALDWIN, D.E., BERK, H.L., PEARLSTEIN, L.D., Phys. Rev. Lett. 36 (1976) 1051; also see Paper IAEA-CN 35/C2, this volume.
[3] BERK, H.L., GORMEZANO, C., STEWART, J.J., submitted to Nucl. Fusion.
[4] POST, R.F., ROSENBLUTH, M.N., Phys. Fluids 9 (1966) 730.

[5] GOTT, Yu.V., IOFFE, M.S., KANAEV, B.S., MOTLICK, A.G., PASTUKHOV, V.P., SUBOLEV, R.J., YUSHMANOV, E.E., 4th Conf. Plasma Physics and Controlled Fusion Research (Proc. Conf. Tokyo, 1974) 1, IAEA, Vienna (1975) 341.
[6] COENSGEN, F.H., CUMMINS, W.F., MOLVIK, A.W., NEXSEN, W.E., SIMONEN, T.C., STALLARD, B.W., 4th Int. Conf. Plasma Physics and Controlled Fusion Research (Proc. Conf. Tokyo, 1974) 1, IAEA, Vienna (1975) 323.
[7] BAKER, W.R., BERKNER, K.H., COOPER, W.S., EHLERS, K.W., KUNKEL, W.B., PYLE, R.V., STEARNS, J.W., 4th Int. Conf. Plasma Physics and Controlled Fusion Research (Proc. Conf. Tokyo, 1974) 1, IAEA, Vienna (1975) 329.
[8] COENSGEN, F.H., CUMMINS, W.F., SHERMAN, A.E., Phys. Fluids 2 (1959) 350; also STEINHAUS, J.F., OLESON, N.L., BARR, W.L., Phys. Fluids 8 (1965) 1720.
[9] STALLARD, B.W., CUMMINS, W.F., MOLVIK, A.W., NEXSEN, W.E., SIMONEN, T.C., TURNER, W.C., Bull. Am. Phys. Soc. 20 (1975) 1231.
[10] NEXSEN, W.E., LOGAN, B.G., COENSGEN, F.H., MOLVIK, A.W., CUMMINS, W.F., Bull. Am. Phys. Soc. 20 (1975) 1232.
[11] SIMONEN, T.C., to be published in Phys. Fluids.
[12] POWERS, E.J., SIMONEN, T.C., to be published in J. Appl. Phys.
[13] TURNER, W.C., CUMMINS, W.F., NEXSEN, W.E., POWERS, E.J., SIMONEN, T.C., STALLARD, B.W., Bull. Am. Phys. Soc. 20 (1975) 1232; also see POWERS, E.J., Phys. Fluids 16 (1973) 1374.
[14] TURNER, W.C., BERK, H.L., STEWART, J.J., submitted to Phys. Rev. Lett.
[15] HALL, L.S., SIMONEN, T.C., Phys. Fluids 17 (1974) 1014.
[16] COENSGEN, F.H., CLAUSER, J.F., CORRELL, D.L., CUMMINS, W.F., GORMEZANO, C., LOGAN, B.G., MOLVIK, A.W., NEXSEN, W.E., SIMONEN, T.C., STALLARD, B.W., TURNER, W.C., LLL Rept. UCID-17037 (1976).
[17] SPITZER, L. Physics of Fully Ionized Gases, 2nd ed., Wiley, New York (1962).
[18] COENSGEN, F.H., CLAUSER, J.F., CORRELL, D.L., CUMMINS, W.F., GORMEZANO, C., LOGAN, B.G., MOLVIK, A.W., NEXSEN, W.E., SIMONEN, T.C., STALLARD, B.W., TURNER, W.C., Phys. Rev. Lett. 37 (1976) 143. Due to an error in the analysis of the Thomson scattering data the correct electron temperature is 0.6 times that reported in Ref. [18].
[19] STALLARD, B.W., LLL Rept. UCRL-51784 (1975).
[20] LOGAN, B.G., LLL Rept. UCID-16851 (1975).

DISCUSSION

ON PAPER IAEA-CN-35/C1

D.R. SWEETMAN: Your values of β seem to be higher than those that would be expected on the basis of the mirror instability? Is that so?

F.H. COENSGEN: The mirror mode limit depends on details of the theoretical model and distribution function. For 2XIIB several simplifying assumptions are violated, such as the long thin approximation; and even the usual MHD approximation that the Larmor radius is small compared to the radial scale length is nearly violated. Hence the precise mirror mode limit is not theoretically known. It is significant that the simulation code of Byers (discussed in paper IAEA-CN-35/C3), which treats large-Larmor-orbit plasmas, does not show a mirror mode limit to the β achieved. In fact, Byers observes a smooth transition to a reversed-magnetic-field equilibrium.

W. HENKES: What is the order of magnitude of the low-energy particle current envisaged to replace the warm plasma stream?

F.H. COENSGEN: Using 2XIIB parameters, Berk's quasi-linear calculations (see paper IAEA-CN-35/C2) give required warm-plasma-stabilizing currents in the range of 80 to 200 A. We are designing a 400-A capability for 2XIIB experiments.

THEORETICAL EXPLANATION OF PRESENT MIRROR EXPERIMENTS AND LINEAR STABILITY OF LARGER SCALED MACHINES*

H.L. BERK, D.E. BALDWIN, T.A. CUTLER,
L.L. LODESTRO, N. MARON, L.D. PEARLSTEIN,
T.D. ROGNLIEN, J.J. STEWART, D.C. WATSON
Lawrence Livermore Laboratory,
University of California,
Livermore, California,
United States of America

Abstract

THEORETICAL EXPLANATION OF PRESENT MIRROR EXPERIMENTS AND LINEAR STABILITY OF LARGER SCALED MACHINES.

A quasilinear model for the evolution of the 2XIIB mirror experiment is presented and shown to reproduce the time evolution of the experiment. From quasilinear theory it follows that the energy lifetime is the Spitzer electron drag time for $T_e \lesssim 0.1\ T_i$. By computing the stability boundary of the DCLC mode, with warm plasma stabilization, the electron temperature is predicted as a function of radial scale length. In addition, the effect of finite length corrections to the Alfvén cyclotron mode is assessed.

INTRODUCTION

Both the 2XIIB [1] and PR-7 [2] mirror experiments have demonstrated stabilization of an ion-cyclotron frequency instability by the axial injection of cold plasma, herein termed a "stream." This conformed to a theoretical prediction that the drift-cyclotron-loss-cone (DCLC) mode would be stabilized by the presence of a low-density warm component [3]. In the following, we describe a quasilinear calculation for the ion evolution together with a model for the time evolution of the electron temperature. The composite theory is shown to be in quantitative agreement with many aspects of the 2XIIB experiment. The diffusion due to fluctuations, competing with transit loss of the unconfined stream, heats the low-temperature stream to partially fill the loss cone of the hotter confined plasma, thereby achieving marginal stability at a low fluctuation level. In the absence of the stream, a higher fluctuation level and a turbulent decay result. Next, we discuss the implication of this stabilizing mechanism in larger-radius machines. Finally, we describe certain finite geometry effects on the anisotropy-driven Alfvén-ion-cyclotron (AIC) mode which is predicted to exist in mirror machines at high β.

* Work performed under the auspices of USERDA, contract No. W-7405-Eng-48.

GENERAL CONSIDERATIONS

Ions are contained in a mirror machine only if $v_\perp^2 > (v_\parallel^2 + 2q\Phi/M)/(R - 1)$, where $v_\perp$ and $v_\parallel$ are the midplane components of the velocity relative to the magnetic field, R is the mirror ratio, q and M are the charge and mass, and Φ is the ambipolar potential which is typically positive and several times $T_e/|e|$ when $T_e/T_i \ll 1$. Particles lying outside this region of velocity space are lost axially in a transit time. When the velocity-space transport rate is slow compared to this transit rate, which is generally the case for mirror-confined plasmas, the distribution function for unconfined particles is small compared to its value for confined particles. The resulting non-monotonic energy distribution can then be subject to microinstabilities, termed loss-cone modes [4,5]. A sufficient level of turbulence results in a velocity diffusion which competes with the axial transit rate. The result is that the low-energy portion of the distribution partially fills in so that it becomes marginally stable. However, the existence of a significant density of unconfined particles implies a large loss flux which must be supplied either from the confined particles or from an external source such as demonstrated by stream stabilization [1].

In the absence of an external source, the requirement for maintenance of a stable distribution implies that the ratio of the lifetimes of confined to unconfined ions will vary as the respective densities. Thus, it was thought that a distribution which is well spread in pitch angle would have a lifetime of only a few axial transit times [6]. However, a distribution that is highly peaked in pitch angle, as results from neutral injection normal to $\vec{B}$ together with diffusion principally in $v_\perp$ and energy drag on cold electrons, has a hole in velocity space that is characteristic of the ambipolar energy. The ratio of densities will then vary as $E_i/q\Phi$, where E_i is the average ion energy. In addition, because the axial flow rate of unconfined ions is here the ion acoustic speed, the lifetime of peaked distribution exceeds that of a well spread distribution of equal energy by a factor $(E_i/q\Phi)^{3/2}$.

If cold ions are supplied, as by an injected plasma stream, the lifetime of confined ions can be further enhanced. The turbulence no longer is required to replenish the loss flux of unconfined ions from the confined ions, but only to heat the injected cold ions to uniformly fill the region $0 < v_\perp^2 < 2q\Phi/M$. The loss flux of unconfined ions is then also an energy flux which, assuming the power comes from the confined ions, results in a lifetime enhancement factor $(E_i/q\Phi)^{5/2}$. In this text, it is

shown that for 2XIIB parameters this lifetime is longer than the Spitzer drag time, so that the lifetime of the energetic ions is determined by this latter classical process.

QUASILINEAR MODEL

To quantify these notions, we have added to an existing two-dimensional (2-D) ($v_\perp, v_\parallel$) Fokker-Planck code, which included Coulomb collisions, charge exchange, and neutral-beam input sources [7], a quasi-linear diffusion in $v_\perp$ and a low-energy source to represent the stream. Particles in the unconfined regions were assumed lost at a rate inverse to their transit time. In addition, a simplified and faster one-dimensional (1-D) code for $F(v_\perp,t) = \int dv_\parallel f(v_\parallel, v_\perp)$, valid when $\langle v_\parallel^2 \rangle \ll \langle v_\perp^2 \rangle$, has been constructed [8,9]. Results of the two codes will be compared here.

The turbulence model is driven by the DCLC for which $k_\parallel = 0$ and $k_\perp a_i > 1$, where $k_\parallel, k_\perp$ are the wave number components relative to $\vec{B}$, and a_i is the mean ion Larmor radius. Near marginal stability, noise is resonant near a cyclotron harmonic m, and the velocity diffusion coefficient is taken as

$$\vec{\vec{D}}(\vec{v}_\perp) = \frac{\hat{v}_\perp \hat{v}_\perp}{v_\perp^2} \sum_k \left| \frac{q\tilde{\Phi}_k}{M} \right|^2 \frac{m^2 \omega_{ci}^2}{\Delta\omega_k} J_m^2\left(\frac{k_\perp v_\perp}{\omega_{ci}}\right) \qquad (1)$$

where $\tilde{\Phi}_k$ is the fluctuating potential, $\Delta\omega_k$ is the correlation frequency determined by the transit rate of ions moving in a non-uniform magnetic field [10], $\Delta\omega_k \approx \omega_{ci}(\langle v_\parallel^2 \rangle^{1/2} \omega_{ci}^{-1} |d \ln B/ds|)^{1/3}$, and s is distance along B. The amplitude $|\tilde{\Phi}_k|^2$ is proportional to the wave energy density,

$$\varepsilon_k = \left| \frac{q\tilde{\Phi}_k}{M\bar{v}^2} \right|^2 \frac{n_e M\bar{v}^2}{\sigma_k}$$

where n_e and $\bar{v}$ are a normalized density and velocity, and σ_k is a time-dependent parameter that is determined by the solution of the dispersion relation and that in this work is modelled as a constant. ε_k is determined by the equation

$$\frac{\partial \varepsilon_k}{\partial t} = 2\gamma_k \varepsilon_k + \alpha_k$$

where α_k is the thermal source of noise, and the growth rate is given by

$$\frac{\gamma_k}{\omega_{ci}} = \sigma_k \frac{\bar{v}^2}{n_0} \int dv^3 \frac{\partial f}{\partial v_\perp^2} J_m^2\left(\frac{k_\perp v_\perp}{\omega_{ci}}\right) \frac{m\omega_{ci}}{\Delta\omega_k} \qquad (2)$$

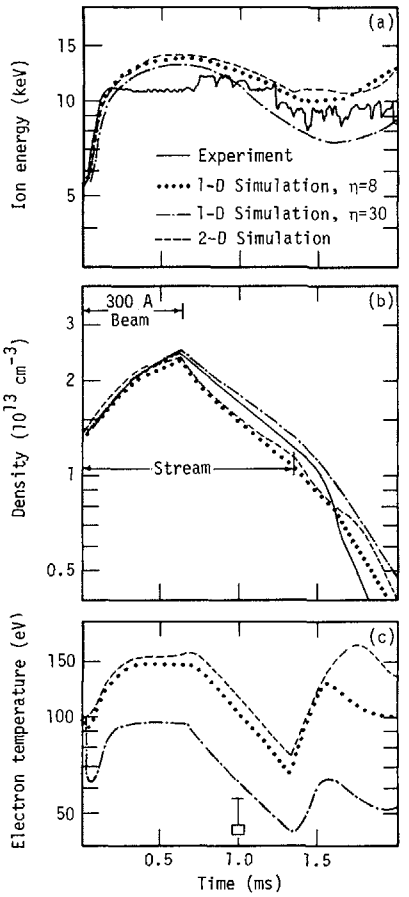


FIG.1. Comparison of the time evolution of the plasma parameters in the 2XIIB experiment with the 1-D and 2-D quasilinear codes. The electron temperature was measured at one point in time as shown.

In a machine such as 2XIIB with a radius of only a few Larmor radii, DCLC is unstable when the "matrix element" on the right-hand side of Eq. (2) is positive over a large range of $k_\perp$. For larger machines, the dispersion relation restricts the range of unstable $k_\perp$, even when the matrix element is positive, and a more realistic form must be used for $\omega(k)$ and σ_k. This case is currently under investigation.

The electron temperature plays an important role in determining both the electron drag rate and the ambipolar potential. It can be calculated

using either the electron Fokker-Planck equation or equivalently from the energy balance equation

$$\frac{d}{dt}\left(\frac{3}{2} nT_e\right) = n\nu_d E_i - \eta T_e J_{loss} \tag{3}$$

where ν_d is the Spitzer ion-electron energy exchange rate, E_i is the mean ion energy, J_{loss} is the electron particle flux per unit volume lost axially, and ηT_e is the mean energy per unit volume of the axially-lost electrons. The identification $\eta T_e = q\Phi + T_e$ reduces the model predictions to those of the electron Fokker-Planck code used in the 2-D code. Larger values of η allow a phenomenological means for accounting for processes such as ionization, secondary emission, etc.; and a value $\eta = 8$, used in the 1-D code, was typical of the values found to describe the T_e history of 2XII [11]. The ratio $q\Phi/T_e$ is determined by the requirement of equal ion and electron loss rates [12]; typically, with stream we find $q\Phi/T_e \approx 3$.

The codes show that the stream reduces the fluctuation level in the plasma, allowing buildup with sufficient energetic beam current and an extended lifetime in the absence of beams. Without stream, the enhanced fluctuations prevent buildup to steady state, and turbulent decay results.

By using the experimentally measured time evolution of the plasma stream and background charge exchange, a quantitative comparison with experiment is possible. In Fig. 1, we compare density, ion temperature and electron temperature measured in the 2XIIB experiment with the predictions of the 1-D and 2-D codes. First of all note that the 1-D code for $\eta = 8$ and the 2-D code agree quite well with each other. As there are some differences in the physics of the two codes, the 2-D code required a stream current 1.5 greater than the 1-D code to predict similar parameters. As both these runs are for moderate values of η, they imply that the electrons in the hot plasma are thermally isolated from the colder external plasma supplying the stream. However, as can be seen in Fig. 1, the electron temperatures predicted by the codes are much larger than the experimental value. Strong thermal contact with the external plasma implies a much larger value of η. A one-dimensional run with $\eta = 30$ is shown in Fig. 1. At this larger value of η, there is better agreement with the observed electron temperature. To obtain the same density values as the experiment, the stream current in the $\eta = 30$ case is a factor of .65 of the $\eta = 8$ case. For a more detailed discussion of the 1-D results, see Refs [8] and [9].

The scaling laws for the steady state follow from the requirement for marginal stability and from Eq. (3) with the loss flux estimated as

$J_{loss} = \nu_t n_u$, where $\nu_t \approx (q\Phi/M)^{1/2}/2L_p$ is the transit rate of unconfined particles, L_p is the axial scale length, and n_u is the unconfined plasma density. Using $q\Phi \approx 3T_e$, we find

$$T_e(\text{keV}) = 3.3 \times 10^{-7} (n^2 L_p E_i/n_u \eta)^{1/3} \tag{4}$$

where E_i is the mean ion energy. For 2XIIB ($R_p/a_i \approx 2$ to 3), n_u at marginal stability is given by $n_u \approx n\lambda q\Phi/E_i \approx 3n\lambda T_e/E_i$, with λ a constant $\approx$ 0.5. For this case, we obtain $T_e = 1.1 \times 10^{-5} (nL_p E_i^2/\lambda\eta)^{1/4}$.
When the stream current J_{strm} is much larger than the beam current, it follows that in steady state $J_{strm} \approx J_{loss}$. When the mean ion energy is roughly the mean input beam energy, which occurs with sufficiently intense beams and stream, both the steady-state density and electron temperature are controlled by the stream and mean ion beam energy,

$$n = 0.7 J_{strm}^{8/11} L_p^{5/11} E_i^{2/11} \eta^{3/11}/\lambda^{5/11} \tag{5}$$

$$T_e = 1.0 \times 10^{-5} J_{strm}^{2/11} L_p^{4/11} E_i^{6/11}/\eta^{2/11} \lambda^{4/11} \tag{6}$$

Note that when these conditions are fulfilled, the steady-state n and T_e are independent of the input beam current. This result manifests itself in the density buildup in Fig. 1. For the first 300 μs, J_{strm} and thus n_u are greater than this minimum value required for stability at the prevailing density, and the density builds up at the beam input rate. After 300 μs, further density increase is determined by the prevailing stream, and the subsequent increase in density while the beam is on requires an increasing stream current with time as inferred from the end loss measurements.

Ions lose energy both by classical drag on the electrons at a rate $\nu_d n E_i$ and via fluctuations that supply the power drain of the unconfined ions given by $\frac{1}{2} q\Phi J_{loss}$, where $\frac{1}{2} q\Phi$ is the average energy of the unconfined ions. From Eq. (3) in steady state, it may be seen that the power drain from electron drag is larger than the turbulent energy transfer by a factor $2\eta/3$, so that the ion energy confinement time is dominated by classical electron drag, with the electron temperature depressed by the presence of the stream.

DRIFT-CYCLOTRON-LOSS-CONE STABILITY

For mirror machines with larger radii, the electron temperature is still given by Eq. (4) with the ratio n_u/n_H determined by the marginal

stability condition. This is evaluated from the flute-averaged dispersion relation of the DCLC mode [10], given by

$$\int_0^L ds\, k_\perp^2 I(\omega, k_\perp, s) = 0 \tag{7}$$

where

$$I = \frac{\omega_{pe}^2}{\omega_{ce}^2} + 1 + \frac{\omega_{pi}^2}{\omega_{ci}^2}\left\{ \frac{\omega_{pi}^2}{k_\perp^2 c^2} - \frac{\omega_{ci}}{k_\perp R_p} \frac{1 + \frac{\beta_\perp}{2}}{\omega + ik_\perp^2 D_e(\omega/k)/\omega_{ci}^2} \right.$$

$$+ \sum_{n\neq 0} \frac{\omega_{ci}^2}{k_\perp^2} \int d^3v \frac{1}{v_\perp} \frac{\partial F_i}{\partial v_\perp} \frac{\omega}{\omega - n\omega_c + ik_\perp^2 D_i(\omega/k)/\omega_{ci}^2} J_n^2\left(\frac{k_\perp v_\perp}{\omega_{ci}}\right)$$

$$\left. + \frac{\omega_{ci}^2}{k_\perp^2} \int d^3v \frac{1}{v_\perp} \frac{\partial F}{\partial v_\perp} \left[J_0^2\left(\frac{k_\perp v_\perp}{\omega_{ci}}\right) - 1 \right] \right\} \tag{8}$$

is the local dispersion relation, and $D_i(\omega/k)$ is the magnitude of the turbulent diffusion coefficient at the phase velocity of the wave. As a representative function, we use

$$F(v_\perp^2) = \frac{(n - n_u)}{v_H^2 - v_h^2}\left[\exp\left(-\frac{v_\perp^2}{v_H^2}\right) - \exp\left(-\frac{v_\perp^2}{v_h^2}\right)\right] + \frac{n_u}{v_u^2} \exp\left(-\frac{v_\perp^2}{v_u^2}\right) \tag{9}$$

In Eq. (8), D_i is obtained from the quasilinear, marginally stable state and can be estimated from the requirement for power balance with the stream. Assuming the turbulence transfers energy from the hot plasma to the unconfined plasma, whose lifetime is a transit time ν_t^{-1}, this balance gives

$$\frac{n v_H^2}{\tau_E} = n_u \nu_t v_u^2 \tag{10}$$

where τ_E is the turbulent-energy lifetime of the hot plasma. By using a diffusive scaling law, we have $D_i(v_H) \approx v_H^2/\tau_E$; and from Eq. (1) we have $D_i(v_\perp) \approx (\omega/kv_\perp)^3 D_i(\omega/k)$ for $\omega/kv_\perp \lesssim 1$ where $\omega \approx m\omega_{ci}$. Hence, using Eq. (10), we find

$$D_i\left(\frac{\omega}{k}\right) = \frac{a_i^3}{L_p} \frac{n_u}{n_H} \left(\frac{kv_H}{\omega}\right)^3 \tag{11}$$

MX, an experiment proposed by Lawrence Livermore Laboratory, has the parameters $B_{vacuum} = 20$ kG and $L_p = 170$ cm. The fraction of warm plasma (n_u/n) required for marginal stability and the implied electron tempera-

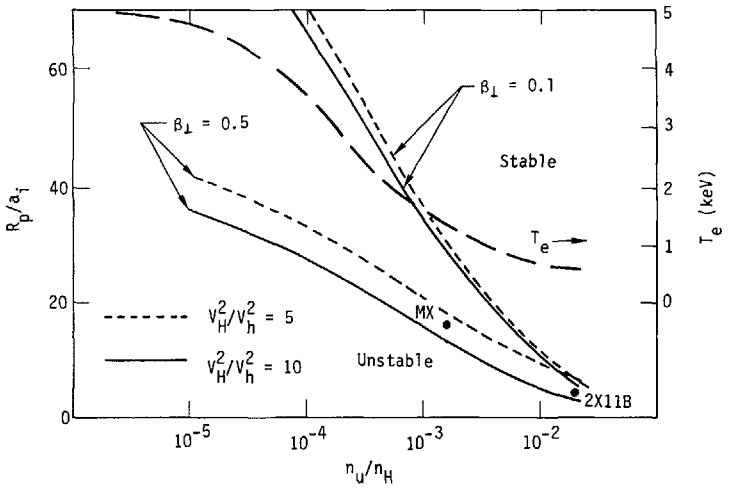


FIG.2. Plasma-radius stability boundary and predicted electron temperature for the MX experiment versus the fraction of warm plasma. Stable regions are for larger radii.

ture at $\beta = 0.5$ (the electron temperature determines the energy lifetime) are plotted in Fig. 2 as a function of plasma radius for two values of $(v_H/v_u)^2$ and $D_e = D_i$. In scaling from 2XIIB to MX, there is a six-fold reduction in the required warm plasma ratio. The marked reduction in the size of the stable radius from the case of no warm plasma to the case with warm plasma is due to two cooperative effects. One is the stabilizing effects of warm plasma and beta reported elsewhere [3,13,14] and the other is orbit diffusion which strongly stabilizes the large $k_\perp$ modes.

ALFVÉN-ION-CYCLOTRON MODE

In addition to inverted populations in velocity space that generate the previously described loss-cone modes, a mirror-confined plasma supports an anisotropic velocity distribution, which is an additional source of instability. A mode of recent concern [15] that taps this source is a left-hand, circularly polarized Alfvén wave. This mode, which will be referred to as the Alfvén-ion-cyclotron (AIC) mode, occurs at a sufficiently large $\beta_\perp$. Previous calculations of this mode [15,16] ignored finite-geometry effects and produced growth rates and frequencies for real $k_\parallel$. In this paper, we present preliminary theoretical results for

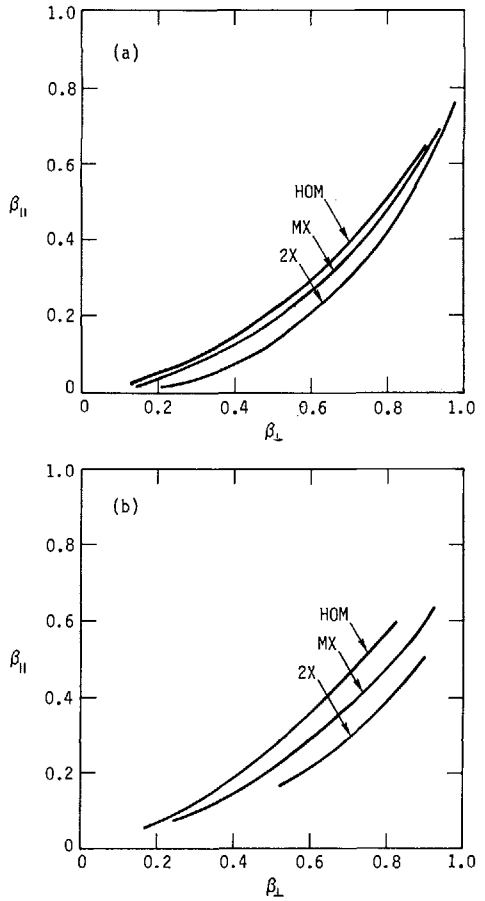


FIG.3. Alfvén-ion cyclotron stability boundaries in the $\beta_{\perp}$–$\beta_{\parallel}$ plane. Boundary curves labelled HOM, MX and 2X correspond to homogeneous plasma and to scale lengths of 25 and 7 ion Larmor radii respectively. (a) and (b) correspond to bi-Maxwellian and collisional ion velocity distributions, respectively.

the stability of this mode in mirror machines of finite extent. Specifically, we determine the boundary between absolute and convective instability ($d\omega/dk_{\parallel} = Im\omega = 0$) and the influence of finite geometry on this boundary by solving the phase integral [3]

$$\int_{-s_t}^{s_t} k_{\parallel}(s)ds = (2n + 1)\pi; \quad n = 0,1,2; \quad \frac{d\omega}{dk_{\parallel}} (s = \pm s_t) = 0 \qquad (12)$$

where s is the distance along a field line. We evaluate Eq. (12) by approximating $k_{\parallel}$ as

$$k_{\parallel}(B) \approx k_{\parallel}[B(0)] + \left.\frac{dk_{\parallel}}{dB}\right|_{B=0} \frac{s^2}{L^2} B(0)$$

The dispersion relation for the AIC mode is given in Ref. [15]. To evaluate stability boundaries, we consider two specific distributions: a bi-Maxwellian distribution (which is a model of the drag-dominated distribution computed by Fokker-Planck codes),

$$f \approx e^{-\alpha_{\perp} v_{\perp}^2} e^{-\alpha_{\parallel} v_{\parallel}^2}$$

and a collisional-type distribution,

$$f \approx e^{-\alpha v^2}\left[\frac{Rv_{\perp}^2}{v^2} - 1 + (2R-3)\ln\left(\frac{Rv_{\perp}^2}{v^2}\right)\right]$$

Our results are depicted in Figs. 3(a) and 3(b), where we plot the boundary of absolute instability for AIC for a uniform plasma and compare it to the shifted boundary obtained from a Wenzel, Kramers and Brillouin (WKB) calculation for 2XIIB and MX configurations.

Due to inhomogeneities, there is a substantial shift of the stability boundary for the 2XIIB configuration. However, the beta observed in that experiment is still in excess of the predicted threshold for AIC. Possible explanations are:

The depression in the field is less than that predicted by the long, thin approximation for the equilibrium, implying less local $\beta_{\perp}$ for the mode.

The simple parabolic expansion of the phase integral is inaccurate, because the WKB approximation typically fails when the calculated frequency shift is comparable to the homogeneous plasma frequency shift.

We have examined the effect on the mode of finite $k_{\perp} \approx 1/R_p$ and find it to be less important than the finite plasma length.

Finally, it should be noted that the SUPERLAYER code described in paper CN-35/C3 in these Proceedings[1] shows buildup through reversal without disruption by AIC, provided the plasma is not too long, i.e. if it is on

[1] McNAMARA, B., et al.

the order of 2XIIB lengths. If it is finite length which stabilizes AIC in 2XIIB, then MX with its longer scale length should be affected by this mode at high beta.

REFERENCES

[1] COENSGEN, F. H., et al., Phys. Rev. Lett. 35 (1975) 1501.

[2] BAIBORODOV, Y. T., et al., 6th Eur. Conf. Controlled Fusion and Plasma Physics (Proc. Conf. Moscow, 1973) 2, U.S.S.R. Academy of Sciences, Moscow (1973) 122.

[3] BERK, H. L., et al., 3rd Int. Conf. Plasma Physics and Controlled Nuclear Fusion Research (Proc. Conf. Novosibirsk, 1968) 2, IAEA, Vienna (1969) 151.

[4] ROSENBLUTH, M. N., POST, R. F., Phys. Fluids 8 (1965) 547.

[5] POST, R. F., ROSENBLUTH, M. N., Phys. Fluids 9 (1966) 730.

[6] GALEEV, A. A., 2nd Int. Conf. Plasma Physics and Controlled Nuclear Fusion Research (Proc. Conf. Culham, 1965) 1, IAEA, Vienna (1966) 341.

[7] FUTCH, A. H., HOLDREN, J. P., KILLEEN, J., MIRIN, A. A., Plasma Phys. 14 (1972) 211.

[8] BERK, H. L., STEWART, J. J., Lawrence Livermore Laboratory Rep. UCRL-78407 (1976) (submitted to Phys. Fluids).

[9] BERK, H. L., GORMEZANO, C., STEWART, J. J., Lawrence Livermore Laboratory Rep. UCRL-78401 (1976) (submitted to Nucl. Fusion).

[10] BALDWIN, D. E., et al., 4th Int. Conf. Plasma Physics and Controlled Nuclear Fusion Research (Proc. Conf. Madison, 1971) 2, IAEA, Vienna (1971) 735.

[11] COENSGEN, F. H., et al., 5th Int. Conf. Plasma Physics and Controlled Nuclear Fusion Research (Proc. Conf. Tokyo, 1974) 1, IAEA, Vienna (1975) 323.

[12] PASTUKHOV, V. P., Nucl. Fusion 14 (1974) 3.

[13] TANG, W. M., PEARLSTEIN, L. D., BERK, H. L., Phys. Fluids 15 (1972) 1153.

[14] GERVER, M. J., Electronic Research Laboratory Rep., University of California, Berkeley (1976) (to be published in Phys. Fluids).

[15] DAVIDSON, R. C., OGDEN, J. M., Phys. Fluids 18 (1975) 1045.

[16] For a list of earlier references, see CORDEY, J. G., HASTIE, R. J., Phys. Fluids 15 (1972) 2291.

DISCUSSION

ON PAPER IAEA-CN-35/C2

R.C. DAVIDSON: We have noted the good agreement between quasi-linear theory and the Livermore mirror experiment, and the similarly good agreement in self-consistent modelling of transport in theta pinches achieved by the Maryland and SAI groups. I would just like to say that it is encouraging to see how a theory as basic as quasi-linear theory can have such an important practical impact on experimental planning and scaling to new devices.

N. WINSOR: Could you indicate how sensitive your results are to the quasi-linear diffusion coefficient model, and how well the mode amplitudes which it assumes agree with experiment? At the higher temperatures of the MX experiment, with lower electron collision frequency, will your scaling be much more sensitive to this model?

H.L. BERK: For mirror parameters like those in the 2XIIB device the results are relatively insensitive to the quasi-linear model, as can be seen by comparing the $\eta = 8$ and $\eta = 30$ results. However, for larger machines such as MX the quasi-linear results will in fact be quite sensitive to the input parameters. Quantitative agreement between theory and experiment has not been obtained for the noise spectrum; but the precise degree of agreement is difficult to ascertain because the wave energy measured depends on the correlation time, the structure of the mode, and so on. However, it is important to note that there is agreement between experiment and theory on the lifetime, and this indicates that the calculated diffusion coefficient is comparable to the experimental. Qualitatively, there is correlation between the experimental and theoretical noise spectra.

R.N. SUDAN: What are your comments about the possibility of modes other than the drift loss-cone mode affecting your scaling as you move towards MX and beyond?

H.L. BERK: We are concerned with several other modes. The short-wavelength convective instability causes concern and MX needs to be designed for less than the axial critical length. Also, in this work we report on the Alfvén-cyclotron instability, which should be observed in both MX and 2XIIB according to our calculations. However, there is no evidence in the 2XIIB experiment that this mode is in fact present. If present in MX, the Alfvén-cyclotron instability will probably limit the β that can be achieved.

THEORY OF MIRROR MACHINES AT HIGH BETA*

B. McNAMARA, D.V. ANDERSON, J.K. BOYD,
J.A. BYERS, R. COHEN, T.A. CUTLER, L.S. HALL,
R.F. POST, M.E. RENSINK
Lawrence Livermore Laboratory,
University of California,
Livermore, California,
United States of America

Abstract

THEORY OF MIRROR MACHINES AT HIGH BETA.

The kinetic and guiding centre fluid theories of high-β plasma containment in mirror machines have been developed in a number of self-consistent models. The geometrical effects of magnetic field and ambipolar potential variation have been incorporated in a bounce-averaged Fokker-Planck code which shows that the square-well model somewhat overestimates the $n\tau$ and β achievable in a mirror field. Simple analytic approximations to the resulting pressure profiles have been incorporated in three-dimensional fluid-equilibrium codes which show the effect of coil geometry on the maximum β. Strongly curved vacuum fields allow higher β, but short plasmas in weakly curved fields tend to reverse the curvature locally before the mirror-mode limit is reached. Adiabaticity of particle orbits is described in terms of general formulas, applicable in high-β plasma equilibria, and is shown to break down close to the mirror-mode limit. Two approaches to increasing the energy multiplication factor Q for mirror machines are investigated. Moving the mirrors apart on a timescale about three times the ion-ion scattering time substantially increases $n\tau$ and improves containment of particles near the loss cone. The SUPER-LAYER particle code has been used to show the existence of stable, axisymmetric, $\beta > 1$ reversed-field equilibria for plasmas a couple of Larmor radii across. The toroidal containment of more than half the ions should enhance Q considerably, and the computer results indicate likely conditions in 2XII for creating reversed-field equilibria by neutral injection.

1. BOUNCE-AVERAGED FOKKER-PLANCK CALCULATIONS

In most previous work [1] on mirror-confined plasmas, the magnetic-square-well model has been invoked so as to reduce the kinetic equations to diffusion equations in velocity space only. Numerical methods for solving these equations are reviewed in Ref. [2]. We have developed techniques for handling a more realistic model which incorporates the spatial variation of the plasma and magnetic field along a flux tube. In this case, we explicitly perform the average over the axial bounce motion; e.g.,

$$\bar{A} \equiv \tau_B^{-1} \oint \frac{ds\, A(s)}{v_{\parallel}(s)} \qquad (1)$$

where A(s) is any arbitrary function of distance s along the field line, the axial bounce period is $\tau_B = \oint ds/v_{\parallel}(s)$, and the particle velocity along the field line is

$$v_{\parallel}(s) = \left[\frac{2}{M}\left(\varepsilon - \mu B(s) - \phi(s)\right)\right]^{1/2}$$

with (ε, μ) the usual constants of the particle motion, energy, and magnetic moment.

* Work performed under the auspices of USERDA, contract No. W-7405-Eng-48.

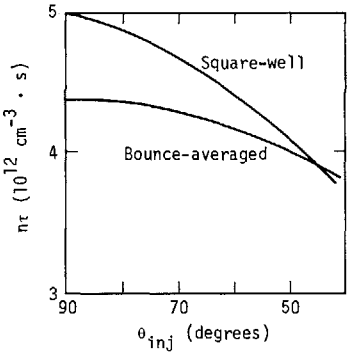


FIG.1. Particle confinement parameter versus source injection angle for magnetic-square-well and bounce-averaged-parabolic models.

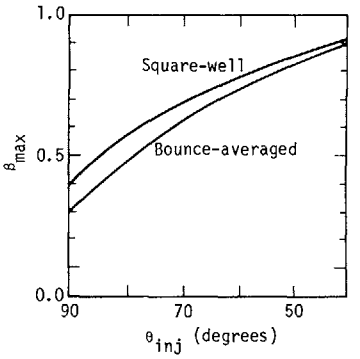


FIG.2. Mirror-mode beta limit versus source injection angle for magnetic-square-well and bounce-averaged-parabolic models.

TABLE I. INPUT DATA FOR COMPARISON BETWEEN MAGNETIC-SQUARE-WELL AND BOUNCE-AVERAGE-PARABOLIC MODELS

Net mirror ratio (R)	5
D^+ injection energy (keV)	50
Injection source width (spatial)	$-0.25 \leq s \leq +0.25$
Electron energy ($\bar{E}_e$)	$0.1\ \bar{E}_i$
Ambipolar potential (ϕ_m)	0
Normalized magnetic field profile	$1 + (R - 1)\ s^2$
(parabolic model)	$-1 \leq s \leq +1$
Local injection angle	Variable

The effect of the bounce-averaging process is indicated in Fig. 1, where we compare results for the particle confinement parameter $n\tau$ from the magnetic-square-well model and from a parabolic-magnetic-well model with bounce averaging. Input data for this comparison are given in Table I. One sees that the magnetic-square-well model yields slightly optimistic (15% higher) values for $n\tau$ with perpendicular injection, but the difference between results from the two models disappears as the injection angle decreases. Similarly, in Fig. 2 we show the maximum $\beta_\perp = 8\pi p_\perp(0)/B_v^2(0)$ for these two models, as limited by the mirror mode.

A further refinement of our model employs the long-thin approximation to self-consistently modify a given vacuum magnetic field due to a finite-β plasma. In this model, we specify only the vacuum magnetic-field profile and the neutral-beam source parameters. From the computed plasma-distribution function, we find the pressure component $p_\perp(B)$ and invert the long-thin relation

$$B_v^2(z) = B^2 + 8\pi p_\perp(B) \qquad (2)$$

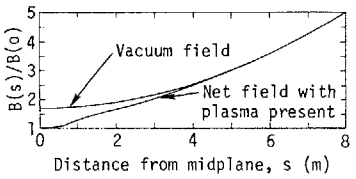


FIG. 3. Normalized magnetic-field strength versus distance from the midplane for reactor plasma.

to find the modified magnetic-field profile B(z). This result is then employed in performing the bounce average on the collision terms and source terms in the kinetic equation, and an iterative process ensures that a self-consistent steady-state result is obtained. As an example of this model we show results for an "optimum" reactor design [3]. Here, the local source current due to ionization of the injected neutral beam is of the form $J(s) = n_b(s)n_i(s)\overline{\sigma v}$, where $n_b(s)$ is the neutral-beam density and $n_i(s)$ is the plasma density. Other input data are as follows: the vacuum magnetic field is the quadratic $B_v(s) = B_v(0)[1 + (R_v - 1)(s^2/L_v^2)]$, with $B_v(0) = 40$ kG, $R_v = 3$, $L_v = 8$ m. The neutral-beam source is defined by $E_{inj} = 150$ keV, $\theta_{inj} = 70° \pm 12.5°$, -150 cm $\leq z \leq +150$ cm. Other parameters are $\overline{E}_e = 0.1\ \overline{E}_i$, $\phi_m = 3\overline{E}_e$, steady-state $\beta_\perp = \overline{0.65}$, mirror-mode limit $\beta_{\perp max.} = 0.7$. The mean value of $n\tau$ over a flux tube is 2.59×10^{13} cm^{-3}/s. In Fig. 3, we show the vacuum magnetic field and the actual self-consistent magnetic field with plasma present. In Fig. 4, the computed plasma pressure $p_\perp(B)$ is compared with a simple analytic model which is used in our magnetohydrodynamic (MHD) equilibrium calculations. The analytic model, which yields a good fit to the kinetic equation results, corresponds to a distribution function of the form

$$F(\varepsilon,\mu) = G(\varepsilon)(\mu B_m - \varepsilon)^n \tag{3}$$

where $n = \frac{1}{2}$, and produces a pressure function of the form

$$\hat{p}_\parallel(B) = \frac{C(B_m - B)^{n+3/2}}{B^n} \tag{4}$$

2. THREE-DIMENSIONAL HIGH-β EQUILIBRIA

The guiding center fluid theory of plasma equilibrium in magnetic mirror wells of Baseball symmetry [1,2,4] is consistent with a pressure tensor of the separable form $\overleftrightarrow{P} = \omega(\Gamma)\overleftrightarrow{\hat{P}}(B)$, where the field-line integral $\Gamma = \oint ds/B\ \hat{p}_\parallel$ is the average, omnigenous, drift surface. Such a pressure tensor can be identified with a microscopic equilibrium distribution function of the form $f = \omega(\Gamma)F(\varepsilon,\mu)$, where F is obtained from the Fokker-Planck equation and the radial profile ω from radial-diffusion calculations. High-β equilibrium fields and pressure distributions have been obtained from two codes using this model. To simplify the comparisons, the following set of profiles was used: the radial profile is specified

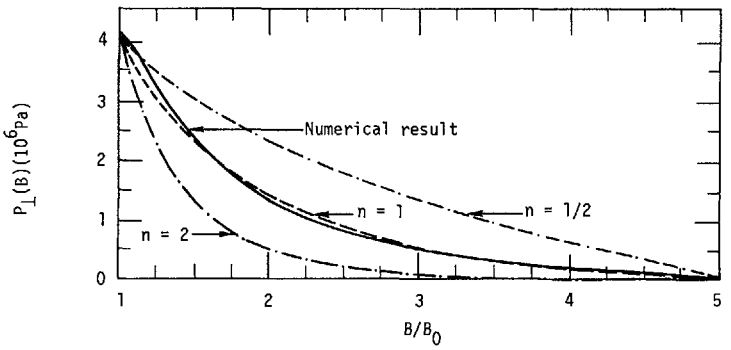


FIG. 4. Plasma pressure versus normalized magnetic-field strength for reactor plasma.

along a line lying in a symmetry plane and passing through the plasma center as

$$\omega(x) = 1 \qquad 0 < x \leq a$$

$$= \left(1 - \frac{(x - a)^2}{(r_p - a)^2}\right)^2 \qquad a < x \leq r_p \tag{5}$$

$$= 0 \qquad r_p < x < \infty$$

This allows peaked or flat profiles to be studied simply, whereas in the case of $a = r_p$ the equilibrium becomes $\vec{\vec{P}}(B)$. The axial profiles are chosen from the class due to Rensink, Eq. (4), or the "ideal" profile

$$\hat{P}_{\parallel} = C(B_m - B)^2 \tag{6}$$

where C is a normalization constant.

The first class represents simple analytic approximations to typical solutions of the Fokker-Planck equations with the following properties:

> For n = 0.5, the distribution is well spread in angle with a singular gradient in velocity space at the loss-cone angle, corresponding to a high particle-loss rate. It is very similar to the ideal distribution, for which the greatest β can be achieved.
> For n = 1, the distribution is still well spread and has smaller particle loss rates.
> For larger n, the distribution becomes quite peaked; the β limits are lower and loss rates are further reduced.

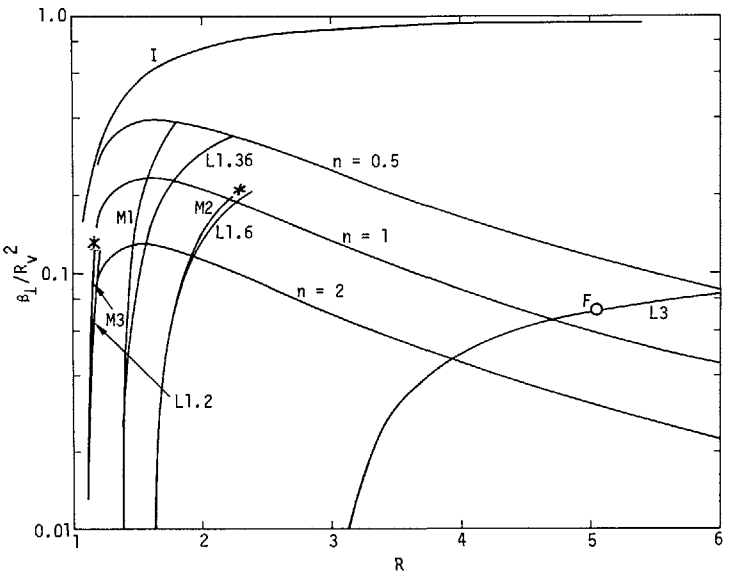


*FIG.5. Log plots of $\beta_\perp/R_v^2$ versus actual mirror ratio. Mirror-mode stability limits are at curves I, n = 0,5, 1, 2. Lowest-order, long-thin approximation to pressure balance gives L curves, labelled with vacuum mirror ratio. Computed results are labelled M (MCGUS). Field curvature weakens at * points. Fokker-Planck result is labelled F.*

The parallel component of the pressure balance equation gives $P_\perp = -B^2\partial(P_\parallel/B)/\partial B$; therefore, $P_\perp$ need not be specified independently. The pressure balance in the direction of the curvature, $\vec{k} = -\hat{b} \cdot \nabla\hat{b}$, where $\vec{B} = B\hat{b}$, is

$$\hat{k}\cdot\nabla(P_\perp + B^2/8\pi) = -k(B^2/4\pi + P_\perp - P_\parallel) \tag{7}$$

Thus,

$$8\pi p_\perp(0)/B_m^2 = \beta_\perp/R_v^2 = \left(\frac{1}{R_v^2} - \frac{1}{R^2}\right)\left[1 + 0(kr_p)\right] \tag{8}$$

Use of $\beta_\perp/R_v^2$ as a parameter allows equilibrium and stability curves to be plotted on the same graph, independent of the profile.

In the guiding-center model, the maximum $\beta_\perp$ achievable is limited by the mirror-mode condition for the existence of equilibrium, $\partial(P_\perp + B^2/8\pi)/\partial B = 0$. This gives either

$$\left(\frac{\beta_\perp}{R_v^2}\right)_{\text{max. (Rensink)}} = \frac{4(R-1)[1+2(n+1)R]}{R^2[3+4nR+4n(n+1)R^2]} \tag{9}$$

or

$$\left(\frac{\beta_\perp}{R_v^2}\right)_{\text{max. (ideal)}} = 1 - \frac{1}{R^2} \tag{10}$$

These curves are shown in Fig. 5 for n = 0.5, 1, 2. For the ideal profile, it is apparent that the $\beta_\perp$ corresponding to the weak curvature pressure balance never reaches the mirror limit. The central field can in principle be depressed to zero for this profile.

The two equilibrium codes, MCGUS and VEPEC, have been applied to a range of fields and pressures. There is not space here for displays of these equilibria, but the general characteristics are as follows. Although the effects of the quadrupole field of the coils are quite strong in shaping the plasma, the drift surfaces remain omnigenous up to the highest β's, validating the connection between fluid and particle models. The plasma drift currents enhance the overall diamagnetism of the plasma, and the well-digging effect is largely confined to the plasma volume. The peak plasma current induced by the coil geometry lies on a closed curve shaped like a baseball seam, a simple consequence of the symmetries.

The effects of coil geometry and pressure profile are summarized in Fig. 5. The L curves are the result of the long-thin approximation for the neighboring computed curves. The curve M1 was run in proposed reactor coils that give a strongly curved field with $kr_p = 0.24$ at the plasma surface. The result diverges from the long-thin approximation to give a higher β, and hence power density, at a lower final mirror ratio, and hence lower Q. The curve has $r_p = 300$ cm and the sharpest radial profile with a = 0. These results differ from the long-thin approximation by an almost constant factor $\tilde{\beta}$(Code) = $\tilde{\beta}$(LTA) × 1.6. Similar results are found at higher mirror ratios. The axial profile was n = 0.5, but other cases would yield nearby curves. Independent of the pressure model, the long-thin approximation is quite accurate for curves like M2, M3, M4 that were produced in the 2XIIB field with $kr_p = 0.06$. The mirror-mode β limits are low enough that the plasma has little effect on the field curvature. Thus, the relation between $\beta_\perp$ and R is insensitive to the pressure profiles but strongly dependent on the field geometry. However, the mirror-mode limit reached on any curve $\beta_\perp$ (R) is sensitively dependent upon the profile, $\hat{P}_{||}$.

The cases M2, M3 were attempts to build a very high-β bubble in the center of a 2XII field by using the ideal profile; M3 with a = r_p, represents a $\hat{P}$(B) equilibrium. The MCGUS code failed to converge above the $\beta_\perp$ indicated by an asterisk in Fig. 5, and this failure is related to the way the field curvature weakens and pressure gradients increase around the maximum plasma current. These equilibria may lead towards reversed-field fluid equilibria which, being topologically toroidal, are not accessible by the MCGUS and VEPEC codes. Only for these high-β bubbles has there been an indication of other than local (mirror) instability, though their stability properties have not yet been computed quantitatively from the energy principle. The most important result for the reactor designer is that weak radial wells ($kr_p \ll 1$) can contain collisional plasmas with $\beta_\perp$ up to the mirror-mode stability limit. Strongly curved field designs are not necessary and require expensive coils and supports. In optimizing the Q of a given design, it is not necessary to

iterate between the Fokker-Planck and equilibrium calculations since the curve of $\beta_\perp(R)$ is insensitive to the pressure profiles and can be generated from model calculations as shown.

3. ADIABATIC CONFINEMENT IN HIGH-BETA EQUILIBRIUM FIELDS

Adiabaticity is an important consideration in the design of high-beta devices. A particle in a mirror field experiences jumps $\Delta\mu$ in its magnetic moment when it passes through the minimum of B on its guiding-center path. The jumps are of order $\exp(-\kappa/\varepsilon)$, where κ/ε is of order of the ratio of the scale length along a field line $L_\parallel = (2B)^{-1/2}\,(d^2B/ds^2)^{-1/2}$ to a gyroradius a_i at the minumum of B. Increasing β lowers $L_\parallel$ and raises a_i, thereby increasing $\Delta\mu$. In particular for a long-thin equilibrium field, κ/ε vanishes when β reaches the threshold for mirror-mode instability, implying that adiabaticity is actually a more restrictive limit on β than the mirror mode.

For a wide variety of fields, $\Delta\mu$ is given to a good approximation by the expression

$$\frac{\Delta\mu}{\mu} \approx \sqrt{\frac{2}{\mu}}\,\nu \mathrm{Re} \int \frac{ds\ \rho_c\ e^{i\psi}}{[1 - (v_\perp/v)_0^2\ (B/B_0)]^{1/2}\ B^{1/2}} \qquad (11)$$

where $\vec{\rho}_c \equiv B^{-1}\,\vec{B} \cdot \nabla\,(\vec{B}/B)$, and $\cos\psi \equiv \vec{v}_\perp \cdot \vec{\rho}_c/(v_\perp \rho_c)$; ρ_c^{-1} is the radius of curvature, and ψ measures the gyrophase. The integral is to be evaluated along a guiding-center path using orbit-averaged values for B, ρ_c and $d\psi/ds$. The subscript 0 denotes values at the minimum of B. The expression in Eq. (11) is valid even for three-dimensional, non-vacuum fields. The integral is evaluated by deforming the contour into the complex s-plane to pass near the singularities of $\rho_c\ B^{-1/2}$ and the stationary points of ψ. For model axisymmetric mirror fields, the results agree with orbit calculations, typically to within about 20% in $\Delta\mu/\mu$, or to a few percent in velocity [5]. It is generally found that

$$\frac{\Delta\mu}{\mu} \approx A\left(\frac{\nu}{v_\perp}\right)_0 \mathrm{Re}\ \exp\,(i\psi_0 - \kappa/\varepsilon) \qquad (12)$$

in which for mirror machines A is a slowly varying function of particle and field parameters, except within a couple of gyroradii of the axis, where A varies linearly with radius. Typically $A \approx 3$ to 5. In Eq. (12), κ is given by

$$\kappa = \frac{1}{i} \int_0^{s_1} \frac{ds}{L} \left(\frac{B/B_0}{[1 - (v_\perp/v)_0^2\ (B/B_0)]^{1/2}} \right) \qquad (13)$$

and $\varepsilon = mcv/(qB_0L)$, where L is an arbitrary scale length, and s_1 is the location of the singularity or stationary point closest to the real s axis. If there is more than one closest singularity Eq. (12) is summed. If the field is nearly quadratic in s, a convenient choice for L is $L_{\|}$. For a quadratic well,

$$\kappa = \frac{1}{2\lambda^2}\left(\frac{1+\lambda^2}{2\lambda}\ \ln\frac{1-\lambda}{1+\lambda}\ -1\right) \tag{14}$$

where $\lambda = (v_\perp/v)_0$.

One may estimate the adiabatic energy limit W, at which the lifetime of a representative particle against loss due to nonadiabaticity is equal to the lifetime against all other processes. Defining Δ to be the fractional change in μ required to lose the representative particle and assuming the jumps are stochastic (no superadiabaticity), we find [5]

$$W = \frac{1.2\times10^{-3}\ \kappa^2 B_0^2 L^2 Z^2/A}{(1-0.039\ \ln A)^2}\quad \text{keV} \tag{15}$$

$$\text{with } A = \frac{A}{2}\left(\frac{50\ \text{keV}}{w}\right)\left(\frac{L_p}{340\ \text{cm}}\ \frac{0.5}{\langle v_{\|}\rangle/v}\ \frac{10^{-2}\ \text{s}}{\tau}\right)^2\left[\frac{15\Delta}{A_0}\ \frac{(v_\perp/v)_{\text{rms}}}{0.59}\ \frac{1}{\sqrt{2}\ (\cos\psi)_{\text{rms}}}\right]^4$$

where L_p is the plasma length, B_0 is in kG, L in cm, and < > denotes a bounce average.

For long-thin equilibria in which the mirror-mode limit is at β less than one, the upper limit s_1 in Eq. (13) is the position in the complex plane where the mirror-mode parameter $B + 4\eta\pi dP_\perp/dB$ vanishes. As β is increased to the mirror-mode limit, s_1 and hence κ and W go to zero. If W is to be greater than some design value, β must be less than a critical value lower than the mirror-mode limit. In large machines such as the Lawrence Livermore Laboratory (LLL) reactor reference designs, this difference is only about 1%; in smaller machines it may be significant.

An estimate for W may be obtained by considering the on-axis variation of B in calculating κ in Eq. (15). This procedure is reasonable when the radial scale length is large compared to a gyroradius, but can severely underestimate W for machines such as 2XIIB. There the well dug by the plasma is only a couple of gyroradii in radius, since there are no finite-energy particles for which the orbit-averaged field is as small as, nor the parallel gradients as steep as, the on-axis values. The energy limit predicted by this procedure is a sensitive function of β for plasmas of axial extent small compared to the scale length of the vacuum axial field, and less strongly dependent on β for longer plasmas. This sensitivity to β is illustrated in Fig. 6 , where the energy limit is plotted as a function of β for a long-thin equilibria corresponding to axial pressure profiles of differing axial extents. Parameters were chosen appropriate to a large mirror experiment such as the proposed MX machine.

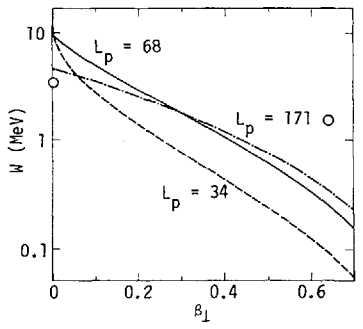


FIG.6. Adiabatic energy limit for MX-like parameters. The curve $L_p = 171$ corresponds to a quadratic $P_\perp(z)$, and the others to Gaussian profiles. The points O are fitted from an MX equilibrium (VEPEC code).

Also shown in Fig. 6 is the result of an analytic fit to a computed MX equilibrium. At $\beta = 0.5$, the deuteron energy limit is 500 keV for the MX design plasma length. At $\beta = 0.5$, the present axial field approximation predicts an energy limit of order 600 MeV for alpha particles in the LLL reactor reference design, but only 16 keV for deuterons in 2XIIB. If the strong radial gradient in 2XIIB is taken into account in the orbit averages, an energy limit of order 60 keV is obtained. If the gyrophase information can be preserved from bounce to bounce so that superadiabaticity occurs, the energy limits are higher by a factor of order 2.

Calculations of the orbits of single particles have been made with the code ORBXYZ, which uses the self-consistent fields generated by the VEPEC equilibrium code. Vector potentials were used in the analysis so that the particles saw $\nabla \cdot B \equiv 0$; otherwise nonphysical effects would destroy the adiabatic invariance. For the results presented here, an MX equilibrium pressure profile was chosen that was close to a collisional profile as deduced from Fokker-Planck studies. The test particle was a 2.2-MeV deuteron with pitch angle 5° from the vacuum loss cone $\theta_{\ell c} = 44°$. The equilibrium field used had $\beta_\perp = 0.52$ and $\theta_{\ell c} = 36°$. Two orbits were studied, one for the vacuum field and the other for the equilibrium field. Changes in the gyro-averaged μ were followed.

In both of these runs, the $\Delta\mu$ contributions from each bounce very nearly cancelled out after a drift period, indicating that the stochastic part of $\Delta\mu$ was small. Numerical estimates of this random part of $\Delta\mu$ allow one to calculate a confinement time based on a random walk towards the loss cone. We summarize the good confinement obtained and compare it with a collision time for deuterons:

Vacuum field:	$\tau_v = 32$ s
$\beta = 0.52$ field:	$\tau_e = 3.6$ s
Collision time:	$\tau_c = 10^{-2}$ s

These anomalously long adiabatic lifetimes of a particle at an energy of order of the energy limit predicted by Eq. (15) may be due to superadiabaticity.

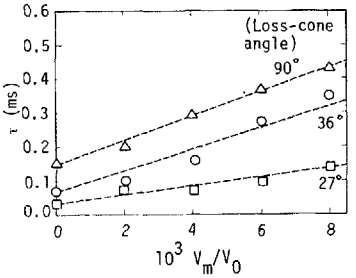


FIG. 7. Confinement time τ(ms) versus relativ. mirror velocity (V_m/V_0) and injection angle, for $R = 5.0$, $n = 5 \times 10^{16}$ cm^{-3}, $E_i = 10$ keV (D^+).

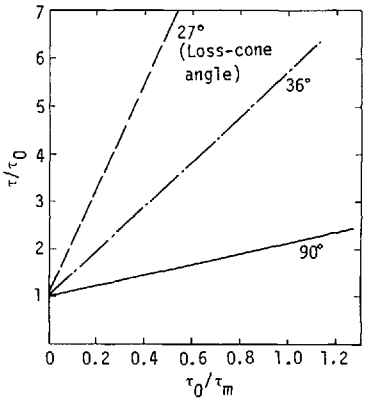


FIG. 8. Confinement enhancement factor τ/τ_0 versus injection angle for the conditions of Fig. 7.

4. TIME-DEPENDENT BETA EFFECTS

Mirror confinement can be enhanced by processes (e.g. time variation of the confining field) that compete with the rates of collisional velocity-space diffusion. Neutral-beam injection can create cyclic, time-dependent, high-beta states in a steady field that could modulate the intensity and the spatial distribution of the confining field. Optimized, this technique could lead to enhancement of the time-averaged Q factor for a mirror system. Two such processes which lead to improved confinement are (1) radial compression and (2) axial expansion (time-dependent mirror separation). Process (1) occurs when beta decreases with time; (2) occurs when the length of the high-beta region increases with time. In a cyclic buildup and decay of plasma density, (2) would be followed by (1) and vice-versa for their inverses. If the rates of (1) and (2) are approximately commensurate with ion-ion collision rates, they can modify the ion loss rate relative to a static situation. A mirror reactor cycle involving optimally programmed neutral injection and direct conversion of escaping ion energies might exhibit a higher Q value than a steady-state operating mode.

We have performed preliminary calculations aimed at elucidating the processes involved in such a cycle. One method, applied to process (2), used a modified version of a previous Monte Carlo code [6]. Approximations made in this code include the assumption of fixed scattering centers and the representation of the effect of particle reflection from a moving mirror as a change in pitch angle. Example results from these calculations are shown in Figs. 7 and 8. Two general results emerge from examination of the data:

> When the distance-doubling time for the moving mirrors is within about a factor of 3 longer than the ion-ion collision rate in a static field, confinement time increases markedly.
>
> The favorable effects on confinement are most marked for particles that are injected near to the loss-cone angle.

Beyond obtaining the qualitative results obtained above, the Monte Carlo results are not being extended; to arrive at quantitatively significant results, we shall depend on the use of one of the LLL Fokker-Planck codes, modified to include the effects of beta-induced changes in the magnetic field.

5. FIELD REVERSAL

Reversed-field mirror configurations have closed field lines containing some fraction of the plasma volume and should greatly improve particle containment and thus enhance Q. A two-dimensional axisymmetric equilibrium code has shown the existence of small-aspect-ratio (fat), reversed-field configurations. Our best working tool for analysing the reversed-field mirror configuration is the SUPERLAYER code [7] developed for the LLL Astron program. Revised to simulate neutral injection, it is now being used to study buildup to field reversal in a mirror machine and to determine properties of the steady state. The code now includes electron drag and charge exchange on the neutral beam, but as yet no angular scattering. The main function of the code is to calculate the self-field generated by the ions and the ion orbits in this field as a function of time. In the past, the code predicted reasonably well both the failure to achieve field reversal by multiple injection of electrons in the Astron experiment and the success achieved at Cornell by injecting a single, high-current pulse.

For present purposes, the main defect of the code is the assumption of axisymmetry (no quadrupole component). We believe this to be of limited importance in determining the equilibrium configuration in the interior region where the closed-field pattern forms. However, imposing symmetry suppresses possible modes of instability that must then be examined either analytically or numerically with other, more complex codes (see below). Also, as of this writing all runs have concentrated on the present 2XIIB parameters ($a/\rho_i \approx 2$); modifications to treat a/ρ_i up to 10 are in progress.

The code is limited in scope, allowing no electron currents or space-charge effects, but including five phase space dimensions in the ion motion. Within these limitations, the code should be able to examine the r,z equilibrium, including all effects of the mirror-tearing mode and the Alfvén ion cyclotron (AIC) mode, as related to the electromagnetic mode with $k_\parallel = 0$ [7]. One rather severe approximation is made: the relevant time scales, τ, such as the drag time or filling time, are shortened considerably, typically by factors of order of 100. The product $I\tau$ is kept consistent with the experiment, and an attempt is made to keep τ long compared to an axial bounce period.

The initial work indicated that field reversal was easily obtainable and persisted in steady state after initial transients if the beams were arranged to form a coherent ring current. This injection prescription is actually unrealistic, and this past year we have concentrated on simulating 2X with realistic injection. Currently, the code predicts that reversal is possible in the 2XIIB experiment provided the beams are focused off-axis; high $\beta_\perp > 1$ is obtainable regardless of the focusing. This condition, however, is accompanied by a slow but steady axial loss of particles (this did not occur with ring-like injection). This loss is persistent, but it is not yet known if it is caused by the physics (non-adiabatic containment?) or by numerical effects. Even if real, the loss rate is sufficiently slow that it may not prevent buildup in a system with

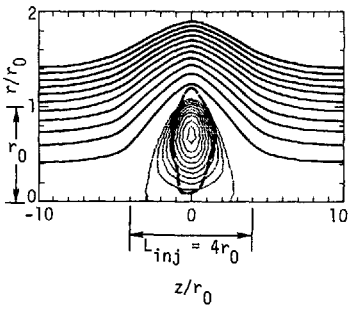


FIG.9. Field lines and half peak density contour (dashed closed line) in the r-z plane for a field-reversed equilibrium. The density of field lines does not indicate field strength due to the geometry. Closed field lines are shown as dotted curves.

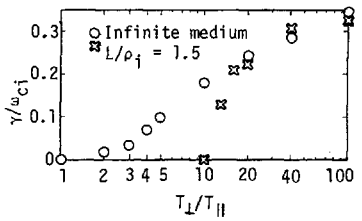


FIG.10. Effect of finite length on growth rate of Alfvén ion cyclotron mode in simulation.

realistic time constants. That is, the loss rate is of the same order as the actual real-time loss rate of hot particles due to electron drag ($\nu_{loss}/\omega_{ci} \approx 10^{-4}$ and $\nu_{drag}/\omega_{ci} \approx 10^{-4}$ for $n = 10^{14}cm^{-3}$, $T_e = 100$ eV).

For 2X-like parameters, we have obtained a strong reversal steady state for $I \approx 600$ A with $\xi = \Delta B/B_{vac} \approx 2$. This case used uniform injection over a length L_{inj} of 20 cm centered at the midplane and over a radius $r_0 = 5$ cm; employed a drag coefficient appropriate to $T_e = 100$ eV; and included charge exchange on the beam. Allowing higher T_e will lead either to higher ξ and β for the same current or to marginal ξ for lower currents.

A typical result is shown in Fig. 9. The mirror ratio R_{vac} over the occupied region is only 1.05; that is, the self-field alone confines the axial pressure. Shown in Fig. 9 are typical field lines in an r-z cross-section indicating a central core of closed field lines. The figure shows that the high-density region, defined as the region enclosed by the contour of half-peak density, is contained nearly entirely within the closed lines. This still leaves a sizable fraction of the total number of particles — perhaps half — outside the closed-line region, because for equal densities the amount of net mass is greater at a larger radius in the open-line region. The plasma has expanded radially to a radius $r = a$, somewhat beyond the injection radius r_0. Much of this contact with the open region is due to the large orbits, $\rho_i/r_0 \approx 1$, in this example. Smaller orbit systems may improve on this.

In the example of Fig. 9, the plasma has pinched in axially to a mean length (full-width half-maximum) of $L \approx L_{inj}/4 \approx r_0$. This is a typical result. Longer axial systems can occur if the injection region is extended. In one example, a steady state occurred for a $L \approx 8r_0$. Even longer systems are subject to breakup due to tearing modes. In essence, the system appears to adjust itself to a finite-length equilibrium with conditions necessary for prevention of the mirror-tearing mode and the AIC mode.

It is not fully resolved how stability to the AIC mode is maintained. That is, the existence of high-β equilibria in many of the code results and in 2XIIB is in conflict with theoretical predictions of limits on $\beta \approx 0.1$-0.2 that are due to the AIC mode. The code should allow both the mirror-tearing mode and also the AIC mode. We have evidence that small

axial scale lengths can add strong stabilizing effects. Figure 10 shows initial results from a linearized code that models instabilities about a given equilibrium. We find complete stability for a case with $T_\perp/T_\parallel = 10.0$, $L/a_i \approx 1.5$; whereas the infinite-medium result gives a growth rate $\gamma/\omega_{ci} \approx 0.08$. However, this stabilizing effect rapidly disappears as the plasma length is increased. Consistent with this result, most of the SUPERLAYER code runs to date have been restricted to systems with only a small number of gyroradii (a/ρ_i, $L/\rho_i < 2$), and a major question is how well these results stand up for larger L/ρ_i, a/ρ_i systems. Although precise limits on lengths have not yet been obtained, a major effort for extending the code work to large L/ρ_i, a/ρ_i systems is underway. In this regard, the one long example referred to above with $L \approx 8r_0$ occurred for a ring-like injection; moreover, this case resulted in generation of considerable axial temperature. That is,

$$\frac{\sum v_r^2 + v_\theta^2}{\sum v_z^2} = 2.6$$

in some sense perhaps equivalent to a "temperature" ratio $T_\perp/T_\parallel = 1.3$, which is close to isotropy. Also, some reversed-field results have been obtained with $a/\rho_i = 4$. This latter result, while still not an ideal steady state, may be most significant since it indicates that one need not take great care in programming the injection when passing from single-orbit to many-orbit size systems.

In progress are the following:

Monte Carlo techniques to simulate classical Coulomb scattering and rf-induced velocity-space diffusion.

Examination of instability modes involving θ perturbations. We are actively developing three-dimensional particle codes that will start from a given steady state and examine the stability to $e^{im\theta}$ modes, specifically the sausage and kink modes, which along with the AIC mode are considered to be the greatest danger.

REFERENCES

[1] RENSINK, M. E., et al., 5th Int. Conf. Plasma Physics and Controlled Nuclear Fusion Research (Proc. Conf. Tokyo, 1974) 1, IAEA, Vienna (1975) 311.

[2] KILLEEN, J., MIRIN, A. A., RENSINK, M. E., The solution of the kinetic equations for a multispecies plasma," Ch. XI, Methods in Computational Physics: Vol. 16, Controlled Fusion (KILLEEN, J., Ed.) Academic Press, New York (1976).

[3] MOIR, R. W., et al., 6th Int. Conf. Plasma Physics and Controlled Nuclear Fusion Research (Proc. Conf. Berchtesgaden, 1976) IAEA, Vienna (this conf.) IAEA-CN-35/I2.

[4] HALL, L. S., McNAMARA, B., Phys. Fluids 18 (1975) 552.

[5] COHEN, R. H., ROWLANDS, G., FOOTE, J., LLL Rep. (in preparation).

[6] POST, R. F., Phys. Rev. Lett. 18 (1967) 232.

[7] DAVIDSON, R. C., OGDEN, J. M., Phys. Fluids 18 (1975) 1045.

DISCUSSION

ON PAPER IAEA-CN-35/C3

D.R. SWEETMAN: It was not clear from you presentation whether or not the theoretical estimates of β for the mirror mode were in agreement with the experimental results from 2XIIB. If not, can you give any explanation for the discrepancy?

B. McNAMARA: The injected 2XII plasma is peaked in angle – this we would model with an $n \gtrsim 1$ Rensnik profile – and is concentrated over the central 80 cm of the well. Thus not all the available mirror ratio is really used and the equilibria at various densities would be on a curve like MZ in Fig.5 of our paper. The quoted field depression of 40% would yield a net mirror ratio over the injection region of 2–2.5 and $\beta_\perp/R_v^2 \sim 0.2$, which is not in conflict with the mirror stability limits. It is more difficult to reconcile the pressure balance with Eq.(8) of our paper. Since $kr_p \sim 0.06$ for 2XII, the maximum possible $\beta_\perp \cong 1$ at $R = \infty$. The 2XII plasma is only 2 Larmor radii across and, if one averages the pressure across an ion orbit, then the pressure balance is satisfied. Note that $\beta_\perp > 1$ is possible in the reversed-field configurations at small r_0/a_i.

H.P. FURTH: What do you expect to see experimentally when the plasma is "mirror unstable"? If the plasma pressure is raised gradually by injection, then it seems to me that in a finite-length mirror machine you will never see an actual fast-growing instability. The presence of "mirror instability" will manifest itself merely in the quasi-static development of equilibrium configurations where the plasma pressure is concentrated in one place along the axis – perhaps to an undesirable extent. Short-wavelength pressure concentrations could arise only transiently, since the lowest-energy state corresponds to complete central coalescence.

B. McNAMARA: The Rensink profiles used in the paper reach the mirror limit at the centre point of the well. This gives a mathematical limit on β since the equations become hyperbolic instead of elliptic and indeed the codes fail to converge. Physically, one would expect the pressure profile to adjust to avoid the condition as more plasma is injected. The limit of this is illustrated by the ideal profile which never reaches the mirror limit unless $R_{vac} \to 0$. The 2XIIB experiment does not appear to have reached an MHD stability limit, the losses being associated with cyclotron noise. It is also interesting that the mirror limit corresponds to loss of adiabaticity. It is likely that the mirror mode limit cannot be reached physically but still represents an upper bound for given injection.

OPEN TRAP WITH AMBIPOLAR MIRRORS

G.I. DIMOV, V.V. ZAKAJDAKOV, M.E. KISHINEVSKIJ
Institute of Nuclear Physics, Siberian Branch of
USSR Academy of Sciences,
Novosibirsk,
Union of Soviet Socialist Republics

Abstract

OPEN TRAP WITH AMBIPOLAR MIRRORS.

Results of numerical calculations on the behaviour of a thermonuclear plasma, allowing for α-particles in a trap with longitudinal confinement of the main ions by ambipolar electric fields are presented. This trap is formed by connecting two small-volume "mirrortrons" to an ordinary open trap. Into the extreme mirrortrons, ~1-MeV ions are introduced continuously by ionization of atomic beams on the plasma, and ~10-keV ions are similarly introduced into the main central region of the trap. By a suitable choice of injection currents, the plasma density established in the extreme mirrortrons is higher than in the central region. As a result of the quasi-neutrality condition, a longitudinal ambipolar field forming a potential well not only for electrons but also for the central ions is formed in the plasma. When the depth of the well for the central ions is much greater than their temperature, their life-time considerably exceeds the time of confinement by the magnetic mirrors. As a result, the plasma density is constant over the entire length of the central mirrortron, including the regions near the mirrors, and an ambipolar field is formed only in the extreme mirrortrons. The distribution of central ions and ambipolar potential in the extreme mirrortrons is uniquely determined by the density distribution of fast extreme ions. It is shown in the present study that an amplification coefficient Q as high as desired can, in principle, be reached in the trap under consideration, allowing for α-particles. However, this requires high magnetic fields in the mirrors and a sufficient length of the central mirrotron. It is shown that for moderate values of Q = 3–8, it is desirable not to confine the central fast α-particles. To achieve a coefficient of Q = 5, it is necessary to create fields of 250 kG in the mirrors, and the length of the trap must not be greater than 100 m.

1. INTRODUCTION

Figure 1 gives a schematic representation of the magnetic field geometry of the trap and the longitudinal distribution of the ambipolar potential φ and plasma density n. In the main central portion of the trap, the magnetic field is uniform. At each end of the trap, there is a pair of magnetic mirrors with field B_m, which form extreme mirrortrons of length L_k. To ensure hydrodynamic stability of the plasma, in addition to the longitudinal barrel-shaped field B, a transverse quadrupole field with gradient g is generated in the extreme mirrortrons.

The behaviour of ions and electrons in the trap was calculated mainly with the same approximations as in Ref. [1]. The Fokker-Planck equation for α-particles in the central mirrortron was solved for the purpose of taking into account the influence of the α-particles generated in a D-T mixture. It was assumed that the α-particles are confined only by the magnetic mirrors, i.e. slow α-particles whose kinetic energy is lower than the depth of the central potential well do not accumulate, but are removed by some means. Since the α-particle concentration under such assumptions is low (of the order of 1%), we considered only their energy transfer to ions and electrons, and neglected the scattering of ions, electrons and α-particles from α-particles. Since it turns out that the density of slow α-particles does not exceed a few percent of their total density, this approximation is justified even when the sub-barrier α-particles are removed from the central mirrortron much more slowly than they would escape into the loss cone.

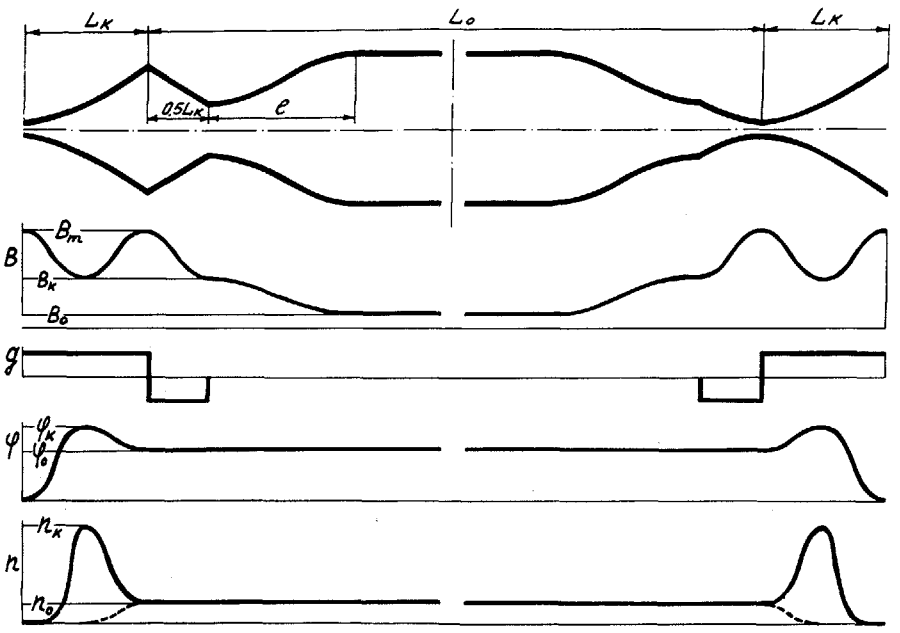


FIG. 1. Diagram of trap.

2. CHARACTERISTICS OF CENTRAL MIRRORTRON

The appreciable gain in the amplification coefficient of the trap is due to the increase in the life-time of central ions τ_{i0}. In accordance with Ref. [2],

$$\frac{n_{i0}}{\tau_{i0}} = \frac{\sqrt{2\pi}\, e^4}{\sqrt{M_i} F(R_0/2R_k)} \frac{n_{i0}^2 \exp(-\Delta\varphi/T_{i0})}{\Delta\varphi\sqrt{T_{i0}}} \left[1 + \frac{T_{i0}}{2\Delta\varphi} - \left(\frac{T_{i0}}{2\Delta\varphi}\right)^2\right]$$

$$\Delta\varphi = \varphi_k - \varphi_0 = T_e \ln \frac{n_k}{n_0}; \quad n_0 = n_{i0} + 2n_{\alpha 0}; \quad F(x) = \sqrt{1+\frac{1}{x}} \ln \frac{\sqrt{1+1/x}+1}{\sqrt{1+1/x}-1} \tag{1}$$

where n_{i0}, T_{i0} are the density and temperature of the central ions; φ_k, φ_0 are the ambipolar potentials according to Fig. 1; n_k is the maximum density of the extreme ions; n_0, $n_{\alpha 0}$ are the densities of electrons and α-particles in the central mirrortron; R_0, R_k are the mirror ratios for the central and extreme mirrortrons; M_i is the calculated ion mass; e is the electron charge. Roughly, from Eq. (1), $\tau_{i0} \sim \tau_i (n_k/n_0)^{T_e/T_{i0}}$, where τ_i is the ion relaxation time. Hence, it is obvious that, in addition to the condition $n_k > n_0$, it is convenient to have $T_e > T_{i0}$. The latter condition is essentially ensured by the fact that the injection energy of the central ions $E_{j0} < \Delta\phi + T_{i0}$. In addition, the temperature of the central ions is maintained constant by the transfer of energy from electrons and α-particles. Electrons acquire energy from fast extreme ions, α-particles, and from the external HF field.

The energy balance for the central ions is given by the equation

$$E_{j0} + \langle E_0^{ei}\rangle + \langle E_0^{\alpha i}\rangle = \left[\Delta\varphi + T_{i0}\left(1 + \frac{T_{i0}}{2\Delta\varphi}\right)\right](1-\alpha_0) + \langle E_{ir}\rangle \alpha_0$$

$$\langle E_0^{ei}\rangle = 4\sqrt{2\pi}\, e^4 \lambda_0^{ei} \frac{\sqrt{m}}{M_i} \frac{T_e - T_{i0}}{T_e^{3/2}} \frac{n_0 n_{i0}}{I_0}$$

$$\langle E_{ir}\rangle = \frac{3}{4} T_{i0} + \frac{2}{\sqrt{\pi}} \frac{1}{\sqrt{M_i}\langle\sigma v_0\rangle T_{i0}^{3/2}} \int W^2 \sigma(W)\, dW$$

$$\alpha_0 = \frac{2I_{\alpha 0}}{I_0}\ ;\ I_{\alpha 0} = \frac{1}{4}\langle\sigma v_0\rangle M_{i0}\ ;\ I_0 = \frac{n_{i0}}{\tau_{i0}} + 2 I_{\alpha 0} \qquad (2)$$

where E_0^{ei}, $E_0^{\alpha i}$ are energies obtained per injected central ion from electrons and α-particles; E_{ir} is the energy of the reacting ion; W is the energy of reacting particles in their centre-of-mass system; λ_0^{ei} is the Coulomb logarithm; σ is the cross-section of the D-T reaction; α_0 is the degree of depletion of the central plasma; $I_{\alpha 0}$ is the current of central α-particles from a unit volume; I_0, v_0 are the injection current into the unit volume and the relative velocity of central ions; m is the electron mass. The quantities related to the α-particles $\langle E_0^{\alpha i}\rangle$, $n_{\alpha 0}$ and others were obtained by solving the Fokker-Planck equation for α-particles from given values of n_{i0}, T_e, T_{i0}, R_0 and of the injection energy of α-particles, equal to 3.52 MeV, and of the injection current of α-particles, equal to $I_{\alpha 0}(1-(1/2R_0))$.

The life-time of all the electrons is determined by the scattering of sub-barrier electrons to which the contributions made by the central and extreme plasmas were considered to be proportional to the probabilities of finding these electrons in the corresponding mirrortrons. Accordingly, the electron balance equation conforming to Ref. [2] is

$$I_0 + I_k V_k/V_0 = 2\sqrt{2\pi}\,(e^4/\sqrt{m}) n_k \exp[-\varphi_k/T_e]$$
$$\times \frac{1}{\sqrt{T_e}}\left[\frac{n_0\lambda_0^{ei}}{F(R_0)} \frac{1 + T_e/2\varphi_0 - T_e^2/4\varphi_0^2}{\varphi_0} + \frac{n_k \lambda_k^{ei}}{F(R_k)} \frac{1 + T_e/2\varphi_k - T_e^2/4\varphi_k^2}{\varphi_k} \frac{V_k}{V_0}\right] \qquad (3)$$

where I_k is the calculated ion current per unit volume of extreme mirrortrons; V_k, V_0 are the calculated volumes of the extreme and central plasmas.

The amplification coefficient for the central mirrortron, equal to the ratio of thermonuclear power to the power supplied from outside, is given by

$$Q_0 = \frac{1}{4I_0} \frac{n_{i0}^2 \langle\sigma v_0\rangle \epsilon}{E_{j0} + \langle E_0^{ei}\rangle + \varphi_0 + T_e(1 + T_e/2\varphi_0) + \langle E_{x0}\rangle - \langle E_0^{\alpha e}\rangle} \qquad (4)$$

where

$$\langle E_{x0}\rangle = \frac{64}{3\sqrt{2\pi}} \frac{\alpha^3 \hbar^2}{m\sqrt{m}} n_0 (n_{i0} + 4n_{\alpha 0}) \sqrt{T_e}/I_0$$

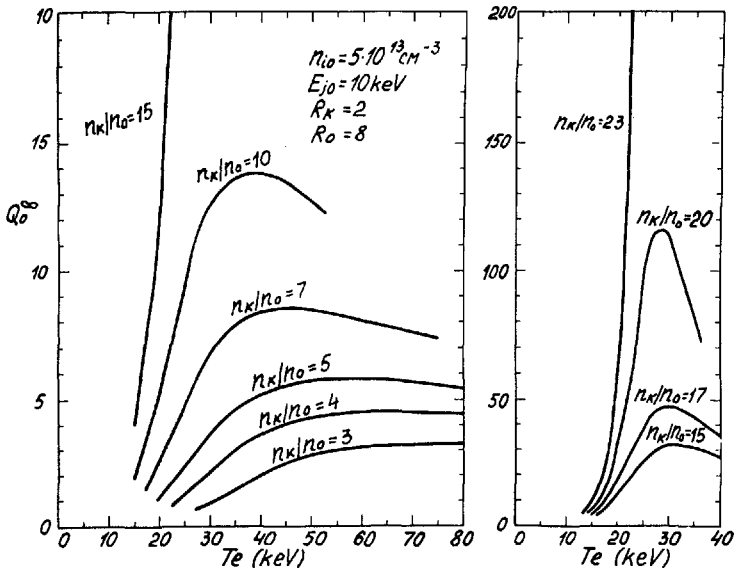


FIG. 2. Amplification coefficient of an infinitely long trap Q_0^∞ versus T_e and n_K/n_0 allowing for fast α-particles.

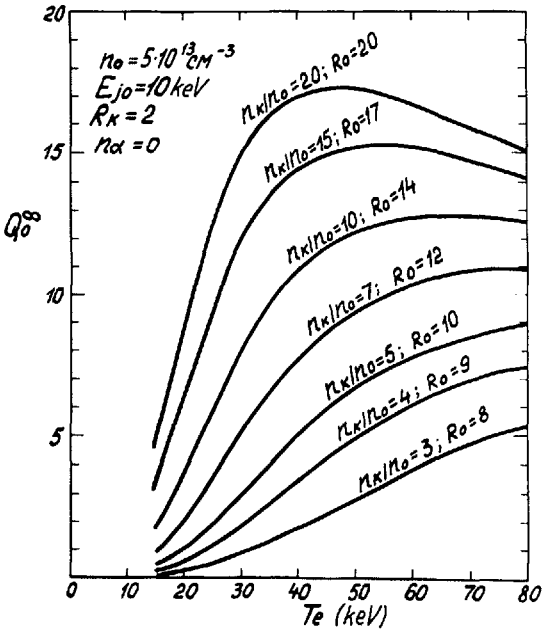


FIG. 3. The dependence Q_0^∞ (T_e, n_K/n_0) neglecting α-particles.

Here $\epsilon = 22.38$ MeV is the thermonuclear energy per nuclear fusion event, including the energy released in the lithium blanket; $E_0^{\alpha e}$ is the energy acquired by the "central" electron from α-particles; E_{x0} is the bremsstrahlung energy per "central" electron; α is the fine-structure constant.

For the energy balance of the trap to be determined by its central portion, it is necessary that the ratio $n_k^2 V_k / n_0^2 V_0$ be sufficiently small. With this condition, in the electron balance equation (3), the second term is much smaller than the first ones, and may be neglected to a first approximation. This means that the external ambipolar potentials φ_k depend weakly on the parameters of the extreme plasma. The amplification coefficient Q_0^∞, corresponding to the condition $V_0/V_k \to \infty$, is 1–3% smaller than the value of Q_0 for real volume ratios. The characteristics of the central plasma when $V_0/V_k \to \infty$ can be determined in terms of the parameters R_0, R_k, n_{i0}, n_k/n_0, T_e and E_{j0}. It follows from the calculations that the coefficient Q_0^∞ decreases as the energy E_{j0} increases. It is, therefore, convenient to inject the ions into a centre with a low energy. In further calculations, we always assumed that $E_{j0} = 10$ keV.

Figure 2 shows the coefficient Q_0^∞ versus the electron temperature and density ratio n_k/n_0. It is evident that, in principle, one can achieve any amplification coefficients of the central portion of the trap. However, the amplification coefficient becomes infinite for a sufficiently high ratio $n_k/n_0 = 23$ when $R_0 = 8$. In this case, $T_e = 24$ keV, and the product of the energy lifetime by density $n\tau_{\epsilon 0} = 2.65 \times 10^{14}$. The mirror ratio has an appreciable influence on the indicated limit. When $R_0 = 20$, $Q_0^\infty = \infty$ at $n_k/n_0 = 20$ and $T_e = 21.5$ keV. Since, in practice, the density of the α-particles heating the plasma may turn out to be lower than the calculated density because of transverse losses, it is useful to consider another limiting case, when $n_\alpha = 0$. In our calculations, in this case, we also neglected the bremsstrahlung losses of electrons since they amount to only $\sim 5\%$ of the power of the α-particles. The influence of mirror ratios is very slight here. Figure 3 shows the functions $Q_0^\infty(T_e, n_k/n_0)$ for this case. It follows from a comparison of Figs 2 and 3 that the heating of plasma with α-particles begins to have a strong influence when $n_k/n_0 \gtrsim 10$.

3. CHARACTERISTICS OF THE TRAP

The extreme mirrortrons are related to the central ones via the electron balance according to Eq.(3) and the electron energy balance according to the equation

$$V_0 I_0 \left[\langle E_0^{ei}\rangle + \varphi_0 + T_e\left(1 + \frac{T_e}{2\varphi_0}\right) + \langle E_{x0}\rangle - \langle E_0^{\alpha e}\rangle - E_{q0}\right] =$$

$$= V_k I_k \left[\langle E_k^{ie}\rangle - \varphi_k - T_e\left(1 + \frac{T_e}{2\varphi_k}\right)\right] \qquad (5)$$

where E_{q0} is the energy of HF heating of electrons per "central" electron; E_k^{ie} is the energy acquired by an "extreme" electron from fast extreme ions. The characteristics of the extreme plasma were found by solving the Fokker-Planck equation for extreme ions from given values of R_k, n_k, T_e and mean energy of extreme ions $\langle E_{ik}\rangle$. As the potential determining the limit of the distribution function we used the ambipolar potential in the external mirrors $\varphi_k^* = \varphi_k - CT_e$, where C is a parameter characterizing the transport of part of the ambipolar field confining the electrons beyond the confines of the mirrortron. From the equilibrium condition of the ion and electron fluxes from external mirrors beyond the confines of the mirrortron, one can estimate that $C \sim 3$. The overall amplification coefficient of the trap is

$$Q = \frac{\epsilon}{4} \frac{n_{i0}^2 \langle \sigma v_0\rangle V_0 + n_k^2 \langle \sigma v_k\rangle V_k}{(E_{j0} + E_{q0}) I_0 V_0 + E_{jk} I_k V_k} \qquad (6)$$

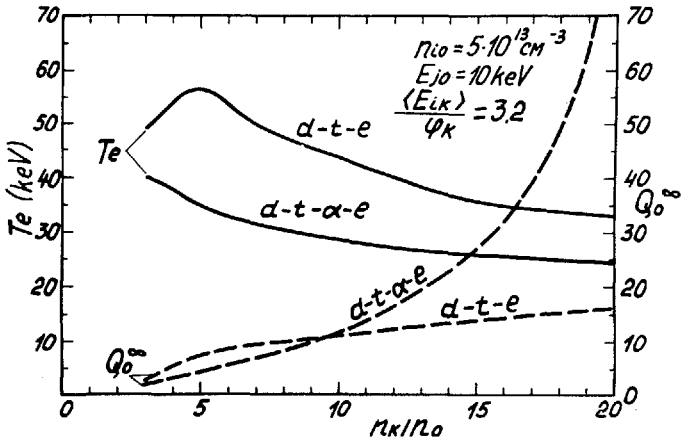


FIG.4. Electron temperatures optimal with respect to the field in the mirrors, and corresponding values of Q_0^∞ as a function of the ratio n_k/n_0, allowing for and neglecting fast α-particles.

where E_{jk} is the energy of ions injected into extreme mirrortrons; v_k is the relative velocity of the extreme ions.

In addition to their main function – to create an ambipolar field confining the central plasma – the extreme mirrortrons can transfer energy into the central mirrortron by means of electrons. The ratio of the power transferred into the centre to the power injected into the extreme mirrortrons is

$$\eta_k = \frac{\langle E_k^{ie} \rangle - \varphi_k - T_e\,(1 + T_e/2\varphi_k)}{E_{jk}} \tag{7}$$

The ratio of the energy consumed by the confinement of ambipolar mirrors to the total power introduced is

$$\gamma = \frac{E_{jk} I_k V_k (1 - \eta_k)}{E_{jk} I_k V_k + (E_{j0} + E_{q0}) I_0 V_0} \tag{8}$$

The magnetic field in the mirrors was taken to be

$$B_m = R_k B_k = R_k \sqrt{\frac{16\pi}{3} \frac{n_k \langle E_{ik} \rangle}{\beta_k}} \tag{9}$$

The volume of the extreme mirrortrons may be characterized by multiplying their length $2L_k$ by the cross-section of the plasma in their central planes S_k:

$$2L_k S_k = \frac{V_k}{\chi}\,; \quad \chi = \frac{B_k}{n_k^2} \left\langle \frac{n_{ik}^2}{B} \right\rangle \tag{10}$$

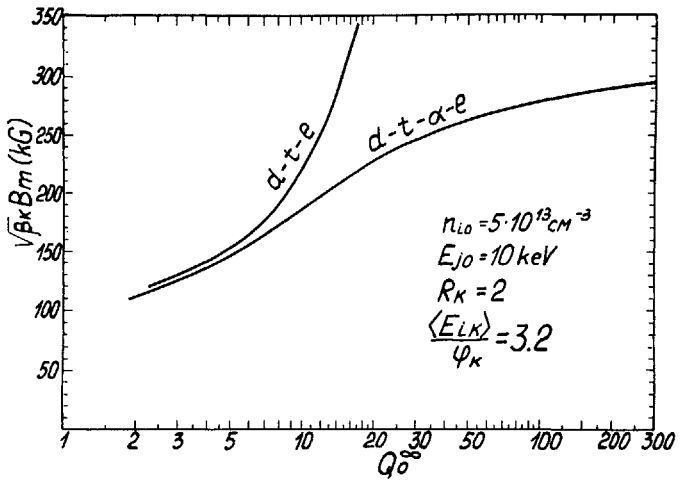


FIG. 5. Minimum fields in mirrors of an infinitely long trap as a function of the amplification coefficient allowing for and neglecting fast α-particles.

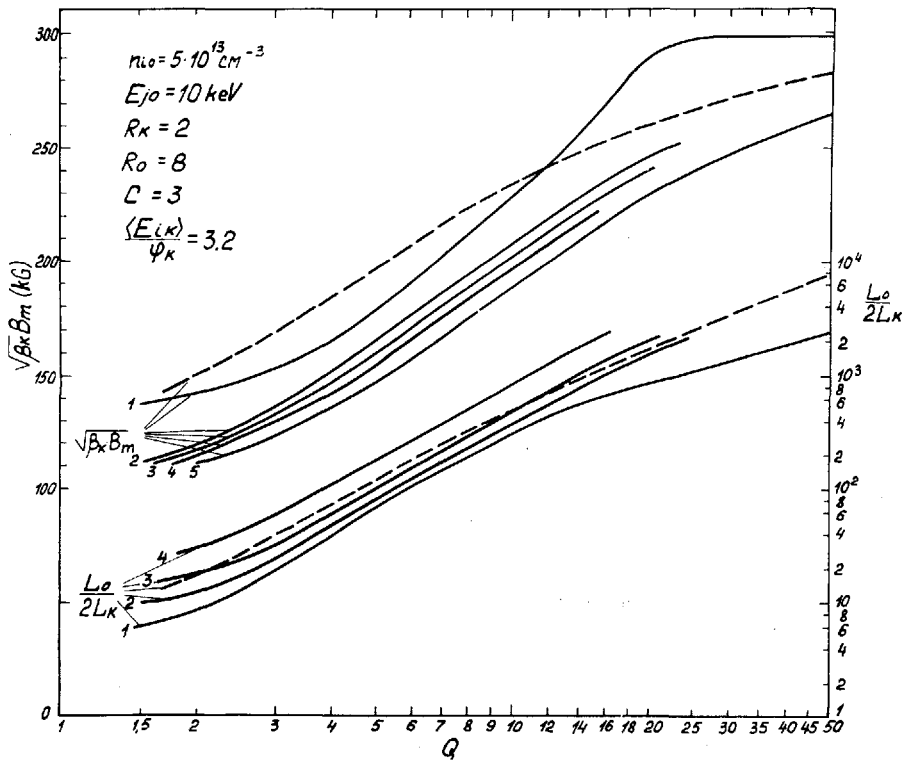


FIG. 6. Fields in the mirrors and relative trap lengths versus amplification coefficient allowing for fast α-particles: 1 – for min $L_0/2L_k$ at $T_e(n_k/n_0)$ according to Fig. 4; 2 – with $\gamma = 26\%$; 3 – with $\gamma = 17.5\%$; 4 – with $\gamma = 9.5\%$; 5 – for $L_0/2L_k = \infty$; dashed curves – for $E_{q0} = 0$, $M_{ik} = 1836$ m.

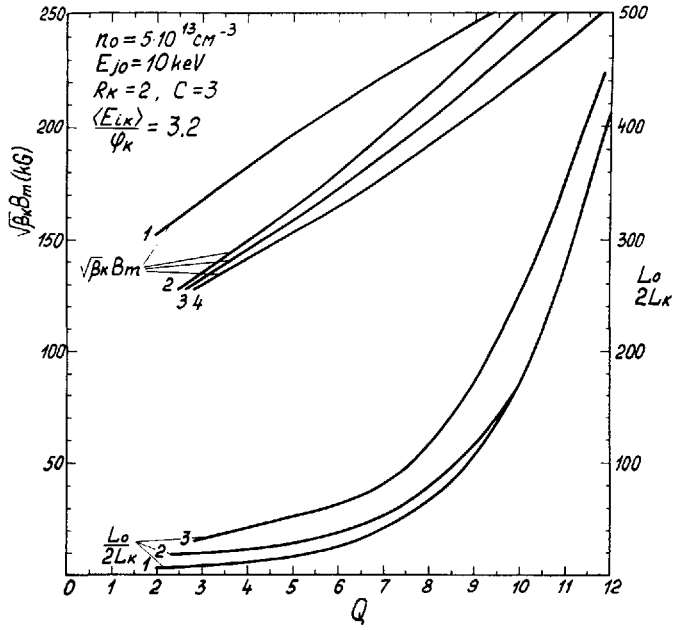


FIG. 7. The functions $B_m(Q)$ and $L_0/2L_k(Q)$ neglecting α-particles: 1 – for min $L_0/2L_k$ at $T_e(n_k/n_0)$ according to Fig.4; 2 – with $\gamma = 16.5\%$; 3 – with $\gamma = 9\%$; 4 – for $L_0/2L_k = \infty$.

where n_{ik}, B are the local plasma density and field in the extreme mirrortrons. The length of the central mirrortron is

$$L_0 = \frac{R_k}{R_0}\frac{V_0}{S_k} + 2\ell\left(1 - \sqrt{\frac{R_k}{R_0}}\right) + L_k\left(1 - \frac{\sqrt{R_k}}{R_0}\right) \qquad (11)$$

where ℓ is the length of the transition portion of the central magnetic field according to Fig.1. In the calculations, it was assumed that $\ell = L_k R_0/R_k$.

For given values of n_{i0}, R_k, C and E_{j0}, the given amplification coefficient of the trap can be obtained for different combinations of the values of n_k, Te and $\langle E_{ik}\rangle$. In the presence of additional HF heating of electrons, to decrease the field B_m in the mirrors, it is necessary to reduce the energy $\langle E_{ik}\rangle$. However, with decreasing ratio $\langle E_{ik}\rangle/\varphi_k$, the anisotropy of the distribution function of ions of the extreme plasma increases, causing its stability to decline. We took the ratio $\langle E_{ik}\rangle/\varphi_k$ equal to its value in a conventional open trap. It follows from the calculations of Ref.3, allowing for the dependence established in Ref. [1] on the mirror ratio in a single mirrortron, that when $R = 2$, $\langle E_i\rangle/\varphi = 3.2$. With such a ratio $\langle E_{ik}\rangle/\varphi_k$, the electron temperatures corresponding to $\min B_m$ at $V_0/V_k \to \infty$ were calculated. The optimum temperature T_e as a function of the density ratio n_k/n_0 for cases with fast α-particles in the central plasma and without them is shown in Fig.4. In the first case, the relatively low value $R_0 = 8$ was taken, for which the number of Larmor radii of the α-particles on the diameter in the central plasma is only one half the number of mean Larmor radii of ions on the diameter in the extreme plasma. In the second case, the value of R_0 was taken from the condition $\beta_0 = \beta_k$, where $\beta_0 = 8\pi n_0 (T_e + T_{i0} + 10\ \text{keV})$. Figure 5 shows the calculated

TABLE I. PARAMETERS OF TRAP AT $\langle E_{ik} \rangle = 3.2\,\varphi_k$
$M_{io} = 4451$ m; $n_{io} = 5 \times 10^{13}$ cm^{-3}; $E_{jo} = 10$ keV; $R_k = 2$; $C = 3$; $\beta_k = 0.4$.

Variant	I			II			III
Q	3	5	8	3	5	8	5
M_{ik}/m	4451			4451			1836
R_0	10.9	12.4	16.25	8	8	8	8
n_k/n_0	3.25	4.1	6.8	4.1	6.1	8.5	9.6
T_e (keV)	50.35	54.5	50.5	37.8	32.9	30.4	29.4
T_{io} (keV)	18.65	23.53	28.15	22.5	24.34	25.86	26.0
$\Delta\varphi$ (keV)	59.35	76.9	96.81	53.34	59.49	65.06	66.5
$\langle E_{ik} \rangle$ (keV)	1057	1218	1260	791	766.3	757.3	745.5
E_{jk} (keV)	1280	1515	1640	955	967	979	1127
$n\tau_{io}$ (10^{14})	7.06	11.37	19.53	2.81	3.51	4.25	4.55
$n\tau_{\epsilon 0}$ (10^{14})	2.08	4.37	5.95	0.792	0.951	1.11	1.19
I_0 (10^{12})	4.06	2.88	2.08	9.56	7.84	6.64	6.25
$n\tau_{ik}$ (10^{14})	2.68	3.22	3.24	1.77	1.62	1.54	0.88
Φ_k/Φ_0 (%)	8.09	7.48	7.59	6.1	4.95	3.83	23.0
Q_0	3.54	5.87	9.53	3.57	6.01	9.64	12.0
η_k (%)	20.01	22.77	27.12	19.76	24.15	26.31	39.36
γ (%)	17.1	16.13	16.75	17.78	17.76	17.46	58.4
P_{j0}/P_j (%)	2.03	1.85	1.84	3.8	4.89	6.31	3.7
$P_{q\hat{0}}/P_j$ (%)	76.5	77.1	75.1	73.4	71.7	70.0	0
P_{rec}/P (%)	35.9	29.1	24.5	37.3	29.5	24.2	28.3
$V_0/2L_kS_k$	87.0	168.8	587.6	119.5	410.3	1230	480.5
χ (%)	29.0	27.9	26.0	27.8	26.3	25.3	25.0
$L_0/2L_k$	19.52	30.53	78.05	32.3	105.0	309.8	122.5
B_m (KG)	214.7	259	339	222	254	298	314
α_0 (%)	12.73	23.76	38.46	6.84	9.04	11.27	12.02
$n_{\alpha 0}$ (10^{11})	–	–	–	7.17	7.07	7.07	6.93
$\langle E_{\alpha 0} \rangle$ (keV)	–	–	–	1779	1726	1695	1682
$I_{\alpha s}/I_{\alpha 0}$ (%)	–	–	–	68.0	70.1	71.8	72.1
$n^*_{\alpha s}$ (10^{13})	–	–	–	0.86	1.29	1.81	2.04
p (%)	4.62	3.34	1.65	5.52	3.4	2.53	1.88

minimum field B_m in the mirrors as a function of the amplification coefficient Q_0^∞. It is evident from Fig.5 that even the minimum values of B_m are very large. In the presence of fast α-particles in the central plasma, the necessary field in the mirrors at high values of Q_0^∞ is much lower. However, at relatively small values of Q_0^∞, the influence of α-particles is insignificant.

It is easy to show that for each value of Q, there is a minimum ratio of the lengths $L_0/2L_k$. Figures 6 and 7 show the minimum ratio of the lengths and corresponding field in the mirrors at optimum temperatures according to Fig.4 and ratio $\langle E_{ik} \rangle/\varphi_k = 3.2$ (curves 1) as a function of the coefficient Q. At a relatively slight excess of the minimum ratio $L_0/2L_k$ for a given Q, the field in the mirrors drops to a value close to its value at $L_0/2L_k \to \infty$. Figures 6 and 7 show the dependences of $L_0/2L_k$ and B_m on the coefficient Q at values of the parameter γ which are lower

than its value at the minimum ratio of the lengths (curves 2, 3 and 4). Figures 6 and 7 pertain to cases with fast α-particles and without them, respectively. It follows from a comparison of these figures that the confinement of fast α-particles leads to an increase in trap length, while the field in the mirrors begins to decrease only when $Q \gtrsim 5$.

It is of interest to examine the trap without additional HF heating of electrons. In this case, $\min B_m$ is not necessarily reached at the minimum value of energy $\langle E_{ik} \rangle$, since as the latter decreases, the efficiency of heating of electrons by the extreme ions declines. To reduce the field in the mirrors in this case, it is convenient to inject lighter ions into the extreme mirrortrons, since their energy is utilized more efficiently in heating the electrons. When $R_k = 2$, $R_0 = 8$, $C = 3$ with fast α-particles in the central mirrortron and injection of protons into the extreme mirrortrons at a ratio $\langle E_{ik} \rangle / \varphi_k = 3.2$, the field in the mirrors is close to minimal. Figure 6 shows the field B_m and ratio $L_0/2L_k$ as a function of the coefficient Q at the indicated parameters (dashed curves). At not too large values of Q, the lack of additional HF heating of electrons causes an increase of the field in the mirrors.

Table I gives the parameters of the trap for three values of the amplification coefficient Q. In variant I, the influence of α-particles is not considered; it is assumed that practically all α-particles are ejected from the central plasma across or along the magnetic field prior to being slowed down. In variant II, the influence of all fast α-particles on the central plasma is considered; it is assumed that slow α-particles are removed from the central plasma, so that their concentration is low. Variant III differs from variant II in the absence of additional HF heating of electrons; instead of deuterons and tritons, the extreme mirrortrons are injected with protons. In addition to the parameters specified above, Table I gives the following ones; Φ_k/Φ_0, the ratio of total injection currents into the extreme mirrortrons and the central one; P_{j0}/P_j, the ratio of the power of ions injected into the centre to the total power introduced into the trap; P_{q0}/P_j, the ratio of the power of HF heating of electrons to the tal power introduced; P_{rec}/P, the ratio of the output power of charged particles to the total output power; $\langle E_{\alpha 0} \rangle$, the mean energy of central α-particles; $I_{\alpha s}$, the current of α-particles entering the potential well; $n^*_{\alpha s}$, the approximate density of slow central α-particles that would accumulate in the centre if they are not removed, neglecting their effect on the plasma; $p = \langle n_{ik} n_{i0} \rangle / \langle n^2_{ik} \rangle$, a coefficient representing the penetration of isotopic central ions into the extreme plasma (averaging over the volume of extreme mirrortrons; n_{i0}, the local density of central ions).

4. CONCLUSIONS

It follows from a comparison of trap variants I and II, Table I and Figs 7 and 6 that for relatively small values of Q but of practical interest, variant I is preferable. In this variant, a weaker magnetic field is required in the main volume of the trap, and the trap length is several times smaller. The absence of a gain from the confinement of fast α-particles (in variant II) at small values of Q is mainly due to the fact that the α-particles together with electrons heat the ions sufficiently effectively, the temperature of the central ions approaches the electron temperature, and thus their life-time decreases appreciably.

In principle, the removal of fast α-particles in variant I can be accomplished by means of HF fields, or by selective violation of the adiabaticity condition for the α-particles, since their energy is much lower than that of the main ions.

One of the possibilities of removal of slow α-particles from the central mirrortron consists in the following: Into the peripheral layer of the central and extreme plasma are, additionally, injected ions of considerably decreased energy so that the electrons and central ions in the layer are markedly cooled, the electron temperature does not exceed the ion temperature, the density of the layer in the centre remains the same, and the density of the extreme ions in the layer is much higher than the density of the layer in the centre. Cooling of deeper plasma layers due to

ion thermal conductivity cannot reduce their density. The removal of energy from ions of the main central plasma increases the separation of the ion temperature from the electron temperature, making it possible to improve the trap parameters. Since radial density and ion temperature are not decreased, a radial transfer of α-particles from the inside to the outer layer will occur. If the α-particles accumulate in this layer, in time they can displace singly charged ions from it along the field, and, as a result of the radial decrease of the ion density, will start being dragged into deeper layers. The fairly intense additional injection of ions into the layer makes it possible to maintain an α-particle density in the layer that is much lower than the ion density, and the α-particles are able to escape through the lowered barriers.

The cooled outer plasma layer can serve as a diverter for the impurity ions as well since the latter will concentrate in this layer. The impurity ions accumulating in the diverter layer can be periodically dumped along the field by means of a brief removal of ambipolar barriers in the layer by disconnecting the additional injection into the layer in the extreme mirrortrons or by cooling the electrons from the ends of the trap.

The situation with conical instabilities is facilitated in the trap under consideration. The neighbourhood of the extreme anisotropic plasma and the penetration of relatively warm isotropic central ions into it may substantially weaken instabilities of relatively low frequency, in particular, the loss-cone drift instability, if the length of the extreme mirrortrons is sufficiently small. Since the electrons in the extreme mirrortrons comprise a small part of all the generalized electrons, the positive feedback due to the heating of electrons by instabilities [4] is aprreciably attenuated. When the electrons are heated additionally, and the ratio of the volumes of the central and extreme mirrortrons is large enough, the power of the injection into the extreme mirrortrons may amount to a few percent of the total power introduced. At the same time, an increase of one order of magnitude in the rate of losses of extreme ions in comparison with classical ones causes a decrease of only tens of percent in comparison with the total amplification coefficient. The last results of the 2XIIB device in Livermore give us reason to hope that a value of $\beta \sim 1$ will be reached. In this case, the vacuum mirror ratio R_k can decrease substantially.

Besides, it is possible that the ratio $\langle E_{ik} \rangle / \varphi_k$ can be reduced according to the stability conditions of the extreme plasma and by increasing the fraction of external ambipolar potentials removed beyond the external mirrors. All this will allow the required magnetic fields in the mirrors to be appreciably reduced.

If their units of measurements are not indicated, all the quantities are expressed in Gauss units (temperature in erg).

In conclusion, the authors express their sincere gratitude to D.D. Ryutov for invaluable discussions and comments, and V.G. Dudnikov and G.V. Roslyakov for useful discussions.

REFERENCES

[1] DIMOV, G.I., ZAKAJDAKOV, V.V., KISHINEVSKIJ, M.E., Fiz. Plazmy 2 (1976) 597.
[2] PASTUKHOV, V.P., Nucl. Phys. **14** (1974) 3.
[3] FUTCH, A.H., et al., Plasma Phys. **14** (1972) 211.
[4] KANAYEV, B.I., YUSHMANOV, E.E., Zh. Ehksp. Teor. Fiz. **67** (1974) 586.

DISCUSSION

ON PAPER IAEA-CN-35/C4

F.F. CHEN: How is simple hydrodynamic stability achieved in the long central region in the 95-metre-long reactor design?

G.I. DIMOV: Thanks to the considerably greater plasma pressures attained in the outer mirrors with "minimum B", the condition of hydrodynamic stability is achieved, on average, over the whole trap. Calculations in the paraxial approximation have shown that the required gradient of the perpendicular magnetic field in the outer mirrors exceeds the value found in a conventional magnetic mirror trap by 10% at the most. It is possible that when the central part of the trap is *very* long it will be necessary to incorporate short "minimum B" segments into the homogeneous field (by appropriate ion injection) to suppress higher modes.

T.K. FOWLER: As Dr. Dimov mentioned, Dr. B. Grant Logan and I have independently considered the triple mirror idea and we agree with his conclusions. I would emphasize the point he made that in view of the high-beta results in the 2XIIB experiment, the magnet field at the mirrors and the injection energy and the length of the machine can be reduced considerably. The best choice of parameters is a matter of economics. As to experiments, I believe that either break-even in a driven machine or ignition in the solenoid could be demonstrated in a device 10 metres in length.

A. SAMAIN: One important advantage of conventional mirror machines is that the impurities are not confined. What would be the situation in the scheme you are proposing?

G.I. DIMOV: It is possible to cool the outer layer of the central ions without permitting any radial decrease of plasma density; this possibility exists because with cooling the life-time of the central ions is increased. In a magnetized plasma at constant density there then occurs, owing to the radial decrease of the ion temperature, a transfer of impurities from within to the outer layer.

Session XXI

REACTOR DESIGN I

Chairman

H.A.B. Bodin
UK

Papers I 1-1 and I 1-2 were presented
by R. Hancox as Rapporteur
Papers I 3-1 and I 3-2 were presented
by W.M. Stacey as Rapporteur

REACTOR COSTS AND MAINTENANCE, WITH REFERENCE TO THE CULHAM MARK II CONCEPTUAL TOKAMAK REACTOR DESIGN

R. HANCOX, J.T.D. MITCHELL
Culham Laboratory, Abingdon, Oxon.,
(Euratom-UKAEA Fusion Association)
United Kingdom

Abstract

REACTOR COSTS AND MAINTENANCE, WITH REFERENCE TO THE CULHAM MARK II CONCEPTUAL TOKAMAK REACTOR DESIGN.

Published designs of tokamak reactors have proposed conceptual solutions for most of the technological problems encountered. Two areas which remain uncertain, however, are the capital cost of the reactor and the practicability of reactor maintenance. A cost estimate for the Culham Conceptual Tokamak Reactor (Mk I) is presented. The capital cost of a power station incorporating this reactor would be significantly higher than that of an equivalent fast breeder fission power station, mainly because of the low power density of the fusion reactor which affects both the reactor and building costs. To reduce the fusion station capital costs a new conceptual design is proposed (Mk II) which incorporates a shaped plasma cross-section to give a higher plasma pressure ratio, $\beta_t \sim 0.1$. Since the higher power density implies more severe radiation damage of the blanket structure, the question of reactor maintenance assumes greater importance. With the proposed scheme for regular replacement of the blanket, a fusion power station availability around 0.9 should be achievable.

1. INTRODUCTION

In recent years several designs of tokamak reactors have been published. Such studies have been encouraged because of growing confidence that the physical feasibility of fusion will soon be demonstrated, but they still assume considerable future progress in plasma physics and technological development. Accepting this extrapolation of present understanding, the objective of such conceptual design studies is to visualise the form of a full scale reactor, to explore the interaction of its many physical and technological requirements, and to assess the practicability of the reactor as the basis of a fusion power system.

The assessment of conceptual reactor designs includes many aspects. For example, the safety and environmental impact of fusion reactors have already been studied in some detail and, whilst much remains to be done, it appears that fusion does have considerable advantages in these respects. Two aspects still requiring more detailed assessment are the capital cost of the reactor, and the practicability of reactor maintenance. If the cost of fusion power is too high, economic considerations will delay its introduction until other fuel resources have been fully utilised. In particular, if the fast breeder fission reactor proves a commercial success, the introduction of fusion reactors could be delayed until well into the twenty-first century, which is beyond the presently envisaged time-scale of fusion development. If reactor design

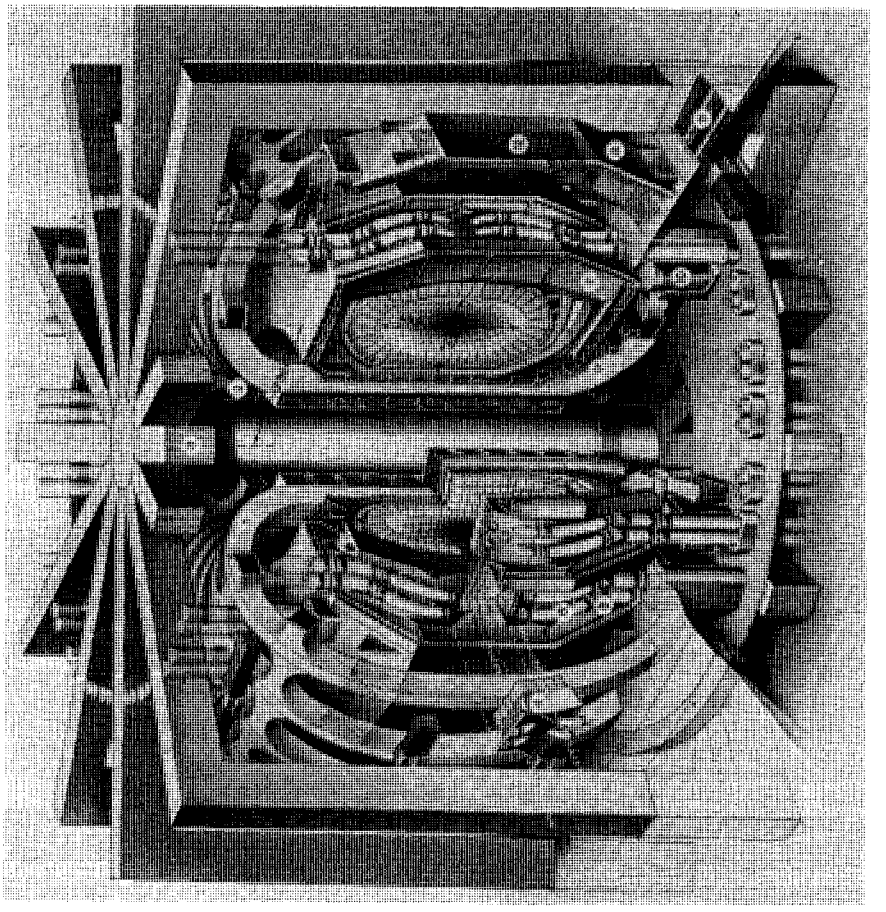


FIG. 1. Culham Conceptual Tokamak Reactor Mk II.

concepts are not developed incorporating facilities for practical maintenance operations, particularly replacement of radiation damaged blanket structure, power generation utilities will not adopt fusion reactors. Reactor availabilities of about 0.9 will be required to ensure a satisfactory return on investment.

The Culham Conceptual Tokamak Reactor Mark I, published in 1972 [1], was considered as a steady state device maintained by diffusion driven plasma currents. It was a 2500 MW(e) reactor with liquid lithium cooling, a refractory metal structure, and niobium-tin superconducting toroidal field windings. A detailed cost breakdown was prepared and a comparison made with a possible fast breeder of the same output power operating at the end of the century, which showed a higher capital cost for the fusion reactor. The only possible maintenance routine for this reactor required complete removal of each of the 32 segments which, including blanket, shield, and magnet, weighed a total of 400 tonnes. This would be a very slow and cumbersome operation. A new conceptual reactor design has now been proposed, the Culham Conceptual Tokamak Reactor Mark II, which seeks to reduce the physical size and cost of the reactor and incorporate facilities for blanket structure replacement with short down-times (Fig.1).

2. COST ESTIMATE FOR THE MARK I DESIGN

The major plasma and physical parameters of the Mk I conceptual design are listed in Table I. A detailed breakdown of materials and weights of each part of the reactor was prepared and costed. All material costs, including that of the niobium-tin superconductor, were on the basis of quantity production for a series of commercial reactors rather than one-off production for a prototype. The specific capital cost of the reactor is 112 £/kW(e) and of the complete power station 357 £/kW(e), at 1976 values, excluding all customer's on-costs and interest during construction. A breakdown of the capital costs of the reactor and of the whole fusion power station are given in Tables II and III. In view of the high thermal efficiency assumed, and consequent high coolant temperature, a refractory niobium alloy was proposed for the cellular structure of the breeding blanket. If corrosion limits would permit the use of stainless steel for much of the blanket structure the estimated capital saving would be around £20/kW(e).

Comparing the fusion reactor cost estimates with similar estimates for a fully developed fast breeder reactor shows that the capital cost of the fusion reactor, up to and including the primary heat exchanger, is more than twice that of the equivalent fast breeder reactor. In addition the fusion power station estimates showed higher costs in the following areas -

1. Power house building and civil works, due to the much larger physical dimensions of the reactor and primary circuit pipe-work.
2. Reactor auxiliaries, including lithium drainage and storage, the magnet cryogenics system, and the vacuum system.

3. Electrical services; additional supplies for magnets, cryogenics, vacuum system, injectors, (divertor), etc.
4. Fuel system; tritium processing plant.
5. Auxiliary plasma heating; neutral injection sources and accelerators.
6. Segment replacement facilities; transportation, examination, and repair facilities for reactor segments.

Fuel cycle costs were also estimated, using 50% enriched lithium for make-up of the natural lithium blanket. The price of enriched lithium was obtained by reference to the capital and operating costs of a UK enrichment plant using a lithium amalgam. Fuel cycle operating costs were estimated assuming continuous operation of the exhaust plasma processing unit and single shift operation of the blanket tritium recovery unit. On this basis the fuel cycle costs for the fusion reactor are substantially less than for a fast breeder reactor, the relative advantage in the early part of the next century being estimated as equivalent to a capital cost around £100/kW(e) in 1976 values. This estimate depends strongly on forecasts of the cost of fissile fuels and fuel reprocessing early in the next century, and cannot be very precise.

TABLE I. PARAMETERS OF THE CULHAM CONCEPTUAL TOKAMAK REACTOR DESIGNS

		Mk I	Mk II
Net electrical power	MW(e)	2500	2500
Gross thermal power	MW(th)	5830	5830
Major radius	m	12.6	7.4
Minor radius (mid plane)	m	2.5	2.1
Aspect ratio		5.0	3.5
Ellipticity		1.0	1.75
First wall power loading	MW/m^2	4.6	6.7
Magnetic field on axis	MA/m	7.6	3.2
Peak magnetic field	MA/m	11.1	6.4
Plasma current	MA	9.7	11.7
Safety factor (at wall)	q	2.5	2.6
Plasma pressure ratio	$\bar{\beta}p$	2.7	1.9
Plasma pressure ratio	$\bar{\beta}t$	0.016	0.093
Plasma density x 10^{-20}	$ions/m^3$	1.8	3.5
Required energy confinement time	s	1.8	1.5

TABLE II. ESTIMATED COST BREAKDOWN FOR A 2500 MW(e) FUSION REACTOR (£M)

Blanket cells and pipework		
Cells	37.9	
Cell supports	2.5	
Inlet/outlet pipework	5.1	
Distribution manifolds	4.3	
Ducts through shield	14.5	
Leak jackets over manifolds and ducts	2.0	
Expansion joints, etc	1.2	
Graphite reflector	3.3	70.8
Shield and supports		
Bedplate	1.3	
Shield, including structure	56.8	
Thermal insulation between cells and shield	6.5	
Primary vacuum seals	5.6	70.2
Magnet system		
Magnet windings	67.6	
Central restraint structure	2.8	
Support structure	0.9	71.3
Primary lithium circuit		
Pipework and valves	22.4	
Pumps and drives	8.9	
Primary heat exchanger	19.9	
Circuit testing	0.8	52.0
Biological shield		
Secondary vacuum boundary	2.5	2.5
Contingency	13.2	13.2
	TOTAL	280.0

Note: The above estimate in 1976 values is based on the Culham Conceptual Tokamak reactor (Mk I) and is for a fully developed reactor. It excludes customer's on-costs and interest during construction, and contains only marginal contingencies.

Combining the capital and fuel cycle costs, these estimates show little difference in the generating costs for the fusion station compared with the fast breeder station. Several items were omitted from the Mk I conceptual design, however, which now appear necessary and should be added to the cost estimate, including poloidal windings and power supplies (13£/kW(e)), a transformer core (22£/kW(e)), and materials for the replacement of radiation damaged blanket structure (37£/kW(e)). A more detailed study of the energy balance in a tokamak reactor operating in a non-continuous mode [2] also suggests that

TABLE III. ESTIMATED COST BREAKDOWN FOR A 2500 MW(e) FUSION REACTOR STATION (£M)

Power house, building and civil works	82.5
Power house, mechanical services	14.1
Site Services, permanent and temporary	34.5
Electrical services	46.1
Control and instrumentation	24.3
Reactor plant	280.0
Reactor auxiliaries	43.6
Maintenance and fuel handling mechanisms	41.3
Fuel injection, heating and recovery systems	40.0
Power generation	287.2
TOTAL	893.6

Note: The above estimate in 1976 values is based on the Culham Conceptual Tokamak reactor (MK I) and is for a fully developed reactor. It excludes customer's on-costs and interest during construction, and contains only marginal contingencies.

the net thermal efficiency is very optimistic. No firm conclusions should be drawn at this early stage but it appears that, whilst there may be strong safety or environmental arguments for the introduction of fusion power, there is no evidence yet that an economic advantage over fission can be anticipated. It is therefore important to find means of reducing the probable cost of a fusion reactor.

3. PARAMETERS OF THE MARK II DESIGN

To reduce the cost of a fusion reactor it is necessary to increase the plasma power density, but without corresponding increases in the costs of the magnetic field and other structures. This requires more efficient use of the magnetic field, leading to an increase of the plasma pressure ratio β_t, and a higher power loading of the first wall of the blanket. The changes made in the design model to develop the Mk II parameters included:-

1. Use of an elliptical plasma minor cross-section. To maintain plasma equilibrium, the ellipticity is limited to 1.75, which is only slightly greater than the maximum design value in the JET experiment [3].
2. Saturation of the flux density in the central core of the transformer. The total flux swing in the Mk II design is about 8.5 T.

3. A maximum toroidal magnetic field of 6.4 MA/m (8.0 T). This is a more severe constraint than was applied to the Mk I design, but is considered necessary because of the size and structural complexity of the magnet windings.

4. A plasma pressure ratio referred to the poloidal magnetic field $\tilde{\beta}_p = \sqrt{R/a}$. This is a slightly more conservative assumption than in the MK I design where $\hat{\beta}_p = R/a$.

5. The inclusion in the cost optimisation routine of the cost of replacement material for the blanket structure after a first wall integrated neutron dose of 10^{27} n/m^2.

The principal parameters of the Mk II design, derived from a cost optimisation, are given in Table I. The low aspect ratio and high plasma pressure ratio result in smaller physical dimensions (R = 7.4 m, a = 2.1 m) and an increased power loading of the first wall. The mean current of 14 MeV neutrons and power loading of the first wall (at 22.4 MeV/reaction) are 1.9 x 10^{18} n/m^{2}s and 6.7 MW/m^2 respectively, and the peak total neutron flux due to geometric effects is 1.5 x 10^{19}n/m^{2}s [4].

The importance of reaching plasma pressure ratios of $\beta_t \sim 0.1$ cannot be overlooked in developing economic Tokamak reactor designs. Any method of improving β, either by field programming or the control of density and temperature profiles, must be a significant part of the experimental programme to demonstrate the practicability of magnetic confinement in the tokamak geometry as the basis of a fusion power system. If the value of β assumed in the Mk II design can be reached, the plasma current and linear dimensions required for a reactor will only be 2 to 3 times larger than in presently conceived experiments. Thus the gap between next-generation devices such as JET and full scale reactors might not be so great as suggested by some earlier reactor designs.

The Mk II design, as described above, is far from complete. Areas not yet investigated in any detail include the form and extent of auxiliary heating systems for start-up (although the cost of neutral injection for ignition is included), the correct location of poloidal field windings, and the control of plasma impurities and their effect on the burn time and need for a divertor. Engineering aspects also to be studied are the design of a divertor system compatible with the concept of blanket replacement, and the energetic and strutural implications of pulsed operation including the need to limit induced currents in the main shield structure. As in other reactor designs means must also be developed for refuelling the reactor if burn times greater than a few seconds are to be obtained.

4. REACTOR MAINTENANCE

An essential requirement of a commercial fusion reactor is that the blanket and adjacent shield structure can be replaced

on a routine operational basis. The high first wall neutron flux in the Mk II conceptual design implies that the radiation damage rate will be comparable with that in the UK Prototype Fast Reactor. It will be important to develop materials which will retain adequate strength and ductility in the first wall environment for a minimum working life of two years.

The whole blanket structure could be replaced during the biennial shut-down for inspection and service of boilers and turbo-alternators - as is common practice for refuelling some types of fission reactors. Since, however, it is intended that the repair and processing of "used" blanket components should be undertaken on site to minimise active material transport, the preferred routine is to replace sections of the blanket on a 4 to 8 week cycle. Blanket segments would be repaired or disposed of as relevant in the time between each replacement operation, to ensure the most effective use of facilities and manpower. If each replacement operation can be completed during a $2\frac{1}{2}$ day weekend a total reactor availability of 0.9 can be attained, including the six week biennial inspection and service.

Unlike a fission reactor, the possibility of flux-levelling does not exist in the blanket of a fusion reactor. Material at the front of the blanket will be severely damaged, whereas material at the back will be less damaged and could be used for several replacement cycles. Material in the bulk of the shield will only be lightly damaged, and will last for the operational life of the reactor. From this situation arises the concept of using the main part of the shield as the reactor structure and primary vacuum envelope. This structure is provided with openings on the outer surface between each pair of toroidal field coils, which are the full height and width of the blanket segments. Each opening is closed by a rigid vacuum-tight door which can be withdrawn radially between the toroidal field coils and the transformer limbs, providing horizontal access to the inner parts of the reactor.

Removal of the doors in the vacuum envelope gives access for cutting the primary coolant distribution piping and for the removal and replacement of the blanket segments inside the main shield structure. Helium is the preferred coolant since leakage after cutting the pipes will not add contamination in the plasma region. The plasma parameters and dimensions of the Mark II design lead to blanket segments of 70 to 100 tonnes weight and 11 metres height. On this scale, the remote handling operations required appear practicable. A more detailed description of the reactor, reactor buildings and work-shops, and discussion of the schedule of servicing operations, has been published elsewhere [5].

The replacement scheme outlined above has many implications. If the time for which the reactor is out of service is to be minimised, the operations must be undertaken with blanket segments that have not cooled to ambient temperature, and therefore an inert atmosphere is required. For adequate access the toroidal field windings must be extended beyond their minimum size in the radial direction and the poloidal windings

may have to be moved vertically to provide enough space. Auxiliary equipment should ideally be above or below the reactor rather than occupying space required for servicing access around the outside. This applies particularly to bulky or complex items such as injector lines for auxiliary heating or refuelling. Instrumentation and auxiliary coolant or control services to the blanket segments and the shield door will have to be remotely disconnected and reconnected. Finally, the need for divertors may greatly complicate the servicing arrangements, and in particular the use of multiple-null poloidal windings in the blanket region may make the replacement of segments impracticable.

The removal of a toroidal or poloidal magnetic winding for repair is considered impracticable. The complex structure required to withstand the centralizing and twisting forces on the toroidal winding and the extensive cryogenic insulation surrounding the superconducting windings do not allow the magnet system to be dismantled easily. Furthermore, the highly active permanent shield structure would have to be partially dismantled to permit removal of a toroidal coil. Superconducting magnet technology must progress to the point at which reliable operation for the life of the reactor is the accepted standard, as with pressure vessels in fission reactors.

The maintenance scheme outlined above is still far from complete. Several areas remain to be considered, such as the possible need for additional cooling to deal with afterheat, or the influence of the detailed positioning requirements of poloidal field windings. The conceptual study has dealt realistically with the essential problem of replacing the first wall, the need to cut coolant pipes, the need for a vacuum envelope, and the need to provide radio-active work-shops for subsequent processing of active blanket segments. It is clear that the maintenance philosophy will have a profound influence on reactor design, and that the requirements and cost of maintenance must be taken into account at an early stage in the design process. Significant progress is required in the development of the remote handling equipment and the processing of active reactor structures if acceptable reactor availability is to be achieved.

5. CONCLUSION

A conceptual tokamak reactor design has been developed (Mk II) with the aim of reducing the estimated capital cost of a fusion power station and incorporating a practical maintenance scheme for the reactor. To meet the first of these objectives it has been necessary to propose smaller physical dimensions than previous designs of comparable power output, with the consequent need for a high plasma pressure ratio ($\beta_t \sim 0.1$) and a high power loading of the first wall ($P_w \sim 6$ MW/m^2). A design concept has been described which takes advantage of these smaller dimensions to facilitate routine replacement of the blanket structure. The implications of these proposals on Tokamak reactor design have been discussed. Whilst further design study is required on many of the reactor sub-systems this, and similar conceptual studies, will lead to

a balanced view of the seriously conflicting requirements of fusion reactors and eventually to practical and economic solutions.

6. ACKNOWLEDGEMENTS

The authors gratefully acknowledge the assistance of their many colleagues who participated in the conceptual reactor studies, and in particular those at A.E.R.E. Harwell involved in the engineering design and at the Reactor Group H.Q. Risley who undertook the cost estimates.

REFERENCES

[1] MITCHELL J T D and HANCOX R, Proceedings of the 7th Intersociety Energy Conversion Engineering Conference, San Diego (1972) 1275.

[2] DARVAS J, et al, Proceedings of the 6th Symposium on Engineering Problems of Fusion Research, San Diego (1975) 48.

[3] JET Project - Design proposal EUR-JET-R5 (1975)

[4] CONSTANTINE G, and PICKETT D, Proceedings of the 9th Symposium on Fusion Technology, Garmisch - Partenkirchen (1976) - to be published.

[5] MITCHELL J T D, and HOLLIS A, Proceedings of the 9th Symposium on Fusion Technology, Garmisch - Partenkirchen (1976) - to be published.

A HIGH-PERFORMANCE NON-CIRCULAR TOKAMAK POWER REACTOR DESIGN STUDY – UWMAK-III

R.W. CONN, G.L. KULCINSKI, C.W. MAYNARD,
R. ARONSTEIN,* R.W. BOOM, A. BOWLES,*
R.G. CLEMMER, J. DAVIS,** G.A. EMMERT,
S. GHOSE,* Y. GOHAR, J. KESNER, S. KUO,†
E. LARSEN, J. SCHARER, I. SVIATOSLAVSKY,
D.K. SZE, W.F. VOGELSANG, T.F. YANG,
W.D. YOUNG
Fusion Technology Program,
Nuclear Engineering Department,
University of Wisconsin,
Madison, Wisconsin,
United States of America

Abstract

A HIGH-PERFORMANCE NON-CIRCULAR TOKAMAK POWER REACTOR DESIGN STUDY – UWMAK-III.

UWMAK-III is a conceptual power reactor design study aimed at understanding the problems associated with using advanced technologies and several new or different design approaches in tokamak systems. Advanced technologies studied include the use of the molybdenum-based alloy, TZM, as the primary structural material, the use of aluminium as the stabilizer and aluminium alloy structure for the NbTi superconducting magnets, and the use of a closed-cycle helium gas turbine power conversion system. New or different design approaches include the study of RF (fast magnetosonic waves) plasma heating, a blanket design where tritium breeding is accomplished only in the outer blanket region, a permanent inner blanket that is basically a hot shield, tritium extraction and recycling processes, and the general design approach to blanket module removal. The maximum module weight is only 42 t. An MHD analysis has determined the non-circular plasma shaped like a characteristic "D" with neutral points on the plasma boundary for a poloidal divertor. The reactor is small (major radius = 8.1 m) with a relatively high β (about 9%) and an average neutron wall loading of 2.5 $MW \cdot m^{-2}$. It is designed to generate 5000 MW(th) during the burn and 1985 MW(e) continuously. The net plant efficiency is about 42%. Aspects of the design study discussed in some detail include the plasma physics analysis, magnet design, blanket and shield neutronic and thermal analyses, tritium extraction, materials performance and radiation damage. A brief discussion is included on the questions of size and costs in tokamak systems and their approximate relation to other advanced power-generating technologies.

1. Introduction

UWMAK-III is a conceptual power reactor design study of a noncircular tokamak with the aim of assessing the prospects and problems associated with utilizing several advanced technologies in a tokamak reactor system. The reactor is designed to produce the same thermal power output, 5000 MW, as our earlier studies, UWMAK-I [1,2] and UWMAK-II [3,4] but it is considerably smaller in physical size. The major parameters characterizing the reactor are listed in Table I and an enlarged cross-section view of the main reactor island is shown in Fig. 1. An overall view of the plant design showing the layout of necessary buildings is given in Fig. 2. The reactor is designed to produce a continuous net electrical output of 1985 MW with a net plant efficiency of 41.9%.

---

* Bechtel Corporation, San Francisco, California.

** McDonnell-Douglas Astronautics Co.-East, St. Louis, Missouri.

† United Technologies Research Center, East Hartford, Connecticut.

Table I

Major Characteristics and Parameters of UWMAK-III

a. General Features

Structural Material	Mo Alloy, TZM
Coolant:	
Inner Blanket	He
Outer Blanket	Lithium (natural)
Shield	He
Fuel Cycle	(D-T), Li
Total Tritium Inventory	35.8 kg
Power Cycle:	
Blanket	Closed Cycle He
Divertor	Na-Steam
Thermal Power During Burn	5000 MW(th)
Average Thermal Power	4735 MW(th)
Average Electrical Power	1985 MW(e)
Net Plant Efficiency	41.9%

b. Plasma Characteristics

Major Radius	8.1 m	Plasma Current	15.8 MA
Plasma Radius	2.7 m	Poloidal Beta	2.2
Shape Factor	1.6	Total Beta	~9%
Height to Width Ratio	~2	q(o)	~1.0
		q (near separatrix)	~3.5
Plasma Shape	"Triangular D"	Current Rise Time	15 s
Magnetic Axis	9.0 m	Plasma Burn Time	1800 s
Plasma Heating Method	RF	RF Power	40 MW
		Toroidal Field Ripple	~1%
RF Frequency	60 MHz		
Mode	Fast Magneto-sonic Wave		

Impurity Control Method - Double Null Divertor + Low Z Liner

c. Blanket Performance Characteristics (R-Z Toroidal Neutronics)

Breeding Ratio	1.25	Max. Temp. in TZM	1000°C
Average Neutron Wall Loading	2.5 MW/m^2	Max. Temp. in Li	980°C
		Max. Temp. in He	870°C
Total Energy Per Fusion	20.1 MeV	Tritium Inventory	1.0 kg

d. Magnet Parameters

Number of Toroidal Field Magnets	18
Magnet Superconductor	NbTi
Maximum Field	8.75 T
On-Axis Magnetic Field	4.05 T
Magnet Stabilizer	Al
Magnet Structure	Al Alloy, 2219
Horizonal Bore	12.75 m
Vertical Bore	24.08 m
Energy Stored in Toroidal Field	108 GJ

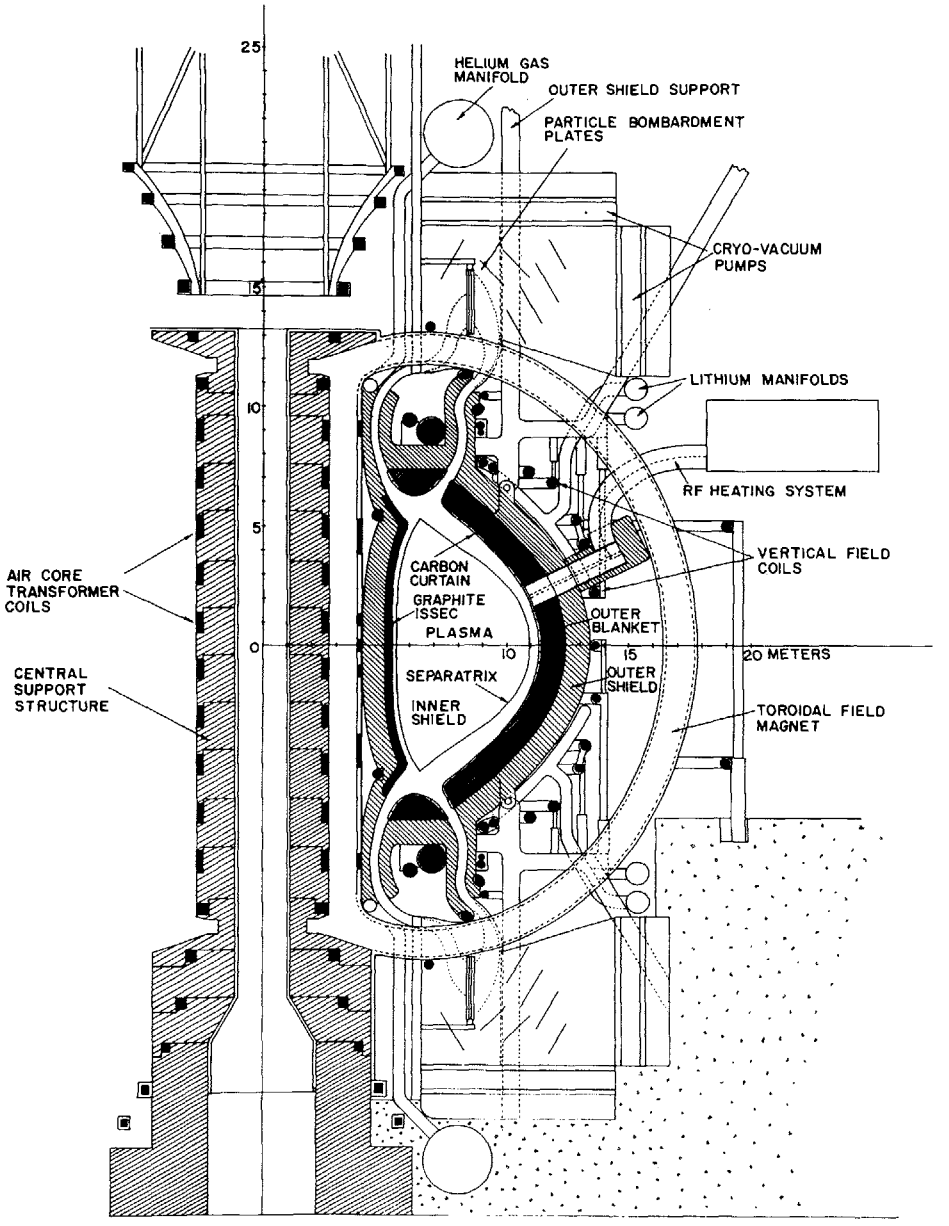


FIG.1. Cross-section view of nuclear island design for UWMAK-III.

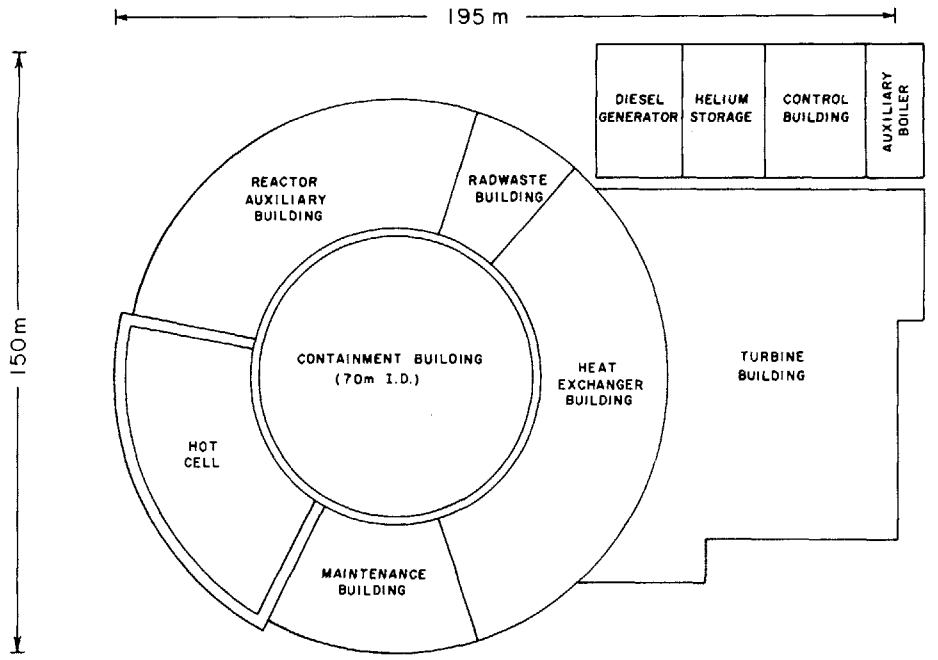


FIG.2. Plan view of building arrangement for a reactor such as UWMAK-III. Note that the area and volumes are, within 20%, about the same as for the Clinch River Fast Breeder Reactor [8].

Before discussing the design study in detail, it is worth enumerating several of the important features and unique aspects of UWMAK-III.

(1) UWMAK-III is substantially reduced in size compared to our earlier studies [1-4]. A comparison of the plasma and toroidal field magnet size and shape between UWMAK-II [3,4] and UWMAK-III is shown in Fig. 3. The size reduction is primarily the result of utilizing a high plasma beta (~9%) and an average 14 MeV neutron wall loading of about 2.5 MW/m^2.

(2) A high-beta "D"-shaped plasma has been designed based on two-dimensional MHD equilibrium studies which show that such plasma equilibria can be found even with discrete external coils located far from the plasma (outside the blanket and shield) and with null points on the plasma boundary.

(3) RF heating has been studied to assess its potential for heating reactor plasmas to ignition conditions [5]. After an initial assessment of various wave heating modes, our efforts were concentrated on the fast magnetosonic wave [6] because of its direct heating of the ions, its accessibility and apparent penetration to the plasma core, and the potential for generating large amounts of RF power at the required frequency (about 60 MHz).

(4) The NbTi superconducting magnet design utilizes an aluminum stabilizer with high-strength aluminum alloy as its structure. In addition to cost advantages, this allows for compatible contraction of both the conductor and the structure on cool-down or warm-up, and reduced activation by neutrons.

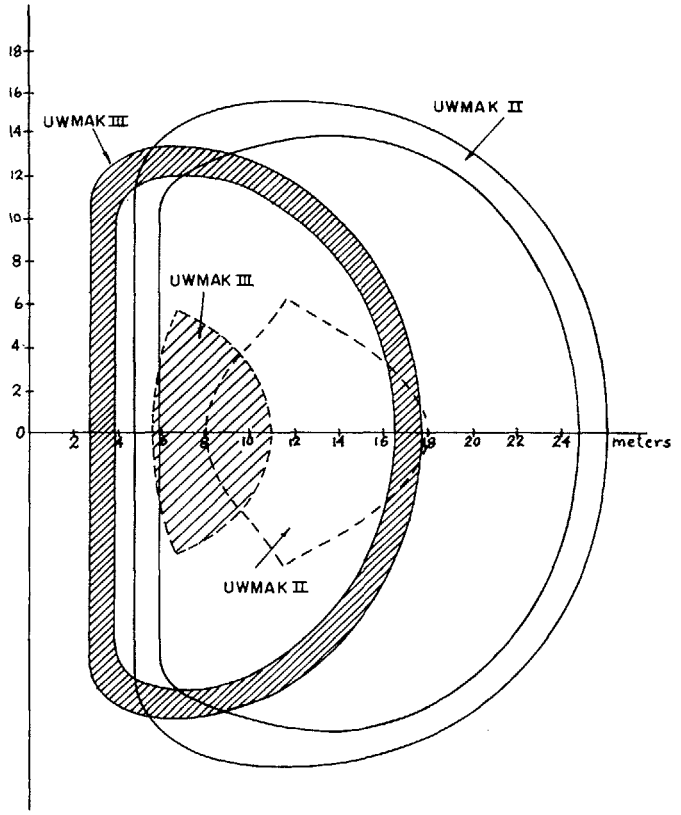


FIG. 3. Comparison of the plasma and toroidal field coils in UWMAK-II [3, 4] and UWMAK-III illustrating the sharp reduction in size.

(5) The molybdenum-based alloy, TZM (99.4% Mo, 0.5% Ti, 0.08% Zr, 0.01% C), is chosen as the primary structural material because of the desire to increase the operating temperature of the coolant while using a material which, unlike vanadium or niobium alloys, is compatible with both helium or liquid lithium coolants. This particular alloy shows a high resistance to radiation damage from neutrons. In addition, the U.S. has a good resource position with respect to Mo.

(6) The blanket design is unique in that tritium breeding takes place only in modules on the outer portion of the torus. A schematic illustration is given in Fig. 4. In the outer blanket, liquid lithium is used as both the coolant and breeder material. The pumping problems are minimized by good access and low magnetic field. The inner blanket nearest the torus centerline is not designed to breed tritium and its first structural wall is protected from radiation damage by a graphite neutron spectral shifter or ISSEC [7]. Thus, the inner blanket is designed as a hot shield and is expected to last for the life of the plant. The outer blanket module will be damaged by radiation and will have to be removed periodically (approximately once every two years). A highly modularized outer blanket design has been developed in which the largest element that must be moved weighs 42 t.

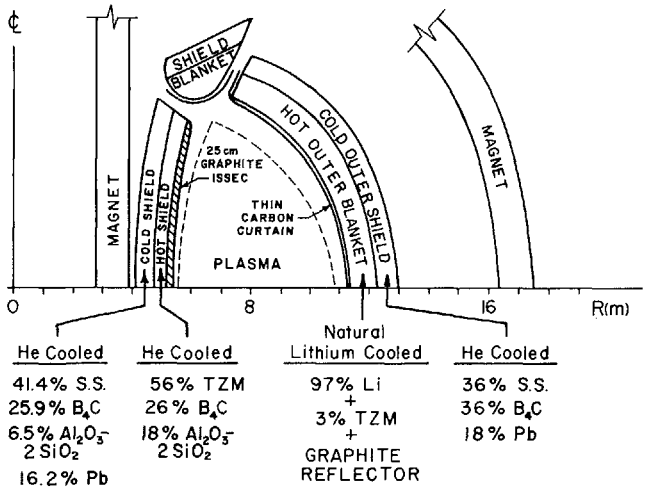


FIG.4. Schematic illustration of the blanket and shield design for UWMAK-III. Tritium breeding is only in the outer blanket.

(7) The blanket neutronics analysis has been carried out using two-dimensional neutron and photon transport in toroidal geometry. This is found to be especially important when the blanket design is not poloidally symmetric. The major radius, R, and the height above the midplane, Z, are used as the main coordinates. Symmetry is assumed in the toroidal angle, ϕ. Existing cylindrical geometry transport codes have been adopted to successfully complete the toroidal neutronics analysis.

(8) A closed cycle helium gas turbine power conversion system has been designed and studied. The helium coolant from the inner blanket goes directly to a helium turbine while the lithium from the outer blanket goes to a Li-Na intermediate heat exchanger. Sodium from the intermediate loop plays the triple role of isolating the tritium-containing lithium from the power cycle, providing a working fluid for thermal energy storage, and protecting the primary structure from high pressures in the event of a leak in a heat exchanger. Thermal storage is required to level the electrical output from the turbines despite the pulsed nature of the tokamak burn cycle.

(9) The plant layout and building design shown in Fig. 2 has produced a compact system design. The primary containment building is, within 20%, the same size as that designed for the 350 MWe Clinch River Breeder Reactor, a demonstration LMFBR [8], and the overall plant size is likewise about the same.

(10) An assessment is made of the materials resource implication of a UWMAK-III type power reactor economy. The most serious problems appear to be associated with the expansion of an established industry rather than the question of sufficient resources.

(11) An economic study has been carried out in collaboration with the Bechtel Corporation using a macro-composite-systems approach in an effort to identify key cost areas in tokamak fusion systems. The resulting estimates have been compared with estimates developed by Bechtel for other advanced, non-fuel-limited approaches to electric power generation.

Table II

UWMAK-III Reactor Cycle

Time (s)	
0-15	Startup: Plasma and divertor currents rise to full value; transformer currents begin to drop.
15-30	RF Heating: Plasma and divertor currents at full value; transformer currents continue to drop.
30-1830	Burn: Transformer currents drop to maximum negative value.
1830-1850	Shutdown: Plasma and divertor currents drop to zero; transformer currents rise to provide negative startup flux.
1850-1890	Pumpout and recharge: First 20 seconds; hydrogen gas pumped into cool plasma, residual gas pumped out. Final 20 seconds; transformer currents reset to initial values.
1890-1900	Final pumpout and refill: Chamber purged and refilled with fresh fuel.

We summarize in this paper details relating particularly to the plasma analysis, blanket and shield design, materials, tritium, overall plant design and system economics. The design of the toroidal field magnet system has been given by Boom, Moses and Young [9] and the analysis of the power cycle is described by Conn and Kuo [10] in other publications. A much more extensive discussion on all aspects of the UWMAK-III study is given in reference 11.

2. Plasma Design and Analysis

Noncircular plasma cross-sections offer the potential for achieving higher plasma β values compared to circular plasmas of equal poloidal beta, β_θ, or safety factor, q [12]. The scaling is

$$\beta = \beta_\theta \left(\frac{S}{qA}\right)^2$$

where A is the aspect ratio and S is the plasma shape factor. Therefore, a detailed MHD equilibrium study has been carried out to determine the plasma shape shown in Fig. 1. The code used to perform this analysis was developed by the MHD group at Princeton [13]. The plasma has been satisfactorily tested for stability against rigid displacements and localized interchange modes. The large triangularity of the shape is the result of forcing the vacuum vertical field to have good curvature.

The plasma burn cycle is summarized in Table II. An air core transformer with superconducting windings located as shown on Fig. 1 is designed to bring the plasma current up linearly from some nominal value to the operating level of 15.8 MA. The vertical or equilibrium field coils actually provide approximately 96% of the startup flux with the OH windings providing the rest. The total flux swing during the current rise phase is 254 V-s.

The flux swing required during the 15-second plasma heating phase and the 30-minute burn is provided by the OH windings alone. The flux swing required, based on a general expression for the plasma electrical conductivity including particle trapping and impurity effects, is 107 V-s. The peak power requirement is 913 MW during the current rise phase and is assumed to be provided by 500 MW off the line and the rest from an inductive energy storage unit similar to that designed for UWMAK-II [3,4].

The plasma reaches a temperature of only 1.8 keV during the ohmic heating phase. Thus, auxiliary heating is required to ignite the plasma and bring it to its steady-state operating condition during the burn period. RF heating has been examined for this purpose and the fast magnetosonic wave at $\omega = 2\omega_{CD}$ has been studied in detail. Analysis shows that the ion cyclotron harmonic absorption term occurs in a vertical band of finite width, Δ, centered at the plasma major radius. The finite width is less than the plasma radius and is due to thermal effects and the 1/R variation of the toroidal field, where R is the major radius. The energy deposited in this slab is then uniformly distributed over the flux surfaces due to the rotational transform. The expression for the ion heating profile is directly proportional to R/r, where r is the local plasma radius, and is therefore strongly peaked at the plasma center.

The existence of toroidal eigenmodes [6] also has a strong effect. In smaller devices, these eigenmodes are well separated but in large reactor systems like UWMAK-III, the density of toroidal eigenmodes in frequency domain becomes a near continuum [5]. This means the eigenmodes will always be available to heat the plasma, but the cumulative effect of all excited modes on the loading of the launching structure and on the heating efficiency is a subject requiring further research.

The theoretical expression for plasma ion heating by the fast magnetosonic wave is used together with a global model of plasma behavior [14,5] to analyse the heatup rate. At the end of the 15-s ohmic heating phase, 40 MW of RF wave heating at 60 MHz is turned on. After 8 s, the plasma reaches ignition and if the RF power is left on for 12 s, the plasma reaches the equilibrium temperature of $T_i \simeq 19$ keV, $T_e \simeq 23$ keV after 15 s. An alternative scenario was also studied in which 200 MW of injected RF is used to rapidly heat the plasma past ignition and then allow alpha heating to take over. This would be an interesting scenario if the plasma can be operated in the "flux-conserving" mode [15].

An important problem with RF heating, in addition to adequate coupling of the waves to the plasma, is the design of a suitable launching structure located on the torus wall. It must be capable of handling 200 MW of power at 60 MHz for a startup period of up to 15 seconds, and it must be designed for the excitation of modes that lead to energy deposition near the plasma core.

An ideal system would have a spectrum which excites lower order poloidal m values. Higher order m values cause the finite ion gyroradius heating to peak further towards the plasma edge, leading to edge heating rather than core heating. In order to excite only low m numbers, the source distribution would have to cover most of the poloidal circumference. A further problem is caused by the fact that for large tokamaks such as UWMAK-III, the minor circumference is large compared to a free space wavelength. This introduces phase shifts of a wave traveling in the poloidal direction which can contribute to a higher order poloidal spectrum and reduce the efficiency. This may be overcome by introducing external circuit phase shifts which correct for the natural phase shift of the wave as it travels in the poloidal sense.

A standard rectangular waveguide launcher flush mounted in the wall introduces a new spectral excitation problem since its toroidal dimension

must be larger than half a free space wavelength for propagation of the dominant TE_{10} mode. This can be overcome by using smaller waveguides, possibly filled with the high dielectric ceramic which reduces the dimension of the guide and excites larger k_{11} values. If the radiation damage and high temperatures introduced into the ceramic can be tolerated, a strip line located over a ceramic dielectric inside a rectangular guide could be envisioned which does not have a cut-off limitation due to small aperture size. The conducting strip would have to be coupled to the torus by making a small loop which is electrically connected to the bottom of the guide.

For the design used in UWMAK-III, a ridged waveguide has been considered in order to reduce the toroidal extent of the guide for improved wave penetration and heating. This reduces the mode conversion potential and provides a means of determining the fraction of wave power initially deposited in the ions. The H-shaped guide would have the inner dimensions of 1 m high by 1 m wide with a gap width of 8.7 cm which is 50 cm in extent. The wave impedance of the dominant TE_{10} mode is 70 ohms and the theoretical power-carrying capability is 30 MW.

If neutron and plasma heating of the guide aperture are not too severe, a guide which is partially or fully filled with a dielectric medium can be considered. A ridged waveguide which is filled with alumina can be designed which is 50 cm wide by 50 cm high with a 10 cm gap. The wave impedance is 40 ohms and a theoretical power transfer of 60 MW can be obtained.

It is evident that several alternatives for the design of magnetosonic wave launching structures exist. From a purely plasma point of view, a wave source distribution is proposed that goes half way around the minor cross-section on the outside edge. A second source located very close to the first but shifted in phase by 180° is proposed in order to set up short wavelengths (λ = 1m) in the toroidal sense. This approach, however, presents some obvious problems with regard to the placement of the vertical field coil and to access. The added complexity led to the design approach shown in Fig. 1. This design was used as the basis for locating the equilibrium vertical field coils used in the MHD analysis described earlier.

The equilibrium plasma conditions during the plasma burn for UWMAK-III have been studied by using both a global plasma energy balance model [14] and a more sophisticated space-time tokamak code [16]. In both cases, thermal equilibria are found which produce 5000 MW_{th} of power. In the latter case, however, the average ion and electron temperatures, the plasma β_θ, and the particle confinement time are found to be significantly lower than those predicted by the global model because the temperature and density profiles are sharply peaked at the axis of the torus.

The plasma and magnetic field parameters are listed in Table Ib-d. The energy confinement time is 1.6 sec while the particle confinement time is 0.55 sec. The fractional burnup is very low, 0.83%, and the fueling rate for D plus T atoms is 1.43×10^{21}/sec. This low fractional burnup and correspondingly high fueling rate results because the diffusion of particles from the plasma is governed by the diffusion coefficient at the plasma edge. The edge condition associated with the use of an unload divertor implies a very low density and therefore a quite collisionless plasma. In turn, this leads to a large diffusion coefficient assuming microinstability scaling [17]. The low value of τ_p in the space-dependent model means the amount of tritium in the refueling cycle will be much larger than heretofore expected on the basis of global model calculations alone. In this case, the fueling rate for tritium is 74.7 kg/day.

Two forms of impurity control are included in the UWMAK-III design, a magnetic divertor and a low Z liner. The magnetic divertor is of the axisymmetric, poloidal double null type such as we have used previously [1-4].

The low Z liner consists of a thick graphite zone (25 cm) on the inner portion of the chamber nearest the centerline and a thin carbon curtain [18], as described in UWMAK-II [3-4], mounted on the outer blanket first wall. The operation of the carbon curtain is similar to that described previously and the temperature during the plasma burn is 1300°C. As such, physical sputtering is expected to dominate. The thick graphite zone on the inner side of the chamber will operate with a much higher surface temperature in the neighborhood of 1800°C. The erosion rate will be governed by physical sputtering and the "possible" formation of acetylene. Low-energy atomic hydrogen studies show effective yield coefficients of 1 to 3 x 10^{-3} [19]. If these values do not increase by more than a factor of 10 at 10-30 keV, then the erosion of the ISSEC will be manageable.

The effectiveness of the divertor in reducing the charged-particle flux to the wall has been estimated using the model described previously [4]. The design of the divertor in UWMAK-III is unique in several ways. Firstly, the particles bombard a thin, solid plate of TZM located outside the toroidal field magnets and the pumping and heat transfer problems are not coupled (see Fig. 1). Placing the bombardment plates outside the TF coils allows the field lines to be fanned out, thus reducing the power density of particles on the plates. Combining this with the relatively small flow conductance back through the slots to the plasma, one expects that there will be little backstreaming of neutrals and impurities.

A pumping scheme for a fusion reactor is complicated by the fact that twice as many pumps as needed in normal operation have to be provided to allow one half of them to be recycled while the outer half are on line. This implies low conductance gate valves, heaters, backup pumps and many ducts and vacuum lines. Nevertheless, a system such as UWMAK-III lends itself to a reasonably simple design. We envisage that all pumping of the main chamber will be by cryopumps that are rectangular in shape and will cover about 65% of the available area in the particle collection chamber. The total pumping area will be 1600 m^2, with only one half of the pumps in use at one time and the pumps would be regenerated every five hours. (Time between regenerations can be as little as 2.5 hours.)

3. Magnet System Design

The design analysis for the UWMAK toroidal field magnets is given elsewhere [9]. To summarize briefly, the toroidal field coils for UWMAK-III shown in Fig. 1 have a modified constant tension "D" shape, corrected for the field variation due to the finite number (18) of coils. The embedded conductor in a solid "D"-shaped alloy aluminum former is used to minimize the material requirements while providing maximum strength and stiffness. This construction was described in detail in the UWMAK-I report [1] and the cold central structure and secondary vacuum wall used in the UWMAK-II [3] design are retained. The superconductor is TiNb superconducting filaments processed in an OFHC copper matrix for convenience but stabilized with high-purity aluminum in the case of the toroidal field magnets. The coils are fully cryogenically stabilized and produce a maximum field of 8.75 T and an axial field at R = 8.1 m of 4.05 T. The smaller size of UWMAK-III has also led to a sharp reduction in the TF coils size. As one measure, we note that the stored energy in the toroidal field of UWMAK-III is 108 GJ compared with 216 GJ in the UWMAK-II design.

A unique feature of the UWMAK-III TF coils is the use of an Al conductor and an Al alloy structure. The use of 316 stainless steel for the structural material in the toroidal field magnets in the UWMAK-I and UWMAK-II designs was predicated on a limiting maximum strain of 0.002 in the copper stabilizer and a desired high stress level to minimize structural volume. Recent work on alloy aluminum reinforced high-purity aluminum stabilizers at the University

of Wisconsin-Madison by H. Segal [20] leads to the possibility of cycling the high-purity aluminum stabilizer to a strain level of 0.0038 with little degradation in its resistivity ratio.

The advantages of using aluminum as the stabilizer and high-strength aluminum alloy as the structure, compared with copper and steel, include lower resistivity, lower weight and cost, easier fabrication, compatible thermal expansion and contraction, lower heat capacity (for cool-down) and lower activation by the small but finite flux of neutrons leaking from the shield. Some disadvantages include lower design stresses, somewhat larger size, and lower heat capacity (for thermal accidents). The potential benefits are clear and further investigations here are clearly suggested.

4. Blanket and Shield Design

A schematic illustration of the blanket and shield design in UWMAK-III is given in Fig. 4 and the philosophy behind this design was given in section 1. A detailed two-dimensional toroidal geometry neutronics and photonics analysis has been completed to determine the nuclear performance of the system [21]. The results are given in Table Ic. An important point to note is that the neutron wall loading is not uniform and this leads to poloidal variations in heating rates and radiation damage which have been included in the thermal hydraulics and materials studies. The wall loading variation as a function of poloidal angle is shown in Fig. 5a.

From a heat transfer viewpoint, the blanket and shield design in Fig. 4 has three distinct components: the hot inner shield, the partial ISSEC zone, and the outer breeding blanket. The heat deposited in the ISSEC zone will be transported to the front and back surfaces of the graphite and radiated away. The analysis indicates that the maximum temperature occurs inside the graphite and is less than 2000°C, assuming the thermal conductivity is degraded similar to nuclear grade material. The surface temperature facing the plasma is somewhat less than the maximum (~1800°C).

The outer blanket is designed to give the lowest value of $\vec{v} \times \vec{B}$ and minimizes MHD effects. Problems of thermal recirculation within a cell are solved by the use of a 10-cm-wide static lithium zone in the middle of the cell for thermal insulation. (The lithium velocity in this buffer zone is sufficient for tritium recovery.) The maximum coolant pressure on the first wall is only 70 psia and the pumping power required is just 2 MW. The maximum temperature of the TZM structure is 1000°C and the lithium exit temperature is 980°C.

The inner hot shield, or inner blanket, is cooled with helium. A 0.5-m-diameter feed tube is introduced between the TF magnets and connected to a manifold running in the toroidal direction. The surface heating load on the inner blanket is 35 W/cm^2 and, together with the space-dependent volumetric heating from the neutronics analysis, leads to a coolant inlet temperature of 488°C and an outlet temperature of 870°C at 1000 psia pressure. These coolant conditions match the temperature of the helium coming from the secondary heat exchanger of the outer blanket cycle such that identical turbines and thermal energy storage can be used. The distribution of coolant tubes within the inner blanket is arranged to be inversely proportional to the heating rate so that the heat load on each coolant is approximately the same.

The blanket cells are approximately 2 m x 2.2 m and the entire outer blanket (which is the part which must be removed because of radiation damage) is built up from these basic modules. The heaviest module which would have to be removed weighs just 42 MT and a sequence of steps have been devised for such a process. The outer shield is designed to swing open so that only blanket module removal would be required.

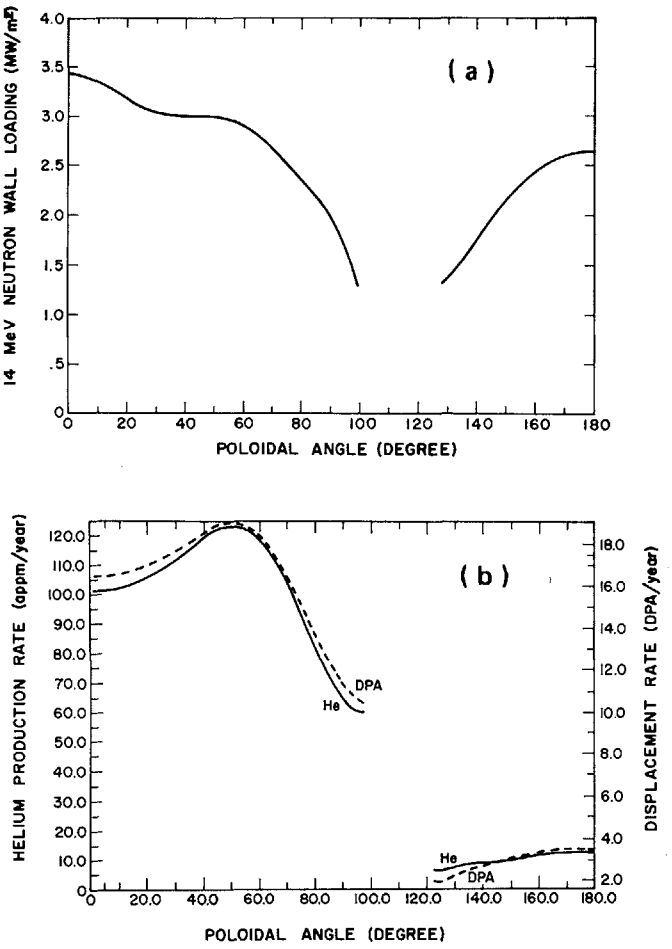


FIG.5. (a) Variation of the neutron wall loading with poloidal angle.
(b) Variation of the helium production rate and atom displacement rate in the first structural wall of TZM.

5. Tritium System Analysis

Extensive details on the tritium systems for both UWMAK-II and UWMAK-III have been given recently by Clemmer, Larsen and Wittenberg [22]. We therefore restrict the discussion here to the problem of removing tritium from the liquid lithium breeder.

Tritium is extracted by diverting about 5% of the liquid lithium in the outer blanket to a niobium window. Niobium is particularly well suited for this purpose because it has a high permeability to hydrogen at these temperatures and it allows us to reduce the tritium concentration in the lithium to a level compatible with subsequent tritium losses to the environment. Other

methods for the extraction of tritium from lithium, such as yttrium beds, molten salt extraction, liquid alloy getters and fractional distillation, were considered but were not found to be as attractive.

However, the niobium window is not without its own problems. The oxygen level in the niobium must be less than 100 ppm or the lithium will erode the surface, even going up grain boundaries to react with oxygen. Also, carbon transport from the TZM will occur, causing embrittlement of the niobium. In addition, at 980°C, niobium will be subject to attack by the oxygen getter in the helium stream and therefore some protective barrier is required. Palladium is the barrier of choice since it has a high hydrogen permeability. A palladium thickness of 0.001 cm deposited by electrodeposition will give a coherent layer of suitable durability. This will require a total of 170 kg of palladium for the calculated surface area of the window. However, the mutual solubility of Nb and Pd is high and it is expected that the palladium will diffuse into the niobium though no firm data exists for the rates of interdiffusion. Therefore, an intermediate yttrium layer is proposed which should minimize the rates of diffusion so that a practical "window" lifetime can be achieved. Yttrium was chosen because it, along with other IIIa elements and some of the rare earth metals, is among the few metals which do not form solid solutions with niobium. The required yttrium layer thickness is estimated to be 2500 Å. This will require a total of 2.0 kg of this element for the calculated surface area of the window. Experimental work is thus required to establish that Nb windows appropriately protected can be operated reliably.

Another important aspect of high-temperature operation in general is that large amounts of tritium could leak through pipes. For example, the high-temperature side of the lithium system is at 980°C and has a tritium pressure of 1.0×10^{-6} torr. The approximate pipe dimensions are $2 \times 10^{6} cm^2$ and 5 mm thickness. Assuming the downstream pressure is zero, the leak through such piping is 92 curies per day. However, to protect the TZM from oxidation, the pipe is double-walled using the outer pipe of stainless steel lined with ceramic insulating material. Since the temperature of the jacket is much lower and the permeability of the ceramic is very low, the release of tritium to the reactor is vanishingly small. However, such double-walled pipe is expensive and may be a factor in the ultimate usability of high-temperature materials.

The overall plant inventory of tritium is estimated to be 35.8 kg. It should be noted that of this only 1.7 kg is in the breeding-recovery cycle. The 34.1 kg in the refueling cycle includes 18.6 kg in reserve storage. The reason the refueling cycle inventory is so large is the small particle confinement time predicted by space-time analysis of plasma performance. The result is a fractional tritium burnup of only 0.8%. Assuming 5% burnup, the refueling cycle tritium inventory would only be 5.5 kg and the total plant inventory would be 7.2 kg.

6. Radiation Effects Analysis

The radiation damage environment in UWMAK-III is much more severe than in previous UWMAK reactors because of the smaller size. The maximum wall loading is ~3.5 MW/m^2 and the average value is ~2.5 MW/m^2 (Fig. 5a). When the back-scattered neutrons are considered, the displacement and helium production rates in the TZM first walls vary in the poloidal direction as shown in Fig. 5b. The maximum dpa rate is ~19 dpa/yr (100% plant factor (P.F.)) in the outer blanket and 3.5 dpa/yr behind the ISSEC shield. The associated helium production rates are 120 appm/yr and ~13 appm/yr at 100% P.F. Extrapolation of this data to present fission neutron and charged particle simulation studies is difficult because of the lack of data. Preliminary analysis reveals that the outer first wall lifetime is likely

to be greater than 6 years for 10% swelling in TZM and the inner TZM walls will not achieve this value in 30 years. There have been no studies with such large amounts of helium in TZM, but again, preliminary analysis reveals that helium levels in the 10-25 appm range actually increase the fatigue and creep life of Mo and TZM after irradiation [23,24]. To be conservative, we have limited the outer TZM wall lifetime to the time required to accumulate 200 appm helium. This criterion requires that some parts of the walls be replaced every 1.5 to 2 years. The electrical resistance increase in the walls of the RF waveguides has been found to be less than 3% per year. Since the lifetime of the modules is 1.5 to 3 years, this increase should represent no particular problem.

The radiation damage to the carbon curtain has been analysed with reference to current dimensional stability data on reactor grade graphites. The analysis reveals that the curtain will last at least 3 years at 1300°C. The situation with respect to the ISSEC is more uncertain. The large majority of data indicates that as the irradiation temperature increases from 1000 to 1400°C, the amount of residual damage decreases [25]. Hence, we expect longer lifetimes (from a swelling standpoint) at 2000°C than at 1400°C. An exact value cannot be given now, but sputtering and vaporization are likely to limit the lifetime to 5 years and hence we have used that value for the lifetime of the ISSEC.

Radiation damage to the superconducting magnets has been analysed and, aside from a few unique areas which are bombarded by neutrons leaking down divertor slots, there are no severe problems. Periodic annealing of the TF coil (~ every 10 years) to room temperature should allow the Al stabilizer to maintain low I^2R losses (less than 10% over normal) in the event of an accident. The degradation of the critical superconducting properties of the TiNb is less than 10% over the plant lifetime.

Finally, analysis of the B_4C, 316 stainless steel and Pb in the shield plus Mylar and organic insulation in the TF coils revealed no insuperable problems.

7. Plant Design and Building Size

The major features of the plant arrangement shown in Fig. 2 include the following: the containment building is centrally located relative to the outer building. It is a reinforced concrete structure lined with stainless steel and it has an inert environment to prevent lithium or sodium fire. The heat exchanger building, radwaste building, auxiliary building, hot cell and the maintenance building are arranged around the containment building. This arrangement makes the plant layout very compact, with maximum utilization of space around the containment, by locating the reactor support systems and facilities close to the nuclear island. This is also expected to offer some economic advantages for piping, cabling and structural considerations. The peninsular arrangement of the Turbine Building orients the axes of the turbine-generators such that any missiles generated by the machines will not strike the containment building.

It is important to note that reducing the size of the nuclear island has produced a concomitant reduction in overall plant size. A perspective on this matter can be obtained by comparing the plant layout for UWMAK-III with that developed for the Clinch River fission breeder reactor (CRBR) [8]. The UWMAK-III systems occupies (not fully) a space 195 m by 138 m. The comparable set of structures for CRBR fits in a space that is 234 m by 159 m. The primary containment building for UWMAK-III is 70 m in diameter by 70 m high whereas the comparable CRBR containment building has a 60-m diameter and is 80.5 high. Only the turbine building in UWMAK-III is significantly larger

and this is because the design electrical output is 1985 MW_e compared to 350 MW_e for CRBR. Thus, tokamak reactors designed with the major characteristics of UWMAK-III (size and shape) will be similar in size to advanced fission reactors, and not appreciably larger.

8. Economic Analysis

An economic analysis for UWMAK-III has been carried out to determine the major cost areas and to indicate where further research effort can yield the greatest cost benefit. It will only be possible to highlight key results here and the reader is referred to reference 11 for the in-depth analysis.

The estimate of direct field cost for UWMAK-III in 4th quarter 1975 dollars is $1154/kWe broken down as follows: land and land rights, $0.5/kWe; structures and site facilities, $285/kWe; reactor plant equipment, $408/kWe; turbine plant equipment, $285/kWe; electric plant equipment, $141/kWe; and miscellaneous plant equipment and special materials, $34/kWe. Direct costs are most easily described since all other costs are derived as percentages thereof. Following Bechtel cost procedures, indirect costs add an additional $986/kWe and owner costs and interest during construction add a final $730/kWe. Note that the percentages applied for indirect costs to UWMAK-III are much higher than in earlier studies [1,3,26].

An analysis of costs by category led to the unanticipated result that the costs of high-temperature refractory metal piping is critical while the costs of the toroidal field magnet system is relatively less important. The piping costs were high because it is necessary to protect refractory metals from the atmosphere to avoid oxide formation and hydrogen embrittlement. Importantly, this is a general characteristic of all refractory metals (i.e. Nb, V, Ta) and is not specific to the use of molybdenum-based alloys. The cost estimate developed for such pipe in the primary system is approximately $10,700/m. As such, about a quarter of the nuclear island costs and about a third of the closed cycle helium turbine plant equipment costs were for the piping. It will be of great interest to redesign UWMAK-III (a relatively small unit physically with R = 8m) using a lower technology structural material such as 316 stainless steel. Clearly, the absolute costs will be reduced significantly. It will be important to determine how much the associated reduction of net efficiency affects the net power costs.

An important auxiliary result is the breakdown by major category of the direct costs: 25% for buildings, 35% for the reactor plant equipment (nuclear island), 25% for the turbine plant, 12% for the electric plant equipment, and 3% for remaining miscellaneous items. Therefore, the nuclear island is 35% of the direct costs while the balance of plant is 65%. The toroidal field magnets were estimated to be 10% of the reactor plant equipment costs or just 3.5% of the total direct costs. This is much lower than anticipated and leads us to conclude that one can afford to pay more for higher magnetic field.

This result may have some very important implications. In particular, it can have an impact on the size of tokamak reactors. There are two reasons one would make a tokamak large. The first is to improve the confinement time of the plasma and the second is to keep the neutron wall loading to a prescribed but low value. A wall loading constraint at some level (high or low) is applicable to all magnetic approaches to fusion and is not specific to tokamaks. On the other hand, increasing the size to improve confinement time is more peculiar to closed line devices like tokamaks than it is to an open-ended system like a mirror machine. However, almost all theories, as well as experience, indicate that the confinement time improves with magnetic field. Therefore, within a given wall loading constraint, tokamaks can be made as

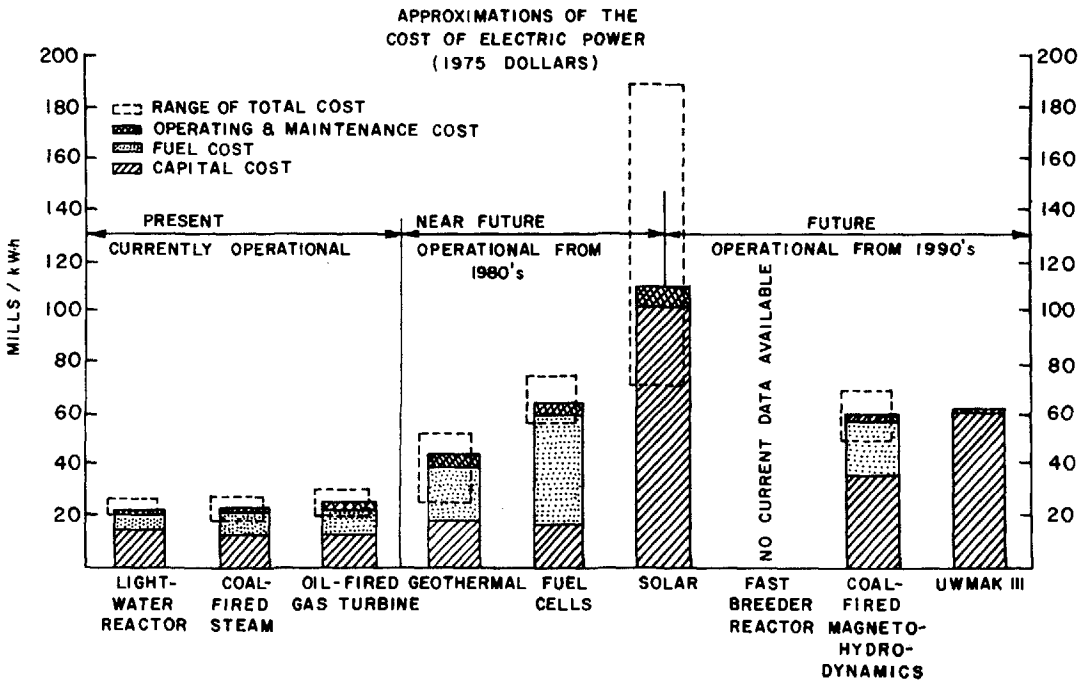


FIG. 6. A comparison of estimated costs for a UWMAK-III type reactor with other non-fuel-limited future energy sources. Costs for all other systems were developed by the Bechtel Corporation. The perspective is that while improvements are clearly required, the UWMAK-III costs are similar to those estimated for other advanced technologies, and not appreciably greater.

small as possible by increasing the magnetic field. The cost penalty on the coils will not be overwhelming whereas keeping the size small will lower the costs of buildings, piping, blanket systems and so on.

A perspective on UWMAK-III costs is provided in Fig. 6 where we plot the range of costs developed by the Bechtel Corp. for other advanced, non-fuel-limited, power-generating sources. Also shown are costs for present-day light water reactors (LWR's) and coal-fired steam plants. Escalation costs are not included and no costs are given for the liquid-metal fast breeder (LMFBR) reactor because no Bechtel developed costs were available. However, as a general gauge, we note that the cost estimate for the Superphenix 1200 MWe commercial prototype LMFBR is about twice LWR costs or 45-50 mills/kWh. The likely range for commercial LMFBRs is 30-50 mills/kWh.

The perspective provided by Fig. 6 is that the estimated cost of a system like UWMAK-III appears to be comparable with estimates developed by Bechtel for other advanced energy power systems that are not fuel limited. Only solar energy costs are well above all others.

Finally, we note that fusion reactor research is still at an early stage, that much inventiveness has already been shown, that there are many remaining directions for improving system design, (higher β [15], blanket designs for extended life at reduced size [27], new and positive information on radiation damage at lower temperatures in stainless steel [28], etc.) and that there is a critical need for new energy sources. Cost estimates at this stage are a guide and we are greatly encouraged to continue with such studies.

Acknowledgement: This research was supported by the Electric Power Research Institute, Palo Alto, California.

References

[1] BADGER, B., et al., "UWMAK-I, A Wisconsin Toroidal Fusion Reactor Design," Nucl. Eng. Dept. Report UWFDM-68, University of Wisconsin, Madison, Vol. 1 (1974), Vol. II (1975).

[2] KULCINSKI, G. L., and CONN, R. W., in Fusion Reactor Design Problems, IAEA, Vienna (1974) p. 51.

[3] BADGER, B., et al., "UWMAK-II, A Conceptual Tokamak Power Reactor Design," Nucl. Eng. Dept. Report UWFDM-112, University of Wisconsin (1975).

[4] Plasma Physics and Controlled Nuclear Fusion Research 1974 (Tokyo Conf., IAEA, Vienna, 1975). See paper by R. W. Conn et al., Vol. III, p.497.

[5] SCHARER, J., CONN, R. W., BLACKFIELD, D., "Study of RF and Neutral Beam Heating in Tokamak Reactors," Nucl. Eng. Dept. Report UWFDM-148, Univ. of Wisconsin (1976).

[6] ADAM, J., et al., in ref. 4, Vol. I, p. 65.

[7] CONN, R. W., KULCINSKI, G. L., AVCI, H., and EL-MAGHRABI, M., Nucl. Technol. 26 125 (1975).

[8] JACOBI, W. M., "Design of Clinch River Breeder Reactor and Selection of Basic Plant Parameters," in J. M. Kallfelz and R. A. Karam, eds, Advanced Reactors: Physics, Design and Economics, Pergamon Press, Oxford (1975.)

[9] BOOM, R. W., MOSES, R., and YOUNG, W., Nucl. Eng. and Design (1976), (in press).

[10] CONN, R. W., and KUO, S., Nucl. Eng. and Design (1976), (in press).

[11] BADGER, B., et al., "UWMAK-III, A Conceptual Noncircular Tokamak Power Reactor Design", Nucl. Eng. Dept. Report UWFDM-150, Univ. of Wisconsin (1976).

[12] OHKAWA, T., VOORHIES, H. G., Phys. Rev. Lett. 22 1275 (1969).

[13] CHANCE, M. S., et al., in ref. 4, Vol. I, p. 463.

[14] CONN, R. W., KESNER, J., Nucl. Fusion 15 775 (1975).

[15] CLARKE, J., "High Beta Flux Conserving Tokamak," ORNL-TM-5429 (1976).

[16] HOGAN, J., Meth. Comp. Phys. 16 (1975).

[17] KADOMTSEV, B.B., POGUTSE, O. P., in L. A. Leontovich, ed., Reviews of Plasma Physics, Consultants Bureau, N. Y. (1970), Vol. 5.

[18] KULCINSKI, G. L., CONN, R. W., LANG, G., Nucl. Fusion 15 327 (1975).

[19] BALOOCH, M., and OLANDER, D. R., J. Chem. Phys. 63 4772 (1975).

[20] SEGAL, H., RICHARDS, T. G., Adv. Cryogenic Engineering, Academic Press, (1975) Vol. 21.

[21] CONN, R. W., GOHAR, Y., MAYNARD, C. W., Trans. Amer. Nucl. Soc. 22 12 (1976).

[22] CLEMMER, R. G., LARSEN, E. M., WITTENBERG, L. W., Nucl. Eng. and Design (1976), (in press).

[23] MICHEL, D. J., SERPAN, C. Z., SMITH, H. H., and PIEPER, A. G., Nucl. Technol. 22 79 (1974).

[24] KINGSBURG, F. D., and MOTEFF, J., Trans. Amer. Nuc. Soc. 12 575 (1969). See also, MOTEFF, J., and KINGSBURG, F. D., Trans. Amer. Nuc. Soc. 10 428 (1967).

[25] GRAY, W. J., MORGAN, W. C., and TINGEY, G. L., Battelle Northwest Lab. Report, BNWL-2078 (June 1976.)

[26] MILLS, R. G., ed., "A Fusion Power Plant," Princeton Plasma Physics Lab. Report, MATT-1050 (1974).

[27] SZE, D. K., LARSEN, E. M., CHENG, E. T., CLEMMER, R. G., "A Gas Carried Li_2O Cooling-Breeding Fusion Reactor Blanket Concept," Nucl. Eng. Dept. Report, UWFDM-151, Univ. of Wisconsin (July 1975).

[28] BLOOM, E. E., WIFFEN, F. W., MAZIASZ, P. J., and STIEGLER, J. O., "Temperature and Fluence Limits for a Type 316 Stainless Steel First Wall," Nucl. Technol. (in press).

DISCUSSION

ON PAPERS IAEA-CN-35/I 1-1, I 1-2

J.P.F. CONRADS: How accurate may we assume the cost estimates for UWMAK-III and Culham Mark II to be?

R. HANCOX: The estimates were prepared by engineers with experience in fission reactor construction, and are therefore reliable from the technical point of view. The uncertainties are in the physics assumptions, which still have to be proved, and those technological areas where our understanding is still very limited, such as refuelling. At this stage of development the cost evaluations can only be estimates, and probably represent lower limits.

C.M. BRAAMS: What coolant are you considering for the Culham Mark II design?

R. HANCOX: In the light of our studies on the Mark I conceptual design, we assumed a liquid lithium blanket with a refractory metal structure, helium-cooled. Alternative breeding materials could be considered and might in fact be advantageous from the maintenance point of view provided adequate breeding is possible.

C.M. BRAAMS: Perhaps I could address a question direct to Mr. Conn, too. From the point of view of reactor safety and public acceptance of fusion reactors, one would prefer to have lithium in the form of a non-volatile chemical. What penalty would you have to pay for choosing a coolant other than liquid lithium?

R.W. CONN: I agree that we should try to use lithium in less chemically active forms, and we are going in that direction in our studies. The choice in UWMAK-III was dictated by the aim of having breeding only in the outer portion of the blanket. The inner portion of the torus is the most difficult to get at and we designed this to be without breeding and to last the lifetime of the plant. But to breed only in the outer blanket requires the use of a form of lithium where parasitic absorption will be low, and a liquid lithium blanket satisfies this requirement. We are, however, now looking at the use of Li_2O as the breding material in a gravity flow system such as those used in the chemical industry. The operating temperatures are low (~450°C) and no intermediate loop is required. This work is in progress.

A.F. KNOBLOCH: One of the most obvious differences between the two concepts described here lies in the design and shape of the poloidal coil system. The Culham Mark II has no internal windings, and in particular no divertor coils. What would be the effect of such internal windings on the servicing scheme proposed for Mark II?

R. HANCOX: A divertor has so far not been included in the Culham Mark II design because it is still uncertain how effective or necessary it will be. Should it prove to be required, we would first consider a bundle divertor similar to the one which we proposed in the European Collaborative Tokamak Reactor Design, since this introduces the minimum additional complications. If a poloidal divertor with windings inside the toroidal field coils should be essential, it would seriously affect our maintenance concept.

A. GIBSON: I wish to return to the question of costs raised a few minutes ago by Dr. Conrads. I notice that the costs quoted for the UWMAK-III are considerably higher than for Culham Mark II (~60% overall and about a factor 2 for the nuclear island). Does this cost difference come directly from the higher wall loading assumed for the Culham design or is it within the cost uncertainty between the two designs?

R. HANCOX: Cost comparisons between reactor designs are complicated by several factors, including different definitions and ground rules. Cost estimates for fusion reactor designs published so far show a wide variation. For this reason I believe it is more helpful to make comparisons, as quoted for the Culham Mark I design, between a possible fusion reactor and a developed fission reactor where the same definitions and rules are applied.

R.W. CONN: One final comment on the meaning of the cost estimates. The economic analysis carried out for UWMAK-III was aimed at finding out where the large cost items lie, not necessarily at assessing accurate absolute costs. For example, we found the cost of the magnet system not to be the large fractional cost most people assume it to be. Thus, higher magnetic fields may not entail as large a cost penalty as heretofore believed. On the other hand, the high-temperature refractory metal structure and piping appear quite expensive and not apparently worth the increased plant efficiency. The only relevant point I make regarding total costs (including an "ignorance" contingency) is that they are within a factor of 2 or 3 of the costs of the much better known systems operating at present.

MIRROR REACTOR STUDIES*

R.W. MOIR, W.L. BARR, D.J. BENDER,
R.J. BURLEIGH, G.A. CARLSON, R.S. DEVOTO,
J.N. DOGGETT, J.H. FINK†, G.W. HAMILTON,
J.D. LEE, M.E. RENSINK, C.E. TAYLOR,
R.W. WERNER
Lawrence Livermore Laboratory,
University of California
Livermore, California

K.R. SCHULTZ
General Atomic Company,
San Diego, California,
United States of America

Abstract

MIRROR REACTOR STUDIES.

Design studies of a fusion mirror reactor, a fusion-fission mirror reactor, and two small mirror reactors are summarized. The fusion reactor uses 150-keV neutral-beam injectors based on the acceleration of negative ions. The injectors provide over 1 GW of continuous power at an efficiency greater than 80%. The fusion reactor has three-stage, modularized, Venetian blind, plasma direct converter with a predicted efficiency of 59% and a new concept for removal of the lune-shaped blanket: a crane is brought between the two halves of the Yin-Yang magnet, which are separated by a float. The design has desirable features such as steady-state operation, minimal impurity problems, and low first-wall thermal stress. The major disadvantage is low Q resulting in high re-circulating power and hence high cost of electrical power. However, the direct capital cost per unit of gross electrical power is reasonable [$1000/kW(e)]. By contrast, the fusion-fission reactor design is not penalized by re-circulating power and uses relatively near-term fusion technology being developed for the fusion power program. New results are presented on the Th-^{233}U and the U-^{239}Pu fuel cycles. The purpose of this hybrid is fuel production, with projected costs at $55/g of Pu or $127/g of ^{233}U. Blanket and cooling system designs, including an emergency cooling system, by General Atomic Company, lead us to the opinion that the reactor can meet expected safety standards for licensing. The smallest mirror reactor having only a shield between the plasma and the coil is the 4.2-m long fusion engineering research facility (FERF) designed for material irradiation. The smallest mirror reactor having both a blanket and shield is the 7.5-m long experimental power reactor (EPR), which has both a fusion and a fusion-fission version.

FUSION MIRROR REACTOR DESIGN

The conceptual design of a mirror reactor is shown in Fig. 1; its parameters are given in Table I. The design is based on a steady-state, mirror-confined D-T plasma sustained by continuous injection of D^0 and T^0. The magnet is of the Yin-Yang type, oriented vertically to allow for lowering the bottom half of the magnet by means of a float. Once lowered, the blanket segments can be removed by a crane. The blanket is a spherical shell, segmented in shapes called lunes (see Fig. 2). Negative-ion injectors sustain the plasma. "Venetian blind" direct converters provide direct energy conversion of plasma end losses. The reactor is enclosed in

* This work was performed under the auspices of the US Energy Research and Development Administration, under Contract No. W-7405-Eng-48.

† On loan from Westinghouse Electric Corporation.

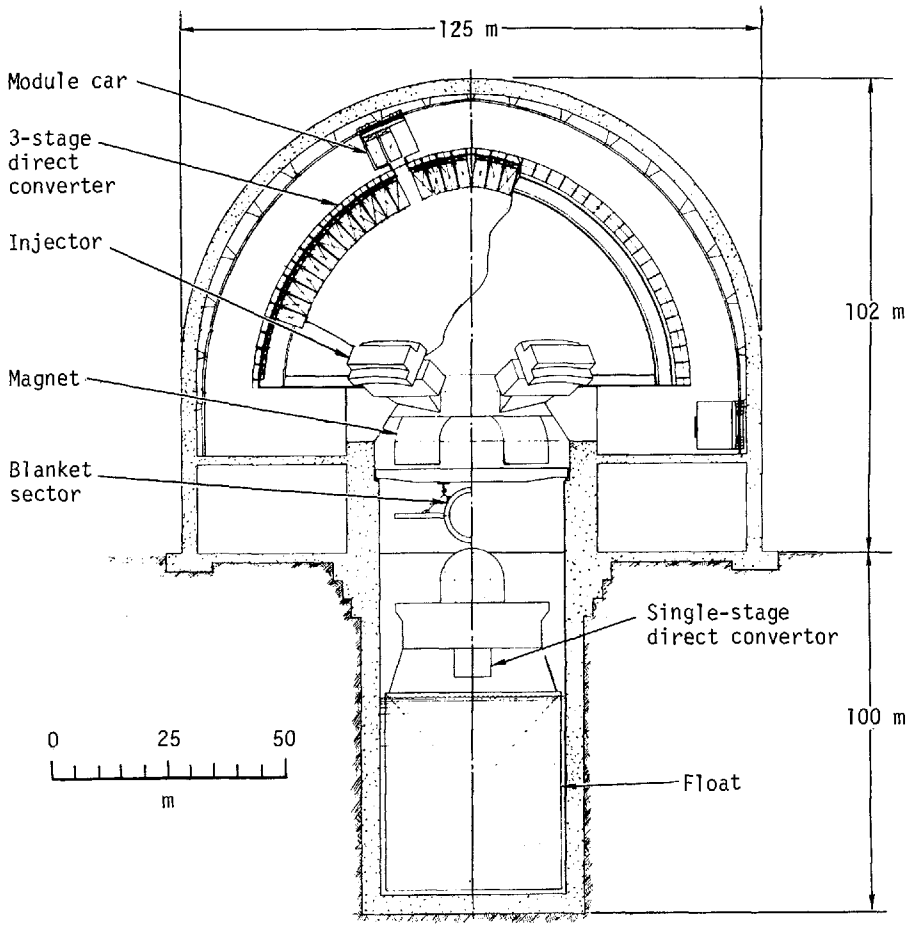


FIG. 1. Mirror fusion reactor.

a reinforced-concrete, dome-shaped building, which is sealed to prevent escape of radionuclides (principally tritium) in case of accidental or routine releases inside the building. Not shown in Fig. 2 is the thermal conversion system consisting of a potassium primary cooling system coupled to a potassium-topped steam cycle.

Blanket and blanket replacement

The blanket and its coolant plena constitute a spherical shell inside the coal that is set with appendages near the midplane for coolant to enter and exit. The shell is divided into an arbitrary number of segments for convenience in handling. With the blanket divided as one slices a melon, the segments may be removed by a simple vertical movement (see Fig. 2).

TABLE I. PARAMETERS FOR MIRROR REACTOR DESIGNS

Parameter	2XIIB	MX	FERF	EPR/fusion-fission	Fusion reactor	Fusion-fission reactor (U-Pu)
L_{plasma}, m	1.6	3.4	4.2	7.5	16.0	15.0
r_{plasma}, m	0.05	0.3	0.25	1.2	3.0	2.4
$B_{0\ vac}$, T	0.6	2.0	3.75	2.3	4.0	2.5
$B_{conductor}$	—	7.0	9.0	8.0	15.0	8.0
R_{vac}	2.0	2.0	2.0	2.5	3.0	2.5
$W_{injection}$, (keV)	20	80	65	100	150	100
$\bar{W}_{ion}$, keV	13	50	83	100	190	100
n_0, cm^{-3}	$\sim 10^{14}$ cm	1×10^{14}	3×10^{14}	1.1×10^{14}	1.6×10^{14}	1.3×10^{14}
β	0.4-1.5	0.5	0.65	0.75	0.75	0.76
$n\tau$, $s\cdot cm^{-3}$	7×10^{10}	$\gtrsim 10^{12}$	2×10^{12}	2.2×10^{13}	5.0×10^{13}	1.8×10^{13}
$Q_{classical}$	—	—	$\sim$0.1	0.7	1.1	0.7
$(\omega_{pe}/\omega_{ce})$	20.0	5.0	6.0	8.3	4.0	8.7
L/a_i	35.0	100.0	110.0	130.0	370.0	280.0
r/a_i	3.0	9.0	8.0	21.0	70.0	45.0
P_{fusion}, MW	—	0.3	3.4	44.0	1270.0	470.0
$P_{electric}$, MW(e)	—	—	—	62.0	450.0	1040.0
Cost, $M	$\sim$10.0	$\sim$100.0	300.0	540.0	2090.0	2300.0
Cost/$P_{electric}$, $/kW(e)	—	—	—	8700.0	4600.	2180.0
Fuel production, kg/yr	—	—	3	190.0	—	2400.0
Fuel cost, $/g	—	—	—	$\sim$200	—	55.0

The neutron and gamma fluxes are attenuated by the blanket and its shield to substantially eliminate radiation damage in materials located behind the shield and to allow contact maintenance outside the reactor. The piping and wiring connections along with the main vacuum seal are outside the irradiated area. During blanket replacement or repair, all joints can be broken and remade in a contact mode, minimizing the need for remote manipulators.

Neutral-beam injector

We have evaluated several different types of very large injectors, ultimately concentrating on the most economical design, one which employs negative ions as a source of neutrals. Figure 3 shows two of the alternatives under investigation. Figure 3(a) shows a positive-ion system [1] in which the fast atoms are produced by charge exchange in a neutralizing duct and the energy of the un-neutralized beam is recovered by an in-line direct converter. Figure 3(b) shows a negative-ion system in which low-energy D^- ions are produced by double charge exchange in a cesium-vapor jet, accelerated to 150 keV, and then converted to fast atoms by photodetachment of the weakly bound electrons.

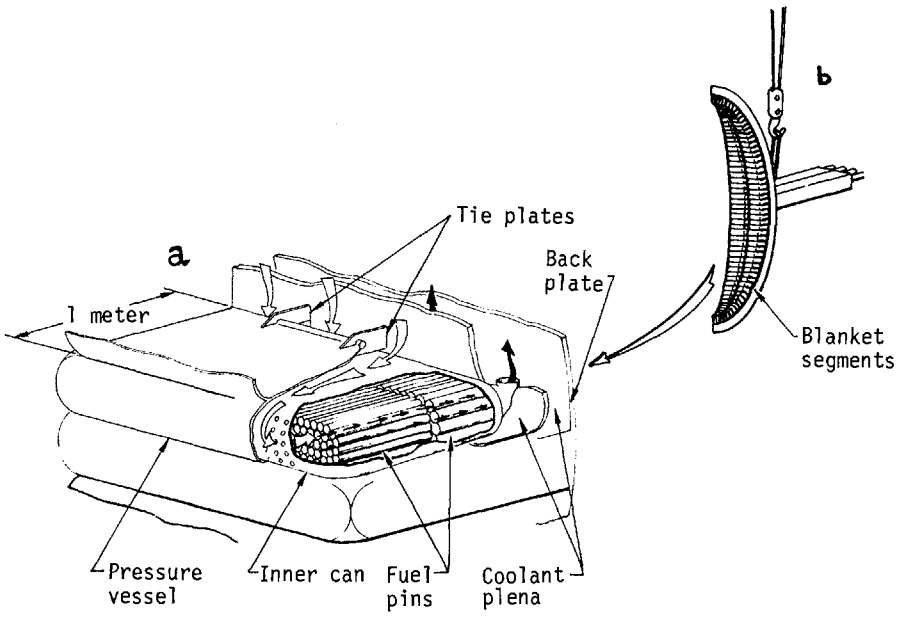


FIG.2. Blanket design, showing (a) segment of a spherical shell called a lune and (b) detail of blanket submodule.

Plasma direct energy converter

The system uses two end-loss direct converters; a simple, one-stage unit receives 20% of the power at one end, and a three-stage, Venetian blind unit (Fig. 4) receives the other 80%. The magnetic mirror at one end is slightly stronger than the other to achieve the 80%-20% split of ion losses due to a process of selective leakage. Together, these direct converters handle 1390 MW with an efficiency of 57% to produce 790 MW of electrical power. Nearly all of the 600 MW that is not directly recovered is converted to high-grade heat (helium at 1000 K) and is processed in a thermal bottoming cycle. Thus, the net efficiency of recovering end losses including thermal recovery is 74%.

The single-stage unit consists of a helium-cooled grounded grid, a water-cooled negative grid, and a helium-cooled positive collector. The efficiency of the unit is high, 52%, because of the +87-kV ambipolar potential in the plasma that allows the collector to be held at 92 kV without any of the ions being turned back.

At the other end, there is a much larger three-stage unit consisting of a helium-cooled grounded grid, a radiatively cooled negative grid, two radiatively cooled collector stages, and a final helium-cooled collector stage. The efficiency of the three-stage unit is 59%, much less than the

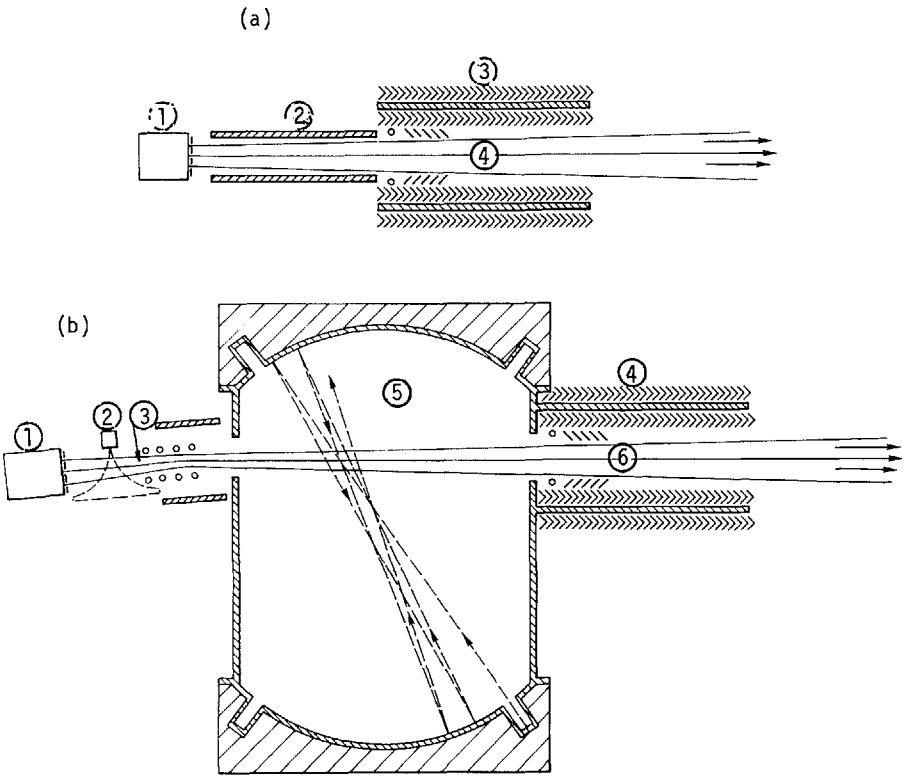


FIG.3. Neutral-beam injector with beam direct conversion, showing (a) the positive-ion system and (b) the negative-ion system. In (a), the details called out are (1) 150-keV D^+ ion source, (2) neutralizing duct, (3) cryogenic gas pumping, and (4) energy-recovery system. In (b), the details called out are (1) low-energy D^+ ion source, (2) Cs jet for double electron capture, (3) 150-keV D^- accelerator, (4) cryogenic gas pumping, (5) photo-detachment optical cavity, and (6) energy recovery system.

79% which is theoretically possible with three collectors and this ion energy distribution. The difference results from the massive grounded grid which not only collects all primary electrons (87 MW) but also intercepts 51 MW of ions. Another large loss is due to the interception of ions on the first two collector stages. This loss is the consequence of the angular spread in the ion trajectories, which is due to the magnetic field at the collector (0.03 T).

Parametric analysis

We characterize the mirror reactor by means of a parametric analysis that couples simplified models of the reactor components in a consistent manner. The analysis, including a cost estimate, optimizes the reactor design; i.e., it minimizes the direct capital cost per unit of net electrical power [$/kW(e)].

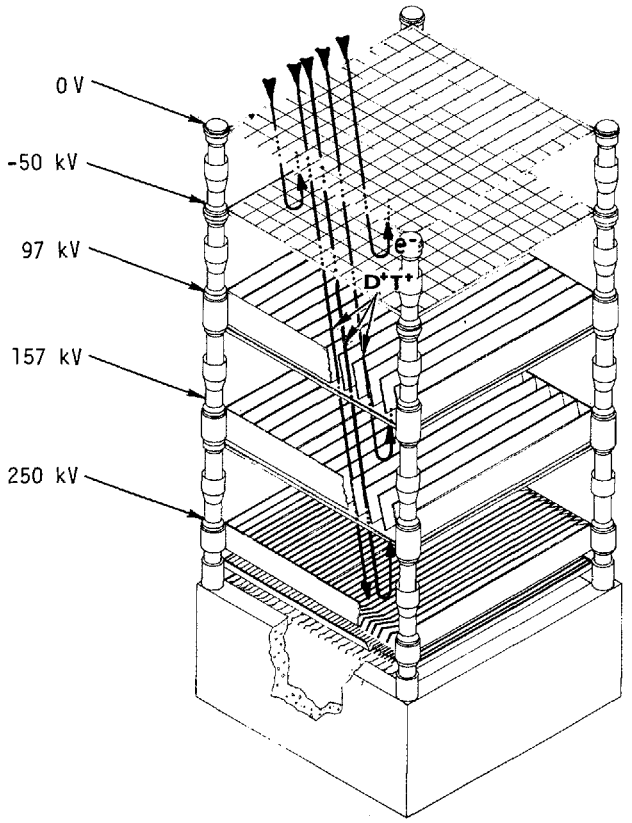


FIG. 4. Modules of the three-stage Venetian blind direct energy converter.

The most critical physics parameter in the design is the plasma Q (fusion power output divided by injected beam power). The value of Q is obtained from a sophisticated Fokker-Plank model [2] for classical mirror-confined plasmas that includes the effects of ambipolar potential, alpha-particle heating, and enhanced mirror ratio due to plasma diamagnetism. An enhancement factor for Q is also introduced to explore the consequences of future improvements in the physics of mirror-confined plasmas. By "enhanced Q" we mean the classical Q predicted by Fokker-Planck calculations multiplied by some constant factor. Thus, enhanced Q retains all of the functional dependences of classical Q.

The maximum β of the plasma (perpendicular kinetic pressure divided by vacuum field magnetic pressure) at the midplane is limited by the magnetohydrodynamic (MHD) "mirror-mode" stability condition [3]; and the long-thin approximation, $R = R_{vac}(1-\beta)^{-1/2}$, is used to relate the net mirror ratio to the vacuum field mirror ratio.

The effects of parametric variations are summarized in Fig. 5. Figure 5(a) shows that the \$/kW(e) cost is sensitive to mirror ratio. An increase in R_{vac} from the optimum results in better confinement (higher Q),

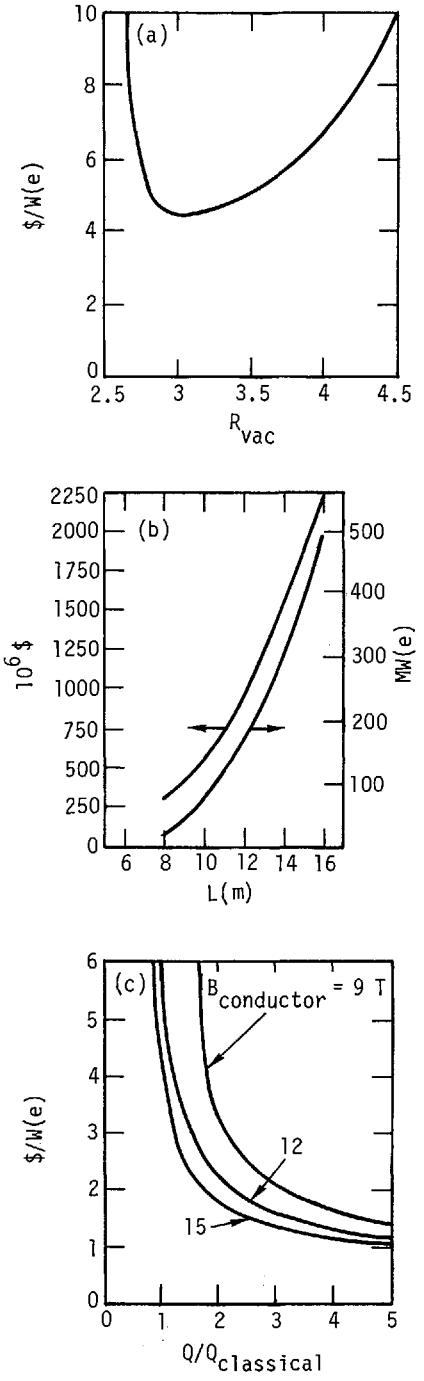


FIG.5. Parametric variations for the mirror fusion reactor, showing (a) relationship between vacuum mirror ratio, R_{vac}, and minimum direct capital (cost) per unit net electric power, $/W(e); (b) dependence of direct capital cost and net electrical power, MW(e), on reactor length, L; and (c) minimum direct capital cost per unit of electrical power, $/W(e), versus Q enhancement factor.

but this positive effect is more than offset by a reduction in central field strength and hence in fusion power. The effects are reversed for a decrease in R_{vac}. Figure 5(b) shows the effect of decreasing the reactor length L below the reference value of 16 m. The direct capital cost and the reactor net power are shown. Lengths less than about 8 m are impossible because the space between the coil and plasma is inadequate for the blanket and shield. Before a minimum size is reached, the cost of electricity rises steeply because the net power decreases more rapidly than the capital cost. Nevertheless, these small reactors may be attractive as experimental power reactors. Figure 5(c) shows the cost of electricity for optimized reactors (optimum mirror ratio, injection energy, and injection angle) as a function of the Q enhancement factor.

We see that the $/kW(e) decreases with both increasing magnetic field strength and Q enhancement. For Q/Q_{cl} greater than about 2.5, the cost reduction with increasing Q enhancement is slow. Also, for high Q enhancement, the relative advantage of high field strength is less than for a lower Q.

Conclusions

Because of its high power density and because plasma losses do not increase with decreasing size, the mirror reactor can be made small and at low cost relative to some other fusion concepts [Fig. 5(b)]. The operating mode is continuous rather than pulsed. Impurity control is automatic. However, the rapid particle loss out the ends makes a mirror reactor with classical end losses have a low Q value; about 75% of the gross electrical power is recirculated back to the injector. The Q value must be raised by a factor of 2 to 3 to reduce the recirculating power fraction to a reasonable value. Further increase in the Q value or major simplifications may be required for economic competitiveness with other energy options. These further increases would allow relaxation of the demands placed on various component technologies.

FUSION-FISSION REACTOR DESIGN

The goal of our fusion-fission (hybrid) design is the production of fissile fuel at minimum cost in blankets containing uranium or thorium. The hybrid reactor [4] looks much the same as the fusion reactor (Fig. 1). The energy gain in the fissioning blanket overcomes the low-Q problems of the fusion reactor, but more important than the fission energy release are the extra neutrons produced by the fissions induced in the highly subcritical uranium or thorium assembly by 14-MeV neutrons. These extra neutrons are used to breed fissile fuel. To be economical fuel producers, hybrids must produce fissile fuel at lower than (1) the cost of mining uranium and isotope separating ^{235}U, (2) the cost of fissile fuel bred by accelerator-produced neutrons, or (3) the cost of the fuel produced in breeder reactors. As power producers, hybrid reactors can have a higher capital cost [$/kW(e)] than fission reactors, but only by a small percent that is proportional to fuel cycle costs. The economic conditions imposed on hybrids to be power producers seems more difficult to achieve than those required for them to be fuel producers.

Fuel Cycle ^{239}Pu and ^{233}U

Using a mirror hybrid system model, we determined the characteristics of optimized hybrid reactors containing either ^{238}U or ^{232}Th in the blanket. Both reactor designs have a thermal rating of about 4000 MW and would produce 2.5 tonnes of fissile fuel per year. The signifcant difference between the two reactors is that the U blanket has an energy multiplication

TABLE II. TIME-DEPENDENT BLANKET PARAMETERS[a]

Fuel type	T	M	Net fissile
Exposure			
U-Mo			
0 MWyr/m^2	1.1	10	1.8
5 MWyr/m^2	1.7	20	1.6
Th			
0 MWyr/m^2	1.1	2.5	0.73
10 MWyr/m^2	1.2	5.0	0.65

[a] T = tritium breeding ratio (atoms/fusion neutron)

M = energy multiplication (blanket energy per fusion neutron divided by 1.4 MeV)

Net fissile = fissile production minus fissile consumption (atoms/fusion neutron)

Exposure = Integrated fusion neutron energy current through the first wall (MWyr/m^2)

about four times greater than the Th blanket. The U hybrid produces 1000 MW of net electrical power, while the Th hybrid just breaks even (i.e., has recirculating power fraction of one). The cost of producing ^{233}U was found to be about twice the cost of producing ^{239}Pu. However, this cost differential may be acceptable because ^{233}U is a better fission reactor fuel than ^{239}Pu.

Blanket design

The blanket consists of 16 replaceable segments that form a spherical shell. This shell occupies the region between the plasma and the coils and has ports for beam injection and plasma leakage. A spherical shell is used so that the fusion neutron current is nearly constant over the surface area of the blanket.

Each segment consists of a collection of submodules assembled into a monolithic structure (see Fig. 2). Each submodule consists of a common-wall pressure vessel containing fuel assemblies. The inner zone of each assembly (~25 cm thick), is fueled with rods containing natural U or Th, unmoderated so as to maximize fission of of ^{238}U or ^{232}Th and to minimize fission of ^{235}U, ^{239}Pu, or ^{233}U. Over 80% of the fission occurring in natural uranium is ^{238}U fission. The outer fuel zone contains Li in the form of $LiAlO_2$ plus graphite for tritium breeding.

For heat removal, the submodules are supplied (in parallel) with high-pressure He coolant from plena that form the back of each blanket module. Inlet He is first used to maintain the pressure vessel temperature below 400°C; it then flows through the fuel and Li zones and finally exits at 530°C. Peak power density in the fuel is ~200W•cm^{-3}.

Representative nuclear performance parameters for this blanket when fueled with either U plus 7 wt.% Mo alloy or Th metal are listed in Table II.

Primary heat-transfer loop and thermal conversion system

The design of the plant is based on technology developed for gas-cooled fission reactors [5]. The He pressure and temperature parameters were set at values typical for fission reactors: 60-atm He pressure, with blanket inlet and outlet temperatures of 280°C and 530°C, respectively. These values permit the use of existing designs of He circulators and steam generators and result in acceptable He ducting dimensions. In general, existing gas-cooled fission reactor technology is directly applicable to the hybrid, although various parameters must be optimized.

We have also considered the safety and licensing of the plant. The hybrid appears to have an advantage over fission reactors in this area because it is possible to eliminate the potential for a criticality accident. This should ameliorate the licensing procedure. However, due to the fuel afterheat power density of up to 10 $W \cdot cm^{-3}$, a total loss of forced cooling in the blanket would probably result in fuel melting, an unacceptable situation from the licensing standpoint. Thus, the major safety consideration is to develop a design in which forced cooling to the blanket can always be assured to a high degree of confidence. To help provide this confidence, the present design includes redundant He circulators and redundant auxiliary circulators of diverse types. Given the verification of this aspect of the plant, it is expected that the hybrid could be licensed.

Conclusions

The design studies show that the mirror concept with classical plasma confinement can produce fissile fuel for burner fission reactors [light-water reactor (LWR), high-temperature gas reactor (HTGR), heavy-water reactor (HWR)] at a competitive cost, (\$55/g Pu; \$127/g ^{233}U). The technology required for the hybrid is less demanding than for a pure-fusion reactor. The safety systems for the fission blanket are comparable to those required for fission reactors. The lack of criticality may off-set safety problems introduced by the more complex geometry. Further design studies are needed to improve the technical feasibility and cost projections.

SMALL MIRROR REACTORS

We studied two classes of small mirror reactors. One, called FERF, is the smallest machine that can accommodate a shield between the plasma and the superconductor. Its purpose is to irradiate many small samples in 14-MeV neutron fluxes of about 10^{14} $n \cdot cm^{-2} \cdot s^{-1}$. The second small mirror reactor, EPR, is the smallest machine that can accommodate both an energy recovery and tritium breeding blanket and a shield between the plasma and the superconductor. There are two versions of EPR: one is a fusion reactor in which breakeven is not achieved; the other is a fusion-fission reactor that produces net power and fissile fuel (see Table I for parameters of these machines).

Fusion energy research facility (FERF)

The purpose of FERF is to provide adequate space and 14-MeV neutron fluence to perform the extensive materials and system testing required prior to the final design of a power reactor.

A secondary but essential purpose for building and operating FERF is to gain experience in the problems associated with the practical integration of the complex subsystems of a fusion reactor into a reliable machine. The purpose of this study was to optimize FERF for the testing of materials and systems.

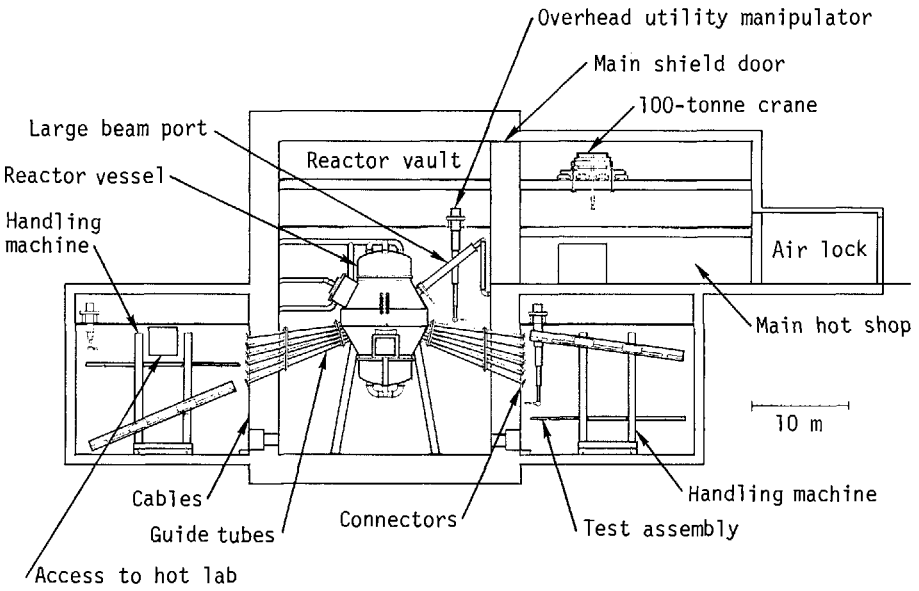


FIG.6. Vertical cross-section through fusion engineering research facility (FERF).

The study is based on a mirror reactor for FERF. The basic geometry and neutron yields are those reported in Ref. [6]. The magnet orientation and supporting structure have been modified to improve access and maintainability (see Fig. 6).

The features that make the mirror machine attractive for FERF are:

- Small size — a mirror machine is smaller and potentially less costly to build and operate than other confinement schemes.
- Reactor level first-wall neutron flux = 1.4×10^{14} $cm^{-2} \cdot s^{-1}$.
- Maintainability — the first wall is easily replaceable.
- d.c. operation — the mirror reactor will operate at steady state for relatively long periods (weeks), providing high availability for irradiations.
- Accessibility — the unique geometry of the Yin-Yang magnet set provides excellent access to the high-flux region of the reactor.

Figure 7 shows the location of the sample tubes and system test facility in relation to the first wall. The tubes have a 60-mm inside diameter and their useful experimental length is 0.5 m. There are 12 tubes per coil lobe for a total of 48. The principal system test facility proposed is a large-diameter port identical to the beam ports, giving access to the central region of the reacting plasma.

A comparison of FERF capabilities to estimated needs for testing fusion reactor materials shows that FERF can provide virtually all the requested space and flux (except for very large blanket sections). However, accelerated testing at a continuous neutron flux $10^{15} cm^{-2} \cdot s^{-1}$ is beyond the practical capability of this or probably any other reactor source.

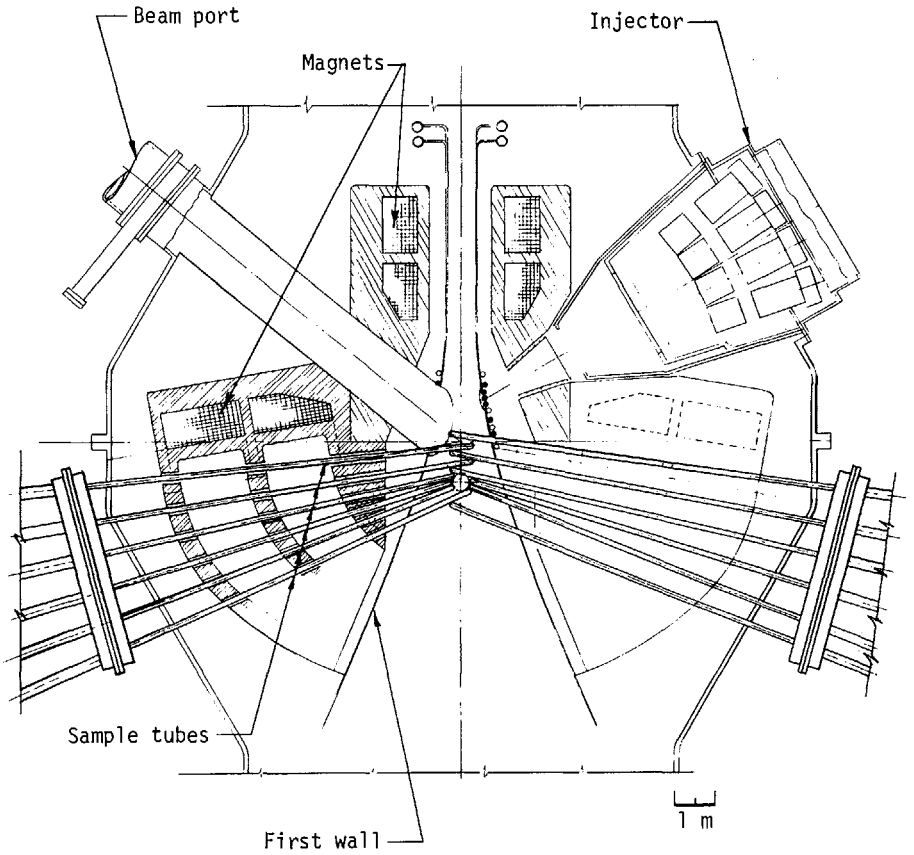


FIG. 7. Vertical cross-section through FERF mirror reactor.

Experimental power reactor (EPR) fusion and fusion-fission reactor

A major step in the development of engineering technology for mirror reactors, after resolution of the plasma physics in MX, will be the design and construction of a test-bed reactor that is capable of incorporating full-scale mirror reactor components. We envision this facility to be the minimum size that permits the inclusion of a blanket and shield inside the coil windings. We use the mirror reactor system as a model to determine representative parameters for this machine.

It was found that a Yin-Yang coil set of 7.5-m mirror-to-mirror length can accommodate a 1-m-thick blanket plus a coolant plenum and shield with a blanket coverage of about 74%. Below the 7.5 m, the wall area available for blanket modules rapidly goes to zero. The EPR utilizes a reactor-grade plasma (100-keV energy) contained in a magnetic field that has a maximum of 8 T at the conductor and a vacuum mirror ratio of 2.5. This results in a first-wall loading of 0.9 MW/m^2.

Because of the low blanket coverage, coupled with the low Q of the mirror plasma, the machine must rely on significant energy multiplication in the blanket for a positive power balance. By configuring the EPR as a hybrid with ^{238}U, we can obtain 300 MW of thermal power in the blanket from 35 MW of fusion neutrons. By employing a plasma direct converter and a steam-cycle thermal conversion system, the resulting plant has a recirculating power fraction of 0.6 and produces 62 MW of net electrical output. In addition, the ^{238}U blanket breeds 200 kg of ^{239}Pu per year. Further parameters for the EPR hybrid appear in Table I.

Conclusion

Small mirror reactors having room for a shield only can be used for material testing (FERF). Somewhat larger mirror reactors having room for a blanket can be used for blanket testing (EPR). A fusion-fission EPR would produce considerable amounts of fissile fuel as well as net power.

REFERENCES

[1] FINK, J.H., BARR, W.L., HAMILTON, G.W., Nucl. Fusion 15 (1975).
[2] KILEEN, J., MIRIN, A.A., RENSINK, M.E., "The solution of the kinetic equations for a multi-species plasma," Methods in Computational Physics, Vol. 16; Control Fusion (KILEEN, J., Ed.), Academic Press, New York (1976).
[3] RENSINK, M.E., et al., 5th Int. Conf. Plasma Physics and Controlled Nuclear Fusion Research (Proc. Conf. Tokyo. 1974) 1, IAEA (1975) 311.
[4] MOIR, R.W., et al., LLL Rep. UCRL-51797 (1975).
[5] SCHULTZ, K.R., et al., General Atomic Company Rep. GA-A14021 (1976).
[6] BATZER, T.H., et al., LLL Rep. UCRL-517617, (1974).

DISCUSSION

ON PAPER IAEA-CN-35/I 2

R.W. CONN: I noticed that the direct costs for the pure mirror fusion reactor were about $4600/kW(e), whereas in UWMAK-III, for example, the direct costs were about $1100/kW(e). We have heard, from Dimov and co-workers and from Fowler and Logan, a discussion of a triple mirror concept which shows substantial enhancement of Q over the classical value of about 1. How much improvement would you anticipate with such systems at higher Q?

R.W. MOIR: Our studies on the mirror reactor with enhanced Q showed direct capital costs of about $1500/kW(e) (Q enhanced by a factor of 2.5) and $1000/kW(e) (Q enhanced by a factor of 5).

A study is under way on the "triple mirror" concept. I do not know what the cost will be, but it will apparently not depend on Q, because Q is high (>3) in any case, and costs related to recirculation will be relatively low if Q is high. Both Dimov and his colleagues at Novosibirsk and Logan and Fowler at Livermore predict a Q greater than 5. The reversed-field mirror reactor, if it is sufficiently stable, will also have a high Q.

PRELIMINARY DESIGN OF A TOKAMAK EXPERIMENTAL FUSION REACTOR

K. SAKO, T. TONE, Y. SEKI, H. IIDA, S. MATSUDA,
H. YAMATO*, N. ASAMI**, F. ETO***, T. IDE†,
T. SUZUKI††, K. MAKI†††, K. IOKI**
Japan Atomic Energy Research Institute,
Tokai, Ibaraki, Japan

Abstract

PRELIMINARY DESIGN OF A TOKAMAK EXPERIMENTAL FUSION REACTOR.

The preliminary design of an tokamak experimental fusion reactor is carried out. This design covers plasma characteristics, reactor structure, blanket neutronics, shielding, supperconducting magnets, neutral-beam injector, electric power supply system, fuel re-circulating system, reactor cooling system, and tritium recovery system. The main design parameters are: reactor fusion power 100 MW, torus radius 6.75 m, plasma radius 1.5 m, first-wall radius 1.75 m, toroidal magnetic field on aixs 6 T, blanket fertile material Li_2O, coolant He, structural material 316 SS, and tritium breeding ratio 0.9.

1. INTRODUCTION

A preliminary design of a tokamak experimental fusion reactor to be built in the near future is under way (1). The goals of the reactor are to achieve reactor-level plasma conditions for a sufficiently long operation period and to obtain design, construction and operational experience for the main components of full-scale power reactors.

The following design bases are provided. The fusion power is to be at the reasonable level of 100MW. A long operation period and a high load factor are to be achieved. The size of the reactor should be as compact as possible from an economical point of view. Niobium tin (Nb_3Sn) superconductor is to be available for toroidal field magnets. The cross-section of the plasma is circular, and gas blanket and mechanical limiters are employed. In order to make the best use of the toroidal magnetic field, the thickness of the blanket and shield on the inside of the torus is minimized at the cost of reduced tritium breeding ratio. The blanket is loaded with lithium oxide(Li_2O) and cooled by helium gas so as to simplify the reactor structure and maintenance scheme and also to attain low tritium inventory. Stainless steel(AISI-316) is used as the main structural material.

---

* On leave from Tokyo Shibaura Electric Co. Ltd., Kawasaki, Japan.
** On leave from Mitsubishi Atomic Power Industries Inc., Omiya, Japan.
*** On leave from Fuji Electric Co. Ltd., Kawasaki, Japan.
† On leave from Sumitomo Heavy Industries, Ltd., Tokyo, Japan.
†† On leave from Kawasaki Heavy Industries, Ltd., Tokyo, Japan.
††† On leave from Hitachi, Ltd., Tokyo, Japan.

TABLE I. MAIN DESIGN PARAMETERS OF THE JAERI EXPERIMENTAL FUSION REACTOR (JXFR)

Fusion power (MW)	100
Reactor dimensions	
Major radius (m)	6.75
Plasma radius (m)	1.5
First wall radius (m)	1.75
Plasma volume (m^3)	300
Plasma	
Mean temperature (keV)	7
Mean density ($10^{14} cm^{-3}$)	1.1
Effective charge	1.6
Confinement time (s)	
Trapped-ion	2.9
Neo-Bohm	2.3
Pseudoclassical	5.7
Injection power (MW) (D-particle with 200keV)	27
Toroidal field (T)	6
Safety factor	2.5
Poloidal beta	2.2
Toroidal beta	0.017
Plasma current (MA)	4
Reactor Structure	
Reactor module/Reactor	8
Blanket cells/Reactor module	284
Injection and evacuation hole/Reactor module	1
Nominal max.1st wall temp(°C)	540
Materials	
Structural material	316SS
Blanket fertile material	Li_2O
Neutronics	
Neutron current at 1st wall (n $cm^{-2}s^{-1}$)	7.6×10^{12}
Neutron wall loading (MW m^{-2})	0.17
First wall displacement damage rate (dpa y^{-1})	0.9
Max. helium production rate in 1st wall (appm y^{-1})	12
Max. hydrogen production rate in 1st wall (appm y^{-1})	36
Tritium breeding ratio	0.92
Nuclear heating per DT neutron (MeV n^{-1})	16.7
Total induced activity at one hour after shutdown (Ci) (after one year operation)	7.5×10^{7}
SCM irradiation effects	
Max. copper displacement (dpa y^{-1})	1.5×10^{-5}
Max. nuclear heating rate (W cm^{-3})	7.8×10^{-5}
Total nuclear heating in SCM (kW)	0.98
Toroidal field magnet	
Number of coils	16
Inner diameter, W/H(m)	7/11
Max. field strength (T)	11.5
Stored energy (GJ)	50
Vertical field magnet	
Magnetomotive force (MAT)	8
Field intensity (T) at plasma center	0.26
Stored energy (GJ)	0.5
Primary winding	
Magnetomotive force (MAT)	60
Maximum field intensity (T)	8
Stored energy (GJ)	2.1
Flux change (Wb)	140
Neutral beam injector	
Deuterium beam energy (keV)	200
Ion beam output (MW)	240
Injection power (MW)	33
Neutral beam gas efficiency (Γ_n/Γ_c)	0.5
Total power efficiency	0.26
Cooling system	
Coolant (10 kg/cm^2)	He
Inlet/Outlet temp. (°C)	300/500
Flow rate (kg/s)	143
Secondary system	He, air-cooled
Tritium inventory	
Fuel recirculating system (kg)	0.3
Tritium recovery system including blanket (kg)	0.1
Total inventory including storage (kg)	0.5
Operation cycle	
Operation period(s)	420
Burn time(s)	300

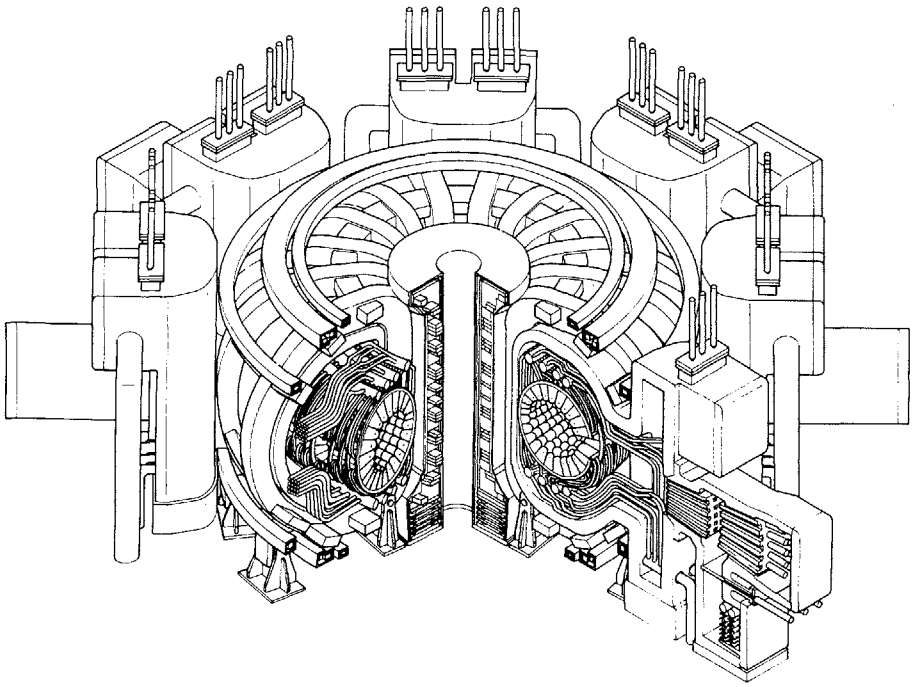


FIG.1. Overview of reactor.

One of the principal questions in the design of this reactor is whether or not the reactor should be self-sustaining. An experimental reactor holding the key to future commercial reactors have many technological problems which must be resolved besides the establishment of a completely self-sustained reactor. The size and power of a self-sustained machine become considerably large for an experimental reactor. We have made the reactor compact by removing the constraint of self-sustaining.

Main design parameters of the reactor are given in Table I and overview of the reactor is shown in Fig.1.

2. PLASMA PROPERTIES

It is difficult to obtain a self-ignition condition at the power level of 100MW with the plasma dimensions listed in Table I. In order to maintain the power balance, stationary heating by 200keV neutral deuteron beam is applied expecting a power amplification by the TCT effect. The impurity assumed is carbon of 2% ($Z_{eff} \sim 1.6$).

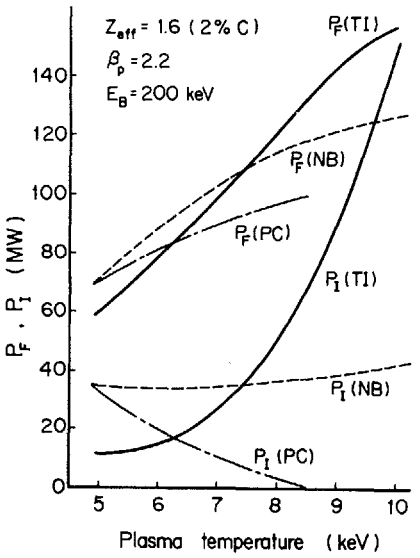


FIG.2. Fusion power P_F and injection power P_I as functions of plasma temperature predicted by various scaling laws (TI: trapped ion, NB: neo-Bohm, PC: pseudoclassical).

2.1 Plasma Parameters and Power Balance

The plasma parameters have been determined in a self-consistent way by taking into consideration the trapped ion(2), neo-Bohm(3) and pseudoclassical(4) scaling laws. Plasma parameters are given in Table I. Figure 2 shows relations between the fusion power and the required injection power at equilibrium. The trapped ion scaling gives 100MW power by 27MW injection power at 7keV.

Calculations with the trapped ion scaling indicate that the operation for larger amount of impurities up to $\sim$ 7% is possible at 7keV with injection power less than 30MW, though the fusion power reduces from 100 to 60MW.

2.2 Fuel Supply to the Plasma

In order to obtain a steady state of the density, fueling by means of a neutral gas surrounding the core plasma is applied in this reactor(5,6). The density and temperature distributions are shown in Fig.3. The neutral distributions are also shown in the figure, where neutral particles are divided into five energy groups. Different energy groups are produced in the different temperature regions of the plasma by charge exchange reactions. The level of impurities estimated from the above neutral distributions is 2 to 3% of the fuel density under the following assumptions: Surfaces of the first wall and the limiters are graphite,

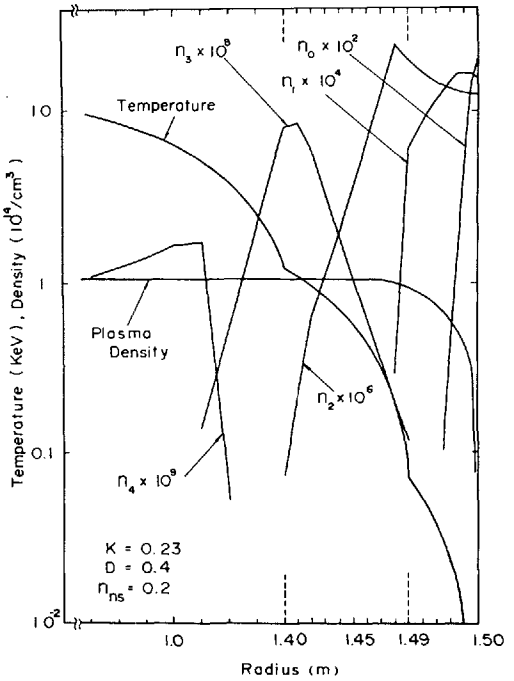


FIG.3. Distributions of the plasma density, plasma temperature and neutral density. Neutral particle density $n_1 \sim n_4$ corresponding to energies of 0.1 eV, 50 eV, 500 eV, 2 keV and 7 keV, respectively.

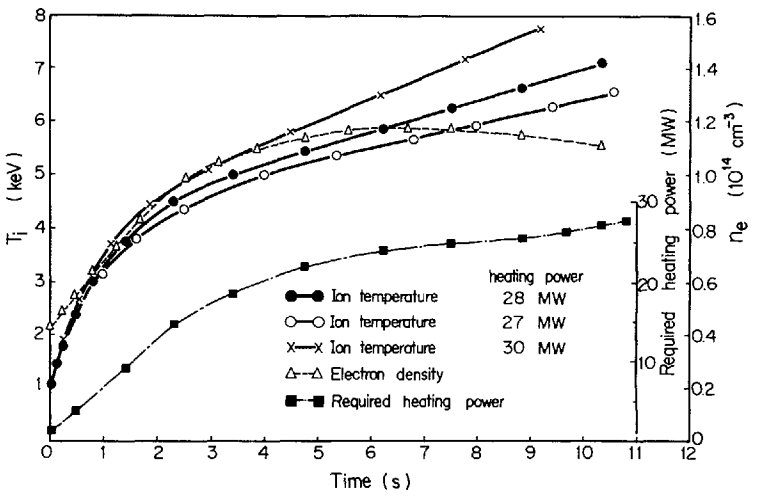


FIG.4. Changes of ion temperature T_i, electron density n_e and required heating power.

contents of impurities are same in the plasma and the surrounding gas, evacuation speeds are same for the impurity and the fuel gas and fueling rate is 4×10^{21}/s.

2.3 Start up

Heating the plasma up to the equilibrium state by constant injection power is investigated. The pseudoclassical scaling-law(4) is applied in the low temperature region below 5 keV and trapped-ion scaling-law(2) applied in the higher region. In the initial state, the low plasma density is desirable to heighten the ion temperature, whereas in the state over several keV the plasma density needs to be higher to some degree to maintain the ion density and the plasma temperature constant. These points must be taken into consideration when the fueling rate and the initial plasma density are decided. Initial values of the ion temperature and the plasma density are 1 keV and 4×10^{13}cm^{-3}, respectively. Under these conditions, the ion temperature, the plasma density and the confinement time can reach in 10 s those in the equilibrium state, 7 keV, 1.1×10^{14}cm^{-3} and 3 s, respectively. The changes of the ion temperature, the plasma density and the required heating power calculated by using zero-dimensional model are shown in Fig.4. The fueling rate of d-t and the neutral beam injection power are 3×10^{13}cm^{-3}s^{-1} and 28 MW, respectively.

3. REACTOR STRUCTURE

3.1 Arrangement of the Reactor

The overview of the reactor is shown in Fig.1. The reactor consists of 8 modules which may be withdrawn in the radial direction for repair. The cross-section of the module is shown in Fig.5. Each module has 284 blanket cells and a cell with a 1.2 meter hole for the neutral beam injection and evacuation. Mechanical limiters employed are so designed that they may be withdrawn in case of failure. The surface of the limiter is covered with graphite. 4 limiters and 4 injectors are alternately installed.

3.2 Blanket Structure

Figure 6 shows the typical blanket cells. Type A cells serve exclusively for shielding purpose; they are used as inner blanket (hatched part in Fig.5). Type B cells are placed in the rest of the blanket for tritium breeding. To protect the first wall from the plasma burst and to moderate impurity problems, graphite layer is installed on the plasma side of the blanket vessel wall.

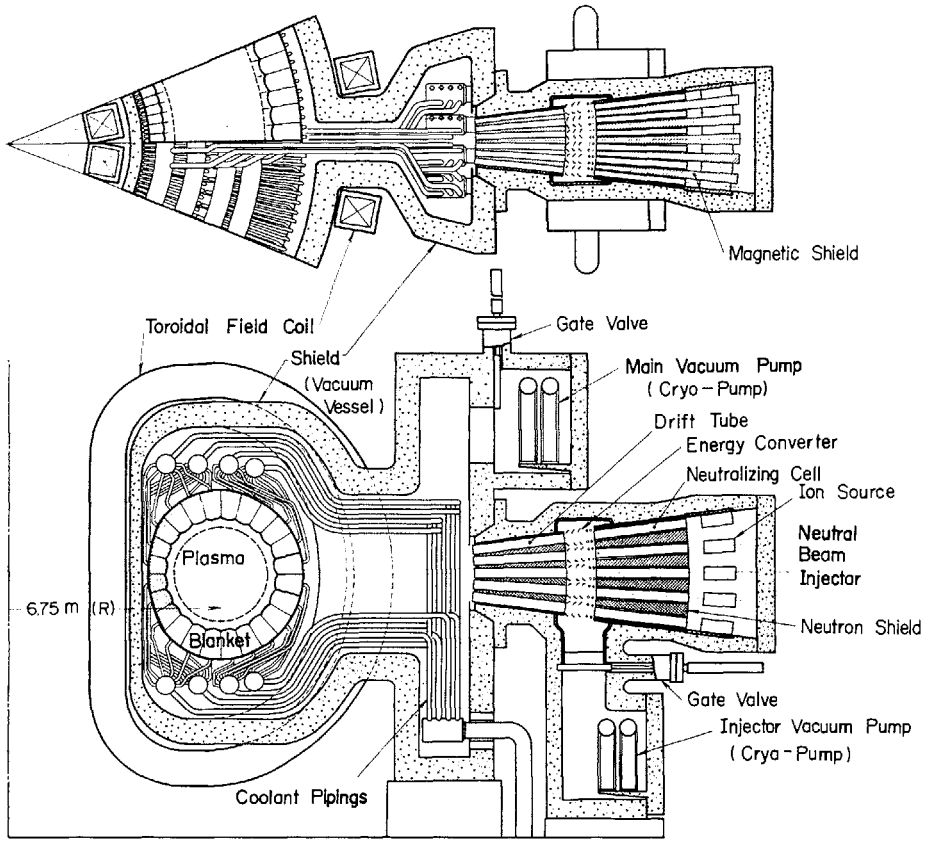


FIG. 5. Cross-sectional view of reactor module.

Heat flux on the surface of the first wall is estimated as 15 W/cm^2 and nuclear heating in the wall is 2 W/cm^3. The nominal temperature of the first wall on the plasma side is calculated as 540°C, that on the coolant side is 500°C. Thermal stress and pressure stress at the spherical dome part of the first wall where the thickness is 5mm, are 7kg/mm^2 and 4kg/mm^2, respectively. The most difficult part of the structural design of the blanket is in designing the side wall of the blanket vessel which has rectangular cross-section, to withstand the high pressure. When the radius of the curvature at the corner of the rectangle is 10cm, and the thickness of the vessel is uniformly 10mm, the maximum pressure stress at the corner becomes about 10kg/mm^2 when the inner pressure is 2kg/cm^2. This means that the pressure balance of the

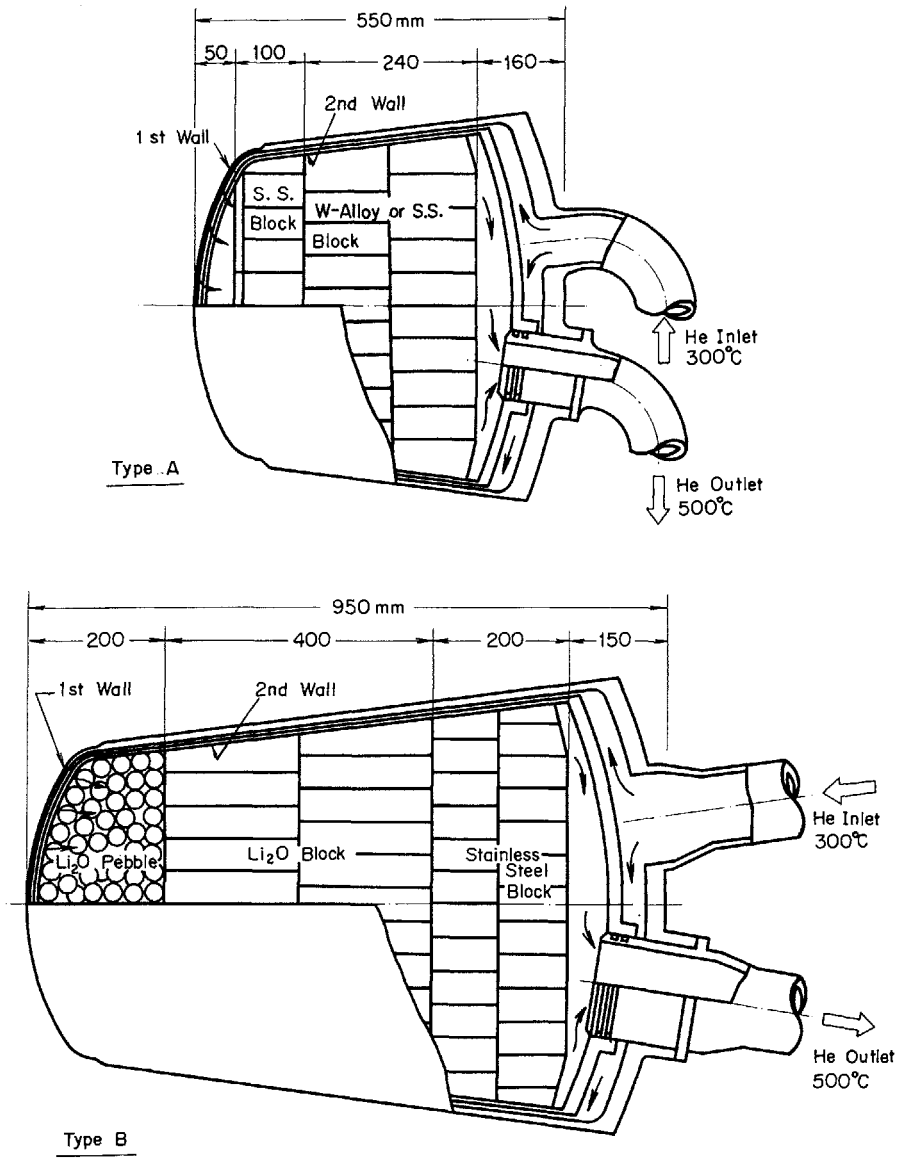


FIG.6. Typical blanket cells.

adjoining vessels is indispensable. The vessel can be designed to withstand higher pressure if the optimal thickness variation of the side wall is considered. The reliability of the pressure balance between the adjoining vessels is not yet fully investigated.

The electromagnetic force induced by the change of the plasma current is estimated to be $\pm 0.4 kg/cm^2$ on the side wall, and the rotating force of a blanket vessel 1.4ton.m, when the plasma current changes at 4MA/0.1s.

3.3 Repair and Maintenance

In this design most of the main components are made exchangeable. In case of major failures such as blanket vessel rupture, magnet failure, etc., the module is withdrawn in the radial direction and the failed section is replaced. Since we consider that this problem to be one of the most important problems in the reactor design, detailed investigation is under way.

4. BLANKET NEUTRONICS

Nuclear characteristics of the blanket are evaluated by using one-dimensional and two-dimensional transport calculation codes ANISN(7) and TWOTRAN-GG(8), respectively. The neutron and gamma-ray multigroup coupled cross-sections and kerma factors were processed using radiation heating analysis code system RADHEAT(9), and MACK(10). Nuclear data of ENDF/B-3 and 4 and secondary gamma-ray production data in POPOP4 Library(11) were used.

Tritium breeding ratio is calcualted to be 0.92 after the application of the correction factor for the toroidal effect and that for the blanket heterogeneity effect (12). Total nuclear heating in the blanket per one incident DT neutron is calcualted as 16.7 MeV. The induced activities of the reactor after long operation periods are studied in detail. The distribution of the radiation dose in and around an extracted reactor module for repair after one year operation and one week cooling period is shown in Fig.7.

5. RADIATION SHIELDING

The superconducting magnets (SCM) of the toroidal coils are shielded so as to suppress the maximum displacements per atom (dpa) of the copper in the SCM to less than 2.5×10^{-5} dpa/y, to minimize the radiation heating in SCM, and to reduce the dose-rate from the induced activation of SCM on the outside of the torus below the accessible level of 2.5 mrem/h.

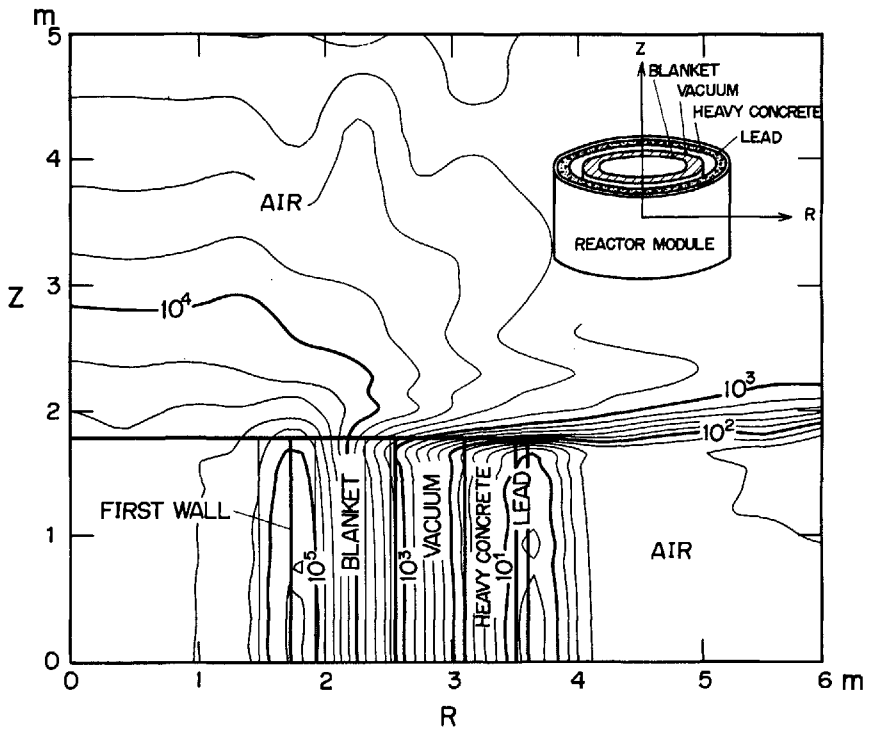


FIG. 7. Distribution of radiation dose-rate (rem·h^{-1}) in and around an extracted reactor module after one year operation and one week cooling period.

Optimal shielding arrangement was pursued for the inner part of the torus, where the effective thickness allowed for the blanket and shield was limited to 80cm. As a result, tungsten (W) instead of Li_2O for tritium breeding is exclusively loaded in this part of the blanket.

If the use of W is found to be unacceptable from the point of long-life induced activity, it will be replaced by stainless steel. In this case, the annealing period of the SCM is halved to about three years. The neutron and gamma-ray fluxes in the inner blanket, shield and magnet are shown in Fig.8. The effect of neutrons streaming through the injection ports on the irradiation of SCM was evaluated by two-dimensional analysis(13). In consequence, the thickness of the heavy concrete shield near the ports was increased by more than 30cm.

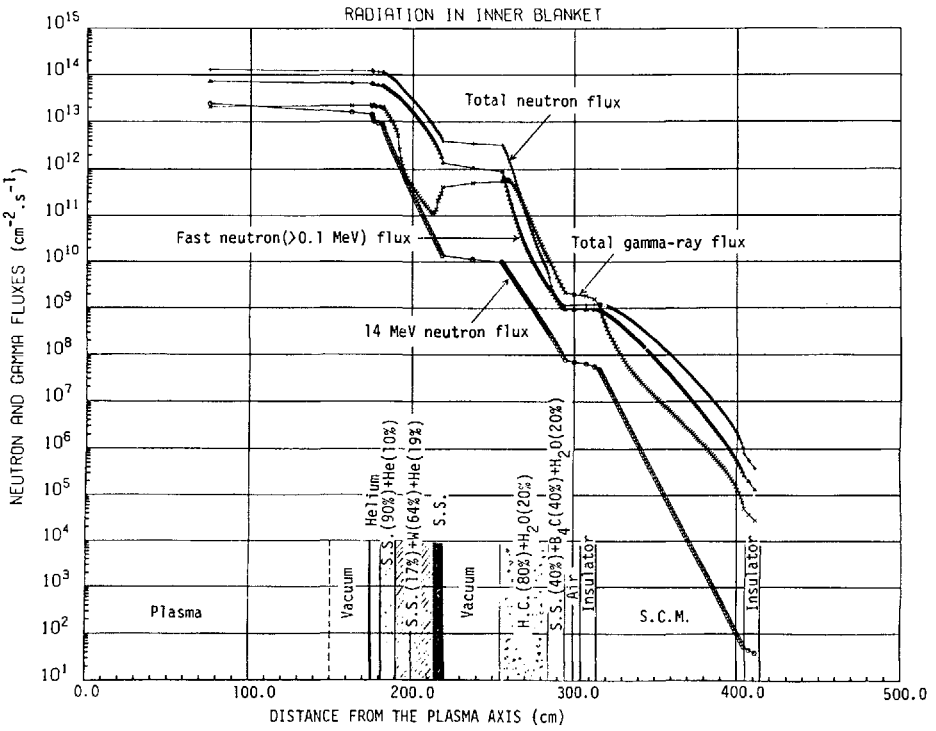


FIG.8. Neutron and gamma-ray fluxes in the inner blanket, shield and magnet.

6. MAGNETS

6.1 Toroidal Field Magnet

The toroidal field magnet is deformed, constant-tension, D-shaped (Fig.9). Because the minimum scale of coil inner bore is limited by blanket and shield dimensions, and the tall coil is rather costly, the constant-tension shape is deformed into lower height. The Nb_3Sn superconductors are employed to produce the maximum field of 11.5 T in coil. The conductors are made of twisted multifilamentary composites, and stabilized by copper matrix. The toroidal magnet consist of 16 coils, and the maximum field ripple of plasma zone is calculated to be 0.6%. The maximum mechanical stress in the coil is computed to be about 30 kg/mm^2. The evaluation of AC pulsing loss is also performed, and the result is nearly 30MJ/one pulse. Other main characteristics are shown in Table I.

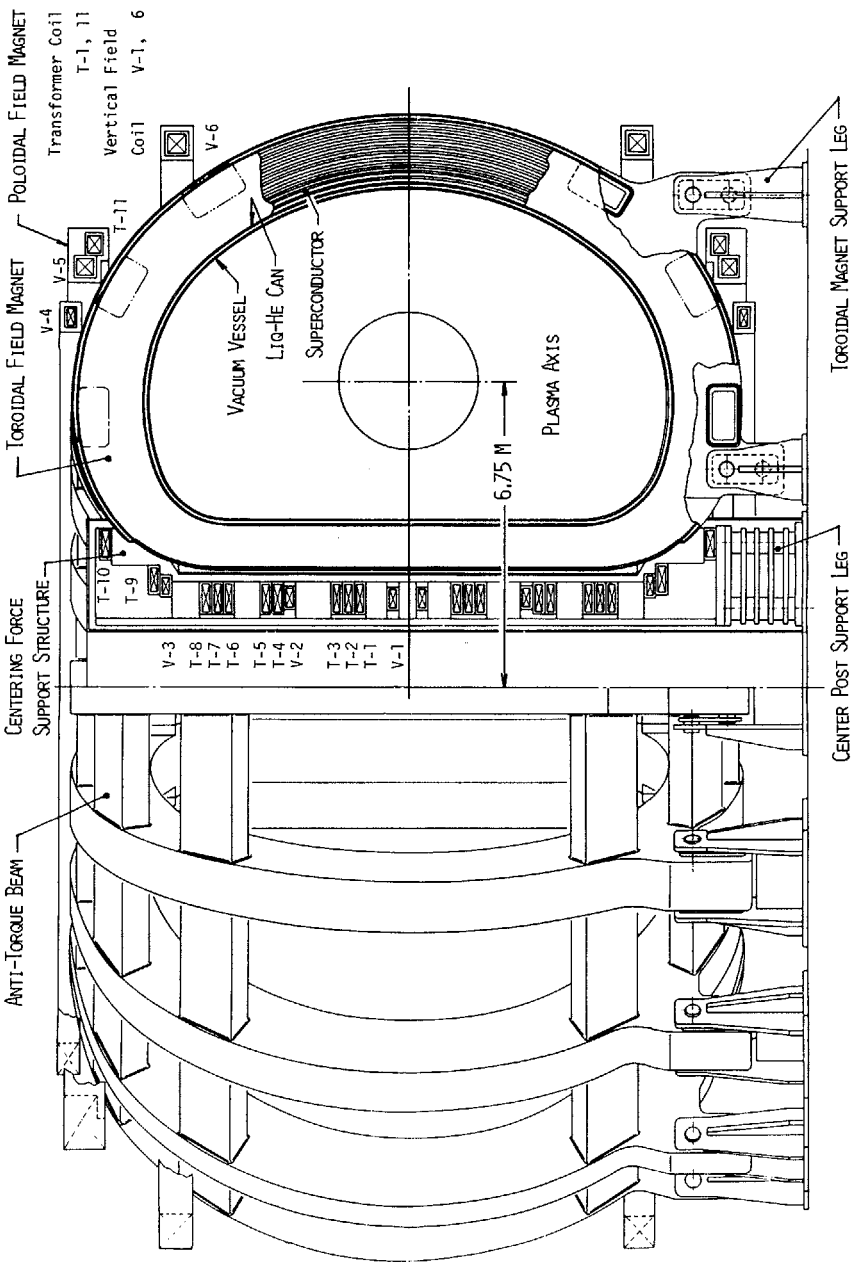


FIG. 9. Superconducting toroidal and poloidal magnets.

6.2 Poloidal Field Magnets

The primary winding and the vertical field magnets are placed outside the toroidal field magnet. The positions of coils are decided by optimizing field configuration using nonlinear programming (14). The vertical field magnet consists of 12 coils and the primary of 22 coils which are shown in Fig. 9. Copper stabilized NbTi superconducting material is used for both of the magnets.

7. NEUTRAL BEAM INJECTOR

About 30MW deuterium beams are injected through the four blanket holes at an energy of 200kV. Each ion source unit consists of 30 ion sources. Suppression of the cold or the unused gas-flow into the torus is required to make the evacuation system compact. In this connection, the concept of the neutral beam gas efficiency is introduced which leads us to the conclusion that the cryo-pumping room should be separated from the torus by small-conductance drift tubes. The divergent loss of neutral beams is reduced by adopting different focal points, namely, the beamlets are focused on the outlet center of the drift tube, and beamlines are focused on the center of each blanket holes.

8. ELECTRICAL POWER SUPPLY SYSTEM

As the transformer coil current swings from positive to negative value during the plasma current rise time, the energy storage is necessary to minimize the peak power. In this design a superconducting inductive energy storage is used. Figure 10 shows the required electric power for each subsystem component.

9. PLANT SYSTEM

9.1 Fuel Recirculating System

Vacuum system consists of 16 cryo-pumps, which are operated 8 at a time, alternately at 2 hours interval. The basic flow diagram of the fuel recirculating system is shown in Fig. 11.

9.2 Reactor Cooling System

Since the reactor is operated periodically, installation of heat reservoirs and application of reactor coolant flow control system are required. The basic flow diagram of the reactor cooling system is shown in Fig.12.

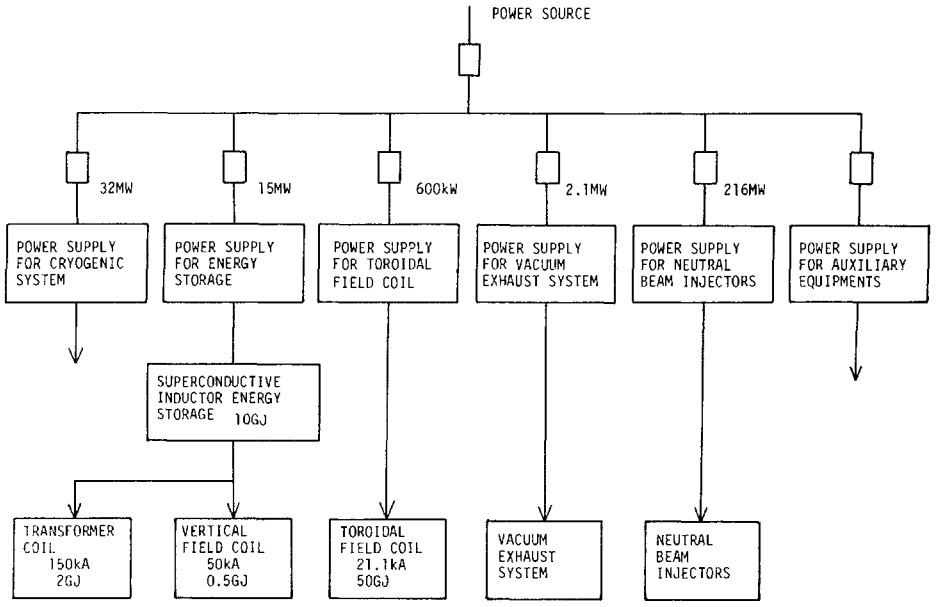


FIG.10. Electrical power supply system.

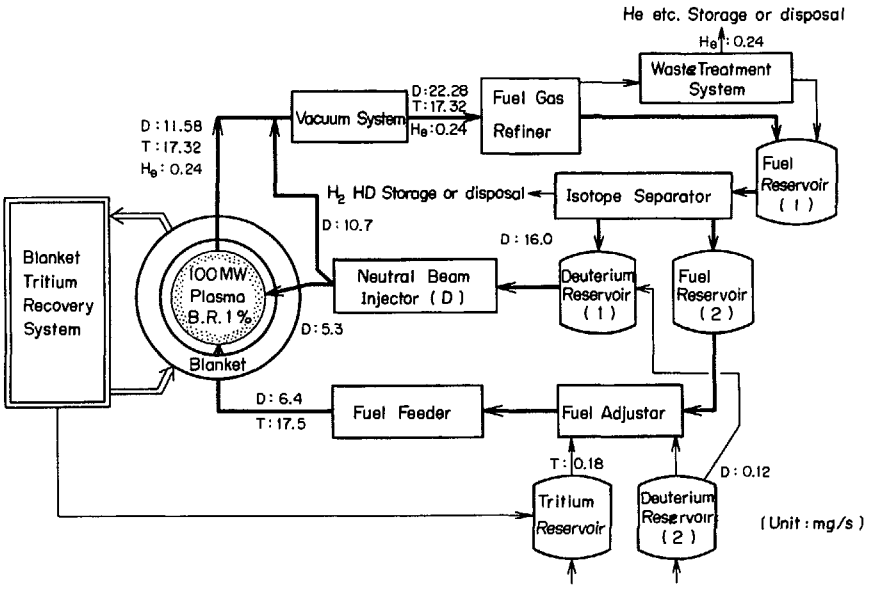


FIG.11. Fuel re-circulating system.

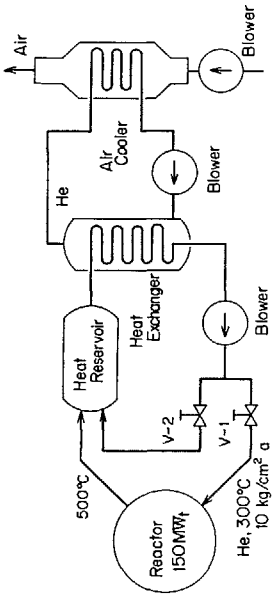


FIG.12. Reactor cooling system.

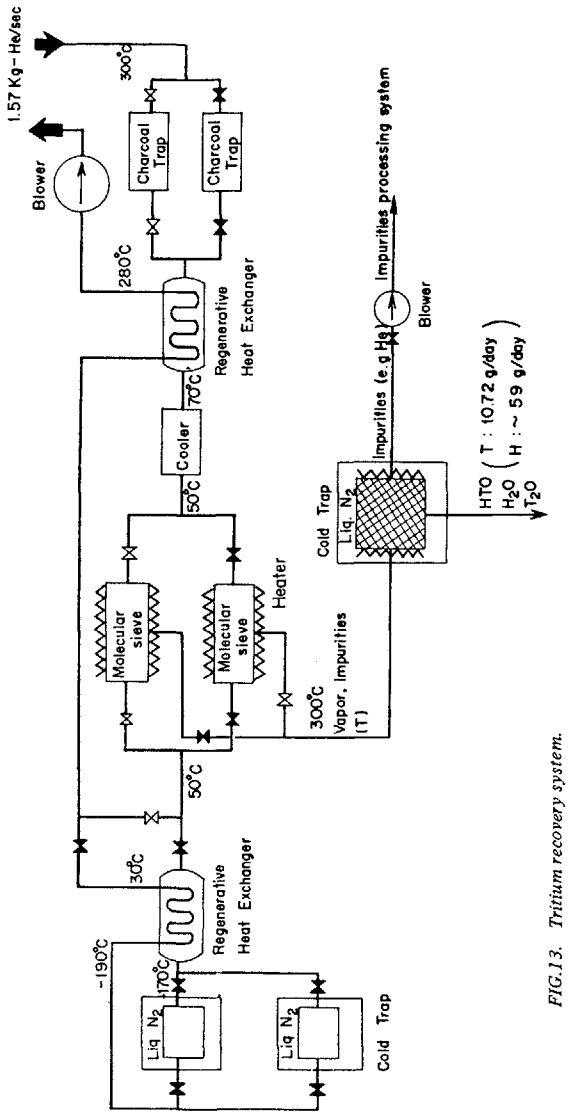


FIG.13. Tritium recovery system.

9.3 Tritium Recovery System

Tritium generated in Li_2O blanket is expected to leak out to the He coolant (15). The tritium is carried by the coolant to the recovery system. The tritium content in the coolant is designed to be 0.1ppm. The flow diagram is shown in Fig. 13. In order to minimize the permeation rate through the heat exchanger tubes, the partial pressure of tritium gas must be extremely low in the main cooling system. An oxidizer is installed at the reactor outlet.

ACKNOWLEDGEMENT

The authors are deeply indebted to Division Head, Dr. S. Mori, and other plasma physicists of the Division of Thermonuclear Fusion Research for the valuable comments and helpful discussions. The authors also thank Drs. T. Naito (Mitsubishi Atomic Power Industries, Inc.) and T. Yamamoto (Fuji Electric Co.) for their contributions to this design.

REFERENCES

(1) SAKO,K., et al., JAERI-M 6670 (1976) (in Japanese).
(2) KADOMTSEV, B.B., POGUTSE, O.P., Nuclear Fusion 11, (1971) 67.
(3) SINNIS, J., et al., Phys. Rev. Lett., 30, (1972) 1214.
(4) YOSHIKAWA, S., CHRISTOFILOS, N.C., Proc. 4th Conf. Plasma Physics and Controlled Nuclear Fusion Research (Madison 1971), Vol.II, IAEA, Vienna (1972) 357.
(5) LEHNERT, B., Proc. Third Int. Symp. Toroidal Plasma Confinement, (Garching, 1973), C1-1.
(6) YAMATO, H., OHTA, M.: Proc. First Topical Meeting on the Technology of Controlled Nuclear Fusion (San Diego 1974), Vol.II, USAEC, (1974) 309.
(7) ENGLE, W.W. Jr., "A User's Manual for ANISN", K-1693 (1967).
(8) LATHROP, K.D., BRINKLEY, F.W., LA-4432 (1970).
(9) MIYASAKA, S., et al., JAERI-M 5794 (1974) (in Japanese).
(10) ABDOU, M.A., MAYNARD, C.W., WRIGHT, R.Q., ORNL-TM-3994 (1973).
(11) FORD, W.E. III., CTC-42 (1970).
(12) IIDA, H., SEKI, Y., IDE, T., JAERI-M 6460 (1976) (in Japanese).
(13) IDE, T., SEKI, Y., IIDA, H., JAERI-M 6475 (1976).
(14) TOI, K., TAKEDA, T., JAERI-M 6018 (1975).
(15) TANAKA, K., et al., Proc. Int. Conf. Radiation Effects and Tritium Technology for Fusion Reactor, Gatlingburg, 1975, CONF-750989, Vol.II.

TOKAMAK EXPERIMENTAL POWER REACTOR STUDIES*

W.M. STACEY, Jr.
Argonne National Laboratory,
Argonne, Illinois

C.C. BAKER
General Atomic Company,
San Diego, California

M. ROBERTS
Oak Ridge National Laboratory,
Oak Ridge, Tennessee,
United States of America

Abstract

TOKAMAK EXPERIMENTAL POWER REACTOR STUDIES.

A description is given of the scoping and conceptual design studies for a tokamak experimental power reactor (EPR) conducted from mid-1974 to mid-1976 at Argonne National Laboratory, General Atomic Company and Oak Ridge National Laboratory. The purpose of these studies was to define the physics and technological features of an EPR which could operate in the mid-to-late 1980s at or near net electrical power production conditions with a plant capacity factor in the range 25–50%, thereby providing perspective on the role of the EPR in the USERDA tokamak programme.

Scoping [1-3] and conceptual design [4-6] studies for a tokamak experimental power reactor (EPR) have been conducted for the past two years at Argonne National Laboratory, General Atomic Company, and Oak Ridge National Laboratory. The purpose of these studies was to define the physics and technological features of an EPR which could operate in the mid-to-late 1980s at or near net electrical power production conditions with a plant capacity factor in the range 25-50%, thereby providing perspective on the role of the EPR in the USERDA tokamak program.

1. DESIGN DESCRIPTION

Salient features of the three designs are illustrated in Figs 1-3. The principal geometric parameters are given in Table I. The design-basis operating parameters are given in Table II.

2. PLASMA PHYSICS

2.1. MHD Equilibrium/Stability and Performance

A range of MHD equilibrium solutions, corresponding to different pressure profiles and degrees of diamagnetism/paramagnetism, is possible for a given toroidal field and design geometry. These solutions require different equilibrium fields, of course, and have associated with them different sets of values for the plasma current, q and β_t.

* Work supported by USERDA and the Electric Power Research Institute (GA).

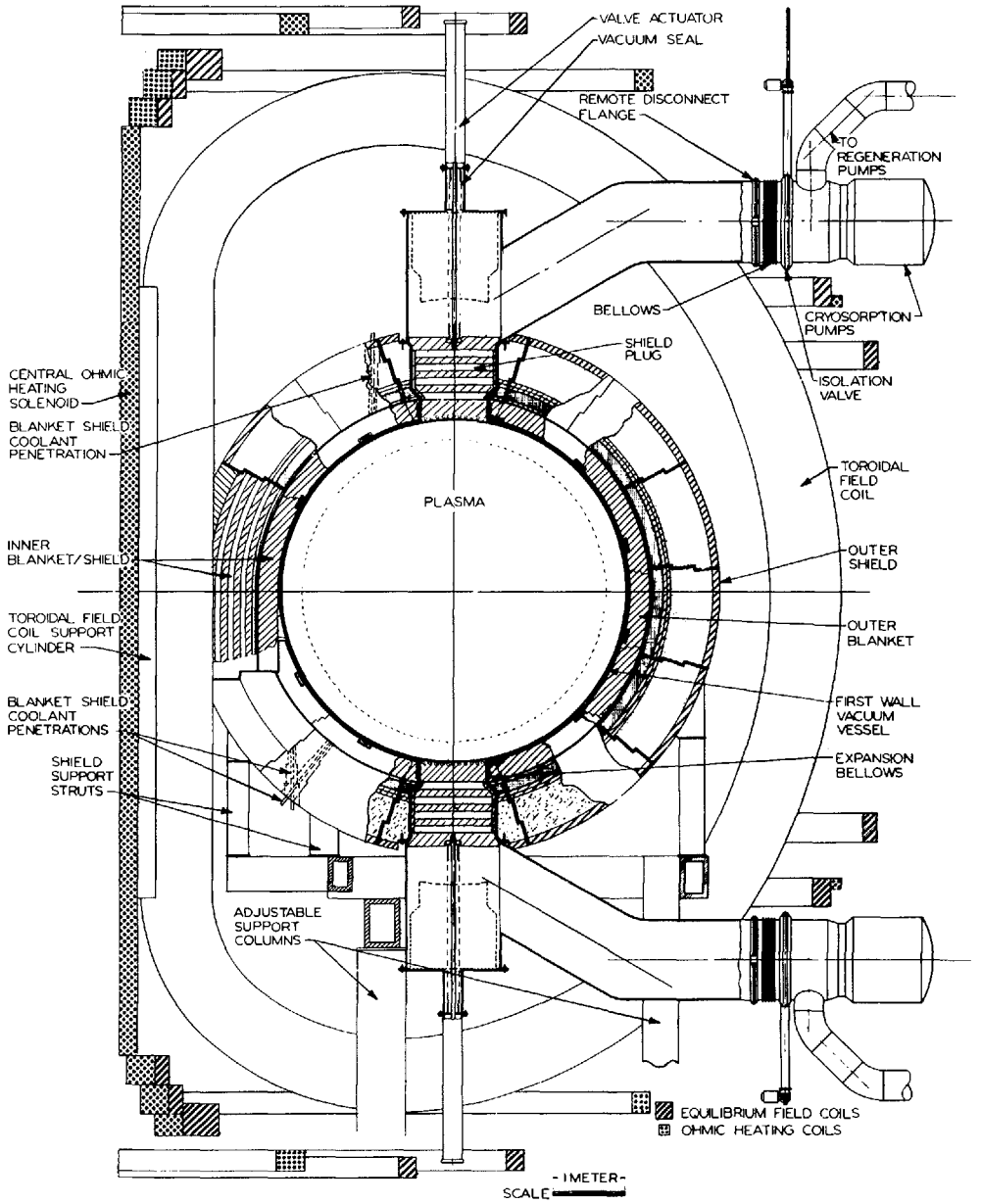


FIG.1. Vertical section of ANL EPR.

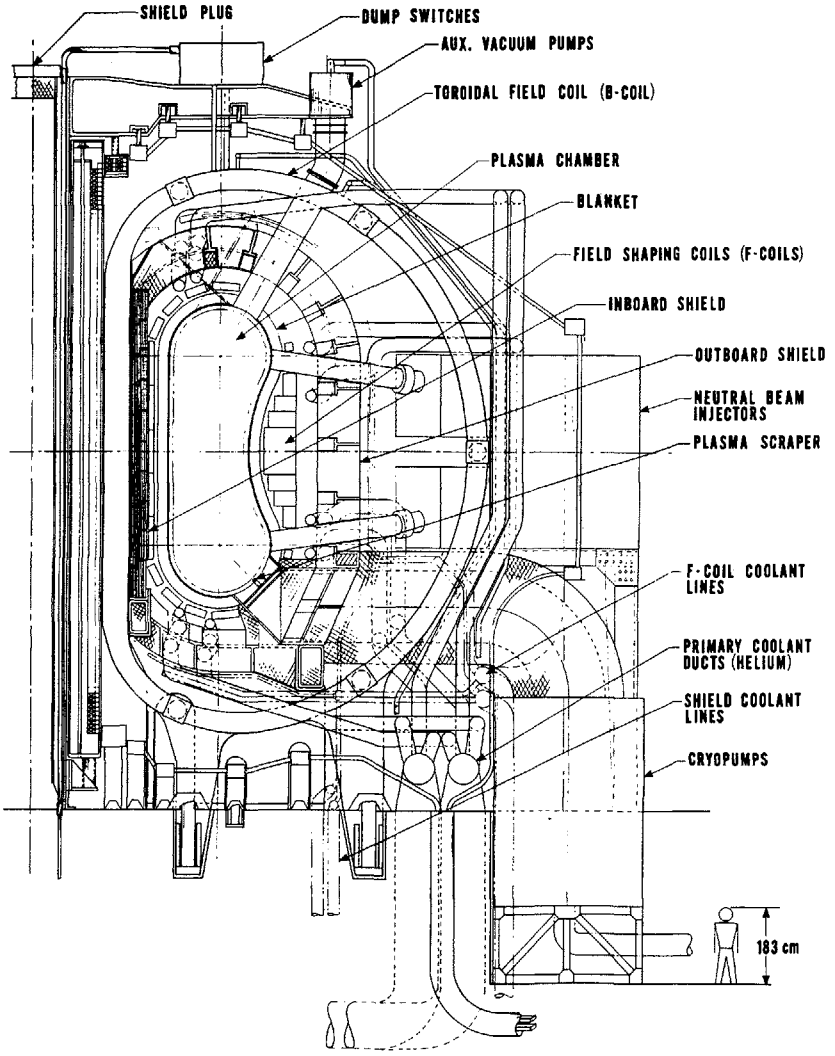


FIG.2. Vertical section of GA EPR.

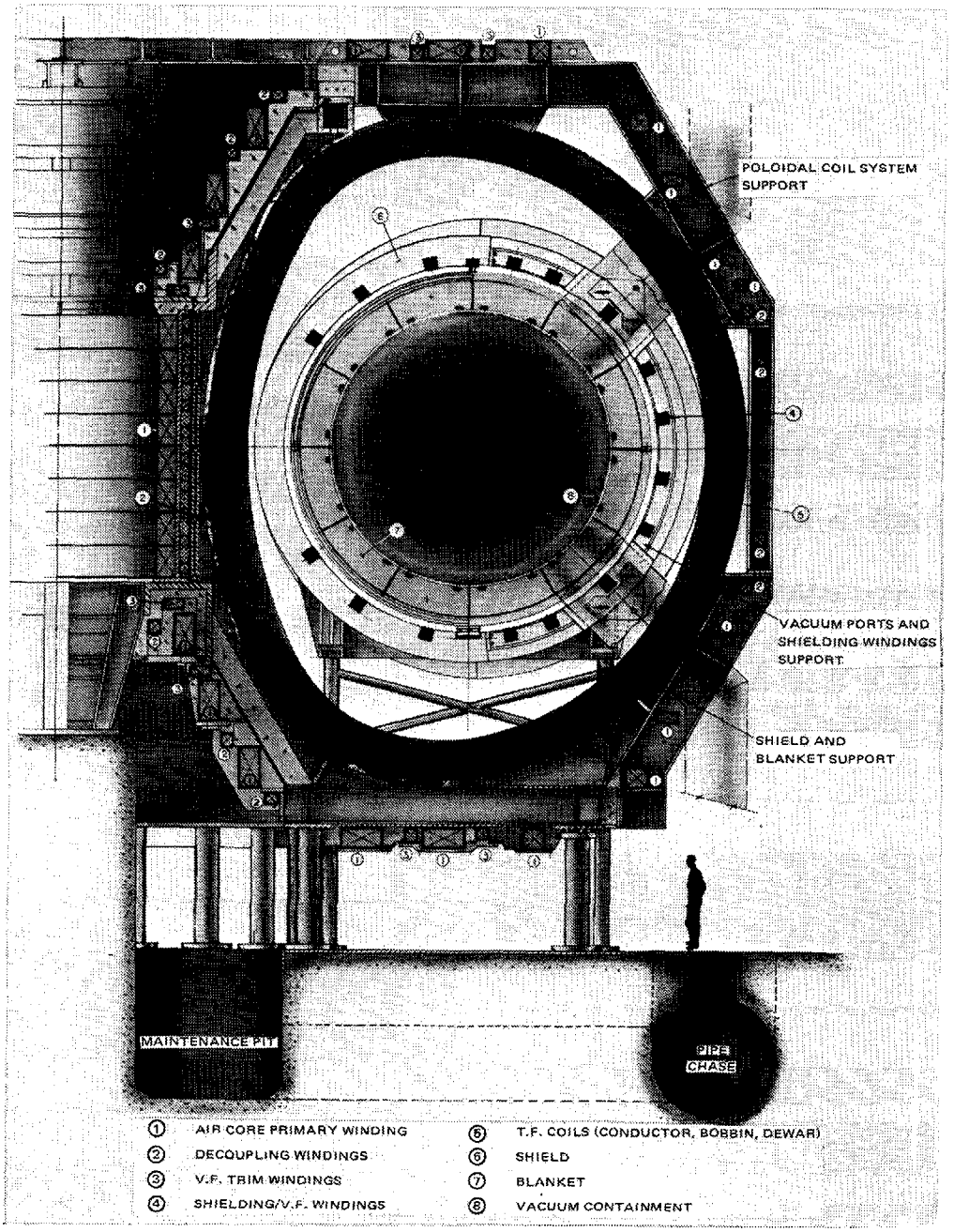


FIG.3. Vertical section of ORNL EPR.

TABLE I. EPR GEOMETRICAL PARAMETERS

	ANL	GA	ORNL
Major radius (m)	6.25	4.50	6.75
Plasma minor radius (m)	2.10	1.12	2.25
Plasma elongation	1	3	1
First-wall minor radius (m)	2.40	1.22	2.25
Blanket thickness (m)	0.28	0.25	0.52
Shield thickness (m)			
inside	0.58	0.40	0.48
outside	0.97	1.00	0.48
Toroidal field coil bore (m)	7.8 × 12.6	8.1 × 12.4	7.4 × 9.7

TABLE II. DESIGN-BASIS OPERATING PARAMETERS

	ANL	GA	ORNL
Duty cycle (%)	75	84	87
Capacity factor = duty cycle × plant availability	50	20	70
Lifetime (yr)	10	10	10

Possible solutions which satisfy $q \geq 1$ for the ANL design are shown in Fig. 4. The solid curves are loci of equilibria varying (from left to right) from highly diamagnetic to highly paramagnetic plasmas, for a given pressure profile exponent, α.[1] Current reversal in part of the torus occurs for solutions to the left of the dashed line. The maximum value of β_t, hence the maximum power density, occurs for equilibria slightly less diamagnetic than those for which current reversal occurs. Thus, the dashed line represents a locus of "optimal" solutions — the value of β_p along this locus is confined to a rather narrow range of $1.8 \geq \beta_p \geq 1.6$. The value of q(a) increases with the peaking of the pressure profile (i.e. with increasing α). The ANL reference design point was chosen by selecting the pressure profile for which q(a) = 3. The pressure profile, with $\alpha = 1.3$, was factored into density and temperature profiles of the same form, but with exponents $\alpha_n = 0.3$ and $\alpha_T = 1.0$, in evaluating the power balance equations.

The MHD stability of the GA Doublet configuration has been examined with respect to localized interchange modes and axisymmetric rigid displacements. Stable equilibria have been determined for high beta conditions ($\beta \geq 10\%$) with the field-shaping coils displaced sufficiently far from the plasma surface to allow for shielding. In the reference design, it was also possible

[1] $p(r) = p_0[1 - (r/a)^2]^{\alpha}$

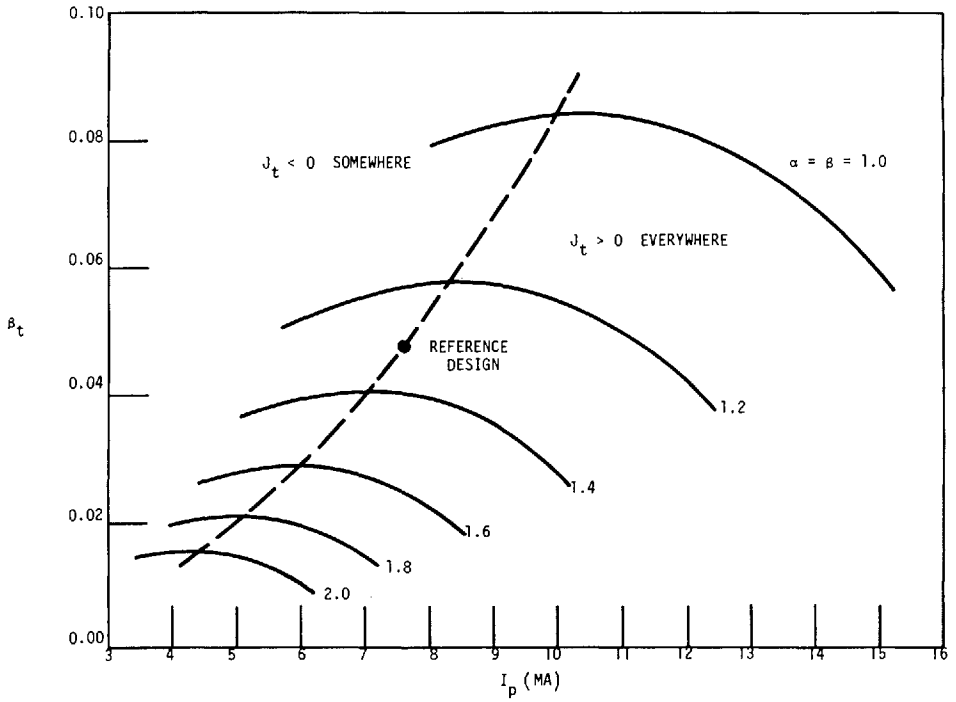


FIG.4. MHD equilibria at B_{max}^{TFC} = 10 T — average total β.

to remove several coils to allow for pumping ports with no adverse effect on the equilibrium or stability. Maximum stable plasma currents and β_t are found by increasing β_p, flattening the current profile and shaping the plasma such that about 50% of the poloidal flux is inside the Doublet separatrix. The reference case assumes that β_p = 1.8 and that the on-axis current density is twice the current density at the limiter. Typical plasma current, pressure, temperature, and densities profiles are shown in Fig. 5.

In the ORNL reference design, account has been taken of the unique features of the poloidal field system design. The design includes vertical field-shielding (VF-S) coils between the plasma boundary and the toroidal coils. Appropriate equilibria produced by this system have been computed for the ORNL-EPR using a free boundary MHD code.

The plasma parameters corresponding to the three reference designs are shown in Table III.

2.2. Impurity Control

The performance of the EPR with a bare stainless steel wall and no means of impurity control would be very poor. Modification of the first-wall surface, a flowing gas boundary, and a divertor were considered.

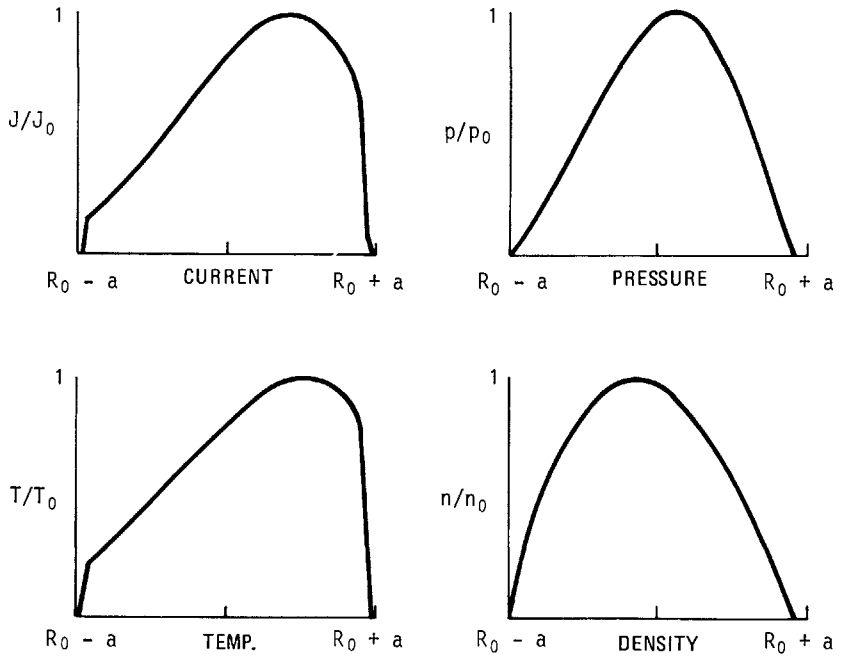


FIG.5. Distributions of plasma current density, pressure, temperature, and ion density in the GA design.

TABLE III. STEADY-STATE PLASMA PARAMETERS

	ANL	GA	ORNL
Average total beta, β_t	0.048	0.10	0.03
Safety factor, q(a)	3.05	2.5	2.5
Plasma current, I (MA)	7.6	11.4	7.2
Average D-T temperature, $\bar{T}_{DT}$	9.6	11.4	12.6
Average D-T ion density, $\bar{n}_{DT}$ (m^{-3})	9.4×10^{19}	1.1×10^{20}	7.0×10^{19}
Effective ion charge, Z_{eff}	1.3	2.0	1.3
Energy confinement, $n\tau_E$ (s/m^3)	2.4×10^{20}	2.7×10^{20}	2.7×10^{20}
Power, P_T [MW(th)]	638	410	410

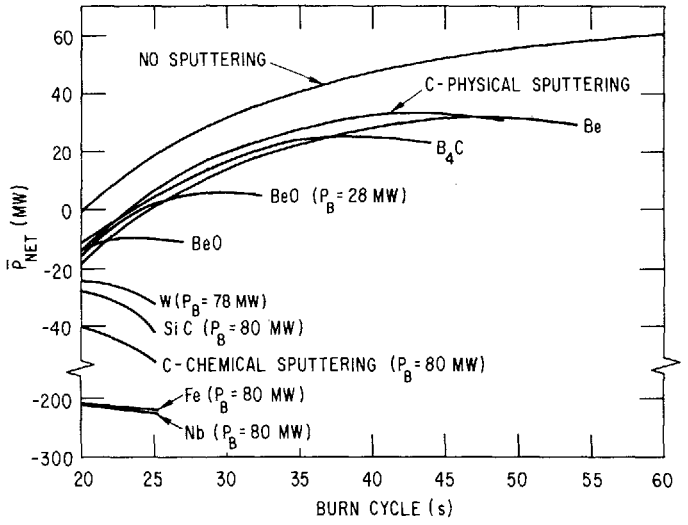


FIG.6. Effect of first-wall surface material on power performance — ANL design.

The net electrical power is plotted as a function of the length of the burn pulse, for several first-wall surface materials, in Fig. 6. Steel, niobium and, to a lesser degree, tungsten surfaces result in very poor performance because large supplemental beam heating ($P_B \approx 80$ MW) is required to offset the enhanced radiation loss due to high-Z plasma contamination. With a low-Z surface the performance is much better, except for carbon in the temperature range ~400-700°C, where chemical sputtering causes excessive plasma contamination. A low-Z material coating on a metal substrate is used for impurity control in the ANL and ORNL designs, and a low-Z standoff liner is used in the GA design.

A flowing plasma boundary concept was selected for additional plasma impurity control for the GA design. Since the plasma boundary region is expected to be collisional, by modifying the impurity diffusion due to ion-impurity collisions, the inward diffusion of impurity ions can be inhibited. This is accomplished by injecting cold fuel at the top of the vacuum chamber and pumping at the limiter located at the bottom of the vacuum chamber. The required throughput is 1.6×10^{23} particles/s. The density profile which results is compatible with concepts on profile inversion for trapped particle mode stabilization and possible edge convection fueling. The flowing plasma boundary is also considered as an ash or alpha-particle removal system.

2.3. Transport Scaling

A multiregime transport model is used to compute the confinement parameters. At high collision frequencies, the particle and electron energy confinement are computed from pseudoclassical theory, and ion energy confinement is computed from neoclassical theory. When collision frequencies are less than bounce frequencies, the confinement parameters are computed from trapped particle (TEM, TIM) theory or pseudoclassical/neoclassical theory, whichever is least favorable. Electron energy confinement times for the GA design are

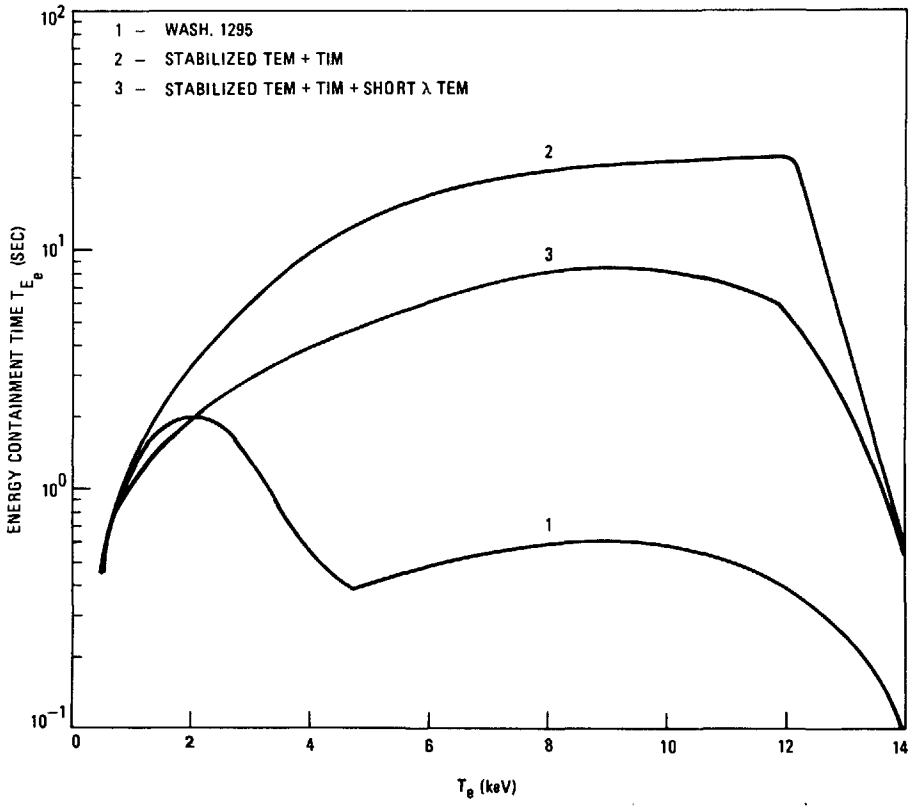


FIG. 7. Energy confinement time as a function of temperature for the GA design.

plotted as a function of electron temperature in Fig. 7. Three transport scenarios are displayed. The temperature, density, and shear profiles used are characteristic of the Doublet configuration with a flowing plasma boundary for impurity control after ignition. The first scenario is essentially that documented in WASH-1295. The second and third scenarios include the effects of stabilization terms on the long-wavelength trapped electron and ion modes, due to shear, Landau damping and ion-ion collisions. The third differs from the second by the inclusion of various short wavelength trapped electron residual modes, and is the transport model adopted for use in the GA design.

2.4. Burn Cycle Dynamics

The basic burn cycle is illustrated schematically in Fig. 8 (times are representative of the ANL design). As the plasma current rises, the equilibrium field must increase to provide MHD equilibrium. The beam heating may be initiated during or after the ohmic heating current ramp.

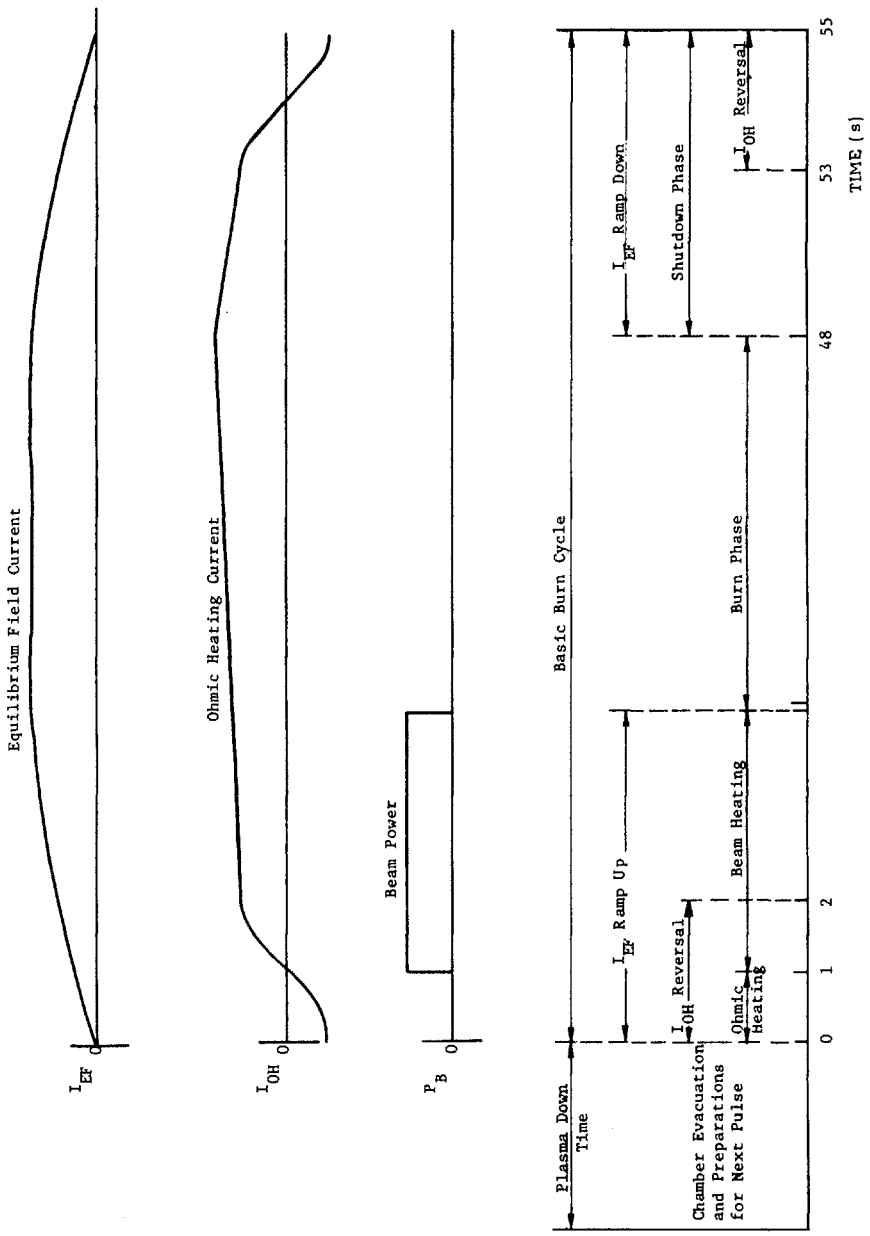


FIG.8. Burn cycle scenario.

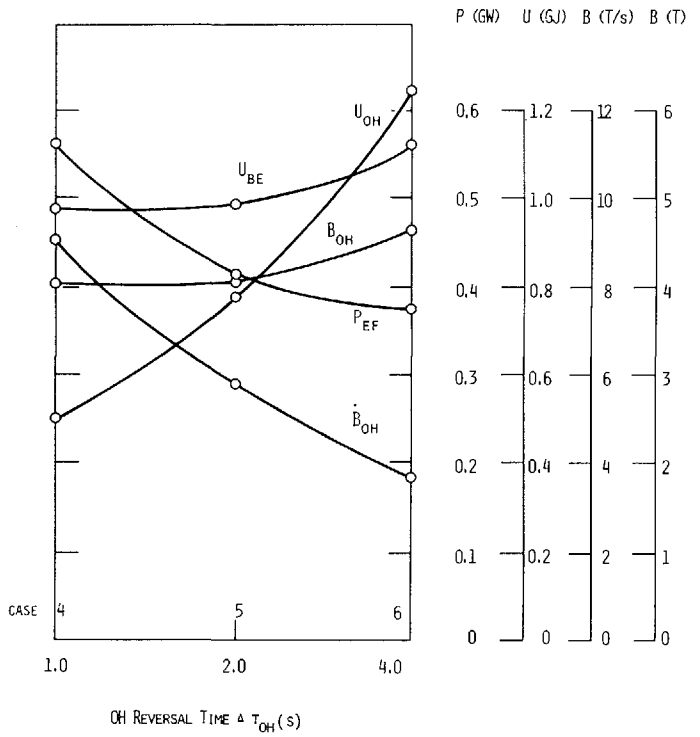


FIG.9. Effect of Ohmic current reversal time on plasma driving and heating system requirements for the ANL design.

The requirements on the plasma driving and heating systems are quite sensitive to the startup procedure. The energy transferred in the ohmic heating system (U_{OH}), the energy transferred into the neutral beam injection system (U_{BE}), the maximum field (B_{OH}) and field rise ($\dot{B}_{OH}$) in the ohmic heating coils, and the maximum power (P_{EF}) transferred by the equilibrium field power supply are plotted in Fig. 9 versus the ohmic heating current reversal time (Δt_{OH}), for the ANL design. By starting up with the maximum plasma current (subject to q and ion sound speed limitations), the required plasma auxiliary heating power is minimized, as illustrated in Fig. 10 for the GA design. The disadvantage is that additional volt-seconds are used during startup. The maximum plasma heating power (and energy) results when startup is accomplished at the maximum allowed β_p. As a result of studies of this type, the requirements shown in Table IV were identified.

Reference case power performance characteristics for the three designs are summarized in Table V. Supplemental beam heating can be provided to achieve this level of energy output even if the energy confinement is inadequate for ignition; however, it would be difficult to achieve net power in

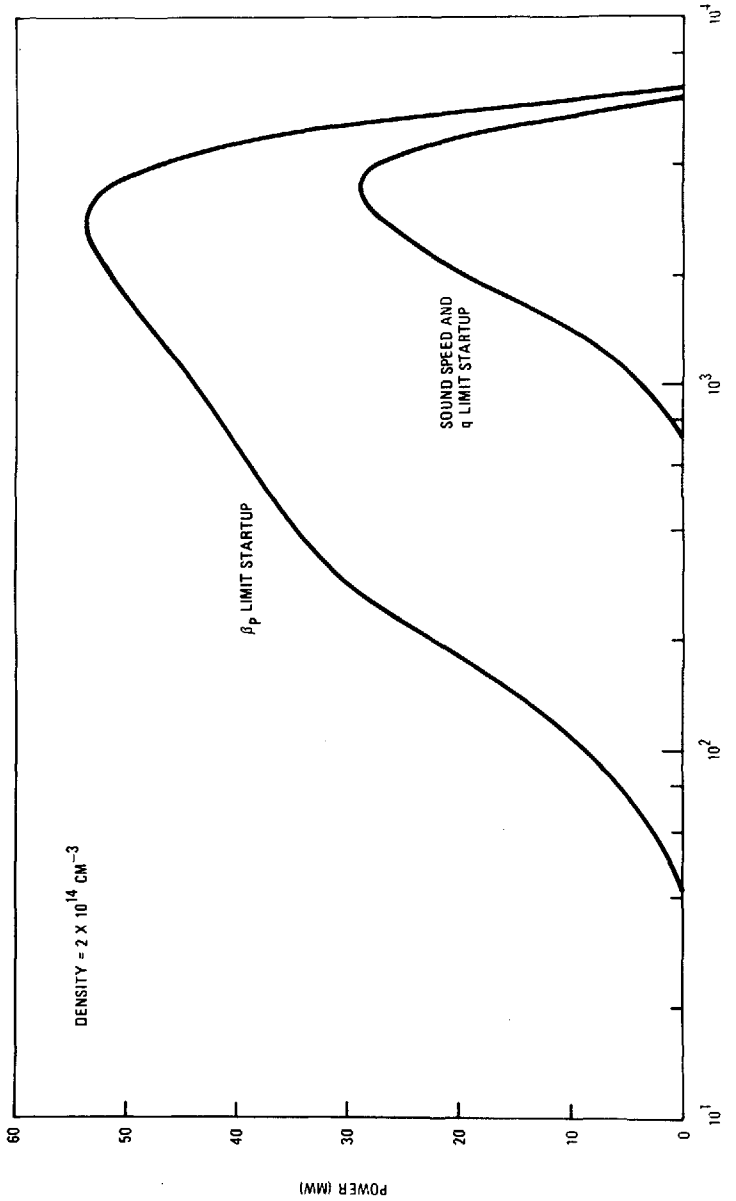


FIG. 10. Auxiliary heating power requirements for the GA design.

TABLE IV. PLASMA DRIVING AND HEATING SYSTEM REQUIREMENTS

	ANL	GA	ORNL
Ohmic Heating Coil System			
Volt-seconds to plasma (V-s)	85	75	110
Maximum power (MW)	1900	2250	2100
Energy transferred (MJ)	1200	1300	1800
Minimum current reversal time (s)	2.0	2.0	2.0
Maximum field in conductor (T)	5.0	5.7	7.2
Maximum field rise (T/s)	6.7	9.6	7.2
Equilibrium Field Coil System[a,b]			
Volt-seconds to plasma (V-s)	50	15	55
Maximum power (MW)	420	117	126
Energy transferred (MJ)	1500	75	76
Neutral Beam Injection System			
Deuteron energy (keV)	180	125	200
Power to plasma (MW)	60	60	50
Energy to plasma (MJ)	300	120	250
Energy to injector (MJ)	1000	800	500

[a] Field-shaping coil in GA design.

[b] Two-coil magnetic system in ORNL design.

TABLE V. REFERENCE BURN CYCLE POWER PERFORMANCE

	ANL	GA	ORNL
Burn pulse length (s)	55	105	100
Downtime between pulses (s)	15	20	15
Energy through first wall (GJ)	16	42	41
Thermal conversion efficiency (%)	30	41	24
Gross electrical power (MW)	72	124	99
Net electrical power (MW)	30	37	7

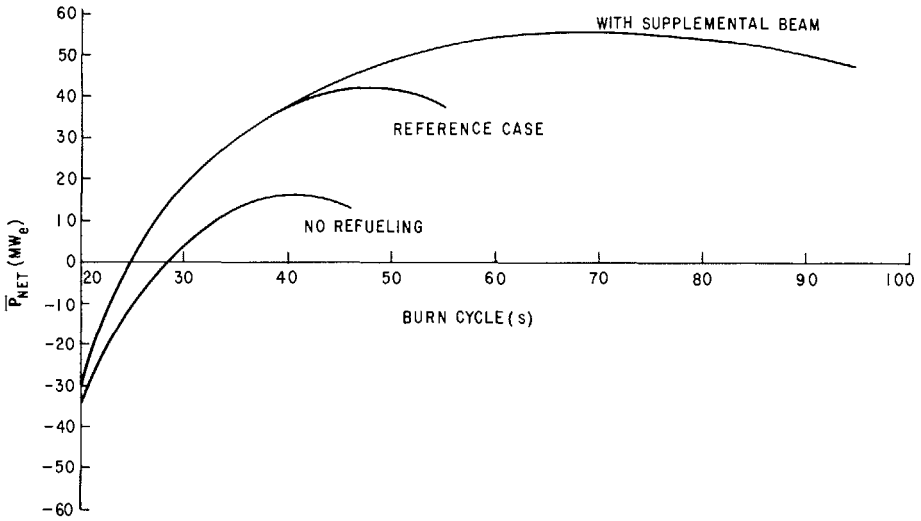


FIG.11. Power performance as a function of operating mode for the ANL design.

this case. Supplemental beam heating can also be used to achieve longer burn cycles by maintaining thermonuclear temperatures against the accumulation of wall-sputtered impurity and helium. It is assumed that the D-T ion density can be maintained during the burn by a combination of recycling and refueling; however, burn pulses up to 30-45 s may be possible without refueling, if recycling is effective. The average net electrical power for the ANL design is shown in Fig. 11 as a function of the length of the burn pulse.

3. TECHNOLOGY

3.1. First-Wall System

A first-wall system which can maintain its structural integrity under the thermal, stress, and radiation conditions imposed by the size of the vacuum chamber and the pulsed mode of operation is one of the more demanding technological requirements for the EPR. The three designs are summarized in Table VI, and the performance characteristics are given in Table VII.

The ANL design consists of a self-supporting vacuum chamber wall consisting of 16 segments, with rib-and-spar support and detachable coolant panels mounted on the inside. The vacuum vessel supports the pressure differential and gravitational loads, while the coolant panels absorb the most severe thermal loads but perform no structural function. The coolant panels are coated on the plasma side with 100-200 microns of beryllium for impurity control.

The GA first wall is formed by disk-shaped silicon-carbide liner plates, which are attached to each blanket module and cooled by thermal radiation to the blanket modules. The vacuum chamber is formed by the modules and seal rings welded between the modules and the support frame.

TABLE VI. FIRST-WALL SYSTEM DESIGN

ANL	GA	ORNL
Free-standing, 2-cm-thick 316 SS vacuum wall with rib and spar support.	Detachable, 1-cm-thick SiC liner plate disks centrally supported by bolting to blanket modules.	Four 90-deg welded segments, 1-cm thick 316 SS, honeycomb interior.
Detachable, 2-cm-thick 316 SS coolant panels.	Cooled by thermal radiation to face of blanket modules.	H_2O coolant at 50 psi; separate first-wall coolant system.
100-200 μm beryllium coating on plasma side.	Graphite filler blocks between modules directly exposed to plasma, cooled by thermal radiation.	Low-Z coating on plasma side.
H_2O coolant at 2000 psi; separate first-wall coolant system.		

TABLE VII. FIRST-WALL SYSTEM PERFORMANCE

	ANL	GA	ORNL
Vacuum Wall[a]			
Surface heat flux (MW/m^2)	0.0	0.27	0.27
Heat deposition (W/cm^3)	5.8	9.7	10.1
Maximum temperature (°C)	<500	600	125
Maximum ΔT during burn (°C)		60	20
Limiting criterion	ductility[b]	thermal fatigue	ductility[c]
Coolant Panel/Stand-off Liner			
Surface heat flux (MW/m^2)	0.13	0.17	NONE
Heat deposition (W/cm^3)	5.8	10.0	
Maximum temperature (°C)	380	1450	
Burn cycle ΔT (°C)	100	120	
Burn cycle thermal strain (%)	0.09	0.001[e]	
Limiting criterion	thermal fatigue[d]	erosion	

[a] Innermost part of blanket in GA design.

[b] 1% at 2.5 MW-yr/m^2.

[c] Unknown, ∿10 MW-yr/m^2.

[d] 5×10^6 burn cycles.

[e] Due to nonlinear temperature distribution in free-standing liner.

TABLE VIII. BLANKET/SHIELD SYSTEM

	ANL	GA	ORNL
Blanket			
Material	316 SS	316 SS	316 SS/C/K
Thickness (m)	0.28	0.25	0.52
Coolant	H_2O	He	He
Maximum temperature in structure (°C)	500	600	536
Maximum heat deposition (W/cm^3)	3.5	9.7	8.4
Bulk Shield			
Material			
inside	SS/B_4C	SS/LiH	B-H_2O/SS/Pb
outside	SS/Pb-mortar/C/Al	B_4C/Pb	B-H_2O/SS/Pb
Thickness (m)			
inside	0.58	0.40	0.48
outside	0.97	1.00	0.48
Fraction of fusion power deposited	0.07	0.01	0.07
Maximum temperature (°C)	90	165	82
Coolant	H_2O	H_2O	H_2O

In the ORNL design, an independently cooled, 1-cm-thick vacuum vessel segment is mounted on the inside of each blanket segment. This vacuum vessel is a composite Type 316 stainless steel structure with a honeycomb interior enclosed between two 0.16-cm-thick plates. Water enters at approximately 100°F and exits at about 250°F at 50 psi pressure. The wall is divided poloidally into 4 quadrants, and with 60 blanket segments there are 240 first-wall "quadrants". Between blanket segments, the wall segments are welded by bellows closures to form a vacuum chamber.

3.2. Blanket/Shield Systems

The blanket/shield system consists of the blanket, the bulk shield, and special penetration shields for the neutral beam lines, vacuum ducts, etc. The thickness of the blanket is chosen such that most of the fusion energy is deposited therein, and the thickness of the bulk shield is determined by magnet protection criteria. There is incentive to minimize the shield thickness on the inside of the torus in order to maximize the toroidal field in the plasma. Features of the three designs are summarized in Table VIII.

The blanket in the ANL design consists of 0.28-m-thick stainless steel blocks, with drilled 1-cm-diameter coolant passages, surrounding the first wall assembly. The bulk shield surrounds the blanket, varying in thickness from 0.58 cm on the inside of the torus, where highly radiation-attenuating material is used, to 0.97 m on the outside of the torus. A shield plug blocks the penetration formed by the vacuum duct during the plasma burn. Special, highly attenuating SS/B_4C shields surround the neutral beam lines after they exit from the bulk shield until they pass the TF coils. A blanket similar to that surrounding the vacuum vessel surrounds the beam penetrations through the bulk shield. The blanket and shield are segmented into 688 electrically insulated blocks to inhibit the development of eddy currents which would distort the penetration of the equilibrium field. The blanket and bulk shield are cooled by H_2O at 2000 psi and atmospheric pressure, respectively.

TABLE IX. COMPARISON OF NEUTRAL BEAM INJECTION SYSTEMS FOR ANL DESIGN[a]

	Design 1	Design 2	Design 3	Design 4
Atomic ion	D^+	D^+	D^-	D^-
Target for $D^+ \rightarrow D^0$	D_2 gas	D_2 gas	D_2 gas	Li plasma
Beam composition (D^+, D_2^+, D_3^+/D^-)	(0.75, 0.18, 0.07/-)	(0.05, 0.03, 0.02/-)	(-/0.95)	(-/0.95)
Ion beam power (MW)	441	338	113	81
No. injectors	12	12	6	6
Gas load/injector (torr-litre)	110	57	41	11
Cryosorption panel area/injector (m^2)	100	80	45	42
Power efficiency	0.34	0.45	0.66	0.77
Net power required (MW)	207	145	91	78

[a]All four systems inject 60 MW of 180 keV D^0 into the plasma.

The main body of the GA blanket, that portion in which fusion neutrons are intercepted and the thermal energy is deposited, is comprised of 1900 cylindrical blanket modules which mount onto the support structure. These 42-cm diameter by 25-cm long modules are fabricated from 20% CW Type 316 stainless steel and incorporate radial coolant holes near the front face with axial coolant passages through the interior. After passing through coolant channels in the module support ring, the 4.9 MPa helium coolant, which enters at 325°C, flows axially towards the blanket wall through coolant holes along the module circumference. The full helium flow is thereby delivered, while it is still relatively cool, to the blanket wall where the heating rates are most severe. The coolant flows radially along the blanket wall, then axially through the module interior in annular passages formed by holes with rod inserts and finally into a plenum and out of the module at 575°C. Metal temperatures do not exceed 600°C, and thermal stresses are maintained within allowable limits by selection of appropriate coolant passage size and spacing. The spaces between modules in the blanket are filled with permanent graphite blocks and graphite rings, which are removable for module maintenance. These graphite sections are cooled by radiation to the blanket modules and reach a maximum temperature of about 1600°C.

Each of the 60 blanket segments in the ORNL design has been divided poloidally into 12 modules. Each module consists of: (1) a helium-cooled liquid metal (potassium or lithium region; (2) a graphite reflector; and (3) stainless steel region. The modular division reduces coolant pressure drop by simplifying the coolant pumping. By breaking the segments into modules, eddy currents are reduced in the lithium also.

3.3. Plasma Heating

Current experience dictates that neutral beam injection be the reference option for plasma heating. The injection heating requirements are indicated in Table IV. The ANL and GA designs are based upon positive ion sources, while the ORNL design is based upon a negative ion source.

Four neutral beam injector systems capable of injecting 60 MW of 180 keV D^0 into the plasma for the ANL design are compared in Table IX. Design 1 is based upon modest extrapolations beyond present results with D^+ sources; design 2 is based upon an improved D^+ source; and designs 3 and 4, which would require considerable advance in source technology, are based upon direct-extraction D^- sources. All designs introduce large ($\sim$1/2 to 1 m^2) penetrations in the shield for neutron and gamma streaming, and design 1 has

TABLE X. TOROIDAL FIELD COIL SYSTEM

	ANL	GA	ORNL
Superconductor	NbTi	NbTi	NbTi/Nb_3Sn
Coil shape	pure-tension D	pure-tension D	minimum-bending oval
No. of coils	16	16	20
Maximum field ripple (%)	1.3	<0.1	2.2
Maximum field (T)	10.0	7.9	11.0
Field at plasma center (T)	4.5	3.9	4.8
Operating temperature (°K)	3.0	4.2	4.0
Stability	cryostatic	cryostatic	cryostatic
Temperature allowance (°K)	0.5	0.8	2/5[a]
Conductor	monolithic	monolithic	cable
Ampère-turns (MAT)	134	89	162
Average current density (A/cm^2)	1463	2039	1790
Cooling	pool boiling	pool boiling	force flow
Stored energy (GJ)	30	16.7	29
Refrigeration power (MW)	14.3	3.6	12.7

[a] 2°K for NbTi/5°K for Nb_3Sn; 12°K instantaneous rise.

very demanding vacuum system requirements. Substantial improvements in power efficiency and corresponding reductions in power requirements and gas loads can be realized if D^+ sources with a very high atomic component are developed, and even more dramatic improvements are promised by direct extraction D^- sources.

Radio-frequency heating is an attractive alternative to neutral beam heating, from the technological point of view. Efficient power sources exist for lower hybrid and ion cyclotron heating. The neutron streaming problem is less severe than with neutral beam injectors, where a straight-line penetration of the shield is intrinsic.

3.4. Toroidal Field Coils

The relatively long burn pulse dictates that the toroidal field coils be superconducting. ANL and GA chose niobium-titanium as the superconductor, because of its good ductility and proven performance in large magnets, while ORNL uses Nb_3Sn on the inside leg, to achieve high fields, and niobium-titanium elsewhere. The TF coil designs are summarized in Table X.

Superimposed pulsed fields from the poloidal coils and the plasma are one of the most difficult problems in the TF coil design. ANL employed an aluminum shield operating at 18°K to shield the TF conductor from the ac heating and out-of-plane load due to the pulsed field. In the GA design,

TABLE XI. POLOIDAL FIELD COIL SYSTEM

	OH Coil			EF Coil			
						ORNL[b]	
	ANL	GA	ORNL	ANL	GA[a]	Shield-EF	Trim-EF
Type	S/C (NbTi)	S/C (NbTi)	S/C (NbTi)	S/C (NbTi)	Cu	Cu	S/C (NbTi)
Coil design	single layer	single layer	pancake	single layer	multilayer	single turn	multilayer
Conductor	cable	cable	cable in conduit	cable	bar	monolithic	cable in conduit
Cooling	He pool boil	He pool boil	He force flow	He pool boil	oil	H_2O	He force flow
Average current density (A/cm^2)	2640	3300	1460	2946	454		
Ampere-turns (MAT)	67	71	61	±18.6	-11.6	7.2	0 (net)
Maximum operational current (kA)	80	450	100	80	75	450	400
Power supply voltage (kV)	48	10	35	21	31[a]		

[a] Field-shaping coil.
[b] Two-coil magnetic system.
[c] For plasma breakdown.

the field-shaping coil system, which is located internal to the TF coils near the plasma, significantly reduces the superimposed pulsed fields in the region of the TF coils. The ORNL design employs an electromagnetic shielding system to resolve this problem.

Unequal currents in the TF coils could create large forces and torques between coils and large bending moments in each coil, which could produce severe damage. The ANL and GA designs are protected against this possibility by series operation, with quench protection provided by discharging the TF coils through large resistors that are activated by switches. In the ORNL design, the TF coils are connected in several parallel loops, with the objective of being able to isolate and discharge only quenched coils.

3.5. Poloidal Field Coils

The poloidal coil system consists of the ohmic-heating (OH) coils, the equilibrium field (EF) or field-shaping coils, and additional coils for plasma initiation and control. The poloidal coil systems designs are summarized in Table XI.

In the ANL design, both the OH and EF coils are superconducting and are located external to the TF coils. The OH and EF coil problems are similar — large stored energy, high operational current, rapid charging and discharging and ring coil configuration. A set of water-cooled copper coils is located inside the TF coils near the plasma and is used to provide ∿500 V for plasma initiation and for equilbrium field trimming.

The GA design uses superconducting OH coils located external to the TF coils and oil-cooled, copper field-shaping coils located internal to the TF coils near the plasma. The field-shaping coils are pulsed at 30 kV to initiate the plasma.

In the ORNL design, the OH coils are superconducting and located external to the toroidal field coils. The EF coils are located both external and internal to the TF coils. The externally located EF coils are superconducting. Those located internally are normal (copper) coils. Their function is to reduce stored energy requirements, enhance the volt-second capability of the device, and to reduce the $\dot{B}$ experienced by the TF coils during the current rise phase of operation. The overall reduction in $\dot{B}$ is about a factor of 5.

TABLE XII. ENERGY TRANSFER AND STORAGE SYSTEMS — MAXIMUM RATINGS — ANL DESIGN

Ohmic Heating Systems	
Drum homopolar generators:	
No. of generators in series	16
No. of drums/generator	6
Total energy transfer (MJ)	1200
Peak power (MW)	1900
Peak voltage (kV)	51
Peak current (kA)	68
Equivalent capacitance (F)	0.897
Rectifier system:	
Type	Inductor-converter bridge
Energy transfer (MJ)	600
Peak power (MW)	66
Peak current (kA)	80
Peak voltage (kV)	0.8
Equilibrium Field System	
Type	Inductor-converter bridge
Energy transfer (MJ)	1500
Peak power (MW)	416
Peak current (kA)	80
Peak voltage (kV)	21
Peak switching frequency (Hz)	1330
Neutral Beam System[a,b] (60 MW)	
Type	SCR, DC/AC/DC at 10 kHz
Energy transfer (GJ)	1
Voltage (kV)	180
Power (MW)	207
RF System (60 MW)[b]	
Type	5-phase inductor-converter bridge
Voltage (kV):	
ICR	18
LHR	64.5
Power (MW):	
ICR	94
LHR	125
Central Energy Storage Inductor	
Type	Superconductive ring dipole inductor
Energy stored (GJ)	3.2
Energy transfer (GJ)	2.4
Peak current (kA)	80
Peak power (MW)	620
Average power from 60 Hz line (MW)	21

[a] Assumes electrical energy recovery in power supply.

[b] Neutral beam and rf are alternative options.

TABLE XIII. TRITIUM FUEL CYCLE

	ANL	GA	ORNL
Burnup (g/day)	64	53	58
Throughput/burnup ratio[a]	50	270	17
Tritium delivery rate (g/hr)	150	600	41
Fuel cycle turnaround time (hr)	4	4	
Plant inventory (kg)	1.5	4.1	5-10
Annual tritium consumption (kG)	16	3.9	18
Enrichment	cryogenic distillation	cryogenic distillation	cryogenic distillation

[a]Design basis value for sizing tritium system.

3.6. Energy Storage and Transfer

In order to operate the poloidal coil and neutral beam systems, gigajoules of energy must be transferred in times on the order of seconds. It will be necessary to store energy on site so that the large power pulses required to initiate and terminate the plasma burn do not perturb the electrical power network.

The energy storage and transfer system for the ANL design consists of a central energy storage inductor (ESI), rectifiers to transfer energy between the ESI and the OH, EF, and neutral beam systems and a rectifier to transfer energy from a substation into the ESI. A separate inertial energy storage unit, consisting of radially stacked homopolar generators, is incorporated in the OH system, so that inductive energy is transferred between the OH coils and the homopolars, with the central ESI making up losses. Electrical energy is recovered directly in the neutral beam system. This energy storage and transfer system is summarized in Table XII.

The system employed in the GA design utilizes three large homopolar motor-generator units, each with a capacity of about 500 MJ, which provide storage for dumping the OH coils and re-energizing them during the flux swing. A conventional type motor-generator with a storage capacity of 800 MJ is provided to store the energy required by the pulse mode operation of the neutral beam injectors. This motor-generator is sized so as to accommodate the excess output when the field-shaping coils are de-energized, thereby leveling the plant output. In addition, a capacitor bank with a storage capacity of 400 kJ supplies an energy pulse to the field-shaping coils, thereby providing the volt-seconds required for initial breakdown of the plasma.

3.7. Tritium Fuel Cycle

The tritium-handling system removes nonmetallic elements and other debris from the spent fuel and enriches, stores and delivers the tritium. Operating parameters for the tritium-handling systems are given in Table XIII. The fuel cycle turnaround time is determined mainly by the regeneration cycle on the cryosorption pumping system for the toroidal vacuum chamber, and minimization of this time is crucial to minimization of the tritium inventory.

TABLE XIV. RADIATION DAMAGE AT DESIGN LIFETIME

	ANL	GA	ORNL
Design lifetime integrated neutron wall load (MW-yr/m^2)	2.5	1.4	10.0
First Wall[a]			
Neutron fluence (n/cm^2)	6×10^{22}	4×10^{22}	1×10^{23}
Yield strength (10^3 psi)[b]	75	29	110
Uniform elongation (%)	>1	nil	>4
Radiation swelling (%)	<4	2	<6
Neutron damage (dpa)	28		110
Helium generation (appm)	540	2100	1290
Hydrogen generation (appm)	1330	740	4240
Blanket			
Maximum neutron fluence (n/cm^2)	5×10^{22}	4×10^{22}	7×10^{22}
Minimum yield strength (10^3 psi)	20	40	60
Minimum ductility (%)	>3	1	1
Maximum radiation swelling (%)	<2	0.3	<2
Maximum neutron damage (dpa)	17	22	10
Maximum helium generation (appm)	230	240	40
Maximum hydrogen generation (appm)	600	500	150
Toroidal Field Coil[c]			
Neutron fluence (n/cm^2)	4×10^{17}	1×10^{18}	2×10^{19}
Neutron damage to Cu stabilizers[d] (dpa)	8×10^{-5}	3×10^{-4}	4×10^{-3}
Radiation dose to insulator (rad)	4×10^{8}	1×10^{9}	2×10^{9}

[a] SiC liner in GA design.

[b] Ultimate.

[c] Maximum values.

[d] Without annealing.

3.8. Radiation Damage

Radiation damage is an important consideration in the design of the EPR. The useful lifetime of the first-wall and innermost portions of the blanket is set by radiation damage criteria and erosion rates of the low-Z liners. Shielding requirements are determined largely by radiation protection criteria for the superconducting TF coils. A summary of radiation damage data at the design lifetime is presented in Table XIV.

TABLE XV. PLANT CAPITAL INVESTMENT DIRECT COST ESTIMATES ($M)

(a) ANL	
Structure and site facilities	67.3
Reactor	248.6
Reactor plant facilities	245.0
Auxiliaries	18.0
TOTAL	578.9
Engineering (25%)	144.7
Contingency (25%)	144.7
GRAND TOTAL	868.3
(b) GA	
Fusion steam supply system:	
Equipment	179.3
Installation	37.4
Engineering	58.5
Indirects	76.3
Contingency	64.5
FSSS TOTAL	416.0
Balance of plant	279.9
GRAND TOTAL	695.9

3.9. Costs

Cost estimates for the ANL and GA designs are given in Table XV.

4. CONCLUSIONS

An EPR operating at or near net electrical power conditions with a capacity factor of 25-50% requires an extrapolation of plasma conditions (confinement, pulse length, etc.) beyond those anticipated for the most advanced experiments (PLT, T-10, D-III, PDX, etc.) that will be operational in the next few years. Advances beyond the current state-of-the-art in certain essential areas of fusion reactor technology (superconducting magnets, energy storage and transfer, neutral injectors, tritium, first-wall, etc.) are also required. Such an EPR represents a significant national investment. To achieve an EPR with these characteristics by the mid-to-late 1980s would be a bold stroke which would go far towards enabling a demonstration of commercial feasibility of fusion power by the end of the century. However, such an undertaking would require significant increases in technology development and EPR design effort as well as an acceleration of the tokamak experimental program, thus an increase in the funding level of the U. S. fusion program.

Moreover, major design decisions would have to be made on the basis of physics information which will become available in the next few years, prior to the operation of the Tokamak Fusion Test Reactor (TFTR) and probably prior to the time at which Doublet-III and PDX reach their ultimate design goals. In addition, several advanced technologies would have to be first demonstrated in a fusion reactor environment in EPR. These factors have led to a consideration of alternatives. At the moment, it appears likely that a less ambitious device which can achieve many of the EPR objectives may be built in the mid-to-late 1980s, and that the EPR may be deferred until the early 1990s.

ACKNOWLEDGMENT

The work reported in this paper was performed by the EPR design teams at ANL, GA and ORNL. The work was supported by USERDA and, in the case of GA, by the Electric Power Research Institute.

REFERENCES

[1] STACEY, W.M., Jr., et al., Tokamak Experimental Power Reactor Studies, Argonne National Laboratory Rep. ANL/CTR-75-2 (1975).

[2] GAC FUSION ENGINEERING STAFF, Experimental Power Reactor Conceptual Design Study — 12-Month Progress Report for the Period July 1, 1974, through June 30, 1975, General Atomic Company Rep. GA-A13534 (1975).

[3] ROBERTS, M., BETTIS, E.S., Oak Ridge Tokamak Experimental Power Reactor Study Reference Design, Oak Ridge National Laboratory Rep. ORNL/TM-5042 (1975).

[4] STACEY, W.M., Jr., et al., Tokamak Experimental Power Reactor Conceptual Design, Argonne National Laboratory Rep. ANL/CTR-76-3 (1976).

[5] BAKER, C.C., et al., Experimental Power Reactor Conceptual Design Study — Final Report for the Period July 1, 1974, through June 30, 1976, General Atomic Company Rep. GA-A14000 (1976).

[6] ROBERTS, M., Oak Ridge Tokamak Experimental Power Reactor Studies — 1976, Oak Ridge National Laboratory Rep. ORNL-TM-5572 (1976).

DISCUSSION

ON PAPERS IAEA-CN-35/I 3-1, I 3-2

G.H. WOLF: You have indicated that sputtering processes (on steel walls, for example) would lead after about 20 s to 200 MW of negative power, but that physical sputtering of carbon would not endanger a positive power output. Since these processes will depend strongly on both the ion energy distribution in the plasma-wall domain and the total power carried to the wall by heavy particles, it would be interesting to know, firstly, what ion temperature or energy distribution was assumed in the near-wall regime to govern these sputtering processes and, secondly, what fraction of the total power from α-particle heating was assumed to be carried to the wall by the ions or neutrals (via charge exchange).

W.M. STACEY: A Maxwellian distribution with a mean energy of 200 eV, corresponding to the assumed plasma edge temperature, was used in the calculations shown here. Other calculations have been carried out for mean energies ranging from 60 eV to 1000 eV. Although the results are, quantitatively, somewhat a function of the mean energy, the qualitative relationships remain approximately the same. For a bare support structure wall to be acceptable, mean energies below ~50 eV would be required.

The plasma energy losses are computed numerically from a rather involved dynamic power balance. The fraction of the alpha or beam power carried to the wall by ions or neutrals varies during the burn cycle, but is small compared to the conduction losses.

K.I. THOMASSEN: From start-up codes used at Los Alamos on the EPR Tokamaks, we find that start-up times of 10 s, as assumed in the Japanese design (IAEA-CN-35/I 3-1) are not realistic because even very low levels of impurities radiate more power than is being put in at this slow rate. Have the authors considered this? Also, the initial rate-of-rise of current must be much faster, and I wonder what initial voltages ($\int \vec{E} \cdot d\vec{\ell}$ around the edge of the plasma) are applied and for how long in order to do this?

T. TONE: A constant impurity level was assumed. However, I can only say that these are points which still require detailed examination.

W.M. STACEY: The US studies (IAEA-CN-35/I 3-2) do indicate that a current reversal time of 10 s would require unacceptably large energy transfer in the ohmic heating system. They point to ~2 s as the optimum for the OH current reversal.

G. CASINI: My question is related to previous comments on impurity control and first wall behaviour. In none of the US experimental reactor projects is a divertor included. Our experience with the FINTOR conceptual design (an experimental minimum-size Tokamak reactor) indicates, however that problems related to the cost and maintenance of such reactors are highly sensitive to whether a divertor is included in the design or not. We feel that maintenance problems should be given considerable weight in any exercise related to power reactors. A point that should perhaps be noted, by the way, is that in the UWMAK full-scale reactors a divertor is always included. How do you feel about this?

W.M. STACEY: We placed emphasis on designing the EPR as simply and cheaply as possible. We have all considered divertors and are aware of the engineering complexities they introduce; our general philosophy was to see if we could get by without them. The ANL calculations indicate that by using a low-Z material (e.g. beryllium) as a first-wall surface to minimize the consequences of impurity contamination, a burn pulse of the order of a minute (longer with some supplemental heating) could be achieved. We felt that this was satisfactory for an EPR.

PURE-FUSION AND FUSION-FISSION REACTOR APPLICATIONS OF HIGH-DENSITY LINEAR CONFINEMENT SYSTEMS

R.A. KRAKOWSKI, R.L.MILLER, R.L. HAGENSON*
University of California,
Los Alamos Scientific Laboratory,
Los Alamos, New Mexico

L.C. STEINHAUER, G.C. VLASES, R.T. TAUSSIG,
P.H. ROSE, A.L. HOFFMAN, D.C. QUIMBY,
G.L. WOODRUFF, H.J. WILLENBERG**
Mathematical Sciences Northwest, Inc.,
Bellevue, Washington,
United States of America

Abstract

PURE-FUSION AND FUSION-FISSION REACTOR APPLICATIONS OF HIGH-DENSITY LINEAR CONFINEMENT SYSTEMS.

Results are presented from systems studies and engineering designs of pure-fusion and fusion-fission (hybrid) reactors based upon high-β pulsed linear plasma confinement. In one concept, classical theta-pinch implosion heating and adiabatic compression is proposed, whereas a second approach proposes the use of intense laser light for pre-heating followed by a modest amount of adiabatic compression by the solenoidal fields. The scientific, technological, and economic potential for fusion or fusion-fission power offered by each concept is described.

1. Introduction

Pulsed linear fusion systems offer several generic advantages for fusion power: high-β and density, high potential for plasma equilibrium and stability, and a simple geometric configuration. The problems of particle/energy end loss and pulsed energy transfer present serious but not insurmountable technological difficulties. The classical linear theta pinch (LTP) and the laser solenoid (LS) represent two examples of this class of fusion device which have been subjected to parametric systems studies and preliminary engineering design.

The LTP and LS differ in the plasma heating method (implosion heating vs laser light absorption, both to varying degrees using adiabatic magnetic compression), and consequently the plasma size, magnet bore and field, and heating efficiency differ considerably. Practical limits on total laser energy force the LS concept to very dense (high magnetic fields) and small diameter plasmas, whereas the LTP requires larger plasma diameters for implosion heating to be effective. Consequently, the LS uses a combined high-field superconductor and several small-bore pulsed coils to achieve the required 30-50 T pulsed fields with minimum joule loss; the LTP

* Work performed under the auspices of USERDA.
** Work supported by EPRI and USERDA.

proposes a more conventional pulsed coil (non-superconducting) that produces $\sim$ 20 T. Both the LTP and LS share the significant advantages offered by linear confinement systems, and both have been considered for either fusion-fission or pure-fusion applications. Although thermonuclear temperatures ($\gtrsim$ 2 keV) and densities ($\sim 10^{22}$ m^{-3}) have been experimentally achieved by implosion-heated pinches [1], rapid plasma streaming from the open ends has limited confinement times to 2-4 μs per meter of pinch length. Hence, pinch lengths in excess of 1 km would be required to satisfy the Lawson criterion. More realistic accounting of energy losses in pulsed systems dictates plasma performance which exceed Lawson's criterion by $\sim$ 10-20, leading to unrealistically long devices. In scaling either the LTP or the LS to a power reactor, the degrading effect of particle/energy end loss on the overall energy balance can be ameliorated by: (a) inhibiting end loss by end stoppering, mirroring, or injection, and/or (b) increasing the nominal 20 MeV/n fusion neutron worth by using a fissile blanket.

2. The Linear Theta Pinch (LTP)

The LTP concept proposes plasma heating/confinement by implosion heating followed by adiabatic magnetic compression. A combination of options (a) and (b) has been conceptualized as the Linear Theta-Pinch Hybrid Reactor (LTPHR) [2,3]. The plasma physics, technological and economic interplay between these options is examined parametrically. The dependence of system performance on blanket configuration and multiplication, the magnitude of implosion heating vs adiabatic compression, locations and dimensions of magnet coils, plasma radius, and burn cycle are examined. Realistic constraints of economics, material strength, neutronic interaction between coil and blanket design, first-wall energy density, and magnetic energy transfer and storage efficiency have been imposed.

2.1 Basic Systems Design

The LTP design consists of a single discharge tube of inner radius 0.1-0.2 m formed by a fractional-turn implosion coil, surrounded by a multi-turn self-supporting compression coil [4]. Hemi-cylindrical blanket modules surround the plasma/coil region, which together form cylindrical modules of $\sim$ 1-2 m length and 1-m diameter. The assembly of modules is situated in a trench-like containment structure, shown schematically in Fig. 1.

2.2 Plasma Physics

Optimum LTP parameters are determined by a time-averaged burn and energy-balance model, which was formulated to agree with a more complete but complex time-dependent burn calculation. The more detailed dynamic calculation properly models alpha-particle thermalization and approximates axial particle/energy losses.

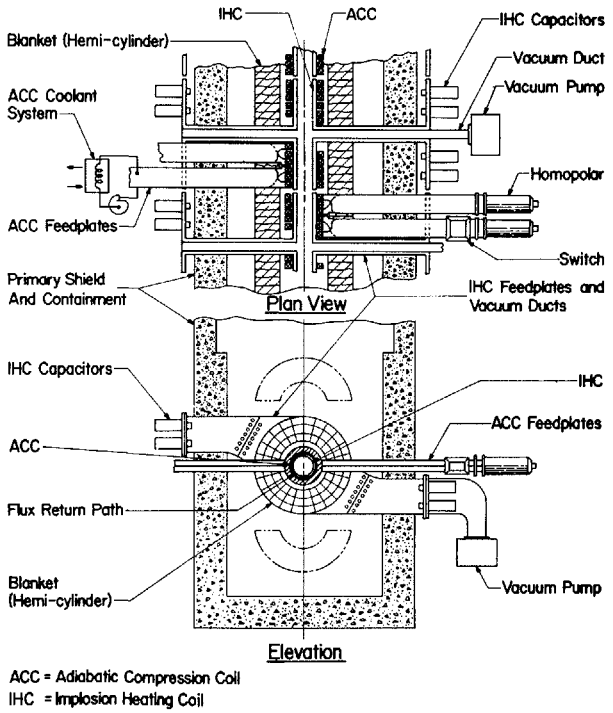


FIG.1. Elevation and plan view of Linear Theta-Pinch Reactor showing essential features of implosion heating coil (IHC), adiabatic compression coil ACC, vacuum system, and biological shield.

2.3 Implosion-Heating and Adiabatic Compression Magnets and Power Supply

The implosion heating coils (IHC) and adiabatic compression coils (ACC) are coaxial and are situated between the plasma and the blanket structure (Fig. 1). The IHC is similar to that described in Ref. [4] and is driven by a high-voltage, low-energy capacitive supply. The ACC is a fully leitzed and transposed 10-turn solenoid with internal structural support. [5,6] A fast-discharge homopolar motor/generator [7] activates the ACC, which is separated from the inner IHC by a flux-return distance determined by the overall system optimization. Both IHC and ACC power supplies are located outside the containment trench and biological shield (Fig. 1).

2.4 Blanket Neutronics

The thermal-neutron $^{232}Th/^{233}U$ blanket described in Ref. [8] was used for all fusion-fission studies to model the decrease in fusion neutron energy worth (480 MeV/n maximum) and tritium breeding ratio (1.56 maximum) with increased coil thicknesses. The neutronic/thermal/hydraulic design parallels that of a high-temperature He-cooled fission reactor, the

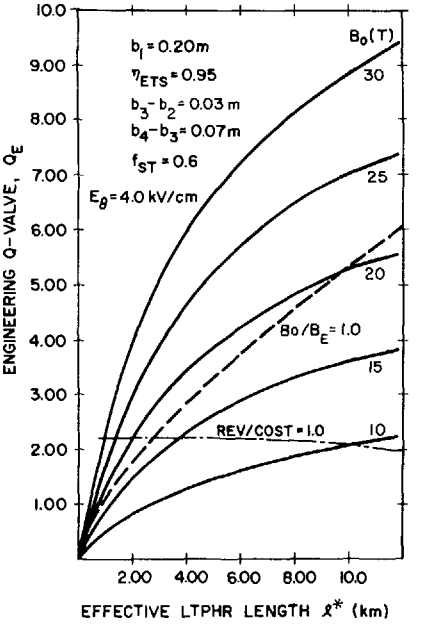


FIG. 2. Dependence of engineering Q-value Q_E (gross electrical power relative to recirculating power) on effective pinch length ℓ^* (actual length times end loss reduction factor) and maximum compression field B_0(T). The minimum Q_E for economic breakeven (REV/COST = 1.0) and maximum Q_E for cyclic fatigue (B_0/B_E = 1.0) curves are also shown. The implosion electric field is E_θ, the energy transfer and storage efficiency is η_{ETS} and optimum values of first-wall radius b_1, IHC return flux path b_3-b_2, ACC winding thickness b_4-b_3 and ACC structural fraction f_{ST} (Ref [3]) have been used.

hemi-cylindrical blanket modules have ∿ 1 m diameter and 1-2 m length, and each module would be completely decoupled from the others. Neutronic optimization of the fusion-fission blanket per se is being made by a separate study.

2.5 LTP Summary

Because of uncertainties in achievable values of certain crucial parameters, a range of operating points is shown in Fig. 2 for the fusion-fission case (LTPHR) in terms of the engineering Q-value Q_E, effective pinch length ℓ^* and maximum compression field B_O. The values of the first-wall radius b_1, IHC flux return thickness b_3-b_2, ACC winding thickness b_4-b_3, and ACC structural fraction f_{ST} represent optimum values [3]. The homopolar energy transfer system efficiency η_{ETS} = 0.95 and implosion electric field E_θ = 4 kV/cm are high but attainable given an adequate development program. The fusion neutron energy worth for the coil thicknesses shown is 412 MeV/n, or roughly 20 times that for the fusion case. All results shown in Fig. 2 pertain to an optimum D-T filling pressure (35 mTorr), the thermal-conversion efficiency is 0.4, and the true length of the device equals the effective length ℓ^* decreased by the reduction in particle end loss relative to the free-streaming case [9]. A purely sinusoidal compression field pulse of half-width equal to one end-loss time has been assumed. The locus of Q_E vs ℓ^* where economic breakeven is expected (REV/COST = 1.0, minimum Q_E) is shown in Fig. 2, as is the case for structural limits (B_O/B_E = 1.0, maximum Q_E).

Intersection of the REV/COST and B_O/B_E curves gives a minimum effective length ℓ^* of 2.8 km, which for a factor of 4 end-loss reduction results in an actual length of 700 m. The compression field B_O in this case is limited to 17 T by the structural constraint, which assures a $> 2.5 \times 10^6$ pulse endurance (cycle fatigue) limit for the ACC structure. Also for this case (REV/COST = 1.0, B_O/B_E = 1.0) Q_E = 2.2, the plasma Q-value (for 20 MeV/n) Q_p = 1.13, and for a 14.1 MeV neutron wall loading of 0.5 MW/m^2 the pulse frequency, electrical power and ^{233}U production rate are, respectively, 1 Hz, 4.64 GWe and 464 kg/y for the particular blanket considered.

The prospect for pure fusion is not promising for this low-Q_p system, considering the attendent factor of $\sim$20 reduction in neutron energy worth. Re-design of the ACC for higher compression fields [10] ($B_O \sim$ 45 T) and increased transfer efficiencies ($\eta_{ETS} \sim 0.98$) leads to $Q_E \sim 1.1$ for a 700-m pure-fusion LTP with a factor of 4 end-loss reduction (ℓ^* = 2.8 km). Furthermore, a flat-top compression field wave form [3] instead of the sinusoid will increase Q_E to 3.0, although ACC switching problems would have to be considered. Increasing the length to 1 km with a flat-top compression would yield a pure-fusion Q-value Q_E = 4.18. The optimism associated with this prediction is embodied in the achievability of the following system parameters: E_θ = 4 kV/cm, B_o = 45 T, η_{ETS} = 0.98, and ℓ^*/ℓ = 4.0.

3. Laser Solenoid (LS)

The LS concept proposes plasma heating by absorption of an axially-directed laser beam together with a moderate amount of magnetic compression. The feasibility of LS reactors was examined during a recent study [11],[12]. Plasma physics and neutronics analyses were integrated with design studies of the hybrid magnet, power supply and other system elements (laser, first wall, tritium recovery) to form point design reactors. Both fusion-fission (using option (b)) and pure fission (using option (a)) designs were developed. The relationship between performance and system parameters was also described in a fusion-fission parameter study [12].

3.1 Basic System Design

The LS employs a single steady superconductor (2 to 3-m inner diameter) enclosing a blanket and radiation shield. Four to ten small bore pulse coils (5 to 6-cm inner diameter) are spaced at intervals in the blanket. Reactor modules are 2 to 5-m in length. The pulse coils are energized in sequence, and the laser beam is directed into the proper tube by an optical transfer system.

3.2 Plasma Physics

The staged heating process (laser heating plus magnetic compression) was optimized to minimize laser energy. Plasma behavior and energy production were analyzed with a time-dependent model, which included axial particle/energy end loss,

alpha-particle thermalization and end loss, and transverse particle diffusion. The end-loss model accounted for the effects of high initial β and transverse diffusion on axial plasma motion [13]. End stoppering with ablating solid DT end plugs was examined, and quasi-steady plasma conditions were described for this configuration.

3.3 Laser

The long-pulse, scalable N_2-CO_2 laser has achieved an advanced level of development for single-pulse systems. Detailed conceptual designs of large repetitively-pulsed modular systems have been made [14]. The present study determined that large laser systems (5 to 50-MJ) could be built in 500 to 1000-kJ modules within limitations imposed by focusing and optical element damage.

3.4 Magnet System and Power Supply

The combined steady superconductor-pulse coil concept has been subject to a detailed feasibility study [15]. The superconducting magnet incorporates a support scheme which essentially eliminates strain in the windings and the surrounding support layer. This design permits a significant reduction in windings thickness compared to conventional support (0.6-m as compared to 1.6-m). Design details were determined for a 20-T superconductor employing layers of NbTi, Nb_3Sn, and V_3Ga. The superconductor can be shielded from field pulsations caused by the pulsed coils.

The pulsed coil incorporates strip-wound layers of laminated conductor and support materials, and is cooled to near room temperature. Materials problems of both magnets were assessed, including difficulties associated with high cyclic stress in the presence of intense radiation (pulsed coil). Cyclic fatigue is handled by frequent replacement (a possibility with linear systems) or by damage healing. Partial healing can be achieved *in situ* by a moderate temperature heat treatment to anneal the displacement damage without allowing mobility of radiation implanted helium atoms.

A power supply design was proposed using electrostatic storage for fast current rise in conjunction with a homopolar generator for pulse flat-topping. The power supply first excludes the field from the plasma tube (permitting creation of a nearly field-free plasma), and then raises it to approximately double the superconductor field.

3.5 Blanket Neutronics

Neutron transport calculations were carried out to determine the effects of a pulsed coil placed between the plasma and the blanket as well as other magnets nearby in the blanket [16]. The dependences of tritium breeding (and fissile breeding in fusion-fission blankets) on magnet thickness, magnet spacing, and blanket parameters were examined. Tritium breeding ratios in excess of unity can be achieved without a beryllium neutron multiplier for pulse coil thicknesses less

TABLE I. LASER SOLENOID REACTOR DESIGNS

	BREEDER A	BREEDER B	FUSION
Dimensions			
Length (m)	300	100	1000
Superconductor I.D.; O.D. (m)	------2.8;3.6------		2.7;4.3
Number of Plasma Tubes	4	4	8
Pulsed Coil I.D.; O.D. (cm)	5.8;13.8	6.2;12.4	5.6;16.8
Thermal Power (MWt)	------4000---------		3570
Laser (N_2-CO_2)			
Laser Pulse Energy (MJ)	12	5.6	43
Electrical Efficiency	----------0.25----------		
Repetition Rate (Hz)	9.3	23	0.39
Absorption	---10 x classical---		classical
Plasma			
Confinement time	----free-streaming-- (self-mirroring)		4 x free-streaming
Q_p (fusion energy/plasma energy)	1.1	0.35	67
First Wall Loading (MW/m^2)	2.4	2.1	2.8
Magnet			
Superconducting Medium	---Nb_3Sn, NbTi---		Nb_3Sn, NbTi, V_3Ga
Superconductor Field (T)	15	15	20
Pulse Coil Conductor	----------Zr-Cu----------		
Pulse Coil Support	---Be-Cu or stainless steel----		
Pulse Coil Field (T)	36	35	44
Maximum Pulse Coil Stress (MPa)	825	825	1,100
Blanket			
Tritium Breeding Medium	Li	Li	LiH
Fissile Breeding Medium	depleted uranium	96% depleted U + 4% Pu	---
Performance			
Net Electrical Power (MWe)	0	0	1000
Circulating Power Fraction	1.0	1.0	0.44
Plutonium Breeding (tonnes/y)	2.3	1.2	----

than about 8-cm and 5-cm for pure fusion and fusion-fission blankets, respectively. The net fissile breeding was between 1.5 and 3.5 atoms per source neutron, depending on fissile enrichment fraction.

Also calculated were radiation damage indices, i.e., stainless steel displacement rates, helium and hydrogen implantation rates, and neutron flux from the shield to the superconductor. Because of the line-source geometry, the

damage indices are somewhat lower than in other geometries, allowing operation at approximately twice the first-wall loading than otherwise possible. Room-temperature pulse-coil operation also minimizes the damage effects of implanted helium atoms.

3.6 LS Summary

All reactor subsystem studies were integrated with the plasma and neutronics calculations to form self-consistent conceptual designs which are summarized in Table I. The two fusion-fission designs correspond to a depleted uranium blanket (Breeder A) and one which is enriched with 10 tonnes of plutonium (Breeder B). These designs are relatively compact, are effective breeders of plutonium, and are based on levels of technology that seem readily accessible in the mid-term. Both are pure breeders, but designs that produce net electrical power have also been developed [12]. The larger pure-fusion design requires a more advanced level of technology and is at least a marginally acceptable power producer. The most serious problems relate to stresses and thermal pulsing of the magnet and first wall and are much less severe for fusion-fission designs.

4. Summary

Conceptual designs of two pulsed, linear high-β fusion systems have been summarized. Both the LTP and LS share many of the significant advantages of linear confinement systems as well as the disadvantages of plasma/energy end loss. Given a need for fusion-fission systems, the required technology and energy balance for both approaches appear reasonable and promising; pure-fusion systems are more uncertain, however. Both concepts envisage the need for moderate to high magnetic-energy transfer efficiencies and design for high cyclic stresses in the magnets. The uncertainty of high implosion-heating voltages is associated with the LTP, whereas the LS requires an efficient, high-energy rapidly-pulsed laser system. Both concepts will benefit significantly by advances in end-stoppering techniques (end plugs, multiple mirrors, cusped ends, etc). The significant advantages of compactness, modularity, favorable plasma equilibrium and stability, high β and density, proven heating machanisms, simple field configurations, direct re-fueling methods, and low sensitivity to plasma impurities give impetus to the resolution of the scientific and technological uncertainties discussed herein.

5. References

[1]. THOMAS, K. S., HARRIS, H. W., JAHODA, F. C., SAWYER, G. A., SIEMON, R. E., "Plasma Experiments on the Linear Scyllac Theta Pinch," Phys. Fluids., 17 (6), 1314 (1974).

[2]. ELLIS, W. R., KRAKOWSKI, R. A., "High Density Linear Systems for Fusion Power," Third Topical Conference on Pulsed High-Beta Plasmas, Culham, England (September 9-12, 1975).

[3]. KRAKOWSKI, R. A., MILLER, R. L., HAGENSON, R. L., "Engineering and Physics Considerations for a Linear Theta-Pinch Hybrid Reactor (LTPHR)," presented at the US-USSR Symposium on Fusion-Fission Reactors, Lawrence Livermore Laboratory, Livermore, CA (1976).

[4]. RIBE, F. L., KRAKOWSKI, R. A., THOMASSEN, K. I., COULTAS, T. A., "Engineering Design Study of a Reference Theta-Pinch Reactor (RTPR), Nucl. Fus. Suppl. on Fusion Reactor Design Problems, IAEA Conf. Culham, England (January 29 - February 15, 1974).

[5]. BARTHOLEMEW, R. J., "Structural Design Aspects of Magnetic Coils for a Linear Theta-Pinch Hybrid Reactor" USERDA Rept. LA-6256-MS, (1976).

[6]. BARTHOLEMEW, R. J., KRAKOWSKI, R. A., HAGENSON, R. L., "Structural Endurance Constraints for High-Field Theta-Pinch Coils," Trans. Am. Nucl. Soc., 22, 20 (1975).

[7]. VOGEL, H. F., BRENNAN, M., DASE, W. G., TOLK, K. M., WELDON, W. F., "Energy Storage and Transfer with Homopolar Machine for a Linear Theta-Pinch Hybrid Reactor," USERDA Rept. LA-6174 (1976).

[8]. KRAKOWSKI, R. A., DUDZIAK, D. J., OLIPHANT, T. A., THOMASSEN, K. I., BOSLER, G. E., RIBE, F. L., "Prospects for Converting ^{232}Th to ^{233}U in a Linear Theta-Pinch Hybrid Reactor," USERDA Rept. ERDA-4, DCTR Fusion-Fission Energy Systems Review Meeting, p 249, December 3-4, 1974.

[9]. FREIDBERG, J. P., WEITZNER, H., "End Loss from a Linear -Pinch," Nucl. Fus., 15, 217, (1975).

[10]. BARTHOLEMEW, R. J., personal communication, LASL (1976).

[11]. STEINHAUER, L. C., VLASES, G. C., TAUSSIG, R. T., HOFFMAN, A. L., ROSE, P. H., WILLENBERG, H. J., QUIMBY, D. C., and WOODRUFF, G. L., Electric Power Research Institute, Report ER-171 (1976).

[12]. STEINHAUER, L. C., TAUSSIG, R. T., "Laser Solenoid Fusion-Fission Design," presented at the US-USSR Symposium on Fusion-Fission Reactors, Lawrence Livermore Laboratory, Livermore, CA (1976).

[13]. STEINHAUER, L.C., Phys. Fluids 19, 738 (1976).

[14]. WILLIAMS, J., MERSON, T., FINCH, F., SCHILLING, F., and FRANK, T., in Proceedings of the First Topical Meeting on the Technology of Controlled Nuclear Fusion, G. R. Hopkins, editor, USAEC Report CONF-740402, p 70.

[15]. MARSTON, P. G., NOLAN, J. J., and AVERILL, R. J., Proceedings of the Sixth Symposium on Engineering Problems of Fusion Research (IEEE, New York, 1976), p 1123; see also "Preliminary Magnet System Study for a Laser Heated Solenoid Reactor," Mathematical Sciences Northwest, Inc., Report 75-134-7 (1975).

[16]. WOODRUFF, G. L. and QUIMBY, D. C., Trans. Am. Nucl. Soc. 22, 14 (1975); see also Mathematical Sciences Northwest, Inc. Reports 75-134-10, 11, 12 (1975).

Session XXII

REACTOR DESIGN II

Chairman

E.E. Kintner
USA

Papers I 9-1 to I 9-3 were presented
by Y. Kolesnichenko as Rapporteur

NEUTRAL BEAM INJECTOR RESEARCH AND DEVELOPMENT WORK IN THE USA

L.D. STEWART, G.C. BARBER, W.K. DAGENHART,
R.C. DAVIS, L.R. GRISHAM*, H.H. HASELTON,
J. KIM, N.S. PONTE, P.M. RYAN, D.E. SCHECHTER,
G. SCHILLING, W.L. STIRLING, C.C. TSAI,
J.H. WHEALTON, R.E. WRIGHT
Oak Ridge National Laboratory (ORNL)**

W.R. BAKER, K.H. BERKNER, W.S. COOPER,
K.W. EHLERS, J.M. HAUGHIAN, D.B. HOPKINS,
W.B. KUNKEL, B.A. PRITCHARD*, R.V. PYLE,
H.M. OWREN, J.W. STEARNS
Lawrence Berkeley Laboratory (LBL)†

O.A. ANDERSON, D.H. BIRDSALL,
D.L. CORRELL, E.B. HOOPER, Jr.,
L.C. PITTENGER, D.S. PRONO
Lawrence Livermore Laboratory (LLL)†

K. PRELEC, T. SLUYTERS, H. HALAMA
Brookhaven National Laboratory (BNL)†
United States of America

Abstract

NEUTRAL BEAM INJECTOR RESEARCH AND DEVELOPMENT WORK IN THE USA.

Neutral beam injection research and development at Brookhaven National Laboratory, Lawrence Berkeley and Livermore Laboratories, and Oak Ridge National Laboratory is described.

The ORNL Neutral Beam Development Program is concentrated on the development and application of tokamak neutral beam injection systems. Tokamak neutral beam development is being carried out for Ormak, PLT, Ormak-Upgrade, PDX and TFTR. Applications have been made to Ormak and are being made to PLT. Basic research in support of the development programme includes work in the areas of plasma sources, ion extraction and beam optics, cryopumping, beam stops and megawatt electrical power systems.

The LBL/LLL Neutral Beam Development Program can be divided into two areas: 1) Development based on positive-ion acceleration and neutralization, primarily for near-term applications on the 2X, BB, MX, and TFTR confinement experiments, and 2) a higher-efficiency-injector programme based on acceleration and neutralization of negative ions, which may be required for fusion reactors and reactor-like experiments. In addition, there is related work (not described here) on negative-ion production and on direct energy recovery.

The objective of the BNL Neutral Beam Program is to develop a 150 keV multiampere (equivalent) neutral injector with essential support systems based on long-pulse, multiampere sources of negative hydrogen and deuterium ions, close-coupled acceleration to the required energy and on neutralization of high-energy negative ions in a gas or plasma jet. High-speed cryogenic and molecular sieve pumps are being developed as part of the programme.

---

* Princeton Plasma Physics Laboratory, Princeton, New Jersey, USA.

** Operated by Union Carbide Corporation for USERDA.

† Work done under the auspices of USERDA.

1. INTRODUCTION

The US neutral-beam-injector research and development work primarily is carried out at ERDA Laboratories: Brookhaven National Laboratory (BNL), Lawrence Berkeley and Livermore Laboratories (LBL/LLL), and Oak Ridge National Laboratory (ORNL).

2. ORNL NEUTRAL BEAM WORK

2.1. ORMAK Neutral Beam Injection

More than 350 kW of neutral beam power have been injected into ORMAK, using three neutral beam systems based on 10-cm-diameter duoPIGatron ion sources [1,2,3]. This power raised the ion temperature in ORMAK to > 1.5 keV and caused the ion temperature to be higher than the electron temperature. To achieve 350 kW, it was necessary to add series floating-deck modulators[4] between the injectors and their respective high voltage supplies. It was also necessary to maximize the transmitted neutral beam power through a careful procedure of aligning the source and beam line, focusing the beam via proper grid curvature and spacing, and optimizing the source operating parameters.

Measured beam line losses were found to be consistent with those expected from inferred line densities. Thus the "choking" effect[5] was not observed over the pressure range and beam current range studied. One of the neutral injection systems is being replaced by a 15-cm duoPIGatron-based system. When this system is operational, it is expected that > 500 kW of neutral beam power will be injected.

2.2 PLT Neutral Beam Injection

1-MW neutral beam injection systems[6,7] for PLT have been designed and constructed, and testing has begun. A facility[8] for testing these and other $\leq$ 60-keV neutral beam systems has been built. Important features of the system are a 3.6-m beam line employing a 60-A, 40-keV ion source, 4 m^2 of cryocondensation pumping providing a conductance limited speed of 2-3 x 10^5 ℓ /sec, a magnet to deflect the unneutralized components to appropriate beam dumps, a tilted, movable, water-cooled calorimeter capable of dissipating peak beam power densities of 25 kW/cm^2, and a cryopanel providing 2 x 10^4 ℓ/sec in the drift tube for additional pumping in this critical region.

2.3 TFTR Neutral Beam Injection

A conceptual design[9,10] was done of the complete Tokamak Fusion Test Reactor (TFTR) neutral beam system, including injectors, beam lines, remote handling, power supplies, and controls. The neutral beam line features three 150-keV, 50-A multistage injectors, loosely coupled gas cells, one common magnet to deflect and dump the residual ion fractions, a 25-MW movable calorimeter, 50 m^2 of cryopumping surface, and a fast shutter.

A test facility[11] was constructed for the development of TFTR injectors and other $\leq$ 150-keV neutral beam systems. Experimental flexibility was achieved by constructing the test stand out of independent vacuum modules and by using a modular power supply capable of supplying a wide variety of voltages and currents. The fast floating-deck modulator for the facility consists of three 60-kV modulators in series [4].

2.4 Ion Sources

A duoPIGatron ion source with a 10-cm-diameter extraction system[2,3] was developed for neutral injection in ORMAK. It produces ion currents of $\leq$ 15 A,, voltages of $\leq$ 40 kV, and pulse lengths of $\leq$ 0.75 sec. In combination, these parameters are limited to 0.2 kJ per pulse.

The duoPIGatron source was modified by adding a line cusp or magnetic multipole[12,13] arrangement in the plasma chamber to augment plasma confinement. A version of the line cusp modified duoPIGatron with a 15-cm-diameter extraction system yields 30 A at a power supply limited voltage of 27 kV.

A line cusp modified duoPIGatron with a 20-cm-diameter extraction system is used on the PLT injectors. It has been operated at 60 A, > 30 keV and > 40 msec. Design goals are 60 A, 40 keV and 300 msec.

A magnetic multipole Mackenzie plasma source, without the duoPIGatron plasma feed, having a 15-cm-diameter extraction system has been built and tested. A noise-free, uniform, 7 x 10^{11}-cm^{-3} hydrogen plasma was produced in this source. The arc power efficiency is better than in the equivalent size modified duoPIGatron source.

2.5 Beam Optics

Experimental beam optics studies, correlated with numerical simulations, [14] have led to improved single-beamlet optics with both one- and two-stage extraction systems. Single-stage systems give half width at half maximum (HWHM) divergence angles of $\gtrsim 0.8^{o}$, with the optimum (smallest) divergences achieved with careful selection of extraction system dimensions and the shape of the first electrode aperture.

Two-stage extraction systems give HWHM divergence angles of $\sim 0.5^{o}$ for beam energies up to 60 keV. It is found both experimentally and with the simulations that the minimum divergence occurs when the ratio of the second (accelerating) gap voltage to the first (extraction) gap voltage is greater than $\sim$4.

2.6 H^+ Enhancement

Increasing the full energy component of the neutral beam by increasing the H^+ component in the plasma source results in better penetration of the plasma by the neutral beam. The H^+ fraction in duoPIGatron ion sources was enhanced by predissociating the hydrogen gas prior to the arc discharge and simultaneously minimizing the recombination rate on internal surfaces. The hydrogen feed was through a $\sim$ 2400-K tungsten oven, which was both a thermal dissociator and a cathode. This gave the beam a H^+ component of 75%, as opposed to a 55% H^+ component without the tungsten oven.

3. LBL/LLL NEUTRAL BEAM WORK

The LBL/LLL Neutral Beam Development Program can be divided into two areas: 1. Development based on positive-ion acceleration and neutralization, primarily for near-term applications on the 2X, BB, MX, and TFTR confinement experiments, and 2. a higher-efficiency-injector program based on acceleration and neutralization of negative ions, which may be required for fusion reactors and reactor-like experiments. In addition there is related work (not described here) on negative-ion production and on direct energy recovery [15].

3.1 Positive-Ion-Based Development

3.1.1 TFTR Neutral Beam System Development

3.1.1.1 Conceptual Design

A conceptual design of a neutral beam system for TFTR has been carried out [16]. This system will use three rectangular sources, producing beams optimally matched to the apertures into TFTR. Pumping is by cryocondensation pumps; a sweep magnet deflects particles into "inertial" beam dumps (i.e., not dynamically cooled during the pulse). A computer system is used for beam diagnostics and control of the system. We expect to complete the engineering design by June 1977.

3.1.1.2 Test Facilities

Large test stands for TFTR and other neutral beam development projects are under construction.

We are completing a new facility[17] at LBL with power supplies capable of producing 150 kV, 20 A, 0.5 sec pulses. The gas load from the test sources is handled by a combination of expansion into an evacuated 170,000 liter volume and pumping by two 0.9-m diameter oil diffusion pumps (65,000 ℓ/sec speed) and two titanium sublimation pumps (16,000 ℓ/sec).

The high voltage power supply for this facility consists of three 50-kV, 20 A, 0.5 sec transformer-rectifier modules connected in series. Shunt regulation is used[18]; switching and fast crowbarring is done by two high-voltage silicon-controlled rectifier assemblies. A good degree of isolation between the neutral beam source and the energy stored in stray capacitance in the power supply is provided by a set of tape-wound cores surrounding the connecting electrical leads; the cores absorb most of the energy in case of a short between accelerator grids.

Early in 1977 a second, independent beam line will be added to this facility, with power supplies capable of 150 kV, 80 A, 30 msec pulses.

Construction is underway on the High Voltage Test Stand (HVTS) at LLL, which will be used for production of 200 keV efficient (D^-) beams, for testing a full-size TFTR module for 0.5 sec and MX sources for 30 sec. This facility will be capable of 200 kV, 25 A, dc, or 120 kV, 65 A, 30 sec, or 80 kV, 80 A, up to 30 sec. Cryocondensation pumping is used throughout, with a total pumping speed of 950,000 ℓ/sec for deuterium. The facility is expected to be operational in mid-1977.

3.1.1.3 Source Development

A first model of a TFTR neutral beam source has been constructed and will be the first item tested on the new LBL test facility. This source will operate with the same beam energy, current density, and accelerator grid geometry of a full-size TFTR source, but will have only 1/4 the area. The accelerator structure has four grids, of molybdenum, with provision for cooling one end of each grid rail. The shapes of the rails were computer-optimized to provide optimum ion optics with minimum interception of secondary particles.

A 15-cm-diameter ("10-Ampere") source has been modified to demonstrate the long-pulse ($\gtrsim$ 1/2 sec) capability required by TFTR and other experiments now being planned. This source has 56 tungsten filaments, operated with dc heater current, and oriented so as to provide a ring-shaped region of magnetic

field (about 45 gauss) between the plasma volume and the outer wall. Langmuir probe measurements indicate that the deuterium ion current density in the central 8 cm diameter region is uniform to ± 1% in space and time for 1 sec pulses at $j_+ = 0.25$ A/cm^2 and to ± 4% for 0.5 sec pulses at $j_+ = 0.5$ A/cm^2. No filament lifetime tests have been performed, but the source has produced in excess of 4000 0.5-sec-long pulses at 0.35 A/cm^2.

This source was coupled to a standard "10-A" accelerating structure with uncooled Mo and W rails, and successfully produced 1.0-sec, 7.5 A deuterium beam pulses at 15 keV ($j_+ = 0.25$ A/cm^2), and 0.75-sec, 15 A pulses at 20 keV ($j_+ = 0.5$ A/cm^2).

Eventual improvements in gas efficiency, control of ion species, ion temperature, and electrical efficiency require a better understanding of the physics of the plasma source. A combined experimental and theoretical advanced development program is underway to achieve this understanding.

3.1.2 MX and BB Neutral-Beam-System Development

Development of 80 keV injectors for the large MX mirror experiment, and 50 keV injectors for the Baseball mirror experiment is in progress; the design of these injectors is based on modification and extensions of the TFTR design.

3.2 Efficient Neutral Beam Production by Negative Ions

Our primary approach is to produce a beam of 1 keV D^+ ions, convert a fraction of them to negatives in a Cs charge-exchange cell, and accelerate the resulting D^- beam first to 100 keV, then at a later date, to 200 keV. A modified LBL "10-A" source is used to produce 10 A of 1 keV deuterium ions in a 10 msec pulse. In the present experiment about 1 A of the beam passes through the narrow apertures of the Cs cell. At least 18% of these 1 keV ions are converted to D^- ions in a Cs cell; these will be accelerated to 100 keV in an accelerator nearing completion. Long pulses at much higher currents will be accelerated to 200 keV after completion of the High Voltage Test Stand.

The transport of a dense, low-energy negative ion beam has been achieved experimentally and also studied computationally; measured profiles (through the beam) of $V_{floating}$, n_i, and n_e show good agreement with those from a computer model. The electron density can be kept low; even some focusing of the beam by plasma potentials should be possible. There are also additional small experiments and theoretical studies of D^- production techniques.

4. BNL NEUTRAL BEAM DEVELOPMENT

The objective of the BNL Neutral Beam Program is to develop a 150 keV multiampere (equivalent) neutral injector with essential support systems based on long pulse, multiampere sources of negative hydrogen and deuterium ions, close coupled acceleration to the required energy and on neutralization of high energy negative ions in a gas or plasma jet. High speed cryogenic and molecular sieve pumps are being developed as part of the program.

4.1 Negative Ion Sources

Three types of negative ion sources are being investigated: magnetron, Penning and hollow discharge duoplasmatron (HDD). Their common features are a cold cathode operation mode and the addition of cesium vapors. A magnetron

source with a cathode area of 13.5 cm^2 was designed and tested [19]. Using six extraction slits with a total extraction area of 1.3 cm^2, H^- currents of up to 0.9 A were obtained in pulses of 10 ms duration and at a pulse rate of 0.1 Hz. The extraction voltage was up to 18 kV and the gas flow about 3-4 torr ℓ/cm^2s. It was possible to extend the pulse length to 20 ms, but due to the arc power supply limitations the H^- yield was only 0.6 A. A small Penning source with a cathode area of 2 cm^2 was tested, yielding H^- currents above 100 mA from a three slit aperture with an area of 0.3 cm^2. Pulse length was 20 ms and the pulse rate 0.1 s. Compared to the magnetron source, a Penning source has a lower arc power efficiency, but its gas efficiency is appreciably better. A larger model, for H^- currents up to 1 A, is under construction. Finally, H^- currents up to 60 mA were obtained from a HDD source,[20] with a current density above 1 A/cm^2 at the extraction aperture. Studies of the cathode temperature control for magnetron and Penning sources are underway, with the goal to design a source capable of operating with pulses of 0.1 to 1 s duration.

4.2 150 kV Test Facility

The accelerating system (150 kV) has been designed by computing particle trajectories in a single slit geometry. At an initial current density of 0.5 A/cm^2 calculations predict a quasi-parallel beam. The 150 kV test facility has been constructed and initial tests with high energy H^- beam have begun. As a part of the focusing system an air core quadrupole was constructed producing a uniform gradient of 0.05 T/cm within a 7 x 7 cm^2 aperture.

4.3 Cryopumping

A 100,000 ℓ/s cryopump was put into operation. Its design was based on small model measurements of properties of frozen hydrogen and deuterium layers. Pumping speed measurements showed values of 120,000 ℓ/s for hydrogen and 100,000 ℓ/s for deuterium, dropping by about 20% with a 0.2 mm thick frozen gas layer.

REFERENCES

[1] JERNIGAN, T. C., et al., Proc. 2nd Symposium on Ion Sources and Formation of Ion Beams, Berkeley (1974).

[2] STIRLING, W. L., et al., Proc. 2nd Symposium on Ion Sources and Formation of Ion Beams, Berkeley (1974).

[3] DAVIS, R. L., et al., Rev. Sci. Instrum. 46, 5 (1975) 576.

[4] PONTE, N. S., SCHILLING, G., Proc 6th Symposium on Engineering Problems of Fusion Research, New York (1976) 683.

[5] RIVIERE, A. C., SHEFFIELD, J., Nucl. Fusion 15, 5 (1975) 944.

[6] HASELTON, H. H., ORNL/PLT Neutral Beam Injection Systems Major Project Proposal, ORNL/TM-5234, Oak Ridge (1976).

[7] HASELTON, H. H., et al., Proc. 6th Symposium on Engineering Problems of Fusion Research, New York (1976) 865.

[8] DAGENHART, W. K., ORNL Medium Energy Neutral Beam Test Facility Major Project Proposal, ORNL/TM-5235, Oak Ridge (1976).

[9] SCHILLING, G., TFTR Neutral Beam Systems Conceptual Design, ORNL/TM-5227, Oak Ridge (1976).

[10] CANNON, D. D., et al., Proc. 6th Symposium on Engineering Problems of Fusion Research, New York (1976) 860.

[11] SCHILLING, G., et al., Proc. 6th Symposium on Engineering Problems of Fusion Research, New York (1976) 191.

[12] LIMPAECHER, R., MACKENZIE, K. R., Rev. Sci. Instrum. 44, 6 (1973) 726.

[13] LEUNG, K. N., et al., Phys. Lett. 51A 8 (1975) 490.

[14] JAEGER, E. F., WHITSON, J. C., Numerical Simulation for Axially Symmetric Beamlets in the DuoPIGatron Ion Source, ORNL/TM-4990, Oak Ridge (1975).

[15] MOIR, R., et al., "Mirror Reactor Studies," paper CN-35/12, this conference.

[16] "TFTR Neutral Beam Injection System Conceptual Design," LBL-3296, August, 1975.

[17] EHLERS, K. W., et al., "120-keV Neutral-Beam Injection System Development," LBL-4471, February 1976.

[18] HOPKINS, D. B., et al., "A Shunt Regulator for 150-kV, 20-A, 0.5-sec Neutral-Beam-Source Power Supplies," LBL-4452, February 1976.

[19] PRELEC, K., SLUYTERS, Th., Proc. 6th Symp. Eng. Problems of Fusion Research, San Diego, p. 430 (1975).

[20] KOBAYASHI, M., et al., (to be published in Rev. Sci. Instrum.).

DISCUSSION

ON PAPER IAEA-CN-35/I 5

R.W. MOIR: At LLL/LBL we are preparing a beam direct converter to operate on the 120-keV, 10-A (10 cm × 10 cm) beam. The purpose of the beam direct converter is to raise the efficiency of neutral beam injectors for energies over 100 keV D^0.

R.F. POST: Do you think that enough research and development work is being done on negative ion beams, so that beams in the 500-keV range will be ready for post-TFTR tokamaks?

L.D. STEWART: I think that we should increase the pace of the research and development programme for producing efficient, high-energy, neutral-beam systems.

DEVELOPMENT OF FAST NEUTRAL BEAM INJECTORS AT FONTENAY-AUX-ROSES

A. BARIAUD, R. BECHERER, J.F. BONNAL,
J. DRUAUX, M. FUMELLI, R. OBERSON,
P.A. RAIMBAULT, F.P.G. VALCKX
Association Euratom-CEA sur la fusion,
Département de physique du plasma
et de la fusion contrôlée,
Centre d'études nucléaires,
Fontenay-aux-Roses,
France

Abstract

DEVELOPMENT OF FAST NEUTRAL BEAM INJECTORS AT FONTENAY-AUX-ROSES.

The fast neutral beam injection system of TFR, based on ten Duopigatrons, is outlined and its evolution briefly described. For the development of high-power injectors, needed for JET and other European confinement experiments, a collaborative programme is being carried out at Culham and at Fontenay. A survey is given of the results obtained at Fontenay on different injector components: the high-current Periplasmatron ion source; water-cooled extraction grids; and energy recovery systems for the residual charged beam fraction.

1. INTRODUCTION

Since 1970, the power of fast neutral beams has grown at a spectacular rate, and successful plasma heating by neutral beam injection has been demonstrated on tokamaks in different countries.

For the next generation of fusion experiments on magnetically confined plasmas, the requirements for the injectors considerably exceed the present state of the art. For JET the demands are 1-MW injectors operating with pulse lengths of several seconds and at an energy of 80 keV (H) or 160 keV (D). Such high-power, high-energy and long-pulse injectors require very high current ion sources, extraction systems with post-acceleration and adequate cooling, very reliable high-power, fast protection systems, and high-speed clean pumping systems for the considerable amount of gas that has to be admitted into the injectors. At the higher energies needed for neutral injection in JET, the neutralization efficiency for protons and deuterons drops to a low value and it would be very interesting to use an efficient energy recovery system for the residual charged beam fraction instead of using a beam dump for the very high power ion beam.

In close collaboration with Culham Laboratory and under the supervision of the JET Group, high-power injectors are being developed at Culham and at our laboratory. At Fontenay the effort is mainly concentrated on the development of the high-current Periplasmatron ion source, of water-cooled extraction grids and of energy recovery systems.

Although the programme is specially aimed at the requirements of JET, it is evident that the results will be of great importance for other confinement experiments like Asdex and Torus II.

2. THE FAST NEUTRAL INJECTORS ON TFR

On TFR the injection of the neutral beams is realized by means of two diametrically opposite injection lines. Each line bears five separate injectors. The gas pumping is realized with water-cooled titanium getter pumps. The beams are injected almost perpendicularly, at an angle of

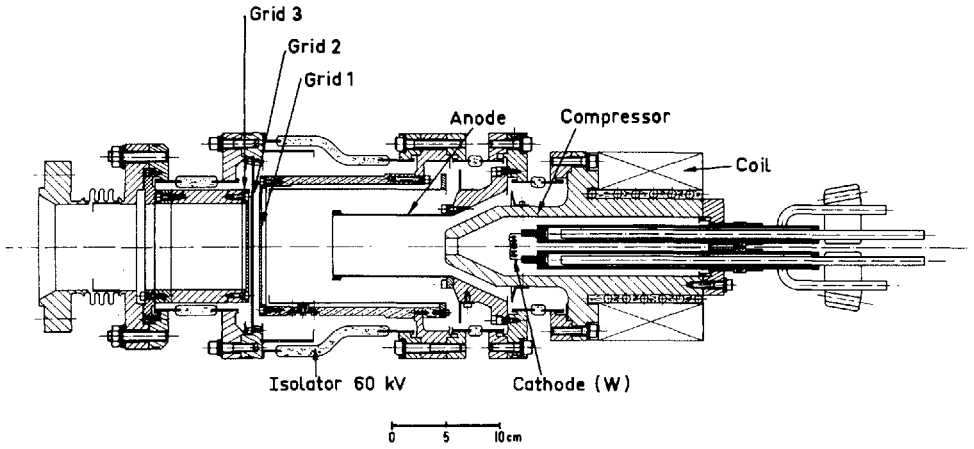


FIG.1. A TFR Duopigatron ion source.

10° with the local meridian plane, which for most particles is sufficient to avoid being trapped in the local mirrors of the toroidal field. The physics of the injection experiments and the results obtained are given in another paper in these Proceedings [1]. For the ten ion sources, Duopigatrons have been chosen, which at the time of decision was the only operational type of multi-ampère source. The injectors had to be mounted very close together for access and efficiency, and a complete modification of the original Oak Ridge design [2] was necessary. An all metal and glass design without any O-ring was adopted (Fig. 1). For the first series of injection experiments in 1975, very conservative operation conditions were chosen to ensure reliable functioning of the ten sources simultaneously [3]. In that period, a power of 450 kW could be injected with deuterium beams of 30 kV. The total extracted power was then 1.2 MW. A series of experiments on a test facility allowed these performances to be considerably improved. The anodes of the sources were modified, which resulted in a more reliable operation at large extracted currents. Furthermore, the extraction grid systems were modified to ensure a better adaptation to the radial plasma density variation and to provide for better beam focusing. With these improvements the total injected power could be raised to 700 kW (D-beam at 30 kV) for a total extracted power of 1.8 MW.

For TFR 600, the diameter of the extraction grids will be enlarged from 8 cm to 10 cm. This should allow the injected power to be raised again by about 50%. For the proposed tokamak Torus II at our laboratory, fast neutral injection is considered at a level of 2 – 10 MW, with 1 MW units, based on the Periplasmatron [4].

3. DEVELOPMENT OF HIGH-POWER FAST NEUTRAL INJECTOR COMPONENTS

This section describes the main results obtained in the development of the Periplasmatron, of cooled extraction grid systems and of energy-recovery systems.

3.1. The Periplasmatron

The idea of the Periplasmatron was conceived after it became clear how difficult it was to obtain a uniform plasma in a Duopigatron and that this would considerably hamper its

extension to high currents. The basic idea is that the plasma would be much more uniform if the primary electrons are shot into the plasma chamber from the outer border. The first encouraging results were obtained with a modified annular Duoplasmatron. The concept of the Periplasmatron has since been proved sane, and very powerful sources can now be realized [5].

In a Periplasmatron the cathode is formed by a ring of tungsten filaments, mounted between two ferromagnetic intermediate electrodes (Fig. 2). With two coils a weak cusped magnetic field is formed which temporarily captures the primary electrons. The anodes are shielded by the magnetic field. The front and back of the chamber are at a quasifloating potential. The spatial distribution of the electrons bouncing in the magnetic well and the rapid diffusion of the plasma through the weak magnetic field assure a nearly uniform plasma density. The conductance between the intermediate electrodes is very large; therefore no pressure drop exists between the cathode chamber and the main plasma chamber, where the pressure is about 1×10^{-2} torr. Consequently no double sheath exists between the intermediate electrodes (as there does in a Duopigatron). At zero magnetic field, thus without any electron capture, the number of ions produced per primary electron is 0.3. This value rises with the magnetic field intensity to attain 1 for a field strength of 40 G at the intermediate electrodes. The mean electron Larmor radius is then about half the distance between the anodes. Up to that field strength the discharge is very quiet. For higher fields it becomes unstable: the collisional electron drift becomes too slow and the arc current can only be maintained by collective motion. The plasma density is a linear function of the arc current (Fig. 3). At 200 A an ion beam of 20 A is currently extracted at 30 keV, using a 14-cm extraction system. At 400 A the source could deliver 40 A, always in a quiet regime.

For hydrogen gas the ion species extracted from the source have been determined by magnetic analysis. At 200 A arc current the ratios of the H^+, H_2^+ and H_3^+ species are 70%, 25% and 5%.

A rectangular version of the Periplasmatron is under study. Its extraction region has a surface of 40 cm $\times$ 10 cm . This source is designed for extracted currents of 50–80 A. Probe measurements have shown that the current density can be 300 $mA \cdot cm^{-2}$ for 250 A arc current.

The ion sources which have so far generally been used for heating experiments are the Duopigatron [6] and the Berkeley sources [7]. These sources are now being modified in order to obtain the high-current, long-pulse operation necessary for TFTR, MX and Doublet III. The performances are improving rapidly and it is difficult to make a balance now. Table I gives tentative data of the most intense Berkeley source, of a long pulse version of that source [8], of the standard and the "two-stage" [9] Duopigatron and of the Periplasmatron.

A special characteristic of the Duopigatron plasma is its high molecular ion content. Furthermore, the specific source power per unit of extracted current for the Berkeley sources and the two-stage Duopigatron is very high, almost twice the specific power of a Periplasmatron.

One of the most important criteria for the choice of an ion source will be its reliability in operation. It can be noticed that the cathode filaments of the Periplasmatron are operated in a very moderate regime. During one and a half years of intense operation not a single filament failure has occurred.

3.2. Water-cooled extraction grids

The only essential limitation to the extension of the pulse length of injection is the heating of the extraction grids. On the injectors now in operation these grids are generally made of copper plates. They heat up adiabatically during the pulse and cool down by conduction between the pulses. (On the Berkeley sources a more complicated slit system is used.) The temperature rise of the grids has to be limited in order to prevent too large an expansion, which would cause the beam quality to deteriorate [10]. For a pulse length of seconds the grids must be cooled or, alternatively, working with very low mean current densities should be accepted.

At Fontenay a series of tests is being made on water-cooled grid systems. Special attention is paid to the technological side of the problem, in order to select an adequate mechanical design,

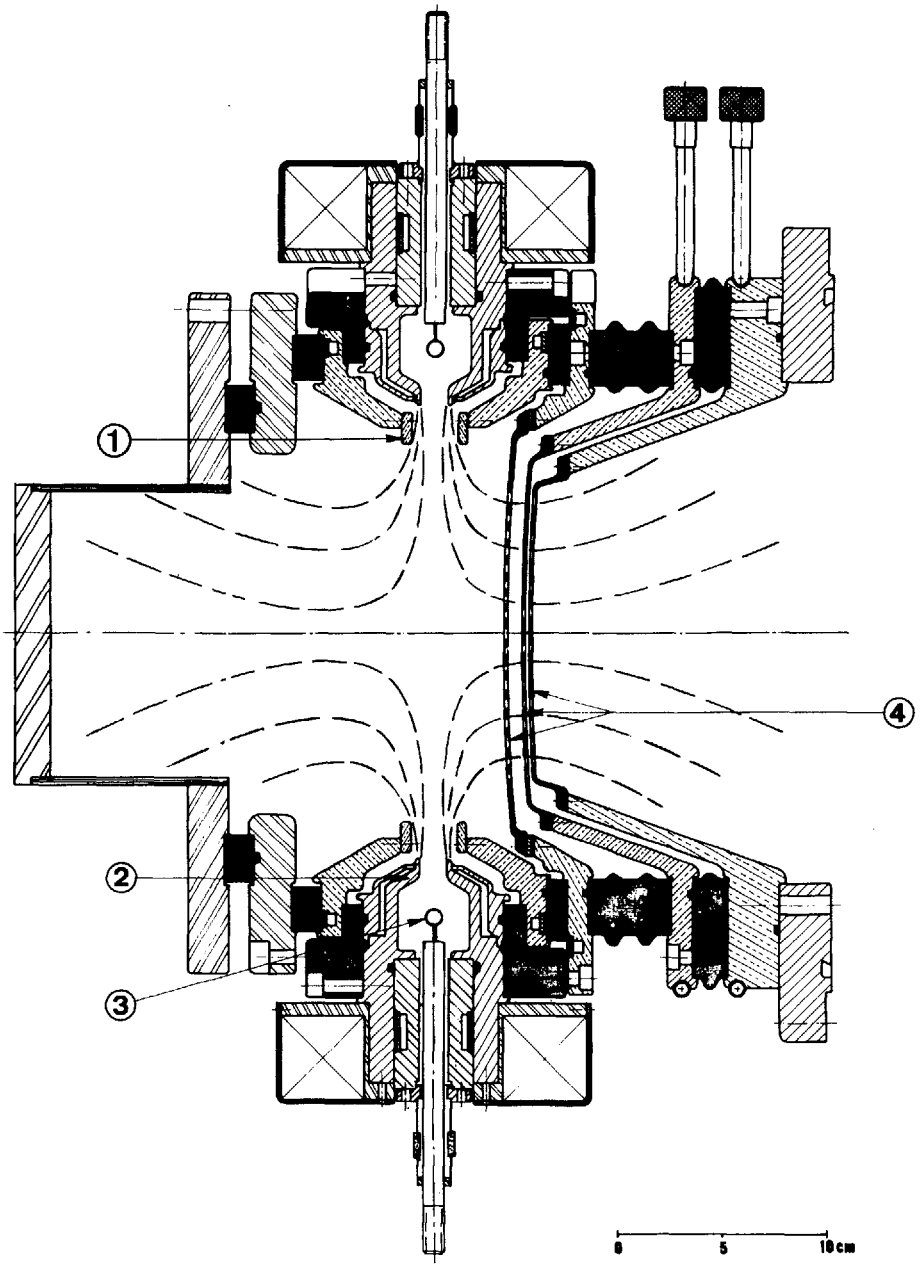


FIG.2. The Periplasmatron ion source: (1) anodes; (2) intermediate electrodes; (3) tungsten spiral filaments; (4) extraction grids.

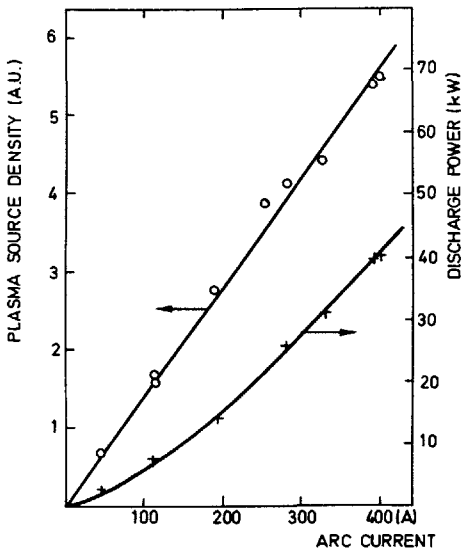


FIG.3. Periplasmatron plasma density and discharge power as a function of the arc current.

TABLE I. TENTATIVE DATA OF MOST INTENSE ION SOURCES

	Berkeley sources		Duopigatron		Periplasmatron	
			Standard	"Two-stage"	Circular	Rectangular
Extr. current (A)	80	7.5	8	40	20 (40)	(60)
Extr. region (cm)	35 × 7	7 × 7	ø 7	ø 20	ø 14	
Current density ($A \cdot cm^{-2}$)	0.5	0.25	0.4		0.2 (0.4)	(0.3)
Pulse length(s)	0.01	1	0.2	0.05	0.2	
Species (%): H^+, H_2^+, H_3^+			40, 50, 10		70, 25, 5	
D^+, D_2^+, D_3^+	75, 18, 7	67, 29, 4				
Source power (kW)	170	35	10	80	25 50	50

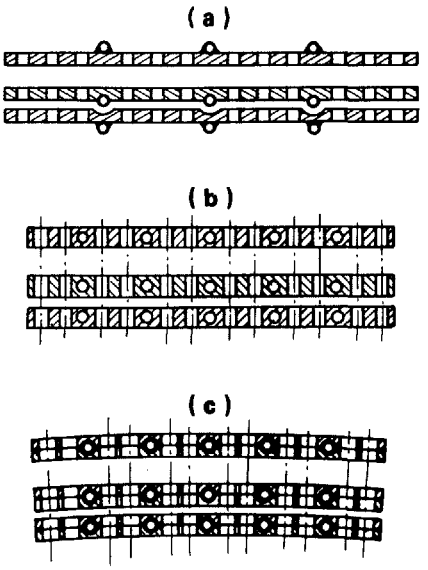


FIG.4. Water-cooled extraction grids: (a) copper tubes silver-soldered on the grids; (b) cooling channels drilled in the copper plates; (c) copper tubing sandwiched in the plates.

without trying for the moment to minimize the power deposited into the grids. Three types of construction have been realized (Fig. 4). A series of measurements with (b)-type grids shows that the relative power deposited in the grids is a weak function of the perveance[1] (Fig. 5). Its minimum lies at a perveance somewhat higher than that for optimum beam transmission. The relative power in the grids agrees fairly well with the figures observed at Oak Ridge [11] except for the third grid, where our values lie a factor of two higher. However, these measurements were made with thick grids without the intention of obtaining good optics; therefore this certainly can be improved. From the measurements it can be deduced that a mean power deposition of 200 $W \cdot cm^{-2}$ in each grid can be handled in continuous operation for this type of copper grid, without too serious effects for the beam optics. At high energy the beam divergence will be less, and consequently the relative power in the grids will be reduced. If, for example, one assumes for an 80-keV hydrogen beam a power deposition of 2% in each grid, then the mean current density could be 100 $mA \cdot cm^{-2}$, i.e. an extracted current density of 330 mA for a system with a transparency of 30%.

For a 1-MW beam this would give an extraction area of, e.g., 50 cm × 12 cm, which seems reasonable.

3.3. Energy recovery systems

In future experiments neutral beams of higher energy have to be used to reach the central region of the plasma. At 30 keV the neutralization efficiency η for protons is high ($\approx$ 80%) but, unfortunately, η drops to a very low value at high energies [12]. For molecular ions, η drops to a low constant value (10–20%) and stays high only for negative ions at higher energy (60–80%).

[1] $I_{extr}/V_{extr}^{3/2}$ = perveance.

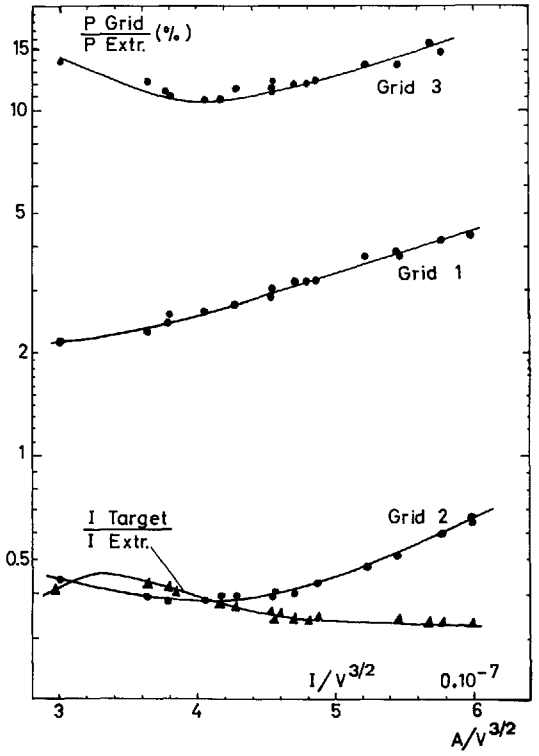


FIG.5. Relative power in the extraction grids and relative current on a target, as a function of the perveance.

Injectors based on negative ions are very complex and in a very early stage of development. Therefore it is important to provide for energy recovery systems, not only in order to improve the energy balance and to reduce the costs of investments, but also because the presence of a very high power ion beam poses serious problems for wall-heating, sputtering and outgassing.

Several systems of energy recovery have been proposed [5, 13–15]. Basic schemes for a recovery system for the case where the source is operated at the earth potential are shown in Fig. 6 and a typical potential distribution in Fig. 7. The ions are accelerated into the neutralizer biased at the high negative voltage corresponding to the desired energy. The residual ions at the exit of the neutralizer are decelerated to a very low energy and captured on suitable electrodes, which are close to earth potential. In principle, the current charge of the neutralizer and thus of the HV system is just the current corresponding to the neutral beam intensity; the residual ions do not charge the HV power supply. An electron suppressor grid is necessary to prevent the ejection of free electrons from the neutralizer and their acceleration to the recovery electrode. Several versions of such a recovery system are possible. In system (a) the whole recovery system is in the beam path, with a transparency as high as possible. However, the power flux, especially on the first row of electrodes, can be very high (some 10 $kW \cdot cm^{-2}$),which limits the possible beam pulse length to 0.2 – 0.5 s. A solution to this problem is to split up the main beam in a number of plane beams, as in system (b).

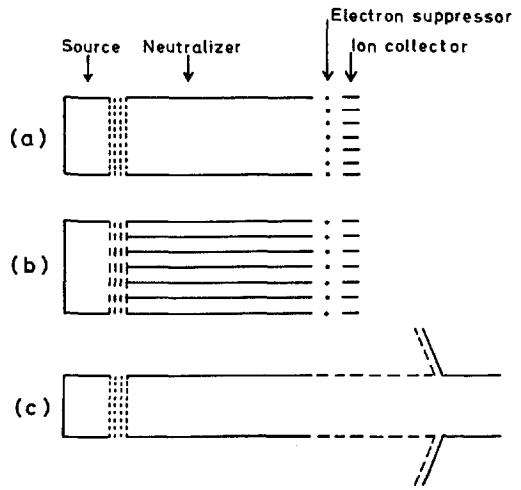


FIG. 6. Three basic energy recovery systems.

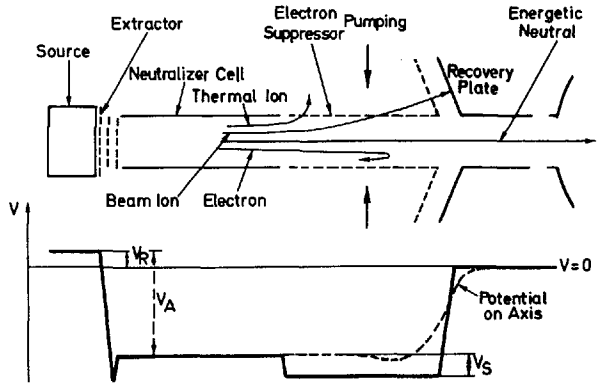


FIG. 7. Injection line with external recovery system.

The difficulty with this system is the necessity for perfect alignment of the individual beams and the need for very low divergence of the beams. Even then the overall transparency of the complete system is very low, and ion sources with a very large extraction area should be used. Detailed calculations of the possibilities and limitations of systems (a) and (b) have been made [16]. The most promising scheme seems to be system (c) (see also Fig. 7). Here the negative potential barrier for the electrons is imposed on the beam by a rather long, highly transparent, cylindrical grid. In the plasma sheath between the neutralizer plasma and the grid, the ions are gradually deflected out of

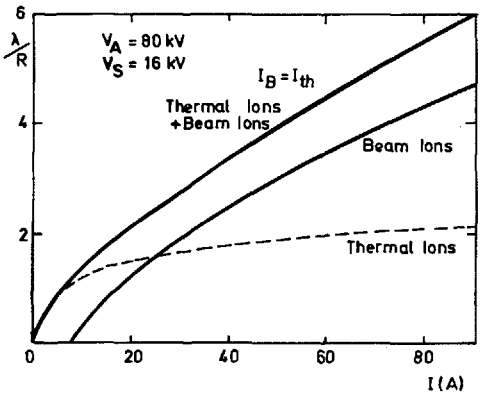


FIG.8. Relative suppression length as a function of the ion beam current and the cold ion current.

the beam path, thus increasing the width of this sheath until finally the sheath thickness equals the radius of the grid. At that point all the electrons are stopped. The remaining part of the ion beam blows up rapidly by its space charge and by the deceleration at the end of the grid; then the ions are captured on the recovery electrodes. The mean fast ion flux on the suppressor grid is much lower than in system (a) and pulses of several seconds are realizable. Numerical and analytical models have been used to derive the scaling laws of the systems, taking into account all the species, i.e. the fast beam ions and neutrals, the ions and electrons formed in the neutralizer, and also those formed in the suppressor region.

In Fig. 8 is shown the suppression length relative to the suppressor radius for different fast and cold ion currents coming from the neutralizer. In this special case the ionization in the suppressor is considered to be negligible. The length is also a function of the suppressor voltage, which in this case was 20% of the acceleration voltage.

Experiments on electron suppression have been made with the system of Fig. 9 to test the calculated scaling laws.

In Fig. 10 are given the measured critical suppressor voltages needed as a function of the extracted ion current for a high (curve b) and low (curve d) pressure in the suppressor grid. These curves can be compared with c and c', calculated for the case of zero pressure in the neutralizer, and a and a' where it is presumed that the ion beam does not expand artificially. It is clear that the reduction of the pressure considerably reduces the suppressor voltage. It also reduces the current to the suppressor system and thus the power loss in this part. At higher energies this power loss is dominated by the interception of a fraction of the fast ions on the grid. The relative power in the suppressor grid is then

$$\frac{P\ grid}{P\ extr} = (1 - T)(1 - \eta) \qquad (1)$$

where T is the transparency of the grid. For 80-keV hydrogen beams this power can amount to about 5% of the extracted power. After electron suppression, the residual ions are decelerated to about 10% of their original energy and then captured on the recovery electrodes. This means that the overall recovery efficiency for one species can be 85%.

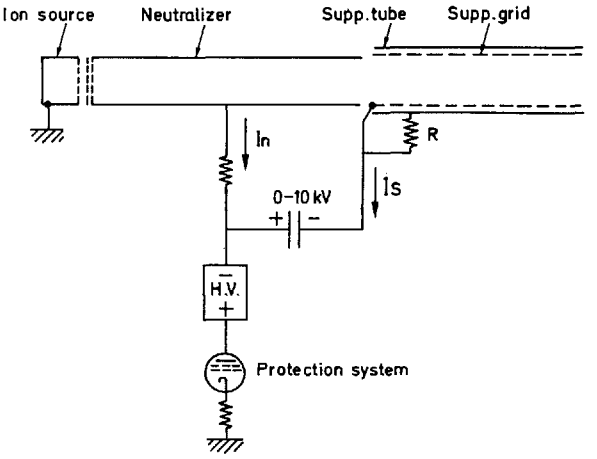


FIG.9. Experimental scheme for the electron suppression measurements.

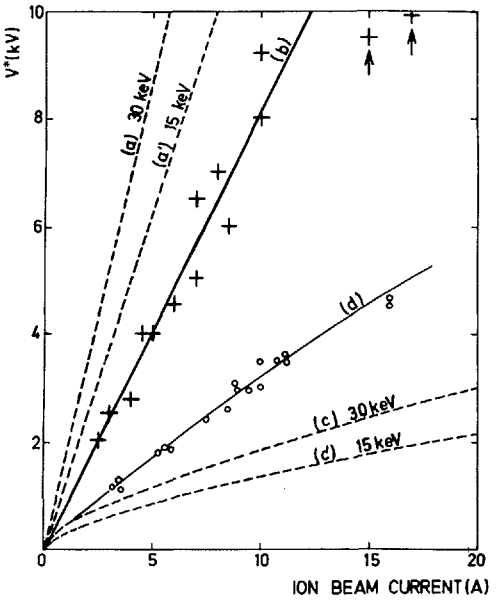


FIG.10. Critical suppression voltage as a function of the extracted beam current.

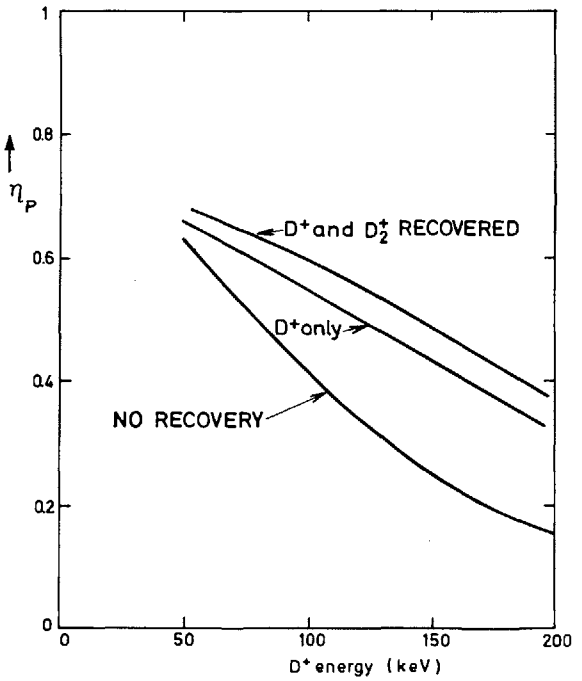


FIG.11. Injector power efficiencies as a function of beam energy.

Neglecting the power spent in the source (which at high energy is of the order of 2% of the total power), the power efficiency of a neutral injector can be given by

$$\eta_p = \sum_k \alpha_k \frac{\eta_{k0}\, T_{kn}}{1 - r_k\,(1 - \eta_{k0})\, T_{ki}} \qquad (2)$$

where α_k is the relative fraction of the species k in the extracted beam (D^+, D_2^+, D_3^+), η_{k0} the neutralization efficiency, and r_k the recovery efficiency. T_{kn} and T_{ki} are the transmission factors for neutrals and ions resulting from the species k. For conservative transmission factors $T_{kn} = T_{ki} = 0.8$ and for an ion beam consisting of 75% D^+ and 25% D_2^+, injector efficiencies are given in Fig. 11, respectively, for $r_1 = r_2 = 0.85$; $r_1 = 0.85$; $r_2 = 0$ and $r_1 = r_2 = 0$, i.e. no recovery at all. It can be seen that around 150 keV the power efficiency can be doubled with a recovery system and that it comes close to the value where injectors around 30 keV are actually working.

4. CONCLUSION

The prospects for realizing medium-energy high-power neutral injectors (up to 100 keV for H; 200 keV for D) are quite positive. Very powerful, long-pulse ion sources will soon be realizable, with extracted currents around 100 A; post-acceleration studies are progressing well [17], and for

long-pulse operation several solutions for the extraction grids will be available. With the help of energy recovery systems, power efficiency can be raised to about 40% at the high-energy limits, which is acceptable at this stage.

REFERENCES

[1] TFR Group, Paper IAEA-CN-35/A4-2, these Proceedings.
[2] STIRLING, W.L., DAVIS, R.C., MORGAN, O.B., STEWART, L.D., Proc. Symp. on Ion Sources and Formation of Ion Beams, Brookhaven, 1971, Rep. BNL 50-310 (1971) 167.
[3] BONNAL, J.F., DRUAUX, J., OBERSON, R., Rep. EUR-CEA-FC 791 (1975).
[4] EURATOM-CEA, Torus II, Rep. EUR-CEA-FC-824 (1976).
[5] FUMELLI, M., BECHERER, R., BERGSTEN, L., VALCKX, F.P.G., Proc. Int. Conf. on Ion Sources, Vienna, 1972, II. Inst. Exp. Phys. (now Inst. für Allgemeine Physik), Vienna Univ. (1972) 289;
FUMELLI, M., Nucl. Instrum. Methods 118 (1974) 337;
FUMELLI, M., VALCKX, F.P.G., Proc. 2nd Symp. on Ion Sources and Formation of Ion Beams, Berkeley, 1974, Rep. LBL-33-99, Suppl. (1974) VI-6-1;
FUMELLI, M., VALCKX, F.P.G., Rep. EUR-CEA 809 (1976).
[6] JERNIGAN, T.C., DAVIS, R.C., MORGAN, O.B., SCHECHTER, D.E., STEWART, L.D., STIRLING, W.L., WRIGHT, R.E., Proc. 2nd Symp. Ion Sources and Formation of Ion Beams, Berkeley, 1974, Rep. LBL-33-99, Suppl. (1974) VI-9-1.
[7] BERKNER, K.H., BAKER, W.R., COOPER, W.S., EHLERS, K.W., KUNKEL, W.B., PYLE, R.V., STEARNS, J.W., ibid. VI-12-1.
[8] EHLERS, K.W., BERKNER, K.H., COOPER, W.S., HAUGIAN, J.M., KUNKEL, W.B., PRICHARD, B.A., Jr., PYLE, R.V., STEARNS, J.W., Proc. 9th Symp. Fusion Techn.,Garmisch-Partenkirchen (1976) paper K1-1.
[9] SCHILLING, G., private communication.
[10] COLE, H.C., HAMMOND, D.P., JONES, E.M., RIVIERE, A.C., SHEFFIELD, J., Culham Lab. Rep. CLM-P 313 (1972).
[11] STEWART, L.D., DAVIS, R.C., JERNIGAN, T.C., MORGAN, O.B., SCHECHTER, D.E., STIRLING, W.L., Proc. 2nd Symp. Ion Sources and Formation of Ion Beams, Berkeley, 1974, Rep. BNL-33-99, Suppl. (1974) II-8-1.
[12] BERKNER, K.H., PYLE, R.V., STEARNS, J.W., Nucl. Fusion 15 (1975) 249.
[13] MOIR, R.W., in Proc. 1st Top. Mtg. on the Technique of Controlled Nuclear Fusion, San Diego (1974).
[14] MOIR, R.W., BARR, W.L., CARLSON, G.A., "Direct conversion of plasma energy to electricity for mirror fusion reactors", Plasma Physics and Controlled Nuclear Fusion Research 1974 (Proc. 5th Int. Conf. Tokyo, 1974) 3, IAEA, Vienna (1975) 583.
[15] BENDER, D.J., BARR, W.L., MOIR, R.W., Proc. 6th Symp. Engineering Problems of Fusion Research, San Diego, 1975.
[16] RAIMBAULT, P., Rep. EUR-CEA-FC 780 (1975).
[17] HOLMES, A.J.T., Proc. 3rd Int. Mtg. Theoretical and Experimental Aspects of Heating of Toroidal Plasmas, Grenoble, 1976, 1, 41.

DISCUSSION

ON PAPER IAEA-CN-35/I 6

R.F. POST: Why do you get a higher H^+ fraction than that obtained with the Oak Ridge source?

F.P.G. VALCKX: The arcs in the duopigatron and the periplasmatron are very different. In the duopigatron the pressure in the intermediate electrode is high, close to 10^{-1} torr; in the periplasmatron the corresponding pressure is 10^{-2} torr. This high pressure is the reason for the higher molecular ion fractions in the duopigatron.

R.F. POST: Why did you choose the Oak Ridge source for TFR?

F.P.G. VALCKX: In 1973, when construction was started on the injection system for TFR, the duopigatron source was the only possible candidate for an intense ion source operating at relatively long pulse lengths (100 to 200 ms). To modify the power system now would be a long and expensive task. If at a later stage we wish to go beyond 1.5 MW injected, we will use periplasmatron sources.

W. HENKES: What is the gas efficiency of the periplasmatron?

F.P.G. VALCKX: The gas efficiency of a source is not an absolute motion; it depends on the gas conductance of the system and the pumping speed on line. The pressure in the source must be about 10^{-2} torr for hydrogen. At 20 A extracted, the gas flow is 7 torr · litre/s.

PULSED ENERGY STORAGE IN FUSION DEVICES*

K.I. THOMASSEN, J.D. ROGERS, F.L. RIBE,
D.M. WELDON, C.E. SWANNACK, H.F. VOGEL
Los Alamos Scientific Laboratory,
Los Alamos, New Mexico

H.G. RYLANDER, W.F. WELDON, K.M. TOLK,
M.D. DRIGA, W.L. BIRD, Jr., H.H. WOODSON
University of Texas at Austin,
Austin, Texas

C.J. MOLE, R.E. STILLWAGON
Westinghouse Electric Corporation,
Pittsburgh, Pennsylvania,
United States of America

Abstract

PULSED ENERGY STORAGE IN FUSION DEVICES.

Research and development on pulsed energy technologies, primarily for pulsed high-β fusion systems, is described. Systems studies at Los Alamos and elsewhere have served to define these required technologies, which include fast-discharging homopolar machines, pulsed superconducting coils and the associated switching technology. Programmes at the Los Alamos Scientific Laboratory, Westinghouse and the University of Texas are described.

INTRODUCTION

Next-generation large fusion devices are of such a size as to require new technologies to meet the requirements for the delivery of pulsed energy. In pulsed high-ß devices this dictates the replacement of capacitative systems by pulsed moderately fast energy transfer systems. We have examined these requirements for a number of fusion systems and are developing pulsed superconducting coils, fast-discharging homopolar machines, and large capacity interrupting switches for these purposes.

This paper gives the results of and describes the pulsed energy-storage programs at present going on at the Los Alamos Scientific Laboratory (LASL), The University of Texas (UT), and Westinghouse Electric Corporation (WEC). These include systems studies, machine design and construction, superconducting coil fabrication and testing, and vacuum interrupter use in magnetic energy transfer experiments. These programs all address the technology of energy transfer in the 100-µs to 500-ms time scale, with energies as large as 60 GJ.

* Work performed under the auspices of USERDA and Electric Power Research Institute.

The fusion devices requiring large, fast energy delivery systems include toroidal and linear theta pinches, liners, toroidal Z-pinches, glass lasers and tokamaks. In the pinches and liners, magnetic fields for plasma compression are driven by these large energy systems, while tokamaks and toroidal Z-pinches require pulsed supplies for ohmic heating. The flash lamp supplies for glass lasers require ∿100 MJ on the 0.1 to 0.5ms time scale.

A toroidal theta-pinch reactor (the RTPR) requires ∿60 GJ delivered in 30 ms, the linear theta-pinch fusion/fission hybrid reactor needs ∿25 GJ in 2 ms, and a liner reactor may require ∿10 GJ on a 1 ms timescale. The ohmic heating coils in present US designs of tokamak EPR's (Experimental Power Reactors) have ∿1 to 2 GJ of stored energy, and the storage currents must be reversed in 0.5 to 2 s to induce plasma current. Tokamak reactor systems require even larger ohmic heating systems. Similar systems are needed for toroidal Z-pinches to ignite the plasma by ohmic heating.

TOROIDAL THETA-PINCH ENERGY SUPPLIES

The LASL Reference Theta Pinch Reactor (RTPR)[1] design has defined requirements on the power supplies to drive the compression coils. A total of 63 GJ must be delivered in 30 ms, held for 70 ms, and returned to storage in 30 ms. A cycle transfer efficiency of 95% is required.

To meet these requirements, WEC advanced the design of a 1.3-GJ homopolar machine (50 of these will be required).[2] Further study under EPRI (Electric Power Research Institute)(auspices of LASL, UT, and WEC) has resulted in a complete conceptual engineering design of this machine. There are eight drum-rotors in the machine which develops 11 kV at 12.25 MA while discharging in 30 ms. A scaled 10-MJ model of this machine is now in final engineering design, with plans to construct it in the next few years. The model machine is a test of high surface speed (277 m/s) operation of solid copper-graphite brushes at high currents (1550 A/cm^2), the superconducting field coils, and operation with high deceleration (30-ms stopping time). The machine will produce 1.55 MA at 719 V.

The model machine, shown schematically in Fig. 1, has two rotors spinning oppositely. Current flows axially along the rotor surface for the length of the machine, with brushes on the inner surface at each end of each rotor. Return current flows on an outer coaxial sleeve to minimize internal inductance. Superconducting NbTi coils, storing ∿8 MJ of energy, provide an average of 2.2 T radial field at the rotor surface. A conceptual design of the machine including electrical, mechanical and thermal considerations has been completed.

TOKAMAK OHMIC HEATING

Joint systems studies by LASL, UT and WEC of homopolar machines and pulsed superconducting coils for tokamak EPR's

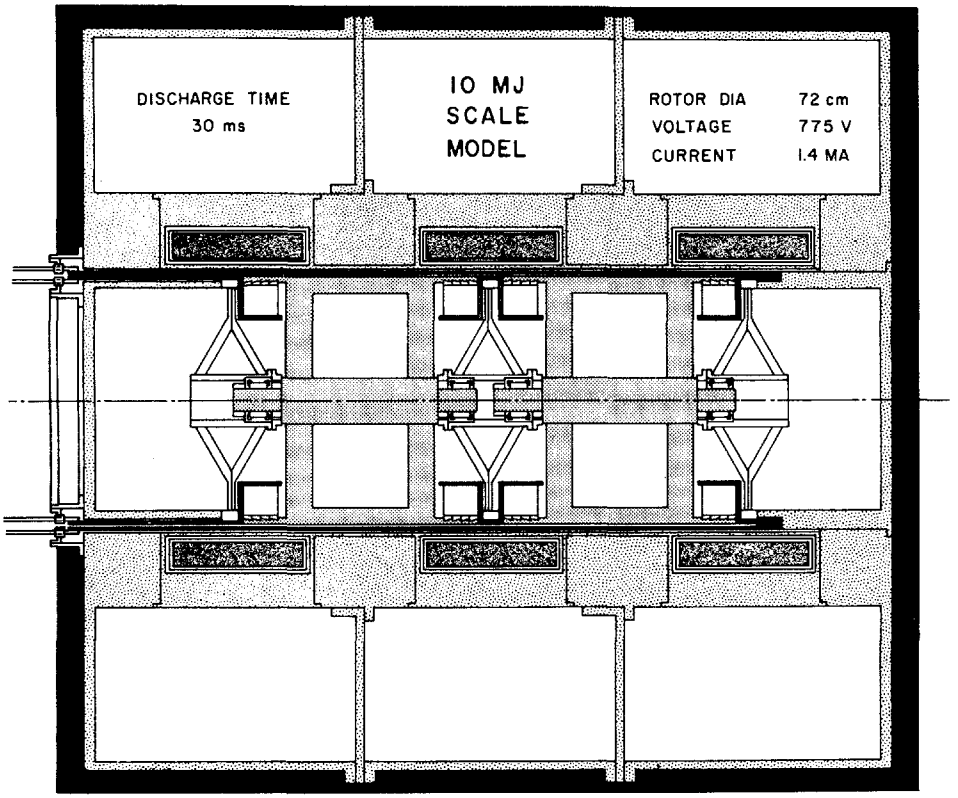


FIG.1. A two-rotor, 10-MJ drum-type homopolar machine.

are under way. As in the high-β systems where the machine load is inductive, the capacitative nature of the homopolar machine is ideal for resonating the energy out of and back into the ohmic-heating coils. The simple circuit of Fig. 2 provides the necessary energization of the plasma, and was used to determine the necessary startup energy, transfer times and OH coil requirements. The OH coil system, its transformer coupling to the plasma, and the plasma inductance and variable resistance, are represented. A zero-dimension code describes plasma current buildup and incorporates resistive heating, bremsstrahlung, line radiation, charge exchange, plasma transport, etc. The power supply (± V) charges the OH coil with R and C bypassed. On turning off this supply, R and C are switched in, giving an initial fast-rising current. On crowbarring R, the homopolar capacitor completes the energy transfer on the several-second time scale and is bypassed during the burn. The circuit is sufficient for establishing the initial rate of change of current (10 to 50 MA/s), stored energy

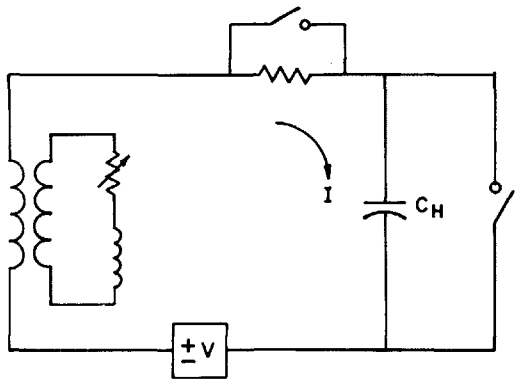


FIG.2. A simplified Ohmic-heating circuit using a homopolar capacitor.

(1 to 2 GJ), the coil primary circuit parameters (peak voltages ∿30 to 60 kV, peak currents ∿150 to 300 kA, and volt-seconds ∿100 to 200) for typical tokamak EPR's. Homopolar machine designs are being carried out by WEC, and superconducting OH coil problems are being assessed at LASL.

HOMOPOLAR MACHINE DEVELOPMENT

Many of the applications described in this paper require very fast transfer times (as small as 0.1 ms). The limitations to extremely fast discharge times for homopolar machines have been studied by UT,[3] and a 1-ms model machine is being constructed. Figure 3 shows the two counter-rotating aluminum rotors which will discharge 10^6 A in 3 ms from a speed of 28 000 rpm into a 30-μΩ, 1/4-μH load at 80% efficiency, or at half speed in 1 ms into a short circuit. The machine capacity is 16.6 F (360 kJ stored) and has a 25-nH, 15-μΩ internal impedance.

The pulsed exciting coil stores 1.2 MJ and has an average magnetic field of 4 T between brushes. The rotors are supported on oil-lubricated hydrostatic journal bearings and are driven by two air turbines.

Concurrent with the machine construction programs (the 1-ms and 30-ms machines), a brush-testing program is in progress at UT. Data taken in air on a steel rotor with surface speeds up to 220 m/s, and with long current pulses applied to the brush, have been described by Ortloff[4] and Casstevens.[5] More recently, a high-speed (450-m/s surface speed) aluminum rotor with various surface treatments is being used in a controlled-atmosphere facility. The gas composition, humidity, and temperature are controlled, and sliding velocity, current, voltage drop, friction force, normal force, and brush and rotor temperatures are monitored. A 60-ms pulse giving current densities of 1550 A/cm can be applied.

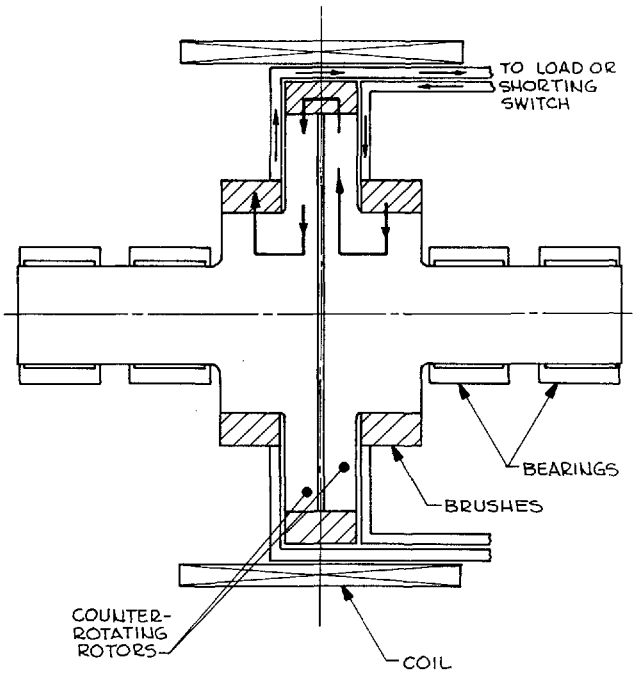


FIG.3. A two-rotor disc-type homopolar to discharge in 1 ms.

MAGNETIC ENERGY TRANSFER AND STORAGE (METS)

The METS program at LASL, begun several years ago, is leading to the development of 400-kJ, 0.7-ms transfer, superconducting coils.[6] The appropriate cryogenic and switching technology is also being developed. These coils are part of a 500-MJ system to drive the Scyllac Fusion Test Reactor[7] (SFTR). Three 300-kJ coils have been constructed and are being tested to determine the ac. losses during discharge. The coils are designed for less than 0.3% energy loss during this rapid transfer and to remain superconducting even during the rapid (0.7 ms) discharge. An earlier 300-kJ coil with a 2700 filament monolithic conductor (6:1, Cu: NbTi) was successfully built and tested by LASL. By design it did not remain superconducting during transfer and had 2-3% losses. Peak current and voltage were 10 kA and 35 kV.

The three 10-kA coils in the present program were constructed by MCA (Magnetics Corporation of America), WEC and IGC (Intermagnetics General Corporation). The IGC coil, shown in Fig. 4, has a single-layer edge-wound cable of 319 multi-strand, 0.39-mm dia. CuNi-Cu matrix NbTi multifilament wires. It is vacuum-impregnated with epoxy resin. In tests

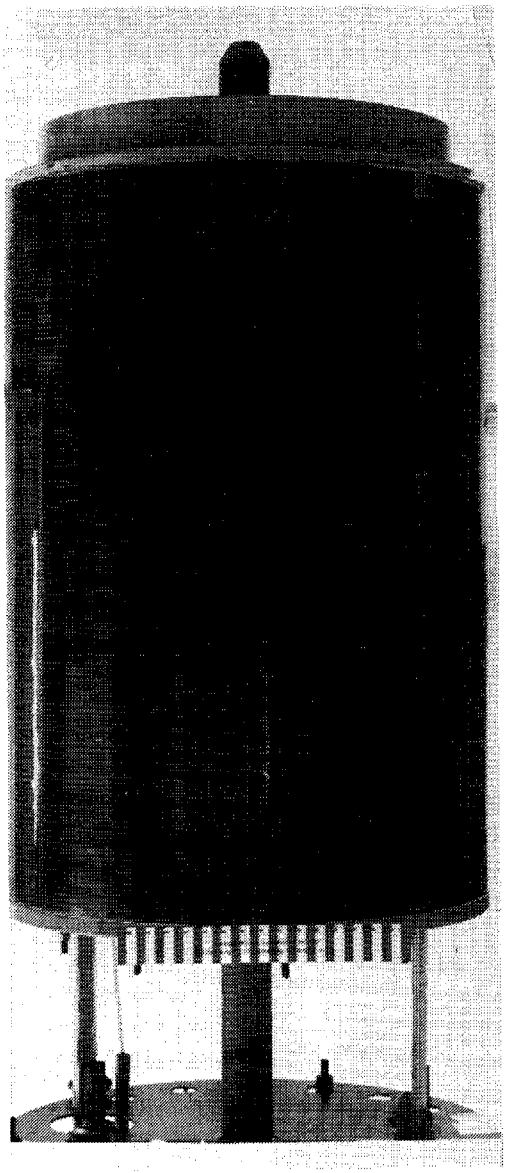


FIG.4. A 300-kJ superconducting storage coil from Intermagnetics General Corp. for 0.7-ms discharge.

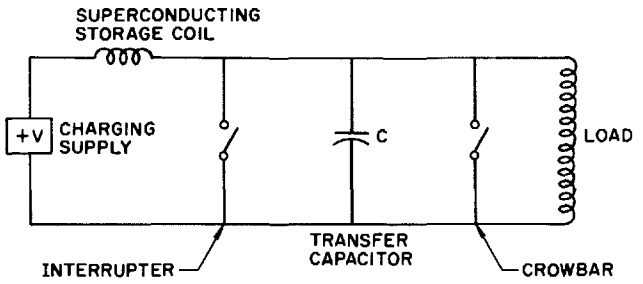


FIG.5. A simplified resonant circuit for transfer between matched inductors through a large capacitor bank.

to date, a normal transition occurred at ∿3 kA so the coil has been disassembled to redesign the supports for the terminals. Motion of the lead-in conductor may be the problem.

The MCA coil uses a single-layer, edge-wound multistrand braid with 1224 monofilament wires. Each wire is 0.127 mm dia., having 1.58:1 Cu:NbTi. The coil has an open structure, with the braid bonded to a "staircase" helical support structure with epoxy resin. Operation of the coil was limited to 4.8 kA by heating damage to the structure from a low current quench while operating without a quench detector circuit. Losses during transfer were found to be less than 0.3%.

Westinghouse is constructing a coil with a 4-layer winding using 72 strands of 0.51-mm dia. Cu matrix NbTi multifilament wires in twelve bundles to form a cable wrapped around an insulated strap. The structure is open to allow ℓHe cooling. This coil has been successfully charged to 10 kA and discharged in 2 ms with 0.8% losses.

In SFTR, 1280 pulsed coils of 381 kJ each will be energized in series and discharged in parallel in a resonant transfer circuit like that in Fig. 5. The individual transfer circuits are first electrically isolated to reduce voltage to ground. This single circuit will be used for component testing of the coil, interrupting switch, crowbar switch and control circuits.

SWITCHING

The major requirements for fast transfer of energy from inductive systems are high current interruption and high voltage hold-off. Dc. switching studies using vacuum interrupters developed for ac. power systems are in progress at LASL and UT. At LASL, the emphasis is on achieving the highest possible power ratings. To date we have interrupted 31 kA and withheld 66 kV using a conventional 7-inch Westinghouse interrupter. Saturable reactors are used in series with the interrupter to limit dI/dt at current zero and improve reliability. Reactors

with ferrite cores, 20-mil silicon iron laminations, 10-mil Permalloy, or special 4-mil silicon iron have been used. Flux ratings ranging from 0 to 0.2 webers are used, with reliability improving at the higher ratings.

At UT, the emphasis is on exploring the pertinent parameters governing interruption (rate of change of current prior to interruption, rate of increase of voltage after interruption, deionization time, conduction time, etc). For example, with a Westinghouse WL23318 bottle, data gathered at 3.2-kA current and 30-kV peak forward voltage, they find a relationship between the fall of commutated current $F = di/dt$, the rise of forward voltage $R = dv/dt$ and the deionization time τ. The relationship is $RF^{1.45}\tau^{-6} = 2 \times 10^{-4}$ where $600 < R < 2000$ v/μs and $3 < F < 80$ A/μs. Plans call for improving the facility to gather data at 10 to 20-kA interrupting currents.

REFERENCES

1. F. L. Ribe, R. A. Krakowski, K. I. Thomassen, and T. A. Coultas, Fusion Reactor Design Problems, Nuclear Fusion Special Supplement 1974, IAEA Vienna (1974) p 99.

2. G. Rostagni, in Pulsed Fusion Reactors, Erice-Trapani (Sicily), September 9-20, 1974 Pergamon Press, Oxford, New York (1975) p 594.

3. M. D. Driga, S. A. Nasser, H. G. Rylander, W. F. Weldon, and H. H. Woodson, IEEE Transactions on Plasma Science Vol. PS-3, No. 4, p 209 (1975).

4. D. J. Ortloff, "The Design of a Brush Test Machine," Master's Thesis in Mechanical Engineering, The University of Texas at Austin, January 1975.

5. J. M. Casstevens, "Measurements of the Friction and Wear Characteristics of Copper-Graphite Sliding Electrical Contact Materials at Very High Speeds and Current Densities," Master's Thesis at the University of Texas at Austin, August 1976.

6. C. E. Swannack, R. A. Haarman, Jr., J. D. G. Lindsay and D. M. Weldon, Proceedings of the Sixth Symposium on Problems of Fusion Research, November 18-21, 1975, San Diego, IEEE, New Brunswick, New Jersey, 75 CH 1097-5 NPS, p 662 (1976).

7. K. I. Thomassen, compiler, "Conceptual Design Study of a Scyllac Fusion Test Reactor," USERDA Report LA-6024, Los Alamos Scientific Laboratory, January 1976.

DISCUSSION

ON PAPER IAEA-CN-35/I 7

F.F. CHEN: Do you think that homopolar energy storage would be feasible in tokamaks (as opposed to theta pinches)?

K.I. THOMASSEN: Extensive studies have been done at Los Alamos, with help from Westinghouse and the University of Texas, on the question of power systems for the start-up of large tokamaks. In experimental power reactors significant savings could, potentially, be achieved if homopolar machines were used to reverse the flux in the Ohmic heating coils. Our comparison was between homopolar machines and a.c. machines, either turbo-alternators or salient pole machines. The savings would be realized largely on the solid-state rectifier system for the a.c. machine, which costs two to three times as much as the machine itself. The a.c. and d.c. (homopolar) machines have similar costs, although more development is required for the homopolar.

REMOVAL OF FOREIGN ATOMS FROM A METAL SURFACE BOMBARDED WITH FAST ATOMIC PARTICLES

S.K. DOLOTOV, S.A. EVSTIGNEEV, S.Yu. LUK'YANOV,
Yu.V. MARTYNENKO, V.M. CHICHEROV
I.V. Kurchatov Institute of Atomic Energy,
Moscow,
Union of Soviet Socialist Republics

Presented by B.B. Kadomtsev

Abstract

REMOVAL OF FOREIGN ATOMS FROM A METAL SURFACE BOMBARDED WITH FAST ATOMIC PARTICLES.

A metal surface coated with foreign atoms was irradiated with periodically repeating ion current pulses. The energy of the ions bombarding the target was 20–30 keV, and inert gas ions were used. A study of the time dependence of the current formed by the dislodged foreign atoms showed that the rate of their removal from the target surface is determined by the sputtering coefficient of the substrate metal.

INTRODUCTION

In plasma devices designed for thermonuclear studies, the walls of the vacuum chamber are exposed to periodic irradiation by fluxes of fast atomic particles. This irradiation causes significant reverse fluxes from the chamber wall, consisting of atoms of the residual gas, which have earlier been adsorbed by the wall surface, and also of atoms of the wall itself. These atoms contaminate the plasma and cause its cooling.

Recent experiments [1, 2] have shown that the sputtering coefficient of layers of adsorbed atoms may have an appreciable magnitude, exceeding the sputtering coefficients of pure metals in some cases, and the sputtering thresholds of the adsorbed layers are unexpectedly low even in the case of chemically adsorbed atoms, when the bond between the foreign and the lattice atoms is fairly strong. Therefore, foreign atoms previously adsorbed by the wall should predominate in the fluxes of atoms from the wall, at least during the first few moments of irradiation. Reducing the fluxes of these atoms is one of the fundamental problems at the present stage of thermonuclear research. Hence the timeliness of the study of the processes involved in the ion bombardment of a solid surface containing foreign atoms.

The importance of these studies is emphasized by a certain peculiarity of the present situation.

It is well known that there exist so-called "lethal densities" [3] of heavy-atom impurities in hydrogen plasma. The achievement of these densities makes the plasma unpromising from the standpoint of obtaining a positive energy yield in a thermonuclear reactor. These densities drop rapidly with growing Z of the impurity atom, and a large flux of light atoms entering the plasma from the wall may prove preferable to a smaller flux of heavier atoms. On the other hand, it is well known from cathode sputtering experiments that the sputtering rate of a metal under imperfect vacuum conditions slows down markedly, until the current density of the bombarding ions reaches a certain critical value. This is obviously explained by the fact that metal sputtering is hindered considerably when the surface carries foreign atoms adsorbed from the residual gas or previously located there. Thus, under certain conditions, foreign atoms may play a positive role, decreasing sputtering of wall metal and penetration of heavy impurities into the plasma. It is possible that this fact can be used by artificially creating a controllable coating of light atoms on the wall.

We performed model experiments simulating the periodic bombardment of a vacuum chamber wall in a high-power plasma device. In these experiments, fast ions bombarded a metal surface initially coated with foreign atoms – adsorbed atoms of the residual gas. Analysis of the results obtained permits us to draw certain conclusions on the behaviour of foreign atoms during ion bombardment and on the mechanism of removal of these particles.

METHOD

To measure the rate of removal of foreign atoms from a metal surface and monitor the state of the irradiated surface, we used the method of ion scattering. In this case, the surface was probed by the bombarding ions themselves. Products of binary collisions between beam ions and surface layer atoms of the target were recorded.

The method of ion scattering is based on the experimental fact that, in the energy spectra of ions scattered by a solid target at a given angle, narrow peaks are observed whose location on the energy scale corresponds to single collisions of an incident ion with an atom of the target. Some of these peaks are formed by ions of the beam, scattered from atoms of the target, while others are formed by recoil atoms present on the surface of the target before the collision. Having measured the energy of a scattered particle and the scattering angle, and knowing the kind of bombarding ions, we can determine the kind of the recoil atoms.

The present study deals with transition processes occurring during the first few moments of ion bombardment. The current of bombarding ions was, therefore, supplied to the target in the form of a pulse with a steep leading edge, and the recording equipment made it possible to record the time characteristics of the process studied.

A diagram of the device is shown in Fig.1. The target was bombarded with singly charged 30-keV argon ions. The maximum current density of the bombarding ions was 300 $\mu A \cdot cm^{-2}$. The beam was supplied to the target periodically; the duration of the pulse was 20 s, the length of its leading edge about 5 ms, and the intervals between the pulses were 120 s. The pressure of residual gases in the target chamber was 1×10^{-7} torr, and thus, the time of formation of one monolayer of residual gas molecules was about 10 s.

The energy spectra were measured by using a spherical electrostatic analyser with a mean trajectory radius of 250 mm and energy resolution of about 0.5%. The ions were recorded with an open multiplier. The signal from the detector output was fed to an oscillograph. The latter was triggered at the instant the next ion current pulse reached the target. Before this, the electrostatic analyser had been tuned to a pre-selected energy interval. The time dependences of the current of scattered ions were thus successively recorded in different parts of the spectrum.

The chamber was evacuated with oil-diffusion pumps which were provided with liquid-nitrogen-cooled traps. For this reason, the residual gas in the chamber consisted mostly of hydrocarbons.

The irradiation conditions, i.e. current density, energy and kind of bombarding ions, were chosen so that the complete cleaning of the metal surface practically attainable at the given residual gas pressure was achieved at the end of the pulse as a result of the ion bombardment. The interval between the ion current pulses was chosen so that an equilibrium coating of the target with atoms of the residual gas would be achieved during this interval.

RESULTS AND DISCUSSION

The procedure described above was used to obtain sets of oscillograms corresponding to those regions of the energy spectrum where calculations showed the locations of peaks of fast carbon and hydrogen ions, formed in binary collisions with the bombarding ions. Carbon and

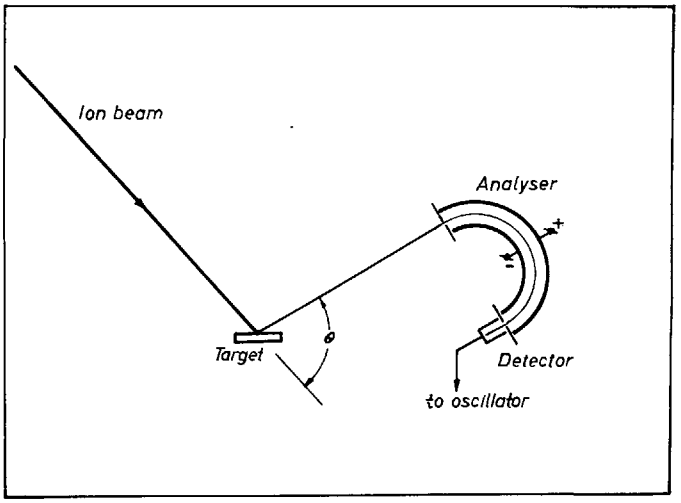


FIG. 1. Diagram of device.

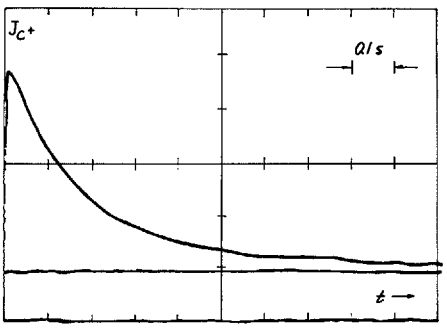


FIG. 2. Typical oscillogram showing time dependence of C^+ ion current. Bombardment of platinum target with 30-keV argon ions.

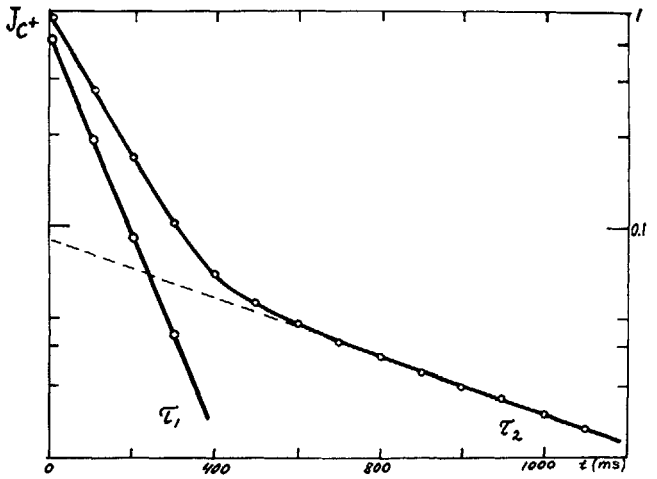


FIG. 3. Time dependence plotted on semilog scale (Ar^+-20 keV; substrate-Au).

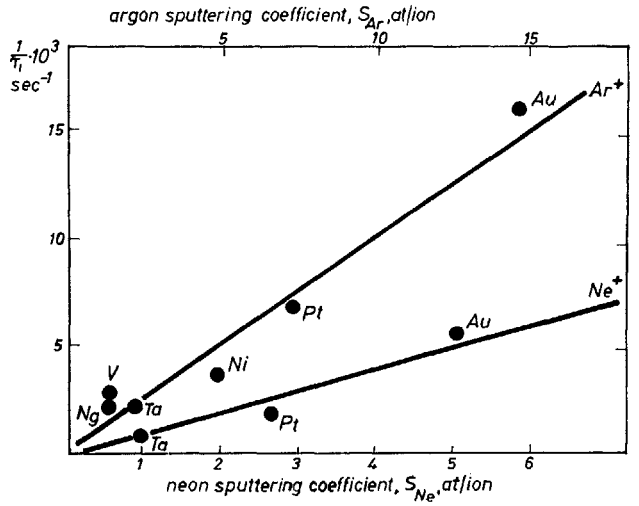


FIG. 4. Time constant of "fast" exponential versus sputtering coefficients of metal substrate.

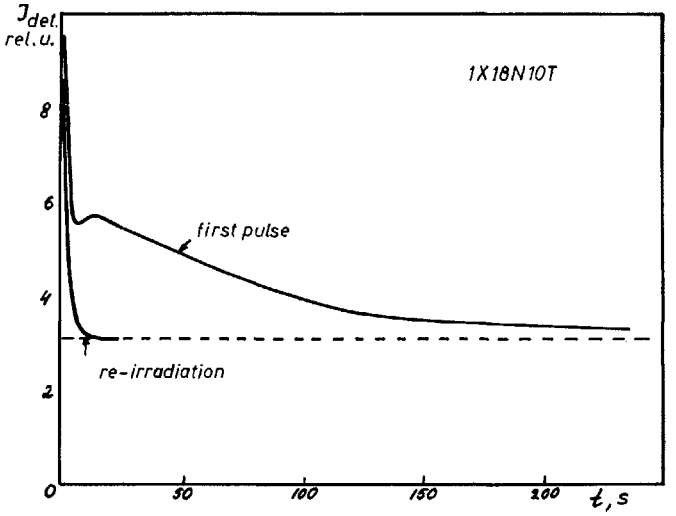


FIG.5. Oscillograms of time dependences of C^+ ion current, obtained during first irradiation of target and repeated irradiations. Target-substrate of 1X18N10T stainless steel.

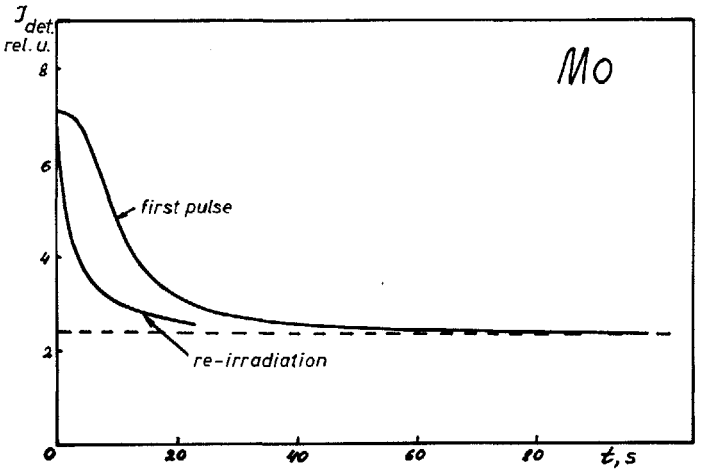


FIG.6. The same in the case of a molybdenum target.

hydrogen should be present on the target surface in the form of components of the hydrocarbons adsorbed from the residual gas.

A typical oscillogram of the detector current, obtained in this energy interval, is shown in Fig.2. It corresponds to the maximum of the peak of C^+ ions. As expected, the flux of carbon ions is maximum at the start of the ion bombardment and decreases with time. We expected the decrease to be exponential. However, it was found that each oscillogram of the time dependence was the sum of two exponentials, one "fast" and the other "slow", characterized by constants τ_1 and τ_2, respectively. A typical example of the time dependence, plotted on a semilog scale, is shown in Fig.3.

The targets on which the experiments were carried out included metals with markedly different sputtering coefficients: niobium, vanadium, tantalum, nickel, platinum, and gold. It was found that the time dependences obtained under the same conditions on targets made of these metals had very different rates of decrease.

To establish the quantitative dependence of the rate of decrease on the sputtering coefficient of the metal used as the target, we plotted $1/\tau_1$ as a function of the sputtering coefficient (see Fig.4). The values of the sputtering coefficients were taken from the paper of Almen and Bruce [4]. The experimental points in Fig.4 are located near curves passing through the origin. The slopes of the curves, corresponding to irradiation with neon and argon ions, differ by a factor of 2.8. The sputtering coefficients by neon and argon differ by the same factor according to the data of Ref.[4].

Thus, the time of removal of foreign atoms from the metal surface during bombardment with fast particles depends on the sputtering coefficient of this metal. This result signifies that the removal of foreign atoms is caused by the sputtering of the metal. One can propose a mechanism of removal based on momentum transfer to the foreign atoms from the metal atoms, which during the sputtering move to the outside, away from the target surface. The presence of a second exponential in the time dependence may be explained by the fact that part of the adsorbed atoms will be knocked into the interior of the target during the ion bombardment. Their removal requires the atomization of several layers of the metal.

Using the method described above, we made a closer study of the removal of foreign atoms during the bombardment of molybdenum and 1X18H10T(SS-316) stainless steel targets.

Oscillograms of time dependences obtained during the first irradiation of the target after it was placed in the scattering chamber were compared with oscillograms obtained during repeated irradiations of the same spot on the target. These oscillograms are shown in Figs 5 and 6. It is evident from Figs 5 and 6 that the total number of carbon atoms knocked out during the irradiation of the targets decreases sharply after the first irradiation. The difference between the number of atoms knocked out during the first irradiation and repeated irradiations is particularly pronounced in the case of a stainless-steel target.

CONCLUSIONS

Foreign atoms knocked out of the wall of a thermonuclear device comprise a significant portion of the flux of impurity atoms into a plasma. Studies of the processes occurring during the bombardment with fast particles of a metal surface covered with foreign atoms are, therefore, of particular interest.

The experiments performed modelled the pulsed irradiation of the wall of a plasma installation. It was shown that the principal mechanism responsible for the removal of foreign atoms is the transfer of momentum to the latter from the sputtered metal atoms of the substrate. The rate of removal of the layer of adsorbed atoms of residual gas is determined by the sputtering coefficient of the substrate metal.

REFERENCES

[1] EVERTS, S.K., McCRACKEN, G.M., J. Appl. Phys. **44** (1973) 3139–3145.
[2] WINTERS, H., SIGMUND, P., J. Appl. Phys. **45** (1974) 4760.
[3] GERVIDS, V.I., KOGAN, V.I., Pis'ma Zh. Ehksp. Teor. Fiz. **21** (1975) 329.
[4] ALMEN, O.E., BRUCE, G., Nucl. Instrum. Methods **11** (1961) 257.

DISCUSSION

ON PAPER IAEA-CN-35/I 8

M.B. GOTTLIEB: I am not sure I understood what the source of the carbon was here. Did it result from volume diffusion to the surface of carbon initially dissolved in the metal, or was it from an external gas?

B.B. KADOMTSEV: The authors say that during surface bombardment a fraction of the surface atoms sorbed at the boundary may penetrate within the metal, so that during the subsequent, slower phase of particle release they are coupled with particles emerging from the body of the metal.

R. HANCOX: The ion beam used in your experiments had an energy of 30 keV, and therefore the proposed mechanism involving sputtering of the base metal is reasonable. Such a mechanism may occur in a reactor; but would you agree that it is not relevant in present plasma physics experiments where predominantly low-energy ions bombard the surface?

B.B. KADOMTSEV: Yes.

DYNAMIC CHARACTERISTICS OF ALPHA-PARTICLE HEATING BASED UPON THE FOKKER-PLANCK EQUATION IN D-T FUSION REACTOR CORE PLASMAS

H. SAITO, M. KATSURAI, H. TSUJI, T. SEKIGUCHI
Department of Electrical Engineering,
University of Tokyo,
Bunkyo, Tokyo, Japan

Abstract

DYNAMIC CHARACTERISTICS OF ALPHA-PARTICLE HEATING BASED UPON THE FOKKER-PLANCK EQUATION IN D-T FUSION REACTOR CORE PLASMAS.

The paper presents an extension of previous work on α-particle heated D-T reactor-core plasma, in which the effect of energy relaxation of α-particles (in the presence of α-particle loss) is included in a more precise manner on the basis of the Fokker-Planck equation. Two basic problems are treated in this paper: (1) the "start-up" or "ignition" problem by means of neutral-beam injection heating, and (2) the determination of α-particle energy transfer function for linear perturbations and the calculation of the growth rate of "thermal instability". Particular emphasis is laid on the discrepancies between the results of our model and those of the "instantaneous-heating model" proposed hitherto by many authors. It is found that an "inertial" property inherent in the energy distribution function of α-particles, as well as a sort of "negative feedback" in the energy transfer to background electrons lead to pronounced effects on dynamics and control of α-particle-heated D-T reactors.

1. INTRODUCTION

In most of the simplified theoretical models proposed hitherto for the problems of "α-particle heating" [1–11], the energy relaxation of the α-particles or the energy transfer from α-particles to the background plasma (i.e. the α-particle heating) is assumed to take place instantaneously with zero relaxation time. These models will hereafter be referred to as instantaneous-heating models (abbreviated as *IH model*). The energy relaxation time of α-particles is in most cases, however, comparable to or even longer than various characteristic times governing the dynamic behaviour of reactor-core plasma.

In this connection, a more accurate new model (referred to as the *Fokker-Planck model*, abbreviated as *FP model*) has recently been developed by some of the present authors [12], which includes the effect of energy relaxation of α-particles in a more precise manner on the basis of the Fokker-Planck equation. This new model depicts a new aspect of the dynamic behaviour of α-particle heating, which originates from an "inertial" property inherent in the energy distribution function of α-particles and cannot be predicted without taking into account a finite energy relaxation time and the energy spread in the distribution function.

This paper presents an extension of Ref.[12] for the purpose of further clarifying the features associated with dynamic and control problems of the α-particle-heated D-T reactor-core plasmas. Particular emphasis is laid on the discrepancies between the results from the IH model and the FP model. The following two basic problems are taken up for comparison:

(1) "Start-up" (or "ignition") by means of neutral-beam injection heating;

(2) Derivation of the *matrix of the energy transfer function* which connects the perturbed electron and ion temperature in D-T-core plasma with the corresponding variations in the amount of energy transfer from α-particles to the core plasma particles in the regime of the linear perturbation, and the calculation of the growth rate of what is called *thermal instability*.

2. BASIC DYNAMIC EQUATIONS

On the assumption that (1) the α-particle and background plasma parameters (density n and temperature T) are spatially uniform as well as isotropic in velocity space, (2) the background plasma electrons and ions (deuterons and tritons) have individual Maxwellian temperatures (T_e, T_i), (3) energy loss from the core plasma occurs through bremsstrahlung radiation and effective particle loss (represented by the effective particle confinement time τ_p), (4) the energy relaxation time of injected high-energy ions in neutral-particle-injection heating is nearly equal to zero because of its relatively low energy as compared to that of the α-particles, and (5) the core plasma ions consist of 50%D-50%T, the basic dynamic equations for particle number and energy conservation can be written as

$$dn_i/dt = -(n_i/\tau_p) - (n_i^2/2)\langle\sigma v\rangle + S \tag{1}$$

$$dn_e/dt \cong -(n_e/\tau_p) + S \tag{2}$$

(the Fokker-Planck equation for α-particles, containing terms describing α-particle generation and loss) (3)

where

$$n_e = n_D + n_T + 2n_\alpha \cong n_D + n_T \cong n_D + n_T + n_\alpha \equiv n_i \tag{4}$$

$$(d/dT)[(3/2)n_iT_i] = W_{\alpha i} - (3/2)(t_{Te}^{-1} + t_{De}^{-1})n_i(T_i - T_e) + (3/2)T_sSG - (3/2)(n_iT_i/\tau_p) \tag{5}$$

$$(d/dt)[(3/2)n_eT_e] = W_{\alpha e} + (3/2)(t_{eT}^{-1} + t_{eD}^{-1})n_e(T_i - T_e)$$
$$+ (3/2)T_s(1-G)S - (3/2)(n_eT_e/\tau_p) - k_b\bar{Z}n_e^2(T_e)^{1/2} \tag{6}$$

where $\langle\sigma v\rangle$ denotes the usual averaged fusion reactivity, t_{jk} (j, k = electrons and D, T ions) the energy equipartition time of the j-th particle colliding with the k-th particle [13], $S(cm^{-3}\cdot s^{-1})$ the intensity of injected neutrals with equivalent temperature T_s, and G is the fraction of injected neutral energy imparted to ions. $\bar{Z}$ is the effective ion charge number of ions and k_b a constant for the bremsstrahlung. The quantities $W_{\alpha i}$ and $W_{\alpha e}$ are the rate of energy transfer from α-particles to ions and electrons, respectively; expressions for them are given in Eqs (7) and (8) of Ref.[12]. The Fokker-Planck equation (Eq.(3)), which essentially describes α-particle conservation, is tediously long and given by Eq.(1) of Ref.[12].

3. "START-UP" OR "IGNITION" OF ALPHA-PARTICLE-HEATED D-T-REACTOR BY NEUTRAL-BEAM INJECTION HEATING

A. Equilibrium state

Before we treat the "start-up" problem, we must establish the equilibrium (or self-sustaining) core plasma conditions for α-particle-heated D-T reactors. This equilibrium can be determined by inserting the conditions d/dt = 0 and T_s = 0 into Eqs (1)–(6) and solving the coupled equations. From considerations of the number of independent variables and of the equations given above, the equilibrium condition is found to be uniquely determined by fixing three physical quantities.

Typical examples of calculated results for the equilibrium condition are shown in Fig.1. In Fig.1a, the values of n (= 10^{14} cm^{-3}) and τ_α (= ∞, 1 s and 0.25 s) are fixed and the required values

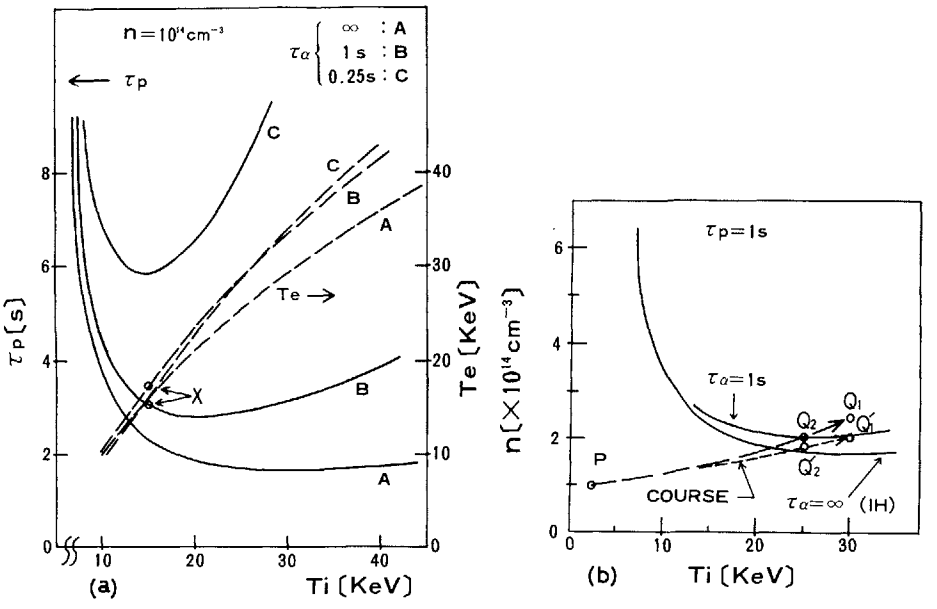


FIG.1. Equilibrium condition of α-particle-heated D-T-reactor core plasma; (a) Required τ_p and T_e versus T_i; (b) plasma density n versus T_i.

of the plasma confinement time τ_p and T_e are shown as a function of T_i, whereas the relation of n versus T_i is given in Fig.1b for fixed values of $\tau_p = \tau_\alpha = 1$ s.

It is to be noted here that, when τ_α is not infinity (or α-particle loss is present), the total amount of energy transfer from α-particles to the background plasma ($= W_{\alpha i} + W_{\alpha e}$) no longer has the form of $n^2 \times$ (function of temperature), and, consequently, the equilibrium state of an α-particle-heated D-T reactor cannot be expressed in the $(n\tau_p - T_i)$-co-ordinate plane, as for the conventional Lawson diagram. Only when $\tau_\alpha = \infty$ do the results coincide with those of the IH model, where representation in an $(n\tau_p - T_i)$-diagram is possible.

B. Start-up

Here, a situation is assumed where the initial plasma (with $n_{DI} = n_{TI} = n_{iI}/2$, T_{iI} and T_{eI}) is heated by a neutral-beam injection heating method (with particle energy T_s and beam intensity S) and is brought to a point in the vicinity of the ignition condition, by taking a route labelled as "course" in Fig.1b. Then, injection heating is cut off and $n_i = n_e \equiv n$ is kept constant hereafter by cold-fuel injection ($T_s = 0$).

In this situation, one concern is the energy partition between electrons and ions in neutral-injection heating [the factor G in Eqs (5) and (6)]. The value of G has already been calculated by Sigmar [14] and Stix [15], and the results indicate $G = 0.8 \sim 1.0$ for the injected ion energy range around 100 keV, which leads to higher T_i than T_e by a factor of about two. To avoid blurring the essential features of α-particle heating, we assume the condition $G = 0.5$ to be fulfilled throughout this paper.

One example of the results of calculation for this "start-up" problem is shown in Figs 2a and b. The conditions are given in the legend.

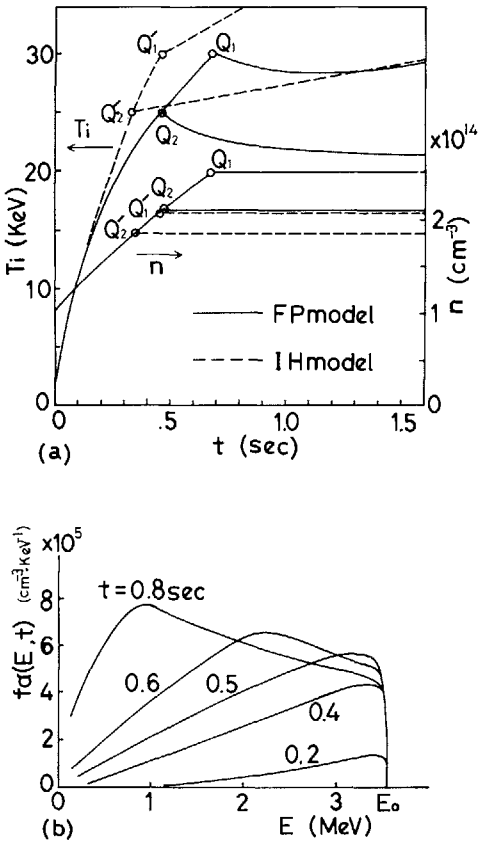


FIG.2. Time history of plasma parameters for "start-up" of α-particle-heated D-T reactors, by means of neutral-beam injection heating; (a) T_i and n versus time t for $\tau_\alpha = \tau_p = 1$ s, the initial plasma condition (the point "P" in Fig.1b): $n_{il} = 10^{14}$ cm^{-3}, $T_{el} = T_{il} = 2$ keV, $T_s = 100$ keV and $S = 4 \times 10^{14}$ cm$^{-3} \cdot$ s^{-1}, (b) the corresponding time evolution of $f_\alpha(E, t)$.

In Fig.2a, the results from the FP model are compared with those from the IH model. When T_i reaches 30 or 25 keV ($\equiv T_c$; the points Q_1, Q_2, Q_1' and Q_2' in the fiture), the injection power is cut off and, hereafter, n_i is maintained at a constant value (2.5 and 2.1 $\times$ 10^{14} cm^{-3}, respectively).

A sharp contrast can be observed between the results from the two models: the IH model predicts a further continuous increase in T_i, exhibiting what is called "thermal instability", whereas the FP model gives just the opposite trend, at least, just after injection heating has ceased. In the former case, effects of time lag due to α-particle thermalization as well as of decrease in the total amount of α-particle heating due to α-particle loss do not exist, and the points Q_1' and Q_2' are located above the equilibrium curve [see Fig.1b]. In the FP model, on the other hand, the situation is just the opposite. Figure 2b shows the corresponding time evolution of the α-particle distribution function (for the case of T_c = 25 keV). The point Q_1 lies well above the equilibrium curve for $\tau_\alpha = 1$ s [see Fig.1b], and, in this case, T_i rises again finally. This is not the case for the T_c = 25 keV case; the point Q_2 lies nearly on the equilibrium curve, and once T_i decreases below T_c, no

re-build-up of T_i occurs and there is no ignition. Thus, there is an appropriate value of T_c which brings the operating point to the equilibrium curve as shown in Fig. 1b at a later instant of time.

These results demonstrate an important feature of start-up (or ignition) and control problems in α-particle-heated D-T-reactors.

4. ALPHA-PARTICLE ENERGY TRANSFER FUNCTION AND GROWTH RATE OF THERMAL INSTABILITY

This section deals with the stability problem of a situation where the operating point lies on the equilibrium curve of the α-particle-heated D-T-reactor core plasma (Fig. 1). The IH model ($\tau_\alpha = \infty$) predicts that the so-called "thermal instability" occurs on the left-hand side of the V-shaped equilibrium curve, and, here, the purpose of our study is to compare the growth rate of this instability as based on the FP model with that given by the IH model.

A. Determination of alpha-particle energy transfer function for temperature perturbation

Since Stacey [16] pointed out that, for τ_p = const, the perturbation of T of the background plasma (δT_i and δT_e) plays an essential role in the thermal instability and density perturbation (δn) is less important, it is assumed here that $\delta n \equiv 0$ through this paper ("temperature mode"). The time variation of δT_j and of the corresponding energy transfer to plasma particles, $\delta W_{\alpha j}$ (j = e, i), is expressed by a Laplace transform,

$$\delta T_j(s) = \int_0^\infty \delta T_j(t) \exp(-st)\, dt \tag{7}$$

where s is the complex frequency, and the discussion refers to the regime of linear perturbation which has been found to be valid for $|\delta T_j|/T_{j0} \lesssim 10\%$. The quantities $\delta W_{\alpha j}$ can be related to δT_j in a matrix form:

$$\begin{pmatrix} \delta W_{\alpha e}(s) \\ \delta W_{\alpha i}(s) \end{pmatrix} = \begin{pmatrix} A_{ee}(s) & A_{ei}(s) \\ A_{ie}(s) & A_{ii}(s) \end{pmatrix} \begin{pmatrix} \delta T_e(s) \\ \delta T_i(s) \end{pmatrix} \tag{8}$$

where the matrix elements $A_{jk}(s)$ stand for the energy transfer function between the temperature perturbation of the k (= e, i) species and the corresponding variation of the α-particle energy transfer to the j (= e, i) species.

The matrix elements may, in principle, be determined by the following procedures: (1) by obtaining the expressions for $\delta W_{\alpha e}$ and $\delta W_{\alpha i}$ from Eqs (7) and (8) of Ref. [12] which contain the variation of the energy-drag factors $\delta P_e(E)$, $\delta P_D(E)$ and $\delta P_T(E)$

$$\delta P_j(E) = [\partial P_j(E)/\partial T_e]_0(\delta T_e) + [\partial P_j(E)/\partial T_i]_0(\delta T_i) \tag{9}$$

and that of the α-particle energy distribution function $\delta f_\alpha(E, t)$, (2) by obtaining the linearized Fokker-Planck (FP) equation for $\delta f_\alpha(E, t)$ from Eq. (1) of Ref. [12], (3) by solving the linearized FP equation for the given time functions δT_e and δT_i with the initial condition $\delta f_\alpha(E, 0) = 0$, and, finally, (4) by calculating $\delta W_{\alpha e}$ and $\delta W_{\alpha i}$ with the help of the calculated result of $\delta f_\alpha(E, t)$.

However, the linearized FP equation is too complex for an analytic solution to be obtained; it has been solved here by numerical analysis. Typical results of computations are shown in Figs 3

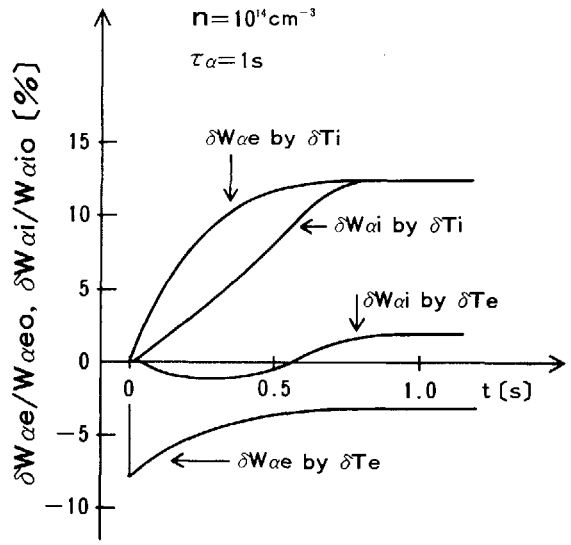


FIG.3. Time response of variation in α-particle energy transfer to plasma electrons and ions ($\delta W_{\alpha i}$ and $\delta W_{\alpha e}$) subject to a step-function-like increase of T_e and T_i; the operating point corresponds to the point "X" in Fig.1a; $T_{i0} = 15$ keV, $T_{e0} = 17$ keV, $n_0 = 10^{14}$ cm^{-3}, $\tau_\alpha = 1$ s, $\Delta T_e = \Delta T_i = 1$ keV.

and 4 for a *step function*-like increase of T_e and T_i. In Fig.3, the step responses of $\delta W_{\alpha e}$ and $\delta W_{\alpha i}$ are shown in the form of percentage variation, and those of $\delta f_\alpha(E, t)$ are shown in Fig.4. The various parameters chosen are given in the legend, and the operating point corresponds to the point labelled as "X" in Fig.1a.

These results may be explained from the physical point of view as follows: under the conditions $w_i \ll v_\alpha \ll w_e$ (w_i, w_e are thermal velocities, v_α is velocity of the α-particles), the energy-drag factors $P_j(E)$ can be written as

$$\begin{aligned} &P_e(E) \cong \alpha n E/T_e^{3/2} \text{ (depending only on } T_e\text{, not on } T_i\text{; } \alpha \text{ is a constant)} \\ &P_D(E) + P_T(E) \cong \beta n/E^{1/2} \text{ (independent of T; } \beta \text{ is a constant)} \end{aligned} \tag{10}$$

so that

$$\delta P_e \cong -(3/2)[P_{e0}/T_{e0}]\delta T_e \quad \text{and} \quad \delta P_{D,T} \cong 0 \tag{11}$$

The physical mechanisms involved are shown schematically in Fig.5. These figures indicate that, as far as thermal-instability problems are concerned, the phenomenon may be explained by the following three main routes, denoted as (1), (2–1) and (2–2), respectively, in the figure. Route (1) shows that δT_e yields δP_e [by Eq.(11)] and, in turn, gives rise to $\delta W_{\alpha e}$ directly without time delay. δT_i leads to a change in the fusion reactivity $\delta\langle\sigma v\rangle$. Routes (2–1) and (2–2) indicate the change in $\delta W_{\alpha j}$ through the perturbation of $\delta f_\alpha(E, t)$, and (2–1) is also through $\delta\langle\sigma v\rangle$ which takes place with a time delay corresponding to the α-particle thermalization time (τ_{th}). Route (2–2) passes through both δP_e and $\delta f_\alpha(E, t)$, which means that δP_e modifies $f_\alpha(E, t)$ with a delay time again characterized by τ_{th} and, in turn, gives an effect on $\delta W_{\alpha j}$ (j = e, i). A qualitative explanation

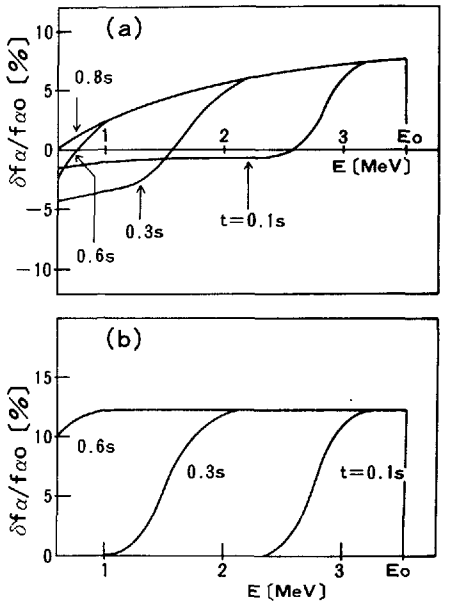


FIG.4. Time evolution of $\delta f_\alpha(E,t)$ corresponding to the conditions of Fig.3; (a) variation due to δT_e, and (b) to δT_i.

of the results given in Fig.3 is possible by considering the three routes shown in Fig.5 in greater detail.

Finally, to obtain the matrix elements A_{jk} of Eq.(8) in analytic form, we approximate the results of numerical analysis shown in Fig.3 by the expressions:

$$\Delta W_{\alpha e}(t) = [-a_2 + (a_2 - a_1)\exp(-t/\tau_e)]\,\Delta T_e, \qquad \Delta W_{\alpha i}(t) = a_3 \Delta T_e$$

$$\Delta W_{\alpha e}(t) = a_4[1 - \exp(-t/\tau_e)]\,\Delta T_i, \qquad \Delta W_{\alpha i}(t) = a_5(t/\tau_i)\Delta T_i \quad (\text{for } t \leqslant \tau_i) \tag{12}$$

$$\text{and } = a_5 \Delta T_i \text{ (constant, for } t > \tau_i)$$

where ΔT_e and ΔT_i are the magnitudes of stepwise variations, a_1 to a_5 are constants, and τ_e, τ_i represent characteristic times. In Fig.3, the step response $\delta W_{\alpha i}$ by δT_e initially exhibits a complex variation but the magnitude itself is not so large so that it has been approximated by a constant (a_3).

In view of the fact that these are the time responses for a step-function-like perturbation of ΔT_j whose Laplace transform is ($\Delta T_j/s$), the Laplace transforms of the expressions (12) yield $A_{jk}(s)$ in analytic form, which can be written as

$$\left(\begin{array}{c|c} -a_1 + (a_1 - a_2)(\tau_e s + 1)^{-1} & a_4(\tau_e s + 1)^{-1} \\ \hline a_3 & (a_5/\tau_i s)[1 - \exp(-\tau_i s)] \end{array}\right) \tag{13}$$

It is, however, uneconomical to determine the values of the constants a_1 to a_5, τ_e and τ_i directly from the results of computer calculations alone. For this reason, these calculations have been carried out here by using the results of a "retardation theory of α-particle energy" which were developed separately by the present authors and will be presented in a separate paper [13].

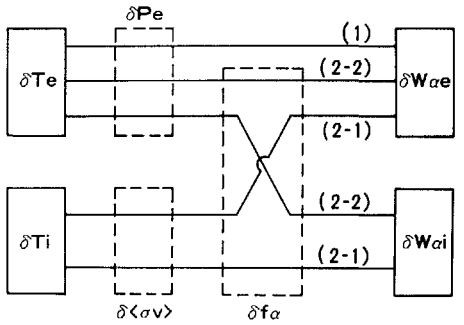


FIG.5. Schematic diagram explaining the physical mechanisms involved in the linear perturbation of α-particle energy transfer.

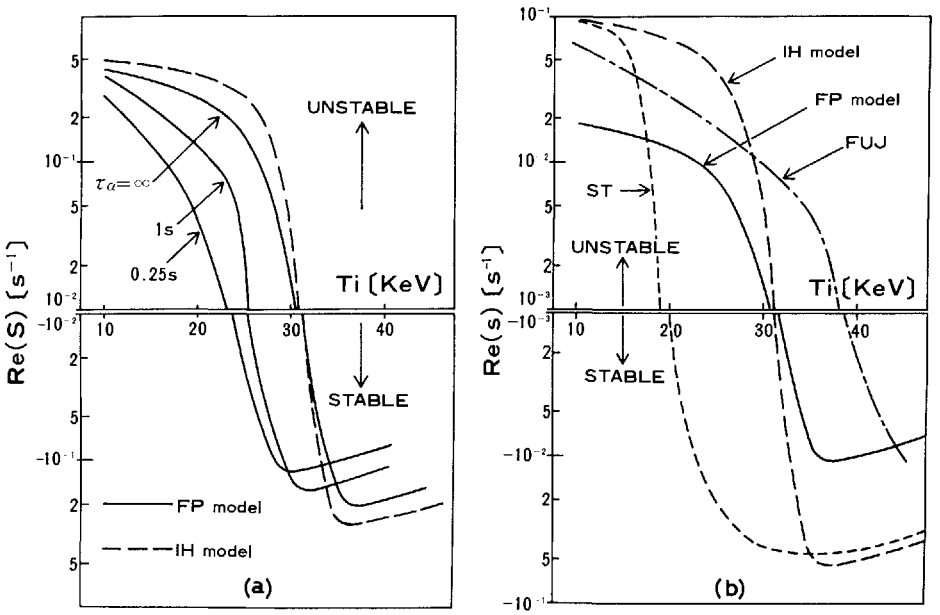


FIG.6. Growth rate [Re(s)] of thermal instability versus T_i; (a) higher plasma density region [$n_0 = 10^{14}$ cm^{-3}, $\tau_\alpha = \infty$, 1 and 0.25 s; corresponding to Fig. 1a], (b) lower density region (2×10^{13} cm^{-3}, $\tau_\alpha = \infty$). The curves denoted as "ST" and "FUJ" are the results from (modified) IH models reported by other authors.

B. Growth rate of thermal instability (temperature mode)

The linearized equations with respect to δT_e and δT_i are derived from the energy equations (5) and (6), and the resultant equations are then Laplace-transformed to yield the relation $[T(s)][\delta T] = 0$, where $[\delta T]$ denotes a vector $\begin{pmatrix} \delta T_e(s) \\ \delta T_i(s) \end{pmatrix}$ and $[T]$ is a matrix given by

$$[T(s)] \equiv \left(\begin{array}{c|c} (3/2)n_0 s - A_{ee}(s) - Y_1 & -[A_{ei}(s) + Y_2] \\ \hline -[A_{ie}(s) + Y_3] & (3/2)n_0 - A_{ii}(s) - Y_4 \end{array} \right) \tag{14}$$

where

$$\begin{aligned} (2/3)Y_1 &= -n_0[K_0 - (\partial K/\partial T_e)_0(T_{i0} - T_{e0})] - S_0 - (k_b/3)\bar{Z}n_0^2 T_{e0}^{-1/2} \\ (2/3)Y_2 &= n_0 K_0, \quad (2/3)Y_4 = -(n_0/2)K_0' - S_0 \\ (2/3)Y_3 &= (n_0/2)[K_0' - (\partial K'/\partial T_e)_0(T_{i0} - T_{e0})] \\ K(T_e) &= t_{eI}^{-1}(T_e) + t_{eD}^{-1}(T_e), \quad K'(T_e) = t_{Te}^{-1}(T_e) + t_{De}^{-1}(T_e) \end{aligned} \tag{15}$$

Here, the variation of the particle equipartition times t_{jk} with δT_i has been neglected.

Finally, the complex frequency for the eigenmodes of the perturbation is determined by a secular equation:

$$\text{determinant of } [T(s)] = 0 \tag{16}$$

Equation (16) can be solved to yield the eigenvalues of s analytically in the case of the IH model in which **two** eigenvalues exist, whereas only numerical analysis is possible for the FP model in which there are **three** eigenvalues. Attention must be paid to the instability (or eigen) mode having the largest real part of the three eigenvalues s [denoted as Re(s)].

Typical examples for the computed results of Re(s) (the growth or damping rate) are shown in Fig.6a for higher plasma density ($n_0 = 10^{14}$ cm^{-3}) and in Fig.6b for lower plasma density ($n_0 = 2 \times 10^{13}$ cm^{-3}), and the results of FP and IH models are compared. It is seen from Fig.6a that, while the discrepancy between the two models is rather small when $\tau_\alpha = \infty$, the tendency of reduced growth rate becomes pronounced in the unstable domain and the stable region is extended to the lower T_i-region, as the value of τ_α decreases. This "stabilizing effect" results from the decrease in the total amount of energy transfer from α-particles with decreasing τ_α, which is accompanied by a severe increase of the plasma confinement time (τ_p) required for the equilibrium condition to be fulfilled (Fig.1a). The T_i-value which gives the minimum value of τ_p decreases with decreasing τ_α (Fig.1a), and this is the reason why the stable region is extended to the lower T_i-region when τ_α decreases. It is to be noted from Figs 1a and 6a that the unstable region expands, to some extent, to the right-hand side of the V-shaped curve representing the equilibrium, in contrast to the case of the IH model.

In case of lower plasma density, shown in Fig.6b, the discrepancy in the growth rate between the two models is further pronounced even when $\tau_\alpha = \infty$. This stabilizing effect in the FP model may be attributed to the inherent characteristics of the α-particle relaxation phenomenon, particularly to a "negative-feedback" effect originating from the matrix element A_{ee} [Eq.(8) and Fig.3], which has already been predicted in our previous article [12]. For comparison, the results of Stacey [16] (ST) and of Fujisawa [11] (FUJ; a modified version of the IH model) are also shown in Fig.6b. The apparent discrepancies among three different results from the IH model may probably be attributed to the difficulty of accurate numerical determination of $d\langle\sigma v\rangle/dT_i$.

5. CONCLUDING REMARKS

As an extension of our previous paper [12], some features of the dynamic and control problems associated with α-particle-heated D-T fusion reactors have been described. These have been obtained by numerically solving the coupled equations consisting of the Fokker-Planck equation for

α-particles (in the presence of α-particle loss) and the particle and energy conservation equations for the background plasma.

It has been found that an "inertial" property inherent in the energy distribution function of α-particles, as well as a sort of "negative feedback" in the energy transfer to background electrons, give rise to pronounced effects on the problem of "start-up" (or "ignition") of the α-particle-heated D-T reactor core plasmas (by neutral-beam injection heating). This is also the case for the "thermal-instability" problem.

Fairly large discrepancies are observed between the results from our new model and those from the "instantaneous-heating" models proposed hitherto by many authors.

REFERENCES

[1] SWEETMAN, D.R., Nucl. Fusion **13** (1973) 157.
[2] McALEES, D.G., CONN, R.W., Nucl. Fusion **14** (1974) 419.
[3] MILLS, R.G., in Nuclear Fusion Reactors Conference (Proc. Conf. Culham Laboratory, 1969) 332.
[4] YAMATO, H., OHTA, M., MORI, S., Nucl. Fusion **12** (1972) 604.
[5] KOLESNICHENKO, Ya.I., REZNIK, S.N., Nucl. Fusion **13** (1973) 167.
[6] STACEY, W.M., Jr., Nucl. Fusion **13** (1973) 843.
[7] HORTON, W., Jr., KAMMASH, T., Technology of Controlled Thermonuclear Fusion Experiments and the Engineering Aspects of Fusion Reactors (Proc. Symp. Austin, 1972) 146.
[8] STACEY, W.M., Jr., Nucl. Fusion **14** (1974) 219.
[9] OHNISHI, M., YOSHIKAWA, H., WAKABAYASHI, J., Nucl. Fusion **13** (1973) 761.
[10] ROSE, D.J., Nucl. Fusion **9** (1969) 183.
[11] FUJISAWA, T., Nucl. Fusion **14** (1974) 173.
[12] TSUJI, H., KATSURAI, M., SEKIGUCHI, T., NAKANO, N., Nucl. Fusion **16** 2 (1976) 287.
[13] SAITO, H., KATSURAI, M., SEKIGUCHI, T., to be submitted to Nuclear Fusion.
[14] SIGMAR, D.J., JOYCE, G., Nucl. Fusion **11** (1971) 447.
[15] STIX, T.H., Plasma Phys. **14** (1972) 367.
[16] STACEY, W.M., Jr., Nucl. Fusion **15** (1975) 63.

THERMAL THERMONUCLEAR INSTABILITY IN A TOKAMAK REACTOR

Ya. I. KOLESNICHENKO, S.N. REZNIK,
Nuclear Research Institute of the Ukrainian SSR
Academy of Sciences,
Kiev,
Union of Soviet Socialist Republics

Abstract

THERMAL THERMONUCLEAR INSTABILITY IN A TOKAMAK REACTOR.

Thermal thermonuclear instability (thermonuclear burning instability) in a tokamak reactor is considered on the assumption that the duration of the plasma pulse is considerably longer than the plasma energy life-time. It was shown previously that this instability gives rise to self-heating of the plasma as a result of which the plasma temperature tends towards the steady-state value T^{st} at which $da/dT > 0$ where $a(T)$ is a function defined by the steady-state equation for the plasma energy balance. In the present paper, the effect of the finiteness of the time taken for thermalization of the highly energetic α-particles (thermonuclear reaction products) and also the finiteness of the time taken for exchange of energy between the electron and ion components of the plasma on the thermal instability is investigated. It is shown that when allowance is made for these factors, the steady states with positive derivatives of da/dT are stable as before. The approximation to these states may however assume the form of damped temperature oscillations about T^{st}. In the case of a non-isothermal plasma, both the function $a(T_i)$ and $a(T_e)$, where T_e and T_i are respectively the plasma electron and ion temperatures, may be used to describe the steady states. The possibility of non-self-sustaining stable thermonuclear burning is also considered in this paper. It is shown that, unlike self-sustaining thermonuclear burning, when additional power is supplied to the plasma, it is possible for a stable steady-state (quasi-steady-state) thermonuclear reaction regime to be established at relatively low plasma temperatures ($T \sim 10$ keV). In this case, the energy released as a result of fusion reactions may considerably exceed the energy supplied to the plasma.

1. INTRODUCTION

It is well known that a positive energy yield in tokamak systems can be achieved at plasma temperatures of $T \cong 10$–20 keV. This temperature is frequently considered to be the "working" temperature of a tokamak. At these temperatures, however, "thermal thermonuclear" instability (thermonuclear burning instability) may develop, owing to the non-linear dependence of the energy release and energy loss of a thermonuclear plasma on the plasma temperature [1]. The development of this instability may result in self-heating of the plasma whereby the plasma temperature increases several-fold within a time of the order of τ_E, where τ_E is the plasma energy life-time [2]. This means that the plasma pressure increases considerably owing to this instability and, as a result, the equilibrium of the plasma column in the magnetic field may be disturbed. If this does not take place, the development of instability terminates in establishing a steady-state plasma temperature which is considerably higher than the temperature to which the plasma was heated by external heating sources.

Investigations carried out recently [3] have shown that the conditions for the development of thermal thermonuclear instability can be expressed by means of the function $a(T)$ (where a is the radius of the plasma column and T is the temperature at the centre of the plasma) which is derived from the steady-state equation for the plasma energy balance. The existence of this function is due to the fact that when a is constant, the thermonuclear reaction energy entering the plasma is exactly compensated by the plasma energy losses only at certain temperatures [4].

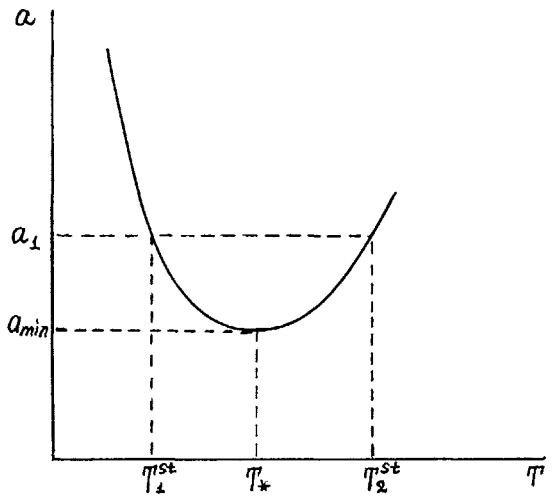


FIG.1. Relationship between steady-state temperature and radius of plasma column.

Only those temperature values for which $da/dT > 0$ are found to be stable, however [3]. If the thermonuclear reaction is the main source of energy, the function a(T) has a minimum for tokamaks (Fig. 1). A state with a high plasma temperature is therefore stable. The development of thermal thermonuclear instability results in the establishment of this particular temperature.

Thermonuclear burning will take place in a reactor when the plasma temperature at the centre of the plasma column is several orders of magnitude higher than the temperature at the periphery. A spatially inhomogeneous plasma was therefore considered in Ref. [3] and in a previous study [4], where the conditions for the steady-state evolution of a thermonuclear reaction were investigated on the basis of the function a(T). At the same time, however, it was assumed in these investigations that the highly energetic α-particles instantaneously yield their energy to the plasma which was assumed to the isothermal. In reality, however, both the α-particle thermalization time (τ_T) and the time taken for exchange of energy between the plasma electron and ion components (τ_{ei}^e) are non-zero and may be comparable to the characteristic times for the variation in the plasma parameters. It is, therefore, important to investigate the effect of the finiteness of τ_T and τ_{ei}^e on the thermal thermonuclear instability. All these questions are considered in Sections 3 and 4 of this paper. A qualitative picture of thermal instability in a homogeneous plasma is given in Section 2 and the effect of the inhomogeneity of the plasma on this instability is discussed. In Section 5 the possibility of achieving a stable thermonuclear reaction at a plasma temperature of $T \cong 10$ keV in a tokamak reactor is considered. This consideration is necessary because stable steady-state temperatures are generally rather high [2]. These aspects are investigated on the assumption that the characteristic time for the variation in the plasma density is considerably greater than the characteristic time for the variation in the temperature.

It should be noted that apart from Refs [1–4] a considerable number of other investigations on thermal thermonuclear instability have recently been carried out (see, e.g. Refs [5–9]). A survey of the results of these investigations is not within the scope of the present paper, however. In a number of investigations in which the dynamics of plasma heating is investigated numerically it was shown that self-heating of the plasma can take place owing to the development of a thermonuclear reaction [10, 11].

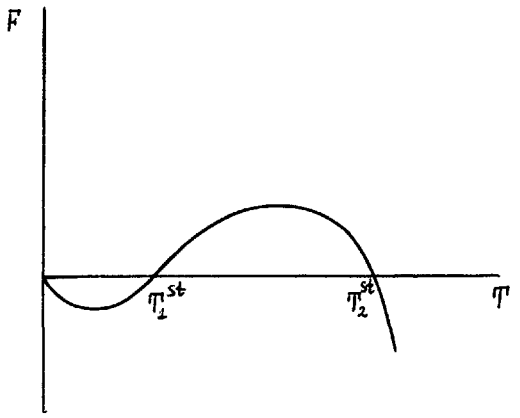


FIG.2. The function $F(T) = Q_+(T) - Q_-(T)$ for $a > a_{min}$.

2. THERMONUCLEAR BURNING INSTABILITY IN HOMOGENEOUS AND INHOMOGENEOUS PLASMAS

First, we consider a simple model of a thermonuclear plasma. It is assumed that the plasma is isothermal and homogeneous and that the thermonuclear reaction is self-sustaining. The plasma density n will be assumed to be constant. When this is the case, the following equation for the plasma energy balance is valid:

$$3n\frac{dT}{dt} = F(n, T, a) \tag{2.1}$$

where

$$F = Q_+(n, T) - Q_-(n, T, a) \tag{2.2}$$

$$Q_+ = \epsilon_\alpha r(n, T),\ r = \frac{n^2\langle\sigma v\rangle}{4},\ \epsilon_\alpha = 3{,}5\ \text{MeV} \tag{2.3}$$

$$Q = \frac{3nT}{\tau_E} + Q_{rad}(n, T, a),\ \tau_E = \frac{a^2}{\chi} \tag{2.4}$$

Here Q_+ is the thermonuclear reaction energy entering the plasma, Q_- are the plasma energy losses due to thermal conduction and radiation (Q_{rad}), r(n, T) is the thermonuclear reaction rate and χ is the plasma thermal conductivity coefficient.

Now we analyse Eq. (2.1). If it is assumed that $F = 0$ (i.e. $dT/dt = 0$), we derive the function a(T) plotted in Fig. 1. This figure shows that two steady-state temperatures, T_1^{st} and T_2^{st}, are possible in a plasma column of radius a_1 (if $a_1 > a_{min}$). When $a = a_1$, the function F is positive in the region $T_1^{st} < T < T_2^{st}$ and is negative outside this region (Fig. 2). The sign of the function F determines the sign of the derivative dT/dt, however. If $T_1^{st} < T < T_2^{st}$, therefore, energy release in the plasma will predominate over energy loss and self-heating of the plasma will take place whereas, if $T < T_1^{st}$ or $T > T_2^{st}$, the converse situation is found. The steady-state value T_1^{st} for which

$da/dT < 0$ is, therefore, found to be unstable whereas T_2^{st} for which $da/dT > 0$ is stable. The temperature T_* where $a = a_{min}$ is the minimum temperature for which thermonuclear burning is stable.

By applying Eq. (2.1) it is readily found that a considerable variation in temperature may take place within a time of the order of τ_E during the development of thermal thermonuclear instability. This instability may, therefore, be an important factor, not only for steady-state systems, but also for the experimental tokamak reactors presently at the planning stage. As the steady-state value T^{st} is approached, the rate of temperature variation decreases. Assuming that, in the vicinity of T^{st}, $T = T^{st} + \delta T$, $\delta T = \delta\hat{T}e^{\gamma t} \ll T^{st}$ we obtain the following expression from Eq. (2.1) in the absence of magnetic bremsstrahlung [2]:

$$\gamma = -\frac{2}{\tau_E}\frac{d\ln a}{d\ln T} \tag{2.5}$$

If the energy losses due to magnetic bremsstrahlung are appreciable, γ is not expressed directly in terms of τ_E, however, as before, $\gamma \sim -da/dT$.

Analysis of the energy balance of an inhomogeneous plasma is considerably more complex. In this case, $T^{st} = T^{st}(\vec{r})$ and, therefore, even if the plasma temperature in a certain region is the same as its steady-state value, it may deviate substantially from T^{st} in other regions. Nevertheless, as the energy balance equation for an inhomogeneous plasma is a parabolic equation, it may be asserted that the development of thermal instability terminates in establishing a stable steady-state radial distribution for the plasma temperature if the plasma column exists for a sufficiently long time. It is, therefore, sufficient to investigate the stability of steady-state distributions of T^{st} with respect to slight perturbations of the temperature $\delta T(\vec{r})$. This problem was solved in Ref. [3].

The initial attitude adopted in Ref. [3] was that the steady states in an inhomogeneous plasma are conveniently described by means of the function $a(T_m)$ where $T_m = T(r = 0)$ is the temperature at the axis of the plasma column [4]. Investigations carried out in Ref. [3] showed that the steady-state temperature distributions with $da/dT_m > 0$ are stable with respect to the fluctuations δT with an arbitrary spatial distribution. In toroidal systems, moreover, owing to the rotational transform of the magnetic field lines, the only increasing form of the fluctuation δT is that whereby either an increase or a decrease in the temperature takes place at every point in the plasma. The general conclusion which can be drawn from the results of Ref. [3] is that the effect of the inhomogeneity on the thermal thermonuclear instability is quantitative rather than qualitative in character. Allowance must be made for the inhomogeneity in order to establish the real curve $a(T_m)$ which is used to determine both the minimum plasma radius necessary for stable thermonuclear burning and the values of the temperature T_2^{st} established as a result of the development of thermal thermonuclear instability. Nevertheless, it is sufficient to confine our considerations to an approximation of a homogeneous plasma to investigate thermal instability in qualitative terms.

3. EFFECT OF THE FINITENESS OF THE α-PARTICLE THERMALIZATION TIME ON THERMAL THERMONUCLEAR INSTABILITY

In investigating the energy balance, it is usually assumed that the thermonuclear reaction energy entering the plasma is defined by the equation $Q_+ = \epsilon_\alpha r$. This equation was also used in the analysis conducted above. Strictly speaking, however, this equation is only valid if the highly energetic α-particles instantaneously yield their energy to the plasma. In practice, however, the variation in the α-particle energy is defined by the equation

$$\frac{d\epsilon}{dt} = -\frac{\epsilon}{\tau_T}, \quad \epsilon(t = t_0) = \epsilon_\alpha = 3.5 \text{ (MeV)} \tag{3.1}$$

where t_0 is the time when the α-particles are produced and τ_T is the characteristic time for the variation in the α-particle energy which depends on the plasma parameters, the α-particle energy at the time t and also on the level of electromagnetic noise in the plasma. If τ_T is predominantly dependent on Coulomb particle collisions it follows that

$$\tau_T = \frac{5 \times 10^{11}\, T_e^{3/2}\,(\text{keV})}{n_e\,(\text{cm}^{-3})}$$

From this we deduce that for the plasma parameters $n \cong 5 \times 10^{13}$ cm^{-3} and T = 20 keV, $\tau_T \cong 1$ s. τ_T can, therefore, be comparable to the characteristic times for the variation in the plasma parameters Δt. It is, therefore, interesting to investigate the effect of the finiteness of τ_T on the thermal thermonuclear instability.

The energy penetrating the plasma is defined by means of an expression in which allowance is made for the finiteness of τ_T:

$$\tilde{Q}_+(t) = -\int_{-\infty}^{t} dt_0\, r(t_0)\, \frac{d\epsilon}{dt}(t, t_0) \tag{3.2}$$

where $d\epsilon/dt\,(t, t_0)$ is the rate of variation at the time t of the energy of the α-particles produced at the time t_0. Evidently, if $\Delta t \gg \tau_T$, $\tilde{Q}_+ = Q_+$.

If Eqs (3.1) and (3.2) are to be used in practical applications, it is necessary to define τ_T more precisely. An expression for τ_T is only known, however, for the case where turbulence is absent and, even in this case, τ_T is an extremely complex function, $\tau_T(T, \epsilon)$. We, therefore, confine our investigations to a model treatment assuming that τ_T = const. As will subsequently become apparent, this treatment enables very definite conclusions to be drawn.

When τ_T = const. it follows from Eq. (3.1) that

$$\epsilon(t, t_0) = \epsilon_\alpha e^{-\frac{t-t_0}{\tau_T}}$$

and, therefore,

$$\tilde{Q}_+ = \frac{\epsilon_\alpha}{\tau_T}\, e^{-\frac{t}{\tau_T}} \int_{-\infty}^{t} dt_0\, r(t_0)\, e^{\frac{t_0}{\tau_T}} \tag{3.3}$$

On substituting Eq. (3.3) into Eq. (2.1) instead of Q_+ and differentiating the equation thus derived with respect to t, we then find after simple transformations that

$$\tau_T \frac{d^2T}{dt^2} + A\frac{dT}{dt} = F_1 \tag{3.4}$$

where

$$A = 1 + \frac{\tau_T}{3n}\frac{\partial Q_-}{\partial T} > 0, \quad F_1 = (Q_+ - Q_-)/3n \tag{3.5}$$

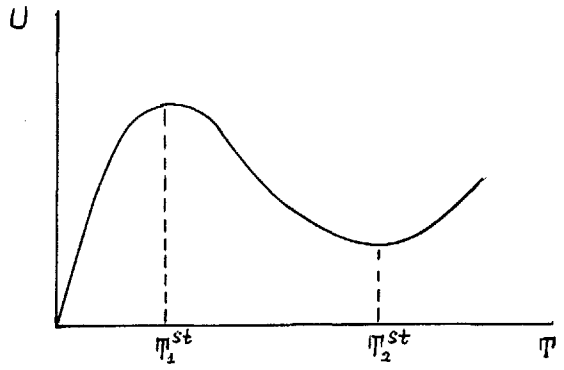


FIG.3. Form of the potential $U(T) = -\int^{T} \frac{1}{3n}(Q_+ - Q_-)\,dT$.

Equation (3.4) is similar in form to the equation for the motion of particles in a potential field where frictional forces are present, where τ_T, T, A dT/dt and the function

$$U = -\int^{T} F_1\,dT,$$

respectively, function as the mass, the co-ordinate, the frictional force and the potential. The form of the potential U(T) is plotted in Fig. 3. This figure shows that the maximum potential corresponds to the steady-state temperature T_1^{st} and the minimum potential corresponds to the temperature T_2^{st}. The system, therefore, tends to undergo transition to the state with $T = T_2^{st}$. In this case, the transition to the steady state may be accompanied by damped temperature oscillations about T_2^{st}. The nature of the process whereby the temperature T_2^{st} is established clearly depends on the relationship between the "frictional force" A dT/dt and the "particle mass" τ_T.

When allowance is made for the finiteness of τ_T, the temperature T_2^{st} for which $da/dT > 0$ is, therefore, stable as before. The approaches to T_2^{st} may, however, be oscillatory in character. To identify the conditions where this will take place, a state deviating slightly from equilibrium is considered, i.e. $T = T^{st} + \delta T$, $\delta T \ll T^{st}$. In this case we derive the normal equation $F = 0$ for T^{st} and the following equation for δT (for conciseness, T is written instead of T^{st}):

$$\tau_T \frac{d^2\delta T}{dt^2} + A\frac{d\delta T}{dt} - \frac{1}{3n}\frac{\partial F}{\partial T}\delta T = 0 \tag{3.6}$$

On representing δT in the form $\delta T = \sum_{i=1,2} C_i \exp(\gamma_i t)$ we obtain:

$$\gamma_{1,2} = \frac{1}{2\tau_T}\left\{-A \pm \sqrt{A^2 + \frac{4\tau_T}{3n}\frac{\partial F}{\partial T}}\right\} \tag{3.7}$$

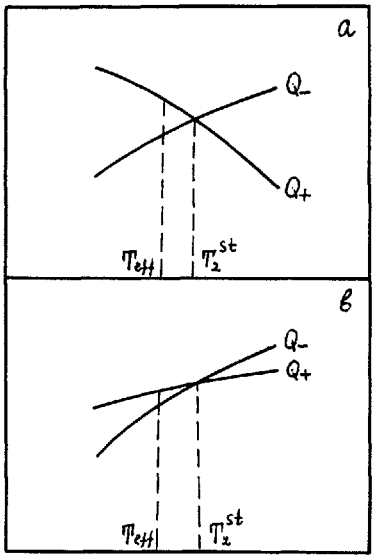


FIG.4. Plasma energy release and energy loss on approaching the stable steady-state temperature T_2^{st} *in the cases* $\left.\frac{\partial Q_+}{\partial T}\right|_{T_2^{st}} < 0$ *(a) and* $\left.\frac{\partial Q_+}{\partial T}\right|_{T_2^{st}} > 0$ *(b).* T_{eff} *is the effective temperature for* Q_+ *on approaching* T_2^{st} *from the left.*

As is to be expected, in the temperature region where $\partial F/\partial T > 0$ (i.e. $da/dT < 0$), the steady states are unstable: $\gamma_1 > 0$. $\gamma_2 < 0$ however and therefore, if a fluctuation δT takes place at the time t = 0, then $d\delta T/dt|_{t=0} = -\delta Q_-$ and the fluctuation will be damped initially.

The region where $\partial F/\partial T < 0$ and therefore $da/dT > 0$ is therefore considered. If the expression under the root sign in Eq. (3.7) is represented as

$$\Delta = \left(1 - \frac{\tau_T}{3n}\frac{\partial Q_-}{\partial T}\right)^2 + \frac{4\tau_T}{3n}\frac{\partial Q_+}{\partial T}$$

we conclude that if $d\langle\sigma v\rangle/dT > 0$ then $\gamma_{1,2} < 0$ and allowance for the finiteness of τ_T does not give rise to oscillations. If $d\langle\sigma v\rangle/dT < 0$ then $\gamma_{1,2}$ may become complex ($R\gamma_{1,2} < 0$). From this it follows that in a device where the stable steady-state temperature is high, $T_2^{st} \gtrsim 70$ keV ($\Delta < 0$), the approach to this value will be accompanied by oscillations in the temperature.

The effect of the finiteness of τ_T can be illustrated by means of Fig. 4 which shows Q_+ and Q_- as a function of T. The finiteness of τ_T has the effect that, at the time t, the energy penetrating the plasma depends on the temperature at the preceding points in time (roughly speaking, at the time $t-\tau_T$). It may, therefore, be asserted that Q_+ depends on a certain temperature T_{eff}. When self-heating of the plasma takes place, $T_{eff} < T$ and, therefore, in the case where $\partial Q_+/\partial T < 0$ when the temperature attains the value T_2^{st}, $Q_+(T_{eff}) > Q_-(T)$ (see Fig. 4) and, as a result, the temperature "races through" the steady-state values. The temperature continues to increase until $Q_+(T_{eff}) = Q_-(T)$ after which the temperature decreases. In the other case where $\partial Q_+/\partial T > 0$ temperature oscillations are clearly not possible as can be seen from Fig. 4. These discussions are clearly applicable for arbitrary values of τ_T and not only for τ_T = const.

4. THERMAL THERMONUCLEAR INSTABILITY IN A NON-ISOTHERMAL PLASMA

The effect of the finiteness of the time taken for the exchange of energy between the electron and ion components of the plasma (τ_{ei}^{ϵ}) is considered. The following equations will be taken as the starting point:

$$\frac{3}{2} n \frac{dT_i}{dt} = F_i(n, T_e, T_i, a) \tag{4.1}$$

$$\frac{3}{2} n \frac{dT_e}{dt} = F_e(n, T_e, T_i, a) \tag{4.2}$$

where

$$F_i = \frac{n\epsilon_{\alpha i}}{\tau_f} - \frac{3}{2}\frac{nT_i}{\tau_{Ei}} + \frac{3n(T_e - T_i)}{\tau_{ei}^{\epsilon}} \tag{4.3}$$

$$F_e = \frac{n\epsilon_{\alpha e}}{\tau_f} - \frac{3}{2}\frac{nT_e}{\tau_{Ee}} - \frac{3n(T_e - T_i)}{\tau_{ei}^{\epsilon}} - Q_{rad} \tag{4.4}$$

and $n = n_e = n_i$; τ_{Ee}, τ_{Ei} are the energy life-times of the electron and ion components of the plasma;

$$\tau_{ei}^{\epsilon} = \frac{3}{2\sqrt{2\pi}} \frac{\mu_i}{m_e} \frac{T_e^{3/2}}{e^4 \Lambda n}$$

μ_i is the reduced mass of the deuterium and tritium ions, Λ is the Coulomb logarithm; $\epsilon_{\alpha e}$ and $\epsilon_{\alpha i}$ are the energies yielded to the electrons and ions by the α-particles and $\tau_f = 4/n\langle\sigma v\rangle$. The following approximate expressions will be applied for $\epsilon_{\alpha e}$ and $\epsilon_{\alpha i}$ [12]:

$$\epsilon_{\alpha e} = \epsilon_\alpha - \epsilon_{\alpha i} \tag{4.5}$$

$$\epsilon_{\alpha i} = \epsilon_\alpha \frac{2}{3}\alpha^2 \left\{ \sqrt{3}\left(\operatorname{arctg}\frac{2-\alpha}{2\sqrt{3}} + \frac{\pi}{6}\right) - \frac{1}{2}\ln\frac{(1+\alpha)^3}{1+\alpha^3} \right\} \tag{4.6}$$

where

$$\alpha = \left(\frac{3\sqrt{\pi}}{8}\frac{m_\alpha}{\mu_i}\left(\frac{m_\alpha}{m_e}\right)^{1/2}\right)^{1/3}\sqrt{\frac{T_e}{\epsilon_\alpha}}$$

and m_α is the mass of the α-particles.

From Eqs (4.1) and (4.2) it follows that the steady states are described by the following equations: $F_i = 0$, $F_e \approx 0$. From this it is apparent that the steady states in a non-isothermal plasma can be described using the two functions: $a(T_i)$ or $a(T_e)$.

The stability of the steady-state temperature values is investigated. Assuming that $\delta T_{e,i} = \delta\hat{T}_{e,i} e^{\gamma t} \ll T_{e,i}^{st}$, from the linearized Eqs (4.1) and (4.2) we derive (T is written instead of T^{st} as above):

$$\gamma_{1,2} = \frac{1}{2}\left\{ -B \pm \sqrt{B^2 - 4C} \right\} \tag{4.7}$$

$$B = -\left(\frac{\partial F_i}{\partial T_i} + \frac{\partial F_e}{\partial T_e}\right), \quad C = \frac{\partial F_i}{\partial T_i}\frac{\partial F_e}{\partial T_e} - \frac{\partial F_i}{\partial T_e}\frac{\partial F_e}{\partial T_i} \tag{4.8}$$

Applying the steady-state equations $F_i = 0$, $F_e = 0$ the expression for C is transformed as follows:

$$C = \frac{da}{dT_i}\left(\frac{\partial F_i}{\partial T_e}\frac{\partial F_e}{\partial a} - \frac{\partial F_e}{\partial T_e}\frac{\partial F_i}{\partial a}\right) = \frac{da}{dT_e}\left(\frac{\partial F_e}{\partial T_i}\frac{\partial F_i}{\partial a} - \frac{\partial F_i}{\partial T_i}\frac{\partial F_e}{\partial a}\right) \tag{4.9}$$

From Eq. (4.9) it follows that, at the temperatures for which the functions $a(T_{e,i})$ have extreme values, $C = 0$, and one of the roots of Eq. (4.7) is equal to 0: $\gamma_1 = 0$. In this case, the second root $\gamma_2 = -B$.

If a definitive answer is to be given to the question of the stability of the steady states, it is necessary to determine the signs of the coefficients in Eq. (4.7). On analysing the expressions for these coefficients, it is found that for moderate transfer coefficients in the plasma ($\tau_E \sim T^{-\ell}$, $\ell > -1$) and for $|T_e - T_i|/T_e < 1$, $B > 0$, and the sign of C is the same as that of the derivative $da/dT_{e,i}$. It, therefore, follows that $\gamma_2 < 0$ and sign $\gamma_1 = -$sign $da/dT_{e,i}$. γ may become complex in the high-temperature region.

It should be noted that in this treatment of the problem no allowance is made for the finiteness of the time taken for transfer of energy from the α-particles to the electrons and ions (τ_{T_e}, τ_{T_i}). By reasoning as in the previous section it can be shown, however, that allowance for the finiteness of τ_{T_e} and τ_{T_i} does not give rise to qualitative effects when $\tau \lesssim 70$ keV.

The criterion for thermonuclear burning stability, $da/dT > 0$, obtained in a simple model of a thermonuclear plasma,is therefore still valid when transition is made to a more realistic description of the plasma.

5. THERMAL INSTABILITY IN THE PRESENCE OF EXTERNAL PLASMA HEATING SOURCES

In the course of a self-sustaining thermonuclear reaction in a tokamak reactor the steady-state plasma temperatures may be extremely high. If the transport processes in the plasma are neo-classical therefore, it is found that $T^{st} \cong 70$ keV for the tokamak parameters $a \cong 100$–200 cm, $\epsilon \cong 0.4$, $B \cong 40$ kG, and $n \cong 5 \times 10^{13}$ cm^{-3} [2]. If a steady-state (quasi-steady-state) thermonuclear reaction is to be achieved in a lower temperature regime, it is therefore necessary to control the plasma energy currents. Another possibility does, however, exist since when the energy input to the plasma is steady-state, a section of the curve a(T) is found to have a positive derivative.

If the energy input to the plasma is steady-state, the steady-state equation for the plasma energy balance assumes the following form:

$$F(n, T, a) + Q_0 = 0 \tag{5.1}$$

where the function F is defined by expression (2.2) and Q_0 is the power input to the plasma calculated per unit volume. Depending on the value of Q_0, three types of curves a(T) can be obtained by applying Eq. (5.1) (Fig. 5). Curve 1 corresponds to the minimum input power and curve 3 to the maximum input power. In the second case, all the steady-state temperatures are stable. An interesting case is the intermediate one where stable states exist in the low-temperature region ($T \cong 10$ keV) for $a < a_{max}$ whereas for $a > a_{max}$ these states only exist in the high-temperature region.

It is readily apparent that if more than one stable state exists in the system, the state with the lowest temperature will be established. In the case shown in Fig. 5, curve 1, therefore, a temperature of $T \cong 4$ keV becomes established, which is of no practical importance. The plasma

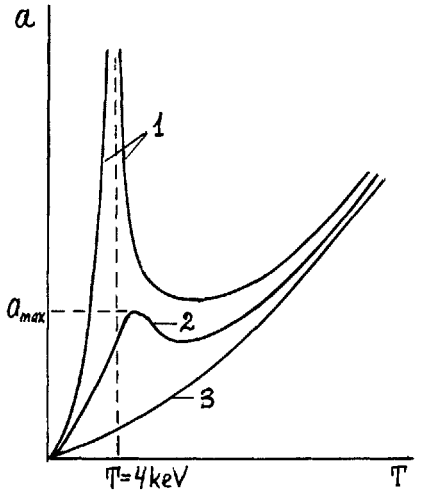


FIG.5. Function a(T) with steady-state energy input into the plasma.

can, however, be heated to the temperature on the right-hand side of this section of curve a(T) where $da/dT < 0$ by the temporary introduction of a high-power supply, and, in this case, the thermonuclear reaction will be self-sustaining,and self-heating of the plasma will take place to high temperatures.

If the input power is sufficiently high, therefore, a stable thermonuclear reaction may be achieved not only in the high-temperature region, but also at a plasma temperature of $T \cong 10$ keV (curves 2 and 3 in Fig. 5). Clearly, the only cases of practical interest are those where the power input into the plasma is small compared with the power released as a result of the thermonuclear reaction. It is, therefore, necessary to calculate the value of Q_0 required to achieve curves 2 and 3 in Fig. 5.

It is readily shown that curve 2 is achieved when

$$Q_1 < Q_0 < Q_2 \tag{5.2}$$

and curve 3 when

$$Q_0 > Q_2 \tag{5.3}$$

where

$$Q_1 = G_{max} = 7.3 \times 10^{-31} n^2 \ (W \cdot cm^{-3}) \tag{5.4}$$

$$Q_2 = \left(G - \frac{T}{\ell+1}\frac{dG}{dT}\right)_{max} \tag{5.5}$$

$$G = Q_- - Q_+$$

$Q_b = bn^2\sqrt{T/4}$, b = const is the plasma energy loss by bremsstrahlung, $g = \epsilon_\alpha \langle\sigma v\rangle - b\sqrt{T}$, and ℓ is the exponent in the law $\tau_E \sim T^{-\ell}$. From Eq. (5.5) it follows that Q_2 has a maximum value for classical transport processes:

$$Q_2 = 10^{-28}\, n^2\ (W\cdot cm^{-3})\, \tau_E \sim \tau_E^{cl} \tag{5.6}$$

$$Q_2 = 3 \times 10^{-29}\, n^2\ (W\cdot cm^{-3})\, \tau_E = \text{const} \tag{5.7}$$

$$Q_2 = 4.3 \times 10^{-30}\, n^2\ (W\cdot cm^{-3})\, \tau_E \cong \tau_E^{Bohm} \tag{5.8}$$

To consider a specific example, let $n = 5 \times 10^{13}$ cm^{-3}, $\tau_E = 10^{-5}\, a^2\, B_\theta$, $B_\theta = 6$ kG, and $Q_0 = 0.078$ W·cm^{-3}. As $Q_0 > Q_2$, we obtain curve 3 in Fig. 5. Any steady-state temperature value is, therefore, stable. In particular, if T = 15 keV we obtain $a \cong 200$ cm. In this case, the energy released as a result of nuclear reactions considerably exceeds the energy input to the plasma:

$$\frac{Q_{fus}}{Q_0} = \frac{\epsilon_{fus}\, n^2 \langle\sigma v\rangle}{4\, Q_0} = 7.5 \tag{5.9}$$

where $\epsilon_{fus} = 22.4$ MeV.

REFERENCES

[1] MILLS, R.G., in Engineering Problems of Fusion Research (Proc. Symp. Los Alamos Scientific Laboratory), LA-4250 (1969).
[2] KOLESNICHENKO, Ya.I., REZNIK, S.N., FURSA, A.D., Fiz. Plazmy 2 6 (1976).
[3] KOLESNICHENKO, Ya.I., et al., Nucl. Fusion 16 (1976) 105.
[4] KOLESNICHENKO, Ya.I., Nucl. Fusion 12 (1972) 419.
[5] OHTA, M., YAMATO, H., MORI, S., in Plasma Physics and Controlled Nuclear Fusion Research (Proc. Conf. Madison, 1971) 3, IAEA, Vienna (1971) 423.
[6] POWELL, C., HANN, O.I., Nucl. Fusion 12(1972) 667.
[7] OHNISHI, M., et al., Nucl. Fusion 13 (1973) 761.
[8] STACEY, W.M., Jr., Nucl. Fusion 13 (1973) 843.
[9] STACEY, W.M., Jr., Nucl. Fusion 15 (1975) 63.
[10] DNESTROVSKII, Yu.N., KOSTOMAROV, D.P., Supplement to "Computing Methods in Plasma Physics", Izd. "Mir", M, 1974.
[11] LYSENKO, S.E., POPKOV, G.N., Nucl. Fusion, Spec. Suppl. (1975) 269.
[12] SIGMAR, D.I., JOYCE, G., Nucl. Fusion 11 (1971) 1147.

STATIONARY TEMPERATURE PROFILE IN A TOKAMAK REACTOR OPERATED IN THE NEOCLASSICAL REGIME

T.F. VOLKOV, Yu.L. IGITKHANOV, M.Z. TOKAR'
I.V. Kurchatov Institute of Atomic Energy,
Moscow,
Union of Soviet Socialist Republics

Abstract

STATIONARY TEMPERATURE PROFILE IN A TOKAMAK REACTOR OPERATED IN THE NEOCLASSICAL REGIME.

It is shown that the neoclassical character of the transport processes allows operation of fusion in a regime where a zone of cold plasma capable of protecting the wall from sputtering is formed near the wall. The possibility of establishing such a regime is determined by the "impermeability" of the reactor plasma with respect to the neutral atoms.

1. Protection of the reactor first wall from sputtering by high-temperature plasma as well as keeping the impurity content in the working volume low are the most important problems on the road to realization of controlled nuclear fusion. One way of solving these problems is to determine and reach a reactor regime which would allow the co-existence of two zones, one of which is a zone of active hot plasma in the centre and the other one is cold plasma at the periphery, capable of protecting the wall against sputtering. The ion temperature in the wall zone should be lower than the threshold energy of the wall material sputtering. The extension of the protecting layer should be larger than the penetration depth of the charge-exchange neutral atoms, which, in turn, depends on the plasma density in this layer. It will be shown later on that the transport equations of neoclassical theory have a stationary solution at which a hot zone of thermonuclear reactions is found to be spatially localized and surrounded by a cold plasma layer similar to a plasma blanket.

2. On the assumption that the energy containment time determined by the neoclassical value of the thermal conductivity (cycle duration) is less than the characteristic time of temperature variations in the reactor volume (time of operation), we shall start from the stationary equation of energy balance:

$$-\frac{1}{r}\frac{d}{dr}\left(r\chi_i\frac{dT}{dr}\right)=Q_F-Q_R \tag{1}$$

where

$$\chi_i = q^2 n\rho_i^2\nu_i\left(1.6+\frac{1}{q^2}+\frac{0.68\,\epsilon^{3/2}}{1+0.36\,qR/\epsilon^{3/2}\lambda}\right) \tag{2}$$

$$Q_F = 3.24\times10^{-9}\frac{n^2}{T_{keV}^{2/3}}\,\frac{\exp\left(-20/T_{keV}^{1/3}\right)}{1+\left(\frac{T_{keV}}{70}\right)^{1/3}}, \quad \left(\frac{keV}{cm^3\cdot s}\right) \tag{3}$$

$$Q_R = 3.32\times10^{-15}\,n^2\sqrt{T_{keV}}, \quad \left(\frac{keV}{cm^3\cdot s}\right) \tag{4}$$

Here χ_i is the neoclassical coefficient of thermal conductivity, presented in the form of an interpolation formula which describes the frequency dependence in all three collisional regimes simultaneously, Q_F is the power of the fusion energy of a 50% mixture of deuterium and tritium nuclei, on the assumption that the time of the energy transfer of alpha particles is small compared with the energy containment time, and Q_R is the power of the bremsstrahlung losses. The current density was taken constant over the cross-section so that $q_0 = B_0/0.2\,R_{j_0}$, $\rho_i = v_{T_i}/\omega_{ei}$, $\lambda = v_{T_i}/\nu_i$, $\epsilon = r/R$ and $T_e = T_i = T$ because the plasma thermalization time is short compared to the energy containment time.

Since the diffusion time is substantially longer than the energy containment time, Eq. (1) can be considered separately from the diffusion equation, i.e. at a certain given density profile, in particular, when the plasma flux flowing across the magnetic surfaces vanishes. Such a stationary solution should be possible for the hot zone of the reactor, in which there are no neutral atoms[1]. In the case of sufficiently large $\beta_\theta = 8\pi p/B_\theta^2$, when the particle fluxes are of a diffusional nature, the density profile to be determined is locally related to the temperature profile and can be found from the compensation condition of the well known expressions for averaged diffusion and thermal diffusion fluxes in each of the three neoclassical regimes. In a highly collisional regime, taking into account the contribution of the longitudinal thermal force [1, 2], i.e. for

$$nv_r = -2D_\perp q_0^2 \left(\frac{0.66}{T}\,\frac{d\,nT}{dr} - 0.27\,\frac{n}{T}\,\frac{dT}{dr}\right) \tag{5}$$

we find – the coefficients of Eq. (5) are known within an accuracy of 10% –

$$nT^{3/5} = \text{const}, \quad \left(\nu_e > \frac{v_{T_e}}{q_0 R}\right) \tag{6}$$

In the weakly collisional region [3],

$$nv_r = -q_0^2 D_\perp \epsilon^{-3/2} n\left(-2.24\,\frac{1}{n}\,\frac{dn}{dr} + 0.62\,\frac{1}{T}\,\frac{dT}{dr}\right) \tag{7}$$

we find

$$nT^{-1/4} = \text{const}, \quad (\nu_e < \epsilon^{3/2} v_{Te}/q_0 R) \tag{8}$$

For the intermediate-frequency regime [3],

$$nv_r = -q_0^2 D_\perp n\,\frac{v_{T_e}}{qR\nu_e}\left(\frac{1}{n}\,\frac{dn}{dr} + \frac{3}{2}\,\frac{1}{T}\,\frac{dT}{dr}\right) \tag{9}$$

we have

$$nT^{3/2} = \text{const}, \quad \left(\epsilon^{3/2}\,\frac{v_{T_e}}{q_0 R} < \nu_e < \frac{v_{T_e}}{q_0 R}\right) \tag{10}$$

[1] Injection of fuel and removal of ash seem to distort the stationary profile to a certain extent.

3. Figures 1, 2 show the results of the numerical calculations of Eqs (1), (6), (8) and (10) for $B_0 = 35$ kG, $q_0 = 3.5$, $R = 5 \times 10^2$ cm. The values of $T_0 = 10$ keV, $n_0 = 0.5 \times 10^{14}$ cm^{-3} and $dT/dr|_0 = 0$ on the axis were taken as the boundary condition. The value of $\lambda = v_{T_i} \tau_i$ was checked at every step and the transport coefficients were used in the corresponding neoclassical regime. A narrow plateau region is formed near the magnetic axis at $r \to 0$ (since, however, the bounce frequency vanishes, this is a purely geometrical factor). Then, a banana region with a thermal conductivity coefficient of $\chi_b = \epsilon^{-3/2} \cdot$ const, independent of both density and temperature profiles, is formed in a large area over the radius. Initially, the temperature profile is flat, and then it decreases to about 300 eV at the boundary of the plateau region. It should be pointed out that the reactor core is located entirely in the banana region and amounts to 60–65% of the working volume. The energy is transported, through thermal conductivity and radiation, outside the core $r > r_a \approx 140$ cm,

$$2\pi r q_T(r) = W_F - 2\pi \int_0^r r Q_R \, dr \tag{11}$$

where

$$W_F = 2\pi \int_0^r r Q_F \, dr$$

is the total power of the fusion energy per unit length of the plasma column, and $q_T = -\chi_i \, dT/dr$. We see from Eq. (11) that $q_T(r)$ should be maximum in this range, and radiation losses decrease proportionally to T. It should be noted that the transport coefficients in the banana regime are responsible for the temperature to drop (for the boundary conditions under consideration) to a very small value at a technically reasonable distance from the axis (Fig. 3), in contrast to the classical regime. This is due to the fact that the classical thermal conductivity value increases as $T^{-1.7}$ with decreasing temperature while the banana thermal conductivity decreases with distance as $\epsilon^{-3/2}$. At $r \gtrsim r_a$, where the released fusion energy in Eq. (1) can be neglected, the tail of the temperature can easily be determined in the banana region as

$$T = T_0 \sqrt{x} \, [0.92 \, I_{-3/7}(0.57 \, x^{7/6}) = I_{3/7}(0.57 \, x^{7/6})] \tag{12}$$

where $x = r^{3/7}/r_0^{3/7}$, $r_0 = B_0^2/2.8 \times 10^{11} R^{3/2} q_0^2$, and the coefficients are determined by matching with the numerical solution. It is seen from Eq. (12) that the temperature decreases almost linearly if $x \ll 1$ is taken into account and a series expansion is carried out.

As the temperature decreases over the radius, the collision frequency decreases too, when one enters the plateau region. Both density $n \sim T^{-3/2}$, and radiation losses, $Q_R \sim T^{-5/2}$, start to become substantial in this region.

Let us note that the plateau region occupies a rather small transition zone over the radius in the regime under consideration. The occurrence of a strongly collisional regime at the periphery with $\nu > v_T/qR$ of dense and cold plasma with a thermal conductivity of $\chi \sim T^{-1.7}$ is of fundamental importance. The latter plays a very essential role in establishing an extended temperature tail. In this regime, the temperature decreases approximately with 115 eV to the ionization potential over a length of about 15 cm (at $T_0 = 9.5$ keV, and about 17 cm).

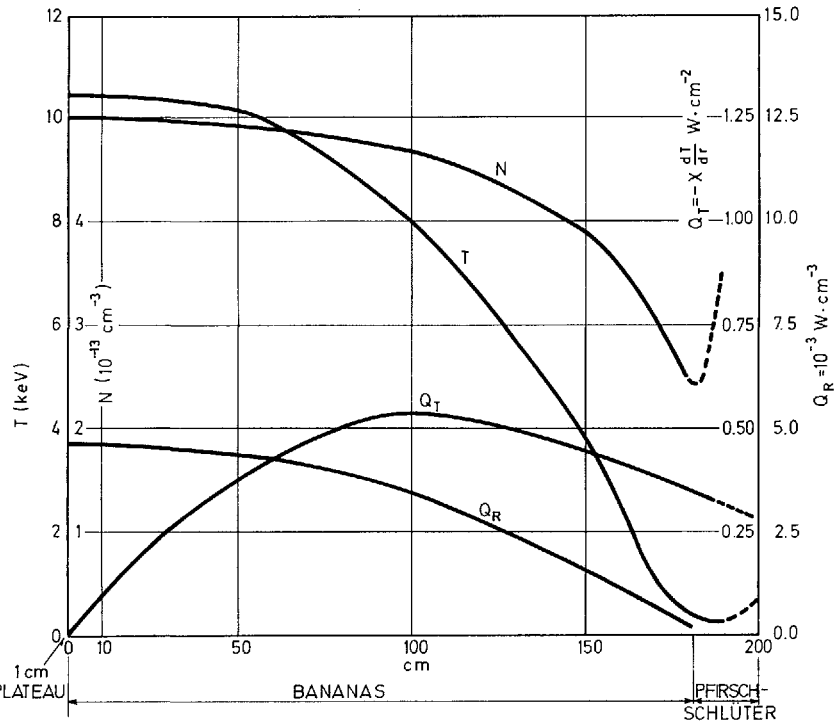


FIG.1. Variation of temperature T, density N, radiation losses Q_R, and thermal-conductivity losses Q_T in the "hot" plasma zone ($T_0 = 10$ keV, $N = 5 \times 10^{13}$ cm^{-3}).

As follows from Eq. (1), we have for the temperature in the strongly collisional regime:

$$T^{-0.7} = a_1 J_0(kr) + a_2 Y_0(kr) \tag{13}$$

where $k = 1.4 \times 10^{-6} B_0/q_0$. The coefficients a_1 and a_2 can be determined by matching with the numberical solution at the boundary of the plateau region. (for $T_0 = 10.5$ keV, $a_1 = 2$, and $a_2 = 0.2$). In our case, $kr < 4$, this corresponds to an extended temperature tail. It should be pointed out that a relatively flat variation of the temperature profile is due to the establishing of a classical regime at the periphery while the temperature gradient is caused by the dominating banana regime over the radius. Note that, as the temperature T_0 decreases, the temperature tail is elongated and becoming flatter. The density continues to grow in the collisional regime $n \sim T^{3/5}$, reaching a value of the order of 1.4×10^{14} cm^3 over a length of 200 cm. The energy lost by bremsstrahlung increases as $Q_R \sim n^2 \sqrt{T} \sim T^{0.7}$ and reaches $\approx 2 \times 10^{-3}$ W·cm^{-3}. In this case, the losses due to thermal conductivity decrease as $q_T \sim T^{-1.7}\, dT/dr$, amounting approximately to 0.26 W·cm^{-2}. If this volume is bounded by an imaginary wall at a distance $a = 2 \times 10^2$ (this corresponds to the current of 6 MA) we find that, for $V = 4 \times 10^8$ cm^3 and $S = 4 \times 10^4$ cm^2,

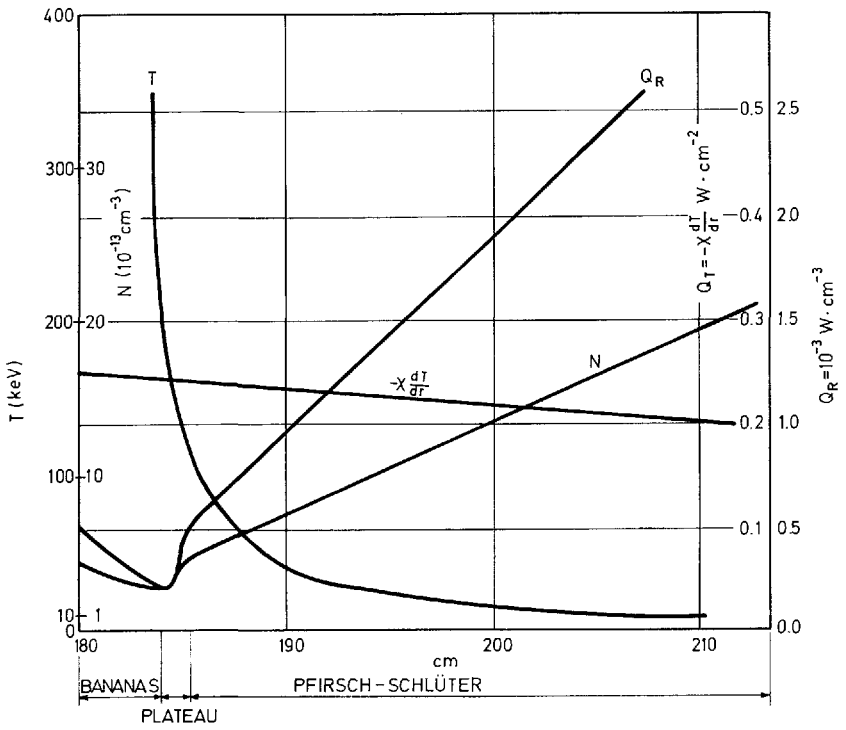


FIG.2. Variation of temperature T, density N, radiation losses Q_R, and thermal conductivity losses Q_T in the "cold" plasma zone.

the total power output of the reactor will be P = 2 MW, where thermal losses constitute $p_T = q_T S = 1.2 \times 10^6$ W and radiation amounts to $P_R = Q_R V \cong 0.8 \times 10^6$ W. For $\tau_E \cong 8 - 10$ s, the energy content is $p\tau_E = 2 \times 10^7$ J. This value is an order of magnitude less than that of T-20 because the reactor core is smaller, owing to the formation of a protection zone.

4. The solution obtained here could provide efficient protection against sputtering if it is realized down to the wall (limiter). This solution will, however, be not valid in the region near the wall; its whole extension is determined by the penetration depth of the neutral atoms flying from the wall material into the plasma; at $n \approx 10^{14}$ cm^{-3}, it is 10–15 cm. At such lengths, the flux at the wall is finite, because of neutral-particle ionization, which fly from the wall in the form of ions and electrons. When the plasma is sufficiently dense at the periphery and the path length of the neutral atoms is small, the whole "re-cycling" process is localized within a sufficiently narrow zone near the wall, which can be concentrated, for example, in the shadow of the limiter. The final answer to the question of the possibility of establishing such a regime is related to the solution of the boundary problem. The above stationary solution, however, which leads to the natural co-existence of hot and cold plasma zones, allows us to assume that the blanket

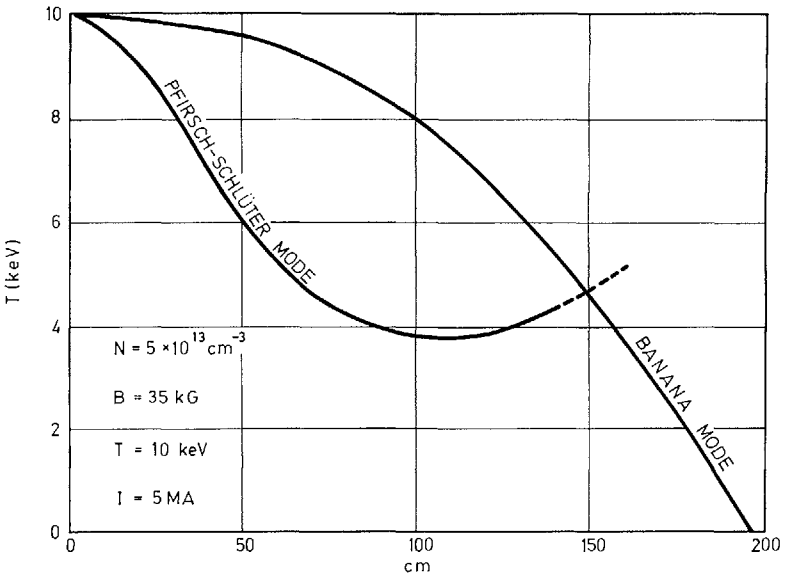


FIG. 3. Variation of the temperature in the banana and highly collisional regimes.

solution for the reactor wall region is consistent with the core parameters. Let us confine ourselves to evaluation of a heat flux which can enter the wall through the wall zone. The main mechanism responsible for heat transport in this region is macroscopic flux of neutrals. By using mainly Refs [4, 5] we can show that the heat flux obtained can be transported by the neutrals, provided a temperature jump takes place, caused by the difference between plasma and wall temperatures. Such a regime is possible since the density of neutral atoms is rather low when the atoms recombining at the wall penetrate deep into the plasma, while the ion temperature is, in the region near the wall, considerably higher than the wall temperature. The plasma flux to the wall

$$nv_r = -2.5 \times 10^{-4} \frac{q_0^2}{B_0^2} \left(\frac{L_k}{10}\right)\left(\frac{n^2}{T\sqrt{T}} \frac{dT}{dr} + \frac{5}{3} \frac{n}{\sqrt{T}} \frac{dn}{dr}\right) \tag{14}$$

and the heat flux

$$\begin{aligned} Q &= Q_e + Q_i + 5\, nv_r T \\ &= -2.5 \times 10^{-2} \frac{q_0^2}{B_0^2} \left(\frac{L_k}{10}\right) \frac{7}{7.2} \left(\frac{n^2}{\sqrt{T}} \frac{dT}{dr} + 0.072\, n \sqrt{T} \frac{dn}{dr}\right) \end{aligned} \tag{15}$$

in the presence of the plasma surface recombination (i.e. $n = 0$ for $r = 0$) are related by

$$Q_0 = \frac{21}{5} (nv_r)\, \Delta T \tag{16}$$

where ΔT is the magnitude of the temperature jump causing the heat flux transfer. The plasma density can be assumed to be low at a distance of one charge-exchange length from the wall, λ_s,

so that the heat flux at the wall is given by

$$Q_0 = 2.5 \times 10^{-4} \frac{q_0^2}{B_0^2} \frac{7}{2} \frac{n_s^2}{\lambda_s} \sqrt{\Delta T} \cong 0.8 \times 10^{17} \Delta T \qquad (17)$$

where $n_s \cong 1.4 \times 10^{14}$ cm^{-3} is the density at the charge-exchange length, $\lambda_s = (n\sigma_s)\sqrt{T_w/\Delta T}$ at the wall temperature $T_w \cong 0.1$ eV, $\sigma_s = 4 \times 10^{-15}$ cm^2 is the charge-exchange cross-section. According to the albedo theory, the ionization probability for a fast neutral is $\kappa = \sqrt{1-\beta}$ where $\beta = \nu_c/(\nu_c + \nu_i)$ since the charge-exchange frequency ν_c is higher than the ionization frequency ν_i. The ionization probability of a slow neutral atom is $\kappa^2 j_n$, i.e. it is smaller than that of a fast particle so that it can be neglected. The total heat flux on the wall can be written as

$$n = Q_0 + \frac{3}{2} j_n \Delta T \cong \left(1 + \frac{5}{14} \frac{1}{\sqrt{1-\beta}}\right) Q_0$$

In the range of $\beta \to 0$ at $\Delta T \cong 10 - 15$ eV, $\Pi \cong 0.2$ W·cm^{-2}, which is of the normal order of magnitude.

Summarizing we point out that the realization of the regime under consideration depends on the possibility of obtaining high densities of cold plasma at the periphery. For this purpose, a poloidal divertor can be used for injection. A conventional divertor is not desirable in this case since its "cleaning" depth is insufficient. However, as Kadomtsev has first pointed out, it is possible to have a diverter design allowing the divertor layer to be of arbitrary width, and, consequently, of arbitrary injection depth. This can be achieved if the external current conductor is tangent to the inner side of the torus or if it is located along an arc whose curvature is inverse to that of the torus. In this case, the field of the external current should cut out the magnetic surfaces of the torus and remove them to the external zone. By varying the curvature of the external conductor, it is possible to vary the blanket depth. These qualitative considerations indicate that it is, in principle, possible to produce a plasma of proper density and an appropriate density profile by fuel injection.

REFERENCES

[1] HAZELTINE, R.D., HINTON, F.L., Phys. Fluids, **16**, (1973) 1883.
[2] SHAFRANOV, V.D., CONNOR, J.W., VATSON, C.J., Pre-print of the Institute of Atomic Energy 2567 (1975).
[3] SAGDEEV, R.Z., GALEEV, A.A., Problems of Plasma Theory, **7** 70 (in Russian).
[4] SAKHAROV, A.D., Plasma Physics and the Problem of Controlled Thermonuclear Reactions, **1** 20 (in Russian).
[5] ZUBAREV, D.N., KLIMOV, V.N., Plasma Physics and the Problem of Controlled Thermonuclear Reactions, **I** 138 (in Russian).

DISCUSSION

ON PAPERS IAEA-CN-35/I 9–1, I 9–2, I 9–3

F. ENGELMANN: I should like to make a comment on paper IAEA-CN-35/I 9–3. I find it very interesting that the authors could show that taking account of the banana, plateau, and Pfirsch-Schlüter regimes allows for steady-state temperature profiles with an edge value of the temperature as low as 10 eV. I should like to point out, however, that for the outermost part of the discharge (typically when $T \lesssim 30$ eV in the example considered), the usual Pfirsch-Schlüter transport coefficients are no longer valid, owing to the appearance of heat transfer between electrons and ions (see ENGELMANN, F., NOCENTINI, A., Nucl. Fusion 16 (1976) 694). In particular, the heat conductivity here decreases considerably, so I should expect the corresponding plasma layer to be narrower than that calculated without allowance for this effect.

With regard to papers IAEA-CN-35/I 9–1 and I 9–2, I should like to ask if cyclotron radiation was taken into account.

Ya.I. KOLESNICHENKO: The stability criterion for thermonuclear burning derived in paper IAEA-CN-35/I 9–2 is very general and remains valid when cyclotron radiation is taken into account. Cyclotron radiation was not taken into account in paper IAEA-CN-35/I 9–1.

With regard to your comment on paper IAEA-CN-35/I 9–3, I should like to point out that the authors now have evaluations which justify the hope that the blanket solution can be made compatible with the reactor core parameters.

J.G. CORDEY: In papers IAEA-CN-35/I 9–1 and I 9–2, were the profiles of temperature and density allowed to vary during the α-particle heating?

Ya.I. KOLESNICHENKO: The radial dependence of plasma temperature and density is not considered in these papers. The plasma is assumed to be spatially uniform, and its finiteness is taken into consideration by introducing phenomenological energy and particle confinement times (τ_E and τ_n). The problem of thermonuclear burning stability with allowance for spatial non-uniformity and boundary conditions has been dealt with in a recent article by us (KOLESNICHENKO, Ya.I., REZNIK, S.N., YAVORSKIJ, V.A., Nucl. Fusion 16 (1976) 105).

Session XXIII

MISCELLANEOUS

Chairman

B.P. Lehnert
Sweden

Papers H 2-1 and H 2-2 were presented
by A. Mohri as Rapporteur

ENERGY PRINCIPLES FOR NON-IDEAL MHD*

H. TASSO
Max-Planck Institut für Plasmaphysik,
Garching,
Federal Republic of Germany

Abstract

ENERGY PRINCIPLES FOR NON-IDEAL MHD.

Energy principles were found for the three-dimensional plasmas of arbitrary geometry with viscosity and finite Larmor radius (FLR) effects and for two-dimensional plasmas of arbitrary shape, taking into account viscosity, FLR effects and resistivity. This allows a scaling-free decision about stability in the same way as for ideal MHD (necessary and sufficient criterion). Rough estimates of growth rates can also be made. Application to tokamaks yields the results: (1) Very plausible explanation of the anomalous skin effect at the beginning of the discharge; (2) Reduction by a factor of 100 of the resistive kink or ideal internal kink growth rate of the $m = 1$, $n = 1$ mode by inclusion of the viscosity parallel to the magnetic field, which explains the observations; (3) Formulation of a condition allowing the use of test functions to study the stability of configurations with stagnation points and magnetic islands. Application to the high-β, $\ell = 1$ stellarator allows the explanation of the stabilization of $m = 2$ by FLR in the present experiments, but parallel viscosity could strongly destabilize plasmas of higher temperatures unless their ideal MHD stability is improved. Finally, an energy principle for all three-dimensional resistive perturbations in the tokamak scaling is given even with FLR and viscosity. Helical perturbations can always be unstable.

Stability problems related to non-ideal effects are becoming more important since, at low ß and with peaked current distributions, tokamaks are only subject to weak instability with respect to major ideal MHD modes; and experiments show that for high-ß stellarators the m = 1 MHD mode is wall-stabilized and the need for finite Larmor radius stabilization of m = 2 is increasing.

The numerical solution of these problems is not easy because of the small growth rates and the various time scales involved. The analytical study of eigenmodes is very tedious [1] and cannot be done without many approximations [2] (scalings) involving geometry and physics which may be of a specific and uncertain nature.

Energy principles can help to afford an insight and allow qualitative and, often enough, quantitative conclusions. This procedure is definitely different from a variational formulation, which is always possible for every equation if one adds to it the adjoint one [3]. These variational principles, such as Lagrangian principles, do not lead to criteria involving the use of test functions but are another formulation of a given set of equations. Nethertheless variational formulations can have numerical advantages.

A well-known example is the MHD energy principle, which has helped to provide general answers to many classes of MHD equilibria. Some precise numerical methods are also based on it. Other examples [4,5] for resistive MHD have also been found.

The aim of this study is to find a general stability equation, probably the most general for which a stability condition involving only test functions can be formulated. This condition is called energy principle

* Work performed under terms of agreement on association between the Max-Planck-Institut für Plasmaphysik and Euratom.

because of its strong analogy to the perturbed potential energy due to virtual displacements. This stability condition should not be purely academic in character but should help us to understand the influence of different physical terms on stability. In fact, as we shall see, it does clear up cases where resistivity, viscosity and finite Larmor radius are involved.

I. GENERAL STABILITY EQUATION

Let us consider the following equation:

$$N\ddot{\underline{\zeta}} + (F+M)\dot{\underline{\zeta}} + Q\underline{\zeta} = 0 \qquad (1)$$

where $\underline{\zeta}$ is a complex multidimensional representation vector in a functional space, N and M are hermitian and positive operators and Q is a hermitian and F an antihermitian operator.

It can be seen that this equation contains several limiting cases: If $F = M = 0$, it is the ideal MHD case [6] for static equilibria. If $M = 0$, $F \neq 0$, it is the case of linearized conservative systems such as the linearized Vlasov equation [7]. If $F = 0$, $M \neq 0$, it is the case of a resistive plasma in 1- [4] and 2- [5] dimensional geometries.

(a) Sufficient Condition for Stability

Let us first recall the definition of the scalar product for 2 vectors $\underline{\xi}$ and $\underline{\eta}$ denoted by (ξ, η):

$$(\xi,\eta) = \int d\tau\, \underline{\xi}^{*} \cdot \underline{\eta} \qquad (2)$$

the Hilbert space to which $\underline{\xi}$ and $\underline{\eta}$ belong being restricted to functions fulfilling specific boundary conditions suggested by physics.

Consider now the scalar product of $\dot{\underline{\zeta}}$ with the left-hand side of eq. (1) and add to the expression its complex conjugate. The $(\dot{\zeta},F\dot{\zeta})$ terms cancel because of the anti-hermiticity of F, and one obtains

$$\frac{1}{2}\left[(\dot{\zeta},N\dot{\zeta}) + (\zeta,Q\zeta)\right]^{\cdot} = -(\dot{\zeta},M\dot{\zeta}) \qquad (3)$$

If Q is positive, i.e. $(\zeta,Q\zeta) > 0$ for all $\underline{\zeta}$, the system is stable owing to the positivity of N and M.

(b) Necessary and Sufficient Condition for Stability

If $M \neq 0$ and if $(\zeta,Q\zeta) < 0$ for any $\underline{\zeta} = \underline{\eta}$, the system is unstable. Together with the previous result this leads to a necessary and sufficient condition.

Proof

The proof is done by demonstrating incompatibility of stable $\underline{\zeta}$ and negative values of $(\zeta,Q\zeta)$. Indeed, it is then possible to choose $\underline{\zeta} = \underline{\eta}$ at a particular time with $(\zeta,Q\zeta) < 0$, and then, integrating eq. (3), we obtain $(\zeta,Q\zeta)$ at later times:

$$(\zeta,Q\zeta) = -2\int_{t_o}^{t} (\dot{\zeta},M\dot{\zeta})dt' - (\dot{\zeta},N\dot{\zeta}) + (\eta,Q\eta) \qquad (4)$$

From eq. (4) it follows that $(\zeta,Q\zeta)$ remains negative and at least finite for all later $t > t_o$. This excludes the possibility that $\underline{\zeta} \to 0$ as $t \to \infty$. An

oscillation of $\underline{\zeta}$ around a finite value at $t \to \infty$ is also in contradiction with eq. (4), the integral becoming infinite because $\dot{\underline{\zeta}}$ vanishes only on a countable set. The last possibility for a stable $\underline{\zeta}$ would be to tend to a constant in time, but this is in contradiction with eq. (1) itself since $Q\underline{\zeta}$ cannot vanish because of eq. (4).

It is appealing to conjecture that the growth will be exponential because any power growth is incompatible with eq. (4). A rigorous proof of exponential growth cannot be done in the same way [4,8] as for $F \equiv 0$, in which case overstability is forbidden. Let us conclude this section by saying that for eq. (1) with $M \neq 0$

$$(\zeta, Q\zeta) \geq 0 \tag{5}$$

is necessary and sufficient for stability.

II. SIMPLEST MODEL AND TIME SCALES

Let us consider a second-order differential equation with constant coefficients which is a particular case of eq. (1):

$$\frac{1}{2}\ddot{y} + (a + i\,b)\dot{y} + c\,y = 0 \qquad \text{with } a > 0 \tag{6}$$

The solution is $y = e^{\omega t}$, with

$$\omega = -(a+ib) \pm \sqrt{(a+ib)^2 - 2c} \tag{7}$$

and $c > 0$ is necessary and sufficient for stability.

a) If $a^2+b^2 \ll |c|$, then $\omega \simeq -(a+ib) \pm i\sqrt{2|c|}\left(1 - \frac{(a+ib)^2}{4|c|}\right)$ (7a)

In the unstable case the growth rate is given by $\sqrt{|c|}$ as expected.

b) If $a^2+b^2 \gg |c|$, then $\omega \simeq -(a+ib) \pm (a+ib)\left(1 - \frac{c}{(a+ib)^2}\right)$

The unstable case gives a growth rate

$$\mathrm{Re}(\omega) = \frac{-a\,c}{a^2+b^2} \tag{7b}$$

c) If $a^2 \ll b^2 \simeq |c|$, then $\omega \simeq -(a+ib) \pm i\sqrt{b^2+2c}\left(1 - \frac{iab}{b^2+2c}\right)$

for $b^2+2c \simeq |c|$

and $\omega \simeq -(a+ib) \pm \sqrt{i2ab}$ for $b^2+2c = 0$

so that $\mathrm{Re}(\omega) \simeq a\left(\frac{b}{\sqrt{|c|}} - 1\right)$ for $b^2+2c = |c|$

$$\mathrm{Re}(\omega) \simeq \sqrt{ab} \qquad \text{for } b^2+2c = 0 \tag{7c}$$

d) If $a^2 \approx b^2 \gg |c|$, then

$$\mathrm{Re}(\omega) \approx \sqrt{|c|} \tag{7d}$$

This particular example shows that despite the fact that the sign of c governs stability independently of the values of a and b, the growth rates are strongly dependent on the relative magnitudes of a,b and c.

III. THREE-DIMENSIONAL PLASMAS WITH THE FULL PRESSURE TENSOR

The macroscopic equations are of the following form:

$$\begin{aligned}
&\rho \frac{d\underline{v}}{dt} = \underline{j} \times \underline{B} - \nabla p - \nabla \cdot \underline{\underline{\Pi}} \\
&\underline{E} + \underline{v} \times \underline{B} = 0 \\
&\dot{\rho} + \nabla \cdot \rho \underline{v} = 0 \\
&p = f(\rho) \\
&\nabla \times \underline{B} = j \\
&\nabla \cdot \underline{B} = 0 \\
&\nabla \times \underline{E} = - \dot{\underline{B}}
\end{aligned} \tag{8}$$

The pressure tensor [9] $\underline{\underline{\Pi}}$ is given by

$$\begin{aligned}
-\Pi_{xx} &= \alpha(\Gamma_{xx} + \Gamma_{yy}) + \beta \Gamma_{xy} + \frac{\beta^2}{4\alpha} (\Gamma_{xx} - \Gamma_{yy}) \\
-\Pi_{yy} &= \alpha(\Gamma_{xx} + \Gamma_{yy}) - \beta \Gamma_{xy} - \frac{\beta^2}{4\alpha} (\Gamma_{xx} - \Gamma_{yy}) \\
-\Pi_{zz} &= 2 \alpha \Gamma_{zz} \\
-\Pi_{xy} &= -\Pi_{yx} = \frac{\beta}{2} (\Gamma_{yy} - \Gamma_{xx}) + \frac{\beta^2}{2\alpha} \Gamma_{xy} \\
-\Pi_{xz} &= -\Pi_{zx} = 2 \beta \Gamma_{yz} + 2 \Gamma_{xz} \frac{\beta^2}{\alpha} \\
-\Pi_{yz} &= -\Pi_{2z} = 2 \frac{\beta^2}{\alpha} \Gamma_{yz} - 2 \beta \Gamma_{xz}
\end{aligned} \tag{9}$$

$$\Gamma_{ij} = \frac{1}{2} \left(\frac{\partial v_i}{\partial x_j} + \frac{\partial v_j}{\partial x_i}\right) - \frac{1}{3} \frac{\partial v_n}{\partial x_n} \delta_{ij}$$

$$\beta = p/\omega_{ci}$$

$$\alpha = \frac{2}{3} \beta \omega_{ci} \tau_{ii}$$

x,y,z are a local system of Cartesian coordinates, z being along the magnetic field. ω_{ci} is the ion cyclotron frequency and τ_{ii} the ion-ion collision time.

After linearizing the system (8) around a static equilibrium and expressing all physical quantities in the perturbed velocity, we obtain (see ref. [10])

$$\rho_o \frac{\partial^2 \underline{v}}{\partial t^2} + \frac{\partial}{\partial t} \nabla \cdot \underline{\underline{\Pi}} + Q \underline{v} = 0 \tag{10}$$

where Q is the MHD stability operator. In order to find out what the properties of the operator $\nabla \cdot \underline{\underline{\Pi}}$ are, let us consider $\underline{\underline{\Pi}}$ in a general coordinate system x^1, x^2, x^3 ; then

$$\int \left[\underline{v}' \cdot (\nabla \cdot \underline{\underline{\Pi}}) \right] \, d\tau = \int v'_r \, \Pi^{rn}_{,n} \, \sqrt{g} \, dx^1 \, dx^2 \, dx^3 \qquad (11)$$

$$= -\int \Pi^{rn} \, v'_{r,n} \, \sqrt{g} \, dx^1 \, dx^2 \, dx^3 + \int \frac{\partial}{\partial x^n} (\sqrt{g} \, v'_r \, \Pi^{rn}) dx^1 \, dx^2 \, dx^3$$

where ,n is the covariant derivative with respect to x^n.

The last integral vanishes because of the boundary conditions on $\underline{v}$, and $\Pi^{rn} \, v'_{r,n}$ can be evaluated in the local coordinates system.

It turns out [10] that the terms in α and $\frac{\beta^2}{\alpha}$ are symmetric and positive definite, and the terms in β are antisymmetric. The pure β terms are due to the finite Larmor radius, the α terms to the magnetic-free viscosity, and the $\frac{\beta^2}{\alpha}$ terms to the magnetic viscosity.

Equation (10) is of the same type as eq. (1); the finite Larmor radius effects correspond to the operator F, and the viscosity to the operator M. The stability is decided by the MHD operator but the growth rates can be affected by F.L.R. effects and viscosity. Let us make estimates of the reduction in MHD growth rates.

We know that the most dangerous MHD modes are nearly divergence-free. This means that

$$\Gamma_{xx} + \Gamma_{yy} = \frac{\partial v_x}{\partial x} + \frac{\partial v_y}{\partial y} = - \frac{\partial v_z}{\partial z}$$

but because of $v_\perp = \frac{E \times B}{B^2}$ and $E \approx \nabla \phi$, $\operatorname{div} v_\perp \approx \frac{v_\perp}{r} \frac{r}{R}$

where r is the radial extent of the mode, and R the large radius of the torus. On the other hand, one has $\Gamma_{xy} \approx \frac{v_\perp}{r}$, so that the ion-ion term dominates the F.L.R. term if

$$\frac{\alpha}{\beta} > \left(\frac{R}{r}\right)^2$$

For an ion temperature of 1 keV, a magnetic field of 30 kg, and a density of 10^{14}, one has $\omega_{ci} \, \tau_{ii} \approx 5 \times 10^4$.

Very roughly, we can associate the coefficient a of eq. (6) with the ion-ion term in eq. (10) by the relation

$$a \approx \frac{\alpha}{n_i M R^2} \approx \frac{kT \, \tau_{ii}}{MR^2} \approx 3 \times 10^7$$

if one takes R ≈ 100 cm.

A full MHD growth rate $\gamma_{MHD} \approx \sqrt{|c|}$ is usually also of this order. If for particular reasons (geometry, near marginality condition) an MHD growth rate is not full, then $a^2 >> |c|$ and eq. (7b) lead to the reduced growth rate

$$Re(\omega) \approx \frac{|c|}{a}$$

a) Tokamak case

The m = 1, n = 1 mode observed [11] in Tokamaks near the magnetic axis has a rather small growth rate [12] (resistive kink or ideal internal kink) of the order of 10^5 to 10^6 s^{-1} compared with typical MHD growth, but still too high to explain the experiment. Viscosity leads to a reduced $\gamma \approx \frac{|c|}{a} \approx 10^3$ to 10^4 which agrees with observation.

b) High ß, l = 1 stellarator

The m = 2 mode has a typical MHD growth rate and for the previous plasma parameters we should obtain $a^2 \approx b^2 \approx |c|$, so that we would have the case (7d) with a small reduction in growth rate.

This mode has rarely been observed [13] in the present experiments, this being due to the fact that $\omega_{ci} \tau_{ii}$ is 2 to 3 orders of magnitude lower ($T_i \approx 100$ eV) than calculated before, so that $a^2 << b^2 \approx |c|$, which is the case of eq. (7c). The F.L.R. stabilization dominates in this case.

The derivation of the pressure tensor as given by eqs (9) is done for $\frac{r_L}{L} << 1$ and $\Lambda_{MFP} << L$, with r_L = Larmor radius, L = inhomogenity length, Λ_{MFP} = mean free path. For incompressible motion the validity of the pressure tensor can be extended [13] to the domain $\Lambda_{MFP} >> L_\perp$ but $\Lambda_{MFP} << L_\parallel$.

IV. TWO-DIMENSIONAL PLASMAS WITH RESISTIVITY AND THE FULL PRESSURE TENSOR

It is well known that resistivity leads [1] to new modes and one can expect a much more difficult behaviour. At present only the 2-dimensional case for straight plasmas can be solved, as we shall see.

The equilibrium is characterized [5] by

$$\underline{j}_o = \underline{e}_z J_o(\psi) \qquad (12)$$

$$\underline{E}_o = \underline{ct} = \underline{e}_z \eta_o(\psi) J_o(\psi)$$

$$\underline{B}_o = \underline{e}_z \times \nabla\psi \; (\underline{e}_z \cdot \underline{B}_o) \; \underline{e}_z$$

$$\nabla^2\psi = J_o(\psi) = -\frac{dP_o}{d\psi}$$

z is the coordinate along the straight plasma; ψ is the meridional magnetic flux; and η_o is the resistivity.

The meridional currents are assumed to be zero in order to have a static plasma in equilibrium, which is important for this kind of formulation but not necessarily for the physical results.

After linearizing the equation of motion we obtain

$$\rho_o \ddot{\underline{\xi}} + \nabla p_1 + \nabla \cdot \underline{\underline{\Pi}}(\underline{\xi}) - \underline{j}_1 \times \underline{B}_o - \underline{j}_o \times \underline{B}_1 = 0 \qquad (13)$$

$$\nabla \cdot \underline{\xi} = 0 \qquad (14)$$

$$\dot{\underline{A}}_1 + \eta_o \nabla \times \nabla \times \underline{A}_1 + \eta_1 \underline{j}_o - \dot{\underline{\xi}} \times \underline{B}_o = 0 \qquad (15)$$

$$\underline{B}_1 = \nabla \times \underline{A}_1 \qquad (16)$$

$$\eta_1 = - \xi \cdot \nabla \eta_o \qquad (17)$$

Apart from the pressure tensor term, these equations are the same as in ref. [5]. Equation (17) is valid as long as the heat conductivity is small enough. This will be discussed later.

Restriction to two-dimensional perturbations leads to

$$\underline{\xi} = \underline{e}_z \times \nabla U = - \nabla \times \underline{e}_z U \,, \quad \underline{B}_1 = - \underline{e}_z \times \nabla A = \nabla \times \underline{e}_z A$$

$$\underline{j}_1 = - \underline{e}_z \nabla^2 A \,, \qquad \nabla \times \underline{j}_1 = - \nabla(\nabla^2 A) \times \underline{e}_z$$

where U and A are two scalars: the stream function and the z-component of the vector potential.

Taking the curl of eq. (13), we obtain

$$- \nabla \cdot \rho_o \nabla \ddot{U} + \underline{e}_z \cdot \nabla \times \nabla \cdot \underline{\underline{\Pi}}(\nabla \times \underline{e}_z \dot{U}) - \underline{B}_o \cdot \nabla (\nabla^2 A) - \nabla \times \underline{j}_o \cdot \nabla A = 0 \qquad (18)$$

$$\dot{A} + \underline{B}_o \cdot \nabla \dot{U} - \eta_o \nabla^2 A + J_o(\underline{e}_z \times \nabla \eta_o \cdot \nabla U) = 0 \qquad (19)$$

If $\nabla^2 A$ is taken from eq. (19) ($\eta_o \neq 0$) and inserted in eq. (18), we obtain the following system of equations in matrix operatorial form:

$$\begin{pmatrix} -\nabla \cdot \rho_o \nabla & 0 \\ 0 & 0 \end{pmatrix} \begin{pmatrix} \ddot{U} \\ \ddot{A} \end{pmatrix} + \begin{pmatrix} \dfrac{-(\underline{B}_o \cdot \nabla)^2}{\eta_o} & \dfrac{-(\underline{B}_o \cdot \nabla)}{\eta_o} \\ \dfrac{\underline{B}_o \cdot \nabla}{\eta_o} & \dfrac{1}{\eta_o} \end{pmatrix} \begin{pmatrix} \dot{U} \\ \dot{A} \end{pmatrix}$$

$$+ \begin{pmatrix} \underline{e}_z \nabla \times \nabla \cdot \underline{\underline{\Pi}}(\nabla \times \underline{e}_z \ldots) & 0 \\ 0 & 0 \end{pmatrix} \begin{pmatrix} \dot{U} \\ \dot{A} \end{pmatrix} \qquad (20)$$

$$+ \begin{pmatrix} -J_o(\psi)\underline{B}_o \cdot \nabla \underline{e}_z \times \dfrac{\nabla \eta_o}{\eta_o} \cdot \nabla & - \nabla \times \underline{j}_o \cdot \nabla \\ \nabla \times \underline{j}_o \cdot \nabla & - \nabla^2 \end{pmatrix} \begin{pmatrix} U \\ A \end{pmatrix} = 0$$

Apart from the $\nabla \cdot \underline{\underline{\Pi}}$ term, eq. (20) is identical with eq. (17) of ref. [5]. Let us investigate the operator $e_z \cdot \nabla \times \nabla \cdot \underline{\underline{\Pi}}$ $(\nabla \times e_z \ldots)$. We know from the previous section and from ref. [10] that $\nabla \cdot \underline{\underline{\Pi}}$ $(\underline{\xi})$ contains α terms which are positive definite operators and pure β terms which are antisymmetric, but if $\underline{\xi}$ is a curl and if $\nabla \cdot \underline{\underline{\Pi}}$ $(\underline{\xi})$ is replaced by $\nabla \times \nabla \cdot \underline{\underline{\Pi}}$ $(\underline{\xi})$, the symmetry properties will not be changed, as the following equation shows:

$$\int d\tau \; v \, \underline{e}_z \cdot \nabla \times \nabla \cdot \Pi \quad (\nabla \times \underline{e}_z \, u) = \int \nabla \times \underline{e}_z v \cdot \nabla \cdot \underline{\underline{\Pi}} \quad (\nabla \times \underline{e}_z \, u) \quad d\tau$$

The symmetry properties of $\nabla \cdot \underline{\underline{\Pi}}$ are thus the same as $e_z \cdot \nabla \times \nabla \cdot \underline{\underline{\Pi}} (\nabla \times e_z \ldots)$.

Then eq. (20) has the same character as eq. (1) and the stability condition is given by the last matrix operator of eq. (20), which is the same as in ref. [5].

This leads to the energy principle derived in [5] for zero pressure tensor and extended here to F.L.R. and ion-ion collisions:

$$\begin{aligned} \delta W = & \int d\tau \; \left(-\frac{dJ_o}{d\psi}\right) (\underline{e}_z \times \nabla\psi \cdot \nabla U)^2 \\ & + 2 \int d\tau \; \left(-\frac{dJ_o}{d\psi}\right) A \, (\underline{e}_z \times \nabla\psi \cdot \nabla U) \\ & + \int d\tau \; |\nabla A|^2 \end{aligned} \tag{21}$$

A simple application to tokamaks is the instability of skin currents. If one localizes a test function with ∇U finite at $dJ_o/d\psi > 0$ and $A \sim 0$, then $\delta w < 0$. This mode is similar to the rippling mode in one-dimensional geometry [1].

Another application would be the stability of configurations with stagnation points (such as Doublet or for islands in tokamaks). This necessitates numerical calculations which are not easy to do because of the stagnation point, but eq. (21) at least allows the problem to be correctly formulated.

V. ALL PERTURBATION WITH RESISTIVITY, VISCOSITY, FLR, IN THE TOKAMAK SCALING

The energy principle of section IV can be extended to three dimensional perturbations if one goes to helical coordinates for the representation of the equilibrium and perturbations and in the approximation of the tokamak scaling $Kr \simeq \frac{B_\theta}{B_z} \simeq \varepsilon$

The proof and calculations are given in [14]. The necessary and sufficient criterion is given by:

$$\begin{aligned} \delta w = & \int \left(-\frac{dj_o}{dr}\right) (\underline{u} \times \underline{e}_r \cdot \nabla G) \, (\underline{u} \times \nabla F_o \cdot \nabla G) \, d\tau \\ & + 2 \int \left(-\frac{dj_o}{dr}\right) (\underline{u} \times \underline{e}_r \cdot \nabla G) \, F \quad d\tau \\ & - \int F \, L \, F \; d\tau \end{aligned}$$

where $\underline{B}_o = f_o(r)\,\underline{u} + \underline{u} \times \nabla F_o(r)$

$\underline{B}_j = f(r,u,t)\,\underline{u} + \underline{u} \times \nabla F(r,u,t)$

$\underline{\xi} = g(r,u,t)\,\underline{u} + \underline{u} \times \nabla G(r,u,t)$

$$\underline{u} = \frac{l\,\underline{e}_z + hr\,\underline{e}_\theta}{l^2 + h^2 r^2} \quad , \qquad hr \simeq \varepsilon$$

$u = l\,\theta - hz$

A test function can always be found to make the system unstable as soon as $\frac{dj_o}{dr} \neq 0$. This test function can be taken as:

$F \simeq 0$ and G concentrated on the side of the resonance ($\nabla F_o = 0$) at which the first integrand is negative which is always possible. Estimate of growth rate can also be done as in section III.

VI. DISCUSSION AND CONCLUSION

The method pursued in this work is of a general character. It allows statements about stability without going to the solution of eigenmodes, which can also be very difficult numerically. It does not imply scalings of sheath thickness [2] as in the boundary layer theory, so that stability boundaries depend on the equations used and not on the particular scalings used to derive a dispersion relation.

This is a very appealing property if, for a physical system, the variable ζ, in which the linearized equations of motion are of the same type as eq. (1), were easy to find. This choice of the representation is crucial and not trivial. Section IV shows how intricate things can be.

The choice of the physical equations themselves is also a basic difficulty. Resistivity, for example, depends on temperature, and temperature depends crucially on heat conductivity along the magnetic field lines. If this had to be taken into account in eq. (17), it would modify the structure of eq. (20), and the symmetry properties of some of the operator might be destroyed atleast for the present representation. The results of Section IV are therefore good as long as eq. (17) holds, which depends on the kind of motion allowed (a weak dependence along B would slightly change eq. (17)) and on the temperature (the heat conductivity is very large for higher temperatures). It is worth while to make some effort to include heat conductivity in the formulation. This point is of importance as well for the nonlinear study of tearing modes [15, 16].

The collisional viscosity as derived in the literature is valid for $\Lambda_{MFP} \ll L$ and $\omega \ll \nu_{ii}$, but for incompressible motion it seems that only $\Lambda_{MFP} \ll L_{\shortparallel}$ is necessary [17]. For the inner plasma of some of the present tokamaks these conditions are barely verified: in fact, $\omega \simeq \nu_{ii}$ and $\Lambda_{MFP} \simeq L_{\shortparallel}$. The need for the study of macroscopic modes with a microscopic theory and a collision operator will therefore increase in the future.

Equation (1) will lead in the unstable case to overstability because of the antisymmetric operator F, which in SectionsIII and IV is related to the F.L.R. effects. In fact, it should be said that not only the F.L.R. effects lead to finite real frequencies but also the Hall [18] term, the finite heat conductivity, compressibility, etc., but in tokamaks it seems plausible that the Hall term is responsible for the main part of the observed real frequency [11] for m = 2 and F.L.R. and Hall term for the m = 1. Unfortunately, the inclusion of the Hall term perturbs [10] the nice symmetry properties of, for example, eq. (10) despite the fact that the stability boundaries do not seem to be altered [19].

The application of the energy principles found in this study to the experiments can be summarized as follows:

A) Tokamak

1) The generalized rippling mode which occurs if the current density is skinned, and which has been found in ref. [5], persist despite F.L.R. effects and collisional viscosity and could explain the anomalous skin effect observed in tokamaks, especially at the beginning of the discharge, when eq. (17) holds best and other modes are weak.

2) A scaling-free investigation of the stability of configuration with stagnation points (divertor, doublet, m = 2 islands) is made possible by the study of the sign of the energy expression given by eq. (21).

3) A rough estimate of the influence of collisional viscosity on the m = 1, n = 1 mode shows a strong reduction of the growth rate as much as a factor of 100. If the original resistive or ideal MHD mode has a growth rate [12] of the order of $10^5 s^{-1}$, then collisional viscosity would reduce it to $10^3\ s^{-1}$. Going to higher temperatures will help.

4) A detailed analysis of helical perturbations can be done by the criterion of section V. A helical perturbation can always be unstable [20].

B) High-ß stellarator

The m = 1 is stabilized by the wall and the m = 2 mode can be stabilized by F.L.R. effects if the ion temperature is not too low and not too large (for $T_i \approx 100$ eV viscous effects are much smaller than F.L.R. effects). For higher temperatures (≈ 1 keV) the parallel viscosity could destabilize again and at the same time reduce the original ideal growth rates, but by a rather small factor (see equation (7d)) because the ideal growth rates are rather big $\gamma \approx 10^7\ s^{-1}$. One can say that as long as the ideal MHD growth rates are so high, viscosity would not help and going to higher temperatures could strongly destabilize by suppressing the F.L.R. effects. For very high temperatures (> 1 keV) the macroscopic theory breaks down and a microscopic treatment is needed.

REFERENCES

[1] Furth, H.P., Killeen, J., Rosenbluth, M.N., Phys. of Fluids 6 (1963) 459; Coppi, B., in Propagation and Instabilities (W.I. Futterman, ed.) Stanford University Press (1963) p. 70.

[2] Glasser, A.H., Green, J.M., Johnson, J.L., Physics of Fluids 18 (1975) 875.

[3] Atherton, R.W., Homsy, G.M., Studies in Applied Math. LIV. 1 (1975) 31.

[4] Barston, E.M., Phys. of Fluids 12 (1969) 2162.

[5] Tasso, H., Plasma Physics 17 (1975) 1131.

[6] Bernstein, I.B., et al., Proc. Royal Soc. A 244 (1958) 17; Hain, K., et al., Z. Naturforschung 12a (1957) 833.

[7] Low, F.E., Proc. Royal Soc. A 248 (1958) 283;
Sturrock, P.A., Ann. Phys. 4 (1958) 306.
[8] Pfirsch, D., Tasso, H., Nucl. Fusion 11 (1971) 259.
[9] Chapman, S., Cowling, T., The Mathematical Theory of Non-uniform Gases, Cambridge Univ. Press N.Y. (1953).
[10] Tasso, H., Schram, P.P.J.M., Nuclear Fusion 6 (1966) 284.
[11] von Goeler, S., et al., Phys. Rev. Lett. 33 (1974) 1201;
Launois, P., Proc. of 7th Europ. Conf. on Contr. Fusion and Plasma Phys. (1-5 Sept. 1975) 1.
Karger, F., et al., This conference, paper CN/35, A-7.
[13] Fünfer, E., et al., Proc. of 7th Europ. Conf. on Contr. Fusion and Plasma Physics (1-5 Sept. 1975) 151.
[17] Dum, C.T., Private Communication.
[15] Rosenbluth, M., et al., Proc. of 7th Europ. Conf. on Contr. Fusion and Plasma Physics (1-5 Sept. 1975) 286.
[18] Tayler, R.J., Nuclear Fusion, Supplement (1962) part 3, 877;
Buti, B., et al., Nuclear Fusion 5 (1965) 17.
[19] Schram, P.P.J.M., Tasso, H., Nuclear Fusion 7 (1967) 91.
[12] Coppi, B., et al., Proceedings of the Annual Meeting on Theoretical Aspects of Controlled Thermonuclear Research (April 7-9, 1976) paper 1 A - 4.
[14] Tasso, H., to be published; see also IPP 6/149 (1976),
[20] This result is well verified by the numerical calculations done by Dibiase, J.A., UCRL-51591 (May 1974).
[16] White, R.B., et al., paper B 2-1, This Conference;
Biskamp, D., Welter, H., paper B 2-2, This Conference.

DISCUSSION

ON PAPER IAEA-CN-35/H1

B.P. LEHNERT *(Chairman):* I agree with you that ion-ion collisions produce viscous effects which can have a strong suppressing influence on the growth rates of MHD instabilities. In particular, if one considers the boundary region of an impermeable plasma, ion-neutral collisions and neutral-gas viscosity also contribute to this damping effect by creating what might be termed a "compound" plasma-neutral-gas viscosity (see LEHNERT, B.P., in Plasma Physics and Controlled Nuclear Fusion Research, Proc. 5th Int. Conf. Tokyo 1974, 2, IAEA, Vienna (1975) 717).

H. TASSO: I did not include ion-neutral collisions in my work but I would in fact expect that they could also contribute to the reduction of growth rates. There are several physical terms which should be added to this theory, namely the Hall term, thermal conductivity and a more fully elaborated Ohm's law, so it is by no means complete. I appreciate your comment.

EXPERIMENTAL STUDIES ON GENERATION AND BEHAVIOUR OF FIELD-REVERSING E- AND P-LAYERS*

H.A. DAVIS, H.H. FLEISCHMANN, S.C. LUCKHARDT,
R.A. MEGER
Laboratory of Plasma Studies,
Cornell University,
Ithaca, New York,
United States of America

Abstract

EXPERIMENTAL STUDIES ON GENERATION AND BEHAVIOUR OF FIELD-REVERSING E- AND P-LAYERS.

Recent results are reported from the Cornell RECE-programme studying the generation and stability of field-reversing electron and ion rings for Astron or Spherator-type devices. Most important, field-reversing electron rings with field-reversal lasting over 220 μs and overall lifetimes up to 1.3 ms were obtained in the new RECE-Christa facility using 2.5-MeV electrons. The ring decay generally is smooth and roughly consistent with a collisional diffusion of the fast electrons in the background gas, except when the toroidal field, B_θ, is permitted to decay too rapidly. Experiments on the smaller RECE-Berta facility show precessional stabilization of weak rings when magnetic multipole Ioffe fields are applied. Experiments using magnetically insulated diode arrangements and microsecond voltage pulses resulted in the generation of intense ion beams with pulse lengths up to 1 μs and current densities up to 30 $A \cdot cm^{-2}$.

I. INTRODUCTION

The use of strong rings of high-energy electrons or ions has been considered for a number of fusion schemes including: i) The generation of absolute minimum-B configurations in the Astron[1] scheme and in its more recent version, the Ion Ring Compressor,[2] in which the high-energy ion ring is to be obtained by adiabatic compression of a low-energy ion ring, or in the small-orbit rings envisioned in the mirror[3] and EBT[4] programs, and ii) the replacement of internal current loops, e.g. in Spherator[5] geometry. Also, high-energy ion rings may be useful in combination with electronuclear breeding schemes.[6] So far, experiments have been limited to electron rings because the field-reversing ion rings needed for an actual reactor are considerably more expensive to produce, and many of the relevant physics questions can be answered with electron rings. The Astron program at Livermore succeeded in creating large-orbit electron rings exhibiting axial field changes of up to 40% from single-pulse injection, but the originally envisioned pulse stacking to enhance this ring strength further did not appear to be workable.[7] Fully field-reversing E-layers with lifetimes of 10 - 20 µsec exhibiting a simple collisional decay and surprising stability were obtained, however, in the Cornell RECE-program in two different machines.[8,9,10] Since then, the RECE-program was aimed at extending the lifetime of these electron rings, testing the limits of ring stability under various conditions, and at developing pulsed-ion sources of the strength necessary for creation of reactor type ion rings. The present paper is to describe some of the most recent results of this effort, most importantly including the creation of field-reversing electron rings with reversal times of up to 220 µsec and overall lifetimes of up to 1.3 ms in the new RECE-Christa device.

* Work supported by USERDA Contract E(11-1) 2319.

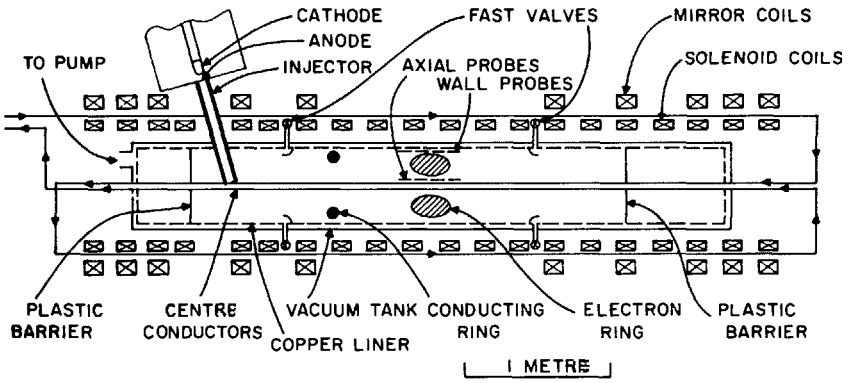


FIG.1. New RECE-Christa facility.

II. RECE-CHRISTA FACILITY

The new RECE-Christa facility shown in Fig. 1 is a scaled-up version of the RECE-Berta facility[9] on which most of our earlier experiments were performed. An intense electron beam is generated by an oil-insulated Marx-Blumlein beam generator (Maxwell Laboratories, maximum diode voltage = 5 MeV, Blumlein impedance = 30 ohms, electric pulse length 80 nsec). The electron beam is generated in a diode consisting of a carbon cathode (5 cm in diameter) and a .0125 mm thick aluminized Mylar anode foil. After the beam propagates through a magnetically shielded injector tube (6 cm inner diameter, 90 cm long) filled with 1-3 Torr of H_2, it is passed through a second foil (0.25 mm titanium) and then tangentially injected (injection radius 12-14 cm, injection angle about 10 deg) into a large vacuum tank. This tank is made from Lucite sections, 60 cm in diameter, and 4 m in overall length. To provide a conducting enclosure for the beam and ring, the entire tank is lined inside with a perforated heavy copper shell, 6 mm thick.

An axial magnetic mirror field, $B_{z0}(z)$, (up to 1 kGauss, mirror ratio less than 2) is produced by a set of solenoid coils and a set of various optional mirror coils. Both sets of coils are energized separately from a DC power supply. Local fine-tuning is accomplished by putting single-turn loops around the tank. In addition, four axial current loops energized from a crow-barred capacitor bank permit a total current of up to 70 kA to flow along the axis, generating a "toroidal" field, $B_\theta \lesssim 1$ kGauss, at the ring radius.

As in earlier RECE-Berta experiments, a steady-state gas filling of a few hundred mTorr of hydrogen is maintained in the tank to allow space charge neutralization and trapping of the injected electron beam. In addition, two pulsed valves directed towards plastic barriers in each half of the tank permit localized gas puffs to be introduced into the regions around the injector and the downstream mirror. The resulting transient local pressure increase (up to $\simeq$ 250 mTorr) appears to be important for the ring trapping process while it does not appear to affect the decay of the trapped ring. A 22-cm-radius copper ring mounted inside the chamber downstream of the injector was found to enhance trapping.

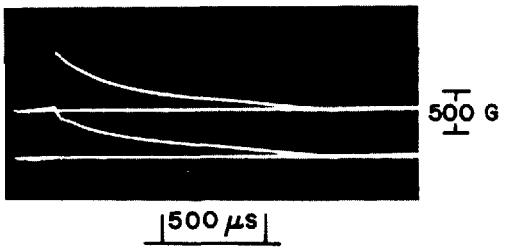


FIG.2. Ring field measured on tank axis.

For diagnostic purposes, mainly various sets of magnetic pick-up loops installed both along the tank axis and on the copper wall are employed. The response times of these probes vary between 50 nsec and 1.5 μsec. The respective signals are integrated through passive RC integrators (RC = 25-100 μsec for the fast probes and RC = 2-5 msec for the slow probes). Also, optical observations and scintillation X-ray detectors are used sometimes.

III. RECE-CHRISTA EXPERIMENTS

Using the above facility, strong electron rings exhibiting axial field-reversal initially and a smooth decay in strength are now observed regularly, using an electron beam energy of about 2.5 MeV, injection currents of ∿ 30 kA, steady-state gas pressures of 300-500 mTorr, axial magnetic fields, B_{zo} = 400-500 Gauss, and axial currents, I_z = 40-70 kA. As shown in Fig. 2, the initial magnetic fields generated by these rings at the ring center at present reach 170% of the applied mirror field, and remain above the field-reversal point for up to 220 μsec. Overall ring lifetimes reach up to 1.3 msec.

Approximate average radii and axial lengths of the trapped rings are derived as in our earlier experiments[9] by comparing the measured magnetic field distributions with those created by a radially thin E-layer having an axial $\cos^2$-distribution of the current density. Typical ring parameters and their time dependence over the first 350 μsec are shown in Fig. 3. As in our earlier experiments,[9] the ring radius, R, equals about 1/2 the wall radius and decreases during the decay. The layer length, however, has a markedly different development. Instead of the continuous increase observed earlier, the lengths of the present electron rings generally shrink quite significantly from L = (3-5)R to L = (1-2)R over the first 100-200 μsec (see Fig. 3) with a slight re-lengthening occurring thereafter. As evident from Fig. 3, the axial shrinkage of the rings coincides with a significant loss in total ring current. It appears that mainly the ends of the axial current distribution are lost while the central component represented by the peak of the current distribution decays much slower. These losses appear even more pronounced when higher mirror ratios and smaller toroidal fields are used. In this case, strong axially-long rings (axial field changes of up to 200% were observed) often become completely unstable during the first 200 μsec. While the origin of the rapid losses and instabilities is not clear at present, it would appear that they concern mainly electrons having large axial momentum.

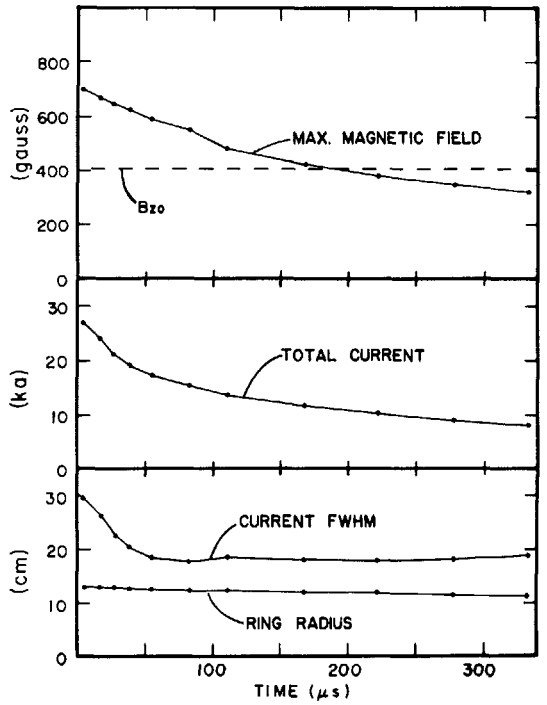


FIG.3. Time dependence of ring parameters.

The decay of the inner ring portions remaining after the first 100-200 μsec roughly agrees with that expected from classical scattering of the fast electrons in the background gas. The experimentally observed decay rate of 0.3 Gauss/μsec at the ring center is somewhat smaller than the value of 0.45 Gauss/μsec obtained from scaling (assuming no toroidal field) the value of 4 Gauss/μsec observed in RECE-Berta. The latter discrepancy, however, can easily be explained by the large experimental uncertainties and by the relatively strong average toroidal field, $B_\theta \simeq (1.5\text{-}2)B_{zo}$ in the ring.

Judging from the smooth decay of the electron rings, it appears that even strong rings are quite stable under the conditions of our experiment, which is similar to that of an Astron-Sperator.[5] To test the stability range in more detail, first experiments have been performed in which the normal crow-barring of the toroidal field was avoided, resulting in a decay of that field component with a quarter-cycle time equal to its rise time of 250 μsec. In this case, periods of anomalous losses occur at various combinations of B_θ/B_o and $\delta B/B_o$ (see Fig. 4). These losses occur on a 20-μsec time scale with periods of stable decay in between. These bursts appear to be accompanied by a positive change of the toroidal diamagnetism of the rings. The dependence of these bursts on other machine and ring parameters is being investigated.

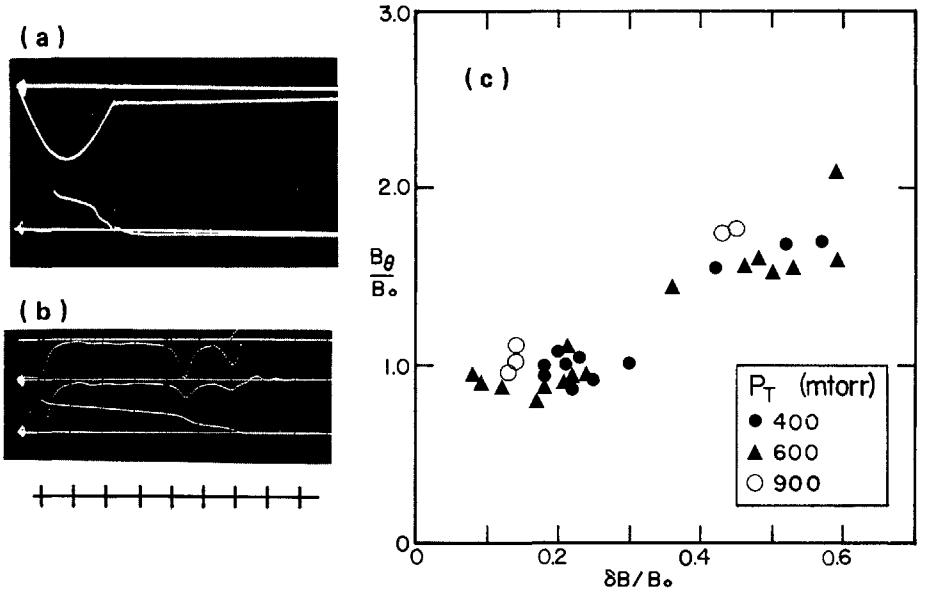


FIG.4. Anomalous electron losses in RECE-Christa.
(a) Time dependence of B_θ and δB on 200 μs/div.
(b) Two unintegrated and one integrated δB traces on 20 μs/div.
(c) Values of B_θ/B_0 and $\delta B/B_0$ at times of peak instability for various pressures.

IV. PRECESSIONAL STABILIZATION WITH GENERAL MULTIPOLE FIELDS

In certain reactor applications in which a toroidal field cannot be applied, and where the resistive decay of the image currents in the wall will render the wall stabilization ineffective, precessional[11] stabilization of the rings by outside fields will be important. Earlier,[12,13] we have shown the capability of quadrupole Ioffe windings to stabilize weak rings with $\delta B/B_0 \lesssim 60\%$. Unfortunately, it appeared—and this result has been reconfirmed since—that rings stronger than this limit exhibit a faster-than-collisional decay, the origin of which is not yet clear. Some theoretical considerations[14] point towards a half-frequency resonance between the average Larmor frequency and the frequency of the quadrupole perturbation experienced by the orbiting electrons. Therefore, further investigations have been performed on the effectiveness of multipole fields of higher order.

A theoretical analysis (to be published elsewhere), again based on Furth's superparticle model[11] of a thin ring, indicates that the precessional mode can also be stabilized by higher-order Ioffe fields, either of positive or of negative order, under the condition that

$$\varepsilon_m^2 \geq \eta \qquad (1)$$

where $\varepsilon_m = B_m(R)/B_0$ is the normalized multipole field strength at the radius of the ring, and where $\eta = (R/B_0)(\partial B_z/\partial r)_R$ is the radial index of the mirror

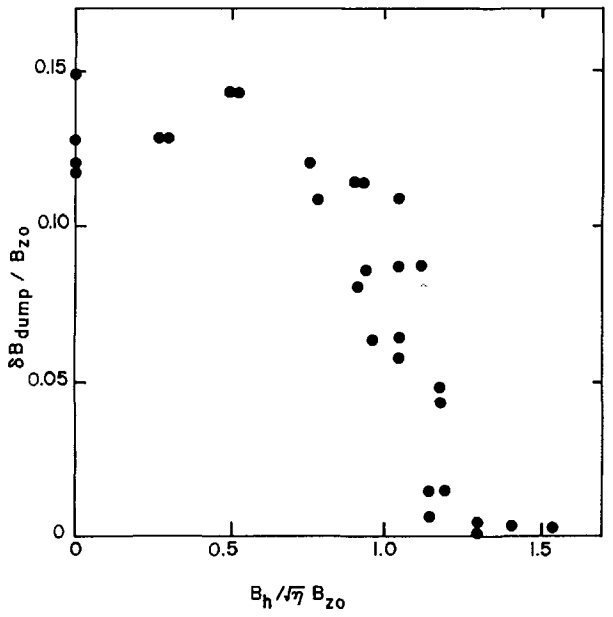


FIG.5. Dependence of dump instability level on normalized hexapole field strength.

field at the ring radius. For a finite-thickness E-layer, Eq. (1) can be generalized to

$$\frac{\epsilon_m^2\,(R)}{R^{2m-2}} \oint r^{2m-2}\, J_\theta \; dA > \frac{(R)}{R^2} \oint r^2\, J_\theta \; dA \qquad (2)$$

where the integral is to be taken over the minor ring cross-section.

To test these predictions, the RECE-Berta facility was fitted with additional hexapole windings energized from a separate capacitor bank. As indicated in Fig. 5, a stable decay of electron rings with $\delta B/B_o \lesssim$ 20-40% was observed. The dependence of the experimentally observed onset of the ring dump on the hexapole field strength, B_h, is also shown in Fig. 5. The experimental stability threshold agrees within about 30% with the theoretically expected critical hexapole field $B_h = \sqrt{\eta}\, B_{zo}$

V. GENERATION OF INTENSE ION PULSES FOR FUTURE ION RING EXPERIMENTS

For single-pulse generation of field-reversing ion rings for plasma confinement experiments, ion pulse densities at least of the order of 100 μAsec/cm^2 will be needed. Towards this aim, earlier experiments[15] testing the performance of magnetically insulated ion diodes, in particular for the generation of ion pulses with microsecond pulse lengths were extended.

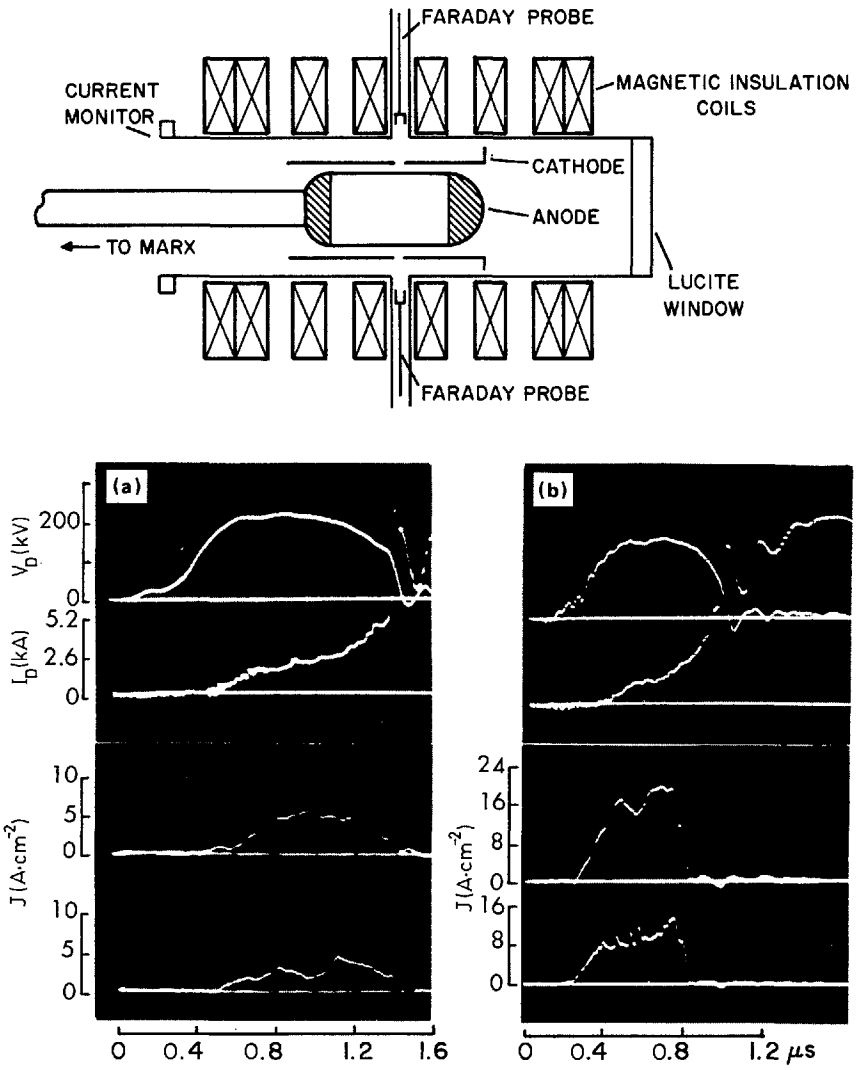


FIG.6. Long-pulse ion generation: experimental arrangement and results (7 mm gap, and B_z = 10 kG). (a) Opposed Faraday probes at cathode mid-plane; (b) probes at anode ends.

For this purpose, the Marx generator of our QUIBLE Blumlein[9] was connected directly to the vacuum diode, providing a positive voltage of 150-250 kV for several microseconds duration. For the diode, again the cylindrical arrangement[16] shown in Fig. 6 was chosen. Magnetic field coils around the diode produced an axial field of up to 20 kGauss. Various anode materials and diode spacings (3-11mm) were used. The generated ion current densities generally were measured using magnetically insulated Faraday cups especially designed to suppress secondary electron loss. The

probes were positioned on opposite sides of the anode behind two holes in the cathode cylinder, or in some cases, a longitudinal array of five similar hole-probe combinations were used to measure the z-dependence of the ion emission. Most reliable operation was obtained employing a nylon filament anode as used by Dreike et. al.[17] and using a 7-mm gap spacing. Typical data obtained in this arrangement are shown in Fig. 6a. A diode voltage, $V_d \sim 200$ kV (top trace) is sustained for about 1.2 μsec using a 10 kGauss field. The pulse is terminated by a distinct break in the voltage signal. This pulse time scaled roughly with $(1/V_d)$, and with B for $B \lesssim 10$ kGauss, leveling off for $B \gtrsim 10$ kGauss. Misalignment of the diode can significantly degrade the pulse length. The Faraday probe currents (lower two traces in Fig. 6) are normally delayed from the initiation of the voltage pulse by about 100-200 nsec. Under the above circumstances, the probes indicate ion current densities of 5 - 10 A/cm^2 in the diode midplane with the larger values normally associated with shorter pulse times. RMS fluctuations between the two midplane probe signals normally amounted to about 25%. The corresponding current densities were roughly proportional to V_d^2. Results from the longitudinal probe array (Fig. 6b) indicated current densities were larger at the ends of the nylon strings by about a factor 2.

At the ends, a total ion emission density per pulse of up to 7 μAmp-sec/cm^2 was obtained for the above conditions, which represents an improvement of almost an order of magnitude over the earlier short-pulse operation of such diodes[17]. As indicated by the Faraday probes, the total high-energy ion current in the diode (up to about 2 kA) generally amounted to 50-100% of the total diode current I_d.

Similar voltage stand-off characteristics and scaling laws were obtained for metallic or graphite anodes, however, with the total diode current suppressed to below 40 Amps.

REFERENCES

1. Christofilos, N. C., Proceedings of the 2nd United Nations International Conference on Peaceful Uses of Atomic Energy (Geneva, 1958), Vol. 32, p. 279; and Lawrence Livermore Laboratory report, UCRL-71189, July 1968.

2. Fleischmann, H. H., Conference on Electrostatic and Electromagnetic Confinement of Plasmas and the Phenomenology of Relativistic Electron Beams, (N. Y. Acad. Sci., New York, March 1974), and Ann. N. Y. Acad. Sci. 251 472 (1975), and Fleischmann, H. H., and Kammash, T., Nucl. Fusion 15 1143 (1975).

3. Condit, W. C., Jr., Fowler, T. K., and Post, R. F., Lawrence Livermore report, UCRL-58002 (Feb. 1976).

4. Dandl, R. A., et al., Plasma Physics and Controlled Fusion Research (Intern. Atomic Energy Agency, Tokyo, November 1974) Vol. II, p. 141.

5. Yoshikawa, S., Phys. Rev. Lett. 26 295 (1971).

6. Fleischmann, H. H., Cornell report LPS 186 (Jan. 1976), and Trans. Am. Nuc. Soc. TANSAO 23 24 (1976).

7. Briggs, R. J., et al., Phys. Fluids 16 1934 (1973), Lawrence Livermore Laboratory report, UCRL-51874 (Aug. 1975).

8. Bzura, J. J., et al., Phys. Rev. Lett. 29 256 (1972).

9. Phelps, D. A., et al., Phys. Fluids 17 2226 (1974).

10. Kribel, R. E., et al., Plasma Physics 16 113 (1974).

11. Furth, H. P., Phys. Fluids 8 2020 (1965).

12. Woodall, D. M., et al., Phys. Rev. Lett. 34 260 (1975).

13. Luckhardt, S. C., et al., Phys. Rev. Lett. 35 1758 (1975).

14. Berk, H. L., and Lovelace, R. V., private communication.

15. Luckhardt, S. C., Renk, T., and Fleischmann, H. H., Bul. Am. Phys. Soc. 21 691 (1975), and Fleischmann, H. H., International Topical Conference on Electron Beam Research and Technology (Albuquerque Nov. 1975), Vol. 2, p. 129.

16. Golden, J., Orzechowski, T. J., and Bekefi, G., J. Appl. Phys. 45 3211 (1974).

17. Dreike, P., Eichenberger, C., Humphries, S., and Sudan, R. N., J. Appl. Phys. 47 85 (1976).

FORMATION OF A HIGH-CURRENT RELATIVISTIC-ELECTRON-BEAM RING FOR PLASMA CONFINEMENT

A. MOHRI, M. MASUZAKI, K. NARIHARA, T. TSUZUKI,
K. YAMANAKA, K. IKUTA
Institute of Plasma Physics, Nagoya University,
Nagoya, Japan

Abstract

FORMATION OF A HIGH-CURRENT RELATIVISTIC-ELECTRON-BEAM RING FOR PLASMA CONFINEMENT.

High toroidal relativistic-electron-beam (REB) ring currents are formed in the toroidal devices SPAC-2, 3 and 4 with aspect ratios of 5, 2 and ~ 1, respectively, by injecting REB (typically 380 keV, 18 kA, 30 ns) either into neutral gas (SPAC-2, 3 and 4) or into plasma (SPAC-4). In the strong toroidal magnetic field of SPAC-2, the attainable ring current is limited so that the safety factor $q \gtrsim 5$. Stable configurations with high magnetic shear can be realized (SPAC-3 and 4). Injection of REB into a dense plasma leads to an REB ring with high magnetic shear (SPAC-4), and the stable state can be maintained by holding the magnetic shear under external control through the toroidal field. The instability of the plasma-ion-beam system is examined in view of a future application of strong ion beams to a pre-heating of the plasma confined by an REB ring before adiabatic compression.

1. INTRODUCTION

The formation of high toroidal relativistic-electron-beam (REB) ring currents will offer new possibilities of plasma confinement. A subject of greatest interest is the generation of magnetic configurations with high magnetic shear by REB currents. The diffusion of magnetic fields in high-magnetic-shear systems as the reversed-field pinch is strongly suppressed if the usual plasma currents are replaced by REB currents. Another subject is the formation of an REB ring of very small aspect ratio. Since the toroidal current can be supplied by the injection of an REB without using Ohmic heating equipment, toroidal devices of very small aspect ratio can be realized, and plasma heating by three-dimensional adiabatic compression can be applied effectively when the plasma temperature is raised in advance, e.g. by injection of high-current ion beams. During the compression, the particle energy of the REB ring becomes high enough to overcome current decay.

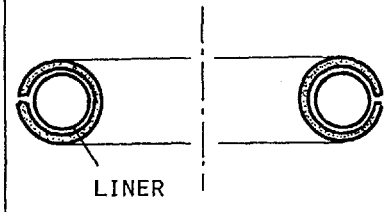
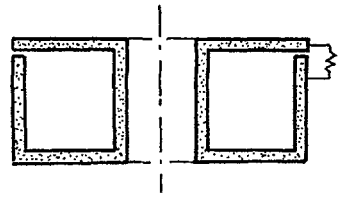
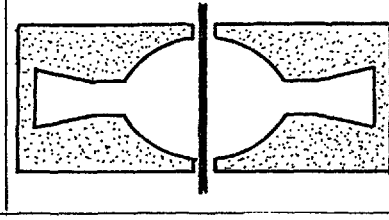
To investigate these possibilities, we carried out a series of experiments to form REB rings with three different aspect ratios (5, 2, ~ 1) by using the toroidal devices SPAC-2[1], SPAC-3 and SPAC-4. The main chracteristics of these tori are listed in Table I. REB's (typically 380 keV, 18 kA, 30 ns) were injected into neutral hydrogen gas of 0.1 ~ 0.2 torr filled into SPAC-2, 3 and 4 and also into a dense plasma prepared in SPAC-4.

PLasma heating by a strong ion beam is a promising method of pre-heating plasma before adiabatic compression. In connection with this possibility, the threshold for the occurrence of an instability is to be discussed.

2. INJECTION METHOD

High-voltage pulses with a pulse duration of 25 ~ 30 ns were delivered to a 4.6-Ω transmission line from a Phoebus-I generator [2] equipped with an air-core step-up transformer. Usually the output voltage of the pulse was 350 ~ 380 kV. An impedance-transforming line is installed between the transmission line and an REB-emitting diode, for the purpose of impedance matching. The diode consists of a grid anode and a graphite or metallic cathode, whose emitting surface is typically

TABLE I. PARAMETERS OF THE TOROIDAL DEVICES

DEVICE	SHAPE OF SHELL	R (CM)	a (CM)	MAX. B_t (KG)	MAX. B_v (KG)
SPAC-2		28	5.5	20	0.2
SPAC-3		12	6	2	0.5
SPAC-4		5~8		1.5	2.0

1.8 cm × 1.5 cm in size. The diode is placed just inside a toroidal metallic chamber and emits an REB parallel to the magnetic field. In all cases reported here, vertical magnetic fields were applied to launch the REB to an equilibrium position [3].

The formation of REB rings is related to the dynamic behaviour of the injected beam and also to the stability of the configuration at the final stage of the formation. The injection of an REB into neutral gas or plasma induces a return current inside. As the return current decays, both the net current and the resultant image current on the metallic wall increase with time. The rise of the magnetic force on the beam, which is caused by the image current, makes the beam orbit adiabatically shrink inwards. This mechanism is similar to the adiabatic trapping of electrons in a betatron [4]. Furthermore, the energy of the self-magnetic field should be supplied from the kinetic energy of the beam electrons, so that the beam orbit deviates towards the major axis of the torus when a vertical field is present.

3. INJECTION INTO NEUTRAL GAS

A rather fast net current rise is required at the injection of the REB so as to achieve an efficient formation of an REB ring, whereas the space charge should be well neutralized by the return current. Therefore, an appropriate presssure of the neutral gas should be chosen, which was found to be 0.1 ~ 0.2 torr for hydrogen in the present experiments.

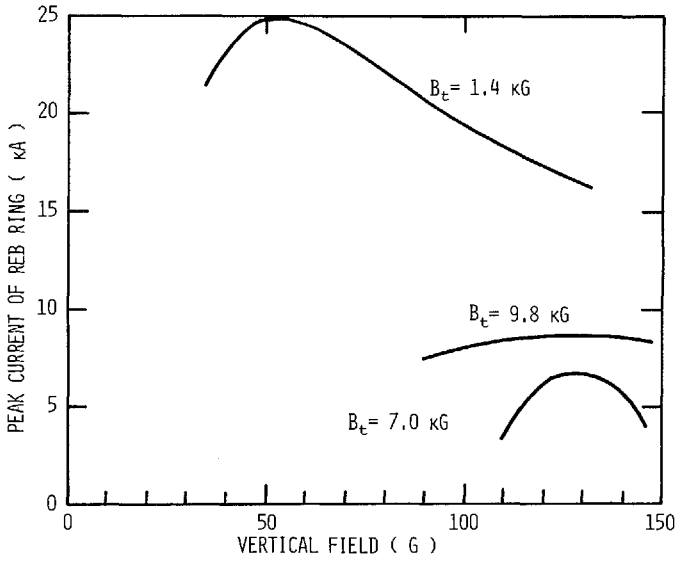
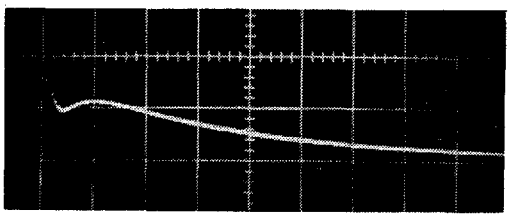


FIG.1. Dependence of REB ring current on vertical field for different toroidal magnetic fields in SPAC-2.



5 μs/DIV.

FIG.2. Decay of REB ring current in a strong toroidal magnetic field in SPAC-2 (B_t= 7 kG, B_v=125 G). The peak current is 7 kA.

3.1. REB ring in a strong toroidal field

The tokamak-like device SPAC-2[1] has a 1.5 cm thick aluminium shell and a liner made of a stainless steel bellows with a thickness of 0.3 mm. Other parameters are listed in Table I. An electron beam (350 keV, 18 kA) was injected into hydrogen gas of 0.15 torr at the peak of the pulsed toroidal magnetic field. Figure 1 shows the change of obtained peak current of the REB ring with the vertical field B_v for three different toroidal fields B_t. In the case of strong B_t (7 ~ 10 kG), the attained maximum current of the REB ring was 7 ~ 8.7 kA, which corresponds to a safety factor of $q_a \geqslant 5$ at the outermost surface. This result supports the theoretical prediction of a current limit [5]. For $q_a \gtrsim 5$, the net poloidal magnetic field rose smoothly with time and reached its peak at about 120 ns after injection. Then it decayed exponentially without distinguishable fluctuations (Fig.2). The decay time of the ring current was 25 μs. The momentum transfer due to collisions with background particles and the classical diffusion of the REB ring in a strong magnetic field [6] cannot account for this decay time. On the other hand, the decay time is in

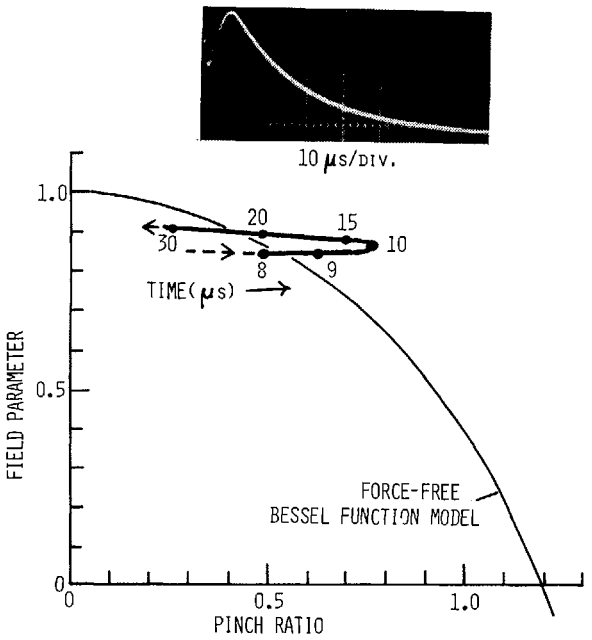


FIG.3. Travel of state in θ-F space after damping of oscillations for REB ring in SPAC-3. B_t=1.5 kG, B_v=210 G. The wave form of the ring current is shown in the inset, where the peak current is 30 kA.

good agreement with that estimated from the spiralling-off of beam electrons as caused by the field error.

In the case of weak toroidal field ($B_t = 1.4$ kG), the current obtained was 25 kA where $q_a \cong 0.3$ (Fig.1). The current decay time was 0.3 μs, which is comparable to the skin time of the liner for the toroidal field. This configuration may be akin to a stabilized pinch with high magnetic shear since penetration of the external B_t would change the configuration to an unstable one.

3.2. REB ring with high magnetic shear

For a further study of the possibilities of achieving a state with $q < 1$, the toroidal device SPAC-3 was constructed. The aluminium shell has a rectangular cross-section, and its poloidal cut is bridged by many resistors to achieve a skin time of 40 μs for the toroidal magnetic field. An external toroidal magnetic field, rising slowly enough to penetrate the shell chamber, was applied, and at the peak of the field, an REB was injected in the same way as was mentioned previously. The filling gas was hydrogen at a pressure of 0.15 torr; in addition, a d.c. vertical field, B_v, was applied. The poloidal field inside the shell rose within 80 ns after the injection. Then, slow radial and vertical oscillations of the current ring followed, but were damped within 8–10 μs. Subsequently, the current decayed smoothly without any noticeable fluctuations. The peak current attained at B_t = 1.5 kG and B_v = 210 G was about 30 kA and the current decay time was 25 μs (inset of Fig.3). Note that, in the case of a low q value, the decay time in SPAC-2 was only 0.3 μs. At the time of the current peak, the toroidal field just inside the chamber wall decreased by 200 G, and the pinch ratio $\theta \equiv B_p(a)/\langle B_t \rangle \cong 0.77$ and the field parameter $F \equiv B_t(a)/\langle B_t \rangle \cong 0.86$.

As the time passed on,the point (θ, F) moved gradually around the θ-F curve of the force-free Bessel-function model introduced by J.B. Taylor [7], as is shown in Fig.3. The current of 30 kA is 1.5 times the Alfvén limit [8] which is ~ 20 kA in this case. Therefore, this state is thought to be nearly force-free [9] if the plasma is cold. These results suggest that there is a possibility of generating high-magnetic-shear systems, similar to the reversed-field pinch configuration, by REB currents.

3.3. REB ring of low aspect ratio

To produce an REB ring with an aspect ratio close to unity, we injected an REB into SPAC-4, which is equipped with a thick aluminium chamber of spherical shape. A central conductor set along the major axis of the device generates a toroidal magnetic field B_t. The REB diode was placed in the gap between the lower and upper halves of the shell. The filling gas in the chamber was hydrogen at a pressure of 0.2 torr.

The toroidal current obtained in the case $B_t = 0$ and $B_v = 1.26$ kG was estimated to be 21 kA, and the decay time of the current was about 6 μs. However, a few cycles of the major-radial oscillation of the ring current were observed immediately after the injection. The period of the oscillation was 1–2 μs. As B_t was increased, oscillations of the ring about the median plane of the torus appeared. Such an oscillation is due to the magnetic interaction of the ring current with induced image currents on the chamber wall. The configuration became nearly symmetric for currents higher than 10 kA.

4. INJECTION INTO DENSE PLASMA

Adjustment of the initial plasma density at the time of REB injection is the first requisite for obtaining a confined-plasma β value necessary for stability. For an efficient formation of the REB ring, fast appearance of the REB-current poloidal field is required as well as sufficient neutralization of space charge. In case of injection into a neutral gas, the suitable range of gas pressures was limited so that the condition was compatible with these two requirements. Therefore, the injection of an REB into a plasma would be more favourable if something could be contrived to impede poloidal-field masking due to the return current of the plasma. SPAC-4 served to carry out this experiment. The molybdenum grid anode of the diode was connected with the outer conductor of the transmission line by a fairly long stem. The connection point is also in contact with the toroidal chamber. Thus, while the diode is working, the anode potential is biased negative to the chamber, owing to the self-inductance of the stem. This potential can be made deep enough to reflect the bulk of plasma electrons which would carry the return current. As a result, a fast rise of the poloidal field is expected. Electron leakage through this potential barrier is sufficient to maintain neutrality of the beam-plasma-system space charge.

Hydrogen plasma was filled into the chamber by a rail-type plasma gun. The maximum plasma density and the electron temperature were nearly 4×10^{15} cm^{-3} and 10 eV, respectively, in the presence of both toroidal and vertical magnetic fields. The REB was injected at the peak of the plasma density. The poloidal magnetic field rose fast within 30 ns, a time which was comparable to the pulse duration of the REB injection.

At first, the time of the REB injection was set during the flat part of the toroidal magnetic field where $dB_t/dt = 0$. In optimum conditions where $B_t = 1270$ G at a radius of 5 cm and the external vertical field $B_{v0} = 600$ G, field reversal with respect to the vertical field was attained to 500%. The ring current was estimated to be about 20 kA. The magnetic energy transferred from the injected REB was about 50 J while the total injected energy was nearly 200 J. Thus, the efficiency of the injection was larger than 20%. In most of runs with $dB_t/dt = 0$, fast damping stages of the ring current appeared successively during the decay (Fig.4a). The damping stages were

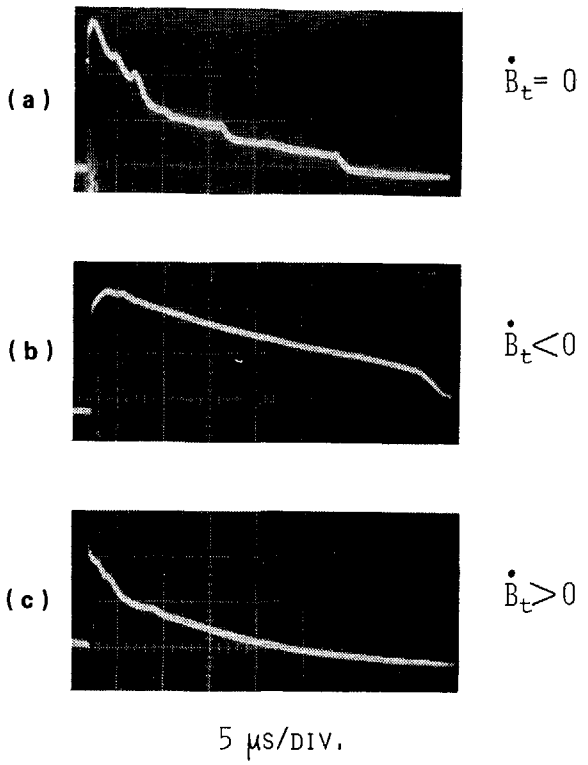


FIG.4. Suppression of instability by controlling the changing rate of the external toroidal magnetic field for the REB ring formed by REB injection into the plasma of SPAC-4. B_t at $t = 0$ is 1040 G at $r = 5$ cm. (a) $\dot{B} = 0$; (b) stable case; $dB_t/B_t dt \cong -10^4 s^{-1}$, (c) unstable case; $dB_t/B_t dt \cong +10^4 s^{-1}$.

accompanied by bursts of hard X-rays and spectral lines of hydrogen atoms. Strong soft X-rays from the wall of the central conductor were also observed in the damping stages. The most violent collapse was observed when the field reversal of B_v was near 100% where the stagnation points degenerated to a point on the major axis. It should be noted that during the decay of the ring current two stagnation points on the major axis approach each other and, thereby, the area enclosed by the separatrix becomes smaller. If the configuration is paramagnetic and stabilized by high magnetic shear, the region in which the plasma is stably confined becomes smaller as the current decays since the pitch-minimum surface of the field lines shrinks gradually. As time passes on, the plasma and the current outside the stable region will be scraped off by instabilities [10].

Decrease of the external toroidal field will help the magnetic shear at the periphery in stabilizing the plasma. The REB was injected in the decay phase of B_t. The wave form of the poloidal field became very quiescent when the rate $dB_t/B_t dt \cong -10^4 s^{-1}$ (Fig.4b). The decay of the current I_b was linear with time for ~40 μs and the half-decay time was about 25 μs. In this case, the rate $dI_b/I_b dt \sim dB_t/B_t dt$. However, the decay became faster after a field reversal of 100% had been reached. A possible explanation of the decay is the spiralling-out of the beam electrons, owing to the error in the magnetic field. The accuracy of the field corresponding to the decay time is estimated to be $\sim 10^{-5}$. This value would be the limit of the accuracy in such a small toroidal device. On the other hand, when a ring was formed in the increasing phase of B_t, violent instabilities

appeared and the current faded out faster (Fig.3c). These results suggest that a stable and long-life REB ring with high magnetic shear can be formed when the toroidal and vertical fields are externally controlled in an appropriate way.

5. INSTABILITY DURING FURTHER HEATING BROUGHT ABOUT BY AN ION BEAM

The production of high-temperature plasma is important in achieving an effective adiabatic compression of the plasma by an REB ring. The high-current ion-beam heating would be effective for this purpose. Favourable heating would be obtained when the ion beams are introduced perpendicularly to the magnetic lines of force and lose their energy while drifting about the magnetic axis in the background plasma. In such circumstances, MHD instabilities may appear. The threshold of an instability is discussed by using a simple model.

We consider a situation where a column of energetic ions is located in a cylindrical cold MHD plasma magnetized by straight lines of force; the column rotates about the plasma axis. Then, this plasma-beam system can be described by a set of equations for the vector potential $\vec{A}$:

$$\vec{B}_0 \times \vec{I} = 0 \tag{1}$$

$$M\left(\frac{\partial \vec{v}_1}{\partial t} + \vec{v}_0 \cdot \nabla \vec{v}_1 + \vec{v}_1 \cdot \nabla \vec{v}_0\right) = e(\vec{E} + \vec{v}_0 \times \vec{B}_1 + \vec{v}_1 \times \vec{B}_0) \tag{2}$$

$$\frac{\partial n_1}{\partial t} + \nabla \cdot (n_0 \vec{v}_1 + n_1 \vec{v}_0) = 0 \tag{3}$$

where

$$\vec{I} = \left(\frac{\mu_0 \rho}{B_0^2}\right) \frac{\partial^2 \vec{A}}{\partial t^2} + \nabla \times \nabla \times \vec{A} - \mu_0 \vec{J}_b$$

$$\vec{B}_1 = \nabla \times \vec{A}, \quad \vec{E} = -\frac{\partial \vec{A}}{\partial t} \quad \text{and} \quad \vec{J}_b = e(n_0 \vec{v}_1 + n_1 \vec{v}_0)$$

Here, M, e and n are the mass, the charge and the number density of the energetic ions, and ρ is the plasma density. The subscripts 0 and 1 designate unperturbed and linearized quantities, respectively.

For the unperturbed magnetic field, $\vec{B}_0 = (0, 0, B_0)$, and the perturbed quantities f written as

$$f = f(r,k) \exp [i(kz - \omega t)] \tag{4}$$

the set of the equations can be reduced to a single differential equation in the low-frequency limit:

$$\frac{d^2 A_\theta}{dx^2} + \frac{1}{x} \frac{dA_\theta}{dx} \left(K^2 - \frac{1}{x^2} - \frac{\lambda^2 k^2 a^2}{\tilde{\omega}^2} x^2\right) A_\theta = 0 \tag{5}$$

where

$$K^2 = \left(\frac{\omega^2}{C_A^2} - k^2\right) a^2, \quad \lambda^2 = ne^2 a^2 / M\epsilon_0 c^2, \quad \tilde{\omega} = \omega/(eB_0/M) = \omega/\Omega, \quad C_A^2 = B_0^2/\mu_0 \rho$$

and a is the radius of the rotating ion column and A_θ the θ component of the vector potential. Under an appropriate boundary condition at the plasma-beam interface, Eq.(5) is solved whence the dispersion relation for the instability becomes

$$\omega^4 - k^2 C_A^2 \omega^2 + (2/3)\lambda^2 \Omega^2 k^2 C_A^2 = 0 \tag{6}$$

Thus, the threshold of the beam ion density, n_c, for the instability is

$$n_c = \frac{3}{8} \frac{k^2 C_A^2}{\Omega^2} \frac{M\epsilon_0 c^2}{e^2 a^2} \tag{7}$$

and

$$\omega = \pm (2/3)^{1/4} (k C_A \lambda \Omega)^{1/2} \exp\left(\pm \frac{1}{2} \tan^{-1} \delta\right) \tag{8}$$

where

$$\delta^2 = \frac{8}{3} \frac{\lambda^2 \Omega^2}{k^2 C_A^2} - 1$$

From Eq.(8) we see that the plasma heated by ion beams does not exhibit any fatal MHD instability when the beam density is low enough.

6. CONCLUDING REMARKS

It has been shown experimentally that toroidal magnetic configurations maintained by high REB currents can be formed by injecting short REB pulses into toroidal chambers. A stable state of low magnetic shear was obtainable for $q \gtrsim 5$ only. Configurations with high magnetic shear could be realized but perfect toroidal field reversal has not yet been attained, mainly because of the low energy of the REB source at hand. A method of injecting REB into plasma was developed, which is very essential to the REB ring scheme for plasma confinement. By this method, a very fat configuration with high magnetic shear like the Astron-Spherator [11] could be formed, where the vertical field reversal reached to 500%. It has also been proved that the control of magnetic shear is very important in stabilizing the system.

REFERENCES

[1] HAMADA, Y., MOHRI, A., Jpn. J. Appl. Phys. **13** (1974) 1624.
[2] MOHRI, A., IKUTA, K., MASUZAKI, M., TSUZUKI, T., Jpn. J. Appl. Phys. **14** (1975) 1777.
[3] MOHRI, A., MASUZAKI, M., TSUZUKI, T., IKUTA, K., Phys. Rev. Lett. **34** (1975) 574.
[4] KERST, D.W., SERBER, R., Phys. Rev. **60** (1941) 58.
[5] LOVELAGE, R.V., Phys. Fluids **19** (1976) 723.
[6] HUMPHRIES, S., Plasma Phys. **16** (1974) 705.
[7] TAYLOR, J.B., in Plasma Physics and Controlled Nuclear Fusion Research (Proc. 5th Int. Conf. Tokyo, 1974) **1**, IAEA, Vienna (1975) 161.
[8] ALFVEN, H., Phys. Rev. **55** (1939) 425.
[9] YOSHIKAWA, S., Phys. Rev. Lett. **26** (1971) 295.
[10] ROBINSON, D.C., Plasma Phys. **13** (1971) 439.
[11] YOSHIKAWA, S., CHRISTOFILOS, N.C., in Plasma Physics and Controlled Fusion Research (Proc. 4th Int. Conf. Madison, 1971) **2**, IAEA, Vienna (1971) 357.

DISCUSSION

ON PAPERS IAEA-CN-35/H2–1, H 2–2

M.S. RABINOVICH: Have you observed the development of a tearing mode in which the ring breaks down into two rings?

A. MOHRI: No, we have not identified an instability of this kind. It was possible to suppress the observed instability by reducing the toroidal field.

H. KNOEPFEL: In connection with toroidal electron beams, a point worth mentioning is that a powerful and simple alternative production method based on the runaway effect exists. At Oak Ridge we have been able in this way to generate reproducibly, in the Ormak tokamak (major radius R = 80 cm), toroidal electron beams with (typically) 60 kA current and 3 MeV mean electron energy, the current decaying with e-folding times of 40 ms.

H.H. FLEISCHMANN: I should like to comment on Rabinovich's question about the occurrence of tearing modes and also on Knoepfel's remarks concerning the relationship of the experiments reported here to the high-current runaway beam generated by the ORMAK group.

In our small machine, RECE-Berta, we sometimes observe (about once in 10 to 20 shots) an apparent axial splitting-off of the ring preceded and followed by normal collisional decay. This effect certainly is reminiscent of a tearing mode. We have no details as yet, but the phenomenon undoubtedly needs to be investigated more thoroughly in view of its potential importance.

The runaway beam experiment and the experiments reported here complement each other. They both aim at obtaining various advantages, for example a reduction of the minimum useful q-value in tokamaks. The difference between the two experiments (apart from the technology of beam generation) lies in the size of the fast-particle Larmor orbits relative to the plasma dimensions: in the runaway discharges the magnetic field is large (i.e. the Larmor orbits are relatively small) whereas in the electron ring experiment the orbit size is comparable with the ring size.

J. BENFORD: How low can the q of a tokamak be made by injection of a relativistic beam, in principle?

A. MOHRI: In our experiments we have not brought the q value below 5 in the tokamak mode. Magnetic shear stabilization is necessary for lower q; our experiments, at least, suggest this tendency.

R.N. SUDAN: The Cornell experiments on electron beam injection into toroidal traps indicate that after trapping for several turns around the torus the energetic electrons are lost to the walls, the loss being accompanied by X-ray emission. Do you see such X-ray bursts during the decay of the toroidal current, indicating the presence of energetic electrons?

A. MOHRI: X-ray bursts were observed only at the injection stage and at the final dump. There was, however, some small emission of X-rays during current decay.

MACROPARTICLE ACCELERATION BY LASER-INDUCED ABLATION PRESSURE

M.D.J. BURGESS, H. MOTZ, P.T. RUMSBY,
M. MICHAELIS*
Engineering Science Department,
University of Oxford,
Parks Road, Oxford,
United Kingdom

Abstract

MACROPARTICLE ACCELERATION BY LASER-INDUCED ABLATION PRESSURE.

It is shown that the theoretical scaling of plasma pressure is very closely obeyed using ordinary Q-switched laser pulses, resulting in velocities of over 2×10^4 cm $\cdot s^{-1}$. The problems associated with increasing this velocity whilst still not rupturing the pellet have also been examined and an experiment aimed at determining the results is described.

1. Introduction

The initial motivation for the experimental work reported here was the testing of several theories [1,2,3] which account for the scaling of plasma pressure with differing laser wavelengths and intensities incident upon various target materials. During the course of these experiments velocities in excess of 10^4cm$\cdot s^{-1}$ were achieved. The first part of this paper will present the results of this work and then it will go on to consider the problems of accelerating pellets to velocities of over 10^6cm s^{-1}.

If such hypervelocities can be reached then one of the criteria for refuelling a quasi steady state fusion reactor will have been satisfied. Gralnick [4] has shown that a 5000 MW(T) reactor would require (e.g.) 1mm radius DT pellets to be introduced at a rate of 85 per second and injection velocities of more than 10^6cm$\cdot s^{-1}$ are required so that the penetration time is less than the pellet disassembly time.

Other possible applications for such laser induced ablation pressures lie in the fields of micrometeorite impact simulation and the production of hypersonic vibrations [5], non-linear acoustics [6] and even the propulsion of a space-vehicle into earth orbit [7].

Of the many methods which have been suggested to achieve hypervelocities with macroparticles [8,9], three ways in particular are favoured: electrostatic, pneumatic and laser-induced acceleration. The first requires voltages (for sensibly sized pellets) which are not yet technologically feasible and are yet sufficiently high to either disrupt the pellet or even to cause field emission. The second method suffers from not only possibly introducing large amounts of driver gas into the reactor system but also from requiring the driver gas to be a high temperature plasma, unless a significant fraction of the pellet is ablated (in rocket fashion) to allow the remaining solid to travel at a higher velocity than the driver gas. Such a plasma/cryogenic pellet launcher of sufficient size and with the necessary launch-rate will be extremely difficult to manufacture.

---

* Present address: Physics Department, Durban, University of Natal.

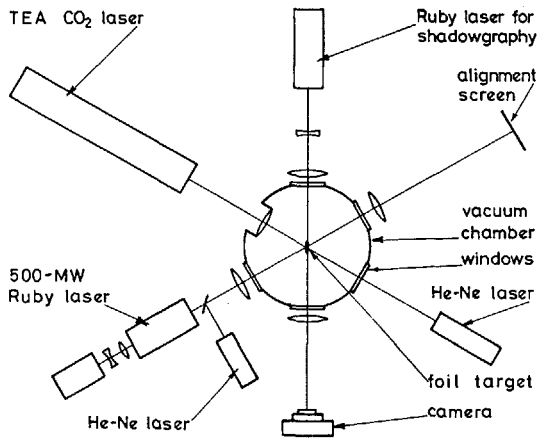


FIG.1. Experimental arrangement.

Velocities of 2×10^6cm s^{-1} have been achieved with 270μg glass spheres for use in micrometeorite simulation experiments using a two-stage accelerator [10] which consists of a light gas gun as the first stage and a coaxial accelerator with a compressor coil as the second stage. However, it is difficult to foresee the necessary three orders of magnitude increase in pellet mass which would be necessary for refuelling purposes.

The method of laser-induced acceleration also has its problems and these, together with an examination of its feasibility, will be discussed in sections 3 and 4 of this paper. Section 5 describes an experiment which is at present underway to extend a normal Q-switched ruby laser pulse and thereby to increase the velocities attained to 10^5cm s^{-1}.

2. Experimental Test of Scaling Laws

Despite differing analytical techniques, the treatments of Cooper [1], Puell [2] and Caruso and Gratton [2] yield essentially the same scaling law for the plasma pressure within the intensity regime of 10^9 to 10^{14} W cm^{-2}. With only minor deviations their models give rise to dependences of the form:

$$P \propto \lambda^{-0.25} I^{0.75} Z^{-0.5} M^{0.4} \qquad (1)$$

where P is the plasma pressure, λ is the incident radiation wavelength, I its intensity, M is the atomic mass of the target material and Z is the average charge state of the plasma created. The very weak dependence on time has been ignored.

The experimental arrangement is shown in Figures 1 and 2. The beams from either a 25MW, 45ns pulsed TEA CO_2 laser or a 500MW, 18ns pulsed ruby laser were focussed onto one side of a thin metal foil to create a plasma. The plasma ablation pressure causes the foil to travel in the direction normal to its surface. Foil velocities were simply determined by exposing shadowgrams with another 40MW, 20ns ruby laser pulse both before irradiation of the foil and after a known delay (typically 24μs).

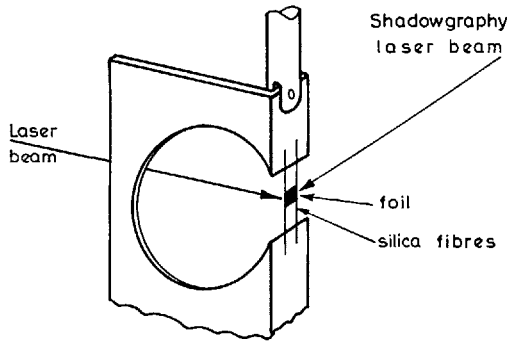


FIG.2. Target foil holder.

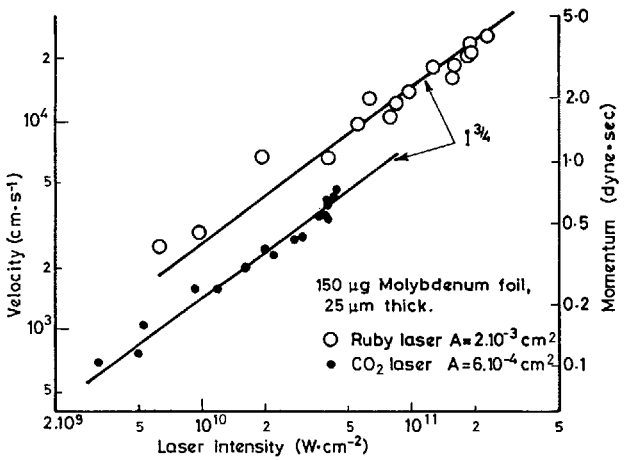


FIG.3. Foil velocity (and momentum) measurements for different ruby and CO_2 laser intensities.

Using 0.15mg Mo foil targets (0.75mm x 0.75mm x 25μm), velocity measurements were made over a large range of laser intensities for both ruby and CO_2 laser irradiation. The velocity measurements and corresponding momenta are displayed in Figure 3.

As the amount of target evaporated during a laser pulse was small compared to the initial target mass, then the plasma pressure is related to the final foil velocity by

$$P(\lambda, I) \propto \frac{mv}{At} \qquad (2)$$

where m is the target mass, A the laser focal spot area and t the time of laser irradiation. Remembering that the mass loss is small, we have for a particular laser wavelength

$$P(\lambda, I) \propto v \qquad (3)$$

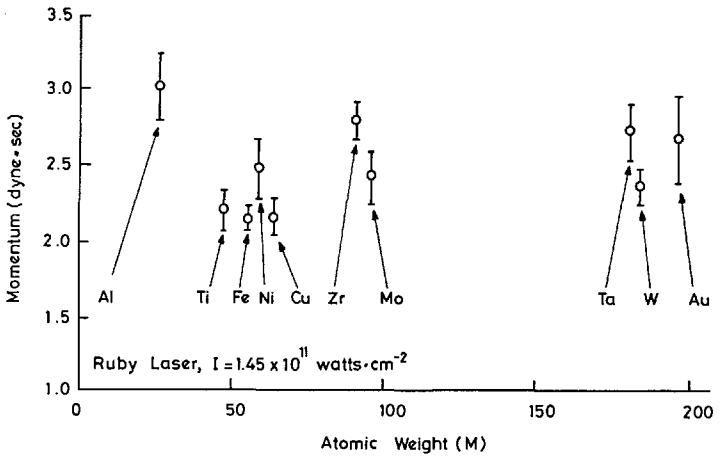


FIG.4. Foil momentum measurements for different target materials.

The experimental points on Figure 3 can be seen to closely obey the $v \propto P \propto I^{0.75}$ dependence for both ruby and CO_2 laser irradiation as predicted theoretically.

The scaling of plasma pressure with laser wavelength can be checked by calculating the ratio

$$\frac{[v/At]_{Ruby}}{[v/At]_{CO_2}} \propto \frac{P_{Ruby}}{P_{CO_2}} \qquad (4)$$

for identical laser intensities. This gives a wavelength scaling of $P \propto \lambda^{-0.2}$, which is close to the theoretical $P \propto \lambda^{-0.25}$.

To check the pressure scaling with M and Z, velocity measurements were made using different foil materials irradiated by the ruby laser at an intensity of 1.45×10^{11} W cm^{-2}. Figure 4 shows the results in terms of momentum acquired by each foil ($mv \propto P$) plotted against atomic mass. To compare these results with theory we need some relationship between M and Z, since Z will increase as M is increased. By extrapolating the $Z \propto M^{0.75}$ dependence found by House [11] between C (M=12) and Fe (M=56) to hold up to the heaviest elements used gives an overall pressure dependence on atomic mass of

$$P \propto M^{0.015} \qquad (5)$$

The roughly flat momentum against atomic mass results shown in Figure 4 agree well with this scaling.

Finally we have noted that for laser shots where the foil and laser beam were incorrectly aligned, very large rotational velocities (over 5 million revs. min^{-1}) were imparted to the foil.

For ruby laser irradiations in the above experiment, the focal spot diameter was adjusted to be 500μm as it was found that for smaller spot sizes the foils were ruptured by the laser pulse at the highest intensities. The exact nature and avoidance of such rupturing are thought to be two of the major problems posed by laser-induced acceleration and these will now be discussed in more detail.

3. Feasibility

The equation of motion for the laser ablated pellet is

$$\frac{mdv}{dt} + \frac{udm}{dt} = PA \qquad (6)$$

where $m = m(t)$ is the remaining solid mass of the pellet at time t of initial mass M_o, v is the velocity of this remaining mass in the laboratory frame, u is the velocity - relative to the remaining mass - of the ejected particles, P is the plasma pressure and A is the effective surface area of the pellet.

Equation (6) can be written

$$v = -\int \frac{udm}{m} + \int \frac{PA}{m}\,dt \qquad (7)$$

so that if we allow the particles to escape at their thermal speed

$$u \sim \left(\frac{k_B T}{m_i}\right)^{\frac{1}{2}} \qquad (8)$$

where m_i is the ionic mass and the temperature is in degrees kelvin.

Mass conservation at the ablating surface gives

$$\frac{dm}{dt} = \dot{m} \sim n_v\, m_i\, A\, u \qquad (9)$$

where n_v is the number density of the ejected particles.

Substituting (8) and (9) in (7) gives

$$v \sim u\int \frac{dm}{m} + \frac{n_v \cdot kT \cdot A}{n_v \cdot m_i \cdot A \cdot u}\int \frac{dm}{m}$$

$$\text{i.e. final velocity} \sim 2u \log_e \frac{M_o}{m(\tau)} \qquad (10)$$

where τ is the pulse length of the incident radiation.

If we assume a plasma temperature of 10eV (10^5 °K), the thermal velocity of ejection

$$u \gtrsim 10^6 \text{ cm s}^{-1}$$

and for more than 63% mass burn-up $v > u$.

However note that for 99% mass burn up, $v < 5u$, and that for effective temperatures much lower than 10eV the mass decrement would have to be unreasonably large.

If, therefore, a low temperature plasma could be created at the laser incident pellet surface and maintained for the length of time required to obtain more than 60% mass loss, then final velocities of over 10^6cm s^{-1} will be achieved.

$$\text{i.e.} \quad \dot{m}\,\tau \gtrsim \frac{60}{100} \cdot M_o$$

Using (9) and evaluating gives: $\tau \gtrsim 1\mu s$

for a 10eV plasma absorbing ruby light at its critical density.

In order to create the plasma initially, the intensity cannot be allowed to fall too low. A laser giving 1J in 10^{-8} s must give 100 J in 10^{-6} s. This amount of energy would be compatible with the amount needed to accelerate a 1mm pellet of DT to the required velocity (40J).

In the experiment described in section 2, molybdenum foils were accelerated to over 10^4cm s^{-1}. The lower atomic mass and correspondingly higher thermal ejection velocity of DT should produce velocities in excess of 10^5cm s^{-1}. However, the Q-switched laser pulses used meant that the light was absorbed in a very short distance ($< 10^{-2}$cm) and so very little mass was lost. Increasing the pulse length to sizeable fractions of a microsecond should give rise to the desired velocity.

4. Problems

We have seen that too low an intensity will not give rise to a sufficiently high ejection velocity for reasonable mass decrements. If too high an intensity is used the hydrodynamic shock induced in the pellet by momentum conservation will exceed the cohesive strength of the material. Caruso [3] has shown that an intensity of 10^{11} W cm^{-2} is sufficient to completely ionise a solid deuterium target (of dimension , $L \sim 10^{-2}$cm) by means of the induced shock.

For the size of pellet we are considering ($L \sim 10^{-1}$cm) the induced shock could be sufficient to vapourise most of the pellet remaining, and thus reduce the penetration distance into the fusion plasma.

Fortunately the maximum amount of momentum transfer per joule of incident laser energy would seem to lie between the extremes mentioned above. Gregg and Thomas [13] have shown that for ruby light incident upon several different materials the optimum value is about 5×10^9 W cm^{-2}, below which a significant amount of energy is conducted away and above which a significant amount of energy goes into increasing both the degree of ionisation and the energy per ion. This is less efficient than if the same amount of laser energy were put into a larger number of ions with less energy per ion.

We shall not in this paper treat the difficult theoretical problem of light absorption and expansion dynamics of the gas behind the pellet.

If, due to misalignment, the pellet were to start rotating then the problem of mass loss by vaporisation would become much more acute.

Finally if the acceleration is too great, the maximum tolerable inertial stress of the pellet will be exceeded. For solid hydrogen, the maximum

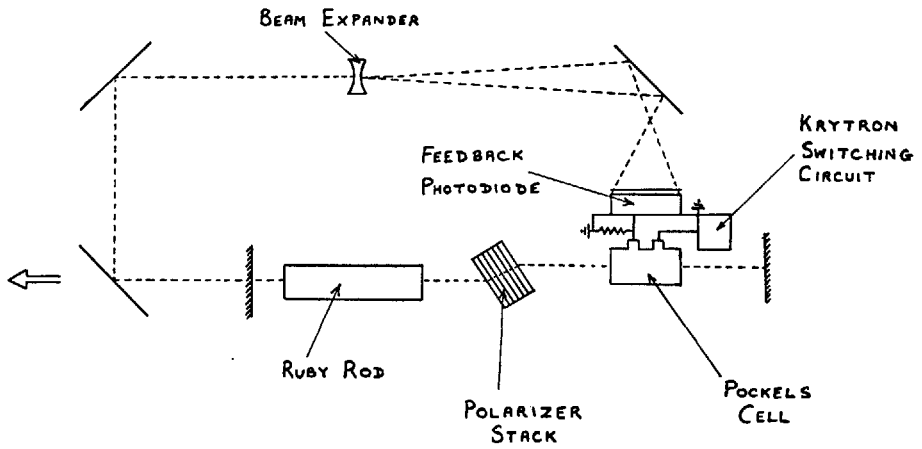


FIG.5. Laser cavity with feedback elements.

allowable stress in 5×10^5 Nm^{-2} [9], which indicates a maximum acceleration of 5×10^8cm s^{-2} for a 1mm pellet. This has to be compared with the value required to reach 10^6cm s^{-1} in 1μs (a very long Q-switched laser pulse), namely 10^{12}cm s^{-2}.

One possible method of overcoming the stress problems would be to encase the pellet in a material of high tensile strength. If molybdenum were to be used, the jacket would have to be over 1cm thick. Unless all this casing is also ablated away, there will be severe impurity problems within the fusion reactor.

On the other hand, if we accept that the pellet will be shattered by a stress exceeding its cohesive strength, it would still travel on and the dynamics of its motion will not be much changed. It is not clear whether it would, in fact, end up as a tightly packed powder and how Gralnick's theory of the action of the reactor plasma would have to be modified.

On account of this uncertainty and the difficulty involved in knowing the important parameters with any degree of certainty, it was decided to empirically determine the result on the velocity of increasing the pulse length and energy, still keeping the intensity below any damaging shock-inducing threshold.

5. Device for Pulse Lengthening and Shaping

There are several methods by which the pulse of the ruby laser used in the experiment described in section 2 may be lengthened. Slower Q-switching (using a rotating mirror) and introducing a non-linear absorbing element into the cavity (two photon absorption) would certainly have the right effect but the method of compound feedback as described by Yeoman et al [14] seemed to offer the best pulse shape.

Following their procedure it is hoped to increase the length of an ordinary Q-switched ruby laser from its present 25ns (FWHM) to several hundreds of nanoseconds, and instead of the normal gaussian output, to approach a ramp-like laser pulse intensity slowly rising with time.

A straightforward KORAD K1 ruby laser cavity will be modified as shown in Figure 5, where the feedback mechanism is fully described in reference [14].

With just negative feedback, a fast rising pulse with an exponential decay is obtained. It is the rapid rise which is thought to be strongly shock inducing and by controlling the feedback voltage this can be reduced to give pulse shapes very close to those desired (e.g. Fig.5(e) of reference [14]).

Having obtained the required pulse, the initial experiments using thin foils of molybdenum will be repeated and the velocities determined in a similar way. The damage threshold can also be examined by simply switching off the feedback and returning to the normal Q-switched pulse and comparing the results with those obtained using the modified pulse.

As this paper is preliminary, the results of the pulse shaping will be reported shortly.

6. Conclusions

In this paper we have shown that the theoretical scaling of plasma pressure is obeyed very closely using ordinary Q-switched laser pulses, resulting in velocities, without fragmentation, of over 2×10^4 cm s^{-1}.

The question as to whether the acceleration method proposed could be useful for reactor refuelling cannot be answered definitely at this stage. It appears that the required pellet velocities can be reached but the fragmentation phenomena and their importance have to be further investigated. Acceleration experiments are proceeding and it is hoped to communicate some results shortly.

References

[1] COOPER, R.S., A.I.A.A. Journal 11 831 (1973).
[2] PUELL, H., Z. Naturforsch 25a 1807 (1970).
[3] CARUSO, A., BERTOTTI, B., GIUPPONI, P., Nuovo Cimento XLVB 2 176 (1966).
[4] GRALNICK, S.L., Nucl. Fusion 13 703 (1973).
[5] ASKAR'YAN, G.A., MOROZ, E.M., J.E.T.P. 43 2314 (1962).
[6] BELOKOGNE, V.A., Proc. VIth Int. Symp. Nonlinear Acoustics, Moscow, p.66 8-10 July, 1975.
[7] PIRRI, A.N., MONSLER, M.J., NEBOLSINE, P.E., A.I.A.A. Journal 12 9 1254 (1974).
[8] LINHART in "Physics of High Energy Density", Acad. Press 1971.
[9] RISØ REPORT No.332 Nov. 1975.
[10] IGENBERGS, E.B., JEX, D.W., SHRIVER, E.L., A.I.A.A. Journal 13 8 1024 (1975).
[11] HOUSE, L.L., Astrophys. J. Supp. Ser. 8 307 (1964).
[12] CARUSO, A., GRATTON, R., Plasma Phys. 10 867 (1968).
[13] GREGG, D.W., THOMAS, S.J., J. Appl. Phys. 37 2787 (1966).
[14] LOVBERG, R.V., WOODING, E.R., YEOMAN, M.L., I.E.E.E. J. Qn. El. QE-11 1 17 (1975).

DISCUSSION

ON PAPER IAEA-CN-35/H3

M.S. RABINOVICH: I should like to make a few comments – firstly of a historical nature. The suggestion that particle acceleration of this kind might be a feasible proposition was put forward twelve years ago by Askaryan amd Moroz in 'Pis'ma Zh. Ehksp. Teor. Fiz'. About ten years ago Askaryan, Shevchenko and co-workers reported the results of experiments in which small metal particles were accelerated to velocities of the order of 10^6 cm·s^{-1}. It is now very important in my opinion, although undoubtedly a difficult problem, to accelerate solid hydrogen as a means of increasing the density of plasmas in stellarators and tokamaks. We are in fact now working on techniques of producing solid hydrogen particles for acceleration and heating in the L-2 stellarator. Finally, I would like to suggest that the fears expressed about particle destruction during acceleration are probably somewhat exaggerated.

R.J. COLCHIN: We have been using a gas-dynamic acceleration technique in the last couple of years to accelerate small hydrogen pellets into Ormak – 70-μm pellets initially, and more recently 220-μm pellets. The velocities attained are about the same as those mentioned by Mr. Motz: 10^4 cm·s^{-1}. We think, however, that we have probably reached the limit attainable with this type of acceleration and are now looking for ways of accelerating larger particles to higher speeds. In general, one wants to accelerate as slowly as possible in order not to break up the pellets, and we are afraid that the shock in the laser system might do just that. One possibility we are working on, therefore, is a centrifuge type of acceleration, which we feel is likely to be gentler than laser-induced acceleration.

I.J. SPALDING: You estimate that a 1-cm thick Mo jacket is required to overcome stresses induced during the laser acceleration. Some three years ago I suggested the use of an annular laser beam to provide guidance and radial confinement. Have you considered whether an annular beam would improve the prospects for reactor pellet-refuelling?

H. MOTZ: No, we have not really examined the question. We know of your suggestion, however, and think it a good one because it would provide lateral stabilization.

GENERATION OF INTENSE ION BEAMS AND THEIR APPLICATION TO CONTROLLED FUSION RESEARCH

P. DREIKE, R.L. FERCH, A. FRIEDMAN,
S. HUMPHRIES, R.V. LOVELACE, G. LUDWIG,
R.N. SUDAN

Laboratory of Plasma Studies,
Cornell University,
Ithaca, New York

D.L. BOOK, G. COOPERSTEIN, A.T. DROBOT*,
J. GOLDEN, S.A. GOLDSTEIN†, C.A. KAPETANAKOS,
R. LEE, W. MANHEIMER, S.J. MARSH #, D. MOSHER,
E. OTT ‡, S.J. STEPHANAKIS, P.J. TURCHI
Naval Research Laboratory,
Washington, D.C.,
United States of America

Abstract

GENERATION OF INTENSE ION BEAMS AND THEIR APPLICATION TO CONTROLLED FUSION RESEARCH.

Successful generation of pulsed multi-kA proton beams in the energy range 0.2 to 1.7 MeV using existing pulsed power technology has been achieved by three different techniques: reflex triodes, pinched electron-beam diodes and magnetically insulated diodes. Peak current densities in excess of 10 kA · cm^{-2} have been observed on the NRL Gamble II machine and over 1.0 kA · cm^{-2} on the Cornell Neptune machine. Peak total ion currents above 200 kA are produced by Gamble II. The potential applications of intense ion beams to magnetic confinement include (i) plasma heating and (ii) ion rings. A summary of continuous theoretical and experimental investigations on these applications is presented.

I. INTRODUCTION

The potential applications of intense, pulsed ion beams to CTR has led to the initiation of programs at both Cornell [1] and NRL [2] on the production of such beams, using existing pulse power technology that was initially developed for the generation of relativistic electron beams. As a result of these programs, pulsed proton beams are presently available at a power level of 0.2 x 10^{12} watts with peak proton currents in excess of 200 kA. Recent results on ion sources are summarized in Sect. II. Intense ion beams offer a potential alternative to high-powered lasers and E-beams for fusion by inertial confinement if the required source [3] brightness $j_i/\theta^2 \simeq 500$ kA/cm^2/rad^2 can be achieved for 10-MeV protons. The power required with ~ 10-MeV proton beams is at least a factor of 10 less than for electrons. Furthermore, beam propagation to target from the diode is less problematical since intense ion beams are charged and current neutralized by electrons that are dragged along by the ions from the source. An ambient neutralizing medium is not required as for electron beams so that propagation in field free vacuum is possible.

---

* Science Applications, Inc.

† University of Maryland.

NRC Research Associate.

‡ On leave from Cornell University.

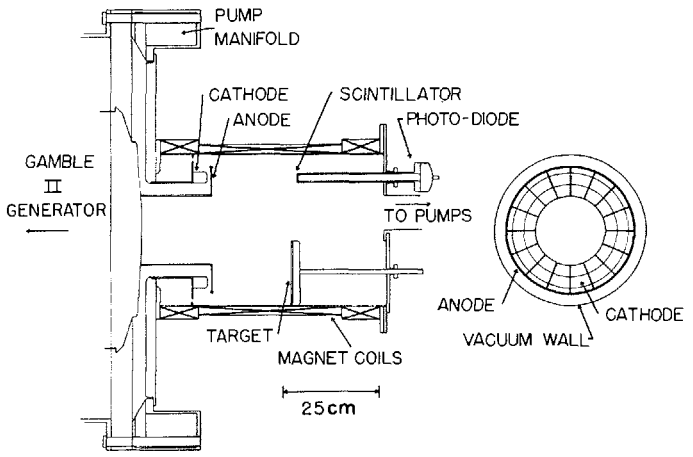


FIG. 1. Schematic of the coaxial reflex triode powered by the Gamble II generator.

Applications of intense ion beams to magnetic confinement include (1) plasma heating and (2) ion-rings. Such ion-rings can be used as internal currents to close the lines of force of a magnetic mirror to reduce end losses and improve the Q factor. Alternatively, by adiabatic magnetic compression the ion energy can be increased so that the ion-ring can operate in the Astron mode, i.e. to provide both plasma heating and confinement. Sect. III is devoted to the formation, stability and compression of ion rings.

II. INTENSE ION BEAM GENERATION

Efficient production of intense ion beams requires: (i) a plasma source capable of supplying a large thermal ion flux uniformly over a large area that must be turned on almost synchronously with the diode voltage pulse and (ii) reduction of the power drain to the electron flow. In the devices described below these difficulties have been circumvented either by reflexing or by magnetically insulating the electron flow.

A. Reflex Triode [1,2]

A schematic of the experiment is shown in Fig. 1. The 0.6 to 1.2 MV, 130 nsec duration positive pulse (base line) from the NRL Gamble II generator is applied to the anode that is constructed from solid 12-μm thick polyethylene film interwoven between thin radial spokes. To maximize the energy delivered to the electrons and ions, i.e. the resistive part of the load in the reflex triode, it is necessary that the inductance of the triode be kept as small as possible.

This is accomplished by designing the triode in such a way that the current flows in a coaxial configuration. For the 20-cm-long anode stalk (inner conductor) of 9.5 cm radius and the 12.7-cm-radius outer conductor, the inductance of the load is about 12 nH. The electrical breakdown in the vacuum gap between the inner and outer conductors is prevented by the externally applied magnetic field. The critical magnetic field B_c required to magnetically insulate the d = 3.2 cm gap between the two coaxial cylinders is less than 1.5 kG. The number of protons in the beam ($\sim 4 \times 10^{16}$) is determined by a nuclear activation technique [2] that measures coincident γ-rays associated with

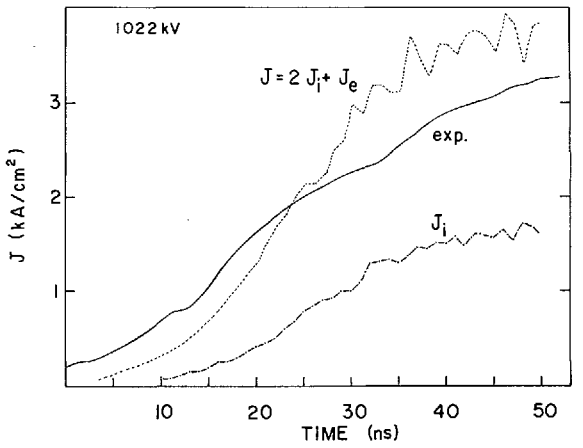


FIG.2. Code-predicted total – – – – – ($J_T = 2J_i + J_e$) and ion current density – · – · – as a function of time for an anode voltage of 1022 kV. The solid line is the observed total current from the experiment of Fig.1.

the annihilation of positrons from the reaction $^{12}C(p,\gamma)^{13}N(\beta^+)^{13}C$. The peak ion current inferred from the measured number of protons by the activation technique and the ion pulse shape determined with the scintillator-photodiode system is in excess of 200 kA, at 1 MeV. This peak current corresponds to a peak ion current density of approximately 1 kA/cm², which is about 59 times greater than that predicted for bipolar flow, when edge effects can be neglected.

The coaxial triode performs very satisfactorily in the range of magnetic field from 2 kG to the maximum tested value of 6 kG. In the absence of external magnetic field, the self-magnetic field produced by the current flowing in the anode stalk inhibits a considerable fraction of the electrons of the hollow beam from reaching the anode and thus the impedance of the diode is appreciably increased.

A 1-D electrostatic computer simulation code developed at NRL, which incorporates both elastic and inelastic scattering by the anode foil, shows that the enhancement of the ion-to-electron current ratio increases with the average number of electron reflections. For large numbers of reflections the triode behavior is found to be highly time-dependent. In this case the total current increases linearly with time until the electric field is driven to zero inside the gap, resulting in current oscillations. Figure 2 shows the ion and the total current predicted by the simulation code for a reflex triode similar to that used in the experiment. The total current is in fair agreement with the observed current.

B. Magnetically Insulated Diode [3,4,5]

A sequence of experiments with co-axial, cylindrical, magnetron-type geometry have been performed with different anode designs and power supplies. This geometry allows the Hall electron current to flow in a closed azimuthal path without producing any build-up of space-charge electric fields which could transport electrons across the gap and cause early breakdown. In one experiment, a small fraction of the radially converging ion beam at one end of the diode was allowed to strike a Lucite conical flashboard which produced a

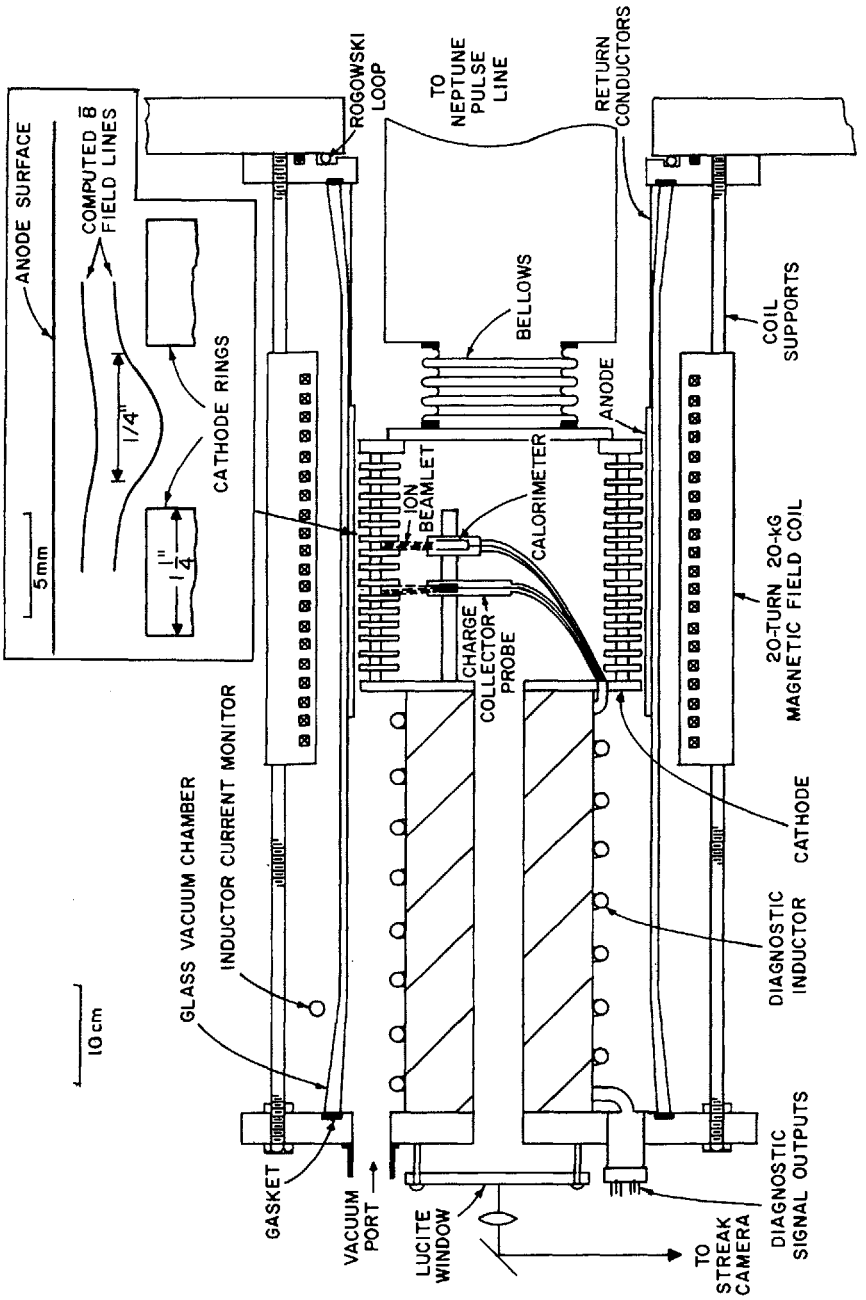


FIG. 3. Schematic of the magnetically insulated diode assembly powered by the Neptune generator.

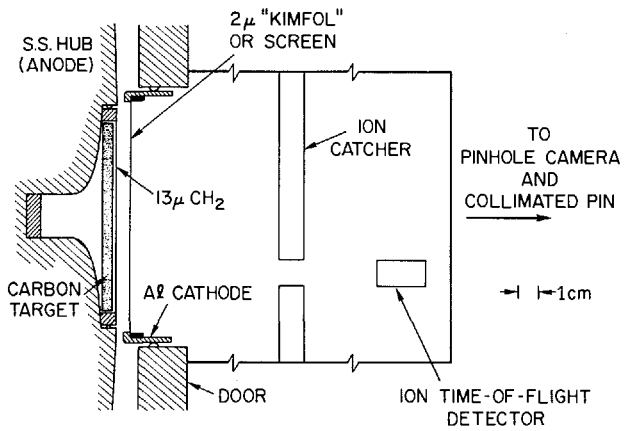


FIG.4. Schematic of the experiment to study the ion production in the self-pinching mode. The diode is powered by the Gamble II generator.

dense plasma. Electrons extracted along the magnetic lines of force from this plasma served to neutralize the converging ion beam as it crossed the magnetic field. Proton currents up to 5 kA were propagated across field lines to within 1 cm of the axis and the maximum current density achieved was 70 A/cm², which agreed with calculations based on geometrical convergence. The beam divergence of less than 3° is inferred from the study of damage patterns.

The diode shown in Fig. 3 is powered by the 500-kV, 250-kA, 70-nsec Neptune machine. The anode is a metal cylinder lined with strips of insulating plastic, machined flush with the inner surface. Metal pins ensure rapid breakdown of the plastic surface on the application of the voltage pulse. The metal cathode, however, has a thickness large enough for the pulsed magnetic field ($\leq$ 20 kG, 150 μsec) used for electron insulation to be shielded from the region interior to the cathode. Proton current densities up to 100 A/cm² with 4.2 mm gap have been measured by several charge collecting probes placed 4 cm behind the cathode holes and located at different z-positions. The total active ion emission area is 1000 cm², indicating total proton currents of $\leq$ 100 kA at energies between 300 - 400 keV for a pulse duration of 70 nsec. The total measured diode current exceeds the proton current, indicating some electron leakage.

C. "Pinched Beam" Ion Source

Efficient production of intense proton beams has also been achieved using the 10^{12}-W Gamble II generator driving a diode in the self-pinching mode. The generator is operated in positive polarity so that ions are extracted from the outer (negative) electrode (Fig. 4) at ground potential and drifted in an evacuated tube. Anodes consisted of stretched 13 μm $(CH_2)_n$ which sometimes was backed by a carbon target. The cathode consisted of a 14-cm carbonate foil or fine-mesh screen recessed about 4 mm from the face of the aluminum ring.

Measured by the nuclear activation technique, in excess of 4×10^{16}, 0.5 - 0.8 MeV protons distributed over a 120-cm² cross-sectional area are routinely produced in a 30 - 50 nsec pulse. The time dependence of the ion current is obtained with a 125 μm-thick NE-102 scintillator-photodiode pair. The 150 - 200 kA average ion currents deduced from these measurements are in good agreement with the diode theory of Goldstein and Lee [6] and represent about $\frac{1}{3}$ of the total diode current.

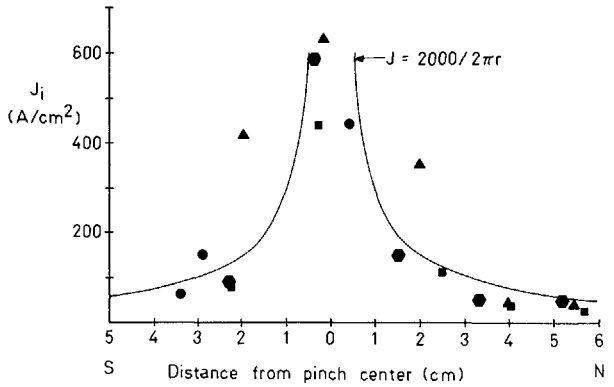


FIG. 5. Measured ion current density as a function of radial position for 4 shots on Neptune; line charge 800 keV, diode spacing 1.4 cm, flat electrodes, Mylar coating on anode. Solid line is an assumed r^{-1} variation. The detectors are located 1 cm from cathode surface with 0.001 cm^2 apertures.

The Cornell Neptune machine (1 Ω at 330 kV) is operated in the "pinched beam" mode with a 0.025-cm nylon sheet clamped to the anode to serve as a rapid source of plasma when subjected to high electric fields of the main voltage pulse. Pinched equilibrium is thus formed early in the pulse. Proton current densities measured by biased charged collectors [7] are in excess of 1 kA/cm^2 and showed a strong radial dependence (Fig. 5). Total ion currents are in excess of 12 kA, indicating an efficiency of 10%.

III. ION-RINGS

A. Injection

An ion-ring is characterized by a field reversal factor $\zeta \equiv \delta B/B_a = Nr_i/R$, where δB is the change in the field on axis due to the ring current, B_a is the applied field, N is the total number of ions in the ring, R is the ring major radius and $r_i = q^2/cm^2$ is the classical ion radius. Since experience with electron rings [8] has shown that single pulse injection offers advantages over slow buildup, the total number of protons N must be injected in a pulse time τ of less than a few cyclotron periods. For R ≃ 10 cm, about 10^{17} protons are required to obtain $\zeta \geq 1$. Two injection techniques are possible in principle: a) injection through a nonadiabatic magnetic cusp [2,9] followed by an axially increasing magnetic field leading to a mirror in which the ring is finally trapped, and b) transverse injection at the end of a magnetic mirror by several injectors placed around the azimuth.

In order to study the physics of the injection process and magnetic compression of these rings a 2-D (r,z) hybrid RING code has been developed. The motion of the ring ions is followed using a particle-in-cell method with a model for the electromagnetic field equations [1]. Because of the large disparity in the electron and ion time scales, electrons are not treated as particles. Quasi-neutrality by the electrons and current neutralization in the r-z plane is assumed. The particles are contained in a cylindrical vessel at the boundaries of which the contribution to the vector potential A_θ from the internal currents is set to zero. The plasma current density J_θ^e is given by

[1] (which neglects the displacement current).

Ohm's law where the conductivity σ is assumed constant within and set equal to zero outside the ring. Inside the ring

$$\nabla^2 A_\theta - A_\theta/r^2 = -(4\pi/c)\ (J_\theta^b + J_\theta^e)$$

where

$$J_\theta^e = \sigma\ [-\partial\ A_\theta/\partial\ ct + (v_z^e\ B_r - v_r^e\ B_z)/c]$$

and J_θ^b is the ring ion current density. The electrostatic potential is obtained from

$$\nabla \cdot \underline{J}^b = -\ \nabla \cdot \underline{J}^e = \sigma\ [-\ \nabla^2 \phi + \nabla \cdot (v_\theta^e\ \hat{\theta} \times \underline{B})/c]$$

The maximum random axial velocity v_z and radial velocity v_r that can be contained in a ring are $v_r/v_o \leq (1 + \zeta)^{\frac{1}{2}}$, where v_o is the mean azimuthal velocity. Thus self-fields are important in maintaining the integrity of the ring during injection and in particular its axial confinement. The influence of self-fields during injection is observed when an annular beam is injected through a nonadiabatic cusp. The injection parameters are so chosen that only single particles injected between r_1 and $r_1 + \Delta r/2$, where r_1 and Δr are the inner radius and thickness of the beam respectively, are able to penetrate the cusp. However, when a beam of sufficient strength is injected, all of the beam particles penetrate. As the beam passes through the cusp its axial motion is converted into rotational motion which reduces the external field by the diamagnetic effect, thus leading to improved transmission.

B. Magnetic Compression

The ring lifetime is determined [10] by the slowing-down time τ_s [$= 0.63 \times 10^{11}\ W_b^{3/2}/n_e$, where W is the ion energy in MeV and n_e the density of electrons in cm^{-3}] of the fast protons by the space-charge neutralizing electrons. The penetration of fields through the ring is determined by the magnetic diffusion time τ_d [$\sim 4\pi\ \sigma\ a^2/c^2 \simeq 3.1 \times 10^{-7}\ T_e^{3/2}\ a^2/Z\ell n$ sec, where a is the minor radius of the ring and T_e is the electron temperature in eV]. When the compression time τ_c satisfies the condition $\tau_d \ll \tau_c \ll \tau_s$ the plasma currents can be neglected.

To assess the effect of high conductivity such that $\tau_d \leq \tau_c \ll \tau_s$, the RING code was used. Particles were initialized with the same energy and canonical angular momentum P_θ, and after a short period necessary to reach equilibrium the external axial field was increased by a factor of 3 over 1.4×10^3 time steps Δt, where $\Delta t = 1/200$ of the initial cyclotron period. Although betatron oscillations are observed in the initial stage, they are damped during compression. The initial cross-section of the ring is in general elliptical with $a_z > a_r$, where $a_z (a_r)$ are the FWHM axial (radial) widths. The beam current I_b and induced plasma current I_e are plotted in Fig. 6 for three identical runs but with increasing plasma conductivity such that $\tau_d/\tau_c|_{t=0} = 0.018$, 0.14 and 0.28, thus covering the range from relatively small to large plasma current. After the induced plasma current decays away, the final compressed ring parameters approach the values that would be attained in the absence of plasma current. As σ increases I_b drops but I_e increases, reinforcing during compression the total current. As a result the transient magnitude of ζ increases as shown in Fig. 7. The quantities $B_a R^3$, $B_a a_r a_z$ and $\zeta/B_a^{\frac{1}{2}}$ remain approximately constant and departures are explained by a more exact analysis. As the conductivity increases, the skin plasma current flows in such a way as to exclude changes of flux and the induction electric field E_θ in the ring interior. Ring compression now takes place through the radial $\underline{J}^e \times \underline{B}$ force which is exerted on the ring ions through a radial electric field E_r.

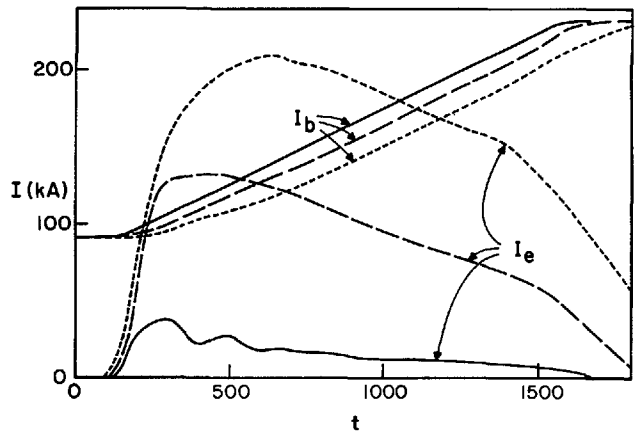


FIG. 6. Total beam and plasma currents I_b and I_e as a function of time during compression for three conductivities $\tau_d/\tau_c|_{t=0} = 0.018$, 0.14 and 0.28.

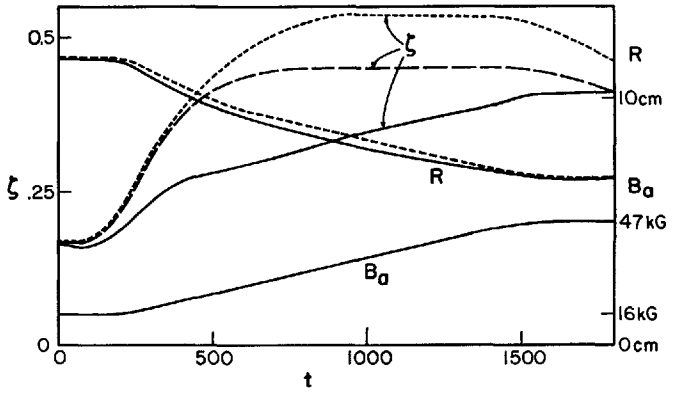


FIG. 7. Applied magnetic field B, major radius R and field reversal factor ζ as a function of time for the three cases of Fig. 6.

Fig. 8 shows the flux lines and contours of constant ion current density for a ring with initial $\zeta = 0.83$ and $\tau_d/\tau_c|_{t=0} = 0.34$ compressed to $\zeta = 1.15$ (field reversal). The profile of J^e is shown as a function of radius at $t \simeq 500\ \Delta t$ and $\zeta = 1.15$. Notice that J^e actually reverses sign towards the minor surface because the driving induction electric field E_θ changes sign when the field reverses sign in the ring interior.

C. Stability

Major progress has been made in developing the theory of low-frequency, MHD stability of high-current ion-rings in a low-temperature background plasma.

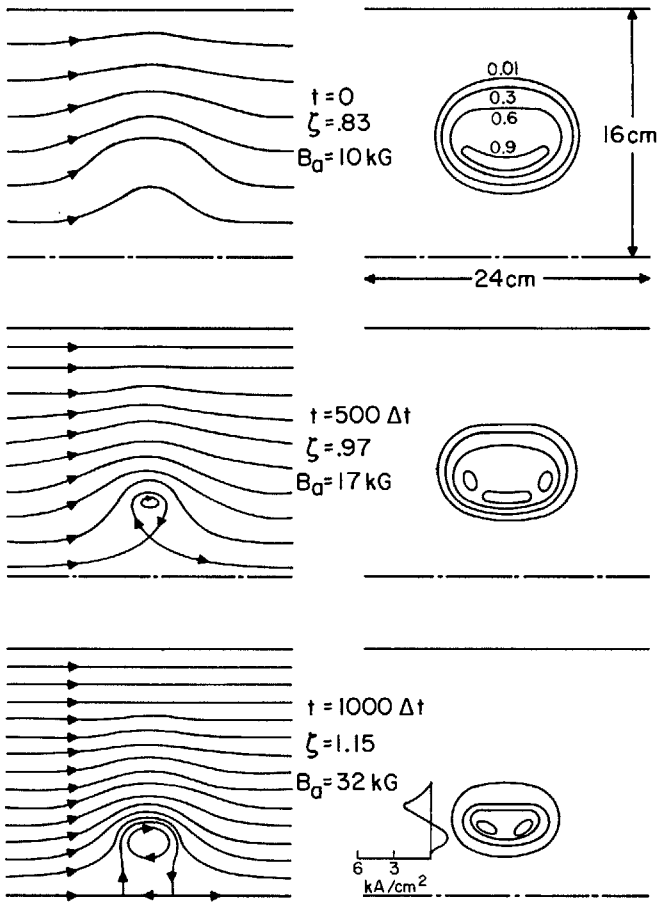


FIG.8. Sketches of field lines and lines of constant beam current density for three different times during compression to field reversal from initial ζ = 0.83. Inset is plot of plasma current density versus radius at z = 0 for t = 500 Δt; $\tau_d/\tau_c \mid_{t=0} = 0.34$ for this case.

Two approaches have been developed. In the first [11], the plasma displacement $\underline{\xi}$ is determined by the dynamical equation

$$n_p m_p \frac{\partial^2}{\partial t^2} \underline{\xi} + q n_b \underline{B} \times \frac{\partial}{\partial t} \underline{\xi} = \underline{F}(\underline{\xi}) - \frac{1}{c} \delta \underline{J}^b \times \underline{B}$$

where $\underline{F}(\xi) \equiv \frac{1}{4\pi} (\nabla \times \underline{\delta B}) \times \underline{B}$ and $\underline{\delta B} = \nabla \times \underline{\xi} \times \underline{B}$. The quantities $\underline{\delta B}$ and $\delta \underline{J}^b$ are perturbations in the total magnetic field and beam current respectively. The main effort is then devoted to obtaining tractable expressions for the operator $\underline{\delta J}^b$ $(\underline{\delta B})$ which is found to be self-adjoint for a number of special but important cases, in particular the kink perturbation $\ell \neq 0$, $m = \pm 1$, where ℓ, m are toroidal and poloidal mode numbers respectively. The resulting energy principle leads to the following condition for the stability of the kink mode:

$$I/I_A < \tfrac{1}{2}(a/R)^2 \qquad (1)$$

where $I_A = m_b c^2 v_o/e$ is the Alfvén current for the ring ions. For comparison, the ring current required for field reversal on axis is $I/I_A > G/2\pi$, where G is a dimensionless factor of order unity.

In the second approach [12], the free energy $C = U - \Omega L_z - \int d^3x\, d^3v\, f \ell n f$ [U and L_z are the total system energy and z-component of the angular momentum respectively, and $\int d^3x\, f \ell n f$ is the ring entropy] is varied to second order in the plasma displacement. The background plasma dynamics are governed by the collisionless, pressureless, two-fluid model and the beam dynamics by the Vlasov equation. The beam equilibrium is given by the rigid distribution $f_o \sim \exp\{-(H - \Omega P_\theta)/T\}$, where H and P_θ are the particle energy and canonical angular momentum, Ω is the mean rotational frequency and T is the temperature.

From the resulting energy principle, $\delta C > 0$ for stability, we conclude that for a long, thin, cylindrical layer with $T \ll mv^2{}_o$ all modes with $\ell \geq 2$ are stable. The mode $\ell = 1$ is stable for $k^2R^2 \geq 0.15$, where k is the axial mode number. For $\ell = 0$, we recover the usual tearing mode by minimizing δC. Since in this case the field curvature is absent, instability is due to the curvature of the orbiting particles. In a layer of finite length the field line curvature also contributes to instability and in the extreme limit of the "bicycle tire" equilibrium the field curvature dominates the orbit curvature. In this case the stability condition turns out to be

$$\ell\Omega > \omega_\beta \tag{2}$$

where $\omega_\beta = (2qv_oI/m_bca^2)^{\frac{1}{2}}$ is the betatron frequency in the self field. On substituting this expression for ω_β in (2) we obtain for stability $I/I_A < \frac{1}{2}\ell^2a^2/R^2$ and the condition (1) is recovered for $\ell = 1$. We are thus led to conclude from both these approaches that the most likely stable, field-reversed ion ring equilibrium is one in which $a_r \sim a_z \sim R$, characteristic of experimentally observed electron rings and those seen in particle simulation studies. Stability to the precession mode follows the standard condition that the external field index should be negative.

Unfortunately, for high frequencies ($\omega > \Omega_i$) no general analysis is applicable and one resorts to a mode by mode analysis. We have examined flute modes $\underline{k} \cdot \underline{B} = 0$ for which the electrostatic and electromagnetic fields are separable in a background plasma density much higher than the beam density. The eigenfunctions and frequencies are obtained from a WKB analysis, ($\omega_e \gg \omega > \Omega_i$), which includes the radial gradient of the magnetic field and beam density. These modes have frequencies around the ion plasma frequency and may be destabilized by resonant interaction with the ring ions. However, when the plasma is confined, its density gradient makes the condition for existence of these modes more stringent and stabilization is possible.

D. Experiments in Progress

Experiments to produce ion rings are under way at both Cornell and NRL. At Cornell the effort is devoted to magnetically insulated diodes with flux-excluding anodes placed in fast pulsed solenoidal coils to achieve field geometries which both insulate against electron flow and provide for efficient ion-ring injection. In one experiment θ-currents induced in a ring anode by pulsed fields produce radial magnetic fields which give the emitted ions rotational velocity and also prevent electron flow across the gap. Other schemes based on the same principle of flux-exclusion anodes are under development. Electron neutralization is provided by plasma flashboards.

At NRL, construction is under way of an experiment in which a p-layer will be formed by passing a 1-MeV, 200-kA proton beam ($> 4 \times 10^{16}$ protons/pulse) through a cusped magnetic field and trapping it inside a magnetic mirror. The trapping is achieved by increasing the magnitude of the near mirror peak using a gate field.

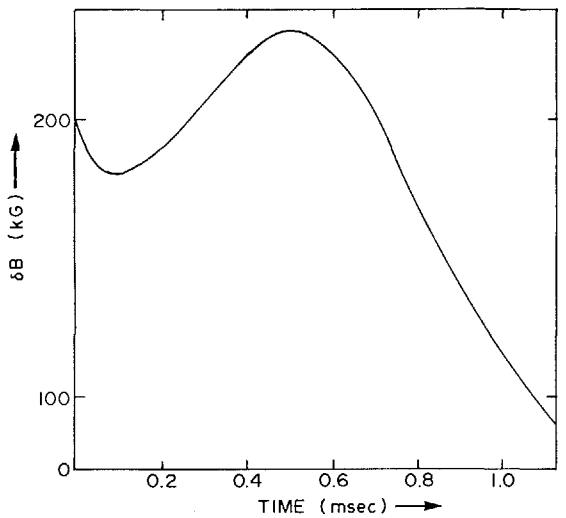


FIG.9. Self-magnetic field of a plasma-loaded ring as a function of time. The various parameters are given in the text. It is important to note that in this model the magnetic compression time τ_c is comparable to the ring-ions' slowing-down time τ_s and thus heating effects play an important role.

Other applications of these intense ion beams presently under theoretical investigation are the heating of plasma in closed field configurations and the implosion of plasma-loaded rings with metalic liners. [13]

In the theoretical model dealing with the heating of plasma in closed systems, the neutralized ion beam propagates across the magnetic field by means of the polarization electric field. Once the beam reaches the plasma, the polarization field is probably shorted out and the beam can only penetrate by displacing the background plasma and field. Vlasov calculations show that this can occur if the beam radius is large compared to a beam ion Larmor radius and if the beam velocity exceeds the Alfvén speed. The beam may be made to stop near the center of the toroidal plasma by means of one or more mechanisms among which the Kelvin-Helmhelz instability appears to be the most promising.

With respect to the implosion of plasma-loaded rings with liners, we are studying the dynamics of charge-neutral ion rings including collisions of beam ions with plasma electrons and ions. The numerical calculations at NRL include the effect of collisional heating and cases where the betatron frequency is not large compared with the gyrofrequency.

Preliminary results show that the dynamical behavior of the system is altered when τ_c becomes comparable to τ_s where τ_c is the magnetic compression time and τ_s the ring ions' slowing-down time. The principal new phenomenon is the production of thermal energy which increases the ring pressure and minor radius, and accordingly reduces the degree of field reversal. Figure 9 shows the result of a calculation for which the time scale of heating by beam target collisions is the same as that for liner implosion. A deuteron beam of 550 keV with T = 25 keV and $n = 5 \times 10^{15}$ cm^{-3} strikes a hot-electron-cold-He_3 target (T_e = 10 keV, T_i < 1 keV) of density 2×10^{16} cm^{-3}. The inner liner radius decreases from 30 cm to 15 cm in 1.0 ms, which would raise the self-magnetic field from its initial value of 200 kG to 800 kG if the scaling law $B \propto R^{-2}$ held. In fact, the field drops initially, owing to the sharp increase in the minor radius, then experiences a modest enhancement.

Since charged reaction products also contribute to the internal pressure of the beam, the use of D-T reactions, producing most of their energy in neutrons (absorbed by the liner), may be advantageous. With a beam energy clamped at 175 keV, however, the increase in scattering collision frequency, which scales as V_{beam}^{-3}, cancels out any advantage. Other reaction configurations, involving higher beam energies, may be of interest.

The work of the Cornell group was supported by ONR and US ERDA.

REFERENCES

[1] HUMPHRIES, S., LEE, J.J., SUDAN, R.N., Appl. Phys. Lett. 25 20 (1974); J. Appl. Phys. 46 187 (1975).

[2] KAPETANAKOS, C.A., GOLDEN, J., YOUNG, F.C., Nuclear Fusion 16 151 (1976); GOLDEN, J., KAPETANAKOS, C.A., Appl. Phys. Lett. 28 3 (1976); GOLDEN, J., et al., Proc. of Int. Top. Conf. on Elect. Beam Research and Tech., Sandia Corp., Albuquerque, N.M., Vol. 1, p. 635.

[3] HUMPHRIES, S., SUDAN, R.N., WILEY, L., J. Appl. Phys. 47 2382 (1976).

[4] SUDAN, R.N., LOVELACE, R.V., Phys. Rev. Lett. 31 1174 (1973).

[5] DREIKE, P., et al., J. Appl. Phys. 47 85 (1976).

[6] GOLDSTEIN, S.A., LEE, R., Phys. Rev. Lett. 35 1079 (1975).

[7] EICHENBERGER, C., et al., LPS Report 188, Laboratory of Plasma Studies, Cornell University, Ithaca, New York.

[8] ANDREWS, M.L., et al., Phys. Rev. Lett. 27 1428 (1971).

[9] KAPETANAKOS, C.A., PARKER, R.K., CHU, K.R., Appl. Phys. Lett. 26 284 (1975).

[10] SUDAN, R.N., OTT, E., Phys. Rev. Lett. 33 355 (1974).

[11] LOVELACE, R.V., Phys. Rev. Lett. 35 162 (1975); Phys. Fluids 19 723 (1976).

[12] SUDAN, R.N., ROSENBLUTH, M.N., Phys. Rev. Lett. 36 972 (1976).

[13] BOOK, D., et al., Paper IAEA-CN-35/E19-1, these Proceedings.

PLASMA CONFINEMENT IN A CUSP FIELD WITH RF PLUGGING

S. HIROE, T. SATO, T. WATARI, S. HIDEKUMA, R. KUMAZAWA,
K. ADATI, T. SHOJI, S. KAWASAKI, T. HATORI, H. OBAYASHI,
T. WATANABE, N. WATANABE*, S. MIYAKE**, A. MIYAHARA,
K. TAKAYAMA
Institute of Plasma Physics,
Nagoya University,
Nagoya, Japan

Abstract

PLASMA CONFINEMENT IN A CUSP FIELD WITH RF PLUGGING.

Plasma loss through a line cusp is substantially suppressed by the application of a r.f. electric field perpendicular to the magnetic lines of force. The frequency of the applied r.f. electric field is chosen around the local ion cyclotron frequency ω_{ci}. To render this effect (referred to as r.f. plugging) pertinent to thermonuclear plasma, several physical characters were investigated. A scaling law of the r.f. plugging of the line loss, including heating effect, was found experimentally, in the range of plasma density $n = 5 \times 10^8$ to 3×10^{12} cm^{-3}. A preliminary experiment on plugging cylindrical plasma was also carried out in a mirror configuration. An instability is observed when the r.f. field is not so strong, but it is stabilized again by increasing the r.f. field.

1. INTRODUCTION

When an r.f. electric field is applied perpendicularly to the magnetic field, a charged particle feels a quasipotential field and is accelerated in the direction of decreasing magnetic field. The potential [1] is expressed by

$$\psi = \frac{q^2 E_{rf}^2}{4m\omega_c^2} \frac{1}{\omega^2/\omega_c^2 - 1} \tag{1}$$

where q is charge, m mass, ω_c cyclotron frequency, ω and E_{rf} the frequency and strength of the externally applied r.f. electric field, respectively. Application to plugging the plasma loss from a cusp field using the ion cyclotron frequency has been made by our group [2–5].

So far, the following interesting results have been obtained:

(1) An r.f. electric field can easily penetrate into the high-density sheet plasma formed at the line cusp;
(2) Plasma loss through a line cusp can be suppressed to a few per cent of that without r.f. field;
(3) Effective ion heating is observed;
(4) Frequencies optimum for plugging and heating lie around the eigenfrequency of the electrostatic ion cyclotron mode.

In this paper, a scaling relation of the r.f. plugging in the line cusp region is experimentally investigated in order to see whether plugging and heating of the plasma can be made relevant to thermonuclear fusion. Experimental data of plugging at the point cusp and of the observed instability are also given.

---

* Faculty of Engineering, University of Tokyo, Tokyo.
** Welding Research Institute, Osaka University, Osaka.

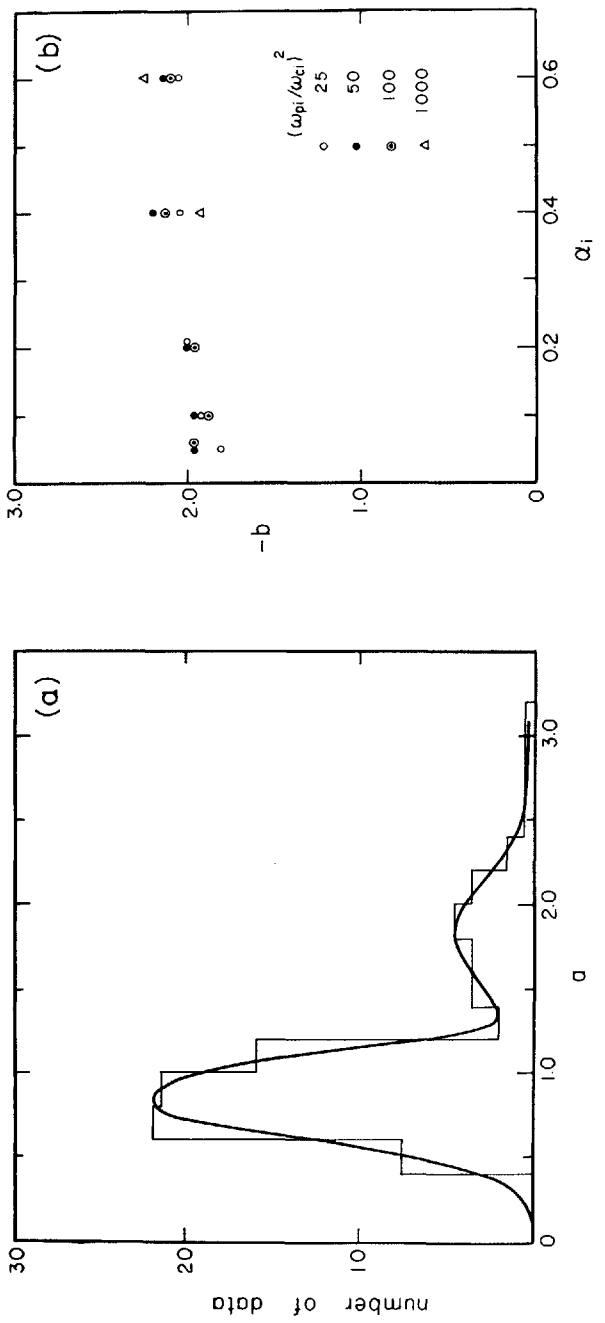


FIG. 1. (a) Histogram for the distribution of index a expressed in the relation $\delta n/(1/\alpha_i) \propto E_{rf}^{a}$. *The total number of data is 94.*
(b) The value of b in the relation $E_{rf} \propto B^{b}$ *versus* α_i *as a parameter of* $(\omega_{pi}/\omega_{ci})^2$.

2. EXPERIMENTAL SET-UP

The experiments were carried out on the TPD-III machine, which has a spindle cusp at its centre. The maximum magnetic field strength at the line (r = 25 cm) and point (z = 37 cm) cusps are 10 kG and 24 kG respectively. A helium plasma produced by a TPD-type plasma source is fed either steadily or in pulsed operation into one of the point cusps through a three-stage differential pumping section. Ion density at the cusp centre ranges from 5×10^8 to 3×10^{12} cm^{-3}. The initial ion temperature T_0 is almost equal to the electron temperature and is 5–30 eV. The r.f. electric field is applied in the line cusp region on ring-shaped parallel plate electrodes of outer diameter 50 cm and inner diameter 34 cm. The maximum voltage applied to the r.f. electrodes is about 5 kV.

The ion density is measured by a Langmuir probe placed at the cusp centre. Ion temperature and loss flux are measured by multigrid energy analysers of retarding potential type placed just outside the line and the point cusps. The temperature measured by this type of analyser is checked by the data obtained from a neutral particle analyser in the case of hydrogen plasma.

3. SCALING LAW OF RF PLUGGING AND HEATING AT LINE CUSP

3.1. Expression of relative loss flux

The effectiveness of r.f. plugging is represented by a parameter α_i, which is defined as the particle loss flux with r.f. field relative to that without r.f. field. The r.f. frequency is chosen to be the optimum, ω^*. For a given plasma, condition α_i is measurable as a function of E_{rf}. If the plugging is mainly due to the quasipotential barrier ψ, the parameter α_i may be written as

$$\alpha_i = \exp(-\psi^*/T_i) \tag{2}$$

where ψ^* is the value of ψ at ω^*, and T_i is the ion temperature. When the potential is very hard and high, the plasma particles are reflected adiabatically without any change of temperature. This was, however, not the case in the present experiment, but the plasma was subject to r.f. heating as well as plugging. The temperature increase is given as a function of plasma and field parameters. This brings a complicated functional dependence of ψ^*/T_i, which may be equal to $\ell n(1/\alpha_i)$, on E_{rf}, B and the normalized plasma density $\omega_{pi}^2/\omega_{ci}^2 \propto n_i/B^2$. Here, the electric field strength E_{rf} is defined as the value of the applied r.f. voltage divided by the separation of r.f. electrodes. The magnetic field strength B is the value under the r.f. electrodes. The ion density n_i is the value at the cusp centre when the r.f. field is not applied. Theory might suggest the following dependence:

$$\ell n(1/\alpha_i) \propto \{E_{rf} B^b (\omega_{pi}^2/\omega_{ci}^2)^c\}^a \tag{3}$$

where indices a, b and c are left to be deduced from the experimental data.

3.2. Experimental determination of indices

As a first step we can observe the relation between α_i and E_{rf}. For given values of B and $\omega_{pi}^2/\omega_{ci}^2$, $\ell n(1/\alpha_i)$ is plotted against E_{rf}, and the index a is estimated. The histogram for the distribution of a is given in Fig. 1(a), where a remarkable concentration of data is found in the

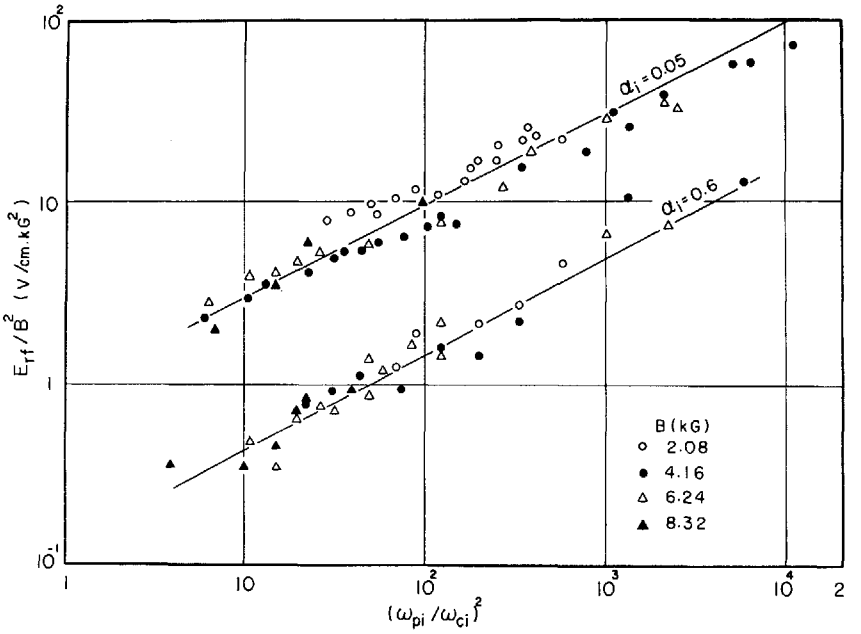


FIG.2. E_{rf}/B^2 versus $(\omega_{pi}/\omega_{ci})^2$ for $\alpha_i = 0.05$ and 0.6.

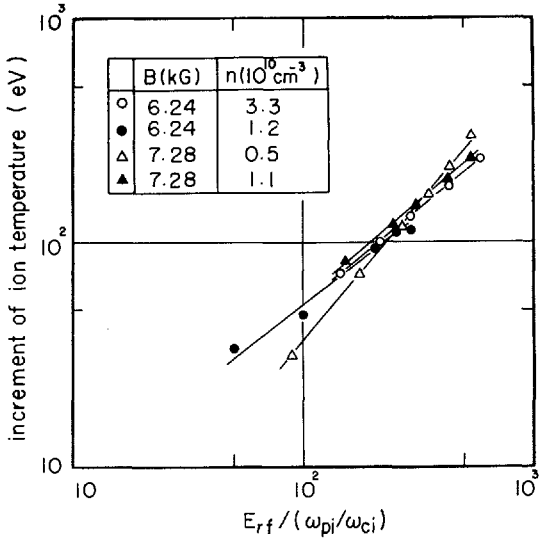


FIG.3. Increment of ion temperature of bulk plasma versus $E_{rf}/(\omega_{pi}/\omega_{ci})$ for some different conditions.

range of $0.6 \leqslant a < 1.2$, with a minor satellite peak around $a \sim 1.8$. This implies that, for the major part of the data, we can write

$$\ell n(1/\alpha_i) \propto E_{rf}^{0.8}$$

Next, the r.f. field strength required to keep a certain value of α_i is investigated as a function of $\omega_{pi}^2/\omega_{ci}^2$ for several magnetic field strengths. Then we can reduce the interrelationship between E_{rf} and B, under the condition of fixed α_i and $\omega_{pi}^2/\omega_{ci}^2$. This is shown in Fig. 1(b), where the index b is plotted against α_i. For a wide range of $\omega_{pi}^2/\omega_{ci}^2$ the data are quite consistent with $E_{rf} \propto B^2$.

Finally, we make plots of E_{rf}/B^2 versus $\omega_{pi}^2/\omega_{ci}^2$ for fixed α_i and B. The experimental results for $\alpha_i = 0.05$ and 0.6 are shown in Fig. 2. They are very well represented by $E_{rf}/B^2 \propto \omega_{pi}/\omega_{ci}$, which implies $c = -1/2$.

Taking these results ($a = 0.8$, $b = -2$ and $c = -1/2$) into account, we can finally obtain

$$\alpha_i = \exp\left[-2.6 \times 10^3 \left\{ \frac{E_{rf}(V/cm)}{B(kG)\sqrt{n(cm^{-3})}} \right\}^{0.8}\right] \tag{4}$$

From the standpoint of the plugging effect, this can be regarded as an empirical relation between the plasma and the field parameters. Equation (4) is, however, only applicable to TPD-III or a machine of similar size, because the scale length (diameter of r.f. electrodes, say) of the system is not given explicitly. If the scale length becomes larger, a smaller value of E_{rf} could be effective to give the same α_i.

3.3. Effect of ion heating

The increment of bulk ion temperature at ω^* is measured and found to be expressed as

$$T_i - T_o \cong T_i \propto E_{rf}/(\omega_{pi}/\omega_{ci})$$

when E_{rf} is sufficiently large (Fig. 3). On the other hand, if we assume that the confinement time of ions in a cusp configuration is proportional to B/T_i, the increment of ion temperature should be linearly dependent on the effective electric field E_{eff}. Comparing this with the result of Fig. 3, we may say that $E_{eff} \cong E_{rf}/(\omega_{pi}/\omega_{ci})$. If this E_{eff} is substituted for E_{rf} in Eq. (1), we have

$$\psi^* \propto \omega_{ci}^{-2} E_{rf}^2/(\omega_{pi}^2/\omega_{ci}^2)$$

These two relations give

$$\ell n\left(\frac{1}{\alpha_i}\right) \propto \frac{\psi^*}{T_i} \propto \frac{E_{rf}}{\omega_{ci}\omega_{pi}} \propto \frac{E_{rf}}{B\sqrt{n_i}} \tag{5}$$

The functional form of the empirical scaling relation (4) agrees approximately with this formula.

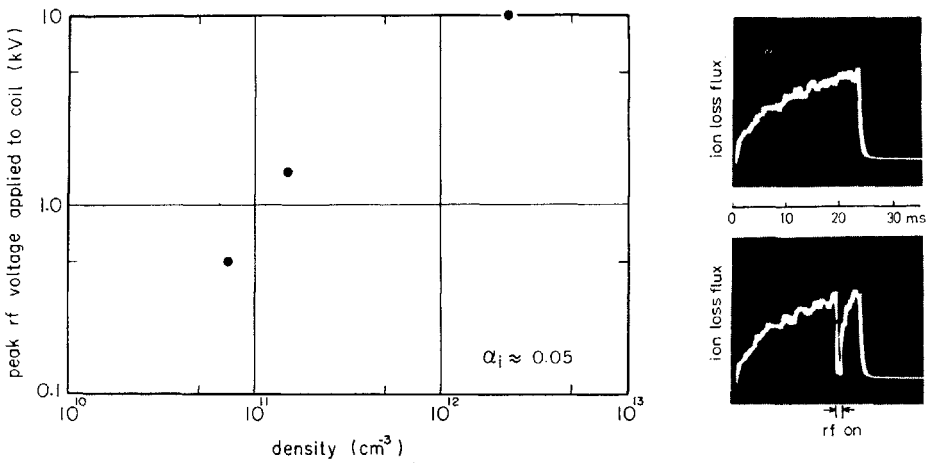


FIG.4. Peak r.f. voltage applied to solenoidal coil set up at mirror throat required to keep $\alpha_i \approx 0.05$ versus ion density. B = 11.3 kG. Photographs are the ion loss flux from the mirror end without (upper) and with (lower) r.f. plug.

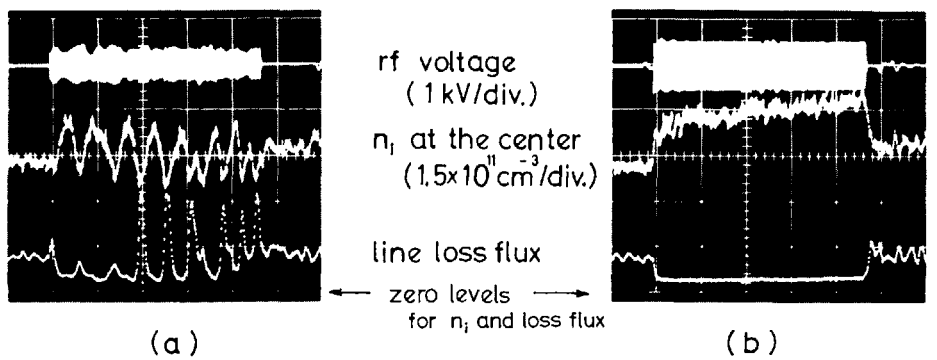


FIG.5. (a) Typical example of instability. $E_{rf} = 200$ V·cm^{-1}; $\omega/2\pi = 4.3$ MHz; B = 6.24 kG. Time scale: 1 ms/div.
(b) Signals after stabilization by increase of E_{rf}. $E_{rf} = 310$ V·cm^{-1}; $\omega/2\pi = 4.3$ MHz; B = 6.24 kG.

4. PLUGGING AT POINT CUSP

A preliminary experiment on the plugging of cylindrical plasma was also carried out in a mirror configuration. The r.f. field was applied to a seven-turn solenoidal coil of 5 cm diameter and 10 cm length. Helium plasma was fed into one of the mirror throats, and the r.f. coil was set up at the opposite mirror throat. By applying the r.f. voltage, the loss flux through the mirror end can be effectively reduced. The r.f. voltage applied to the r.f. coil required to reduce α_i to about 0.05, plotted against the ion density measured at the centre of the mirrors, is shown in Fig. 4.

5. INSTABILITY AND ITS STABILIZATION

An instability is observed when the r.f. field of moderate strength is applied at the line cusp. One typical example is shown in Fig. 5(a). The top trace is the r.f. electric field, the middle trace is the ion density measured at the cusp centre, and the bottom trace is the loss flux from the line cusp. The time variation of the loss flux is observed to be a series of spikes and their peak values exceed the level without r.f. field. The decrease of ion density corresponds closely to the increase of the loss flux. Since this instability is easily suppressed by an increase of E_{rf} above a critical value, as shown in Fig. 5(b), it has little effect on the scaling law of r.f. plugging. The critical electric field strength is an increasing function of ion density and a decreasing function of the frequency of the applied r.f. field.

ACKNOWLEDGEMENTS

The authors wish to thank S. Fujiwaka for the design of the r.f. electrodes. They are also indebted to Dr. K. Akaishi for useful discussions about the vacuum system of the TPD-III machine and to Y. Kubota for the design and maintenance of the 2.5-MW(e) d.c. power supply.

REFERENCES

[1] DOW, D.G., KNECHTLI, R.C., J. Electron. Contr. 7 (1959) 316.
[2] SATO, T., et al., Proc. 3rd European Conf. on Controlled Fusion and Plasma Physics, Utrecht, 1969, p.21.
[3] MIYAKE, S., et al., J. Phys. Soc. Jpn. 31 (1971) 265.
[4] WATARI, T., et al., Phys. Fluids 17 (1974) 2107.
[5] HIROE, S., et al., Nucl. Fusion 15 (1975) 769.

Session XXIV

FOCUS, LINER, WALL CONFINEMENT

Chairman

F. Hofmann
Switzerland

Papers E 18-1 to E 18-5 C were presented
by A. Bernard as Rapporteur
Papers E 19-1 and E 19-2 were presented
by A.E. Robson as Rapporteur

NEUTRON PRODUCTION IN THE DENSE PLASMA FOCUS

H.J. KAEPPELER
Institut für Plasmaforschung,
Universität Stuttgart,
Stuttgart,
Federal Republic of Germany

Abstract

NEUTRON PRODUCTION IN THE DENSE PLASMA FOCUS.

To analyse the phenomena in the dense plasma focus leading to neutron production, several theoretical approaches were made recently. As MHD calculations are still not capable of treating the fully compressed phase of the focus, particle calculations were carried out, showing that neutron production due to beam-beam collisions plays an essential role besides that due to beam-target collisions. These particle calculations, however, consider laminar dissipations only. To obtain a consistent theory of phenomena, however approximate, in the plasma focus, an analytical treatment was carried out, recently extended to include neutron production due to both acceleration and thermal processes. Expressions for neutron production time are given and the transfer of energy from accelerated particles to thermal distribution is discussed.

The analytical treatment commences from the definition of the minimum compression radius [1,2,3]

$$r_m = \frac{c^2}{4\pi\sigma_s w} \tag{1}$$

where c is the velocity of light, σ_s the turbulent electrical conductivity of the collapsing sheath and w the compression velocity. After compression of the plasma to r_m, there ensues a quiescent stage defined by the electron heating time [3,4] which, for a focus of the NESSI type [5], lasts for approximately 10 to 15 nsec. After this time, the electron temperature has increased from a rather low value of 50 to 100 e V [6], causing an increase of the electrical conductivity sufficient for the onset of m=0 instabilities. The damping of m=0 instabilities in the plasma focus is discussed elsewhere [3,4,7]. The initially low electron temperature of 50 to 100 e V is completely consistent with this analytical model, as the experimentally observed value r_m 1 to 2 millimeters follows only for an electrical conductivity of 10^{13} sec^{-1} [3,4].

The m=0 instabilities are responsible for strong local electric fields

$$E = \frac{1}{\sqrt{2\pi c^2 \rho_a}} \left(\frac{I_o}{c r_a}\right)^2 \left(\frac{r_a}{r}\right) \tag{2}$$

(ρ_a, r_a = density and plasma radius at onset of instabilities, I_o = maximum current) in which the deuterons are accelerated to mean energies

$$\varepsilon = \frac{e}{c} \frac{I/c}{\sqrt{2\pi\rho_a r_a^2}} \qquad \frac{I}{c} = \frac{e}{c} w \frac{I}{c} \tag{3}$$

if the m=0 contraction goes to $r = \lambda_i$ (λ_i = ion mean free path).

In the treatment of neutron production, three temporal quantities are of importance:

(a) the decay of the density field $\qquad t_\rho = \frac{r}{A} \sim \frac{r}{v_{th}} \approx t_r \tag{4}$

(b) the decay of the velocity field $$t_v = \frac{\rho r^2}{\eta} \frac{1}{1+Ha^2} \sim \frac{r}{v_{th}} \frac{r/\lambda_i}{Ha^2} \quad (5)$$

(c) the decay of the temperature field $$t_r = \frac{\rho r^2}{\eta} \frac{1}{1+\omega^2\tau^2} \sim \frac{r}{v_{th}} \frac{r/\lambda_i}{\omega^2\tau^2} \quad (6)$$

The neutron yield

$$Y = W\, V\, t_N = \left(\frac{\rho_a}{m_i}\right)^2 \langle q_R v \rangle \quad \pi z r_a^2 \quad t_N \quad (7)$$

for neutrons from acceleration processes follows with the aid of (5):

$$Y_b \sim |\rho_a r_a^2|^2 \frac{q_R}{1+Ha^2} \frac{1}{I_o^{1/2}} \quad (8)$$

The symbols in the above equations are W = production rate, V = volume, t_N = specific neutron production time, Ha = Hartmann number, q_R = reaction cross-section, A = Alfvén velocity, v_{th} = thermal velocity, η = viscosity, ω = gyro-frequency, τ = collision time. For the variation of σ_s with current, a specific assumption using Steenbeck's minimum principle was made [4]. Using Trunk's condition [8] for the critical acceleration as a scaling law [3,4],

$$\frac{I_o^2}{\rho_a r_a^2} = \frac{I_o^2}{\rho_o R_o^2} = \text{const} \quad (9)$$

and assuming a mean variation of q_R with ε in the range of interest, there follows for (8), with $q_R \sim \varepsilon^{5/2}$,

$$Y_b \sim I_o^4 \quad (10)$$

If, on the other hand, an analytical expression for n in the power law $q_R \sim \varepsilon^n$ is derived,

$$n = \frac{1}{2} \frac{\text{const}}{\sqrt{\varepsilon}} - 1 = \frac{7}{2} \frac{10^3}{I_o^{1/2}} - 1 \quad (11)$$

there follows, instead, for the neutron production due to acceleration processes

$$Y_b \sim I_o^{4 + \frac{7}{2}\left(\frac{10^3}{\sqrt{I_o}} - 1\right)} \quad (12)$$

There is also a certain amount of neutron production from thermal processes

$$Y_{th} \sim I^4 \quad (13)$$

which is calculated from Eqs (7) and (6) with the assumption of $p \sim B^2$ [3,4], a necessary condition for thermal phenomena.

For the interpretation of these results, a relation for the critical density

$$\rho_{crit} = \left[\frac{m_i^3 c^2}{3^2 2^3 \pi^{7/2} e^4 \sigma_s \ell n \Lambda}\right]^{2/5} \frac{(I_o/c)^{6/5}}{R_o^2} \quad (14)$$

is introduced. The condition

$$\frac{\rho_o}{\rho_{crit}} > 1 \quad \text{is equivalent to} \quad \frac{r_a}{\lambda_i} > 1 \,.$$

As

$$\frac{\rho_o}{\rho_{crit}} \sim I_o^{4/5} \quad (15)$$

it is evident that the possibility of thermalization, possibly enhanced by kinetic instabilities [9], increases with increasing current. At the same time, the exponent in the law for the neutron yield due to acceleration processes decreases below 4 for currents greater than 10^6 ampères, while the exponent in the thermal neutron yield remains constant. This means that not only thermalization increases in large devices but also the thermal neutron yield increases in importance for large devices. Finally, Eqs (14) and (15) indicate a procedure to design a plasma focus either towards acceleration or towards thermal yield. This may be a further criterion to distinguish between Mather and Fillipov devices [10].

REFERENCES

1. Kaeppeler, H.J., and Ruhs, N., Physics Letters 49A 383 (1974).
2. Kaeppeler, H.J., and Ruhs, N., Bull. Amer. Phys. Soc. Ser. II 19 945 (1974).
3. Kaeppeler, H.J., Report IPF-74-7, Stuttgart (1974).
4. Kaeppeler, H.J., Basic physical phenomena, neutron production and scaling of the dense plasma focus, Submitted to Phys. Fluids (1976).
5. Rapp, H., Report IPF-74-1, Stuttgart (1974).
6. Bernard, A., Coudeville, A., Durantet, J., Jolas, A., Launspach, J., de Macureau, S. and Watteau, J.P., Phys. Fluids 18 180 (1975).
7. Kaeppeler, H.J., Second International Congress on Waves and Instabilities in Plasmas, Survey Lectures, K 1-46, Innsbruck (1975).
8. Trunk, M., Plasma Physics 17 237 (1975).
9. Kaeppeler, H.J., Ruhs, N., Trunk, M., and Decker, G., 7th European Conference on Controlled Fusion and Plasma Physics, Vol. I, p. 63, Lausanne (1975).
10. Bernard, A., Plasma Focus, 3rd Topical Conf. on Pulsed High-Beta Plasmas, Culham (1975).

DYNAMICS OF 120 AND 20 kV PLASMA FOCUS DEVICES WITH RESPECT TO DENSITY AND CURRENT DISTRIBUTION, AND NEUTRON AND X-RAY EMISSION

G. DECKER, B. NAHRATH, T. OPPENLÄNDER,
G. PROSS, B. RÜCKLE, H. SCHMIDT,
M. SHAKHATRE, M. TRUNK
Institut für Plasmaforschung,
Universität Stuttgart,
Stuttgart,
Federal Republic of Germany

Abstract

DYNAMICS OF 120 AND 20 kV PLASMA FOCUS DEVICES WITH RESPECT TO DENSITY AND CURRENT DISTRIBUTION, AND NEUTRON AND X-RAY EMISSION.

The experiments had two goals: (1) Better understanding of the dynamics and neutron production of the focus phase and (2) improved scaling of the neutron yield by operating a high-voltage focus. For the first goal, experiments with a 30-kJ/16-kV plasma focus of the Mather type (NESSI) were performed. The simultaneously applied diagnostics include interferometry, X-ray photography with channel plates, magnetic probes and scintillator/photomultiplier detectors for measuring hard X-ray and neutron emission. In the established chronology one can distinguish five phases in the development of the plasma focus: A compression phase is followed by a short (8 ns) very dense phase, where the density peaks at a minimum radius ($t = 0$, authors' chronology). The plasma cylinder expands to a relatively long-lasting (30 to 70 ns) quiescent phase before instabilities occur. This short unstable phase is followed by a decay phase during which the neutron emission peaks. Important correlations between the plasma parameters and the neutron emission are discussed. Secondly, on the assumption that the neutron yield scales with a high power of the current, it was concluded that a high-voltage focus could result in higher neutron yield as compared with a lower voltage device of the same energy. The proper adjustments of the discharge parameters necessary due to the very short current risetime were investigated.

For the further development of the neutron-producing plasma focus of the Mather type we had two main goals: (1) Improved understanding of the neutron-producing mechanism by refined and simultaneously applied diagnostics; and (2) Improved efficiency of neutron production by operating a plasma focus in the 100-kV regime, not yet used.

Part I

We have made considerable efforts to advance the development of suitable diagnostic tools for space- and time-resolved measurements of density distributions and soft X-radiation as well as current measurements in the converging sheath. Though the plasma focus in general shows the same features from shot to shot at a certain geometry and pressure, the dynamics can differ from shot to shot on a short time scale, i.e. in the ns range. We therefore found it necessary to make simultaneous measurements of the density distribution, soft and hard X-ray emission, current in the dense focus region, as well as intensity and duration of the neutron output.

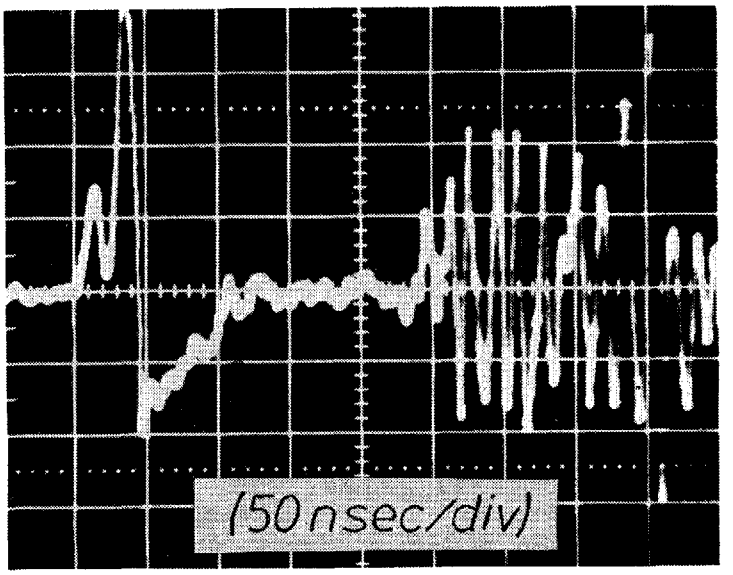


FIG.1. Magnetic probe signal proportional to $\ddot{B}$.

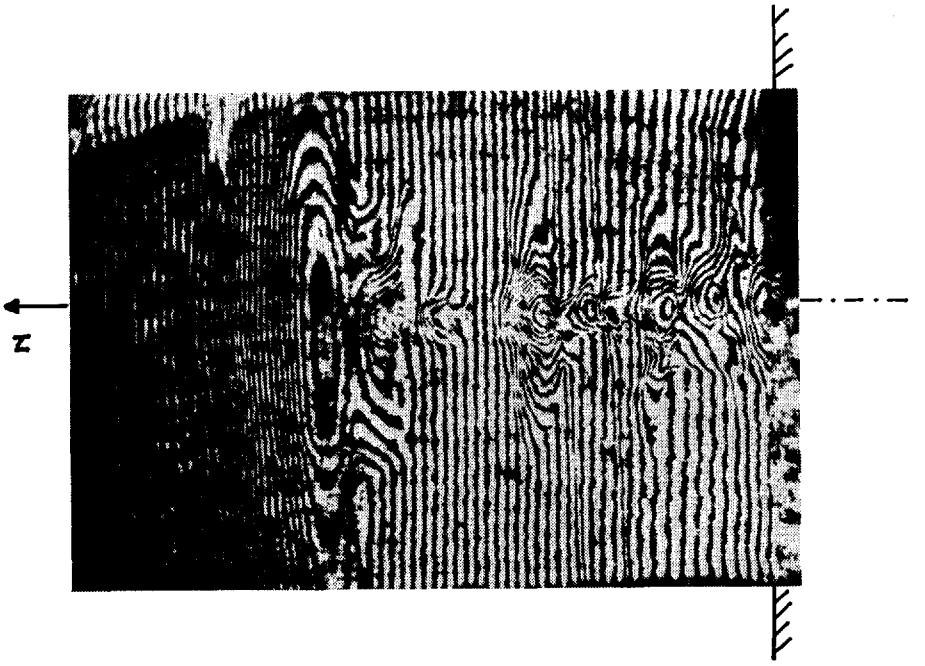


FIG.2. Interferogram.

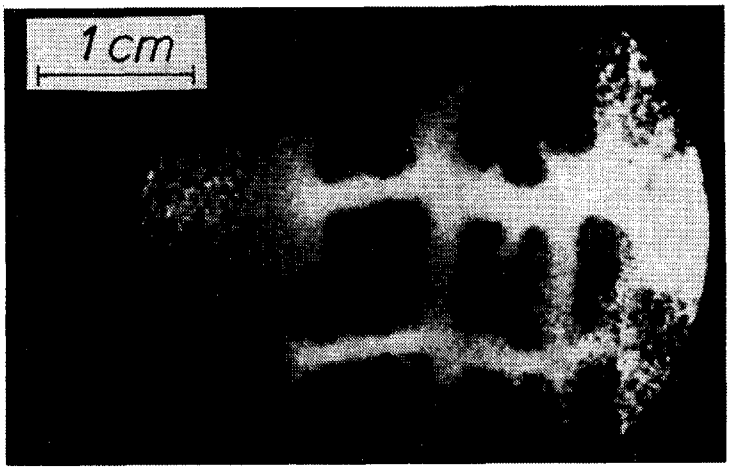


FIG.3. Double pinhole X-ray image taken simultaneously with Fig.2.

The measurements were performed with our NESSI device (Mather type; hollow inner electrode; $r_i = 3.3$ cm; $r_a = 6.2$ cm; $\ell = 28$ cm; $L_0 = 24$ nH) operating at 30 kJ/16 kV and $p = 1.5$ torr. Four interferograms (N_2 laser; 337 nm; exposure 0.5 ns) were taken at 10-ns intervals, employing optical delay lines. Two soft X-ray images were taken simultaneously through two pinholes of 0.3 mm diameter, 5.2 mm apart. By means of a pulsed channel plate (40 mm diameter) these images were obtained through 10-μm and 50-μm Be foils, respectively, with an exposure time of 3 ns in a 1 : 1 imaging ratio. The magnetic probe (4 windings 0.7 mm diameter) with a diameter of 1.1 mm is positioned at (r,z) = (33,10) mm. The probe is connected to a transformer and the signal is proportional to $\dot{B}$. The overall risetime is 1.3 ns. The neutron diagnostic (silver activation counter; scintillator/photomultiplier) is conventional.

It is important and necessary to refer to a distinct time mark in the chronology of the plasma focus. A very convenient, reliable and local event for the time correlation is the minimum radius. A sharp signal at the end of the compression phase can be obtained either by a beam deviation method [1,2] or by simply imaging an axial point of the plasma focus onto a photodiode with fast response time. We have used this last method for our measurements. The light intensity peaks with the density and therefore with the minimum radius of the plasma cylinder. In our chronology, we choose this time (measured at (r,z) = (0,10) mm) as $t = 0$. Only when the $\dot{I}$-signal shows one single dip does this dip occur at $t = -10$ ($\pm$ 5) ns. If there is more than one dip, there is no fixed time difference between the $\dot{I}$-dips and $t = 0$ ($r = r_{min}$).

Besides the rough distinction of three phases (ignition, running-down and focus phase), we can distinguish in the last phase (the focusing phase of the plasma focus) five subphases: we call them compression phase, very dense phase, quiescent phase, unstable phase and decay phase, with the following typical behaviour.

In the *compression phase* ($t < -5$ ns) the plasma is radially accelerated. Maximum compression velocities of 4×10^7 cm $\cdot$ s^{-1} have been observed. Usually there occur Rayleigh-Taylor instabilities and variations in the value of the radial density gradients from shot to shot (observed by interferometry). Soft X-radiation is observed with the channel plate from $t = -30$ ns in regions coinciding with the interferometrically measured plasma cylinder. Even at this early

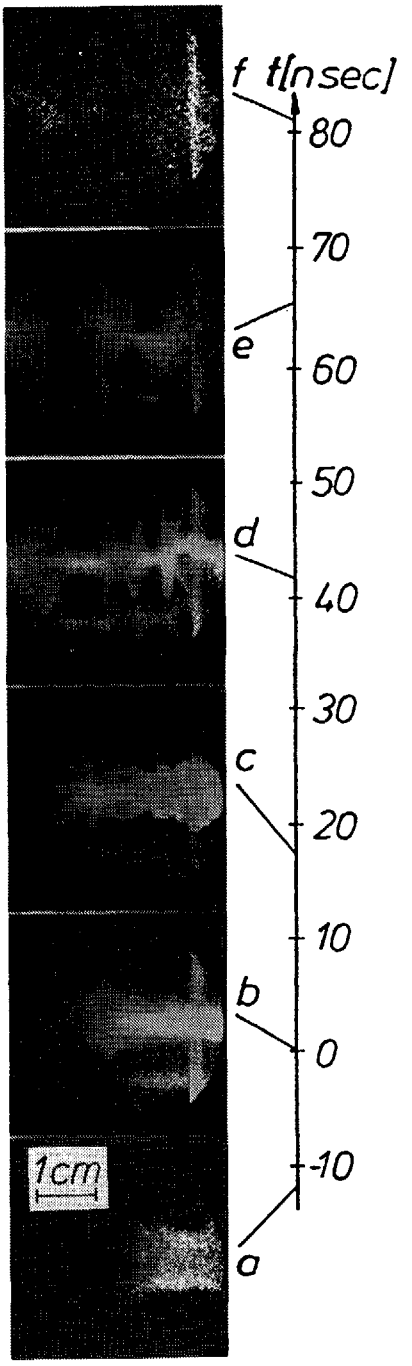


FIG.4. Sequence of double pinhole soft-X-ray images.

stage of the focus development, hard X-rays and some neutrons can be detected. The current in the sheath amounts to 290 kA at a total current value of 590 kA, i.e. only about half of the total current can act as a driving force for the compression. This phenomenon, which is pressure-dependent in its value, has also been observed for another of our plasma focus devices. The two dips in the $\ddot{B}$-signal indicate a step structure in the current sheath (see Fig.1).

The *very dense phase* ($-5 < t < +5$ ns) persists typically only 8 to 10 ns (half-width of the density). At a minimum radius of $r_{min} \approx 1.5$ mm the density on the axis is about 2.5×10^{19} cm^{-3}. In this phase we observe from the soft X-ray emission some heating of the electrons, i.e. the soft X-radiation becomes harder. The diameter in this phase seems to be determined by diffusion processes [3].

The plasma expands rapidly to a *quiescent phase* ($10 < t < 40$ ns) with a radius of 3–5 mm. Due to the expansion, the density drops to 2×10^{18} cm^{-3}. During this phase the density decreases further (to about 1×10^{18} cm^{-3}) whereby the plasma cross-section remains nearly constant, i.e. there is a strong axial flow with velocities in the order of 5×10^7 to 10^8 cm · s^{-1}. No increase in the electron temperature is observed from the pinhole pictures, i.e. the plasma is relatively cold ($100 < T_e < 500$ eV).

After the long-lasting quiescent phase, $m = 0$ instabilities develop rapidly, resulting in distinct plasma sections 5 to 10 mm in length and $\leqslant 0.5$ mm in radius. Figures 2 and 3 (taken simultaneously at $t = 60$ ns) demonstrate this phase and also show the similarity between the density structure and the soft X-ray image. In this *unstable phase* ($40 < t < 60$ ns) the plasma is heated to the keV range (see Figs 3 and 4d). In the probe signal, strong oscillations start (Fig.1). The neutron emission (dN/dt) is still increasing. The density is, according to our observations, always and at all locations less than at $t = 0$. High electric fields are generated and particles are accelerated to high energies. Fast electrons give rise to a burst of hard X-rays at about this time. (The fast ions ionize the gas on their path and form an ionizing wave (bubble) [4] propagating in the axial direction with up to 2×10^8 cm · s^{-1} [5].)

In the *decay phase* ($t > 60$ ns) the density falls to at least $n < 2 \times 10^{17}$ cm^{-3} (beyond the detection limit in the interferograms). We observe some clouds (Fig.4e, f) in the soft X-radiation at that time. For even later times (90–200 ns) the existence of a large hot and thin plasma cloud (with a diameter of at least 70 mm) could be inferred from the fact that the surface of the magnetic probe emitted soft X-rays at these times. At about $t = 90$ ns the neutron emission has its maximum. The neutron signal has a faster rise time than decay time, with a half-width of about 250 ns.

DISCUSSION AND CONCLUSIONS

We attribute the oscillations in the magnetic probe signals to the strength of the $m = 0$ instabilities and conclude that a strong development of these instabilities is mandatory for high neutron output [6]. We further find that for a high neutron yield (for constant external parameters) the following conditions are necessary but not sufficient:

(a) The current in the converging sheath (not only the total current) must be high.
(b) The converging sheath in the compression phase must be narrow, i.e. there must be high density gradients.
(c) The lifetime of the very dense phase must be short (there is no correlation to the value of the density in the very dense phase, however).

We can conclude that although we could establish a number of correlations not known earlier between the features of the plasma focus, there is still no clear understanding of the influences on the neutron production in the plasma focus. A study of the possibilities of influencing the development of the $m = 0$ instabilities, e.g. by external means, seems appropriate. Also, the decay phase, where very strong neutron emission occurs, needs to be analysed in detail.

Part II

HIGH-VOLTAGE FOCUS

From MHD calculations [7] it became apparent that a higher current for a constant bank energy may be obtained by using relatively higher voltages – provided the inductance of the bank can also be kept constant and is not too large compared with the inductance of the load. From the higher current a higher neutron yield is to be expected [8]. Consequently a 120-kV/24-kJ device with $L_0 = 35$ nH was constructed. The current risetime, 500 ns, is roughly a factor 5–10 faster than in most conventional (20–40 kV) devices.

Initial experiments with a centre electrode radius (33 mm) typical for a Mather-type plasma focus of this energy range, resulted in no neutron production because it was not possible to adjust the plasma motion (by length and pressure variation) so that compression occurred at anywhere near maximum current. In particular, the time for radial compression was always too long. It was impossible to reduce this time by applying very low pressure ($\leqslant 0.5$ torr) because of the appearance of spikes in the breech region at the beginning of the discharge, accompanied by a strong X-ray burst, and preventing a proper sheath formation [9]. We therefore reduced the centre electrode radius to 25 mm and could produce neutrons in a rather small pressure range around 1 torr (centre electrode length 70–130 mm; voltages ~ 85 kV; energy ~ 12 kJ). A further reduction of the centre electrode radius to 12.5 mm (outer electrode radius 30 mm) resulted in much more reliable neutron output allowing operation between 4 and 25 torr (centre electrode length 60–100 mm; voltages ~ 85 kV; energy 12 kJ). Neutron output has now reached 5.3×10^9 for the best shots, which is about five times more than the best shots of our 12-kJ, 20-kV, 70-nH device. Further improvement seems likely.

MHD calculations predict higher densities and plasma temperatures for such a fast high-voltage device, even if only the same current should be reached.

REFERENCES

[1] SCHMIDT, H., et al., Proc. 7th Europ. Conf. Controlled Fusion and Plasma Physics, Lausanne, 1975, Vol.1, p.57.
[2] RÜCKLE, B., Rep. IPF-76-1, Stuttgart (1976).
[3] KAEPPELER, H.J., Basic physical phenomena, neutron production and scaling of the dense plasma focus, submitted to Phys. Fluids, 1976; and Rep. IPF-74-7, Stuttgart (1974).
[4] BERNARD, A., et al., Phys. Fluids **18** (1975) 180.
[5] SCHMIDT, H., Verh. Dtsch. Phys. Ges. (VI) 10 (1975) P-75.
[6] OPPENLÄNDER, T., PROSS, G., The plasma focus current in the compression phase, to be published in Plasma Phys.
[7] TRUNK, M., Plasma Phys. **17** (1975) 237.
[8] BERNARD, A., 3rd Top. Conf. on Pulsed High-Beta Plasmas, Culham, 1975, Pergamon, Oxford (1976), paper C1.1.
[9] PROSS, G., Rep. IPF-75-4, Stuttgart (1975).

PRELIMINARY RESULTS OF THE 1-MJ PLASMA FOCUS EXPERIMENT

C. MAISONNIER, J.P. RAGER, C. GOURLAN,
M. GALANTI, P.D. MORGAN*
Associazione Euratom-CNEN sulla Fusione,
Centro Gas Ionizzati,
Frascati, Rome,
Italy

Abstract

PRELIMINARY RESULTS OF THE 1-MJ PLASMA FOCUS EXPERIMENT.

The paper describes the first year of operation with the 1-MJ Plasma Focus at Frascati. The facility, which is routinely operated at 700 kJ, has proved to be technically very reliable. Successive modifications of the two different experimental chambers (Filippov and Mather type) have led to a continuous improvement in the performance of the experiment, though the neutron yield is still a factor of ten below the value predicted by the scaling law. The role of the breakdown conditions and of the current distribution have been investigated experimentally. A critical discussion of the problems connected with the scaling of Plasma Focus experiments to high energy levels is presented.

1. INTRODUCTION

Observations made on low-energy plasma focus devices (stored energy $W_0 < 150$ kJ) have shown that: (a) the neutron yield increases as W_0^2 (10^{11} neutrons per shot at 100 kJ in deuterium), (b) a very large fraction (up to 20%) of W_0 can be transferred to the dense plasma or to energetic beams, (c) this transfer results from strong turbulent phenomena taking place immediately after maximum compression, when the plasma column is disrupted by an $m = 0$ instability. Moreover, plasma foci being very simple devices, extrapolation to high energies is attractive.

The main purposes of the 1-MJ system built at Frascati are, therefore: (a) to check whether scaling laws hold with increasing energy, (b) to prepare solutions to technological problems appearing at higher energy levels, (c) to clarify the mechanism of turbulent heating.

Three facilities have already been operated above 150 kJ, at Physics International (500 kJ in D-T) [1], Los Alamos (480 kJ) [2] and Limeil (380 kJ) [3]. The last two facilities were most successful, giving neutron yields of the order of 10^{12}.

At Frascati, on the 1-MJ condenser bank (40 kV, 8 nH) [4], both Filippov- and Mather-type heads have been used; their geometrical dimensions were extrapolated from successfull low-energy devices using simple scaling rules [5]. The facility is very reliable, being routinely operated at 700 kJ. After a year of experimentation, its neutron yield has grown progressively through many geometrical modifications to a level which is presently still an order of magnitude below the expectation. In this paper, we present a review of the results obtained, so far, with various geometries, and make a tentative critical discussion of the rules of extrapolation.

2. DESCRIPTION OF THE 1-MJ FACILITY

Both Filippov- and Mather-type experiments have been tested on the 1-MJ bank. Stray inductances in the collector amount to 3 nH for the Filippov and 8 nH for the Mather configuration, including the insulator gap.

---

* Present address: Euratom-UKAEA Association for Fusion Research, Culham Laboratory, United Kingdom.

2.1. Filippov configuration

Pending the availability of the high-purity alumina insulator under development, a 822-mm-diameter, 100-mm-high pyrex cylinder has been used. The radial and axial interelectrode gaps were about 80 mm. The outer electrode (cathode) was continuous. Successive modifications aimed at limiting reflection-induced restrikes along the insulator by using a squirrel-cage cathode configuration and limiting long-duration voltage overstress across the insulator ($U < 20$ kV) by ressorting to smaller interelectrode gaps ($\cong 40$ mm).

2.2. Mather configuration

It has an anode diameter $2R_0 = 370$ mm and an anode length $H = 500$ mm (excluding insulator). The outer electrode is a cylindrical squirrel cage of 450 mm inner diameter. The alumina insulator has a diameter of 350 mm, and its height is $D = 100$ mm. The electrode material is A 304 stainless steel. Successive modifications aimed at improving the matching at higher filling pressure by reducing the anode length (250 mm), improving breakdown conditions by using either a shorter alumina insulator (50 mm), pre-ionization, or a larger radial gap, and at improving performances in the high-pressure regime by a using pyrex insulator (50 and 100 mm high). A new Mather head is now being assembled (Fig.1).

2.3. Measurements

The measurements of the voltage U (at the collector input) and of dI/dt, allow a monitoring of the apparent inductance of the discharge:

$$L^* = \frac{\int_0^t U\,dt}{I} = L + \frac{\int_0^t R\,I\,dt}{I}$$

where L and R are, respectively, the inductance and the resistance inside the experimental chamber. Accurate calibrations guarantee an accuracy of 5%. Measurement of the current density distribution j in and behind the sheath ($\partial B/\partial t \propto vj$, v being the sheath velocity) with a series of magnetic probes along one of the Mather gun generatrices as well as a comparison of the L* values at particular times (initial, end of rundown t_m, end of collapse t_c) with values deduced on the assumption of an ideal current distribution concentrated in a thin sheath, provide information on breakdown, run-down, and collapse conditions. Preliminary information on the collapsed phase has been obtained by using interferometric holography (Filippov geometry). The total neutron yield is measured side-on by using Geiger tubes.

3. EXPERIMENTAL RESULTS

Performances obtained with the original configurations were disappointing, expecially in the case of the Filippov geometry, in which an early chocking of the implosion was observed, with the maximum inductance limited to 10–20 nH. Modifications to the cathode geometry as referred to in Section 2 allowed reproducible operations at higher pressure and voltage. Typical results are: $N = 3 \times 10^{10}$ at 20 kV, 0.6 torr D_2 and $N = 7 \times 10^{10}$ at 30 kV, 1 torr D_2.

The Mather gun configuration is more effective, yielding $N = 2.5 \times 10^{11}$ at 33 kV, 2.2 torr D_2 in its original configuration. The best reproducible relative performance (referred to the known

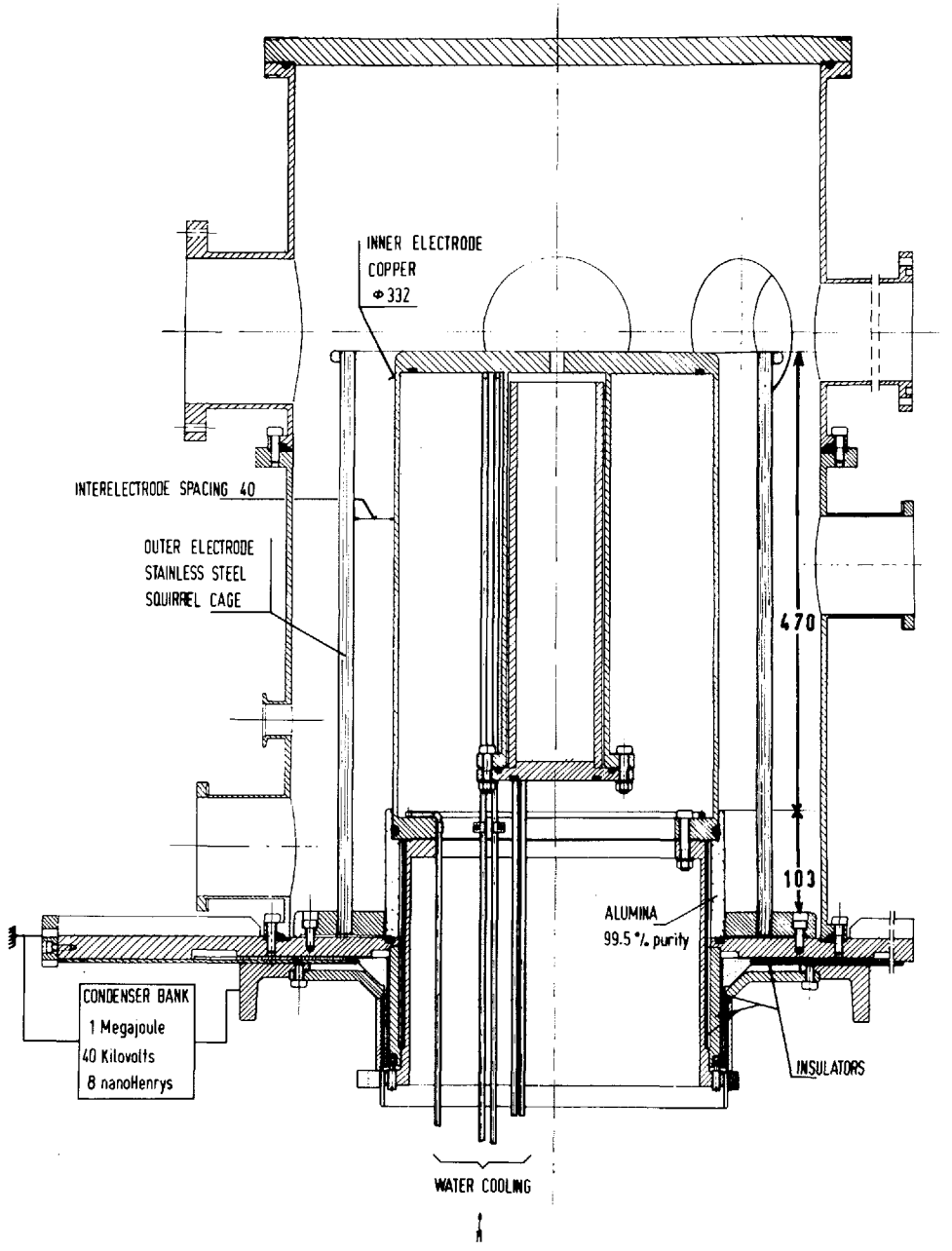


FIG.1. A sketch of the Mather-type 1-MJ experimental chamber.

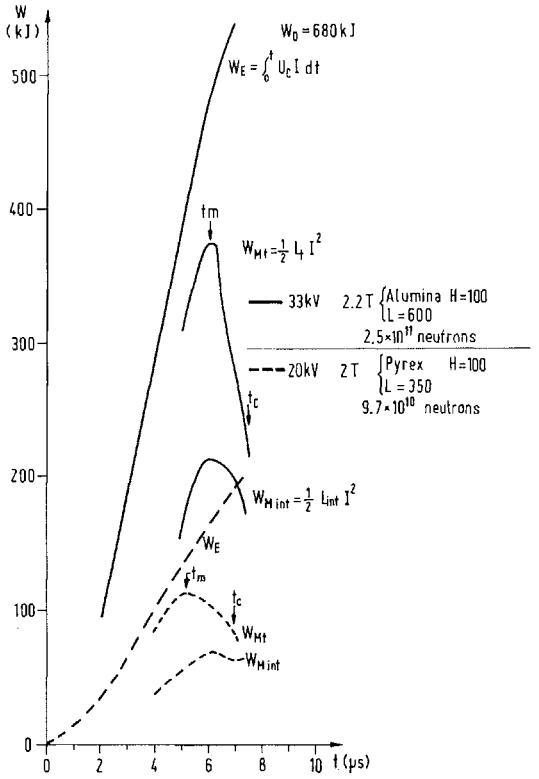


FIG.2. Energy balance for Mather-type experimental chambers (U_c is the voltage across the condenser bank, L_t is the total inductance, L_{int} is the experimental chamber inductance).

scaling laws) has been achieved by using the short gun 100-mm pyrex insulator combination: 10^{11} at 20 kV, 2 torr D_2.

A general tendency of any kind of configuration is a degradation in the scaling of neutron production with increasing energy.

3.1. The role of matching between source and load

By varying the gun length and the pressure regime it is established that the matching is satisfactory (Fig.2) and not critical, in the range of filling pressures of interest. Typical values for dL/dt run-down are 3–4 mΩ (a weak function of the filling pressure). Figure 2 shows that, at a time t_m corresponding to the start of the collapse, 45–55% of W_0 is stored into total magnetic energy and that at a time t_c corresponding to the dI/dt peak, 75 to 80% of W_0 has flown out of the condenser bank. The current value at $t = t_m$ is close to I_{max} within a broad range of initial pressures p_0.

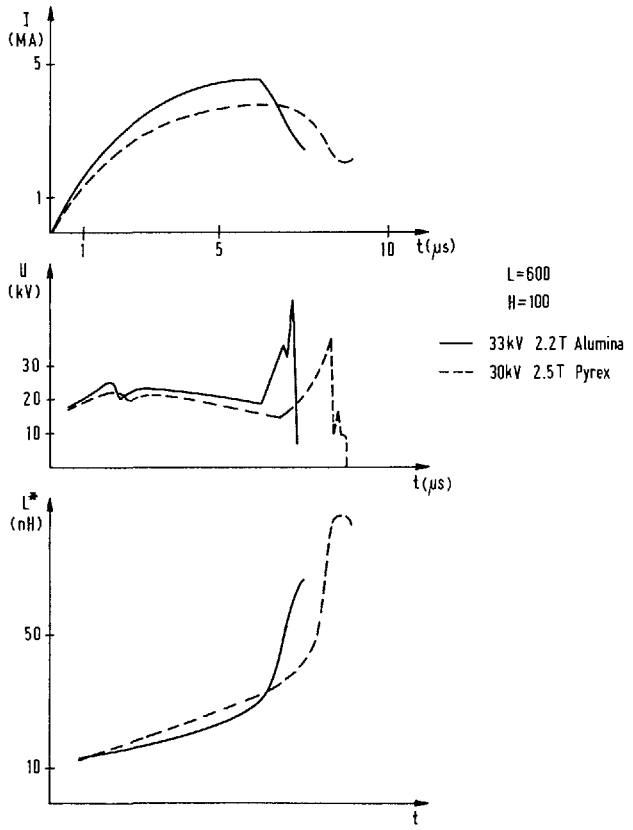


FIG.3. Inductance, voltage and current evolutions in time for two kinds of insulators (Mather-type experimental chamber).

3.2. Breakdown and current distribution in and behind the sheath

The use of interferometric holography on the Filippov experiment demonstrated that, though the electron content has increased by a factor of 10 over that obtained on the MIRAPI experiment for a factor-of-10 increase in energy, the maximum density has hardly changed (a few 10^{19} cm^{-3}). These results are quite reproducible and are not correlated with the neutron yield. Maximum inductances, conversely, give ideal current-carrying pinch diameters of about 50 mm for good shots and 125 mm for bad shots, though the compressed high-density pinches have identical diameters and electron contents ($\cong$ 40 mm). Such correlations were interpreted in terms of diffuse current distributions around the dense pinch, and attention was focused on breakdown conditions and current distributions behind the pinch.

Results obtained using the more versatile Mather gun can be summed up as follows: The use of the short gun ($H \ll 2\pi R_0$) enhanced the importance of breakdown and current sheath structure. In particular, when an alumina insulator is used, a sudden drop in neutron yield is observed at filling pressures above 2 torr (a pressure far below that required by the scaling law (5–8 torr), and the behaviour is very erratic at high energy levels. Under nominal conditions (ΔR_0 = 40 mm, D = 100 mm), the breakdown is usually diffuse, characterized by the appearance of a magnetic

field everywhere in the annular volume delimited by inner-outer electrode cylinders and the insulator height. The main current sheath stagnates for quite a long time (1 μs) in the vicinity of the insulator (see $L^*(t)$ in Fig.3). It is observed that the current density distribution varies noticeably as a function of the insulator material and the pressure regime. For instance, a short alumina insulator ($\Delta R_0 \cong D$) improves breakdown and azimuthal symmetry and gives better neutron yield reproducibility at a higher energy level. The return current in the squirrel cage is only a fraction of the total current, demonstrating the existence of a diffuse current distribution behind the pinch. In a long gun ($H \cong 2\pi R_0$), the sheath reaches the end of the gun carrying a larger fraction of the total current than in a short gun, and reproducibility is improved. The use of a pyrex insulator gives much better azimuthal symmetry, and a higher fraction of the current flowing in the squirrel cage. Coupled to the short gun, it allows neutron production even at high pressures and gives much less erratic behaviour at the high energy level. Using pyrex, $L(t_m)$ is very close to its ideal geometrical value and highly reproducible, while $L(t_c)$ is systematically higher than when alumina is used, which reflects the fact that the current distribution is better and the collapse is more effective.

4. DISCUSSION

The experimental effort undertaken up to now aims at improving the design of the plasma focus heads. To analyse the reasons of their partial success, let us review what we know about the rules for extrapolation, which concern:

(1) Matching

For the condenser bank to be fully discharged at the time of maximum compression, one should maintain approximately constant the following expressions: $W_0^2 U_0^{-2} R_0^{-4} p_0^{-1}$ for a Filippov-type [5] or $W_0^2 U_0^{-2} R_0^{-2} H^{-2} p_0^{-1}$ for a Mather-type device (provided $L_0 \ll L_p$, where L_p is the pinch inductance). These conditions, which are not critical, can easily be satisfied in our devices with reasonable pressures (1–10 torr).

(2) Sheath formation

A uniform breakdown, the formation of a well defined sheath which carries all the current and does not "leak" particles behind, and the absence of subsequent re-strikes are of fundamental improtance. As practically all devices, whatever their energy level, work in the same range of voltages (30–50 kV) and their initial inductances decrease only slowly with increasing energy, power is initially fed at approximately the same rate in large and small machines. But the energy required to ionize and lift the sheath increases with the size of the machine, so that the larger the device, the longer lasts the interaction between insulator and plasma. Consequently, at low energy levels ($\leqslant$ 100 kJ), it takes only a limited effort to obtain a good sheath formation, whereas at higher levels it is much more time-consuming to find the right compromise between many and poorly known requirements [2] under active study at present. At about 400 kJ, for two devices (Limeil and Los Alamos) satisfactory working conditions have been attained. In our experiment, the Filippov head is waiting for the pure alumina insulator still under construction. The Mather head, in its version with a $H = 500$ mm, $R_0 = 40$ mm pyrex insulator and stainless-steel electrodes, seems to provide a uniform breakdown and a satisfactory run-down: the internal inductance of the gun at the end of the run-down is exactly what it should be (34 nH), implying that the whole current is concentrated in a thin sheath. But it is observed that the radial implosion proceeds too slowly compared to numerical calculations implying a rather diffuse current distribution during this phase as it has been observed experimentally in the Filippov geometry. This problem is being tackled, at present.

(3) Plasma heating

For the temperature of the plasma during neutron production to be optimum (~ 10 keV), the energy available for each particle in the pinch, $W_0 R_0^{-2} h^{-1} p_0^{-1}$, should remain constant (h, the axial dimension of the hot plasma, seems to be rather independent of R_0, of the order of a few centimetres, and connected with the axial wavelength of the m = 0 instabilities which disrupt the pinch). But to reach the right temperature, this energy should be effectively transferred from the magnetic field to the plasma through a mechanism of turbulent heating, whose effects have clearly been observed but whose nature is still obscure. We are, then, not yet able to write down the corresponding criteria. If one ventured to say that turbulence will start when the drift velocity of the electrons reaches some constant critical value (for instance, the thermal velocity of the ions, in the case of ion-acoustic waves), $I_p R_0^{-2} p_0^{-1}$ should have a given value. Assuming h = ct, a consequence of these two conditions would be that $L_p W_0$ remains constant.

As the inductance of the gun (L_p-L_0) is practically independent of the gun size, an absolute energy limitation would result.

Anyway, for a given energy W_0, it seems advantageous to have I_p as large as possible, then L_0 will be small. The best geometry in this respect is the Filippov one, and L_0 has to be kept minimum. The experimental study of the conceivable limit due to these phenomena will be started as soon as the radial implosion is under effective control.

REFERENCES

[1] GATES, D.C., DEMETER, L.J., NOETH, A.A., Proc. Am. Nucl. Soc. **1** (Augusta, USA, 1971) 39.
[2] MATHER, J.W., in Plasma Physics and Controlled Nuclear Fusion Research (Proc. 4th Int. Conf. Madison, 1971) **1**, IAEA, Vienna (1971) 561.
[3] BERNARD, A., et al., in Controlled Fusion and Plasma Physics (Proc. 7th Europ. Conf. Lausanne, 1975) **1**, Lausanne (1975) 60.
[4] GOURLAN, C., KROEGLER, H., MAISONNIER, C., VILLA, G., in Energy Storage, Compression and switching (Proc. Int. Conf. 1974), Plenum Press, New York and London (1974) 337.
[5] MAISONNIER, C., International School of Fusion Reactor Technology "Ettore Majorana", Pulsed Fusion Reactors—Erice, Pergamon Press, Erice, Italy (1974) 131.

DYNAMICS OF A NON-CYLINDRICAL Z-PINCH AND THE PARTICLE ACCELERATION MECHANISM

V.V. VIKHREV, K.G. GUREEV, S.K. ZHDANOV,
V.M. KORZHAVIN, B.A. TRUBNIKOV
I.V. Kurchatov Institute of Atomic Energy,
Moscow,
Union of Soviet Socialist Republics

Abstract

DYNAMICS OF A NON-CYLINDRICAL Z-PINCH AND THE PARTICLE ACCELERATION MECHANISM.

The dynamics of a plasma in a Z-pinch is considered theoretically, and it is shown that: (1) anisotropic hydrodynamics with magnetic visconsity is a correct collisionless MHD model for the plasma; (2) this model enables the drift instability of the Z-pinch boundary which results in turbulent diffusion with the "Bohm" coefficient $D \sim cT/eB$ to bc investigated; (3) this coefficient in accordance with the formula $\lambda \sim \sqrt{2Dt} \sim \sqrt{a/J_0}$ defines the length of the sausage-type instability which is the same as that observed; (4) as a result of the partial replacement of the conduction current by a displacement current, a wave in which the condition $E > B$ is inevitably satisfied develops and this results in acceleration of both the ions and the electrons; (5) allowance for the Hall effect results in increased escape of plasma from the sausage-type instability; (6) transverse-current instabilities play an important part in the dynamics of the final stage of the plasma focus, and the anomalous conductivity due to these instabilities gives rise to increased heating and cessation of radial plasma confinement; (7) the neutron yield from the plasma focus may be explained quantitatively by a thermonuclear mechanism on the basis of a simple model for the development of the plasma focus.

1. COLLISIONLESS MHD MODEL FOR A PLASMA WITH MAGNETIC VISCOSITY

As will subsequently be shown, sausage-type instabilities in non-cylindrical Z-pinches develop against a background of strongly turbulent surface drift waves which have formed the subject of a number of previous studies although these have only concerned a plasma with a plane boundary. It is necessary to generalize the methods developed previously to apply to a pinch with a cylindrical geometry. This generalization can be carried out within the limits of a single-fluid MHD model, if a transition is made to the collisionless limit $\nu \sim \langle n\sigma v\rangle \to 0$ but allowance is made for the finiteness of the Larmor radius of the ions. In the isotropic hydrodynamic equation:

$$\rho \dot{\vec{v}} = -\nabla p + \frac{1}{c}[\vec{J} \times \vec{B}] - \nabla \cdot \hat{\pi} \qquad (1)$$

the passage to the limit $\nu \to 0$ is difficult to achieve as the viscosity tensor in the strong magnetic field $\vec{B}$ is known to assume the form $\hat{\pi} = \hat{\pi}^0 + \hat{\pi}^{(1)}$, where $\hat{\pi}^0 \cong P_i/\nu_i(\hat{\delta} - 3\hat{h}\hat{h})[\vec{h}(\vec{h}\nabla)\vec{v} - \frac{1}{3}\mathrm{div}\,\vec{v}]$, $\vec{h} = \vec{B}/B$, and $\hat{\pi}^{(1)}$ is the magnetic viscosity tensor. This difficulty is only apparent, however, and is removed when a transition is made to anisotropic hydrodynamics. Equation (1) is compared with the ideal anisotropic MHD equation of Chew, Goldberger and Low in accordance with which

$$\rho \dot{\vec{v}} = -\nabla \cdot \hat{p} + \frac{1}{c}[\vec{J} \times \vec{B}] \qquad (2)$$

where $\hat{p} = p_\perp \hat{\delta} + (P_\parallel - P_\perp)\hat{h}\hat{h}$ is the pressure tensor. The term with the zero trace

$$\hat{p} \equiv \frac{p_\parallel + 2p_\perp}{3}\hat{\delta} + (p_\parallel - p_\perp)(\hat{h}\hat{h} - \frac{1}{3}\hat{\delta})$$

is isolated in the tensor $\hat{p}$ and we take advantage of the fact that the pressure in Eq. (1) is isotropic, i.e. the difference $\Delta p = p_{\parallel} - p_{\perp}$ is assumed to be small. As Δp varies during motion of the plasma due to the adiabatic variation and as a result of collisional relaxation, it is readily shown [1] that

$$p_{\parallel} - p_{\perp} = \frac{p}{\nu} [\operatorname{div} \vec{v} - 3\vec{h}(\vec{h}\nabla)\vec{v}] \tag{3}$$

and therefore the trace less part of $\hat{p}$ coincides with the tensor $\hat{\pi}^{(0)}$. As far as we are aware, the possibility of interpreting $\hat{\pi}^{(0)}$ in this way has not been noted previously. From this it follows that anisotropic hydrodynamics with magnetic viscosity is the correct collisionless MHD model for the plasma. A strict derivation of the viscosity tensor of a collisionless anisotropic plasma is presented in the present paper.

2. DRIFT INSTABILITY OF THE PINCH BOUNDARY

On considering drift waves within the limits of the anisotropic model proposed above with allowance for magnetic viscosity for a non-cylindrical Z-pinch, we derive the following equation:

$$\frac{1}{r}\frac{\partial}{\partial r}\left[r^3\rho\left(1-\frac{\omega_0}{\omega}\right)\frac{\partial\Psi}{\partial r}\right] - k_z^2 r^2 \rho\left[1 - \frac{\omega_0 + \delta\omega_0}{\omega} - \frac{g_{eff}}{\omega^2}\kappa_{eff}\right]\Psi = 0, \quad \Psi = \frac{v_r}{r} \tag{4}$$

which is similar to the familiar equation for a plane symmetric plasma [2]. In this equation, ω_D is the drift frequency, $\delta\omega_D$ is the correction for the cylindricity, $g_{eff} = 2P/\rho r$ is the effective acceleration, and κ_{eff} is the effective thickness of the transitional layer. The following dispersion relationship is derived from Eq. (4) in the sharp-pinch-boundary approximation:

$$\omega = \omega' + i\gamma, \quad \omega' = \frac{1}{2}\omega_B(kR_i)^2, \quad \gamma = \sqrt{|k| g_{eff} - \frac{1}{4}(kR_i)^4 \omega_{Bi}} \tag{5}$$

where R_i and ω_{Bi} are the Larmor radius and the frequency of the ions respectively. By applying relationship (5) we obtain from a well-known equation [3] the turbulent diffusion coefficient

$$D_{turb} = (\gamma^2/\omega' k^2)_{max} = \frac{3}{2} cT/e_i B \tag{6}$$

which also determines the length of the sausage-type instability.

3. CHARACTERISTIC LENGTH OF THE SAUSAGE-TYPE INSTABILITY IN A PINCH

As follows from Eq. (5), the growth rate $\gamma(k)$ is maximum for $k = k^*$, as determined from the relationship $g_{eff} = k^{*3} R_i^4 \omega_{Bi}^2$ which corresponds to the wavelength $\lambda^* = \pi a (R_i/a)^{2/3}$. These increasing oscillations are found to be comparatively short-wave and rapid as, under real conditions, it is generally found that $R_i/a \sim 10^{-3}$ at the boundary of the Z-pinch and the plasma focus. Perturbations such as the "macro"-sausage-type instabilities observed in pinches are evidently rather different. The length of the sausage-type instability formed in a Z-pinch was investigated experimentally in Ref. [4] and it was found that it is satisfactorily approximated by the empirical relationship $\lambda = 2 \times 10^5 A(\text{cm}) \sqrt{j_0 (A \cdot s^{-1})}$ where j_0 is the initial current rise rate. The satisfactory

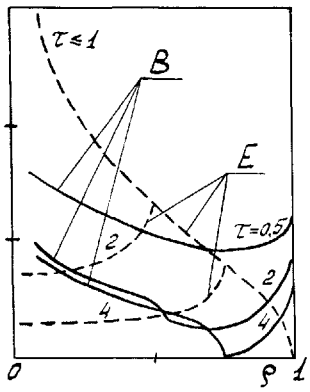


FIG.1. Profiles of E and B for a linearly decreasing current:

$J_0(t) = J_0 - (J_0 - J_1)\tau$, for $\tau = t/T \leqslant 1$.

$J_0(t) = J_1 < J_0$ for $\tau \geqslant 1$, $\rho = x/ct$.

nature of this approximation was also confirmed by the experimental results given in Ref. [5]. This type of equation can be derived from simple dimensional concepts if the conventional equilibrium equation $\nabla p = 2T\nabla n = 1/c\,[j \times B]$, where $j = env$ is rewritten in "diffusion" form $nv_z = D\nabla_r n$, $D = 2cT/eB$ and the value D is considered the "effective" diffusion coefficient which is defined from the equation $\Delta x = \sqrt{2Dt}$ giving the root-mean-square displacement of the particles within the time t. Perturbations with $\lambda < \Delta x$ are smoothed in a similar process, and we therefore have the characteristic parameter $\lambda_{eff} = 2\Delta x$ which yields an equation virtually identical with the empirical relationship given above, if it is assumed that $B = 2J/ca$, $J = \dot{J}_0 t$ and, in accordance with Ref. [4], that $T = 10$ eV.

This derivation assumes the form of a dimensional calculation but the fact that the effective length of the sausage-type instability is dependent on the same diffusion coefficient as in Eq. (6) clearly indicates that the sausage-type instabilities observed in Z-pinches are formed against a background of developing drift wave turbulence.

4. PARTICLE ACCELERATION MECHANISM DURING TERMINATION OF SAUSAGE-TYPE INSTABILITIES.

It has already been established that particles accelerated to energies of 300 keV and higher are observed in powerful pulsed discharges. As was first shown by one of the present authors [6], as a result of the blocking of the conduction current and its partial replacement by the displacement current $j_{disp} = (1/4\pi)(\partial/\partial t)\epsilon E_z$ during the development of the sausage-type instability, the field E_z should increase and this can accelerate a certain proportion of the plasma particles. This type of acceleration mechanism can be refuted by the concept that particles, particularly electrons, cannot be accelerated at right angles to the magnetic field. If the electric field E is stronger than the magnetic field B, however, the particle motion will cease to assume a drift character and acceleration is found to be possible. This possibility is investigated in a number of model examples in Ref. [7]. As compared with the problem investigated previously, [8], allowance was made for

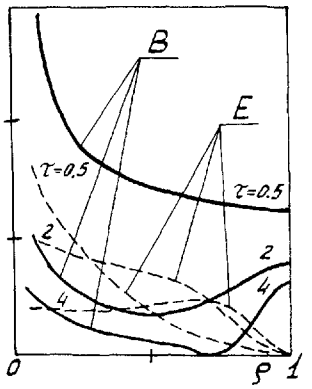


FIG.2. The same for the current $J_0(t) = J_0 - [(J_0 - J_1)/(t^2 + T^2)]t^2$, $\tau = t/T$, $\rho = x/ct$.

such factors as the non-instantaneous but gradual nature of the current cessation process, the presence of a surrounding plasma column, the transition to a boundary problem with the condition $E = -\sqrt{B/C}$ at the plasma boundary and the incomplete cessation of the current. In Ref. [7], it was shown that an electromagnetic wave develops under these conditions and during the development of this wave the condition $E > B \approx 0$ is inevitably satisfied and it is therefore possible for both ions and electrons to be accelerated. The accelerating field $E \approx 20\ kV \cdot cm^{-1}$ determined from comparison with the experimental results at the point where $B = 0$ is found to be of the same order as that used in the model in Ref. [9]. Figures 1 and 2 show the development of the fields E_z and B_φ for two laws of current decrease. At a certain value of $\tau = t/T = \tau^*$ it is evidently found that $B = 0$, $E \neq 0$ at a certain distance from the axis. Under real conditions, strict axial symmetry can hardly be expected with the result that the situation $E > B \cong 0$ means that it is possible for repeated parallel breakdown to occur and in a number of cases this is observed on the X-ray photographs of the discharge.

5. INFLUENCE OF HALL EFFECT ON THE DYNAMICS OF A DISCHARGE IN A NON-CYLINDRICAL Z-PINCH

A plasma focus is obtained as a result of the collapse of a Z-pinch sheath during which compression of the pinch is accompanied by escape of material parallel to the axis. The loss of material results in an increase in the temperature in the plasma focus as compared with the linear Z-pinch. The curvature of the sheath is one of the reasons for the loss of material in the plasma focus. The increase in the curvature of the sheath in a non-cylindrical Z-pinch may be due to current slippage along the anode surface which is caused by the small Hall electric field produced by the plasma along the highly conductive surface of the electrode [10].

It is essential to make allowance for the Hall effect in a plasma if the Hall electric field is predominant compared with the Ohmic field, i.e. if the plasma electrons are magnetoactive, $\omega_{eH}\tau_{ei} > 1$ and if the exchange parameter η [10] expressing the ratio of the current velocity of the electrons to the hydrodynamic velocity of the plasma is greater than or equal to unity. Estimates and calculations [11] show that the parameter η in a non-cylindrical Z-pinch is substantially less than unity right up to the point where the sheath converges at the discharge axis. Nevertheless, it is necessary to make allowance for the Hall effect as this results in a substantial variation in the dynamics of the discharge compared with the results obtained in Ref. [11].

The influence of the Hall effect on the dynamics of a sheath in a non-cylindrical Z-pinch is considered within the limits of two-dimensional MHD calculations. The calculations are performed in the cylindrical co-ordinates r and z in a fixed rectangular lattice measuring 10 cm × 2 cm. The z-axis coincides with the axis of the system and the r-axis coincides with the surface of the anode. When setting up the calculations, allowance was made for diffusion and transport of the magnetic field, variation in the density within the limits of the equation of continuity, motion under the effect of a ponderomotive force and the inherent pressure of the plasma, heat exchange between ions and electrons, ion, κ_i, and electron, κ_e, thermal conductivity, the viscosity tensor of the ions, Ω, and also the viscous heat release θ. The following equations were taken for the plasma density n, the velocity $\vec{v}$, the magnetic field $\vec{H}$ and the temperature T_i and T_e:

$$\frac{\partial \vec{H}}{\partial t} = -\frac{c^2}{4\pi}\,\mathrm{rot}\left(\frac{\mathrm{rot}\,\vec{H}}{\sigma}\right) + \mathrm{rot}\,[\vec{v} \times \vec{H}] \tag{7}$$

$$\frac{\partial n}{\partial t} = -\,\mathrm{div}\,(n\vec{v}) \tag{8}$$

$$Mn\frac{d\vec{v}}{dt} = -\,\mathrm{grad}\,(nT_i + nT_e) + \frac{1}{4\pi}\,[\mathrm{rot}\,\vec{H} \times \vec{H}] + \mathrm{Div}(\Omega) \tag{9}$$

$$\frac{3}{2}\frac{\partial}{\partial t}(nT_i) = \mathrm{div}(\kappa_i\,\mathrm{grad}\,T_i) - nT_i\,\mathrm{div}(\vec{v}) - \mathrm{div}\left(\frac{3}{2}nT_i\vec{v}\right) + \frac{3m}{M}\,n\,\frac{T_e - T_i}{\tau_{ei}} +$$

$$+ \mathrm{div}(\Omega\vec{v}) - \vec{v}\,\mathrm{Div}(\Omega) \tag{10}$$

$$\frac{3}{2}\frac{\partial}{\partial t}(nT_e) = \mathrm{div}(\kappa_e\,\mathrm{grad}\,T_e) - nT_e\,\mathrm{div}(\vec{v}) - \mathrm{div}\left(\frac{3}{2}nT_e\vec{v}\right) + \frac{3m}{M}\,n\,\frac{T_i - T_e}{\tau_{ei}} \tag{11}$$

As the Hall effect has little influence in the plasma considered, it is only important to allow for this effect at the boundary between the plasma and the electrode. As the electrode is highly conductive and the tangential component of the electric field at the boundary of the two media is continuous, it follows that the radial electric field near the electrode $E_r|_{z=0} = 0$. This condition gives

$$\left.\frac{\partial H}{\partial z}\right|_{z=0} = \frac{\omega_{eH}\,\tau_{ei}}{r}\,\frac{\partial}{\partial r}(rH) \tag{12}$$

which is used as the boundary condition for the magnetic field. When the boundary condition (12) is used instead of the normal condition $(\partial H/\partial z)|_{z=0} = 0$, this gives a qualitatively different result for the solution of the MHD equations when modelling the motion of a shell in a non-cylindrical Z-pinch.

The geometry and parameters of the discharge were taken as those characteristic of a non-cylindrical Z-pinch [12], the initial gas pressure was 1 torr and the current magnitude was 1.5 mA. It was initially assumed that the sheath was displaced from the axis by a distance r ~10 cm and moves at a velocity $v_r \sim 10^7$ cm·s^{-1}. The plasma compression coefficient in the sheath was initially taken as 4 and the temperature $T_e = T_i = 30$ eV. The temperature of the unperturbed gas was assumed to be 1 eV.

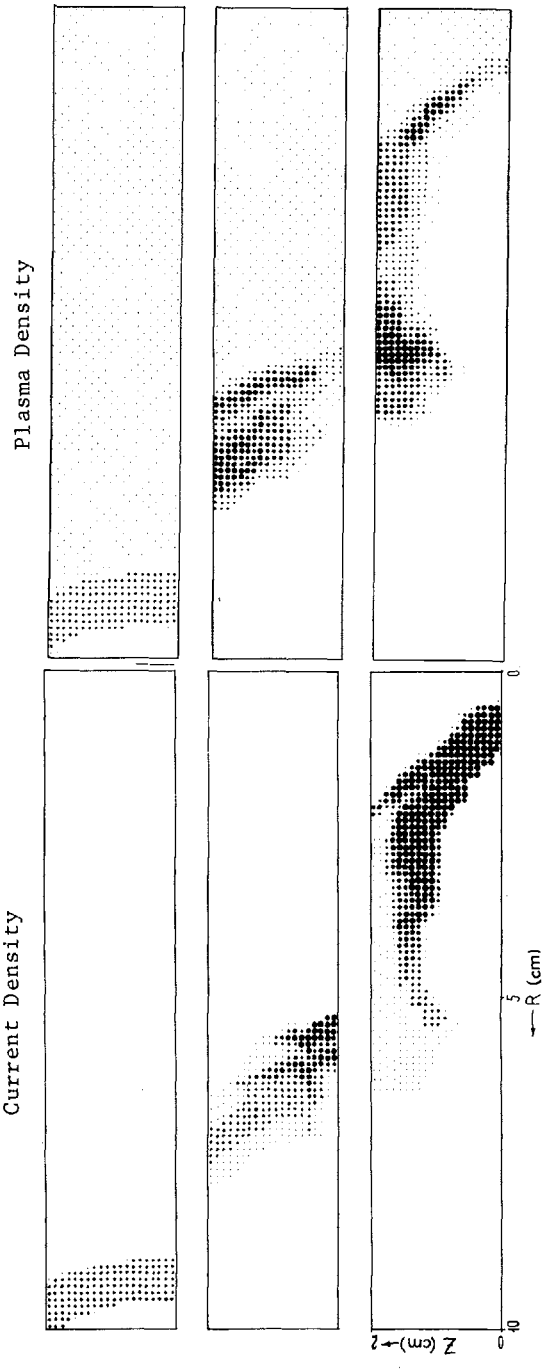


FIG. 3. Computer graphs of the current density and plasma density for three points at times t = 0, 0.23 and 0.34 μs.

Computer graphs of the plasma density and the absolute current magnitude for three points at times t = 0, 0.23, and 0.34 μs are given in Fig. 3. Calculations showed that during motion of the sheath the magnetization parameter for the electrons in the sheath becomes greater than unity. The absence of an electric field parallel to the electrode in the region adjacent to the electrode results in a reduction in the plasma conductivity in this region by a factor of $1 + \omega_{cH}^2 \tau_{ei}^2$ in the direction perpendicular to the electrode. In this magnetoactive plasma near the electrode the current is forced to flow along the anode and the current component perpendicular to the anode only becomes appreciable near the front of the sheath where the low electron temperature ensures that the magnetization parameter is also low. The radial component of the current gives rise to the formation of a magnetic field which repels the plasma from the anode. The drift of plasma from the anode results in a reduction in the mass of the sheath in the layer near the anode and increases the radial velocity at this point. The sheath becomes increasingly convex (Fig. 3) which facilitates the release of gas from this region of sheath and thereby results in further substantial acceleration.

During development of the discharge the influence of the Hall effect increases in the region adjacent to the electrode. This is due to the increased velocity of the sheath which results in heating of the plasma and thereby increases the magnetization parameter of the electrons, and is also due to the increase in the magnetic field strength as the sheath approaches the axis of the system.

During the final sheath compression stage the plasma density at the axis of the discharge is found to be negligibly higher than the initial density. This slight increase in density in the plasma focus is due to the formation of a magnetic field which repels the plasma from the anode and also to the escape of plasma from the sausage-type instability due to the curvature of the sheath. The small number of particles in the plasma focus cross-section results in an increase in the current velocity of the electrons in this region and at the major radius anomalous plasma resistivity begins to be observed in the sheath from the axis.

These calculations show that the curvature of the sheath in a Z-pinch which results in the formation of a plasma focus can be produced by current slippage along the anode in the region adjacent to the electrodes as well as by the geometry of the electrodes.

6. EFFECT OF ANOMALOUS CONDUCTIVITY ON THE DYNAMICS OF THE PLASMA FOCUS

The break-up stage which determines the life-time of the plasma focus is an important phase in the development of the plasma focus. During collapse of the sheath at the chamber axis, the majority of the energy initially stored in the capacitor bank is converted into magnetic field energy in the discharge current and only a small proportion (1–2%) is transformed into thermal energy in the plasma focus. As a result of the processes which take place at the break-up stage, up to 10–20% of the initial energy may be transferred to the plasma [13]. The remaining energy is returned to the capacitor bank and dissipated in subsequent half-cycles. When solving the problem of the life-time of the plasma focus, it is first of all necessary therefore to clarify the physical processes which prevent a more complete transfer of magnetic field energy to the plasma and result in decay of a thermonuclear plasma.

A theoretical description of the plasma focus within the limits of a two-dimensional MHD model does not enable the lifetime to be obtained as it results in continual compression and total rupture of the plasma column [11]. In the kinetic description of the ions [14] the column does not undergo rupture although the current velocities of the electrons described by MHD equations with classical transport coefficients attain relativistic values and substantially exceed the threshold of a number of current instabilities [15]. Under these conditions it becomes necessary to make allowance for turbulent transport coefficients and, in particular, the anomalous conductivity of

the plasma. A number of experimental observations indicate that the plasma focus undergoes a transition to the turbulent state before the final stage is reached [13, 16, 17].

The condition for turbulence of the plasma column can be represented as follows:

$$N_1 < 2.6 \times 10^{16} \frac{1+\alpha}{\xi^2} \text{ cm}^{-1} \tag{13}$$

where N_1 is the linear density, $\alpha = T_e/T_i$ and $\xi = U_{thresh}/v_{Ti}$ is the ratio of the threshold velocity to the ion thermal velocity. When the plasma escapes from the focus region along the z-axis, the linear density decreases and from a certain point onwards condition (13) begins to be satisfield for the instability which has the lowest excitation threshold. The plasma conductivity becomes anomalously low and is defined by the expression

$$\sigma = \frac{\sigma_{Coul}}{1 + \nu_{eff}\tau} \tag{14}$$

where σ_{Coul} is the Coulomb conductivity of the plasma, τ is the Coulomb electron-ion collision frequency, and ν_{eff} is the effective collision frequency, the value of which depends on the type of instability which develops. The transverse current instabilities have the lowest excitation thresholds, particularly the electron acoustic instability and the lower hybrid drift instability which has characteristic frequencies and growth rates of the order of the lower hybrid frequency $\omega \sim \gamma \sim \sqrt{\omega_{Be}\omega_{Bi}}$ and an effective collision frequency [18]

$$\nu_{eff} \cong \left(\frac{u}{v_T}\right)^2 \sqrt{\omega_{Be}\omega_{Bi}} \tag{15}$$

whereby 85% of the energy obtained as a result of turbulent heating is expended on heating the ions.

A one-dimensional MHD model of a completely ionized plasma in which allowance was made for the double temperature properties of the plasma, the diffusion and transport of the magnetic field, the radial motion of the plasma, the viscosity, the Joule and viscous heat release and also the escape of plasma along the axis was used to describe the dynamics of the formation and break-up of the plasma focus. The numerical solution was carried out in a Langrangian system of co-ordinates. The plasma conductivity was defined by Eqs (14) and (15). The characteristic time for escape of the plasma $\tau = \Delta z/v_z$, where Δz is half the height of the plasma focus and the velocity v_z was determined by solving the equation

$$\frac{dv_z}{dt} = \frac{(P_i + P_e)_t - P_0}{nM\Delta z} - \frac{v_z}{\tau} \tag{16}$$

where $(p_i + p_e)_t$ is the gas dynamic pressure of the plasma at the time t and p_0 is the initial pressure. The time dependence of the discharge current was defined by the electrical equation for the circuit. The following plasma parameters were taken as the initial conditions: $r = 2.5$ cm, $T_i = T_e = 5$ eV, $n = 3.5 \times 10^{17}$ cm^{-3}, $J = 8 \times 10^5$A and $\Delta z = 0.5$ cm.

The calculated time dependences for the radius of the plasma column, the linear density, the ion temperature, the current and the neutron radiation intensity are plotted in Fig. 4. Continuous compression evidently does not take place in the given model. When the linear density decreases to 10^{17} cm^{-1}, the diameter of the pinch attains its minimum value of 0.5 mm. In this case, the current velocities begin to exceed the instability threshold by a considerable margin and the resistivity of the plasma column becomes anomalously high. This results in a

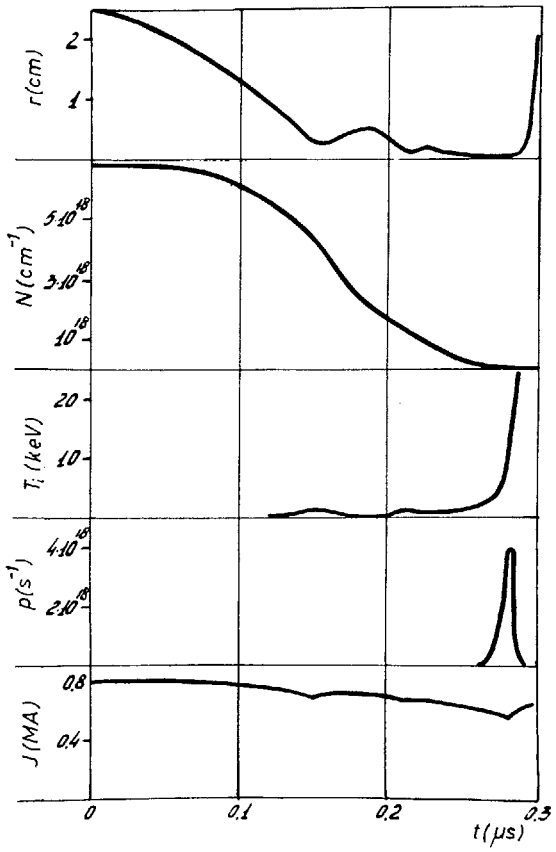


FIG.4. Variation of pinch radius r, linear density N, ion temperature T_i, neutron radiation intensity P, and current J with time.

considerable excess voltage and an anomalously high degree of plasma heating. As a result of the rapid increase in the gas-kinetic pressure, the radial confinement of the plasma is disturbed and the plasma column begins to expand. The ion temperature at the instant of maximum compression is 6 keV and the average plasma density over the cross-section was 5×10^{19} cm^{-3}. Although the pinch temperature continues to increase during the expansion stage, the neutron radiation decreases due to the drop in pressure in the pinch, and virtually ceases within a few nanoseconds after expansion of the pinch has begun. The total neutron yield was 3×10^{10} and the neutron pulse duration was 30 ns. The anomalous conductivity results in a substantial increase in the rate of diffusion of the magnetic field into the plasma and the skin layer thickness increases to half the radius of the column. The electric fields in the plasma attain values of $10^5 - 10^6$ V·cm^{-1}.

The anomalous conductivity, therefore, results in a substantial release of heat in the plasma and thereby disturbs the radial confinement of the plasma. The dynamics of the plasma focus with allowance for anomalous conductivity agree with the experimental results. Certain discrepancies in the duration and total yields of neutron radiation, which is of a thermonuclear

origin in the given model, are completely admissible as the one-dimensional model only approximately describes the escape of plasma along the axis and does not make allowance for the possible development of MHD instability such as the "sausage-type instability".

7. A SIMPLE MODEL FOR THE DEVELOPMENT OF THE PLASMA FOCUS

Numerical modelling of the plasma focus shows that in the final compression stage the plasma density and temperature are constant over the radius of the plasma column and the magnetic field pressure at the pinch boundary is equal to the plasma pressure to a high degree of accuracy

$$\frac{H^2}{8\pi} = 2nT \tag{17}$$

These properties in the final stage of compression of a Z-pinch were used in Ref.[19] to investigate the dynamics of sausage-type instabilities of a plasma column.

As well as averaging the plasma parameters over the radius, we also average over the height of the plasma column. Let N be the number of ions incident per unit height of the pinch. $N = \pi r^2 n$ where r is the radius of the pinch and n is the average plasma density in the pinch. If τ is the characteristic time for escape of particles from the plasma focus, it follows that

$$\frac{dN}{dt} = -\frac{N}{\tau} \tag{18}$$

The energy balance in the plasma focus without allowance for losses due to the thermal conductivity of the plasma and radiation is defined by the following equation:

$$3\frac{d(NT)}{dt} = 5\frac{NT}{\tau} - 2\pi r\frac{H^2}{8\pi}\frac{dr}{dt} \tag{19}$$

The last term in this equation describes the work performed by the magnetic field in compressing the plasma column.

The development and breakup of a plasma focus with a constant current J flowing through the focus is considered. Assuming that the magnetic field strength $H = 0.2\ I/r$, where J is the current in amperes, Eq.(17) gives

$$J^2 = 400\ NT = \text{const} \tag{20}$$

From Eqs (19) and (20), it follows that

$$\frac{dr}{dt} = -\frac{5}{8}\frac{r}{\tau} \tag{21}$$

From Eqs (18) and (20), we obtain

$$\frac{dT}{dt} = \frac{T}{\tau} \tag{22}$$

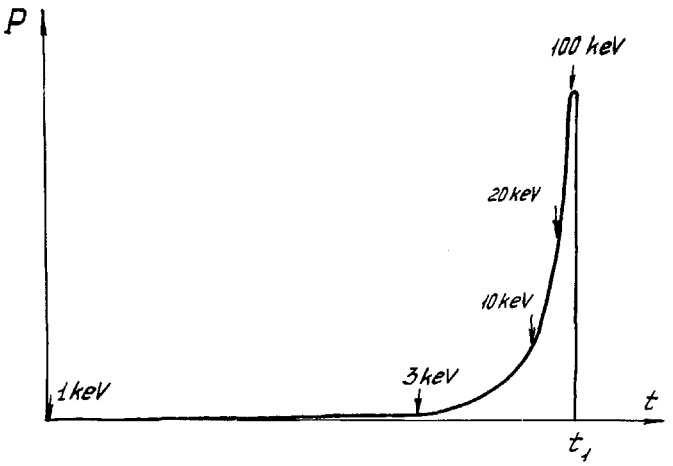


FIG.5. Neutron radiation intensity as a function of time in the case of radial escape of material. Arrows show the plasma temperature at certain points in time. The initial temperature is 1 keV.

The plasma density n varies with time in accordance with the equation

$$\frac{dn}{dt} = \frac{1}{4}\frac{n}{\tau} \tag{23}$$

Equations (22) and (23) show that during escape of material from the plasma focus, the plasma temperature and density in the plasma focus increase.

Loss of mass in the plasma focus is due to escape of material through the ends of the plasma column and also to radial drift of particles, i.e.

$$\frac{1}{\tau} = \frac{1}{\tau_e} + \frac{1}{\tau_r} \tag{24}$$

where τ_e is the characteristic time for escape of plasma along the pinch and τ_r is the corresponding time for escape in the radial direction. Numerical modelling of the development of the plasma focus with allowance for escape of plasma along the axis showed that τ_e can be approximately defined as

$$\tau_e \cong \frac{\ell}{2v^*} \tag{25}$$

where ℓ is the length of the plasma focus and v^* is the characteristic velocity equal to the speed of sound and also, owing to condition (17), to the Alfvén velocity.

Radial escape of mass in the plasma focus may occur if the length of the focus is at least several times greater than the transverse dimension. In this case MHD instability such as the sausage-type instability develops, as has been shown by the experimental results of Ref.[13] and modelling in Refs [11, 19]. The results of the development of this instability have not yet been completely investigated although it should be noted that the development of this instability should not result

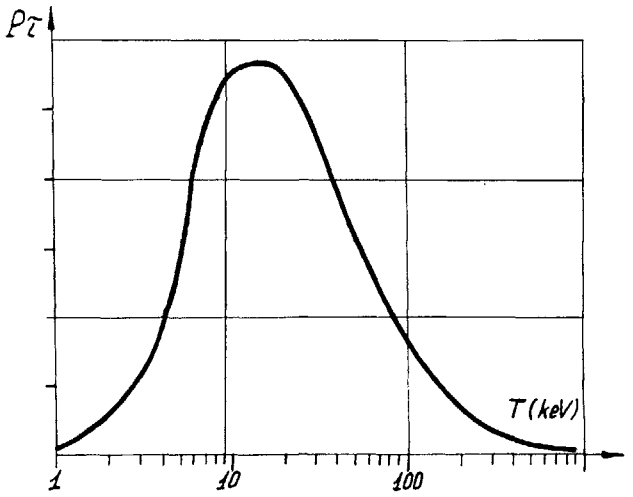


FIG. 6. Relative contribution to neutron radiation made by a plasma at different temperatures.

in a general escape of plasma from the axis of the system. This instability clearly results in the escape of individual layers and clusters of plasma into the region occupied by the magnetic field around the plasma focus. It is assumed that the characteristic time for the radial escape of material is defined by the expression

$$\tau_r = \frac{kr}{v^*} \tag{26}$$

where k is a coefficient indicating the extent to which the time for the radial escape of plasma from the plasma focus exceeds the radial transit time. The value of k can be determined, in principle, from experimental interferograms of the plasma focus, i.e.

$$k = \frac{\ell^*}{d} \tag{27}$$

where ℓ^* is the characteristic length of the section of plasma focus with the diameter d, which is not disturbed by MHD instability with the mode m = 0. Calculations give values of k between 2 and 10 with the most probable value being $k \sim 5$.

The development of the plasma focus is considered for two cases where the particle drift is due to one of the mechanisms noted above. If the escape of material is only due to radial disturbance of the plasma focus, $\tau = \tau_r \sim r/\sqrt{T}$ and therefore from Eqs (21) and (22) it follows that

$$\frac{d\tau}{dt} = -\frac{9}{8} \tag{28}$$

or

$$\tau = \frac{9}{8}(t_1 - t) \tag{29}$$

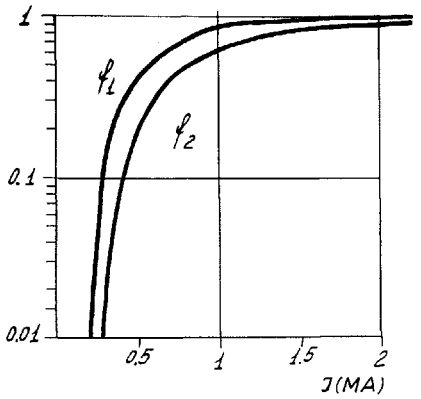


FIG.7. Factors f_1 and f_2 as functions of the current flowing through the plasma focus.

where t_1 is the plasma focus existence time, $t_1 = \frac{8}{9}\frac{kr_0}{v^*}$, r_0 is the initial radius of the plasma focus and $v_0^* = v^*|_{t=0}$. Applying the solution of Eq.(29) we obtain

$$N = N_0 (1 - t/t_1)^{8/9}$$

$$T = T_0 (1 - t/t_1)^{-8/9}$$

$$n = n_0 (1 - t/t_1)^{-2/9}$$

$$r = r_0 (1 - t/t_1)^{5/9} \qquad (30)$$

The intensity of the neutron radiation from the plasma focus as determined by the expression

$$P = \ell N n \sigma(T) \qquad (31)$$

where $\sigma(T)$ is the thermonuclear d-d reaction cross-section, is plotted in Fig.5 as a function of time. The highest intensity is obtained at a temperature of 100 keV with the neutron radiation rapidly ceasing after this temperature has been obtained. Figure 6 shows the contribution made by the plasma at a certain temperature to the neutron radiation. The area below the curve in Fig.6 determines the neutron yield. The largest contribution to the neutron radiation is clearly made by a plasma at a temperature of 10–20 keV. The reduction in the contribution made by the plasma at higher temperatures is attributable to the decrease in the number of particles found at this temperature and also to the reduction in the existence time for this plasma. The total neutron radiation from the plasma focus as a result of d-d reactions with allowance only for radial escape of material is equal to

$$\int_0^{t_1} p\,dt = 0.4\, k\ell J^3 n_0^{1/2} T_0^{-1/8} \qquad (32)$$

where the current J is expressed in MA, T_0 is in keV and n_0 is in cm^{-3}.

In the previous section it has been shown that in the equilibrium state of a Z-pinch the quantity of particles in the cross-section cannot be less than 2.6×10^{16} cm^{-1} otherwise, even if the current distribution over the cross-section is uniform, the current velocity of the electrons will be greater than the thermal velocity of the ions which results in an anomalously high degree of heating in the pinch, and thereby causes the pinch to expand and the neutron radiation to cease. If allowance is made for this fact by integrating in Eq.(32) up to the point where the quantity of particles in the cross-section is equal to 2.6×10^{16} rather than up to time t_1, it is found that the neutron yield must be multiplied by a certain factor f_1 which depends on the magnitude of the current. The dependency $f_1(J)$ is shown in Fig.7. At currents greater than 1 MA, the factor f_1 approaches unity. This means that at high current magnitudes the plasma focus is disturbed because of MHD instabilities up to the point where the plasma temperature in the focus attains 100 keV, and the anomalous heating expands the pinch when the neutron radiation has virtually ceased. Equation (32) with allowance for the factor f_1 assumes the form:

$$N_{1\,dd} = 0.4\, k \ln_0^{1/2}\, T_0^{-1/8}\, J^3 f_1(J) \tag{33}$$

If the time for escape of particles from the plasma focus depends on the escape of plasma through the ends, it follows that $\tau \sim T^{-1/2}$ and the plasma parameters vary with time as

$$\tau = \frac{1}{2}\,(1 - t/t_1), \qquad \text{where } t_1 = \frac{\ell}{v^*}$$

$$N = N_0\,(1 - t/t_1)^2$$

$$T = T_0\,(1 - t/t_1)^{-2}$$

$$n = n_0\,(1 - t/t_1)^{-1/2}$$

$$r = r_0\,(1 - t/t_1)^{5/4} \tag{34}$$

The neutron radiation for d-d reactions is in this case defined by the expression

$$N_{2\,dd} = 2 \times 10^{-9}\, I^2 n_0 T_0^{-1/4}\, J^2 f_2(I) \tag{35}$$

where the current I is expressed in MA, the initial temperature in the plasma focus T_0 is in keV and n_0 is in cm^{-3}. Figure 7 shows the factor f_2 as a function of the current.

As the escape of particles from the plasma focus generally takes place due to both mechanisms, the neutron yield can be approximately represented as follows

$$N_{dd} = \frac{N_{1\,dd}\, N_{2\,dd}}{N_{1\,dd} + N_{2\,dd}} \tag{36}$$

On comparing this equation with the experimental results, it is frequently found that the neutron radiation is slightly higher than that observed experimentally. From Eq.(36) it follows that the neutron yield from the plasma focus depends on the average current at the instant of singularity, on the plasma density in the focus and on the length of the focus. The neutron radiation is very slightly dependent on the initial temperature T_0 with the neutron yield decreasing with increasing T_0.

It should be noted that within the limits of this model for the development of the plasma focus, any mechanism of heat removal from a high temperature plasma promotes an increase in the neutron yield from the plasma focus. This is because the temperature is not dependent on the heating but on the current flowing through the plasma focus and the quantity of particles in

the cross-section. Removal of heat promotes an increase in the plasma density and therefore an increase in the neutron radiation intensity. This apparently paradoxical situation is achieved as the energy necessary for the equilibrium condition (17) to be satisfied enters the plasma from the magnetic field which compresses the plasma.

REFERENCES

[1] TRUBNIKOV, B.A., ZHDANOV, S.K., Fiz. Plazmy **4** (1976).
[2] MIKHAJLOVSKIJ, A.B., Vopr. Teor. Plazmy **3** (1963) 185.
[3] KADOMTSEV, B.B., Vopr. Teor. Plazmy **4** (1964) 300.
[4] OSOVETS, S.M., et al., Zh. Ehksp. Teor. Fiz. **64** (1973) 1228.
[5] ALEKSANDROV, V.V., et al., Zh. Ehksp. Teor. Fiz. **64** (1973) 1222.
[6] TRUBNIKOV, B.A., Plasma Physics and Problems of Controlled Thermonuclear Reactions, 1, Izd. Akad. Nauk, USSR, Moscow (1958) 289.
[7] TRUBNIKOV, B.A., ZHDANOV, S.K., Zh. Ehksp. Teor. Fiz. **68** (1976) 538.
[8] TRUBNIKOV, B.A., Plasma Physics and Problems of Controlled Thermonuclear Reactions, Vol. 4, Izd. Akad. Nauk, USSR, Moscow, (1958) 87.
[9] GARY, S.P., Phys. Fluids, **17** (1974) 2135.
[10] BRUSHLINSKIJ, K.V., MOROZOV, A.I., Vopr. Teor. Plazmy, Atomizdat, Moscow **8** (1974) 88.
[11] D'YACHENKO, V.F., IMSHENNIK, V.S., Vopr. Teor. Plazmy, Atomizdat, Moscow **8** (1974) 164.
[12] GUREEV, K.G., FILIPPOV, P.V., FILIPPOVA, T.I., Fiz. plazmy **1** (1975) 120.
[13] MAISONNIER, CH., PECORELLA, F., RAGER, J.P., SAMUELLI, M., STRANGIO, C., MESSINA, A., in Plasma Physics and Controlled Nuclear Fusion Research (Proc. 5th Int. Conf. Tokyo, 1974) **3**, IAEA, Vienna (1975) 99.
[14] ZUEVA, N.M., IMSHENNIK, V.S., et al., Preprint IMP Akad. Nauk. USSR, 73, Moscow (1975).
[15] GRIGOREVA, L.I., LONGINOV, A.V., PYATAK, A.I., SIZONENKO, V.L., SMERDOV, B.I., STEPANOV, K.N., CHECHKIN, V.V., in Plasma Physics and Controlled Nuclear Fusion Research (Proc. 4th Int. Conf. Madison, 1971) **3**, IAEA, Vienna (1971) 573 (in Russian); English translation: Nucl. Fusion Supplement 1972 335.
[16] GRIBKOV, V.A., et al., Pis'ma Zh. Ehksp. Teor. Fiz. **15** (1972) 329.
[17] BERNARD, A., et al., Phys. Fluids **18** (1975) 180.
[18] GUDBLUD, I.P., et al., Zh. Ehksp. Teor. Fiz. **64** (1973) 2084.
[19] IMSHENNIK, V.S., OSOVETS, S.M., OTROSHCHENKO, I.V., Zh. Ehksp. Teor. Fiz. **64** (1973) 2057.

STRUCTURE OF CURRENT SHEATH AND FAST-PARTICLE BEAMS IN THE FOCUS EXPERIMENT

A. BERNARD, A. COUDEVILLE, J.P. GARÇONNET,
A. JOLAS, J. DE MASCUREAU, C. NAZET
Commissariat à l'Energie Atomique,
Centre d'études de Limeil,
Villeneuve-Saint-Georges,
France

Abstract

STRUCTURE OF CURRENT SHEATH AND FAST-PARTICLE BEAMS IN THE FOCUS EXPERIMENT.

Magnetic-probe measurements are presented that deal with the structure of the plasma sheath and the current distribution in a co-axial tube of the Mather type. Fast particles produced by turbulence are studied. The electron beam bombards the anode and generates X-rays whose energy spectrum is measured. For the purpose of obtaining more accurate information on the ion beam characteristics various types of targets were used, in particular a target of deuterated polyethylene. These investigations were made under various initial conditions and different pressure regimes. Moreover, the range of operation of the Focus experiments towards low current intensities was studied. Experimental arrangements are compared for which neutron emission varies over six orders of magnitude.

1. INTRODUCTION

The results obtained previously with a diagnostic ensemble [1, 2] showed that the characteristic phenomena of the Focus experiment were due to microscopic instabilities generated by the interaction between electric current and plasma. These micro-instabilities are known to manifest themselves through different effects: plasma heating due to high resistivity exceeding that given by Spitzer, particle acceleration up to high energies, and finally an 'anomalous' plasma radiation.

The impedance of the plasma sheet being the result of a variable inductance and a resistance, we have to measure the inductance independently in order to deduce the resistance from voltage and current measurements. Previous measurements [3] proved that the current sheet was not identical with the filament and, for a knowledge of the current distribution, the magnetic field was measured with isolated probes placed at several points in the tube.

Another aspect of turbulence is the particle acceleration up to high energies. Electrons and ions, bombarding the anode and the gas, simultaneously generate X-ray bremsstrahlung and neutrons. To study the X-ray radiation, we have developed an equipment yielding spectral and time resolutions simultaneously. The duration of the deuteron beam emission was determined with the help of a solid deuterated target.

Moreover, two new low-energy equipments were installed. The smaller one, with maximal current of 40 kA, permits comparative studies in a much larger zone of operation to be carried out.

2. CURRENT DISTRIBUTION

The results presented were obtained with a Mather-type co-axial tube. The bank energy is 27 kJ at 40 kV. The inner electrode has a diameter of 50 mm and is 250 mm long, the end face

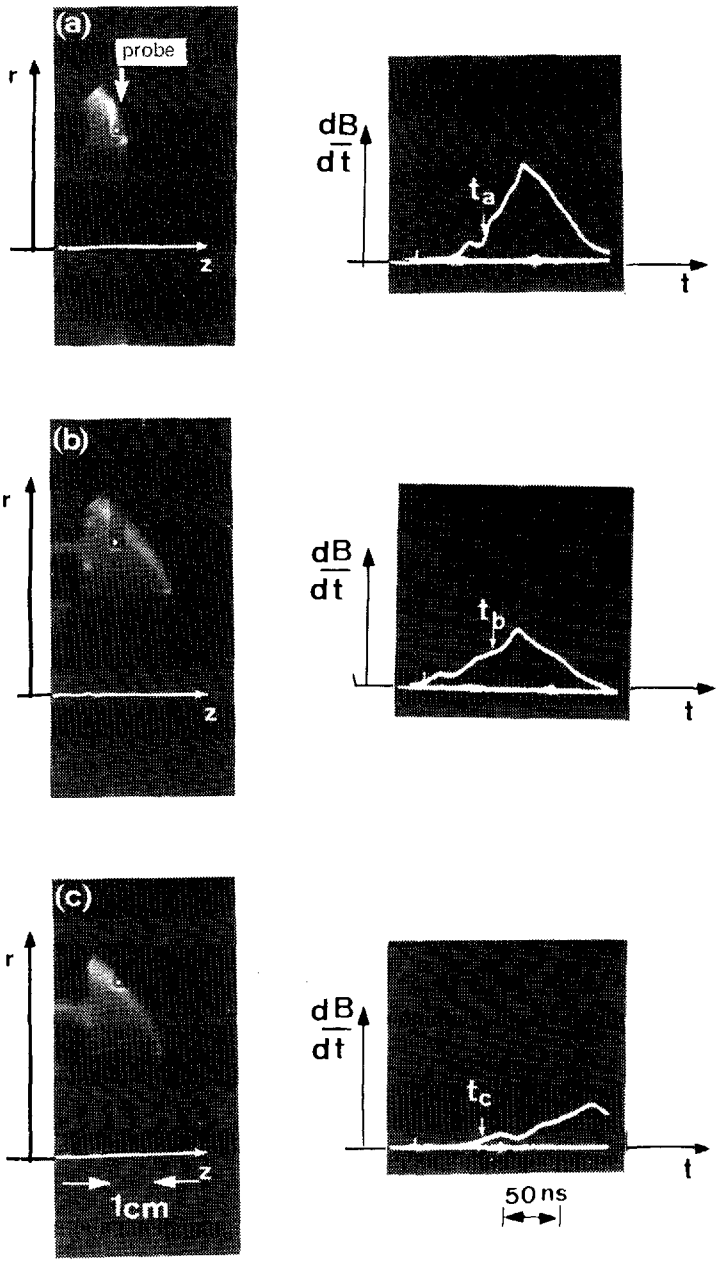


FIG.1. Photographs of the plasma sheath and magnetic probe signals at three radial positions 18 mm distant from the end of the anode. a) r = 28 mm; b) r = 37 mm; c) r = 42 mm (white dot shows exact position of probe loop).

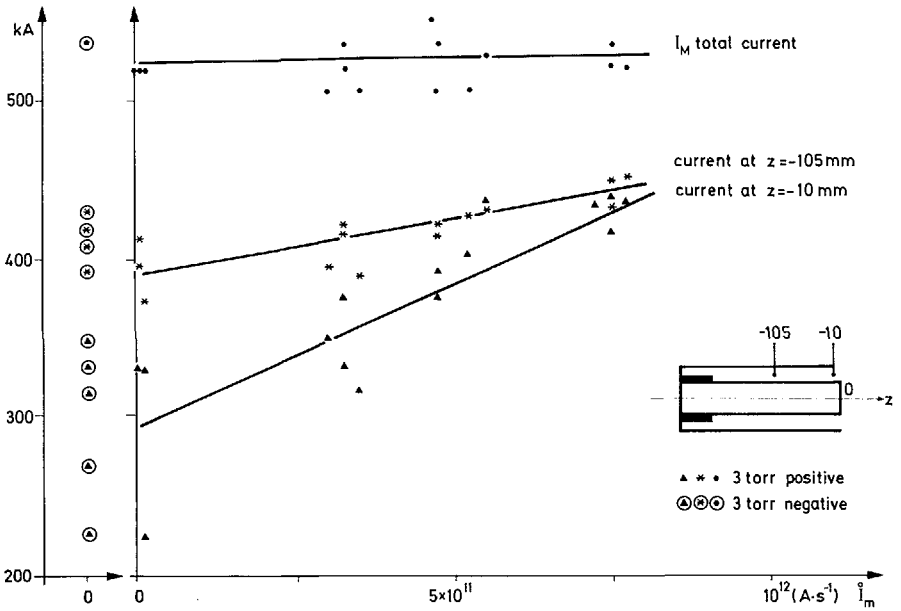


FIG.2. Current driven by the plasma sheath as a function of the minimum of the current derivative I_m at the time of singularity. For each discharge the maximum total current I_M is given.

is a solid plate. The external electrode consists of 20 parallel bars of 230 mm length, uniformly distributed over a diameter of 100 mm. The total electric current I and its derivative $\dot{I}$ are measured by a Rogowski loop placed on a co-axial cable. The current reaches 530 kA at the moment of singularity. To measure the position of the current sheet as a function of time, as well as its structure, magnetic probes were developed. They are oriented such as to be sensitive to time variations of the azimuthal magnetic field component dB_θ/dt. Figure 1 shows the signals obtained when the plasma has reached the end of the electrode after axial propagation, at three different radii. The studies were made for an initial pressure of 3 torr of hydrogen. At every shot a photograph is carefully re-adjusted with respect to the signal obtained. From our measurements we see that the sheet velocity (1.3×10^7 cm $\cdot$ s^{-1}) as well as the current I can be taken as constant on the probe during the passage of the plasma over the probe. Then the signal obtained is proportional to the radial current density j_r. The current was found to circulate in a shell that presents a structure and is the thicker the greater the distance from the central electrode. A first current sheet is perfectly correlated with the position and the thickness of the luminous shell, but the greatest part of the current (85%) circulates in a second shell situated behind the luminous zone.

In Fig.2 we plotted, as a function of the extremum of the current derivative $\dot{I}_m$ at the moment of singularity, the values of the shifted current measured in the middle of the tube ($z = -105$ mm) as well as at its end ($z = -10$ mm). At every shot, the maximum total current I_M is also given. Now, we see that the shifted current is always only a fraction of the total current, the more important as the shot is efficient. The photographs taken at the same pressure but with negative polarity also follow this rule. These results stress the importance of the phases of breakdown and propagation in the subsequent phenomena.

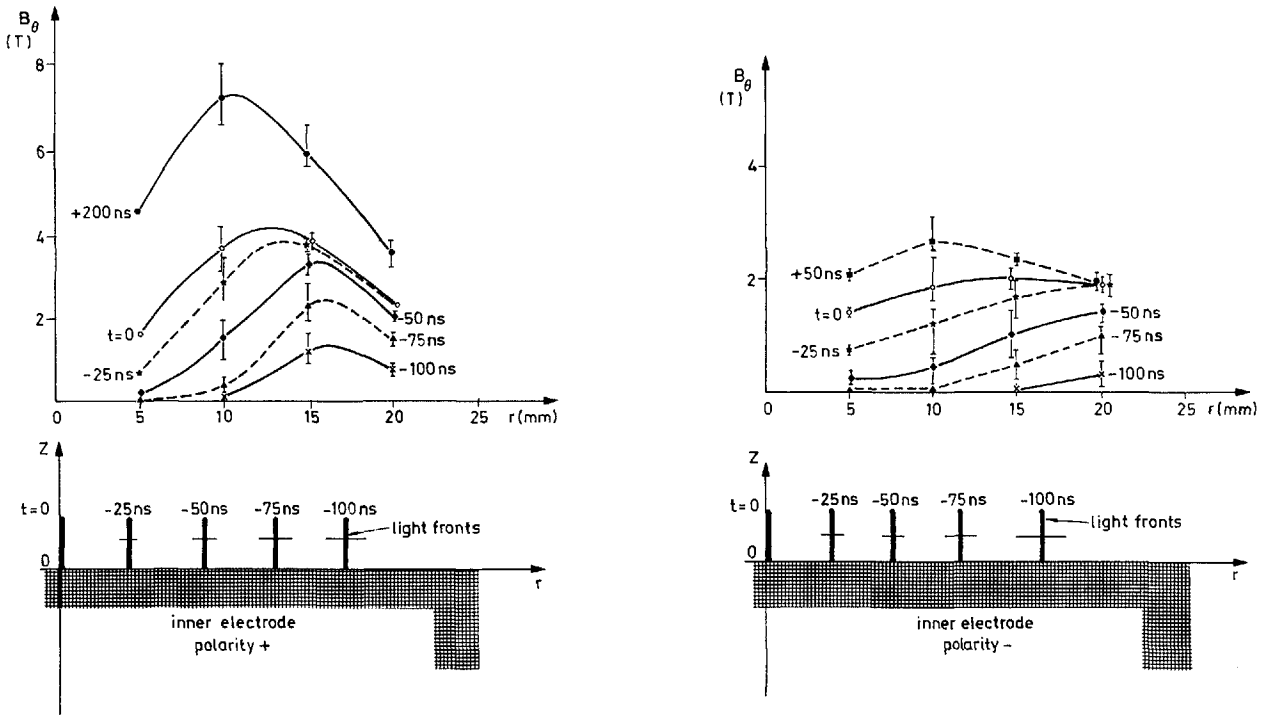


FIG.3. Magnetic induction distribution during the radial compression: $t = 0$ corresponds to the focusing of the luminous sheath to the z-axis.

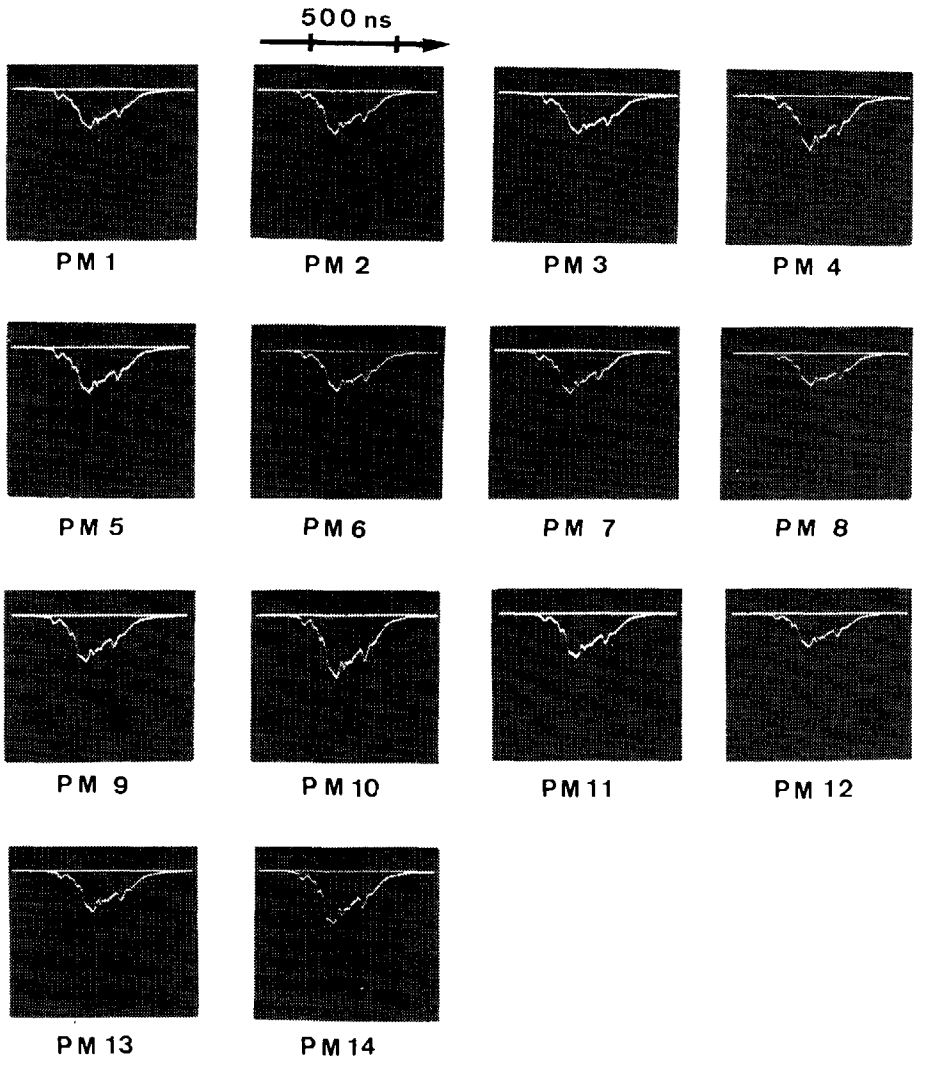


FIG.4. Oscillograms of the X-ray signals obtained at 5 torr of hydrogen with a copper anode. The detectors are not filtered. The good isotropy of the emission should be noted.

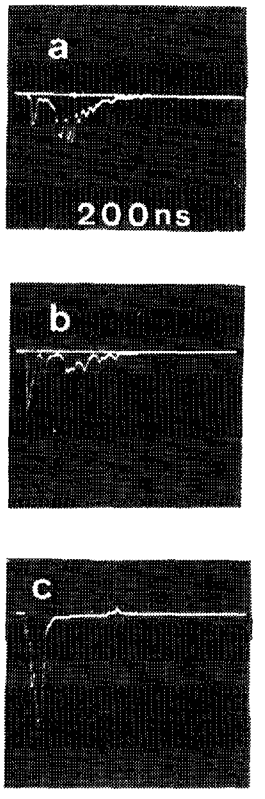


FIG.5. Signals obtained with an anode equipped with a patch of Cu-Ni-W alloy.
a) 2 torr of H_2, hemispheric end;
b) 1 torr of H_2, hemispheric end;
c) 1.5 torr of H_2, hemispheric end with a cylindrical mouth-piece.

Studies of the radial compression phase are in progress at present for this 40 kV-experiment. Figure 3 shows the results obtained for an experiment fed by a bank of 27 kJ at 20 kV. From time-integrated probe signals obtained at different positions we can draw the mean radial distribution of the magnetic induction at different times. We see (Fig.3) that the magnetic induction continues to grow after the focusing of the luminous sheath while the maximum remains at a radius of 12 mm. This indicates that there is no focusing on small radii of the greatest part of the shifted current. For negative polarity, we observe a magnetic induction half of that measured for positive polarity. For this experiment (27 kJ, 20 kV), the mean maximum maximum resistance is found to be 150 kΩ for positive operation and generally one fifth of this value for negative operation.

3. ELECTRON BEAMS AND X-RAYS

The X-ray emission was studied on a 27 kJ – 40 kV experiment where both form and nature of the anode and the initial hydrogen pressure were varied. The X-ray emission can be

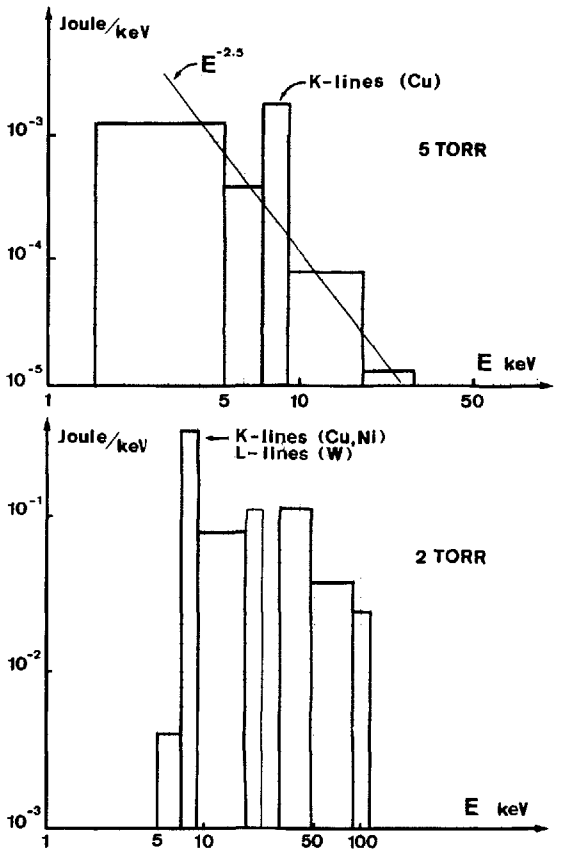


FIG.6. (top) Spectrum at 5 torr of H_2, with copper anode, observation at 90° to the electrode axis. (bottom) Spectrum at 2 torr of H_2, anode with a patch of Cu-Ni-W alloy, observation at 55°.

observed in three directions: at 90°, 55° or 20° relative to the electrode axis; in one of these directions 14 detectors provided with adjustable collimators allow us to analyse the energy spectrum of the X-ray photons by means of the Ross filter method. Each detector consists of an inlet window, a thin beryllium membrane, and a scintillator connected with a fast photomultiplier. The set of the detection chain has a rise-time below 1.5 ns and is linear on an intensity scale of 10^4.

Observing successively the plasma (the electrode being outside the field) and afterwards the end of the electrode in the region where it suffers erosion, we found the X-ray emission from the plasma to be negligible compared with that resulting from the interaction between electrons and anode.

The influence of pressure is considerable, not only on the X-ray intensity but also on the spectral distribution and its development with time. The oscillograms shown in Fig.4 permit a relative calibration of the 14 detectors. By their similarity, the signals received at 5 torr showed that the emission was axially symmetric; the duration which reaches 300 ns, on the average, is also to be noted.

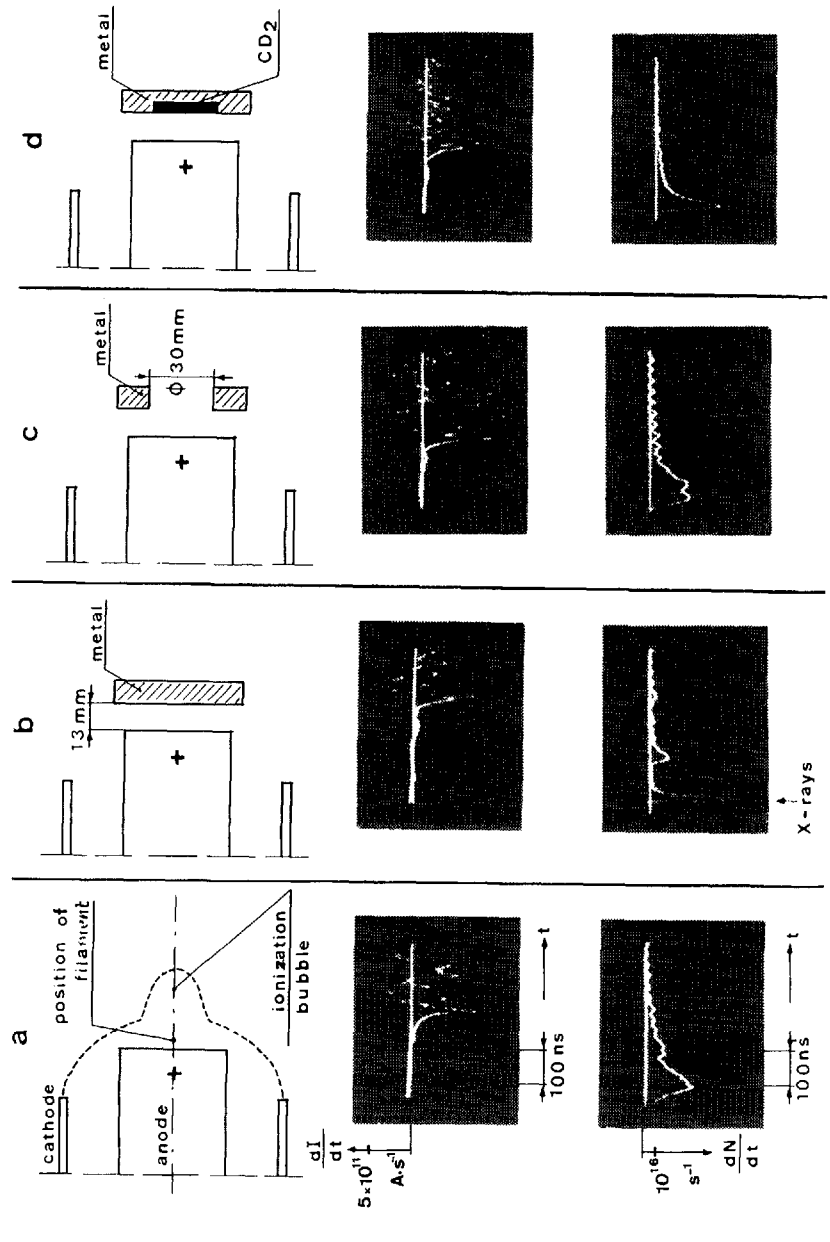


FIG. 7. Time derivative of current (upper row) and neutron pulse (lower row) without time correspondence between the two rows (in b the pulse of hard X-rays is also seen). The initial pressure was 1.5 torr of D_2. The mean number of neutrons is (a) 3×10^9, (b) 5×10^8, (c) 3×10^9, and (d) 2.5×10^9.

At lower pressures the emission is observed to become stronger and its total duration decreases while peaks appear which are narrower than 50 ns. The three oscillograms of Fig.5 illustrate this development at low pressure. Moreover, the oscillogram (c) shows the influence of the anode geometry. In this case at the hemispherical end of a copper electrode (diameter 50 mm), a Cu-Ni-W bar (93% W) was inserted; its diameter was 6 mm and its length 10 mm. This type of mouth-piece plays an important role because of its nature (high Z) in the efficiency of the interaction, and because of its shape, in the focusing of the electron beam; the X-ray pulse is thus often concentrated to a single and very intense peak which is yet narrower, about 20 ns.

At every shot the use of 14 detectors in pairwise arrangement and provided with suitably equilibrated filters makes it possible to obtain the spectrum in 7 energy bands. It is necessary to stress the perfect time resolution of the system of detection, and also the fact that the absolute calibration of the detectors allows us to measure the total X-ray energy emitted in all the spectral bands observed.

Figure 6 shows two types of spectra obtained at 5 and 2 torr with a reduced number of bands. In the 5-torr spectrum we plotted the curve of $E^{-2.5}$ which is in good agreement with experiment at high energies. These spectra show clearly that the radiated energy grows as the pressure is reduced, and that the spectrum is shifted towards higher energies which proves the presence of electrons accelerated up to energies above 100 keV. Moreover, in the energy band between 7.1 and 9 keV a maximum is observed which corresponds to the principal K-lines of copper and nickel and the L-lines of tungsten.

4. DEUTERON BEAMS AND TARGET BOMBARDMENT

In Mather-type experiments, the fast deuterons give rise to an ionization bubble [1] and, simultaneously, to nuclear fusion reactions when bombarding the deuterium contained in the chamber. With the apparatus described in Section 2, we performed experiments in which we used obstacles and targets in order to detect the deuteron beam. In normal operation, Fig.7a, the neutron emission amounts to $N = 3 \times 10^9$ at a pressure of 1.5 torr (low pressure). When a metallic plate is placed 13 mm off the end of the anode, the singularity of the current derivative remains virtually unchanged, Fig.7b, but N decreases (to 5×10^8) and so does the half-width of the dN/dt curve. If the plate has a hole 30 mm in diameter, Fig.7c, we have the results of case a again. This experiment shows that the filling gas contained between the anode and the rear chamber wall (300 mm), which is passed through by the ionization wave, represents a gaseous target in which the deuteron beam, in this case, generates 80% of the neutrons at 1.5 torr. This gaseous target must be considered to be thick for the component of the deuteron distribution which generates the main part of neutrons. Actually, when displacing the metallic plate, we could verify that most of the neutrons are generated within the first 55 mm, while, in the case of a thin target, the neutron production would be uniform throughout the chamber.

We replaced the gaseous target by a solid one of CD_2, 5 mm thick and 30 mm in diameter, inserted into the metallic plate, Fig.7d. In case d, N is 5 times the value of case b and dN/dt is twice as high as in the cases a and c. With a CD_2 target, when its stopping cross-section and the target deuteron density are taken into account, the bombardment as well as the nuclear reactions take place within a very thin layer and, consequently, in a negligible time; there is no artificial prolongation of the neutron emission due to the propagation time of the deuterons in the target. The duration of the neutron emission is then identical with the duration of the deuteron beam.

For an initial pressure of 1.5 torr we have an average neutron yield of 2.5×10^9 with the CD_2 target by D(d,n)He reactions, Fig.7d, and a very similar yield when a D_2 target is used. It is shown [4] that the thick-target neutron yield of a deuteron target is smaller in CD_2 than in D_2.

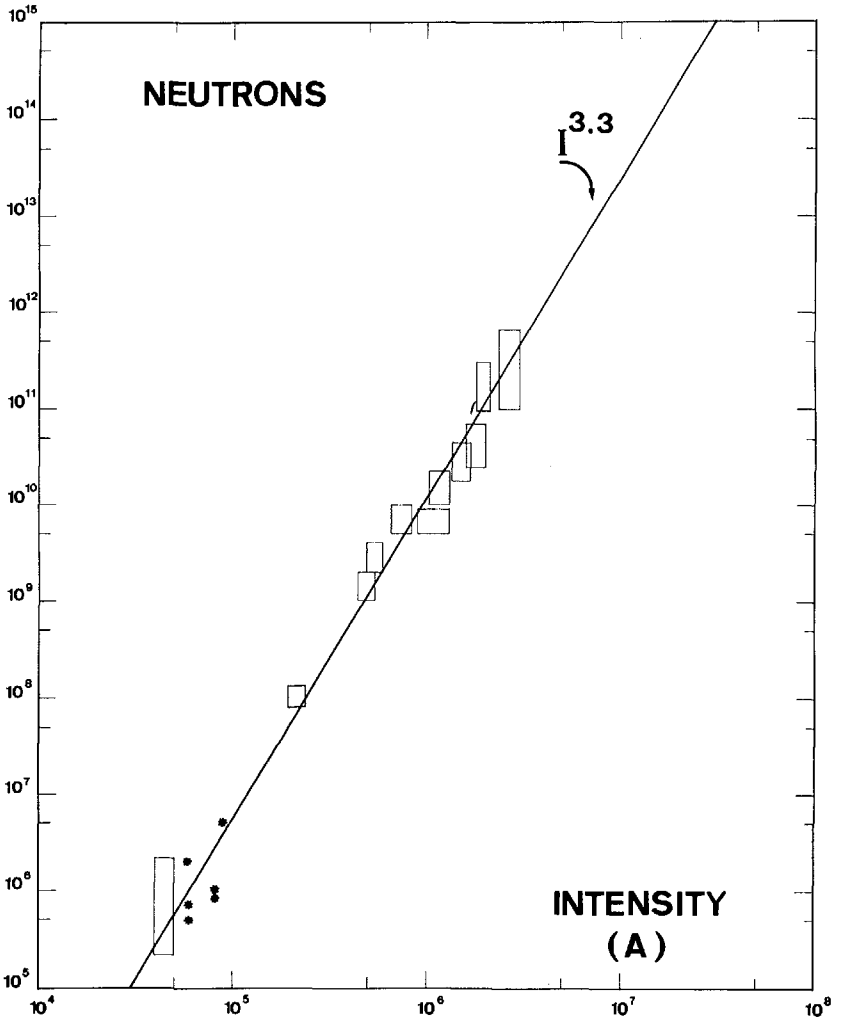


FIG. 8. Extrapolation of the neutron emission as a function of the current.

TABLE I. CALCULATIONS FOR QUANTITIES CORRESPONDING TO SIMPLE ELECTRICAL DIAGRAM

Device		Number of neutrons	I_M	I_p	I_m	V_p	$V_p I_p$	$V_p I_p^{-1}$
Energy kJ	Voltage kV		kA	kA	10^{11} A·s^{-1}	kV	W	Ω
0.44	40	8×10^5	43	41	0.4	15	6.15×10^8	0.37
3.28	40	10^8	215	195	5.5	83	1.6×10^{10}	0.43
27	40	5×10^9	530	520	8	110	5.7×10^{10}	0.21
191	30	1.2×10^{11}	1960	1470	78	430	6.3×10^{11}	0.29
340	40	6×10^{11}	2550	1920	83	520	10^{12}	0.27

The nuclear reactions observed in CD_2 (case d) have then to be attributed to a high-energy component (E > 600 keV) of deuterons that generate only few neutrons in the gas (case c), which, at these energies, represents a thin target.

These experiments confirm the importance to be attributed to the bombardment of gas by a fast deuteron beam. The use of a CD_2 target makes it possible to know the duration of the beam. The Focus experiment thus represents a source of intense ion beams providing easy access to irradiation of various targets.

5. GENERAL CHARACTERISTICS OF PHENOMENA OBSERVED FROM 40 TO 2500 kA

It is well known, at present, that, in comparing various experiments of the 'Focus' type, the value of the electric current at the moment of interaction is a fundamental parameter. In the following we shall denote by I_M the total current circulating in the tube at the beginning of the singularity and by I_p the current when the singularity has reached its maximum. To verify the scope of the phenomena, it was tried to extend the range of operation towards low values of I_M. The lowest point was obtained under the following conditions: capacity 0.55 μF, voltage 40 kV, stray inductance 360 nH, hollow inner electrode 5 mm in diameter, 100 mm long, the length comprising the pyrex insulating sleeve, outer electrode consisting of parallel bars with a mean diameter of 40 mm. Operation is optimum if the initial pressure is 2 torr of deuterium. Then $I_M = 43$ kA and the mean neutron emission is $N = 8 \times 10^5$ neutrons per shot.

Let us now examine the experiments performed at Limeil, where, at present, I_M ranges from 43 to 2550 kA. In Fig.8 the quantity N is plotted as a function of I_M. The slope of the straight line compatible with these points shows that N grows in proportion to $I_M^{3,3}$. The stars on this curve correspond to measurements performed not in a 'Focus' discharge but in a Z-pinch experiment of non-cylindrical symmetry [5]. It seems, then, that we are confronted with a very general phenomenon for which N varies over six orders of magnitude.

Because of the large range investigated it is interesting to carry out some order-of-magnitude calculations for quantities corresponding to a simple electrical diagram. In Table I, we give for each mode of operation I_M, I_p, $\dot{I}_m$, the extremum of the current derivative, the maximum value of the pinch voltage defined as $V_p = V_c - L_c \dot{I}$ (V_c is the voltage across the gun and L_c is the gun inductance assumed constant during the singularity).

$V_p I_p$ represents the maximum power of the machine. It is worth noting the high powers obtained with rather modest energy banks. We also see that the maximum impedance $V_m I_m^{-1}$ varies little for all these machines.

6. CONCLUSIONS

In the Focus machines, breakdown and current propagation appear to be much more complex than had been imagined before and even the concept of a unique front must be given up. In this paper, we are just beginning to become familiar with the fine structure of the sheath. This knowledge is important for an understanding of the energy transfer phenomena at the moment of the singularity and for the determination of the parameters to be chosen in the case of an extrapolation at a high level.

As in the intensity measurements of the laser light scattered by the plasma [2], we see that the filling pressure which determines the quantity of matter present in the filament at the instant of the singularity, is a fundamental parameter in the X-ray emission and in the interaction between the deuteron beam and a deuterated target. The micro-instabilities which give rise to the anomalous density fluctuations are experimentally well linked with the particle accelerations.

The time characteristics of the deuterium beam were determined and it was shown that it is possible to let them interact with targets placed very close to the anode.

The characteristic facts of the Focus experiment occur in a very large current (or energy) range and the observation already made in the past that the number of neutrons grows faster than the stored energy is confirmed. The size of this range as well as the good agreement obtained with another experiment, also of the Z-pinch type, as regards the neutron emission, shows that the physical mechanisms concerned is very general and is, possibly, to be connected with the fact that the plasma impedance at the moment of singularity remains unchanged. All these results are promising as regards an extrapolation to higher current strengths.

REFERENCES

[1] BERNARD, A., COUDEVILLE, A., JOLAS, A., LAUNSPACH, J., de MASCUREAU, J., Phys. Fluids 18 (1975) 180.

[2] BERNARD, A., COUDEVILLE, A., GARÇONNET, J.P., GENTA, P., JOLAS, A., LANDURE, Y., de MASCUREAU, J., NAZET, C., VEZIN, R., in Plasma Physics and Controlled Nuclear Fusion Research (Proc. 5th Int. Conf. Tokyo, 1974) 3, IAEA, Vienna (1975) 83.

[3] BERNARD, A., in Pulsed High Beta Plasmas (Proc. 3rd Top. Conf. Culham, 1975) Paper C1 (1975) 1; BERNARD, A., JOLAS, A., GARÇONNET, J.P., de MASCUREAU, J., NAZET, C., COUDEVILLE, A., BEKIARIAN, A., Commissariat à l'Energie Atomique, France, Note No. 268/76 (1976).

[4] BERNARD, A., COUDEVILLE, A., GARÇONNET, J.P., JOLAS, A., de MASCUREAU, J., NAZET, C., Commissariat à l'Energie Atomique, France, Note No. 1945 (9.11.1976).

[5] WATTEAU, J.P., Commissariat à l'Energie Atomique, France, Report CEA-R-3523 (1968).

EXPERIMENTAL VERIFICATION OF A THEORY OF THE CURRENT SHEATH IN THE PLASMA FOCUS

M. VARGAS, F. GRATTON*, J. GRATTON*,
H. BRUZZONE, H. KELLY
Laboratorio de Física del Plasma,
Facultad de Ciencias Exactas y Naturales,
Universidad de Buenos Aires,
y
Dirección General de Investigación y Desarrollo,
Ministerio de Defensa,
Buenos Aires,
Argentina

Abstract

EXPERIMENTAL VERIFICATION OF A THEORY OF THE CURRENT SHEATH IN THE PLASMA FOCUS.

An axisymmetric model for the kinematics of the current sheath which, combined with the circuit equation, gives complete analytical solutions, was tested in a small plasma focus. Optical and electrical methods were employed to determine the shape, positions and times of the current sheath evolution. In the ordinary range of working pressures, changing the external inductance from 130 nH to 33 nH, and from statistics of a large number of shots, it was found that the theory gives a satisfactory account of the kinematical and electrical properties.

A theory of the current sheath (CS) evolution consisting,briefly, of a snow-plough axisymmetric model where the CS motion is treated like that of an ideal mathematical surface [1, 2], was tested by experiments. The theory leads to a partial differential equation for the CS profile in the z, r plane of the device (see Fig. 1) which is solved by the method of characteristics. An interesting feature of this model is that the CS kinematics coupled with the electric circuit (with variable self-inductance of the plasma, L(t)) have solutions represented by analytical formulae. Improvements of the theory including CS structure effects are given in the next paper [3].

The experiments were performed with a low-energy plasma focus with a hollow inner electrode ($V_0 = 13-17$ kV; $C = 6\ \mu$F; $L_0 = 33$ nH (for sizes see Fig. 1)). The outer electrode was suppressed and a back collector plate inserted to permit the return of the current,I. Thus lateral image converter photographs could be obtained and the real CS profile compared with the model. The CS kinematics was determined by two methods:

(a) From photographs taken at recorded times t_e, the measurement of the CS position z at $r = R_1$ gives the parameter

$$\tau = a \int_0^t I\, dt/CV_0 = 2z_1/R_1$$

* Member of Consejo Nacional de Investigaciones Científicas y Técnicas, Argentina (CONICET).

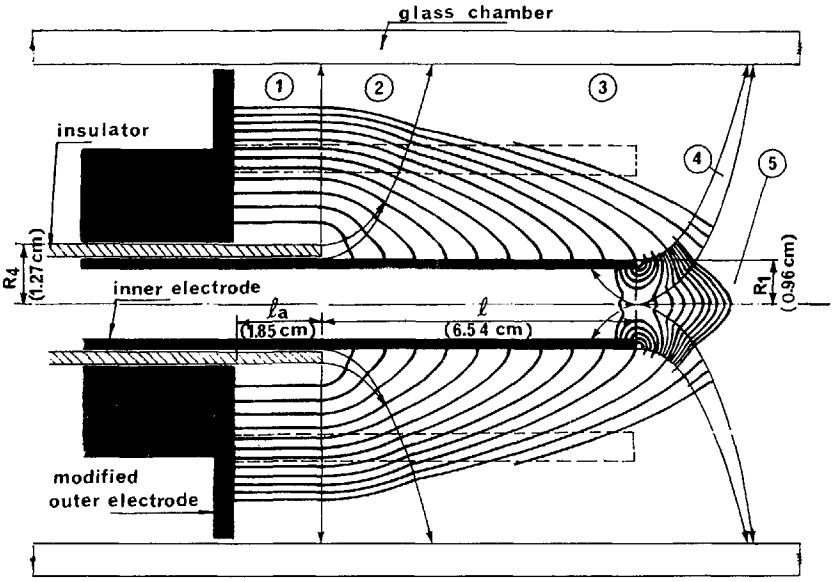


FIG.1. Evolution of current sheath according to the model.

which together with the values of the (non-dimensional) numbers

$$a = 2CV_0/R_1^2\ (2\pi\rho_0)^{\frac{1}{2}} \quad , \quad \lambda = L(t)/L_0$$

where ρ_0 is gas filling density, allows a computation of the time t_t (when CS reaches z_1) predicted by the theory.

(b) The lateral image of the electrode is formed by the optics of a 35-mm camera on a metal plate with a row of pin-holes. The passage of the CS front consecutively illuminates the holes and a photomultiplier allows a recording of the time t_e. A comparison with t_t is performed as in (a) by computing z_1 from the known position of the holes.

Observations were made varying $P_0 = 0.2-0.3$ torr, $L_0 = 33-130$ nH, $V_0 = 13-17$ kV, in D_2, argon and air. From many photographs we confirmed a general agreement between the CS shape and the model (Figs 1 and 2). The theory of characteristics allows for a natural division of the CS motion in zones which appear in the photographs: divergent pinch on the insulator (1); travelling profile along the electrode (3); roll-off at the electrode edge (4). Note the change in slope in correspondence with the insulator edge zone (2). The pinch column formation is not predicted by the zero-thickness model and it must be inserted ad hoc in the theory. The "bubble" (5), which is accounted for in the model, starts in the photographs at a position on the axis shifted with respect to the electrode end. A careful verification of the CS shape in argon and air (averaged on 130 shots $P_0 = 1-2$ torr, at 33 nH and 130 nH) fits remarkably well with the model in regions (1) to (3). Yet in D_2 (about 100 shots) the real profile stands slightly more erect on the electrode than the theoretical one. The difference could be explained by the structure corrections treated in Ref.[3] which predict this effect. The corrections in shape simultaneously comprise a decrease

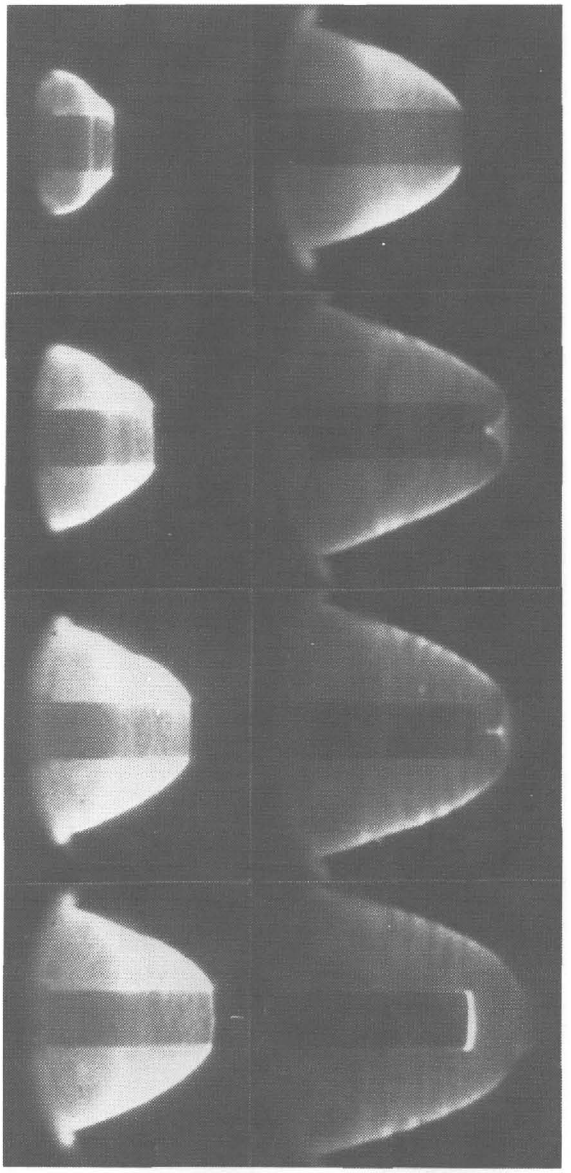


FIG. 2. Sequence of photographs showing stages of current sheath motion. Left-hand side: Argon, 0.6 torr; Right-hand side: Air, 0.4 torr.

TABLE I. t_e VERSUS t_t CORRELATIONS
(at $V_0 = 17$ kV; $P_0 = 0.2$–0.3 torr; $L_0 = 33$ nH); least-square parameters: $t_e = mt_t + b$.

Method		Deuterium[a]		Argon		Air	
		A	B	A	B	A	B
n:	number of data	46	22(X 7)	21	19(X 7)	15	6(X 10)
m:	slope	1.2	1.12	0.97	0.91	0.92	0.92
b:	intercept	0.120	0.182	0.190	0.350	0.150	0.300
r:	correlation coefficient	0.98	0.98	0.89	0.92	0.96	0.92
s_m:	standard deviation of m	0.04	0.04	0.11	0.09	0.07	0.06
s_b:	standard deviation of b	0.005	0.006	0.025	0.021	0.020	0.010

[a] With 0.6% O_2 + 2.18% N_2 in volume.

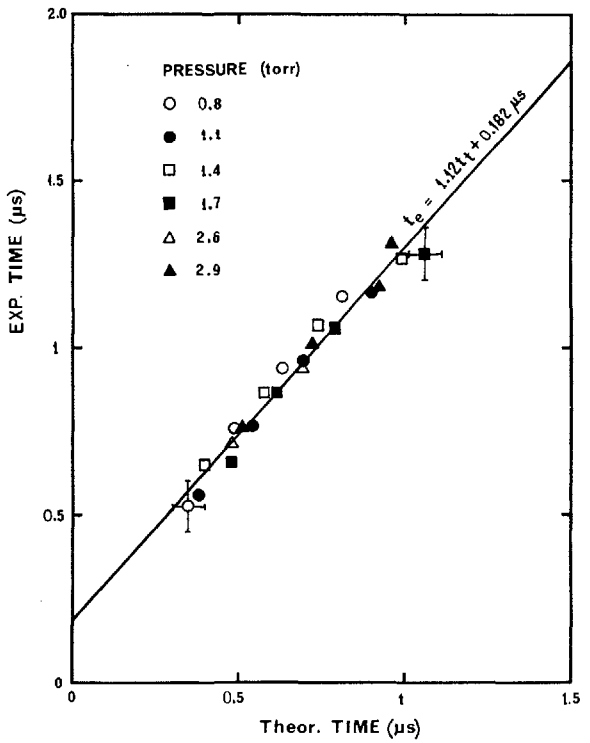


FIG. 3. Comparison between theoretical and experimental times for deuterium.

of the CS velocity (compared with the zero-thickness theory). The measurements in D_2 confirm this fact (see Table I). In Fig.3, t_e (obtained by method (b)) versus t_t is shown as an example at 33 nH ($P_0 = 0.2-0.3$ torr; $V_0 = 17$ kV). The correlation is excellent. The least-square line is $t_e = (1.12 \pm 0.04)\, t_t + (0.182 \pm 0.006)$ μs. On the assumption that the difference in the slope is all due to structure effects (and thus disregarding systematic errors) a CS velocity 16% smaller would be required. This corresponds to the case $F = -1/12$ of Ref.[3]. The initial delay of about 200 ns is significant and we interpret it as due to a transitory initial stage where ionization, formation of the CS and acceleration occur. The starting time for the model is thus delayed with respect to the switching time of the apparatus. We found a similar retardation comparing the focus time given by the $\dot{I}$ peak and the theoretical time for the same event as a function of the pressure ($P_0 = 1-3$ torr, D_2, averaging 200 shots). The correlation was found adequate if a constant initial time of 200 ns was added to t_t. Table I also contains results of time comparison for argon and air that provide convincing support, within experimental error, to the (zero-thickness) theory. For a change, at the high value of 130 nH, statistics of 25 shots in D_2 ($V_0 = 13-16$ kV; $P_0 = 0.85-2.7$ torr) gave $t_e = (1.10 \pm 0.04)\, t_t + (0.02 \pm 0.01)$ μs and $r = 0.99$, which is quite satisfactory.

We conclude that the model is reliable in its kinematical and electrical aspects in the ordinary working range of pressures of our device.

ACKNOWLEDGEMENTS

We are grateful to the Stevens group for their constant support. A grant from the Argentinian CONICET has contributed in part to this research.

REFERENCES

[1] GRATTON, F., VARGAS, M., Proc. 7th Europ. Conf. Controlled Fusion and Plasma Physics, Lausanne (1975) 64; and in High-Beta Plasmas (EVANS, D.E., Ed.) Pergamon, Oxford (1976).

[2] VARGAS, M., "Un modelo bidimensional analítico para el plasma focus", Physics Seminar, Facultad de Ciencias Exactas y Naturales, Buenos Aires (April 1976).

[3] GRATTON, F., VARGAS, M., Paper IAEA-CN-35/E18-5(b), these Proceedings.

MAGNETIC TENSION AND THICKNESS IN THE CURRENT SHEATH DYNAMICS

F. GRATTON*, M. VARGAS
Laboratorio de Física del Plasma,
Facultad de Ciencias Exactas y Naturales,
Universidad de Buenos Aires
y
Dirección General de Investigación y Desarrollo,
Ministerio de Defensa,
Buenos Aires,
Argentina

Abstract

MAGNETIC TENSION AND THICKNESS IN THE CURRENT SHEATH DYNAMICS.

A theory of the current sheath dynamics for a plasma focus including finite thickness effects is briefly communicated. Inner radial magnetic fields related to the filamentary structure are shown to be necessary for the sheath stability. The theory allows for analytic solutions in the stationary coaxial stage giving the slope and velocity of the sheath.

A set of equations which include finite thickness effects for the (axisymmetric, time-dependent) current sheath (CS) dynamics for a plasma focus has been derived. The physical magnitudes are averaged through the CS structure. Inner radial magnetic fields B_t are taken into account and it can be shown that they play an important role in the CS stability. These fields, measured by several authors, are associated with the observed filamentary fine structure of the CS [1].

The CS profile in the z,r plane of the device is given by $\zeta = \zeta(x, \tau)$ where $\zeta = z/R_1$, $x = r/R_1$ and

$$\tau = 2\int_0^t u_1(t)dt/R_1 \qquad u_1 = I(t)/R_1(2\pi\rho_0)^{\frac{1}{2}}$$

(I is the current in e.m.u.; R_1 is the inner electrode radius; and ρ_0 is the gas filling density) as in Ref.[2]. Neglecting acceleration effects, the quantity

$$f(t) = (\langle \rho_i v_t^2 \rangle + \langle p_i \rangle + \langle B_{\theta i}^2 \rangle/8\pi - \langle B_t^2 \rangle/8\pi)\, r\delta$$

is shown to be independent of r. Here ρ_i, p_i, $B_{\theta i}$ are internal density, pressure, and azimuthal magnetic field, respectively, and the plasma within the CS (whose thickness is δ) flows towards the outer electrode with velocity v_t. When $\delta = 0$ the model [2] which allows for analytic solutions of the CS motion and electrical circuit is recovered.

An iteration scheme based on the $\delta = 0$ solutions fails near $r = R_1$ due to a non-uniform convergence of the solutions towards the $\delta = 0$ case. For the coaxial stage under the hypothesis that $F = f(t)/\rho_0 u_1^2(t) R_1^2$ is invariant in time, solutions for stationary travelling profiles can be obtained. Letting

$$u = -\sin\varphi = \zeta_x(1 + \zeta_x^2)^{-\frac{1}{2}}$$

---

* Member of Consejo Nacional de Investigaciones Científicas y Técnicas, Argentina (CONICET)

(φ is the angle between the CS normal and the inner electrode),

$$\eta = 2c^2 x^2$$

($c = u/2u_1$, where u is the CS velocity at x = 1), the following equation can be derived:

$$F\, du/d\eta = -(1 - u^2 - 1/2\eta) \tag{1}$$

A linear perturbation stability analysis shows that all the solutions with $F > 0$ are unstable in time. Stability requires negative F, which means dominant magnetic tension in the CS (note that, in computer simulations, artificial viscosity is used to quench numerical instabilities; thus the above effect does not appear). As is widely confirmed in practice, $\varphi = 0$ at $r = R_1$. The presence of the filamentary structure also gives physical support to this boundary condition. Then, for $\eta = 2c^2$, $u = 0$.

The CS velocity is the solution of an eigenvalue problem for Eq.(1) requiring $u \to -1$ for $\eta \to \infty$. Only one profile satisfying the above conditions exists for each $F < 0$ value, determining a related unique eigenvalue $c^*(F)$. When $c \neq c^*$, no physically admissible solution of Eq.(1) can be found. The present eigenvalue problem corresponds to that of the self-similar solutions of the second kind for non-linear partial differential equations which, as is known, are connected to the existence of uniformly propagating regimes with a velocity unknown in advance. It can be shown that the eigenvalue solutions of Eq.(1) for $h = -1/4F$, h a positive integer, are given by:

$$u = -(1 + 2d\,\ell n\, v/dz) \quad , \quad z = 2\eta/F$$

$$v = \sum_{r=0}^{h-1} \binom{h-1}{r} z^{h-r}/(h-r)! \tag{2}$$

The condition $u = 0$ for $z = 4c^2/F < 0$ determines c as the real root of maximum modulus of the polynomial equation which ensues. The first values are: $h = 1$; $F = -1/4$; $c = 0.3535$; $h = 2$; $F = -1/8$; $c = 0.4045$; $h = 3$; $F = -1/12$; $c = 0.4261$. As $F \to 0$, $c \to 1/2$ as given by the zero-thickness theory [2]. Compared with the $\delta = 0$ model, for negative F we have smaller CS velocities; the radius of curvature at the inner electrode $R_c = -F/(4c^2 - 1)$ is different from zero, and thus the CS profiles stand more erect on the electrode.

ACKNOWLEDGEMENTS

Thanks are due to Dr. V. Nardi for his kind interest in our work. Helpful discussions with Dr. C. Ferro Fontán are gratefully acknowledged.

REFERENCES

[1] NARDI, V., Phys. Rev. Lett. **25** (1970) 718(c) and literature quoted therein.
[2] GRATTON, F., VARGAS, M., Proc. 7th Europ. Conf. Controlled Fusion and Plasma Physics, Lausanne (1975) 64; and High-Beta Plasmas, (EVANS, D.E., Ed.), Pergamon, Oxford (1976).

SOME PROPERTIES OF THE NEUTRON YIELD IN A LOW-ENERGY PLASMA FOCUS

H. BRUZZONE, R. DELELLIS, R. GRATTON*, H. KELLY,
M. MILANESE, J. POUZO
Laboratorio de Física del Plasma,
Facultad de Ciencias Exactas y Naturales,
Universidad de Buenos Aires,
y
Dirección General de Investigación y Desarrollo,
Ministerio de Defensa,
Buenos Aires,
Argentina

Abstract

SOME PROPERTIES OF THE NEUTRON YIELD IN A LOW-ENERGY PLASMA FOCUS.

The measurement is reported of the average neutron yield $\bar{n}$ of a low-energy plasma focus device, as a function of the filling pressure p, for three different values of the external inductance L_0. The variation of $\bar{n}$ in successive shots performed with the same gas is investigated. Data on reproducibility are given.

EXPERIMENTAL RESULTS

We measured the neutron yield in a small Mather-type plasma focus ($C = 6\ \mu F$; $V_0 = 17$ kV; $E_0 = 0.867$ kJ; $r_i = 0.95$ cm; $r_e = 2.7$ cm) for three different combinations of external inductance L_0 and electrode length ℓ:

(a) $L_0 = 51$ nH; $\ell = 10.3$ cm
(b) $L_0 = 43$ nH; $\ell = 10.3$ cm
(c) $L_0 = 33$ nH; $\ell = 8.8$ cm

The detector employed was an activation counter similar to the one described in Ref. [1]. More than 300 shots have been performed for each set of parameters, the gas being renewed after sequences of five shots.

In Fig. 1 we report the average neutron yield $\bar{n}$ taking into account only the first discharges in each sequence. In Fig. 2 we compare $\bar{n}$ calculated as described before with the value of $\bar{n}$ obtained from the subsequent shots for configuration c. The bars represent the mean square dispersion. Configurations a and b show analogous behaviour and present similar relative dispersion (of the order of 30%).

In each sequence we observed an increase of the pressure ranging from 0.05 torr to 0.4 torr per shot. There is an approximate proportionality between the pressure increase and $\bar{n}$.

---

* Member of Consejo Nacional de Investigaciones Científicas y Técnicas, Argentina (CONICET)

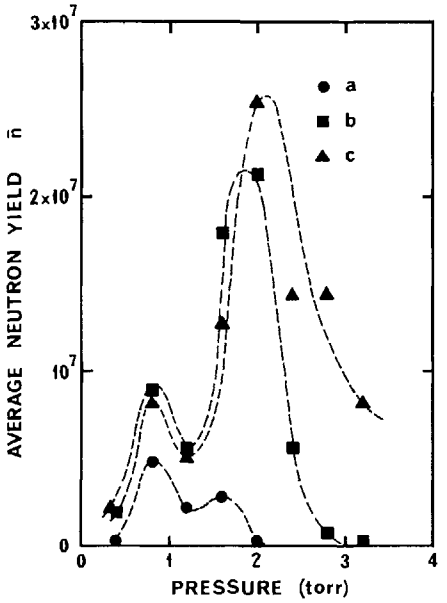


FIG. 1. $\bar{n}$ versus p for (a) $L_0 = 51$ nH, $\ell = 10.3$ cm; (b) $L_0 = 43$ nH, $\ell = 10.3$ cm; (c) $L_0 = 33$ nH; $\ell = 8.8$ cm.

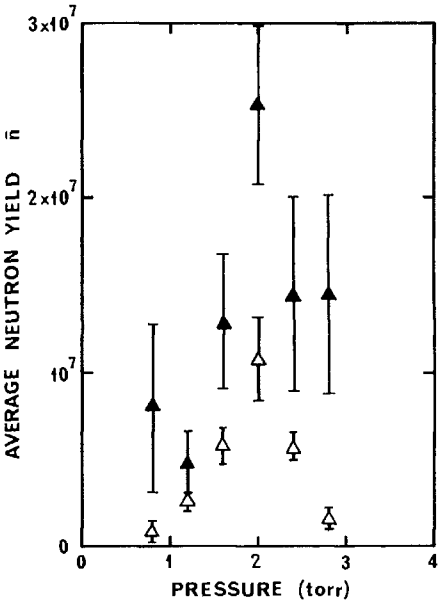


FIG. 2. $\bar{n}$ versus p for $L_0 = 33$ nH; $\ell = 8.8$ cm.
▲: average neutron yield calculated with first shots;
△: average neutron yield calculated with subsequent shots.

COMMENTS

The results reported in Fig.1 show two maxima of $\bar{n}$ as a function of the filling pressure. The change of the parameters of the device from configuration a to c leads to a considerable increase of $\bar{n}$, probably due to the decrease of L_0; furthermore, the position of the "high pressure" maximum seems to shift to the right, and, as a general fact, the increase of $\bar{n}$ is more pronounced in the high-pressure region.

The values of $\bar{n}$ obtained in this work agree reasonably well with those reported in Ref.[2] for a similar device (with lower external inductance), thus confirming that the neutron yield in small plasma focus is considerably higher than those predicted by the scaling law $\bar{n} \sim E_0^2$ based on larger devices. On the other hand, our device shows a high dispersion in the neutron yield (in some shots the neutron yield exceeded the average value by about an order of magnitude).

ACKNOWLEDGEMENTS

This work was in part supported by the Consejo Nacional de Investigaciones Científicas y Técnicas and was under the auspices of the Comisión Nacional de Energía Atómica.

REFERENCES

[1] HUDDLESTONE, R.H., LEONARD, S.L., Plasma Diagnostic Techniques, Academic Press, New York (1965) Ch. 12, p. 569.

[2] MICHEL, L., SCHONBACH, K., FISCHER, H., Appl. Phys. Lett. **24** (1974) 57.

DISCUSSION

ON PAPERS IAEA-CN-35/E 18–1, E 18–2, E 18–3, E 18–4, E 18–5

W.H. BOSTICK: I should like to make a comment which relates not only to these papers but also to paper IAEA-CN-35/H 4 presented by Mr. Sudan at the last session. The deuteron beams produced by even a small plasma focus (~ 10 kJ) can be estimated to carry about 100 kA of current with energies of ~ 10 keV to 1 MeV. The duration of production of each beam is $\leqslant$ 5 ns, and there can be several beams per shot.

SPACE-TIME STRUCTURE OF NEUTRON AND X-RAY SOURCES IN A PLASMA FOCUS*

W.H. BOSTICK[+], V. NARDI[+§], W. PRIOR[+§]

[+] Stevens Institute of Technology,
Hoboken, New Jersey,
United States of America

[§] Istituto Elettrotecnico Nazionale Galileo Ferraris,
Torino,
Italy

Abstract

SPACE-TIME STRUCTURE OF NEUTRON AND X-RAY SOURCES IN A PLASMA FOCUS.

Systematic measurements with paraffin collimators of the neutron emission intensity have been completed on a plasma focus with a 15–20 kV capacitor bank (hollow centre electrode; discharge period $T \sim 8\ \mu s$; D_2 filling at 4–8 torr). The space resolution was 1 cm or better. These data indicate that at least 70% of the total neutron yield originates within hot-plasma regions where electron beams and high-energy D beams ($\gtrsim 0.1-1$ MeV) are produced. The neutron source is composed of several ($\gtrsim 1-10$) space-localized sources of different intensity, each with a duration $\lesssim 5$ ns (FWHM). Localized neutron sources and hard ($\gtrsim 100$ keV) X-ray sources have the same time multiplicity and are usually distributed in two groups over a time interval 40–400 ns long. By the mode of operation used by the authors one group of localized sources (Burst II) is observed 200–400 ns after the other group (Burst I) and its space distribution is broader than for Burst I. The maximum intensity of a localized source of neutrons in Burst I is much higher than the maximum intensity in Burst II. Secondary reactions $T(D,n)^4He$ (from the tritium produced only by primary reactions in the same discharge; no tritium was used in filling the discharge chamber) are observed in a time coincidence with the strongest D–D neutron pulse of Burst I. The neutron signal from a localized source with high intensity has a relatively long tail of small amplitude (area tail $\lesssim 0.2 \times$ area peak). This tail can be generated by the D–D reactions of the unconfined part of an ion beam in the cold plasma. Complete elimination of scattered neutrons on the detector was achieved in these measurements.

1. INTRODUCTION

D-ion beams with an ion energy $E \gtrsim 0.1-1$ MeV/deuteron are usually produced in plasma focus discharges with deuterium when fusion reaction occurs. Observations have been made with a variety of diagnostic methods (e.g. analysis of damage on witness plates [1,2], induced $D(^{27}Al,p)^{28}Al$ reactions in an Al witness plate [3], ion-energy magnetic analyser [4]. The directed energy of an ion beam determines the observed anisotropy of the neutron energy spectrum [1,5,6]. The production of a multiplicity of ion beams and of electron beams [7–9] in a single discharge has been related to the observed fine structure of the plasma focus (filamentation of the current sheath, intensity anisotropy of X-ray localized sources within the axial pinch) and specifically to the decay of its filamentary magnetic structure [1,7,9]. The relative amount of D–D reactions occurring in the hot-plasma region and eventually in a cold-plasma region (because of ion beams) is of critical importance in assessing the efficiency of the plasma focus as a neutron source and as a possible fusion-energy source.

* Work supported in part by AFOSR (Washington, DC), CNR (Italy), NATO Scientific Affairs Division (Brussels), AES Inc. (New York), Jersey Central and New Jersey Power and Light Company.

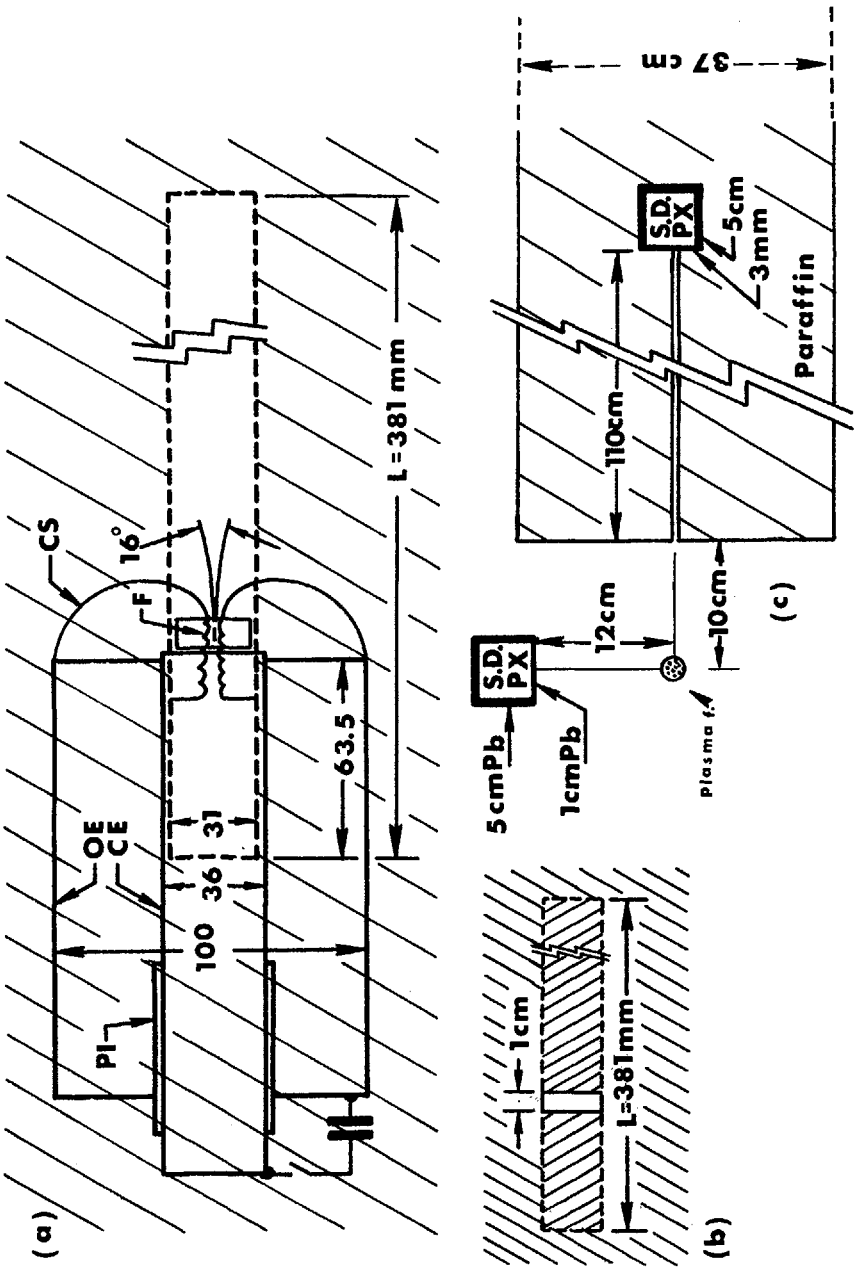


FIG.1. Collimator and plasma focus geometry (lengths are given in mm in the upper part); scintillation detector (SD) and photomultiplier (PX) are in the lead box.

A space-resolved analysis of the neutron source in the plasma focus (with a space resolution of 2.5 cm) indicates that a fraction $> 50\%$ of the neutron emission originates within a hot-plasma column (dia. ~ 25 cm, length ~ 6 cm in a 27-kJ experiment [10]) along the discharge axis. We have made collimated measurements of the neutron intensity (time-resolved) with a space resolution of 1 cm to see whether the sources of the pulsed neutron emission are localized in space to the same extent as space-time-localized X-ray sources can be ($\leqslant 0.5$ mm long, 1–3 ns full width at half maximum (FWHM)).

A clear-cut answer from our data is that indeed the source of a single neutron pulse emitting up to 70% of the total neutron yield (in our plasma focus mode of operation) can be localized within $\lesssim 1$ cm inside the hot-plasma axial column. These data also set an upper limit for the fraction of the neutron yield which can be originated in the cold plasma. Our data are consistent with a beam-cold-plasma emission substantially smaller than 30% of the total yield.

By our mode of operation (low voltage) of the plasma focus, two groups of neutron pulses occur [7,9] as by other experiments at higher voltage and with larger capacitor banks [11]; the first group of neutron pulses (Burst I, from neutron emission onset ($t = 0$) to $t = 80$–100 ns) has in our case a maximum intensity which is usually much higher (by a factor $\gtrsim 2$–10) than the maximum intensity of the second group of pulses (Burst II, at $t \cong 200$–300 ns). If an ion beam is not confined within the hot plasma region, a possible evidence for this non-confinement (via space distribution of the neutron source) should be expected, especially by Burst-I pulses where ion beams with the highest energy are produced preferentially [12].

2. EXPERIMENTS

A 45-μF capacitor bank at 15 kV was used to power our plasma focus with a hollow-centre electrode (anode); the electrode current I on the electrodes (max.$I \cong 0.5$ MA) had a period of 8 ns. A schematic view of plasma focus and paraffin collimators is shown in Fig.1. Two scintillation detectors (circular cylinders of Ne-102; dia. 16 mm, length 50 mm; photomultiplier cathode with the same diameter) for neutrons and X-rays were used in each discharge. For a δ (~ 0 ns)-input the width Δ of the output signal from the whole detector system – signal display by Tektronix 7704 oscilloscopes – was $\Delta \lesssim 5$ ns.

The 381-mm-long paraffin gap parallel to the discharge axis was used for two purposes:

(a) To verify the effectiveness of the paraffin arrangement in eliminating scattered neutrons from the detector. This was done by comparing width and shape of the neutron signal of the detector inside the paraffin with the signal of a detector outside.

(b) To normalize the relative amplitude of the signal from the two detectors in a convenient location for measurements as in Fig.1(c) (respectively at 12 cm and 120 cm in a direction orthogonal to the electrode axis). The amplitude in volts of the neutron signal was made to coincide for non-collimated (i.e. outside the paraffin) and collimated detectors by a convenient choice of the sensitivity of the two detectors. Collimation for 1-cm space resolution was then achieved by reducing the width of the paraffin gap from $L = 381$ mm to $L = 10$ mm. For $L = 10$ mm, only a fraction of the NE-102 circular-front surface (3/5 of the diameter) is exposed to the neutron emission; consequently, the signal amplitude of the collimated detector must be multiplied by a factor 1.4 to regain the same normalization/calibration of the uncollimated-detector signal.

Both NE-102 detector-photomultiplier systems were surrounded by lead walls 5 cm thick on five sides to eliminate scattered X-rays and γ-rays from the signal. The collimated detector was screened in the front direction by 3-mm Pb to have a small-amplitude signal from the hard ($\gtrsim 90$ keV) X-ray pulses, which are emitted at the same time as the neutron pulses of Burst I [9];

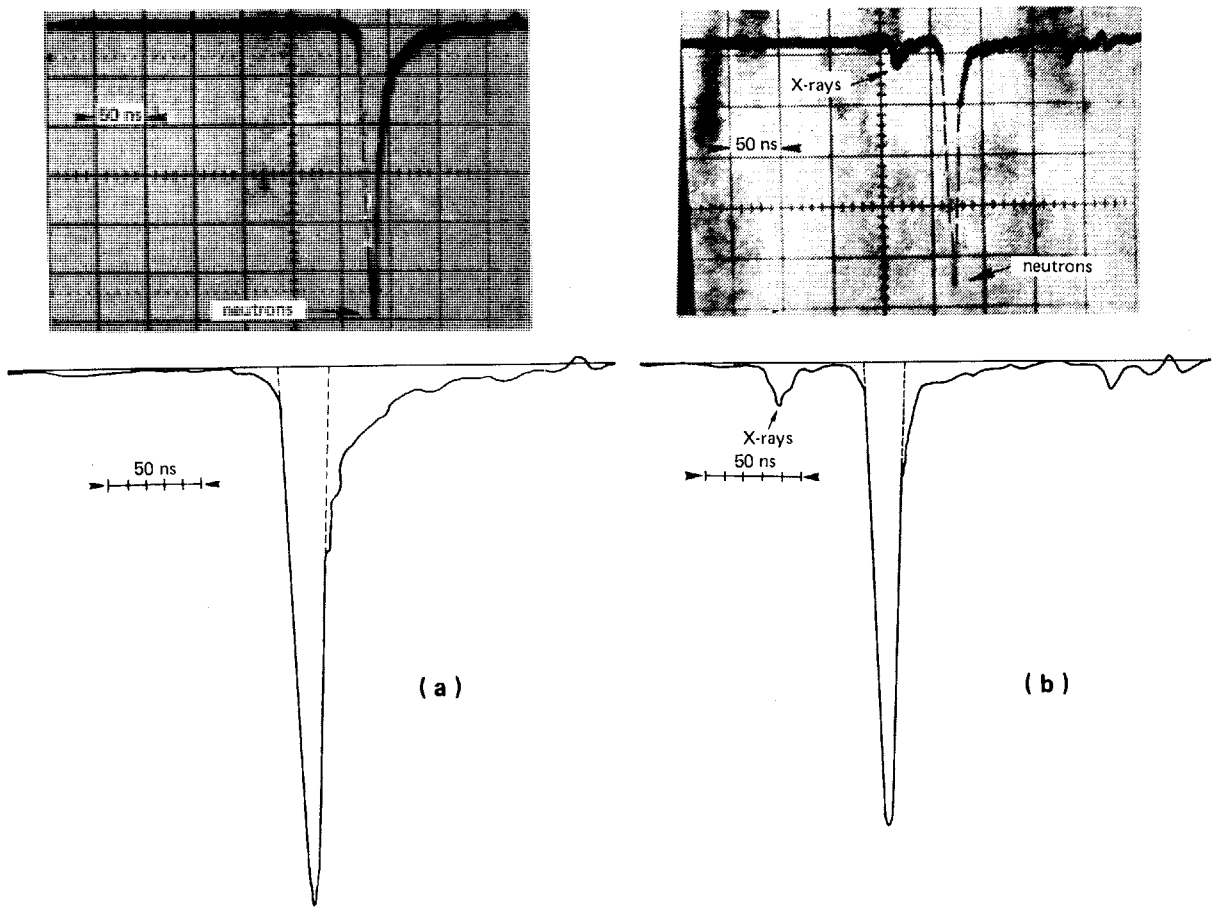


FIG. 2. Scintillation detector signal from (a) uncollimated and (b) collimated detectors (dashed lines separate peak area from tail area). Time increases from left to right (50 ns·cm^{-1}); signal-amplitude scale is 0.2 V·cm^{-1} in (a), 0.1 V·cm^{-1} in (b); the amplitude a_b of the signal in (b) is normalized to the same amplitude scale of (a) by multiplying a_b by the normalization factor $\lambda = 0.7$ (= 1.4/2). Neutron yield in this discharge $n \cong \bar{n} = 10^8$.

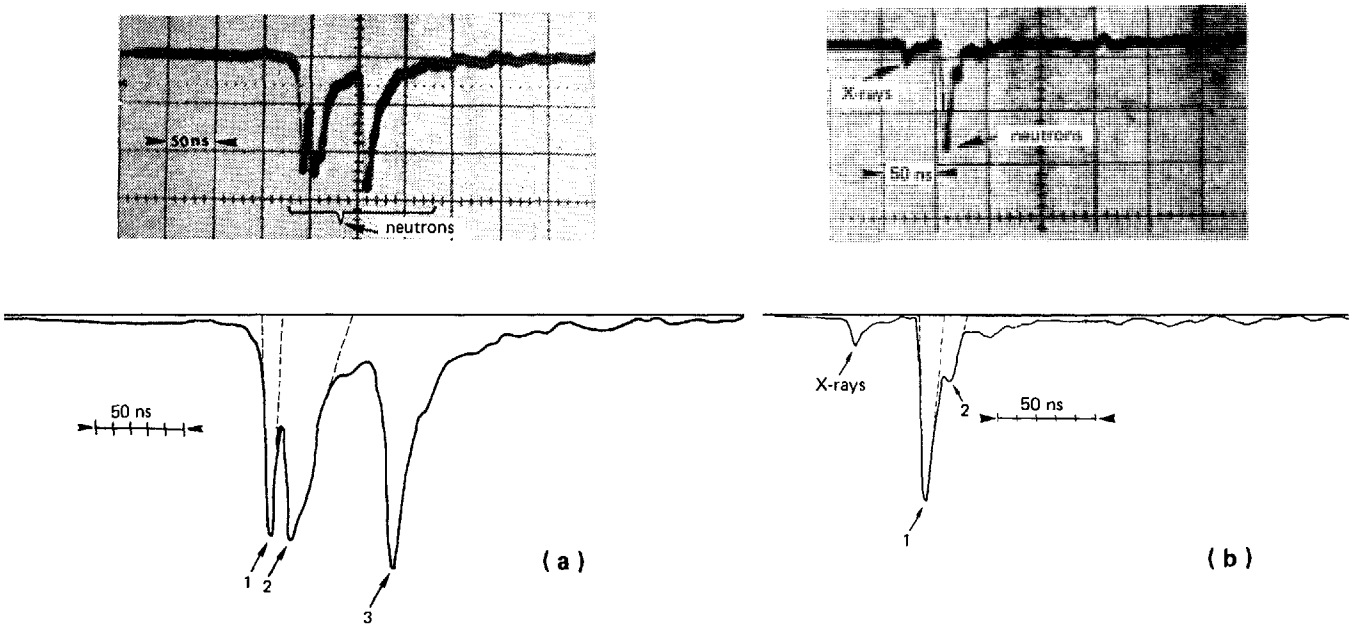


FIG.3. Scintillation detector signals ((a) uncollimated and (b) collimated detectors). Dashed lines indicate the peak resolution used in constructing the histogram of Fig.4(b). Normalization factor signal amplitude in (b) to signal amplitude in (a) is $\lambda = 0.7$. *Neutron yield* $\cong 10^8$.

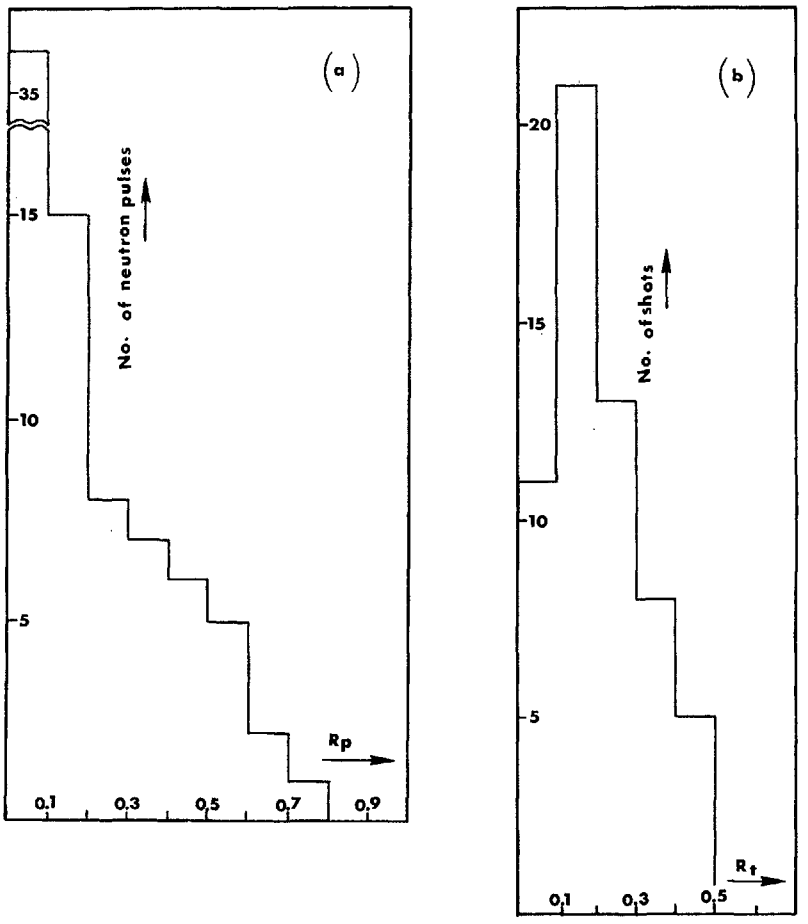


FIG.4. (a) Distribution of resolved neutron pulses (from many discharges) as a function of R_p, the ratio of time-integrated amplitude under a single peak (without tail) for a pair of collimated and uncollimated signals. (b) Distribution of the number of discharges as a function of R_t, the ratio of the time-integrated neutron signal for total emission.

1-cm Pb in front of the other detectors did eliminate from the signal any appreciable contribution from the X-rays at the chosen level of sensitivity of the detectors. The highest peak in the initial small X-ray signal by the collimated detector is used as a time mark (to define the same t = 0 on the signal of both detectors). This is necessary to identify which of the neutron pulses is eventually eliminated because of the collimator. The uniform increase of the total neutron yield versus τ_0^{-1} (τ_0 is the delay between this X-ray peak and the leading edge of the neutron signal) that we have observed [1, 12] by our mode of operation confirms that this initial X-ray peak is a meaningful and reliable time mark; the pulsed emission of 14-MeV neutrons from T(D,n)^{4}He secondary reactions (the tritium is produced by primary reactions in the same discharge; no tritium was used in the filling with pure D_2) coincides with this X-ray peak [9, 12]. The small distance (12 cm) of the non-collimated detector reduces the contribution of scattered neutrons to the initial peak to a

negligible level and makes it possible to record all neutron pulses by minimizing the pulse distortion due to neutron-energy dispersion and neutron time-of-flight. The 1-cm collimator gap points to a 1-cm segment of the axial plasma column starting from the end of the anode, where localized sources of X-rays with the higher intensity are most frequently detected by X-ray pinhole-camera photographs [13]. The discharge chamber was filled with 5.6 torr of deuterium and the neutron yield n had a mean value $\bar{n} \approx 10^8$ neutron/shot with a maximum of $n = 4 \times 10^8$. The distance 120 cm between collimated detector and source was large enough to separate by time-of-flight ($\sim$ 50 ns) the hard X-ray signal from the onset neutron signal and small enough to induce only a negligible neutron-pulse distortion due to neutron-energy dispersion. The bulk of the accelerated unconfined ions is ejected in a 16° cone along the discharge axis; a component with a maximum of ion energy (> 200–300 keV) remains inside a cone with an even smaller aperture ($\sim 6°$ at a distance of 12 cm from the anode end). The cone aperture has been assessed in a previous experiment [2] by the diameter of the damaged area on an aluminium plate (the ion energy in that experiment was evaluated by the skin thickness of the blisters which are produced by the ion bombardment on the witness plate); we have not observed any damage on any plates in the 90° direction from the discharge axis; this indicates that most of the ion beams are ejected within the narrow axial cone $< 16°$.

Scattered neutrons do not contribute to the signal of the collimated detector. This is proved by the fact that, in a discharge with several resolved neutron plates on the ND signal, some of the peaks are completely wiped out in the CD signal (e.g. peak 3 of Fig.3(a)). Any contribution of scattered neutrons to the tail of a neutron peak in the ND signal would further reduce our estimated upper limit of the possible contribution to this tail from neutrons produced by D-beam-cold-plasma interaction.

3. MEASUREMENTS

The neutron pulses of Burst I have a full-width at half-maximum (FWHM) $\tau \cong 2-10$ ns (after correction for instrumental broadening $\sim$ 5 ns) by the 12-cm distant non-collimated detector (ND) signal; an expected velocity dispersion increase of the FWHM broadening of a pulse in the 120-cm distant collimated detector (CD) signal – due to the greater distance of the detector from the source and to neutron energy spread – is observed to be $\sim 1.5-2$ ns in those few cases where there is actually a measured increase. In most of the shots the effect of the collimator is to reduce amplitude and FWHM of a pulse, or to eliminate completely or partially some of the neutron pulses. The shape of a single neutron pulse may remain substantially unaffected by the paraffin collimator except for some reduction of the pulse amplitude (up to $\sim$ 25–30% of the time-integrated amplitude) and for a substantial reduction (usually by more than 50%) of the area (time-voltage) under the tail of the pulse. A typical example of such a pulse is shown in Fig.2(a,b). Burst I in this case is formed by a single large neutron pulse (a peak with a relatively small tail) on both detectors. The ratio area tail (A_t)/area peak (A_p) is $\sim$ 0.38 in the ND signal and $\sim$ 0.23 in the CD signal. The ratio $R_p = A_{pc}/A_{pn}$ = (area peak CD-signal)/(area peak NC-signal) for the pulse of Fig.2 has the value $R_p = 0.51$. A Burst I (from a different discharge) which is formed by at least three distinct pulses is shown in Fig.3(a,b); for pulse 1 we have $R_{p1} = 0.52$, and for pulse 2 $R_{p2} = 0.10$; pulse 3 is completely wiped out in the CD signal. Pulses which follow the first pulse – in a multiple-pulse signal – are eliminated by the paraffin collimator in many discharges; the first pulse is instead eliminated only in a few discharges.

The partial reduction of a pulse amplitude and of FWHM indicates that part of the source falls off the view of the collimator gap. By inspection of all ND–CD signals, we conclude that frequently what appears as a single peak is actually composed of many pulses which are emitted within a time interval $\lesssim$ 5 ns (peaks 1 and 2 of Fig.3(a) are examples of it); a clear indication of a composite pulse is a reduction of FWHM with an increased regularity of the pulse profile (with a triangular shape) on the CD signal.

A summary of the results from our analysis of 58 consecutive discharges by the same conditions is reported in Fig.4. The histogram of Fig.4(a) gives the distribution of the number of pulses (from all discharges) versus R_p; two (or more) pulses which were eventually not resolved on both detector signals have been considered as a single pulse. The histogram of Fig.4(b) gives the distribution of the number of discharges versus R_t (= ratio of the time integral of the neutron signal from the CD over the time integral of ND-neutron signal). Time integration of neutron signals and of single neutron pulses and separation of neutron pulses have been made by a planimeter on a magnified projection (X 4) of each original oscilloscope trace.

4. DISCUSSION

The upper limit of ~ 0.7 for R_p also sets an upper limit for the amount of neutrons that might be produced by interaction -- during a pulse-- of unconfined ions with the cold plasma. In a single pulse this upper limit is then 30% of the neutron emitted in the pulse; a lower value for this upper limit seems more realistic if we consider that part of the pulse source which is outside the view of the collimator gap may still be located in the hot plasma rather than in the cold plasma. It is apparent (e.g. by Fig.2) that part of the tail of a peak is made of a multiplicity of unresolved small-amplitude pulses within the hot plasma. The distribution of Fig.4(b) suggests that at least half of the total neutron emission is emitted by a few (2–3) high-intensity pulses forming Burst I with the possibility that any amount of these pulses (including all or none of the pulses) have a source located within the field of view of the collimator gap. The values of parameters as area of peak (A_p), area of tail (A_t), FWHM (τ) of the signals of Fig.2 are representative of all our neutron signals by our mode of operation at 5.6 torr. The small tail of the CD signal is most likely due to an intrinsic tail in the neutron production by small-amplitude sources within the 1-cm window. The area A_{tc} under this tail should be subtracted from the area of the tail of the ND signal (A_{tN}) in comparing emission from localized sources (A_p) with the contribution from the neutrons which are produced by the ion-cold-plasma interaction. After making this subtraction for the signals of Fig.2, the ratio of the beam-target neutrons produced in the cold background to the neutrons (A_{pN}) produced in more localized sources becomes $\lesssim 26\%$.

5. CONCLUSION

A large fraction of the total yield of D-D neutrons originates in many discharges within a 1-cm long region of the hot plasma column at the end of the anode. The localized source ($\leqslant 1$ cm) of these neutrons can produce in some discharges up to 50% of the total neutron yield. It is consistent with all our data to consider that another 20% of the yield originates within hot plasma regions outside the field of view of the collimator aperture. In some discharges the total neutron yield is produced by a single pulse (a peak plus a tail). The tail of a neutron peak in the detector signal sets an upper limit for the neutrons which can be produced by ion-beam-cold-plasma interaction; this upper limit is $< 30\%$ of the total neutron yield at our pressure of 5.6 torr.

REFERENCES

[1] BOSTICK, W.H., NARDI, V., PRIOR, W., in Proc. 3rd Top. Conf. Pulsed High-Beta Plasmas, Culham, 1975, Pergamon, Oxford (1976).

[2] BOSTICK, W.H., NARDI, V., PRIOR, W., CHOI, J., FILLINGHAM, P.J., CORTESE, C., J. Nucl. Mater. **63** (1976) 695.

[3] GULLICKSON, R., SAHLIN, H., Rep. Lawrence Livermore Lab. (1975).

[4] KROMPHOLZ, H., MICHEL, L., SCHONBACH, K.H., FISCHER, H., Rep. Technische Hochschule, Darmstadt (July 1975).
[5] BOSTICK, W.H., NARDI, V., PRIOR, W., Ann. N.Y. Acad. **251** (1975) 2;
BOSTICK, W.H., NARDI, V., PRIOR, W., RODRIGUEZ-TRELLES, F., CORTESE, C., GEKELMAN, W., Proc. Int. Conf. Energy Storage, Compression and Switching, Turin, 1974, Plenum, New York (1975);
NARDI, V., BOSTICK, W.H., PRIOR, W., Proc. Int. Conf. Physics of High Magnetic Field, Grenoble, 1974, CNRS, p. 129.
[6] PATOU, C., SIMONNET, A., WATTEAU, J.P., Phys. Lett. **29A** (1969) 1.
[7] BOSTICK, W.H., NARDI, V., PRIOR, W., Controlled Fusion and Plasma Physics (Proc. 6th Europ. Conf. Moscow, 1973) **2** (1973) 395.
[8] GRIBKOV, V.A., Proc. Int. Conf. Energy Storage, Compression and Switching, Turin, 1974, Plenum, New York (1975) 271.
[9] BOSTICK, W.H., NARDI, V., PRIOR, W., "Observation of 10^8 Gauss fields and production of 14-MeV D–T neutrons in a deuterium plasma", Plasma Physics and Controlled Nuclear Fusion Research 1974 (Proc. 5th Int. Conf. Tokyo, 1974) **3**, IAEA, Vienna (1975) 109.
[10] BERNARD, A., et al., "Etude de l'émission neutronique et de la turbulence dans l'expérience focus avec une résolution temporelle de l'ordre de la nanoseconde", ibid. 3, 83.
[11] MORGAN, P.D., et al., Controlled Fusion and Plasma Phys. (Proc. 6th Europ. Conf. Moscow 1973) **2** (1973) 391.
[12] BOSTICK, W.H., NARDI, V., PRIOR, W., Controlled Fusion and Plasma Physics (Proc. 7th Europ. Conf. Lausanne 1975).
[13] BOSTICK, W.H., NARDI, V., PRIOR, W., J. Plasma Phys. **8** (1972) 7.

STABILIZED IMPLODING LINER FUSION SYSTEMS

D.L. BOOK, A.L. COOPER, R. FORD, K.A. GERBER,
D.A. HAMMER, D.J. JENKINS, A.E. ROBSON, P.J. TURCHI
Naval Research Laboratory,
Washington, D.C.,
United States of America

Abstract

STABILIZED IMPLODING LINER FUSION SYSTEMS.

A new concept in imploding liner plasma compression is described in which a liquid metal liner is imploded by pistons driven by high-pressure gas, and stability of the inner surface against Rayleigh-Taylor modes is achieved by rotation. The principle has been demonstrated by using a water liner to compress air. This 'captive liner' offers the possibility of stable, reversible implosion-expansion cycles in which the plasma energy is recovered into the driving system, leading to reactor cycles with low Q and, hence, small size. A new method of setting up closed-field confinement geometries inside a liner using a rotating electron beam is described. Plasma currents induced by the beam provide initial plasma heating and generate the containment geometry. Persistence of plasma currents 100 times longer than the beam duration has been observed. Development of these methods could lead to a very compact thermonuclear reactor operating in the manner of a reciprocating engine.

I. INTRODUCTION

In recent years, the use of imploding liner flux compression techniques [1] to create and confine fusion plasmas at megagauss magnetic field levels [2] has received renewed attention in the U.S.A. [3, 4], U.S.S.R. [5, 6], and France [7]. This interest arises from the relatively short confinement times (10^{-4} - 10^{-5} sec) required to achieve fusion energy gain in the higher density plasmas (10^{18} - 10^{19} cm^{-3}) allowed by ultrahigh magnetic fields; thus simple, axi-symmetric high beta plasma-field configurations can be reconsidered since system dimensions are now greatly reduced.

In previous papers [3, 8] we have derived the basic scaling laws for liner compression of theta-pinch systems, based on incompressible liner dynamics. The scaling laws may be summarized as follows:

$$Q \propto B_O r_O \rho^{\frac{1}{2}}; \quad E/L \propto Q^2/\rho; \quad L \propto Q/B_O^2$$

where Q is the ratio of nuclear energy released per cycle to plasma energy at peak compression, B_O is the confining magnetic field and r_O the plasma radius at peak compression, ρ the density of the liner material and L the length of the system, assumed to be open-ended. Results of numerical calculations show that unrestricted end loss leads to $L > 10^3$ m, even with $B_O = 1$ MG, so a reactor should include some means of inhibiting end loss. Cusp ends [3] and cold end plugs [9] have been proposed, as have systems with closed field lines [10]. In this paper we assume that the end loss problem is tractable, and devote most of our attention to the radial dynamics of the system.

The energy density of a plasma in pressure balance with a field of 10^6 gauss is comparable to the energy density of high explosive. The recovery of the energy of the plasma, to which may be added the energy of the charged reaction products, is therefore of some concern, and it is desirable that the compression stage should be followed by a controlled expansion in which the plasma energy is recovered into the original driving source. If this

can be achieved efficiently the value of Q needed for an economical reactor, and hence the size and energy per unit length, can be greatly reduced. The principle of efficient reversible energy transfer is a central feature of theta pinch reactor designs [11]; to apply it to a liner system requires a method of controlling the liner motion at all times. To this end we have developed a concept which we call the rotationally stabilized captive liquid liner.

2. ROTATIONALLY STABILIZED LINER IMPLOSIONS

Liquid metal liners are desirable for a reactor, since they can be readily recycled and the liquid metal can perform the multiple functions of a heat transfer medium, tritium breeding blanket, neutron absorber and replaceable first wall. The obvious difficulty associated with a liquid metal liner is the Rayleigh-Taylor instability of the outside surface as it is being accelerated inwards by the driving source, and the corresponding instability of the inside surface as it is decelerated upon the compressed plasma (the payload).

It has been shown theoretically [12] and demonstrated experimentally [13] that the inner surface may be stabilized by providing the liner with sufficient initial angular momentum that the effective gravity at the inside surface is directed into the liner throughout the motion, that is to say $\ddot{r} - r\omega^2 \leq 0$, a condition which is most severe at turn-around. The stability criterion can be expressed in terms of the ratio R of the energy in rotation to the energy in the compressed payload, both taken at peak compression. A simple model is used in which each radial element of the liner has the same angular momentum, which is conserved during the implosion, so that the angular velocity varies inversely as the square of the radius. $R/(\gamma - 1)$ is then a function only of the dimensionless thickness parameter b, where $\pi b^2 r_0^2$ is the volume of liner material per unit length and γ is the ratio of specific heats of the payload [Table 1]. If the compression ratio is sufficiently large, the greater part of the rotational energy is derived from the driving source and the initial rotational speed requirement can be quite modest.

The outside surface of the liner is not stabilized by rotation, but controlled motion can be achieved by eliminating the outer free surface altogether and driving the liner by means of pistons. This leads to the concept of the captive liquid liner, shown schematically in Fig. 1. A thick-walled metal cylinder rotates inside a stationary pressure vessel. The cylinder wall is bored with a large number of radial cylinders, each containing a piston. Initially (Fig. 1a), the pistons are at their outermost radial positions and the radial cylinders are filled with liquid metal. The entire cylinder block is rotated at sufficient speed to provide for stabization of the inside liner surface. Fast valves admit high pressure gas to the pressure vessel, driving the pistons and the liquid metal radially inward.

If the cylinder block maintains constant angular velocity, each element of fluid will enter the central region with the same angular momentum, which will be conserved during the implosion. The velocity distribution in the radial direction will therefore be the same as used in deriving Table I. If, due to the decrease in the moment of inertia of the whole system, the cylinder block increases its angular velocity during the implosion, the imploded liner will have a distribution of angular momentum that increases with radius. In either case, Rayleigh's condition [14] for the stability of the rotating fluid, $\frac{d}{dr}(r^2\omega)^2 \geq 0$ will be satisfied. The radial kinetic energy of the liquid metal and the pistons is transferred during implosion

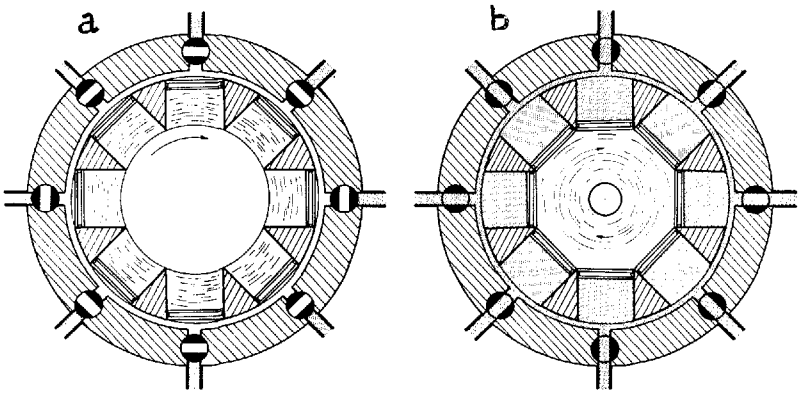


FIG.1. Captive liquid liner principle: (a) initial state,(b) compressed state.

TABLE I. RATIO R OF ROTATIONAL ENERGY TO PAYLOAD ENERGY AT PEAK COMPRESSION

b	1	5	10	25	∞
R/(Y - 1)	3.59	1.43	1.28	1.19	1.00

to the internal energy of the adiabatically compressed payload and to rotational energy of the liner, achieving the final imploded state shown in Fig. 1b. The process can then reverse, with energy returning via the kinetic energy of pistons and liner material to the internal energy of the driving gas.

Note that with free pistons, as shown here, the instability is not entirely eliminated, but can develop with an azimuthal wavenumber n/2, where n is the number of pistons. Complete stabilization could be obtained by mechanically linking the pistons to ensure that they moved in phase; in fact there are many possible variations on the simple arrangement of Fig. 1, including direct mechanical drive.

The cyclic behavior of a piston-driven rotating liquid liner implosion has been demonstrated experimentally using liners of water driven by helium gas at about 7 atm. acting on eight free pistons. Fig. 2 shows a sequence of high-speed photographs of an imploding rotationally stabilized liner, initially 14 cm diameter, compressing a trapped volume of air, initially at low pressure. The cylinder block is made of plexiglass so that the positions of the pistons can be seen. Interaction of the fluid elements from neighboring cylinders gives rise to the surface perturbations evident in the photos. An initial annulus of liquid, 1 cm thick, in addition to the fluid in the cylinders, has been provided to reduce the extent of these

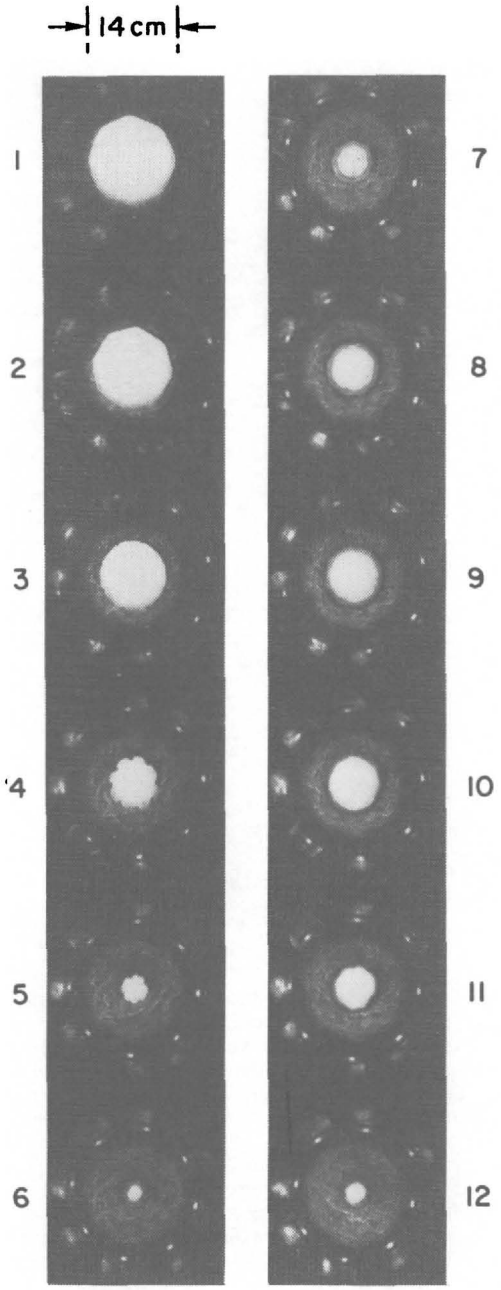


FIG.2. Framing camera photographs of imploding water liner. Rotation speed: 1100 rpm. Exposure time: 25 μ s. Time between frames: 1 ms.

TABLE II. $B_c = (8\pi\rho c_s^2)^{\frac{1}{2}}$

Material	Li	Na	Pb	Hg	Al	Cu
B_c (MG)	1.8	1.3	3.2	2.6	4.3	5.6

perturbations. Note that on the second implosion cycle, the initial annulus is larger and the inside surface is smoother. The annulus should probably have a thickness about equal to a piston diameter; this is supported by preliminary evidence from a sixteen-piston device. Four complete implosion-reexpansion cycles were recorded before the motion was damped out.

The captive liner may be regarded as a pressure amplifier. Assume that the pistons are driven by a constant pressure p_1, and that the linear compression ratio of the inside surface is α. Then equating the work done by the driving gas to the energy of the system at peak compression and noting that $\alpha \approx b$, we obtain,

$$\frac{p_o}{p_1} = \frac{\alpha^2(\gamma - 1)}{1 + R(\alpha, \gamma)}$$

where p_o is the pressure of the compressed payload. As an example, consider $p_o = 40$ kbar, corresponding to a magnetic field of 1.0 MG, and $\alpha \approx b = 30$. Then with $\gamma = 5/3$, $p_1 = 118$ bars. Thus megagauss fields can in principle be obtained by the use of quite modest driving pressures.

The amount of initial rotation required to stabilize the motion can be expressed in terms of the linear speed of the inside surface of the cylinder block u_θ, and is given by

$$u_\theta = v_A/b(\ell n\ (1 + b^2) - 1)^{\frac{1}{2}}, \text{ where } v_A = B_o/(4\pi\rho)^{\frac{1}{2}}.$$

Continuing the above example, a heavy liner material ($\rho = 10$) requires $u_\theta = 12.5 \text{m.sec}^{-1}$, while a light material such as lithium ($\rho = 0.5$) would require $u_\theta = 56 \text{m.sec}^{-1}$. Again, these are quite modest requirements.

3. EFFECT OF COMPRESSIBILITY

When $B_o^2/8\pi \geq \rho c_s^2$, where c_s is the speed of sound in the liner material, the effect of compressibility must be included in the dynamics of thick liners. Due to the finite transit time of a sound wave through the liner, the inside surface can turn round while the outer region of the liner is still imploding; thus less than the full energy of the liner is delivered to the payload.[1] The characteristic magnetic field for this effect is given by $B_c = (8\pi\rho c_s^2)^{\frac{1}{2}}$ and is listed in Table II for a variety of liner materials.

A one-dimensional fluid code incorporating the equation of state of liquid metals has been used to study the effect. Fig. 3 shows a sequence of pressure profiles through the liner, in which the pressure wave traveling back after peak compression can be clearly seen. In this case the pressure in the wave was about 20% of the peak pressure, and the efficiency of energy transfer to the payload was 50%. Fig. 4 shows the radius of the inside surface, normalized to the turn-around radius r_o of an incompressible liner

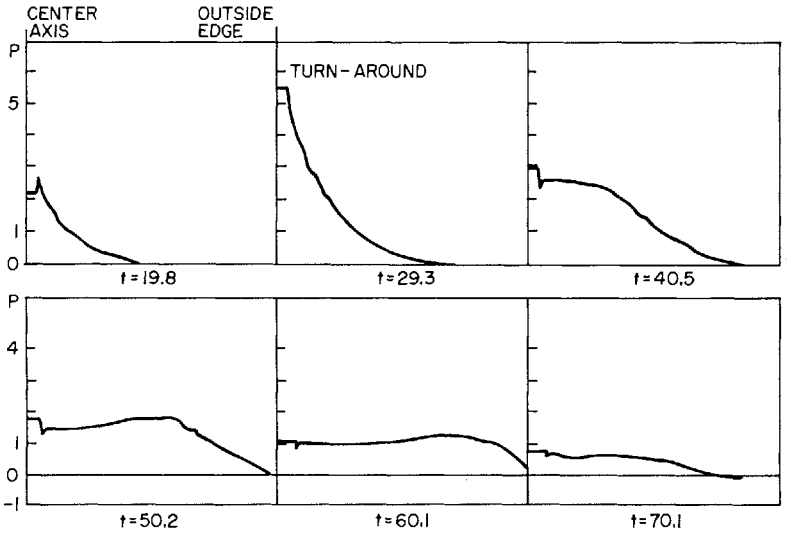


FIG.3. Pressure versus radius for compressible liner. Pressure in units of 0.01 ρ_s^2, time in units of r_0/c_s, $b = 40$. Initial implosion conditions such that an incompressible liner would have achieved peak pressure 0.25 ρc_s^2.

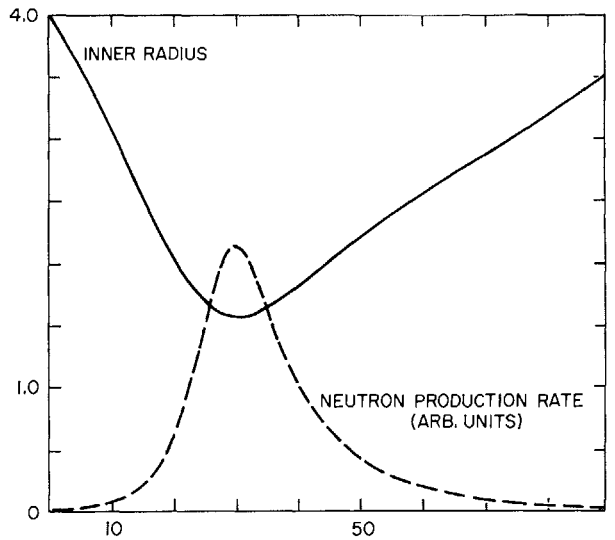


FIG.4. Inner radius and neutron production rate versus time for compressible liner. Radius in units of r_0, time in units of r_0/c_s. Other conditions as for Fig.3.

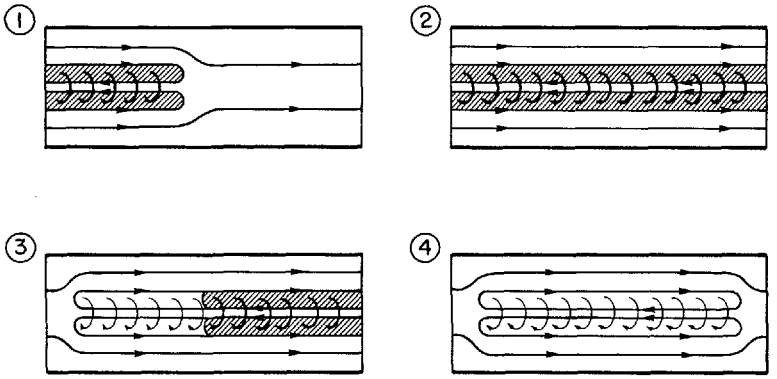


FIG.5. Creation of reversed-field plasma configuration by rotating electron beam: (1) beam enters neutral gas, (2) plasma is formed and heated, (3) beam leaves plasma, inducing plasma currents, (4) plasma currents persist.

of the same energy and mass, against time in units of r_o/c_s. Also shown is the neutron production rate from a D-T plasma compressed to a peak temperature of 18 keV. The lack of symmetry with respect to turn-around in these curves arises from compressibility effects.

The energy that is not delivered to the payload is not dissipated, but remains as wave energy in the liner; it should therefore be possible, at least in principle, to recover this energy into the driving source. Apart from its effect on the detailed motion, the main effects of compressibility are to increase the driving pressure required to reach a given final state, and to increase the axial loading on the ends of the system due to the backward wave. There will also be some modification to the criterion for rotational stabilization.

4. PLASMA PRODUCTION BY ROTATING ELECTRON BEAMS

The creation of the initial plasma for compression by the liner is a significant problem, since many conventional methods of plasma production, such as theta or z-pinches, cannot be used inside the conducting liner. A possible new method is the use of a rotating relativistic electron beam, which offers the potential not only for producing the plasma but also for establishing a closed-field confinement geometry from currents induced in the plasma by the beam.

Hollow rotating electron beams in which the magnetic field on axis is in the opposite direction to the guide field are well within the capabilities of present technology. Consider the injection of such a beam along a guide magnetic field into an initially neutral gas. The sequence of events is illustrated in Fig. 5. The electric field E_θ generated by $\dot{B}_z$ at the beam front breaks down the gas and induces a return current j_θ^* in the opposite sense to the beam current j_θ. If $|j_\theta^*| \ll |j_\theta|$, the magnetic field of the beam is hardly affected, but the plasma is heated ohmically by j_θ^* as well as by direct beam-plasma interaction. When the beam pulse ends, the conductivity of the plasma is sufficiently high that the current induced by the $-\dot{B}_z$ at the beam tail is equal in magnitude and direction to the beam current and therefore, tends to maintain the configuration established by the beam. The field lines must close at the ends of the system thus forming the configuration of the reversed-field theta pinch.

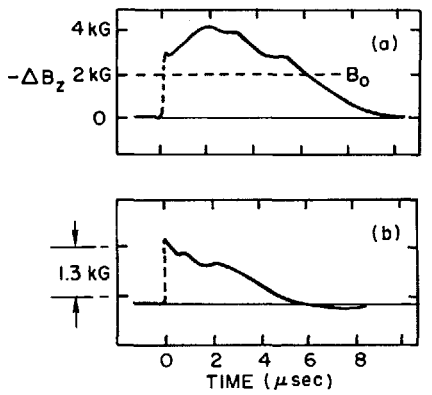


FIG.6. Integrated signal from magnetic probe on axis. B_0 = ambient magnetic field. (a) ΔB_z, (b) $B\theta$.

To test this concept an experiment has been performed in which a 4 cm radius hollow beam of 1.2 MeV electrons, 30 kA current and 60 ns duration, is passed through a non-adiabatic magnetic cusp to produce a rotating beam with approximately equal azimuthal and axial velocity components [15]. The beam is injected into neutral hydrogen at 85 mtorr in an axial magnetic field of 2 kG. The plasma density and temperature are measured by Thomson scattering immediately after the beam pulse, and the magnetic field components ΔB_z and B_θ outside the beam are measured by magnetic probes. Typical probe traces are shown in Fig.6. The plasma density was 5.5×10^{15} cm^{-3} and the electron temperature was 13 eV. The ordinate of Fig.6(a) is scaled to give ΔB_z on axis, assuming flux conservation inside the metal chamber. The ambient field is reversed by the beam, and plasma currents persist after the beam has passed, decaying with a time constant of about 5 μsec. This is consistent with resistive decay at the measured electron temperature, assuming classical resistivity.

In these experiments, a B_θ is generated comparable to ΔB_z since the beam velocity components are comparable; thus, the magnetic field configuration resembles a belt pinch rather than a reversed-field theta pinch. In principle, the pitch angle of the rotating beam can be adjusted to vary the ratio ΔB_z, B_θ as required.

These experiments establish the principle of this method of plasma production, although the temperatures achieved were very low. More powerful electron beams are available, and should be capable of producing the ~ 100 eV initial plasma required for liner compression. If powerful beams were injected into preionized plasma, the net current $j_\theta - j_\theta^* \ll j_\theta$ could still be adequate to reverse the field, and the large j_θ^* could generate strong turbulent heating of the plasma. When the beam passed out of the system the plasma current would fall to $j_\theta - j_\theta^*$ which would, with suitable choice of parameters, be below the threshold for turbulence, and thus leave a quiescent plasma.

5. COMPRESSION OF CLOSED-FIELD CONFIGURATIONS

Since plasma and field are mixed in the reversed field configuration, the ratio $\bar{\beta}$ of plasma energy to total payload energy is always less than unity. Furthermore, adiabatic compression in the radial dimension only

leads to a decrease in β. The scaling laws, which have previously been derived for the case of $\beta = 1$ now have to be modified; in particular, Q is approximately proportional to $\bar{\beta}^2$.

Compression of a beam-generated reversed field theta pinch has been studied using a simple model in which the radial distribution of plasma pressure is scaled according to the return current heating, and is in equilibrium with the magnetic pressure distribution determined by the same return currents. The initial density is uniform, and two cases are studied; in the first case the plasma heating rate is proportional to j_θ^2, as might arise from an ion-acoustic instability, and in the second case the heating is proportional to j_θ^3 as might arise from the electron-electron two-stream instability. With a radial compression ratio of 30, $\bar{\beta}$ goes from an initial value of 0.59 to a final value of 0.19 in the first case, and from 0.74 to 0.32 in the second. While these results show that $\bar{\beta}$ is sensitive to initial conditions, more detailed calculations which include the reaction rate profile are needed to determine the Q for any given case.

6. CONCLUSIONS

The rotationally stabilized captive liner principle transforms the imploding liner fusion concept from a succession of disruptive explosions into something more akin to a reciprocating internal combustion engine. This concept inevitably leads to very thick liners at peak compression; although this may have the practical advantage that the liner can also serve as the tritium breeding blanket, liner velocities will be lower than with thin liners, especially since compressibility effects in thick liners are likely to limit the maxium magnetic field for efficient operation to $\sim$ 1-1.5 megagauss, while thin liners could probably operate at somewhat higher fields. The efficient reversible energy transfer made possible by the captive liner allows reactor cycles with $Q \sim 2$-3 rather than $Q \geq 20$ necessary for systems without direct energy recovery, and this advantage more than compensates for the lower fields. However, these slower systems do require effective plasma confinement at the ends, indicating the need for closed-field configurations. The use of electron beams to provide the initial plasma and a reversed-field configuration in situ is an attractive new possibility; furthermore, the technology of producing these beams is already less than an order of magnitude from what would be required for a reactor.

Many problems remain in implementing this concept; apart from the technical problems of liquid liners, there is the question of the stability of closed field configurations at the high values of β necessary if a reactor is to be of reasonable size. One of the most serious problems is the inevitable evaporation of the inside surface of the liner at the megagauss field level and the consequent contamination of the plasma. Preliminary calculations indicate that the metal vapor will be ionized by contact with the hot plasma and be confined to an outer layer $\delta \ll r_0$ on the time scale of the reaction, but more theory and experiments are needed to resolve this question.

ACKNOWLEDGEMENT

The assistance of Dr. John Gardner in providing the SHASTR code adapted for the compressible liner calculations is gratefully acknowledged.

REFERENCES

[1] KNOEPFEL, H. Pulsed High Magnetic Fields, North Holland-Elsevier, Amsterdam (1970).
[2] LINHART, J.G., KNOEPFEL, H., GOURLAN, G. Nucl. Fusion Supp. Pt. II (1962) 733.
[3] BARCILON, A.I., et al. Plasma Physics and Controlled Nuclear Fusion Research (Proc. Conf. Tokyo 1974) Vol II IAEA, Vienna (1975) 567.
[4] ROBSON, A.E. and TURCHI, P.J. Proc. 3rd Topical Conference on Pulsed High Beta Plasmas, Culham, 9-12 Sept 1975.
[5] ALIKHANOV, S.G., KONKASHBAEV, I.K. Nucl. Fusion Supp. (1975) 123.
[6] VELIKHOV, E.P. Comments on Plasma Physics & Controlled Fusion 1 (1972) 171.
[7] RIOUX, C., JABLON, C. Nucl. Fusion 15 (1975) 425.
[8] ROBSON, A.E. Annals N.Y. Acad. Sci. 251 (1975) 649.
[9] SCHAFFER, M.J. Submitted to Nucl. Fusion.
[10] ES'KOV, A.G. et al. Nucl. Fusion Supp. (1975) 155.
[11] BURNETT, S.C., et al. Los Alamos Sci. Lab. Rep. LA-5121-MS (1972).
[12] BARCILON, A.I., BOOK, D.L., and COOPER, A.L. Phys. Fluids 17 (1974) 1707.
[13] TURCHI, P.J. et al. Phys. Rev. Lett. 36 (1976) 1546.
[14] CHANDRASEKHAR, S. Hydrodynamic and Hydromagnetic Stability, Oxford Univ. Press (1961) 273.
[15] KAPETANAKOS, C.A. et al. Phys. Rev. Lett. 34, 1156 (1975).

INVESTIGATION OF MODEL THERMONUCLEAR SYSTEMS WITH LINERS

S.G. ALIKHANOV, V.P. BAKHTIN, V.M. BRUSNIKIN,
I.S. GLUSHKOV, R.Kh. KURTMULLAEV, A.L. LUNIN,
A.D. MUZYCHENKO, V.P. NOVIKOV, V.V. PICHUGIN,
V.N. SEMENOV, G.E. SMOLKIN, E.G. UTYUGOV,
I.Ya. SHIPUK
I.V. Kurchatov Institute of Atomic Energy,
Moscow,
Union of Soviet Socialist Republics

Abstract

INVESTIGATION OF MODEL THERMONUCLEAR SYSTEMS WITH LINERS.

One of the well-established types of thermonuclear reactor is a plasma compression system using an imploding liner. Over a number of years, two approaches have been adopted for building this type of system at the Kurchatov Institute of Atomic Energy: (1) a straight Z-pinch liner compressing a magnetized plasma by gas-kinetic pressure; (2) a quasi-spherical liner compressing a compact plasma formation in a closed magnetic field.

1. A STRAIGHT Z-PINCH LINER SYSTEM

In this system the plasma is heated and confined directly by means of an imploding straight cylindrical thin liner. The axial magnetic field is only used for thermal insulation of the plasma in the radial direction. In the longitudinal direction the plasma is confined by the fixed ends of the system. The rejection of magnetic confinement was mainly due to power enginering considerations.

Using a simplified model of a liner device with allowance for compressibility we derive the following expression for the energy input per unit length of any given liner system

$$Q' = \frac{10^3 (n\tau)^2 T^2}{(\gamma-1)\rho_0} \left(\frac{P_0}{P}\right)^{1/\gamma} \frac{(1-\xi)^2}{\xi} \left[\frac{MJ}{cm}\right] \qquad (1)$$

where $n\tau$ is expressed in 10^{15} cm$^{-3}\cdot$s, the temperature T is in 10^4 eV, the pressure P is in 10^6 atm, ρ_0 is the initial density of the liner material in g$\cdot$cm^{-3}, γ and P_0 are constants from the adiabatic curve for cold compression, $P = P_0[\rho/\rho_0)^{\gamma} - 1]$; ξ is the ratio of the potential compression energy of the liner material to the plasma energy. By minimizing the energy needed to produce a neutron we obtain $\xi = 0.5$. In this case, in accordance with Eq.(1) for $n\tau = 1$, T = 1, P = 1, i.e. for the maximum pressure possible during magnetic confinement, the energy input per unit length of the system is found to be greater than 100 MJ$\cdot$cm^{-1}, which is not feasible in practice. The energy input per unit length can be reduced if the plasma pressure is substantially increased which means a transition to gas kinetic confinement. Gas-kinetic confinement of a magnetized plasma was previously considered in detail in Ref. [1]. A characteristic feature of gas-kinetic confinement is that the dense and relatively cold plasma in the region near the walls causes substantial radiation losses. Flow of plasma to the walls arises owing to the low thermal conductivity of the hot magnetized plasma. If there is no turbulence, the plasma flow rate is determined from an equation obtained from numerical calculations [1] for a wide range of values of P and H:

$$v \cong 3.3 \times 10^3 \, (P/H)^{0.32} \qquad (2)$$

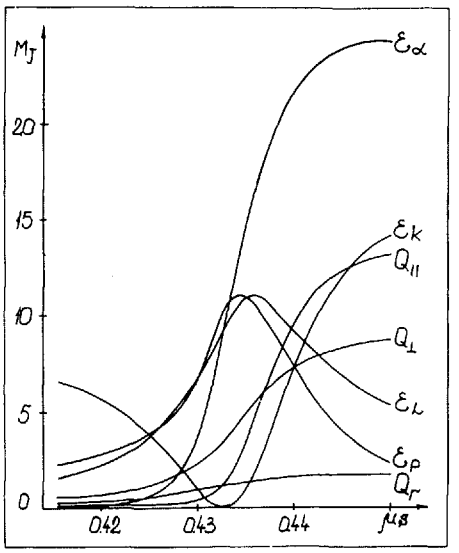


FIG.1. Results of numerical calculations for a Z-pinch liner type of thermonuclear system. $\mathcal{E}_p$, $\mathcal{E}_\alpha$, $\mathcal{E}_L$, $\mathcal{E}_k$ *are, respectively, the plasma, alpha particle, internal liner and kinetic energies;* $Q_{\|}$, $Q_\perp$, Q_r *are, respectively, the longitudinal, radial and radiation energy losses.*

The flow of plasma to the walls was investigated experimentally in a recently published report by Feinberg [2]. The measured value was, however, four times greater than that obtained from Eq.(2) which is possibly due to the existence of turbulence or to some uncertainty in measuring the plasma parameters.

Assuming that the transfer coefficients in our case are based on Coulomb collisions, the requisite energy input per unit length is given by the expression

$$Q' \cong \frac{20(n\tau)^2 T^2 \beta^{0.32}}{p^{0.68}} \left[\frac{MJ}{cm}\right] \tag{3}$$

The need for pressures higher than 10^8 atm in liner fusion becomes increasingly obvious when the total energy of the system is considered, as this is otherwise found to be unrealistically high.

In this case it is also essential to use gas-kinetic confinement in the axial direction [3]. The requisite length L of the system at these pressures is found to be small although the relationship $nL \cong 5 \times 10^{22}$ must be satisfied when this method of confinement is used [3]. The longitudinal losses of heat which are not due to the plasma flow can play a positive part in the thermonuclear burning process.

It is to be anticipated that if allowance is made for all the losses of energy from a plasma compressed by a liner, the requirements imposed on the power engineering and the pressure will be even more stringent. Numerical calculations performed on a one-dimensional model with allowance for the compressibility of the liner material confirmed this assumption. Figure 1 gives the results of calculations on one of these variations which has not been optimized with respect to initial parameters. An iron liner 3 cm long, with an initial diameter of 2 cm and a mass of 4.5 g, was considered.

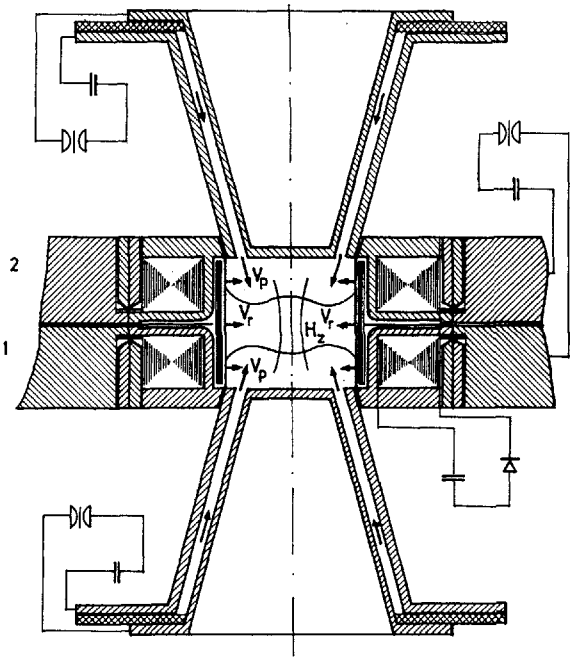


FIG.2. Schematic of the LN-20 device.

The existence of a powerful flux of energy from the plasma results in heating and ionization of the inner layers of the liner. The pressure in the liner and the potential compression energy of the liner were divided into two components: elastic and thermal. All the thermal effects were calculated on the assumption of an ideal plasma and liner material. The equation of state was calculated from the Saha equation by using an approximation method proposed by Yu.P. Raizer [4]. The values of P, V, T, obtained in these calculations agree satisfactorily with the data calculated by using the Thomas-Fermi method with allowance for quantum and exchange corrections [5]. The calculation procedure and the results of optimizing this system will be given in greater detail in a separate publication.

From the calculations noted above, it follows that the required liner velocity is 10^6-10^7 cm·s^{-1}. In this case it is not possible to accelerate the metal liner by simply passing a current through it, owing to thermal limitations on the velocity. The possibility of accelerating the shells by means of a current flowing through the layer of plasma immediately adjacent to the liner is therefore considered. Numerical investigations of the structure of this layer in the hydrodynamic approximation have shown that the characteristic thickness is only dependent on the magnetic field strength:

$$\lambda \cong 5.5 \times 10^4 \, H^{-1} \tag{4}$$

and the flow rate of the magnetic field penetrating the layer is given by

$$U \cong 1.3 \times 10^3 \, H^{0.32} \tag{5}$$

which is substantially lower than the liner velocity. Highly efficient acceleration is thus ensured.

The LN-20 device on which it is proposed to carry out all the model experiments was built in accordance with this programme. The power supply system for the device comprises three capacitor banks. The main bank (2 MJ, 50 kV) is used to accelerate the liner, a fast bank (90 kJ, 50 kV) is used to produce the preliminary plasma and a slow bank (350 kJ, 5 kV) supplies the initial magnetic field coils. The design of the device is shown in Fig.2. Solid-steel discs 1 and 2, 110 cm in diameter and 10 cm thick, act as the current collectors. The principal component is the compression chamber which should combine high voltage strength with vacuum and mechanical strength, and should also include the magnetic field coils and the plasma injection system. It should also be simple to manufacture (frequent replacement) and convenient to assemble and disassemble. The design chosen meets these requirements satisfactorily.

Experiments were first carried out to investigate the symmetry and stability of compression of thin-walled liners (R_0 = 6 cm, ℓ = 11 cm, δ = 0.1 cm). Helium at an initial pressure of 20 atm was used as the gas simulating the plasma. When the liners were manufactured with 5–10% tolerances, the shell was accelerated with a reasonable degree of stability although during deceleration caused by the counter pressure of the helium, the liner lost stability and collapsed. If the deviation in thickness was less than 3–5%, compression was stable and fairly symmetrical. Recent experiments on plasma compression with a magnetic field were carried out using liners manufactured to tolerances better than 1%, with more than hundredfold compression being achieved. The preliminary plasma was produced by two conical co-axial injectors located at the ends of the compression chamber. The initial hydrogen plasma parameters obtained to date are: density ~ 3×10^{17} cm^{-3} and temperature ~ 10 eV. The first series of experiments was carried out to compress a plasma located in a longitudinal magnetic field ($H_0 = 10^4$ G). In Fig.3 the solid lines give the theoretical results and the dots give the experimental results. The time history of the H_α line was measured although the relationship between the broadening of the spectral line and the density of a plasma completely confined by a cold wall requires special consideration. The measured density is approximately an order of magnitude greater than that anticipated in the hot region. This is because the cooler regions with higher densities are the main contributors to the radiation of this line. The results of these measurements provide qualitative confirmation of plasma compression and heating. The results of the magnetic probe measurements agree with the theoretical results. Streak photographs showed that the compression was highly symmetrical. The values of the apparent radius given in Fig.3 and obtained from streak photographs may be greater than the real liner radius even at the instant of maximum compression due to a certain escape of plasma in the end region. The authors consider that one of the most important results of these experiments is that no invasion of impurities is observed right up to the point where the end port through which the spectroscopic measurements were taken is destroyed. It should be borne in mind that the main objection to liner fusion is that it is possible for cumulative jets of sheath material to be formed and these will penetrate into the hot plasma region. Although these were not observed in our experiments additional experimental data is necessary before definitive conclusions can be drawn.

2. SYSTEM WITH A THREE-DIMENSIONAL IMPLODING LINER

Another approach is described in this section in which the dimensions of the system and the energy are minimized by using a shaped liner to achieve quasi-spherical compression of a compact plasma formation in a magnetic field with closed field lines [6]. The closed magnetic configuration eliminates end losses and enables the length of the system and therefore the total stored energy to be reduced by several orders of magnitude for the same energy density. Three-dimensional quasi-spherical compression has a number of advantages as it is possible to achieve higher degrees of compression for the same change in the linear dimensions. The experimental arrangement [6] presupposes that the boundaries of the plasma pre-heating chamber and the liner compression

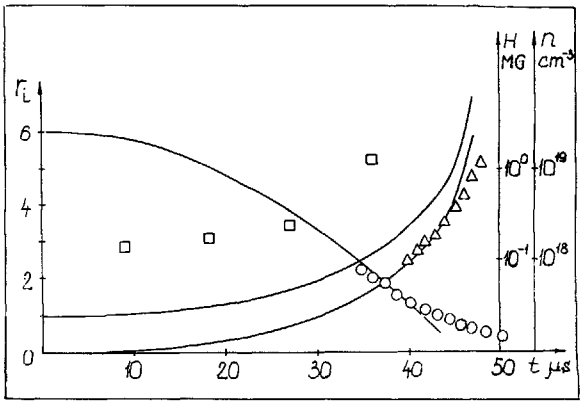


FIG.3. Comparison of experimental and theoretical results for model compression of a plasma with a magnetic field on the LN-20 device.

chamber should be fixed in space which enables a new approach to the problem of radiation resistance of the walls, impurities, etc.

Calculations on the orders of magnitude characterizing the system as a whole show that it is possible to fulfill the Lawson criterion with moderate parameters for the liner (velocity $v = 10^5$ cm·s^{-1}, degree of radial compression $K_r = 10$) and the accumulator (W = 10–20 MJ).

A number of types of systems with quasi-spherical compression of the plasma with a closed magnetic structure are considered:

1. Magnetic confinement and compression of a plasma toroid in a combined (poloidal and toroidal) field including the following cases: (a) a tokamak-like structure with the Kruskal-Shafranov safety factor $q \geqslant 2$; (b) a purely poloidal field (q = 0); (c) a purely azimuthal field formed by currents flowing through the plasma.

2. Non-magnetic confinement and compression of a toroid by means of a cold gas layer (the magnetic field in this case is only used to thermally insulate the plasma).

Investigations to carry out this programme are divided into the following categories: (1) development work on the formation, heating and transportation of a plasma toroid with a closed magnetic configuration [7–9]; (2) investigation of the dynamics of the quasi-spherical collapse of a shaped liner [10] and model experiments to investigate the behaviour of a plasma during liner compression; (3) theoretical investigations on non-magnetic confinement and optimization of the liner system [10].

The results of experiments and numerical modelling relevant to the building of a three-dimensional plasma compression system using a metal liner will be presented: these include the dynamics and stability of the sheath motion, the limiting strength parameters, the gas and plasma pressures, the magnetic field pressure,etc.

2.1. Experimental results on compression of a magnetic field and a gas

Experiments to investigate the dynamics of a liner were carried out on the LNT device (Fig.4a). A shaped aluminium liner (2) 20 cm long, 10 cm in diameter and weighing 200–500 g was accelerated by a field produced by a pusher coil (1) (H_c = 250 kG, rise time τ = 40 μs, power supply from capacitor bank W = 500 kJ, U = 5 kV). A closed shell is formed at the instant when the ends of the liner come into contact with the central conductor (3). The gas and azimuthal

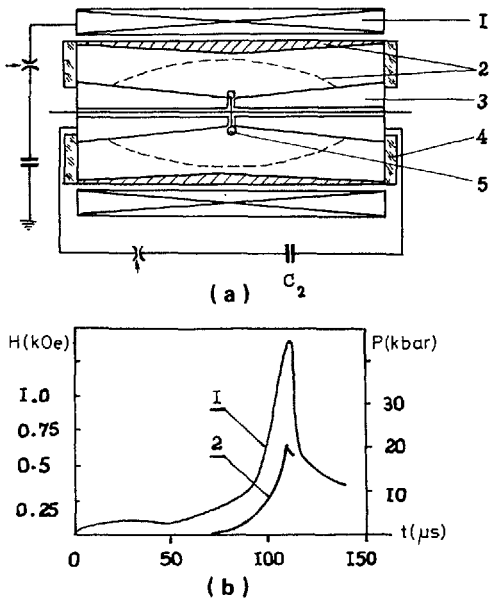


FIG.4. (a) system for measuring the magnetic field and gas cumulation: 1 – pusher coil; 2 – shaped aluminium liner; 3 – central conductor; 4 – rod; 5 – magnetic probe; (b) oscillograms of the field (1) and the gas pressure (2).

magnetic flux of the current flowing through the rod (4) trapped in the sheath at this instant undergo compression during subsequent motion of the liner. In these experiments the plasma pressure was simulated by a gas (He) which is admitted into the liner cavity beforehand at an initial pressure of up to 1 atm.

The aim of this investigation was to examine the possibility of obtaining a collapsible quasi-spherical shell and achieving high degrees of compression of a magnetic flux and a gas using this shell.

The magnetic field in the chamber was measured by using a magnetic probe (5) (see Fig.4a), and the gas pressure was measured by ceramic and quartz piezoelectric gauges and a crusher manometer. Streak photographs of the liner were taken end-on and side-on simultaneously through slits in the driver coil.

The formation of a closed shell and the quasi-spherical collapse of this shell was established experimentally. A sharp increase in the magnetic field and in the trapped gas pressure was recorded during the cumulative phase (Fig.4b).

The velocity of the liner as determined from the streak photographs was of the order of 0.7×10^5 cm·s^{-1} at the centre of the cross-section and 10^5 cm·s^{-1} at the edge. The maximum volume compression coefficient at turnaround was $K \sim 10^3$. Oscillograms of the signals from the magnetic probe (1) and the piezoelectric gauge (2) are given in Fig.4b and these demonstrate the cumulative increase in the field and pressure in the cavity. The magnetic field strength when the liner stopped was 10^6 and the amplification factor was up to 30. The piezoelectric gauges and the crusher manometer record the maximum pressure as $2 \times 10^4 - 10^5$ atm. These figures agree with the data calculated from the compression coefficient.

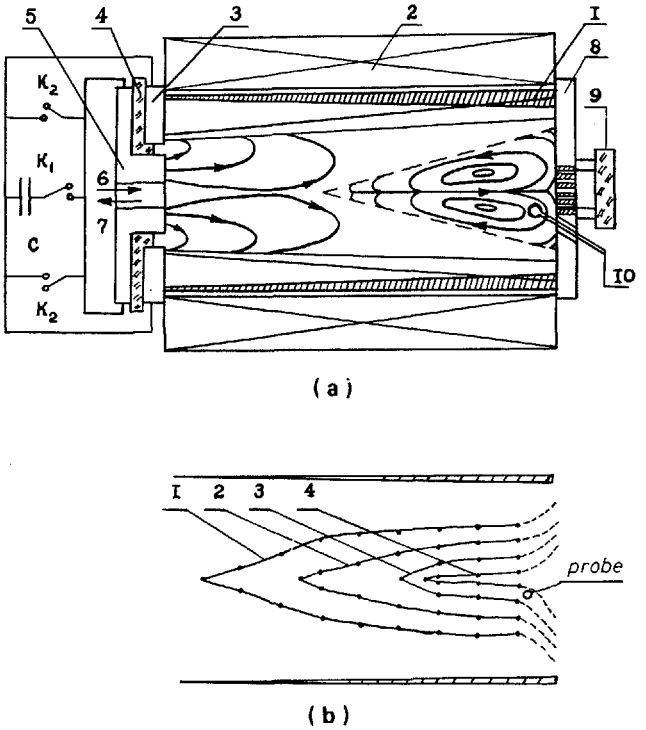


FIG.5. (a) Experimental arrangement for plasma compression by a three-dimensional cumulative liner: 1 – liner; 2 – pusher coil; 3,4,5 – plasma injector elements; 6 – outlet; 7 – wall; 8 – right-hand end wall; 9 – insulator; 10 – single-turn probe. (b) position of the inner surface of the liner at the times: 1) 82 μs, 2) 98 μs, 3) 118 μs, 4) 142 μs.

Particular emphasis should be given to the rapid increase in the power generated by the liner at the cumulative phase. The field rise rate in particular attained 3×10^{11} G·s^{-1} (in the driver coil 6×10^{9} G·s^{-1}).

The mechanisms described are reproducible. The motion of the liner as a whole is regular and symmetrical. In the majority of cases however, azimuthal corrugation of the sheath was observed in the initial stages of motion. It is important to note, however, that under experimental conditions (evidently because of the non-uniform distribution of the liner thickness over the length) the degree of corrugation noticeably decreases or even disappears at the centre of the liner.

2.2. Experiments on plasma compression

The results obtained (that it is possible to achieve a high degree of compression and an increase in power in a liner cavity) enabled the transition to be made to model experiments (with energies of W = 0.5 MJ) to investigate the properties of the plasma during compression by a liner. The main aim of these experiments was to investigate general problems of liner compression, namely vaporization of the liner walls, interaction of plasma with the liner, and the behaviour of a high-density plasma at high energy densities.

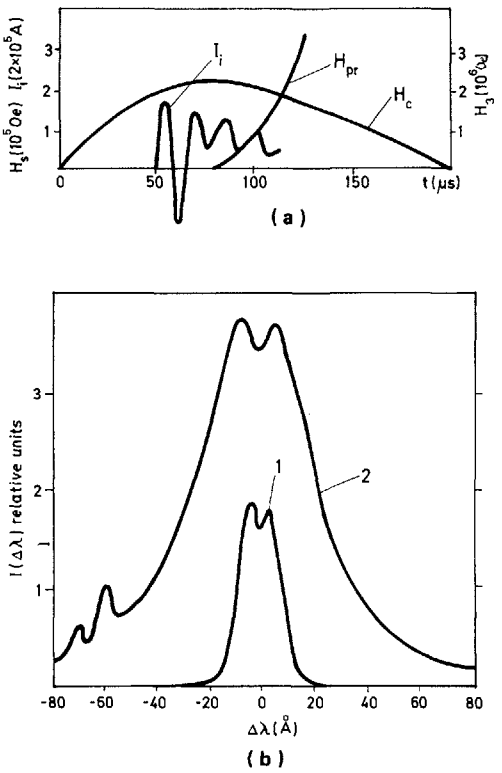


FIG.6. (a) Oscillograms of the solenoid field H_s, the injector current I_i and the probe field H_{pr}. (b) profiles of the H_β line in the injector plasma (1) and in the plasma compressed by the liner (2).

Preliminary experiments were carried out on the LNT device described above with a slightly altered liner shape (see Fig.5a). An asymmetric liner with a linearly increasing wall thickness from 0.3 mm at the left end to 4 mm at the right end was used to provide facilities for plasma diagnostics. The liner (1) together with the right-hand end wall (8) and elements of the plasma injector (3, 4, 5) at the left end limited the vacuum cavity in which the preliminary plasma was produced and where compression took place. During motion the liner collapsed towards the right-hand end wall which consists of a solid-steel disc. Apertures through which the plasma radiation was fed to a spectrochronograph consisting of a combination of a spectrograph STE-1 and a high-speed slow-motion camera LV-03 were located at the centre of the disc immediately adjacent to the region of cumulation. A single-turn probe (10) with an oscillograph was used to monitor the variation in the magnetic field in the plasma during convergence.

The initial plasma was produced by an injector with a coaxial electrode system. The inner electrode (5) is a metal ring in an end insulator (4) and the outer electrode was formed by a metal ring (3) and the liner (1) which was in contact with this ring. The capacitor bank for the plasma injector with a capacitance of C = 27 μF was charged to a voltage of U = 4 X 10^4 V (oscillation period T = 16 μs) and could be crowbarred by the spark gap K_2 at the instant of maximum current when the left end of the liner (during compression) approached the discharge gap of the injector.

During collapse of the left-hand (light) end of the liner the external supply circuit of the plasma injector is interrupted, and the current flowing through the plasma closes the circuit inside the liner forming a closed current toroidal configuration. This type of formation is shown schematically in Fig.5a at the right end of the vacuum volume for a certain point in time (the position of the inner wall of the liner at this point is shown arbitrarily by the dotted lines).

The toroidal current configuration of the plasma formation should have a diffusive magnetic field distribution and it is to be expected that it will be MHD-stable. It may also be assumed that the diffusive field distribution should have a favourable effect on an independent plasma formation which is not attached to the external electrodes and fields during distortion of the external sheath (liner). It should also be noted that the magnetic field attains a maximum strength in the inner region of the torus and a minimum strength in the outer region i.e. near the liner walls. This should substantially reduce the limitations on the maximum attainable magnetic field strength in a plasma during compression by a liner.

The operation of the plasma injector was preliminarily investigated outside the liner in a separate vacuum cavity. A semi-transparent metal cone simulated the liner at the instant when the crowbar was connected and enabled optical plasma diagnostics facilities to be used side on. Streak photographs were taken of the discharge and time-resolved recordings were made of the Stark contour of the H_β line. The electrical parameters of the discharge were also measured. The results indicate that in the working range of hydrogen pressures used (from tenths of a millimetre to several millimetres of mercury) a plasma injector excites a powerful stable current jet with a charged particle density of the order of 10^{16} cm^{-3} (measured from the half-width of the H_β line). The central section of the jet 2–3 cm in diameter has a tendency to exhibit a pinch effect without the appearance of MHD instability. The maximum discharge current is 400 kA and is slightly attenuated within 30–50 μs after the switch K_2 has made contact (see Fig.5a).

Figures 5 and 6 give the experimental results on three-dimensional compression of a plasma by a liner. Figure 6a gives oscillograms of the magnetic field H_s produced by the driving coil, the current I_i of the plasma injector and the signal H_{pr} from the magnetic probe. Figure 5b shows the positions of the inner wall of the liner at various points in time obtained by means of streak photographs of the external boundary of the liner (taken through slits in the side of the solenoid) and subsequent scaling. The figures show that at the instant when the left-hand end of the liner collapses (approximately 80 μs after the initiation of motion) the magnetic field in the plasma begins to increase, and this is recorded by the probe. The maximum field strength recorded by the probe prior to destruction is approximately 3.5 MG.

The smooth variation in the integrated magnetic probe signal gives reason to assume that noticeable MHD instabilities are not present in the plasma. Low-frequency, low-amplitude oscillations with varying degrees of regularity were also observed on the un-integrated probe signal during the cumulation process which may indicate that an internal periodic structure is present in the plasma.

Figure 6b shows the profile of the H_β line during plasma compression before the cumulative phase is reached. The half-width of the line corresponds to the plasma density $n \sim 10^{17}$ cm^{-3}. As cumulation is approached, the half-width of the H_β line continues to increase and the plasma radiation intensity recorded in the region $\delta\lambda = 250$ Å with its centre on the H_β line substantially increases and the proportion of the continuum in the total radiation flux grows considerably. Approximate calculations on the plasma temperature T from the intensity of the H_β line and the continuous radiation gives a value above several tens of electronvolts.

From the results presented in this section and given in Figs 4b and 5b it is apparent that the volume compression coefficient attains $K \sim 10^3$ and higher values of n and T for the plasma could be anticipated in the cumulative phase. Insufficient experiments have been carried out to date on liner compression for reliable measurements of these parameters to be given, and, therefore, we only attempt to give rough estimates of these parameters below.

2.3. Results of numerical modelling

A new problem arises in a system with a three-dimensional converging liner, namely the choice of an optimum shape for the liner and driving field. The liner shape should be such that the following conditions are fulfilled: (1) the shape of the closed shell at all stages of its motion should be approximately quasi-spherical to ensure a minimum level of losses and optimum conditions from the point of view of plasma stability; (2) the transfer of energy from the storage system to the plasma should be as efficient as possible. In this case the problem of energy optimization does not only involve optimizing the electrical system but includes minimizing the losses of kinetic energy during collapse of the end sections of the sheath.

Appropriate calculations were performed on a model comprising a liquid, incompressible, infinitely thin liner compressing a gas and a magnetic azimuthal field in a closed cavity. The liner profile and the shape of the driver coil were varied during the calculations. The qualitative concepts used in the initial choice of liner profile were as follows: the majority of the kinetic energy and therefore of the sheath mass should be contained in the central section which forms a closed cavity in the final state (the length of this section with a compression coefficient of $K \sim 10^3$ is of the order of 1/10 of the initial length of the liner). In accordance with this distribution of mass and energy, the driver coil should consist of independently supplied sections in order to impart the majority of the momentum to the central section of the liner.

Calculations have shown that when using a driver coil consisting of three sections with relative lengths of 0.5; 1.5; 0.5, supplied by capacitor banks with relative energies of 0.15; 0.7; 0.15, 40% efficiency is achieved (profile of the liner thickness 1 : 16) and the proportion of energy lost at the ends is 24%. The volume compression coefficient in this case is 10^3.

The authors are grateful to E.P. Velikhov for constant interest and support with this work.

REFERENCES

[1] ALIKHANOV, S.G., GLUSHKOV, I.S., in Controlled Fusion and Plasma Physics (Proc. Europ. Conf. Lausanne, 1975); Dokl. Akad. Nauk SSSR **26** 3 (1976) 547.
[2] FEINBERG, B., Plasma Phys. **18** (1976) 265.
[3] ALIKHANOV, S.G., KONKASHBAEV, I.K., Nucl. Fusion **14** (1974) 341, in Plasma Physics and Controlled Nuclear Fusion Research (Proc. 5th Int. Conf. Tokyo, 1974) **2**, IAEA, Vienna (1975) 577.
[4] RAJZER, Yu.P., Zh. Ehksp. Teor. Fiz. **36** (1959) 1583.
[5] KALITKIN, N.N., KUZ'MINA, L.V., Preprint IPM, No. 35 (1975).
[6] ES'KOV, A.G., et al., 3rd Conf. on High Beta Plasmas, Culham (1975).
[7] ES'KOV, A.G., et al., in Controlled Fusion and Plasma Physics (Proc. 6th Europ. Conf. Moscow (1973) **1**, Moscow (1973) 599.
[8] ES'KOV, A.G., et al., in Plasma Physics and Controlled Nuclear Fusion Research (Proc. 5th Int. Conf. Tokyo, 1974) **3**, IAEA, Vienna (1975) 71.
[9] ES'KOV, A.G., et al., in Controlled Fusion and Plasma Physics (Proc. 6th Europ. Conf. Moscow 1973) **1**, Moscow (1973) 595.
[10] KURTMULLAEV, R.Kh., et al., in Plasma Physics and Controlled Nuclear Fusion Research (Proc. 5th Int. Conf. Tokyo, 1974) **2**, IAEA, Vienna (1975) 753.

ENERGETIC ASPECTS OF FAST-FUSION REACTORS WITH DENSE LINERS OF MEDIUM VELOCITIES (10 to 100 km · s^{-1})

C. RIOUX
Laboratoire de physique des plasmas,
Université Paris Sud, Orsay,
France

Abstract

ENERGETIC ASPECTS OF FAST-FUSION REACTORS WITH DENSE LINERS OF MEDIUM VELOCITIES (10 to 100 km · s^{-1}).

The paper deals with energetic problems of fast fusion reactors in which cylindrical liners implode at 'intermediary' velocities, i.e. 10 to 100 km · s^{-1}. The heat transfer between plasma and liner are reduced by a longitudinal magnetic field at $\beta \gg 1$. First of all, the global energy regime of the process is studied, for a dense and thin liner, as a function of velocity and thermonuclear combustion rate. Then the results are applied to the model of a simple liner consisting of a cold, thin metallic tube accelerated by a magnetic field. Finally for this model, orders of magnitude of energies are given that can be applied in the construction of an effective reactor.

1. INTRODUCTION

The fast-fusion reactors making use of inertial plasma confinement were studied mainly for velocities of several kilometres per second or several hundred kilometres per second [1–4]. The present paper considers the medium range of 10 to 100 km · s^{-1}. A dense but transparent plasma is subject to an implosion by a cylindrical liner, lateral heat transfer being impeded by a magnetic field, with $\beta \gg 1$. First the global energy regime of the process is investigated for an arbitrary dense and thin liner, as a function of the velocity and the thermonuclear combustion rate. The results obtained are then applied to the model of a simple liner consisting of a thin and cold metal tube accelerated by a magnetic field. Finally, for this model the orders of magnitude of energy are given as applicable in the designing of an efficient reactor.

Problems of stability, initial plasma heating and technological realization are not considered. The system of units is the MKSA, the temperatures are given in keV. The numerical values are taken from Refs [5–8].

2. DESCRIPTION OF EXPERIMENTAL ARRANGEMENT

The D-T mixture to be burnt is placed inside a thin and cold metallic cylinder which is imploded by a strong magnetic field (see Fig.1). The initial plasma heating up to a temperature of a few 10^{-1} keV is achieved by an external process, such as a CO_2 laser or relativistic electron beams. The fast implosion of the cylinder heats the plasma in an adiabatic compression to a temperature above 5 keV where fusion reactions may take place in considerable quantities. The heat transfer between plasma and liner are kept within acceptable limits by a longitudinal magnetic field with $\beta \gg 1$. This field also confines the helions within the plasma. The reaction comes to ignition before adiabatic compression is finished but it develops principally after repulsion.

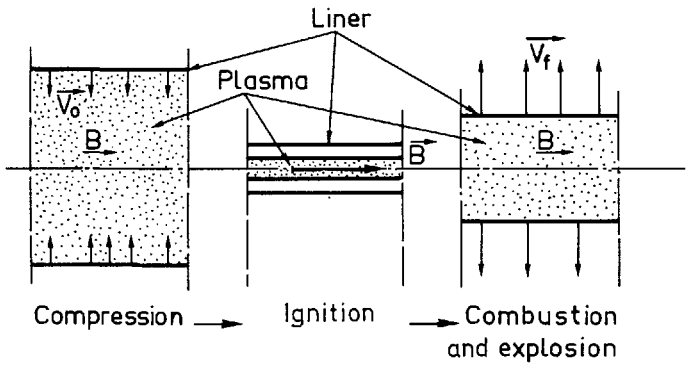


FIG.1. Time development of liner-plasma system: initial states, at repulsion, after combustion.

The liner, consisting of a metal sheet, is accelerated by, e.g. strong longitudinal currents distributed over the thickness. It is very thin at the beginning; during implosion, its inner radius is reduced by a factor of 20 to 30. One aims at achieving a good efficiency for both liner acceleration and transfer of kinetic energy from liner to plasma. So the liner is not vaporized during acceleration and its final thickness is little higher at the radius of repulsion.

The plasma density depends on the nature and the velocity of the liner. Being of the order of 10^{24} to 10^{25} m^{-3} at the beginning, it reaches 10^{27} m^{-3} at the moment of repulsion.

3. LINER ENERGY AS A FUNCTION OF COMBUSTION

A global investigation of the plasma-liner interaction [9] shows that for an arbitrary given system, the energy W_F produced in the fusion reaction can be written in the form

$$\frac{W_F}{W} = f\left(\frac{W}{L}\ \chi\bar{\omega},\ T_0,\ \frac{n_0 r_0}{2V_0}\right) \tag{1}$$

where W is the kinetic energy of the liner, L the length of the system, $\bar{\omega}$ the specific mass of the liner, r_0 the initial plasma radius, V_0 the initial liner velocity, χ the initial liner cross-section divided by the plasma cross-section at repulsion, and T_0 and n_0 are the initial plasma temperature and density, respectively.

For a 'thin' system $\chi \ll 8.6$; in practice, $\chi = 6$ is taken for a well optimized system [10].

The parameter $(W/L)\chi\bar{\omega}$, which defines the necessary energy level per unit length of the liner, is important. For each value of W_F/W we have a pair $[T_0, n_0 r_0/2V_0]$ of initial values linked with a plasma whose w is minimum. So we can write the inequality

$$w \geqslant w_m\left(\frac{W_F}{W}\right) \tag{2}$$

Figure 2 shows w_m as a function of W_F/W; the fusion energy produced is a growing function of w_m.

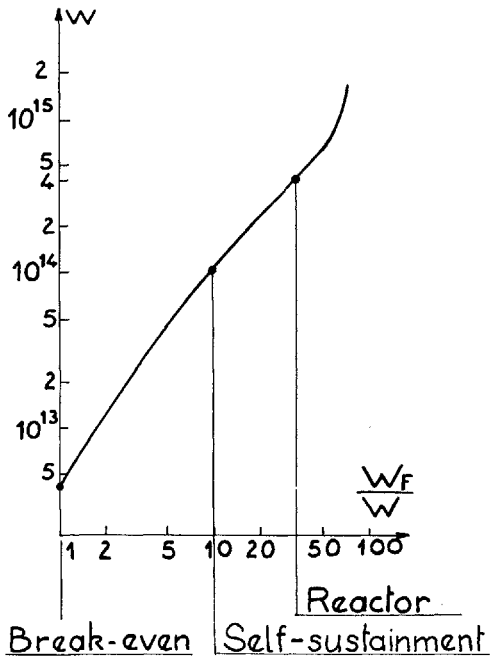


FIG.2. $W=(W/L)\,\bar{\omega}\chi$ as a function of the ratio W_F/W.

The global energy involved is a function of the length which itself depends on the means used to confine the extremities. The preferred structure of the latter being undetermined, we are restricted to considering three reasonable cases:

(0) no confinement of extremities; self-destruction of plasma starts at the ends where two rarefaction waves are built up;
(I) the extremities consist of two inert cold plugs which confine the plasma [11, 12];
(M) plasma and helions are limited by two magnetic mirrors (supposed to be stable).

Under these conditions it can be shown that the global energy of the liner will read as follows:

$$W=\frac{1}{\bar{\omega}^2\chi^2V^2}\;G\left(w,\,T_0,\,\frac{n_0r_0}{2V},\,V\right) \tag{3}$$

Equations (1) and (3) permit the determination of the total energy of the system as a function of the thermonuclear production yield. Also here pairs of optimum values of $[T_0', n_0'r_0/2V]$ for which W is minimum will exist. We have

$$W\geqslant\frac{1}{\bar{\omega}^2\chi^2V^2}\;G_m\left(\frac{W_F}{W},\,T_0,\,V\right) \tag{4}$$

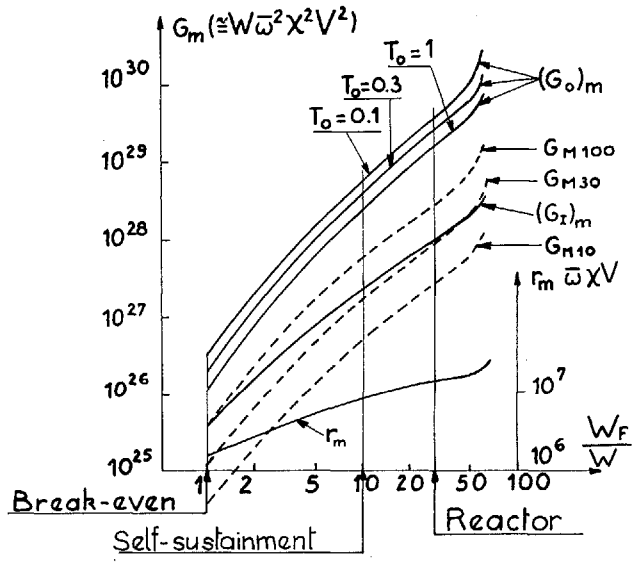


FIG.3. Values of $G_m \cong W\bar{\omega}\chi^2 V^2$ *for three types of axial confinement: no confinement* (G_0)*, 'inertial' confinement* (G_I) *and 'magnetic' confinement* (G_M)*.*
G_0 *is plotted for three initial temperatures,* $T_0 = 0.1$ *keV, 0.3 keV, 1 keV;* G_m *is plotted for three velocities* $V = 10, 30, 100$ *km* $\cdot s^{-1}$.

The function G_m is represented in Fig.3 in the three forms $(G_m)_{(0)}$, $(G_m)_{(I)}$ and $(G_m)_{(M)}$. In practice, $(G_m)_{(I)}$ depends neither on T_0 nor on V_0. $(G_m)_{(0)}$ depends particularly on T_0: we have plotted it for three initial temperatures $T_0 = 0.1$, $T_0 = 0.3$, and $T_0 = 1$.$(G_m)_{(M)}$ is a linear function of V which has been plotted for $V = 10^4$, $V = 3 \times 10^4$ and $V = 10^5$. The diagram shows immediately that non-confined systems require higher energies and are thus of less interest.

In practice, the pairs of values $[T_0', n_0' r_0/2V]$ where W is minimum differ but little from $[T_0, n_0 r_0/2V]$ where W/L is minimum. This fact suggests the approximate relation

$$W \gtrsim \frac{1}{\bar{\omega}^2\chi^2V^2}\, Q(w_m, T_0) \tag{5}$$

where

$$Q_{(0)} \cong 1.8 \times 10^6 \frac{1}{T_0^{4/9}}\, w_m^{1.57},\ Q_{(I)} \cong 6.5 \times 10^9\, w_m^{1.25},\ Q_{(M)} \cong 40\, V\, w_m^{1.5} \tag{6}$$

As regards the dimensions, the liner radius at the instant of repulsion is

$$r_m \cong \frac{0.8\, w^{1/2}}{\bar{\omega}\chi V} \tag{7}$$

On the other hand, the Bohm-type heat transfer at $\beta \gg 1$ which is adopted requires the use of the relation [9]

$$2 \times 10^7 \frac{\beta}{V^2} \ll 1 \tag{8}$$

to obtain an acceptable heat transfer.

In practice, Eq.(8) entails

$$V \gtrsim 10^4 \tag{8'}$$

Equation (8') defines the lower limit of the range of intermediary velocities.

4. EFFICIENCY

Denoting the ratio of the energy supplied to the plasma by compression to the energy fed to the electric network by η_T, we can estimate whether the inequality [9]

$$\eta_T \frac{W_F}{W} \gtrsim 8 \text{ or } 10 \tag{9}$$

must be satisfied if the reactor obtained is to be effectively exploitable. For a simply self-sustained supply central station or, rather, an exploitable supply central station where part of the energy is accumulated through direct conversion, the following condition is sufficient:

$$\eta_T \frac{W_F}{W} \gtrsim 3 \tag{10}$$

For realizable values $W_F/W \cong 50$, the inequalities (9) and (10) yield $\eta_T \gtrsim 20\%$ and $\eta_T \gtrsim 6\%$, respectively. These values are easily achieved if the liner is accelerated by weakly dissipative electromagnetic processes.

If we agree to take $\eta_T = 0.3$, it is necessary to achieve a ratio $W_F/W \gtrsim 10$ for self-sustainment and $W_F/W \gtrsim 30$ for a reactor.

5. ELECTROMAGNETIC ACCELERATION OF LINERS

The efficiency η_T can be written as

$$\eta_T = \eta_G \eta_A \eta_P$$

where η_G is the efficiency of the generator, η_A the efficiency of the liner acceleration and η_P is the efficiency of energy transfer from liner to plasma; η_G can be high if the generator is on an electrotechnical basis; η_P is high if the liner remains 'thin' at the instant of repulsion, i.e. if its thickness is not much larger than the repulsion radius of the plasma; η_A is high if the acceleration entails only Joulean losses of low relative values.

To outline the problem of magnetic propulsion we restrict ourselves to a very simple solution, where the liner consists of a thin cylinder of dense material (initial radius and thickness r_0 and e_0) carrying a surface current, say an axial one (z-pinch). The liner is assumed to be accelerated over a distance much smaller than r_0 so that it rapidly reaches the initial velocity V introduced above. For the latter we shall have

$$V \neq \frac{1}{2}\,\mu_0\,\frac{1}{\bar{\omega}}\exp\left(\int_0^t j^2\,dt\right) \tag{11}$$

where j is the mean current density in the liner.

For the compression of a thermonuclear plasma we have a given T_0, which indirectly leads to a fixed ratio $\lambda = r_0/r_m$ (for attaining the start-up temperature) and a given W_F/W which yields $w = (W/L)\chi\bar{\omega}$.

The energy per unit length of the liner W_L/L, can be written in the form

$$\frac{W_L}{L} = \frac{2\pi}{\mu_0}\,\frac{\bar{\omega}^2}{k}\,V^3 r_0 \tag{12}$$

where

$$k = \int_0^t j^2\,dt$$

When we write $W_L/L = W/L = w/\chi\bar{\omega}$ and introduce (7) we obtain

$$V^2 = 2.5 \times 10^{-7}\,\frac{k}{\bar{\omega}^2}\,\frac{1}{\lambda}\,w^{1/2} \tag{13}$$

For the three confinement types we can deduce the following relations (with $\chi = 6$):

$$W_{(0)} = 2 \times 10^{11}\,\frac{1}{k}\,\frac{1}{T_0^{4/9}}\,\lambda w^{1.07},\quad W_{(I)} = 2 \times 10^{14}\,\frac{1}{k}\,\lambda w,\quad W_{(M)} = 2.5 \times 10^{3}\,\frac{1}{\bar{\omega}k^{1/2}}\,\lambda^{1/2} w^{5/4}$$

(14, 1; 2; 3)

6. SKIN EFFECTS

For conducting material carrying a homogeneous current, k has an upper limit of k_0 beyond which the material will lose its condensed-phase properties. If skin effects exist, the liner is heated up heterogeneously and $k \ll k_0$ (at least, if there is no ionization). To evaluate the effect let us compare e at a thickness characteristic of skin effects:

$$\delta = \left(\frac{\rho r_0}{\mu_0 V}\right)^{1/2}$$

so we obtain

$$\left(\frac{e}{\delta}\right)^2 = 0.2\,\mu_0\,\frac{\chi}{\lambda^3}\,\frac{1}{\rho\bar{\omega}}\,w^{1/2} \qquad (15)$$

The influence of e/δ on the behaviour of the liner is difficult to estimate as it depends on the law of current rise and on the more or less great importance of the liquefied or vaporized parts tolerated [13]. On the whole, we can admit $k \cong k_0$ as long as $e \lesssim 2\delta$. For material such as copper for which $\bar{\omega} = 8.9 \times 10^3$, $\rho = 2 \times 10^{-8}$ and $k_0 \cong 10^{17}$, condition (15) with $e = 2$ will read $w^{1/2} \lesssim 4.7 \times 10^2 \lambda^3$. For $\lambda = 25$ the relation will be satisfied up to $W_F/W \cong 10$. From then on we must admit $k < k_0$.

7. DISCUSSION

The relations (14) stress the influence of k on the energy level W. For a perfect solid conductor (copper) the energies and dimensions involved are the following (with $\lambda = 25$ and $T_0 = 0.3$ keV):

a) $W_F/W = 1$ $(w = 5 \times 10^{12})$

The $V = 5 \times 10^3$; this velocity is insufficient to satisfy inequalities (8). The conditions do not fit systems of intermediary velocities.

b) $W_F/W = 10$ $(W = 10^{14})$

Then $V = 1,1 \times 10^4$, $W/L = 1.8 \times 10^9$ J · m^{-1}

$W_{(0)} = 81 \cdot 10^9$, $W_{(I)} = 5.5 \times 10^9$, $W_{(M)} = 1.2 \times 10^9$

Only the confined forms are acceptable from the energetic point of view. The velocity is at the lower limit of the validity range.

c) $W_F/W = 30$ $(W = 3 \times 10^{14})$; $k = k_0$ admissible

Then, $V = 1.5 \times 10^4$, $W/L = 5.4 \times 10^9$ J · m^{-1}

$W_{(I)} = 12 \times 10^9$ J, $W_{(M)} = 5 \times 10^9$ J

Velocities and energies are convenient.

The energy levels dealt with above concerned liners of a very simple conception: thin, cold and metallic. They might constitute an upper limit of energies usable in such a type of reactor. Considerable improvements of the factor k can be achieved when more complex liners or better adapted current regimes are used. However, even with the above results, a central station of 1000 MW, of total efficiency 20%, can be envisaged, with about ten liner implosions per minute. The necessary technology does not go beyond the actual possibilities when a pulse generator with kinetic storage is used.

Summing up, we can say that even for very simple liners the use of intermediary velocities (> 10 km · s^{-1}) yields an energetically reasonable solution as regards the realization of exploitable fast-fusion reactors.

REFERENCES

[1] ROBSON, A.E., Report of NRL Progress (June 1973) 7.
[2] CHURAEV, V.A., LOBANOV, K.M., FEDYAKOV, V.P., DYATLOV, V.D., TIMONIN, A.M., Sov. Phys.-Tech. Phys. **20** (1976) 873.
[3] LINHART, J.G., Nucl. Fusion **10** (1970) 24.
[4] BOBIN, J.L., Nucl. Fusion **14** (1974) 553.
[5] SPITZER, L., Physics of Fully Ionized Gases, Interscience (1955).
[6] ROSE, D.J., CLARK, M., Plasma and Controlled Fusion, M.I.T. Press and John Wiley, New York - London (1963).
[7] BRAGINSKY, S.I., Reviews of Plasma Physics **1**, Consultants Bureau, New York (1965).
[8] Handbook of Chemistry and Physics, The Chemical Rubber Publishing Co. Cleveland (1962).
[9] RIOUX, C., submitted to Nucl. Fusion.
[10] SOMON, J.P., JABLON, C., submitted to Nucl. Fusion.
[11] ALIKHANOV, S.G., KONBASHBAEV, I.K., CHEBOTAEV, P.Z., Nucl. Fusion **10** (1970) 13.
[12] ALIKHANOV, S.G., KONBASHBAEV, I.K., Nucl. Fusion **14** (1974) 341.
[13] RIOUX, C., Internal Report LF 61 (June 1976).

THEORY AND CALCULATIONS OF NON-MAGNETIC DENSE-PLASMA CONFINEMENT

G.E. VEKSHTEJN, V.V. MIRNOV,
D.D. RYUTOV, P.Z. CHEBOTAEV
Institute of Nuclear Physics,
Novosibirsk,
Union of Soviet Socialist Republics

Presented by E.P. Kruglyakov

Abstract

THEORY AND CALCULATIONS OF NON-MAGNETIC DENSE-PLASMA CONFINEMENT.

In the present paper, the possibility of non-magnetic confinement of a thermonuclear plasma at a temperature of $T \sim 10^4$ eV and a density of $n \sim 10^{17} - 10^{18}$ cm^{-3} in a long cylindrical tube is considered. Non-magnetic confinement, in this case, means that the radial pressure of the plasma is balanced by the rigid walls of the tube rather than by the magnetic-field pressure (this would require a field of the order of 1 MG). The role of the magnetic field only involves reducing the transverse thermal conductivity of the plasma which can be achieved with moderate magnetic fields (such that $\beta \equiv 16\,\pi nT/H^2 \gg 1$). The characteristic features of non-magnetic confinement are clarified. These include the excitation of radial plasma flows, the formation of a dense layer of cold plasma near the walls and an increase in the part played by bremsstrahlung losses. Analytical solutions describing the behaviour of a plasma pulsed and quasi-steady-state heating by a high-current electron beam are found. The results of numerical calculations aimed at determining the parameters of a 'critical' reactor are present.

1. INTRODUCTION

The possibility of non-magnetic confinement of a thermonuclear plasma at a temperature of $T \sim 10^4$ eV and a density of $n \sim 10^{17} - 10^{18}$ cm^{-3} in a long cylindrical tube is considered in this paper. Non-magnetic confinement means in this case that the radial pressure of the plasma is balanced by the rigid walls of the tube rather than by the magnetic-field pressure (this would require a field of the order of 1 MG). The role of the magnetic field only involves reducing the transverse thermal conductivity of the plasma which can be achieved with moderate magnetic fields (such that $\beta \equiv 16\,\pi nT/H^2 \gg 1$). The plasma is assumed to be longitudinally confined by some other method such as by a multi-mirror magnetic field [1]. The range of plasma densities indicated above, $n \lesssim 10^{18}$ cm^{-3}, corresponds to the limiting pressures which can be produced in non-destructible systems [2].

2. ROLE OF RADIATION LOSSES AND CONVECTIVE TRANSFER

The main differences between non-magnetic plasma confinement with $\beta \gg 1$ and traditional systems with low β values are that in plasmas with $\beta \gg 1$ the gas-kinetic pressure $P = 2nT$ should be uniform throughout the cross-section[1]. The importance of this factor can be illustrated most clearly by using an example of a problem with initial conditions. Let the plasma temperature and density be uniform throughout the cross-section at time zero. As a result of interaction with the walls, the layer of plasma adjacent to the walls is cooled down and compressed (nT is independent of r!). This cold layer of plasma removes heat from the adjacent sections of hot plasma which, in turn, cool down and are compressed, etc. A flow of hot plasma towards the walls of the tube

[1] We bear in mind that the typical duration of a single operational cycle of the device is generally so long that the inertia of the plasma can be disregarded.

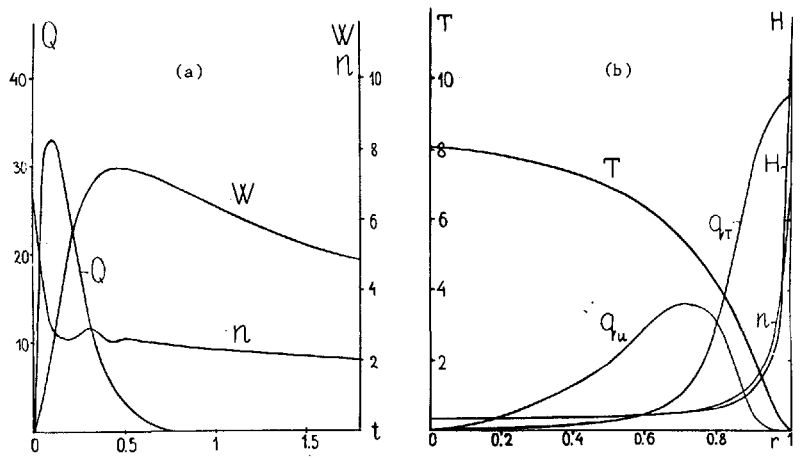


FIG.1. Non-magnetic confinement of a plasma with classical transfer coefficients.
(a) Power Q of heating source referred to unit length of plasma column, energy content W per unit length of plasma column and density n at system axis as a function of time. The radial distribution of the heating power density is given by Eq.(2) with $S \sim [exp(1-r^2/R^2) - 1]$. *Units of measurement:* $t = 3.3 \times 10^{-6}$ *s,* $n = 6 \times 10^{17}$ cm^{-3}, $W = 4 \times 10^4$ $J \cdot cm^{-1}$ *and* $Q = 1.1 \times 10^8$ $W \cdot cm^{-1}$. *The values* n_0 *and* H_0 *at* $t = 0$ *are given as* $n_0 = 4 \times 10^{18}$ cm^{-3} *and* $H_0 = 10^5$ *G,* $R = 3.2$ *cm.*
(b) Radial distributions of the plasma parameters at the time $t = 1.1$ *when the heating source has virtually been switched off. T is the plasma temperature (in units of* 1.5×10^3 *eV), n the plasma density (in units of* 4×10^{18} cm^{-3}, *H the magnetic field strength (in units of* 10^5 *G), q the energy flux (in units of* 3×10^9 $W \cdot cm^{-1}$, *referred to the unit length of the system and passing through the surface of a cylinder of radius r (*q_u *is the convective flow of energy and* q_T *is the thermal flow). We note that the relationship* $q_u + q_r \sim r^2$ *which is accurately fulfilled is characteristic of systems with* $\beta \gg 1$. $R = 3.2$ *cm.*

is stimulated. As the thickness of the cold plasma layer is small compared with the cross-section of tube it may be asserted that the hot plasma is "eaten away" by the walls.

The flow rate of the hot plasma depends on the thermal conductivity of the transitional region between the hot and cold plasma: the higher the thermal conductivity the faster the cooling process (and therefore the compression) of the section of hot plasma in contact with the cold plasma and therefore the higher the flow rate.

The heat flow due to this radial flow of plasma will be described as convective. The existence of this heat flow may, under certain circumstances, result in a substantial reduction in the life-time of the hot plasma as compared with the simple formula:

$$\tau \sim \frac{R^2}{\chi} \tag{1}$$

where R is the radius of the tube and χ is the coefficient of thermal conductivity in the hot region.

The relationship between convective and diffusive flows depends on the temperature dependence of the coefficient of thermal conductivity χ. In the classical case, the coefficient of thermal conductivity is relatively small in the hot region but large in the cold region and as a result, the convective flow is very considerable. The converse situation is achieved with Bohm thermal conductivity. In this case, therefore, the convection effects are insignificant and the plasma cooling time can be calculated from Eq.(1).

The more important case of classical thermal conductivity is considered in slightly greater detail. As has already been noted, after a hot plasma has been produced, a thin layer of dense cold plasma is formed near the walls and this "eats away" all new sections of hot plasma. The thickness of this layer adjacent to the walls increases with time and the heat flow through the layer decreases. Under these conditions the bremsstrahlung from the transitional region between the hot and cold plasma may become an important factor. In actual fact, the bremsstrahlung intensity $Q_{rad} = An^2\sqrt{T}$ for $nT = \text{const}$ is proportional to $T^{-3/2}$ and becomes very substantial in a cold plasma.

In Ref.[3], it was shown that, given classical transfer coefficients,the whole of the heat flow entering the transitional layer between the hot and cold plasma can be removed from this layer in the form of radiation. The hot plasma flow rate appropriate to these conditions is found to be of the order of

$$u \cong \sqrt{\frac{\chi}{\tau_{rad}}}\,\beta^{1/4}$$

where χ is the classical thermal conductivity in the hot plasma region, τ_{rad} is the radiation cooling time for the hot plasma ($\tau_{rad} = 3nT/Q_{rad}$), and β is the ratio of the gas-kinetic pressure to the magnetic pressure in the hot plasma region. The cooling time for the hot plasma under these conditions increases proportionally to the first power of the radius: $\tau \sim R/u$. This solution clearly is only formulated for fairly large tube radii when the layer adjacent to the wall is sufficiently thick to suppress the heat flow before a considerable (of the order of unity) quantity of hot plasma is "eaten away".

Numerical calculations [3] show that, for the values of $\beta \sim 10 - 10^3$ of practical interest, the transition to the conditions where $\tau \sim R$ takes place at very large values of R which correspond to a confinement time considerably exceeding the Lawson time. These values of R also correlate to a very high energy per unit length of the device proportional to R^2 which is difficult to achieve in practice. Numerical illustrations are, therefore, given for smaller radii when radiation is still of minor importance.

The statement of the problem to be solved numerically comprises the following. At zero time a uniform cold plasma fills a cylindrical tube with a uniform longitudinal magnetic field (the walls of the tube are assumed to be ideally conducting). An external heating source chosen to simulate plasma heating by a relativistic electron beam is then switched on. It is assumed that the beam energy flux at the cathode S is known as a function of the radius and the time. Under real conditions, the magnetic field is frozen into the cathode. As,on the other hand, the beam electrons move along magnetic surfaces, the definition of the function S(r,t) uniquely determines the distribution of the heating power by volume[2]:

$$P(r,t) = \frac{S(r_0, t)}{L}\,\frac{r_0\,dr_0}{r\,dr} \qquad (2)$$

Here L is the length of the plasma, and r_0 and r are, respectively, the radii of the magnetic surface at the cathode and in the plasma. If the magnetic field in the plasma is known as a function of the radius and the time, the dependence $r_0(r,t)$ can be determined from the differential equation $H(r,t)r\,dr = H_0 r_0\,dr_0$ where H_0 is the initial uniform magnetic field (the time is contained in the equation as a parameter).

[2] In general terms, the beam liberates energy non-uniformly over the length. As a result of the high longitudinal thermal conductivity, however, the energy liberation is averaged over the length of the plasma and in the calculations it can be assumed that Q is not dependent on Z. It is naturally assumed that the plasma is thermally insulated from the ends.

A system of equations for the transport of plasma at right angles to the magnetic field was solved numerically for a heating source with a power defined by the method indicated above [4]; the electron and ion temperatures were assumed to be equal.

Figure 1b shows the important part played by the convective flow of plasma noted above. This corresponds to the time when the beam is virtually switched off and the plasma is cooling down. Energy is clearly removed from the hot plasma region into the layer adjacent to the walls by a convective flow and is then transferred as a result of thermal conductivity. In this case the plasma cooling time is found approximately an order of magnitude less than the estimated time (1), (see Fig.1a).

In the subsequent qualitative treatment of theproblem it is essential to make allowance for the fact that the magnetic field is frozen in the plasma, as is readily apparent from Fig.1b. This clearly results from simple calculations: $D_m = c^2/4\pi\sigma \ll \chi$ (where c is the speed of light and σ is the plasma conductivity) which are valid in the hot plasma region.

The situation when micro-instabilities have developed in the plasma and the transfer coefficients are anomalous is now considered. Under these conditions the upper estimate of the energy which must be supplied to the plasma to satisfy the Lawson criterion can be obtained if (as was assumed in Refs [5, 6]) a Bohm coefficient of thermal conductivity is assumed: $\chi = \chi_B$ (1/16) (cT/eH). As this assumption is evidently too pessimistic however, it will subsequently be assumed in the calculations that $\chi = \chi_B/5$.

In calculations using the Bohm (or "abbreviated" Bohm) coefficient of thermal conductivity the problem of choosing an expression for the thermoelectromotive force then arises (see Refs [5, 6]). Simple arguments show that the drift instabilities resulting in anomalous thermal conductivity are relatively weakly dependent on the thermoelectromotive force and the plasma conductivity. In calculations using the Bohm thermal conductivity therefore, the thermal forces and conductivity were assumed to be classical, which is, in fact, in accordance with the assumption that the magnetic field is frozen in the plasma (with the exception of the narrow layer adjacent to the walls).

As it is highly improbable that the thermal conductivity is classical under real conditions, the subsequent content of this paper refers to a case when $\chi = \chi_B/5$. As was noted previously, in the case of Bohm thermal conductivity the problem of the thermal balance of the plasma is simpler than in the case of classical conductivity and the estimate given by expression (1) is in this case fairly close to the real value. The problem of determining the parameters of a critical reactor with greater accuracy still remains. The results of analytical and numerical calculations of relevance in this respect are presented in the following two sections.

3. CERTAIN ANALYTICAL SOLUTIONS

It is useful to have analytical solutions for various limiting cases to interpret the numerical calculations. Two of these analytical solutions are presented below. The first of these corresponds to a beam of short duration when the thermal conductivity can generally be disregarded during the heating process. The second refers to the converse limiting case when it is necessary to solve a steady-state problem in order to determine the temperature and density distribution.

The first case is considered. Disregarding all dissipative effects and transfer processes,the equation describing the energy balance in the plasma assumes the form:

$$\frac{3}{2}\frac{\partial p}{\partial t} + \frac{1}{r}\frac{\partial}{\partial r}\left(\frac{3}{2}pur\right) + \frac{p}{r}\frac{\partial}{\partial r}(ur) = P(r,t)$$

where the heating source power is defined by equation (2). Applying the frozen in conditions for the magnetic field $H/H_0 = n/n_0(r_0)$, where $n_0(r_0) = n(r,0)$, Eq.(2) is rewritten as follows:

$$P(r,t) = \frac{f(r_0)}{L} g(t) \frac{n(r,t)}{n_0(r_0)} \cdot \tag{3}$$

It is assumed that $S(r_0,t) = f(r_0)g(t)$.

By virtue of the condition $\beta \gg 1$, the plasma pressure is uniform over the column cross-section and is only a function of time. On integrating Eq.(3) over r with allowance for the boundary condition $u(R,t) = 0$ we find the dependence p(t):

$$p(t) = p_0 + \frac{4}{3R^2} \int_0^t g dt' \int_0^R \frac{f(r_0) r_0}{L} dr_0$$

The spatial density distribution is calculated from Eq.(3) written in Lagrangian variables (r_0,t):

$$\frac{\partial}{\partial t} \left(\frac{p^{3/5}}{n} \right) = \frac{2}{5} f(r_0) g(t) / L p^{2/5} n_0(r_0)$$

The solution of this equation satisfying the initial conditions assumes the form:

$$\frac{n_0(r_0)}{n(r,t)} = \left(\frac{p_0}{p} \right)^{3/5} + \left[1 - \frac{p_0}{p} \right]^{3/5} f(r_0) R^2/2 \int_0^R f(r_0) r_0 dr_0 \tag{4}$$

To seek the density distribution in Eulerian co-ordinates, we must relate the variables r and r_0. Applying the relationship $n_0(r_0) r_0 dr_0 = n r dr$, we find

$$r^2 = \left(\frac{p_0}{p} \right)^{3/5} r_0^2 + \left[1 - \left(\frac{p_0}{p} \right)^{3/5} \right] R^2 \int_0^{r_0} f(r_0') r_0' dr_0' \Big/ \int_0^R f(r_0) r_0 dr_0 \tag{5}$$

On analysing Eqs (4) and (5), we find that the density distribution established after the beam has been switched off is essentially dependent on the profile of the beam. Graphs illustrating the functions n(r) and T(r) are plotted in Figs 2a and 2b for the two specific dependences:

$$f_1 = A \begin{cases} 1 & r_0 < a \\ 0 & r_0 > a \end{cases}, \qquad f_2 = A(e^{1-r^2/R^2} - 1)$$

The curves are plotted on the assumption that the initial distribution $n_0(r_0)$ is uniform and the ratio $p/p_0 \gg 1$. Although the density near the walls is much higher than at the centre, in the first case only approximately half of the particles are concentrated in the layer near the walls and in the second case only a small proportion of the particles are concentrated near the walls. In both cases, therefore, the density at the centre does not decrease very noticeably after heating.

By applying Eqs (4) and (5) the converse problem can be solved and the beam profile which ensures the given density and temperature distribution after heating can be determined.

The steady-state heating problem for the Bohm thermal conductivity coefficient is now considered. The statement of the problem is as follows: let a beam giving a radial heating power distribution Q(r) be injected into a cylindrical tube of radius R filled with a plasma with a uniformly

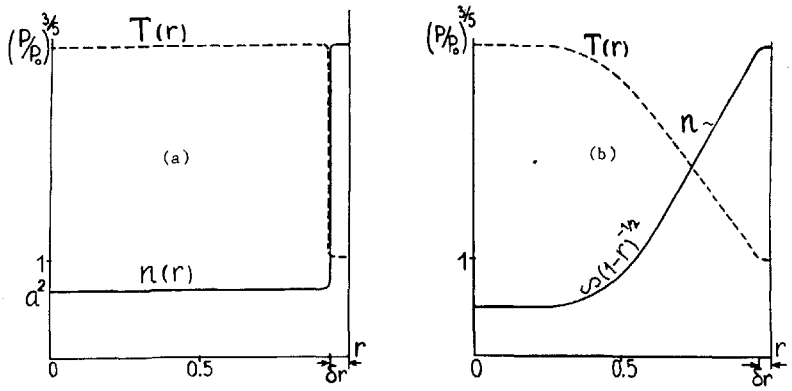


FIG.2. Graphs giving analytical solutions for the radial distributions n(r) and T(r) formed after heating a plasma with the initial parameters n_0, T_0 by a beam of short duration. The density is measured in units of n_0, the temperature is normalized to the value $T_0(p/p_0)^{2/5}$, $p/p_0 \gg 1$ is the ratio of the pressure after heating to the initial pressure, r is the radius referred to R and a is the position of the beam (in units of R).

(a) Heating by a beam with a stepped profile:

$$S(r_0, t) = \begin{cases} g(t) & r < a \\ 0 & r > a \end{cases}$$

Width of the layer adjacent to the wall:

$\delta r \sim (p_0/p)^{3/5}(1-a^2)$

(b) Heating by a beam with a smooth profile:

$S \sim [\exp(1-r^2)-1]$ $\delta r \sim (p_0/p)^{6/5}$.

distributed density n_0, temperature T_x and magnetic field H_0, beginning at a certain point in time under steady-state conditions. To simplify the calculations it will subsequently be assumed that the beam is annular in shape and therefore $Q(r) = Q\delta(r-a)/2\pi a$, where Q is the total heating power supplied per unit length of the plasma column.

A steady-state distribution n(r) and T(r) is established in the plasma within a time of the order of the heat conduction time following the initiation of injection (this is assumed to be small compared with the beam duration). The magnetic field at this steady-state stage can still be assumed to be frozen in the plasma as the field diffusion time is considerably greater than the time taken for the rearrangement of n and T as a result of the thermal conductivity, as was noted previously.

If explicit expressions for n(r) and T(r) are known from the solution of the steady-state problem, the thermonuclear yield Q_{nucl} can be calculated. The operating conditions of a reactor in the critical regime are expressed by the equality

$$Q_{nucl} = Q \tag{6}$$

By varying Q in this relationship with the beam position remaining constant, the value of R corresponding to the minimum thermal energy stored in the plasma can be determined. If the position of the beam is then varied, the optimum heating variant whereby the thermal energy is also at a minimum with respect to this parameter is then determined.

The first part of the problem stated, i.e. the search for steady-state profiles n(r) and T(r) is solved analytically. With this aim in view the equation of heat transfer and the condition for uniform pressure over r are written in dimensionless variables:

$$\frac{\partial T^2}{\partial r} = \begin{cases} 0 & r < a \\ -Q/r & r > a \end{cases} \tag{7}$$

$$nT + n^2/\beta_0 = \text{const} \tag{8}$$

The frozen-in condition for the magnetic field H = n was used when deriving relationships (7) and (8), where H and n are respectively normalized to H_0 and n_0. The values r and a are normalized to R, the unit of measurement for the temperature $\tilde{T} \equiv 10^4$ eV, Q is measured in the quantities $\pi n_0 \tilde{T} D_{B.} = \pi n_0 \tilde{T}^2 c/80eH_0$ and the constant factor $\beta = 16\pi n_0 \tilde{T}/H_0^2$.

From equations (7) and (8) it is apparent that when $r < a$ the density and temperature are uniform with respect to r. If their values in this region are designated as n_a and T_a, the solution for $r > a$ is written in the following form:

$$T = (T_x^2 - Q \ln r)^{1/2} \tag{9}$$

$$n = -\frac{\beta_0 T}{2} + \left(\frac{\beta_0^2 T^2}{4} + \beta_0 n_a T_a + n_a^2\right)^{1/2} \tag{10}$$

The constant in Eq.(9) is determined from the boundary condition at the wall $T(I) = T_x$. The value of T_a contained in Eq.(10) can be determined from relationship (9) taking account of the temperature continuity at the point $r = a: T_a = (T_x^2 - Q \ln a)$. The parameter n_a should be sought from the equation of conservation of the total number of particles:

$$a^2 n_a + 2\int_a^1 nr\,dr = 1$$

Subsequent calculations were carried out numerically. The thermonuclear yield was calculated assuming that the plasma is an equicomponent mixture of deuterium and tritium. The initial equation (see Ref.[7]) for the thermonuclear yield calculated per unit length of the plasma column assumes the form:

$$Q_{nucl} = 4.73 \times 10^{-25}\, n_0^2 R^2 \gamma \tag{11}$$

where R is measured in cm, n_0 is in cm^{-3}, Q_{nucl} is in W/cm, the energy liberated in one fusion event is assumed to be equal to 17.6 MeV and the dimensionless factor γ is dependent on the profile n(r) and T(r) and is expressed by the integral

$$\gamma(Q,a) = 2\pi \int_0^1 r\,dr \frac{n^2}{T^{2/3}} \exp\left(-\frac{9.27}{T^{1/3}}\right)$$

We note that R is not contained in Eqs (7) and (8) or the boundary conditions, and therefore n(r) and T(r) are dimensionless, and as a result γ is only parametrically dependent on Q. In this context, condition (6) must be considered as an equation defining the critical radius of the system

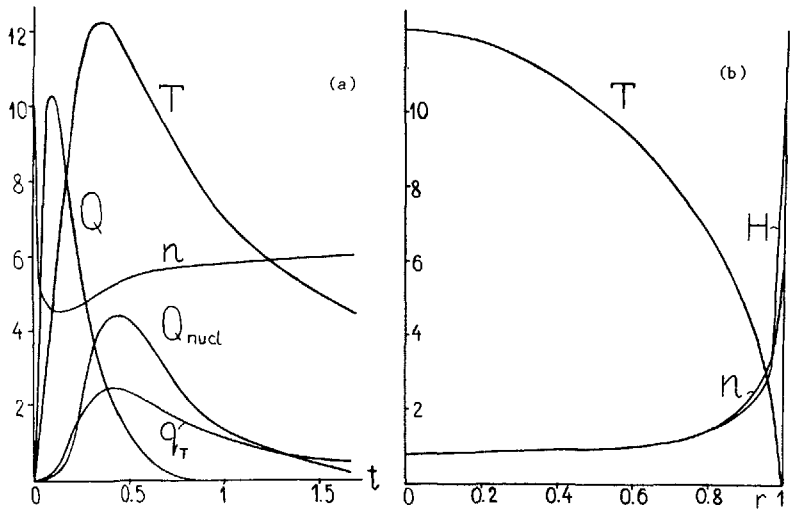


FIG.3. Non-magnetic confinement of a plasma with a Bohm thermal conductivity coefficient.
(a) Power Q of the heating source, thermonuclear yield Q_{nucl}, heat flow q_T through the chamber walls (all the values are referred to the unit length of the plasma column and the units of measurement are 5.4×10^8 W·cm^{-1}), density n and temperature T at the axis of the system (units of measurement, respectively, 10^{17} cm^{-3} and 10^3 eV) as a function of time. Units of measurement of $t = 4 \times 10^{-4}$ s.
(b) Radial distributions of the plasma prameters at the time t = 0.4 when the temperature at the axis attains a maximum. n is the plasma density (in units of 5×10^{17} cm^{-3}), T the plasma temperature (in units of 10^3 eV), H the magnetic field strength (in units of 5×10^4 G) and radius r referred to R = 7.14 cm.

when the input power is equal to the thermonuclear yield. From (6) and (11) it is evident that the dependence of R_{crit} on Q is determined by the relationship $R^2_{crit} \sim Q/\gamma(Q,a)$. The total thermal energy of the plasma is expressed by the integral

$$W = 6\pi R^2 w(Q,a),\ w(Q,a) = \int_0^1 nTr\,dr$$

Under critical conditions therefore, the dependence of W on Q is described by the factors $W \sim Qw(Q,a)/\gamma(Q,a)$. Using this representation it is readily shown that the value W as a function of Q has a minimum. The minimum corresponding to the variation in Q with fixed beam positions were determined numerically. By comparing the values corresponding to the different values of a we determined the optimum beam position a_0 when W has an absolute minimum. The corresponding optimum parameters for the plasma and the beam are as follows: $a_0 = 0.05$ R, R = 6.3 cm, $n_a = 2.8 \times 10^{17}$ cm^{-3}, $T = 1.22 \times 10^4$ eV, $W = 2 \times 10^5$ J·cm^{-1}, $Q = 3.1 \times 10^8$ W·cm^{-1}, and the bremsstrahlung power $Q_{rad} = 1.2 \cdot 10^8$ W·cm^{-1}. In this example, the values of n_0, H_0 and β_0 were assumed to be equal to $n_0 = 10^{18}$ cm^{-3}, $H_0 = 10^5$ G, and $\beta_0 = 80$.

4. NUMERICAL CALCULATIONS ON THE NON-STEADY-STATE PROBLEM

Figure 3 is plotted to illustrate the numerical results obtained for the case when $\chi = \chi_B/5$. This corresponds to the following conditions: radius of tube 7.1 cm, initial plasma density 10^{18} cm^{-3} and initial magnetic field 10^5 G.

The function S describing the radial distribution of the beam power near the cathode (see Eq.(2)) was taken as follows: $S \sim [\exp(1-r_0^2/R^2) - 1]$. Figure 3a shows the total beam power as a function of time.

In the numerical example quoted the beam parameters were taken such that the reactor was "critical", i.e. such that the energy yield of the thermonuclear reactions[3] was equal to the total beam energy per pulse. In this case, allowance was not made for heating of the plasma by α-particles as,in the case under consideration,the Larmor radius of the α-particles was of the order of the radius of the tube. The beam energy necessary to achieve critical conditions was found to be equal to 6×10^5 J·cm^{-1}. It is interesting to note that this agrees with the critical energy in the steady-state problem considered above within a factor of 3.

In accordance with the assertions made in section 3, the plasma energy life-time which can be calculated as (3–4) 10^{-4} s on the basis of Fig. 3a for the case of Bohm thermal conductivity agrees fairly well with the value calculated from expression (1). The difference between the Bohm thermal conductivity and the classical thermal conductivity noted in Section 2 becomes apparent at this point.

Another interesting result of this numerical analysis is that the radiation losses for the example considered are less than 30% of the total energy input.

In conclusion, we note that in all the analytical and numerical examples considered above allowance was made for the cold rigid wall by introducing simple boundary conditions $V_r|_{r=R} = 0$ and $T|_{r=R} = T_x$ where T_x is not dependent on time. In numerical calculations conducted previously [5, 6] it was observed that the behaviour of the plasma in the hot region varies only slightly for a wide range of variation in T_x (from 3–30 eV). This indicates that wall effects do not exert a very substantial influence on the model as a whole.

Results relating to the role of impurities produced during vaporization of the thin surface layer of the wall and penetrating into the hot plasma in various quantities can be found in Ref.[8].

5. CONCLUSIONS

The main conclusions which can be drawn from these results are as follows:

Firstly, the nature of the cooling processes for a plasma with $\beta \gg 1$ is dependent on the function $\chi(T)$ to a significant extent: when the thermal conductivity is classical,convective flow and (in certain cases) bremsstrahlung play an important part whereas, when the thermal conductivity is of the Bohm type,these effects are of little importance and the plasma energy life-time can be calculated from Eq.(1).

Secondly, even if the assumption on the thermal conductivity is not very optimistic ($\chi = \chi_B/5$), the energy input to the plasma necessary to satisfy the Lawson criterion is found to be fairly low $(2–6) \times 10^5$ J·cm^{-1} (depending on the distribution of the heating sources over the cross-section), which is acceptable with a total plasma column length of up to 10 m (see Ref.[9]). Non-magnetic confinement is therefore found to be a completely realistic possibility.

It will subsequently be interesting to consider the importance of any possible axial asymmetry of the heating and also to investigate the processes in the layer adjacent to the wall in greater detail.

[3] It is assumed that the densities of the deuterium and tritium are the same.

REFERENCES

[1] BUDKER, G.I., MIRNOV, V.V., RYUTOV, D.D., Pis'ma Zh. Ehksp. Teor. Fiz. 14 (1971) 320.
[2] BUDKER, G.I., in Plasma Physics and Controlled Fusion (Proc. 6th Europ. Conf. Moscow, 1973) 2, Moscow (1973) 136.
[3] VEKSHTEJN, G.E., Prikl. Mat. Tekh. Fiz. 6 (1976) 31.
[4] BRAGINSKII, S.I., Questions of Plasma Theory, Atomizdat, Moscow (1963) 183 (in Russian).
[5] CHEBOTAEV, P.Z., RYUTOV, D.D., SPECTOR, M.D., VEKSHTEJN, G.E., in Plasma Physics and Controlled Fusion (Proc. 6th Europ. Conf. Moscow, 1973) 411.
[6] VEKSHTEJN, G.E., RYUTOV, D.D., SPEKTOR, M.D., CHEBOTAEV, P.Z., Prikl. Mat. Tekh. Fiz. 6 (1974) 3.
[7] ARTSIMOVICH, L.A., Controlled Thermonuclear Reactions, Fizmatgiz, Moscow (1963) (in Russian).
[8] VEKSHTEJN, G.E., RYUTOV, D.D., CHEBOTAEV, P.Z., Fiz. Plazmy 1 3 (1975) 401.
[9] RYUTOV, D.D., Usp. Fiz. Nauk 116 (1975) 340.

DISCUSSION

ON PAPER IAEA-CN-35/E 21

C.M. BRAAMS: Could you comment on the effectiveness of multiple mirrors for axial confinement in the case where $\beta \gg 1$?

E.P. KRUGLYAKOV: The work described here relates to the case where $\beta \gg 1$, say of the order of 100 or 1000. Hence we are dealing essentially not with magnetic confinement but with wall confinement. The role of the magnetic field is merely to suppress transverse thermal conductivity (radial heat losses) in the plasma.

Session XXV

SUMMARY OF THE CONFERENCE

Chairman

B.B. Kadomtsev
USSR

SUMMARY OF MAGNETIC CONFINEMENT (EXPERIMENTS)*

R.S. PEASE
United Kingdom Atomic Energy Authority,
Culham Laboratory,
Abingdon, Oxfordshire,
United Kingdom

Some 65 of the 150 papers presented at this excellently organized and planned Conference reported new experimental information on the magnetic confinement of high-temperature matter. Contrary to some fears that the reduction to two years of the interval between Conferences would lead to a paucity of new material, these papers reported important new advances in several areas; and the Conference was both timely and fruitful.

The largest bulk of the new material dealt with plasma confinement in systems of the tokamak type. The greatest interest centred on the first results from two new tokamaks, PLT at Princeton, USA, and T-10 at the Kurchatov Institute, Moscow, both being larger than any hitherto operated (minor radius 37 cm for T-10, 40 cm for PLT), and using larger currents, up to 600 kA (A 1, A 2). The new experimental information presented with great care indicates that substantial increases in the confinement time are achieved with these large assemblies. Although neither apparatus has yet been worked up to maximum current or magnetic field, nor optimized for maximum confinement time, energy confinement times between 40 and 60 ms are reported. In their presentations, both Drs Stodiek and Strelkov avoided detailed discussion of the scaling laws, arguing that these initial results were too preliminary; but it does seem that the agreeably simple scaling law $\tau_e \propto a^2 B_\theta$ used in earlier Soviet tokamaks may be a shade too optimistic for the data obtained so far. In T-10 and PLT electron temperatures of a kilovolt and more were readily obtained, together with ion temperatures of up to 1 keV, and sustained for periods of up to 1 s. The Princeton tokamak was able to operate in a mode of exceptional MHD quiescence, which may well lead to important advances. The results obtained on these two machines are in substantial agreement; perhaps the most noticeable difference being the lower value of Z_{eff} in T-10, in part owing to the fact that PLT was largely operated in helium.

Both groups reported that the discharges in these new tokamaks had essentially all the characteristics – turbulent start-up phase, MHD activity in a steady state, confinement time improving with density, disruptive instabilities in some circumstances – seen in smaller tokamaks. It seems, therefore, that increasing the size of tokamaks has not so far produced any new problems, and has already produced improved confinement times, though we shall have to await further observations before the full extent of the improvement is known.

The second great advance reported from the tokamak experiments is the achievement of operation at high densities. By these means the Alcator Group (A 5) have increased the product $n\tau_e$ to a record value of 10^{13} cm^{-3} · s, at a cost of only a modest drop in the average electron temperature. A similar result was obtained by the Pulsator Group at Garching (A 6). But it may well turn out that the record value of density is now held by the 10^{15} cm^{-3} in the SPICA device at Jutphaas (E 6), when operated as a tokamak with $q \sim 1.5$. The value of $n\tau_e$ achieved in Alcator approaches that expected from ion conductivity in the plateau – Pfirsch-Schlüter transition regime. The upper density limit is still determined by the onset of disruptive instabilities.

---

* This summary talk was also published in Nucl. Fusion 16 6 (1976) 1047.

The main reason given for these improvements is first, the improved cleanliness of the machine; second the use of supplementary pulse gas feed after the discharge is established; and thirdly (in the case of Alcator) the use of high toroidal fields (80 kG) which hold off disruptive instabilities to higher values of the density than with low fields.

A third major advance is the application of powerful neutral injection heating to tokamaks. Several groups have reported that ion temperatures have been doubled (A-4.1, 2, 3; A 17), both the Ormak Group and the TFR Group achieving ion temperatures of nearly 2 keV with several hundred kilowatts of injected neutrals. Almost equally interesting is the fact that the increase of ion temperature is proportional to the beam input power. This corresponds to a constant ion energy confinement time and is therefore better than would be expected of the plateau regime in which these tokamaks are usually thought to operate. It is in agreement with neo-classical calculations in the Ormak case. On the other hand, no increase of electron temperature was observed; this result tends to emphasize the magnitude of the electron thermal conduction leaks, even though the ordinary Ohmic power is considerably larger than neutral injection power to the electrons. A more direct attack on the electron heating problem will be of great value in providing an independent control of T_e, as indeed was initiated on the Russian tokamak TM-3 some years ago.

Substantial experimental studies were reported by several groups, especially the TFR team, on the details of the energy balance as a function of minor radius (A 4-1, A 3, A 8, A 11). In the inner regions of the discharge, $q \sim 1$ and there is MHD turbulence and a rapid transfer of heat apparently explicable by this turbulence; in the outer region, the MHD activity is apparently and, as expected, suppressed, and the heat is conducted across the lines of force, presumably by microinstability. A new result reported by the TFR Group is that the amplitude of the fluctuations interpreted as a dissipative trapped electron mode fails by a factor of ten to account for the heat loss. There is strong independent evidence both from other tokamak experiments and from the Levitron (D 12) that the current-driven drift wave is present, and it is perhaps not necessary to blame everything on the trapped electron mode. A substantial spectrum of drift waves was observed also by the Princeton Group using microwave scattering, and in this case quite substantial spatial variations of intensity are seen. If the Levitron observations are, as indeed appears, related to tokamak conditions, then the improvement of confinement time with density may soon saturate at the limit of $u/v_e = 3 \times 10^{-3}$ found in the Levitron.

It would appear that in general the observations agree on the high cross-field conductivity due to MHD turbulence in the inner regions; that the ion thermal conductivity is close to neo-classical, but that the electron thermal conductivity is up to a hundred times neo-classical, at least at low densities, for reasons which are not yet identified, but could be a variety of drift-wave-type fluctuations, of which a current-driven mode seems to be the most nearly identified on the results reported at the Conference. Radiation and charge-exchange transport is mainly predominant in the last stages of transport to the walls in the outer regions.

Tokamak research was also marked by some careful experimentation on disruptive instabilities by the Garching, TFR and Japanese Groups (A 7, A 8, A 9). These are phenomena now known for many years – they occurred in stellarators. The most obvious fact of disruption is that the current stops. We seem to be no nearer an explanation of this fact. However, the main conclusion of the detailed observations is that a major disruption appears to be caused by an interaction between an $m = 1$ disturbance in the inner region (where $q \approx 1$) and an $m = 2$ tearing mode (due to too steep a current density gradient) in the outer regions. In principle, it seems that this should be controllable and disruption ought to be capable of suppression by feedback mechanisms.

The Conference was interested by the account from Culham of the bundle divertor (A 17) and from Japan of the DIVA axisymmetric divertor experiment (A 18). Both experiments were conducted at fairly low currents, so that although it appears that the divertor produces substantial favourable effects on the influx of impurities and background gas, we do not yet see these improvements reflected in decisively increased density, temperature and confinement times. However, the

prospects now offered of a positive method of dealing with impurities are likely to be of great importance.

Finally, a number of papers dealt with the study of shaped cross-sections (A 10 - 3, 4, 5, 7). Alarmed by the low value of β obtained in ordinary tokamaks, a number of experimentalists have studied shaped cross-sections in the hope that higher values of β can be obtained. When these experiments have operated in a normal tokamak mode, there has been no big increase in the values of β obtained (about 1%). It may be, of course, that the heating methods have been too weak. When operated as a belt pinch (A 10-1, 2, 6 and E 8), encouragingly higher values of β are obtained, about 10%; but the penalty here is that the discharges are very much cooler, and last less than 100 ms. I do not understand the reason for this severe penalty. A final point in the experimental studies of tokamaks is the achievement in Tuman II, in Tosca and ATC, of a plasma column well-isolated from any material limiter and showing substantially improved confinement times. The reasons for this improved confinement time are by no means clear, but the phenomenon may turn out to be very important.

The next major event I need to deal with are the results of experiments on stellarators. The importance of the results reported may be gauged in the following way. The main outcome of the massive experimental and theoretical attack on the stellarator system made at Princeton on the C-stellarator during the 1960s was that stellarators suffer from Bohm diffusion and this appeared to be largely unexplained and incurable and led to a typical value of 500 μs confinement time at 100 eV electron temperature. The present results reported from Cleo, Wendelstein VII-A, and L-2 (D 1, D 2, D 5) show electron temperatures up to 900 eV and energy confinement times in the range 1-8 ms. There are some differences between the observations, which is perhaps not surprising at this early stage, and which can no doubt be explained, but it seems fairly clear that energy confinement times of about 20 Bohm times are established. The results represent a clear and major advance on the old C-Stellarator data, which do not depend on any particular interpretation. Dr. Suprunenko and his colleagues have very impressive results in terms of Bohm diffusion from the Uragan II apparatus (D 6) which, however, is relatively small-scale; and he made the point that the results obtained from a wide variety of apparatus agreed rather well with the so-called pseudo-classical theory which, in effect, attributes the success of these new stellarators to the much larger poloidal flux built into them. As is well-known, this poloidal flux was particularly small (equivalent to no more than 10 kA) on the C-Stellarator.

The possibility that stellarators might actually turn out to be better than tokamaks provoked some discussion. But the role of the strong Ohmic heating current used in all these experiments is not clear. It may be that there are mechanisms, such as the inward E $\times$ B drift or the enforced closure of some lines of force that make stellarators behave better when they are Ohmically heated. On the other hand, if the current-driven instability is as important as appears from the Levitron, then Ohmic heating would lower the performance. At all events, there will be great interest in the generation of plasma by non-Ohmic methods in these traps and the subsequent measurement of confinement times. Furthermore, it may then be possible to re-investigate the problem of the bootstrap current in these new and more striking conditions.

The simplest high-beta toroidal system which, because it is axially symmetric, is theoretically a clear-cut system, is the reverse-field pinch. A number of papers (E 1, E 2, E 3 and E 7) reported the successful establishment of this configuration for currents up to about 60 kA, with beta of the order of 30%, densities of up to 10^{16} and a low temperature lasting for perhaps up to 50 μs being obtained. The difficulty is, however, that when these configurations are produced by rapid programming of the fields, they tend to have too high a value of beta, and the resulting instabilities become serious at currents above 60 kA. However, experiments from Los Alamos clearly showed the benefit of size scaling; and experiments from Padua showed that the generation of the reverse field by the relaxation process was equally effective; it is indeed probably the best method in the long run.

The high-beta stellarator, being unsymmetric, does not have the theoretical simplicity of the reverse-field pinch and extremely complicated geometries have been evolved hopefully to secure equilibrium and stability. There were three particularly interesting experimental results first the 9-metre helical theta pinch at Jülich successfully demonstrated stabilization of the m = 1 mode by conducting wall effects with a fat discharge as predicted by theory (E 23). Secondly, a detailed experimental study of the finite-Larmor-radius stabilization showing numerical agreement with theory for the m = 2 mode on the ISAR T-1 apparatus at Garching (E 9). And, finally, the success achieved at Los Alamos by the feedback stabilization of the column, thus increasing the life-time nearly threefold, an encouraging indication of the possibilities of this technique at higher powers (E 10). Nonetheless, all these high-beta systems are still characterized by short-duration and rather collisional plasmas; until these problems of MHD equilibrium and stability can be satisfactorily solved on a routine basis, real research on their confinement properties cannot start. It is therefore encouraging that the main experimental results obtained were in agreement with theory, and therefore it should be possible to predict the conditions required to advance the performance of these important systems.

Of the remaining toroidal confinement systems, fundamental results were reported from the Superconducting Levitron at Culham (D 12) and from the Octupole devices at Wisconsin and General Atomics. A number of papers dealt with configurations determined in part by fields generated by ion and electron beams whose energy – usually relativistic – introduces terms by which they are stabilized (H 2, H 4). The Cornell Group continues to hold out substantial hope of ring-shaped beams of electrons (or ions) being able to generate new toroidal configurations. In their RECE experiment, they successfully sustained several tens of kiloamps in what became a D-shaped tokamak minor cross-section with relativistic electrons for over 200 μs. – The most important example of this principle in action is the Elmo bumpy torus at Oak Ridge (D 7), where the key feature of the field, $\oint d\ell/B$ stabilization, is provided by rings of trapped energetic electrons. Here the microwave power has been increased so that ion and electron temperatures in the range 100–200 eV and beta values of approximately 1% are obtained. The open-ended magnetic systems were relatively sparsely represented. However, the one paper (C 1) giving new experimental results on mirror machines reported substantial and important new results. The report on the 2XII mirror machine at Livermore describes the new results obtained by installing and operating a powerful neutral injection assembly, giving a total of 370 amperes equivalent of neutral deuterons at 15–20 kilovolts. With this massive 5 MW injection system, densities of up to 10^{14} cm^{-3} have been obtained together with high values of β – around 70%. The injection is sufficiently powerful to be self-sustaining in the absence of the initial target plasma, that is, "burn-out" has been achieved. The paper also reports results establishing the nature of the microinstability which can afflict mirror machines; it is the drift loss-cone cyclotron mode; it can be and is suppressed in accord with theory by adding a small stream of warm plasma to smooth out the sharpest features of this loss-cone in the ion velocity distribution. This brings the conclusions of the Livermore Group and of Dr. Ioffe's Group at the Kurchatov Institute into agreement, and is an important advance since Tokyo.

Thus these experiments seem to establish a relatively satisfactory general understanding of the plasma physics of mirror machines; and our problem now is to apply it to achieving something nearer reactor conditions. For the difficulty revealed by these experiments is one common to all open-ended systems: the electrons are too cold. Thus, although the ion losses are correctly described as being near-classical, the major effect is a slowing down of the ions on the cold electrons. The electron temperature is less than 100 eV; and the maximum observed value of $n\tau_e$ averaged over an ion orbit is 2×10^{10} cm$^{-3} \cdot$ s, a value which is in agreement with collisional slowing down theory. If we extrapolate using the same theory ($n\tau \propto T_e^{3/2}$), then it appears that the electron temperatures required in a reactor will approach 10 keV, a difficult though not impossible target for an open-ended system. The studies also need to be extended towards fatter plasmas containing many ion Larmor radii in the plasma radius.

TABLE I. PLASMA PARAMETERS IN TOROIDAL PINCHES

Year	τ_e (s)	T_i (K)	$n\tau_e$ ($cm^{-3}s$)	Sustainment time (s)
1955	10^{-5}	10^5	10^9	10^{-4}
1960	10^{-4}	10^6	10^{10}	3×10^{-3}
1965	2×10^{-3}	10^6	10^{11}	2×10^{-2}
1970	10^{-2}	5×10^6	5×10^{11}	10^{-1}
1976	5×10^{-2}	2×10^7	10^{13}	10^0
Needed for a reactor	10^0	10^8	10^{14}	$\gtrsim 10$

Finally, then, to another linear system, the plasma focus which, however, holds out the possibility that a transverse magnetic field will restrict thermal conduction losses along the axis. The plasma focus is one of the most fascinating physics devices we have: it is very simple, it routinely produces ion and electron temperatures of several kilovolts, it produces far more neutrons per shot than does a tokamak, the neutron yield Y_n increases more rapidly than the stored energy ($Y_n \propto I^{3.3}$). In the papers presented (E 18-1, 2, 3, 4 and 5), interesting new information came from the Limeil and Stuttgart groups, who have embarked on a more detailed diagnostic programme particularly using probes. Direct measurement of anomalous resistance is made in an attempt to link the onset of turbulence with the ion acoustic instability. Ion-ion interaction due to an ion acceleration along the axis is responsible for most of the fusion reactions. By using thin deuterated polythene targets, it was shown that in low pressure conditions more than 80% of the neutrons are produced by directed bombardment. Additional heating has also been used on these plasmas (G 14-1, G 14-4). Powerful CO_2 laser beams were unexpectedly well absorbed due to non-linear effects; but it would appear that power levels have to exceed about 10^9 W for there to be any significant changes in macroscopic parameters – a useful lower limit check on the power input to the electrons. Direct estimates show power input increasing with current, being typically about 10^{11} W. The energy loss time is 10^{-9} s and for this case the transverse magnetic field seems to restrict the electron thermal conduction which would otherwise exceed 10^{12} W.

Do we have a good picture of the main physical processes in the plasma focus? Apart from the initial compression phase – which is well described by 2D computer codes – the answer is no. However, careful measurements of relatively simple quantities, such as are described in these papers, particularly for the phase after the first bounce, may lead to the main framework. The question of how the current leaves (and enters) the electrodes also may reward attention: it seems to me that the ion acceleration process may well be intimately linked with this. The plasma focus may well turn out to combine some of the features of the gas blanket system and of the twin component system, with ion energy and current determined by the Alfvén-Lawson limit.

In a short review such as this, many interesting and important papers have been overlooked. New methods of heating plasma by RF techniques and by lasers were described. Diagnostic tools were improved. First, a rejuvenation of infrared spectroscopy (A 13) has obviously been of great value to the diagnosis of runaway electrons in tokamaks. Secondly, a most elegant and simple technique has been developed at Princeton (A 11) for the direct and unambiguous measurement of q(r) in a tokamak; almost equally elegant is the direct measurement of Z_{eff} by what would be called Rutherford back-scattering in a solid state context.

The key information we seek in our studies of each system is: under what conditions can Lawson's confinement criterion ($n\tau > 10^{14}$ cm$^{-3} \cdot$ s) be satisfied in a hydrogen plasma at temperatures of 10-20 keV subject only to the constraint that the conditions should hold out some prospect of leading to a practical thermonuclear reactor? Just as we were warned in the past against being overly influenced by theoretical considerations, so perhaps now we should not be overly influenced by reactor considerations. Of course, everyone wishes to see the work successfully realized in a reactor. But as this review shows, experiments on magnetic confinement are still in the research stage where the greatest economy in our work is secured by concentrating on understanding the phenomena, and being prepared for the unexpected to turn up.

Table I indicates the general rate of progress that we have been reaching with tokamak systems over the past twenty years or so. One can see the surprisingly steady progress that has been maintained. Furthermore, looked at logarithmically, we have now covered the greater part of the total distance. What remains is difficult, but the difficulties are finite and can be summed up by saying that we do not yet have an adequate understanding of or control of the cross-field electron thermal conduction.

SUMMARY OF MAGNETIC CONFINEMENT (THEORY)*

M.N. ROSENBLUTH
The Institute of Advanced Study,
Princeton, New Jersey,
United States of America

INTRODUCTION[1]

Let me perhaps begin by making several observations of a general character.

(1) It becomes quite clear to anybody who tries to read through and understand the theoretical papers presented here that fusion theory has become a mature branch of theoretical physics. The papers are all of high quality; we have heard a great number of new, interesting and correct results sometimes even all three in the same paper. There is by now a large and effective international community of experts.

(2) Computational physics is playing an increasingly important role in plasma theory. In fact, I strongly suspect that by the next IAEA meeting this summary will have to be given by a computer! There are many examples we have heard here where progress has been achieved by a detailed interplay between experiment, analytic theory and computation. This trend will certainly become increasingly strong as we try to understand highly non-linear phenomena in complex geometries.

(3) No basically new types of instabilities have been discovered for some years. An optimistic interpretation might be that all of these problems have been by now identified. Rather, the novel proposals here were generally on the positive side – such as the new heating scheme of Canobbio [G 6] based on destruction of the third invariant, the novel scheme for obtaining field reversal with ion beams as presented by Sudan [H 4] and the triple mirror scheme of Dimov [C 4] and Fowler (Fowler, T.K., Logan, G., Lawrence Livermore Laboratory, Int. Rep., submitted to Phys. Rev. Lett.) for greatly increasing the Q of open traps.

(4) Some very important relevant areas of physics were not treated here. I have particularly in mind the questions of surface physics which seem to dominate many experiments. How do we account for the differing Z_{eff} reported for T-10 and PLT? [2] I think we will have to bring these studies out of the kitchen before too long.

(5) By far the most vivid impression which I have had at this meeting however is the extent to which the rather exotic topics with which theoreticians amused themselves 5 or 10 years ago have now become recognized as the central issues of fusion physics which are dominating the experiments.

---

* This summary talk was also published in Nucl. Fusion 16 6 (1976) 1047.

[1] As this summary was presented orally, references in the text have been made to first authors or to those who gave the oral presentation of the results at the meeting. The purpose of such references was to jog the memory of the audience concerning the topic discussed, without excessive name-dropping (some papers having 20 authors). Certainly, there is no intention of assigning priority to one or another of the authors, and no attempt has been made to ascertain the previous history (if any) of the ideas discussed.

[2] While the formal oral presentations seemed to indicate a large difference in impurity content between T-10 and PLT, more detailed discussion at the evening sessions seemed to show that there may be more differences of interpretation than anything else. This specific matter obviously requires and will receive further clarification, but it remains true that scientific study of surface questions in fusion experiments has been inadequate.

In this connection I have attempted to organize the papers presented here into five major theoretical topics. Most of the theoretical papers are indeed concerned basically with one or another of these topics:

I – Neo-classical transport (impurities)
II – Ideal MHD theory and finite Larmor radius (β enhancement)
III – Tearing modes (disruptions)
IV – Drift waves, trapped-particle modes (anomalous transport)
V – Drift cone mode (mirror confinement).

In particular, I should point out with some perverse theoretical pride that items III, IV, and V are now clearly identified as principal culprits leading to confinement limitations in present experiments.

I. NEO-CLASSICAL THEORY

Let me first discuss very briefly the studies made here of neo-classical transport, dealing primarily with impurity diffusion. As all of us are aware, most tokamak experiments up to now seem to be consistent with the possibility that while electrons behave anomalously owing to fluctuations, ion behaviour is still classical. Whether this can remain true as we pass into the more collisionless domain of trapped-particle modes is very questionable. Nonetheless, it appears worthwhile to investigate the classical predictions for impurity distribution. The classical calculations and the results are both very complicated. I am somewhat worried that these authors may not have considered the point stressed by Ware (Hazeltine, R., et al., Plasma Physics and Controlled Nuclear Fusion Research (Proc. 5th Int. Conf. Tokyo, 1974) **1**, IAEA, Vienna (1975) 589) that $Ze\,\phi_{pol} > T$ for high Z impurities. Let me give just a few conclusions of these authors:

(1) For these purposes, the Pfirsch-Schlüter regime must be further subdivided depending on the relative collisionality of ions and impurities [B 8–3]
(2) For an exact steady state, it is necessary that a cold dense plasma blanket form near the wall (T = 0). Under these conditions, impurities may tend to concentrate near the outside [B 7].
(3) Taking all these factors into account, neo-classical impurity concentrations as predicted by transport codes tend to be not so peaked as feared, and may perhaps be subject to some external control [B 8–1, B 8–2]. Anomalous convection may also have a uniformizing effect.
(4) A simple argument on a related topic [B 6] shows that since radiation losses go like n^2 and peak at intermediate temperatures, a maximum density limit is predicted for a given energy input. This limit is compatible with that observed in many experiments.

II. IDEAL MHD THEORY AND FINITE LARMOR RADIUS (FLR)

The greatest number of papers has been in this category. I cannot discuss them all. Perhaps the main thrust of the ideal -MHD papers has been an attempt to find toroidal configurations capable of sustaining a high-β plasma and studying their stability. Before proceeding to discuss these, I should like to point out, however, that we have seen, over the past few years, particularly in the work at Garching [E 9] and Los Alamos [E 10] a rather remarkable vindication of the fine points of MHD theory. Quite complicated toroidal systems involving three sets of helical windings have been used in the θ-pinch experiments. Analytic work has successfully predicted the equilibrium and the growth rates of sharp-boundary m = 1 modes, while remarkable 3 D

computer simulation [E 11] has extended the considerations to diffuse profiles, comparing well with experiment. Considering that the energy involved in these modes is only a tiny fraction of that stored in the plasma, it is quite reassuring that such a delicate balance can be correctly treated and shows that the MHD equations in their appropriate limit are, indeed, valid.

This work has been extended at this Conference to a quantitative formulation for this geometry of the finite-larmor-radius (FLR) corrections [E 9, E 16] which explain the suppression of m = 2 modes. I believe, however, that there remains an open question – whether the FLR overstable modes are not still subject to slow growth based on dissipative or resonant effects. The elegant paper by Tasso [H 1] shows that such residual growth is generally to be expected in kinetically stabilized systems although the growth may be slow and hard to estimate.

In any case, the evident success of MHD theory in these cases lends credence to the varied proposals made here for improving the beta of toroidal systems. Papers by Lortz [E 9] and Todoroki [E 12] indicate the possibility of attaining configurations which are at least interchange-stable with β's of up to 10%, in bumpy torusses with elliptical cross-section. The absence of tearing modes in such zero-transform configurations is another strong argument in this direction. High-β doublet equilibria [B 11–1] were also presented and their evolution discussed by Grad [B 9].

A number of computational papers [B 11–2, B 11–3] considered the problem of axisymmetric instabilities in shaped systems such as PDX. The danger that the plasma can only be repelled from the wires by strong skin currents or feedback is clear. Computational results of Troyon [B 11–4] for the MHD spectrum of non-circular small-aspect-ratio tokamaks showed that, for a vertical elongation of two, the internal kink stability criterion is less stringent than the Mercier criterion.

Turning to stellarators, Shafranov [D 8 –1] has now simplified the theory of a figure-eight stellarator to the point where MHD calculations become feasible. In particular, it is shown that the stability window between the various m-number kink modes become wider as the transform is supplied in larger part by external windings as opposed to Ohmic currents.

Interest in reversed-field pinches was greatly stimulated by the Tokyo paper of J.B. Taylor, (Plasma Physics and Controlled Nuclear Fusion Research (Proc. 5th Int. Conf. Tokyo, 1974) 1, IAEA, Vienna (1975) 161), which showed that under the constraint of the constancy of the flux constant, $K = \int A \cdot B \, d\tau$, a certain force-free current distribution ($\vec{j} = \lambda \vec{B}$ where λ is independent of position) represents the minimum energy state for the system, hence, stable against MHD and tearing modes. Further, in the case of reversed-field pinches with proper parameters such a system could be shown to be stable even if surrounded by a small vacuum region. Moreover, owing to the positive stability of the system, it is clear that some window for finite stable β must be present. We have heard at this meeting several important extensions of this theory. Jukes [E 5] while not able to prove general stability for useful finite-β systems, has verified Taylor's conjecture that K indeed remains effectively constant for the tearing mode. Moreover, detailed calculations reported on by Culham [E 2] indicate that carefully tailored MHD-+ tearing-mode-stable profiles with β up to 50% may be found. Whether such profiles can be maintained in the presence of dissipation, or whether they are immune to microinstability remains to be seen.

Finally, in this category of β-enhancement, some favourable developments have been reported on even for the simple tokamak. In particular, the ORNL group [B 10] have made the point that by varying the arbitrary functions $p(\psi)$ and $I(\psi)$ in the Grad-Shafranov equilibrium equations, a wide variety of possible equilibria may be found. In particular, a natural possibility to explore would be that which could be obtained by rapid heating, e.g. by neutral beams. In this case, as the pressure is increased, the rotational transform remains constant as a function of toroidal flux.

Such flux-conserved tokamak equilibria have been found capable of supporting average β's of up to 30%, well above the conventionally accepted values. Clearly, these equilibria depend very strongly on the "cementing" together under considerable stress of the poloidal and toroidal fluxes, and one may wonder about the effectiveness of the self-dug magnetic well against ballooning and tearing modes in the presence of such a large apparent energy reservoir. Nonetheless, if calculations support the stability of the FCT, it will be perhaps the most direct route to usable toroidal β's.

III. TEARING MODES (DISRUPTIONS)

It is now almost universally agreed that the internal disruptions observed in tokamaks are $m = 1$ tearing modes and the theory of these saw-tooth oscillations can now be said to be reasonably well understood in terms of a cycle of Ohmic heating and current peaking followed by an $m = 1$ tearing mode which flattens the profile. The major disruptions clearly involve an $m = 2$ tearing mode, although we are still far from a quantitative or complete story on these.

As discussed by Kadomtsev [B 1], the energy reservoir which can be tapped by magnetic reconnection drives the disruptions. Following Taylor, he pointed out that if free reconnection were possible, a minimum energy state consistent with the constancy of $K = \int A.B\, d\tau$ or, equivalently, of $\int \psi d\phi$, (with ψ and ϕ the poloidal and toroidal fluxes) would be reached with a constant-current density profile, inconsistent with tokamak wall boundary conditions. Such a reconnection evidently implies an expulsion of poloidal flux, i.e. a negative voltage spike. Fortunately, such reconnections cannot take place freely as in a diffuse pinch, but only near the rational surfaces. Moreover, from the linear theory, one sees that island formation is strongly energetically inhibited except for low m-numbers, by analogy with the familiar plane-slab case in which only long wavelength are unstable. Thus, $m = 1$ is always highly unstable for $q < 1$, $m > 2$ is stable for most profiles and $m = 2$ is usually weakly unstable. In this connection, Furth (Glasser, A.H., Furth, H.P., Rutherford, P.H., submitted to Phys. Rev. Lett.) pointed out that by choosing a current profile suitably flattened around the $q = 2$ surface, all tearing modes can be made linearly stable. Evidently, if sufficient external control over the profile can be maintained, this might solve the disruption problem.

In any event, for practical purposes, we need to consider chiefly the $m = 1$ and 2 modes and the possible coupling between them. This coupling may be linear, owing to toroidal effects, or non-linear.

Coppi [B 13] has pointed out that, at high density, ion viscosity may effectively stabilize the $m = 1$ mode. In the definitive paper given by Bussac [B 3] the linear theory of the $m = 1$ and 2 modes for circular tokamaks has been perfected, including kinetic effects and toroidal coupling. Perhaps the principal result of the Bussac paper is to show that unless the shear near the $q = 1$ surface is very small the linear coupling is quite weak, the two modes $m = 1$ and $m = 2$ being essentially independent. If the shear is extremely weak, as may result from previous $m = 1$ tearing, it is found that the $m = 2$ mode can drive the $m = 1$ mode to fairly large amplitude. Whether the locking of frequencies observed before disruption is this coincidental driving of the $m = 1$ mode or is a more fundamental non-linear interaction such as postulated by Kadomtsev remains unclear. Such non-linear coupling could occur through a driven $m = 3$, $n = 2$ mode, for example.

The non-linear tearing behaviour of the $m = 1$ and $m = 2$ modes has been investigated rather completely numerically in the uncoupled cylindrical limit [B 2–1, B 2–2, B 2–3]. The situation for the two modes is quite different.

The $m = 1$, which is nearly neutrally stable according to ideal MHD theory, is observed to proceed very rapidly into the non-linear regime, leading to complete reconnection of the flux around the $q = 1$ surface on a time scale much faster than the $\eta^{-1/2}$ postulated by Kadomtsev. It may be guessed that finite-island size here leads to an MHD-unstable configuration, thus giving rapid growth. In any event, the consequence is to prevent any current peaking within the $q = 1$ surface.

The island width, w, of the $m = 2$ mode grows slowly according to the Rutherford theory, $\dot{w} = \eta\Delta'(w)$, in the weakly non-linear regime (Rutherford, P.H., Phys. Fluids **16** (1973) 1903). Unfortunately, $\Delta'(w)$ nearly tends to zero for large island size so that whether the island growth saturates or not depends in great detail on the complex evolution of the transport coefficients (White, R.B., Monticello, D.A., Rosenbluth, M.N., Waddell, B.V., PPL/MATT-1267, submitted to Phys. Fluids). That is roughly the present state of the art. What are the remaining questions

to be answered? The simplest, I believe, has to do with the non-linear kinetic effects not included in the fluid Ohm's Law hitherto used in the simulations. The linear effect of these is well known. For example, they cause the m = 2 island to rotate at the diamagnetic frequency ω_e^* and to grow at a greatly reduced rate. It is a relatively straightforward matter, now under investigation, to determine whether the non-linear behaviour of the mode is strongly influenced by this possibly non-uniform rotation or other kinetic efforts. This may be crucial to the behaviour of disruptions at higher temperatures.

The question of the non-linear interaction of the modes in toroidal geometry is much more complicated. A 3-D code which is capable of satisfying the subtle constraints of flux conservation would be required for a definitive answer. To give an example of the complexities involved -- it is well known that a helical current in toroidal geometry gives rise to a region of ergodic flux around the magnetic islands. It is also known that within infinite-conductivity theory such such ergodic regions cannot form owing to flux freezing, very complex magnetic "necks" evolving in their place [B 1]. It is not known how this ergodic formation scales with resistivity, or whether it can occur explosively. Certainly, there is experimental evidence during disruptions for the opening up to flux surfaces, and I think it is a safe prediction that any satisfactory theory of disruption must understand this highly non-linear process.

It should also be stressed that many other mysteries remain in tokamaks, e.g. anomalous skin penetration, damping of rotation associated with neutral injection, and rapid influx of gas input through an "opaque" plasma.

IV. DRIFT WAVES, TRAPPED-PARTICLE MODES (ANOMALOUS TRANSPORT)

In the rather crucial area of anomalous transport, the situation now is very unclear. On the one hand, waves of the predicted frequency and wavelength have been definitely seen in tokamaks [A 4–2, A 11] as well as in simpler experiments such as the Wisconsin multipole [D 11] although in tokamaks the frequency spectrum is greatly broadened. Moreover, their amplitude is at least of the right order to explain the anomalous transport. On the other hand, the empirical scaling laws $D \approx n^{-1}$, $n_{max} \approx B/R$ are not yet understood in any simple way [A 5]. Perhaps they merely result from the complex interplay of many factors in the present regimes. We do not know.

The only very simple and appealing explanation of the observed scaling in tokamaks and the Levitron [D 12] is that given by Coppi [B 13] – that the critical parameter is (v_d/v_{the}) and that we are dealing with current-driven drift modes. This is difficult to understand, however, since the effects of temperature gradients and finite gyroradius appear to be much more important, at least in linear theory.

Certain definite progress can be claimed. It has become clear that the linear structure of these modes is really complex and two-dimensional. Taylor [D 10] and Cordey (private communication) have shown, in particular, that shear stabilization may not occur in realistic geometries. This has been verified in the 2-D computations of Tang [B 15–2]. These latter calculations have also identified the important destabilizing effect of curvature drifts in the trapped-electron regime, as well as a strong stabilizing effect at large $k\rho_i$.

The non-linear theory has been clarified in certain simple cases. For example, Terasima [D 9] has studied the case where only a few unstable drift modes exist and has determined that stabilization occurs by a flattening of the density profile, as verified in simulations by Okuda [B 14]. The Princeton group [B 15–2] has shown that wave steepening and consequent ion Landau damping may cause the dissipative trapped-ion mode to be less dangerous than hitherto assumed.

Finally, there has been a rather heroic effort by Horton [B 14] to synthesize, with many doubtful but necessary assumptions, what is now known about microinstabilities as applied to present tokamak regimes. These are characterized by the bulk of the particles being in the plateau regime, but with important parts of the distribution being collisional and other parts trapped, forcing

a detailed numerical evaluation of growth rates. One can then derive a non-linear equation in which the linear mode growth is balanced against non-linear ion Landau damping. This permits a calculation of the mode spectrum and hence of anomalous transport. In view of the many "best guesses" which had to be made, the results are surprisingly close to experiment.

To sum up – the microinstability picture is very complicated. No detailed understanding exists, but I think a strong case may now be made that these waves are a determining factor in anomalous transport. If so, we must be very cautious in assuming that the present rather favourable scaling will persist into the high-temperature regime of trapped-particle instabilities.

Another question of considerable importance which should be studied further is the presumably favourable effect of high β (due to diamagnetic well) on these electrostatic modes. At the same time, higher β may lead to the possible destabilization of Alfvén waves, a topic which has only begun to be considered. Thus, if β enhancement schemes prove successful, microinstability-induced transport may be quite different from that in present experiments. Unfortunately, several interesting papers along these lines by Mikhajlovskij and his co-workers were withdrawn from this meeting.

V. DRIFT CONE MODE (MIRROR CONFINEMENT)

The past year has seen a rather dramatic resurgence of the fortunes of the mirror concept. Paradoxically, this has been initiated by the realization that the long-predicted drift cone mode has indeed been present and limiting the confinement time in all experiments. The new element of understanding was a more careful quasi-linear calculation of the effects of the mode, as reported by Berk [C 2] which showed that it produced a diffusion in perpendicular energy whose magnitude is determined by the condition that the loss cone be filled with untrapped plasma to a level capable of stabilizing the mode thus yielding agreement with experimental life-times. This interpretation was confirmed by the injection of external plasma streams which were observed to quench the r.f. activity. Since the unstable drift modes have phase velocities $\omega/k_\perp \sim (\rho_i/r)\, v_{th}$, it is clear that in larger traps the loss cone need only be filled to a rather low level to stabilize the mode so that end losses from the streaming plasma need not be excessive.

The mirror concept with its minimum-B stability has always had a considerable appeal to the theoretician because of its simplicity, but it has also been realized that the Q-values obtainable were very marginal, primarily owing to the unfavourable ambipolar potential.

Papers by Jassby [B 12–2] and Cordey [B 12–1] showed that the competitive system of counter-streaming beam tokamaks could achieve Q's of 5–10 although at lower β's than may be obtainable with mirrors. It would seem that there are less unknowns with respect to stability problems for this approach.

Several schemes for Q-enhancement of mirrors were presented here. For example, Sudan [H 4] has presented a computation showing the possibility of producing a "reversed-field" trap with high-energy ion beams and compression.

A rather simple scheme (the triple mirror) has been proposed by Dimov [C 4] at this meeting (and independently by Fowler and Logan at LLL) to circumvent the ambipolar problem. As described in paper [B 12–1] the geometry consists of two conventional minimum-B mirror end-plugs which are joined by a long solenoidal simple mirror section. By injecting and trapping high-density and high-temperature ions into the minimum-B sections, the electron density and hence the ambipolar potential [$n_i \equiv n_e \equiv \exp(e\phi/T)$] may be controlled so as to confine the relatively cool, low-density and nearly isotropic thermonuclear ions in the solenoidal central sector. Since the latter may be made arbitrarily long compared to the end-plugs, and with low loss rate, high Q, and even ignition, can be obtained, in principle. The practical interest depends critically on the β which may be reached stably. High β is required since the design is limited by the mirror fields while the pressure in the reacting solenoid is low compared to that in the end plugs.

A number of theoretical questions arise – the β-limiting ballooning instability caused by the curvature in the joining region, the β limit for shear Alfvén waves in the end plugs, drift wave diffusion in the solenoidal section, the drift cone mode in the anisotropic end plugs, and the usual question of whether the electrons can be thermally insulated from the walls.

A particular problem of interest is the following: The drift cone is known to be primarily flute-like. That is to say – the field lines are equipotentials of the fluctuations. Thus, even though the isotropic plasma is physically removed from the end plug, it may act in the same way as the stabilizing streams to short out the drift cone mode of the end plugs, at the same time as the plugs are line-tying the ballooning and drift modes of the central plasma. The detailed properties of this novel symbiotic system present many challenges for the theorist.

CONCLUSION

To conclude we may say that no new, unpleasant theoretical surprises have emerged in the past few years. Even though many mysteries remain, it appears that previously identified modes of instability are indeed principal obstacles to confinement. The linear theories of these are now generally well in hand, and a beginning, partly analytic and partly computational, has been made in uncovering their non-linear properties. Finally, a great number of imaginative proposals for enhancing Q, controlling instabilities and raising β have been made here. It is precisely this almost endless variety of possible methods available for improving confinement, which can be properly evaluated once understanding has been achieved, that leads me to feeling optimistic about eventual success. Finally, for those of you who remain pessimistic about totally controlling the behaviour of a complex fluid, I suggest consideration of the remarkable meteorological controls exerted during this past week by our hosts.

SUMMARY OF INERTIAL CONFINEMENT*

O.N. KROKHIN
P.N. Lebedev Institute of Physics
of the USSR Academy of Sciences,
Moscow,
Union of Soviet Socialist Republics

I shall try to give a brief account of the work being done on inertial confinement as reported at this Conference. To some extent, of course, what I say will be my own subjective evaluation, and some of my conclusions may well turn out to be erroneous and be disproved in the course of further investigations. But this is a reflection of the present status of research, where we have contradictory findings on a number of questions and quite a gulf between the experimental results obtained so far and the full-scale experiments currently being planned.

I shall touch on the following subjects:

1. The interaction of laser radiation with a plasma, including absorption and reflection questions, the generation of fast electrons and ions, and anomalies in the processes of energy transfer in a plasma.
2. The results of experiments on the compression of microballoons filled with D and T.
3. The results of experiments on the application of electron beams in systems with inertial confinement.

THE ABSORPTION OF LASER RADIATION

So far there is no common view concerning the mechanism of laser energy absorption and the amount of laser energy absorbed. It is clear that with radiation fluxes of more than 10^{12} W · cm^{-2} (wavelength 1 μm) a contribution to absorption is made by the linear transformation of light energy into a plasma electron wave in the region where the density is close to critical and also by the parametric build-up of electron and ion oscillations. The significance of linear transformation is indicated by results presented in practically all papers at this Conference. In particular, in the paper from the Los Alamos Scientific Laboratory [F 3] it is stated that virtually all the absorbed radiation energy is associated with resonance absorption due to the steep gradient of the density profile close to the critical density in the case of large radiation fluxes, the character of the interaction of the radiation with the plasma hardly changing with variations in the wavelength (1 μm and 10 μm), which is attributable to the very steep density profile. This is in agreement with the findings of authors from the Lawrence Livermore Laboratory [F 4], who have calculated the absorption to be as much as 60% for an angle of incidence of 30°, and those of a group of investigators from the University of Osaka [F 5], who report experimental results of up to 10^{17} W · cm^{-2} for a neodymium laser and 10^{14} W · cm^{-2} for CO_2. The presence of a parametric effect is indicated by the existence of a $(3/2)\omega$ frequency in the scattered radiation (Centre d'études de Limeil, Los Alamos Scientific Laboratory, Lawrence Livermore Laboratory, University of Osaka, University of Rochester, Lebedev Institute of Physics) [F 1, F 2, F 3, F 4, F 5]. The indeterminacy of the experimental results is evidently due to the fact that the linear transformation and parametric effects are closely intertwined and, moreover, any hydrodynamic turbulence is an additional cause of parametric and resonance absorption.

---

* This summary talk was also published in Nucl. Fusion 16 6 (1976) 1047.

TABLE I. TARGET COMPRESSION

$V/V_0 < 1:1000$ (KMS, LLL)

– several hundred (Rochester, Osaka, Lebedev Institute)

$T \sim 1.5 - 1.7$ keV, $N_n \gtrsim 10^7$ (KMS)

$N_n \sim 10^9$ (LLL)

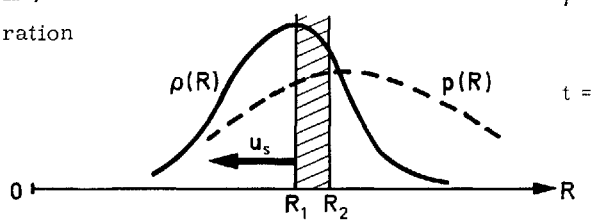
Stability of the compression?

a) small γt

b) saturation

$$\gamma = \left[-\frac{1}{\rho 2} \frac{\partial \rho}{\partial R} \frac{\partial p}{\partial R} \right]^{1/2}$$

$$t = \frac{R_2 - R_1}{u}$$



$R_1 - R_2$ – unstable region (very thin!)

1. $$u \sim \int_{R_1}^{R_2} R(\rho - \bar{\rho}) \frac{1}{\rho} \frac{\partial p}{\partial R} dR \approx \frac{1}{2} \left[\frac{\rho(R_1)}{\bar{\rho}} - 1 \right] [p(R_2) - p(R_1)] (R_2 - R_1)$$

2. $$\epsilon_{kin} = \int_{R_1}^{R_2} \rho \frac{v^2}{2} dR \approx \frac{1}{2} \rho v^2 (R_2 - R_1)$$

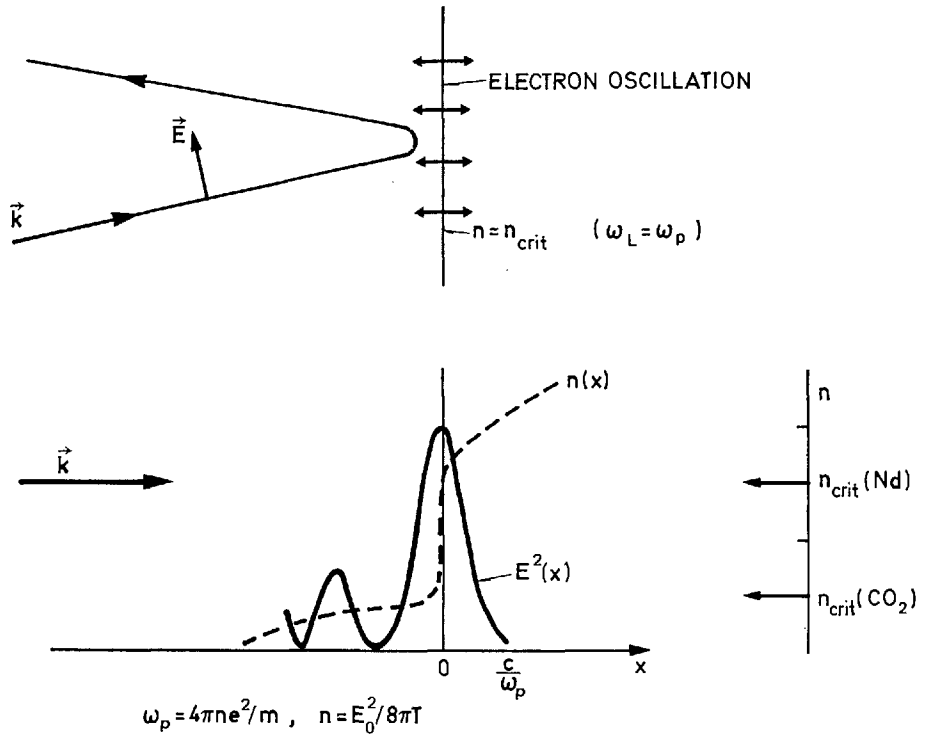
3. $\Delta R/R \sim (u/\epsilon_{kin})^{1/2}$

In present experiments, $u/\epsilon_{kin} \sim 10^{-4}$ (!)

Another problem is the occurrence of fast ions and electrons at high radiation flux densities (10^{15}–10^{16} W · cm^{-2}) (Los Alamos Scientific Laboratory, University of Osaka, University of Rochester, Lawrence Livermore Laboratory, Centre d'études de Limeil) [F 1, F 2, F 3, F 4, F 5], which reduce the mechanical momentum transmitted to the solid target.

Despite some uncertainty about the experimental values for absorbed energy, this problem is probably not critical, because sufficiently effective absorption and momentum transfer can be achieved by a suitable choice of flux density and target design. The appearance of fast electrons is associated with strong resonance absorption, which increases owing to the steep density gradient close to the critical density. The same thing accounts for the appearance of fast ions with energies

TABLE II. RESONANT ABSORPTION, FAST-PARTICLE GENERATION



1. Electron acceleration: $T_e \sim e E_0 L_{eff}$, $L_{eff} \sim c/\omega_p$ (LASL) (LLL)
2. Overheating due to energy transport inhibition (KMS)
3. Result of ponderomotive forces

of 50–100 keV (see the paper from the Ecole Polytechnique, Palaiseau) [G 3–4]. Fast ions can also result from the effect of large ponderomotive forces and from the suppression of heat conduction from the region with critical density to denser layers of material. The latter effect may be due to the appearance of strong magnetic fields as a result of inhomogeneous irradiation or to anomalous resistance in the turbulent plasma. Finally, one should note the Brillouin component in scattered radiation observed by a number of investigations [G 3–4, F 4, F 5]. Of course, the occurrence of this component is something which one may quite reasonably expect, but it can scarcely play a major role in the overall energy balance as there is no reason to expect a large-amplitude ion-acoustic wave to build up owing to large gradients, dispersal velocities and non-linearities and to small coherent interaction lengths.

TABLE III. OUTSTANDING PROBLEMS

1. Laser-plasma interaction:
absorption, reflection, superthermal electrons and ions, anomaly of heat transport
2. Target compression:
temperature measurement, neutron generation, stability problem
3. E-beam interaction with a plasma

Summing up these investigations, one can say that, despite the divergence of the experimental data, and the large number of different interpretations, the various points of view can be reconciled by assuming that we are dealing with a number of interacting processes. I feel I must also mention here the excellent techniques and devices employed – including fast cameras (some sensitive in the X-ray region), X-ray microscopes and pinhole cameras with a resolution of 5 μm [F 1, F 2, F 4, F 5, F 9, F 10].

A great deal of information on corona dynamics is provided by spatially resolvable fast scans of the regions in which the second and (3/2) harmonics are generated [F 2, G 3–4].

THE COMPRESSION OF MICROBALLOONS BY LASER RADIATION AND THE PROBLEM OF STABILITY

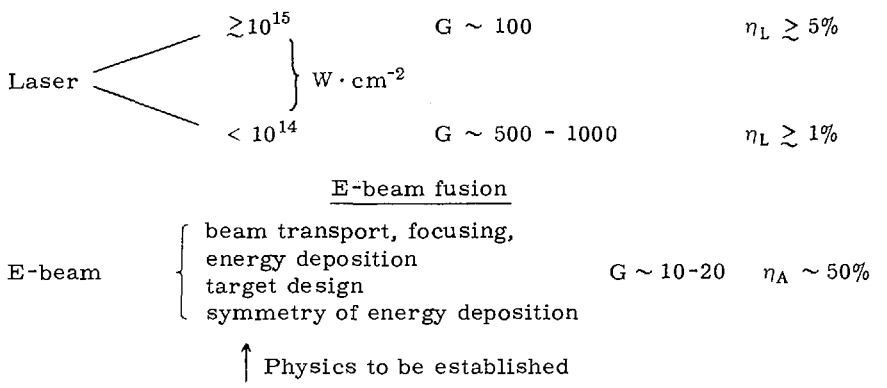
If the instabilities can be sufficiently suppressed, multi-layer hollow targets of fairly large dimensions may result in energy amplification coefficients of several hundred to a thousand for an energy input of the order of 0.1–1 MJ. At least this is suggested by numerical calculations with two-dimensional gas-dynamic programs [F 1, F 3, F 5].

Under certain conditions, Rayleigh-Taylor instabilities can destroy thin sheaths with $10 < R/\Delta R < 100$. In the slowing-down process, at the instant corresponding to maximum compression, it is also possible for the DT-fuel to become mixed with the sheath compressing it. It should be stressed that the Rayleigh-Taylor instability zone is narrow compared with the total thickness of the sheath. The build-up close to the ablation front, i.e. in the region where $\partial p/\partial R$ and $\partial p/\partial R$ have different signs, is determined by the growth rate

$$\gamma = \left\{ -\frac{1}{\rho^2} \frac{\partial p}{\partial R} \frac{\partial p}{\partial R} \right\}^{1/2} \tag{1}$$

The growth rate relates to a comparatively thin layer of material which becomes mixed inside the sheath in proportion to the degree of evaporation, involving new portions of unperturbed material. Owing to the finite, small time in question, this restricts the build-up despite the large growth rate values. In the actual calculations, the value of γt is low (in the range 1–10).

TABLE IV. LASER AND E-BEAM FUSION



E-beam advantages: higher efficiency, more energy available

E-beam problems : transport, focusing, deposition

The excess "potential energy" of the layer, which can be converted to a turbulent form of energy, amounts to

$$u = \int_{R_1}^{R_2} R dR \, (\rho - \bar{\rho}) \, \frac{1}{\rho} \frac{\partial p}{\partial R} \tag{2}$$

The destructive effect of turbulence on the sheath compression process can be estimated from the relationship between the quantity u and the kinetic energy ϵ which the layer receives as a result of the acceleration process:

$$\epsilon = \int_{R_1}^{R_2} \rho \frac{v^2}{2} \, dR \tag{3}$$

Typical u and ϵ (in erg · cm^{-2}) for a microballoon with an initial radius of R = 50 μm illuminated by a 20 J, 2.5 ns laser pulse are $3 \times 10^{10} (R_2 - R_1)$ and $4 \times 10^{14} (R_2 - R_1)$, respectively.

In this case one can expect sheaths with $\Delta R/R \sim (u/\epsilon)^{1/2} \sim 10^{-2}$ to be fairly stable. In fact, the situation may be better, for – as we said earlier – the value of γt is low and it is more than likely that instabilities will not be able to develop to their full extent. The comparatively high stability of the sheaths corresponding to this example was demonstrated in experiments performed by KMS Fusion Inc., in the paper describing which a volume compression factor of 2000 was reported [F 10]. Compression factors of several hundred have been obtained at a number of other

laboratories – the University of Rochester, the University of Osaka, Lawrence Livermore Laboratory, Los Alamos Scientific Laboratory and the Lebedev Institute of Physics [F 2, F 4, F 5] (Table I).

Spectral measurements of alpha particles performed by KMS Fusion Inc. showed that the temperature at the centre attained 1.5 – 1.7 keV after compression. These results have been confirmed by measuring the ratio of the DD and DT reactions, although the error interval is large owing to the inadequate statistics.

Is it possible to make any predictions regarding the future of laser fusion in the light of the latest results reported at this Conference and elsewhere?

It would seem reasonable to say that laser fusion is based on a clear conception of the heating of thermonuclear fuel. As recent physical investigations have shown, the conditions for the interaction of laser radiation with a target can be optimized by a suitable choice of target design and of the magnitude and shape of the incident flux. Gas-dynamic instabilities (Rayleigh- Taylor instabilities) are evidently not a critical obstacle to the production of targets with amplification coefficients of several hundred. Progress in laser technology will undoubtedly lead to the development of sufficiently powerful lasers which have efficiencies of the order of 1–5% and which will enable the energy cycle to be closed.

However, it is still difficult to visualize the extent and complexity of future technological advances in the production of targets and the development of reliable lasers with long service life (essentially the production of optical components and powerful high-voltage electronic devices). It should be noted that such devices will have to be competitively priced. Although we are still far from the stage where serious consideration has to be given to these questions, we need to have a rough idea of the future problems involved in laser fusion.

These questions will take on great significance if it becomes possible in the next few years to perform experiments with substantial thermonuclear burning. At the moment a "plateau" has been reached in experimental research on laser fusion: physical experiments are being conducted and devices in the 10-kJ range and above are being constructed at several laboratories – "Shiva" (10 kJ) at the Lawrence Livermore Laboratory, "Del'fin (10 kJ) at the Lebedev Institute of Physics, a CO_2 laser (up to 100 kJ) at Los Alamos Scientific Laboratory, Gekko XII and Lekko III at the University of Osaka, etc. When the construction of these devices has been completed, we shall be able to conduct experiments at a completely different level. It is quite probable that by the end of 1977 or the beginning of 1978 these experiments will have started and that we shall hear some impressive results at the 7th International Conference.

INVESTIGATIONS WITH ELECTRON BEAMS

So far electron beam powers of up to 10^{12} W have been achieved with beams which can be focused to about 2–4 mm. It is planned to have accelerators with powers of around 10^{14} W operating at the Sandia Laboratories and the I.V. Kurchatov Institute of Atomic Energy by 1980 [F 6, F 7].

Experiments on the interaction of "high-current relativistic beams with targets" (as a rule metallic films) indicate an energy contribution of the order of 30–40% resulting from the strong effect of the proper magnetic field of the beam, which causes the electrons to traverse the plasma repeatedly, thereby increasing the energy losses [F 7] (Table II).

In experiments performed at the I.V. Kurchatov Institute of Atomic Energy with conical models of spherical compression, it has been assumed that volume compression by a factor of 1000 of the DT gas under the sheath is achieved [F 7]. Control experiments in which the target geometry was varied suggest that gas-dynamic heating of the plasma takes place and 10^7 thermonuclear neutrons appear.

It must be said that we still do not have enough experimental and theoretical experience in this field and that there remain problems concerning beam transport and focusing, the processes of interaction with the plasma and the level of energy input into the plasma. There also remains the problem of a suitable design of target in view of the fact that the beam is axially symmetric and the magnetic field energy is high. Table III summarizes outstanding problems in this field.

In conclusion I should like to say how I think systems with inertial confinement based on lasers and on electron beams may develop (Table IV).

With lasers, there are two possibilities – the development either of efficient lasers (which, of course, is a good thing in any case) or of very complex targets with high amplification.

With electron beams, there is no need to have large energy amplification coefficients, but future target design and the experimental approach adopted will depend on the physics of interaction and transport.

SUMMARY OF REACTOR SYSTEMS*

K.-H. SCHMITTER
Max-Planck-Institut für Plasmaphysik,
Garching, Federal Republic of Germany

This year, prior to this Conference, there have already been two large Fusion Technology Symposia. This may explain the declining number of contributions to the topic "Reactor Systems" since Tokyo 1975. About a dozen papers, predominantly relating to tokamak reactor problems – with two exceptions, i.e. mirror reactor design studies and a study devoted to reactor applications of high-density linear confinement systems – were presented.

The material discussed at the Conference will be surveyed in the following order:

I. Reactor design studies
   A. Tokamak systems
      a) Power reactors
      b) Experimental reactors
   B. Other systems
      a) Mirrors
      b) Linear theta-pinches
II. Plasma-wall interaction
III. Neutral injectors
IV. Energy storage and transfer
V. Plasma burning instabilities

It is no secret that the tokamak principle as a power reactor suffers from low power density and/or, in conjunction with maintenance and repair, from accessibility problems.

Both tokamak power reactor design studies presented included, among other topics, these two problems:

The Culham MK II 5800 MWCth) Design Study [I1–1] seeks to reduce the physical size and simultaneously the specific reactor cost by elevation of the first-wall neutron loading to more than 5 $MW \cdot m^{-2}$. The total beta required is about 9%. The design is specially marked by its servicing capability, which is required to allow replacement of neutron-damaged blanket segments as a routine periodic operation. This is necessary in order to attain sufficient reactor availability. For MK II, which does not include a divertor, the removal of a toroidal or poloidal magnet winding for repair is considered to be impracticable, thus making extremely reliable superconducting magnets necessary. This crucial requirement is not only specific to the Culham MK II scheme. It also applies to more or less all tokamaks with superconducting poloidal windings inside the toroidal magnet.

UWMAK III [I1–2] belongs to the latter family. This very detailed 5000 MW(th) power reactor design of the Wisconsin group uses a non-circular plasma cross-section like MK II and roughly half of the first wall loading of MK II, but includes a double-node divertor. Tritium breeding is accomplished in outer blanket modules. These only have to be removed periodically whereas the inner blanket is basically a permanent, hot shield. This latter concept seems to be favourable for achieving easy blanket servicing. Among the different, most interesting advanced technologies applied in UWMAK III, the superconducting magnet design utilizing aluminium stabilization and a high-strength aluminium-alloy structure should be mentioned as an important

---

* This summary talk was also published in Nucl. Fusion 16 6 (1976) 1047.

contribution to large-toroidal-superconducting-coil-system technology. In an analysis, the costs of the high-temperature refractory metal TZM used as main structural material turned out to be more important in UWMAK III than the toroidal field magnet costs. Interesting results could probably be expected from a re-design of UWMAK III with stainless steel as a structural material at lower coolant temperature.

As a last step, preceding a demonstration power plant, a sort of experimental power reactor (EPR) will presumably be required. In the US fusion programme, such an EPR will conceivably be a tokamak configuration without divertor and with a thermal power of $\triangleq 0.5$ GW. The scoping and conceptual design studies for an EPR [I 3–2] performed during the last two years at Argonne National Laboratory, General Atomics and Oak Ridge National Laboratory, resulted in two design with circular plasma cross-section and one design with doublet-type plasma cross-section. Non-breeding EPR's would require about 16 kg of tritium per operational year. Besides the costs, the procedure for transporting these rich quantities of tritium might present a substantial problem. The EPR studies are in many respects very detailed and will be, to a certain extent, of general significance to fusion technology beyond EPR. This might apply, in particular, to first-wall systems, energy storage and transfer, and superconducting magnet systems. For instance, the ORNL magnet design with supercritical helium cooling and electromagnetic shielding of the toroidal field coils should be mentioned here.

The Japanese Experimental Cold-Gas-Blanket Fusion Reactor, presented by the TOKAI group [I 3–1], should breed tritium, but is based on the assumption that self-sustaining is already unnecessary at this stage. Stationary heating by 200-keV neutral deuterons is applied, power amplification being expected as a result of the TCT effect. With trapped ion scaling at a plasma temperature of 7 keV the power amplification calculated for 7% impurities was quoted as 2! The assumed β_{tor} of 1.7% is conservative, and thus for a thermal power of 100 MW a peak toroidal field of 11.5 T will already be necessary, requiring niobium-3-tin magnets. A more detailed design study for these high-field magnets would certainly meet with wide interest, because tokamak reactor cost analyses suggest extending toroidal magnet technology beyond niobium-titanium towards higher fields.

This takes us to the minority of the 'non-tokamak studies', beginning with the mirror reactor. This concept is claimed to have attractive features: For instance, mirror reactors are probably technically more feasible than toroidal reactors with small aspect ratio, would cause fewer accessibility problems, and permit continuous operation. Nevertheless, the prospects for fusion mirror reactors have been considered gloomy so far because of the large re-circulating power which has to be handled efficiently. The Livermore mirror conceptual design and parameter studies [I 2] indicate that Q, the ratio between fusion power output and the injected beam power input, must be raised by a factor of 2–3 above the classical value predicted by Fokker-Planck calculations to reduce the re-circulating power fraction to a reasonable value. A 'Field Reverse Mirror' design study is now being performed. Q values of about 5 were forecast to be attainable with this new concept.

An enhancement of the energy multiplication using a mirror hybrid system is another way of achieving the required Q rise with classical plasma confinement. The Livermore design study states that with such a system fissile fuel for burner fission reactors can also be produced at a competitive cost. If, compared with the fission breeder, the advantage of the lack of criticality can offset the disadvantage of enhanced safety problems caused by a more complex structure, the concept could be quite interesting.

The systems study of the other "non-tokamak reactor" was based on the pulsed-linear-high-beta confinement principle. The theta-pinch implosion-heated and the laser-light-pre-heated schemes studied at Los Alamos in co-operation with Mathematical Sciences, Inc. [I 4] might have a chance, provided there is a need for fusion-fission systems. A technological "no go"does not seem to exist although the solution to the identified problems of energy storage and transfer, materials, and laser technology will not be easy to achieve. But when judging linear fusion reactor

schemes, one should always bear in mind the technical advantages of linear structures over toroidal ones.

Impurity production ranks as one of the major aspects in connection with the reactor first-wall problem. A significant quantity of impurity flux into the plasma is created by atoms desorbed from the first wall. The subject of an experiment at the Kurchatov Institute was an investigation of residual gas desorption from different wall materials such as molybdenum and 316-stainless steel [I 8]. A 20–30 keV ion bombardment proved the desorption rate to be dependent on the sputtering coefficient of the wall material.

A method of protecting the first wall from erosion by the formation of a zone of dense, cold plasma near the wall was discussed in another Kurchatov paper [I 9–3]. The temperature of the ions near the wall should be below the threshold erosion energy of the wall material and the thickness of the protective zone should exceed the depth to which the re-charging neutrals penetrate. The Kurchatov group arrived at the result that neoclassical transfer permits a steady-state solution where the hot thermonuclear zone is localized in space and limited by a sort of "cold plasma blanket". To ensure the required plasma profiles a separate poloidal fuel injection divertor might be required.

Additional heating is not only necessary for bringing fusion reactors to ignition; the importance of neutral injection heating for current and future experiments is still increasing. Already the next generation of experiments requires neutral injectors with performances beyond those offered by the present state of the art. As the neutralization efficiency of protons and positive molecular ions drops to low values with increasing beam energy, energy recovery systems and/or negative sources must be developed. Fonteny-aux-Roses has opted for the recovery scheme. Convertor types of negative ion sources are being studied at Livermore and Berkeley, and Brookhaven National Laboratory is investigating three different types of negative ion sources. But most attention at Oak Ridge, Livermore, and Fontenay is still being paid to the development of neutral injectors based on positive ion acceleration and neutralization, particularly in the direction of longer pulses, higher currents and energies, with really substantial progress having been made during the last two years. Large facilities for testing the PLT-, TFTR- and other neutral-beam injectors have now been completed or are under construction [I 5, I 6].

Energy storage and transfer is one of the technological key problems in fusion and is most difficult to solve for pulsed devices. Inductive storage systems have their transfer problems when terminated by inductive loads. Therefore, the promising results of studies of the potential of homopolar machines for energy storage at Los Alamos and Austin together with industry deserve wide interest [I 7]. The capacitive nature of the homopolar machine is favourable for resonating charge and discharge operations, together with inductive loads like tokamak poloidal windings or high-beta devices. It would be very desirable if more practical experience and experimental data with homopolar systems were soon to become available for high-beta and tokamak applications!

It is still an open question whether thermonuclear burning instabilities of the plasma could become a severe problem in connection with α-particle heating or not! New studies of this question were performed at the University of Tokyo [I 9–1] and at the Ukrainian Academy of Sciences Kiev [I 9–2]. Both considered the effect of α-particle relaxation on buring instabilities under self-sustaining as well as non-self-sustaining conditions. The Tokyo group found with their model, based on the Fokker-Planck equation for constant plasma confinement and spatial uniformity of temperature and density, a stabilizing "feedback" effect in the energy transfer to the background electrons. The Ukrainian group, including non-uniform spatial distribution as well as non-isothermal plasma in their study, defined a sort of stability criterion.

In conclusion, we should like to mention that still more effort is felt to be required to shift the wall loading constraint – which, by the way, applies more or less to all magnetic confinement systems – towards higher values at an acceptable life-time, cost and working temperature. This might be made possible not only by improving material properties but also by devising new blanket schemes.

As it has not yet been proved experimentally that the beta constraints can be removed, very-high-field superconducting magnets might still be required for a reduction of the reactor size. These have to be extremely reliable if their repair is impracticable as is assumed for many tokamak designs. An assessment of the reliability of relevant superconducting systems is urgently required. This might provide substantial contributions to a discussion of the credibility of different magnetic confinement systems as fusion reactors.

CHAIRMEN OF SESSIONS

Session I	R. WIENECKE	Federal Republic of Germany
Session II	V.P. SMIRNOV	Union of Soviet Socialist Republics
Session III	G.H. McCALL	United States of America
Session IV	V.S. STRELKOV	Union of Soviet Socialist Republics
Session V	P.H. REBUT	CEC
Session VI	J.A. PHILLIPS	IAEA
Session VII	R. TOSCHI	Italy
Session VIII	K. YAMAMOTO	Japan
Session IX	D. PFIRSCH	Federal Republic of Germany
Session X	M.S. RABINOVICH	Union of Soviet Socialist Republics
Session XI	A. GIBSON	United Kingdom
Session XII	H.R. GRIEM	United States of America
Session XIII	J.F. CLARKE	United States of America
Session XIV	K. HUSIMI	Japan
Session XV	V.D. SHAFRANOV	Union of Soviet Socialist Republics
Session XVI	R.L. FREEMAN	United States of America
Session XVII	T. CONSOLI	France
Session XVIII	K. TAKAYAMA	Japan
Session XIX	F. HINTZ	Federal Republic of Germany
Session XX	R.F. POST	United States of America
Session XXI	H.A.B. BODIN	United Kingdom
Session XXII	E.E. KINTNER	United States of America

Session XXIII	B.P. LEHNERT	Sweden
Session XXIV	F. HOFMANN	Switzerland
Session XXV	B.B. KADOMTSEV	Union of Soviet Socialist Republics

SECRETARIAT OF THE CONFERENCE

Scientific Secretaries:	J.A. PHILLIPS A. BELOZEROV	Division of Research and Laboratories, IAEA
Administrative Secretary:	Caroline DE MOL VAN OTTERLOO	Division of External Relations, IAEA
Editors:	J.W. WEIL Yu. BALASANOV Miriam LEWIS	Division of Publications, IAEA
Records Officer:	S.A. EDMINSTER	Division of Languages, IAEA

LIST OF PARTICIPANTS

ARGENTINA

Ferro Fontan, C.	Laboratorio Física del Plasma, Facultad de Ciencias Exactas y Naturales, Universidad de Buenos Aires, Ciudad Universitaria, Pabellón 1, 1428 Buenos Aires
Gratton, J.	Laboratorio Física del Plasma, Facultad de Ciencias Exactas y Naturales, Universidad de Buenos Aires, Ciudad Universitaria, Pabellón 1, 1428 Buenos Aires

AUSTRALIA

Brennan, M.H.	The Flinders University, School of Physical Sciences, Bedford Park, S.A. 5042
Cheetham, A.D.	The Flinders University, School of Physical Sciences, Bedford Park, S.A. 5042
How, J.A.	The Flinders University, School of Physical Sciences, Bedford Park, S.A. 5042
Pugatschew, A.A.	Department of Physics, University of Essex, Wivenhoe Park, Colchester, Essex, England
Storer, R.G.	The Flinders University, School of Physical Sciences, Bedford Park, S.A. 5042
Watson-Munro, C.N.	Wills Plasma Physics Department, University of Sydney, N.S.W. 2006
Weber, P.E.	The Flinders University, School of Physical Sciences, Bedford Park, S.A. 5042

AUSTRIA

Cap, F.	Institute for Theoretical Physics, University of Innsbruck, Innrain 52, A-6020 Innsbruck
Friedmann, H.	Institut für Radiumforschung und Kernphysik der Akademie der Wissenschaften, Boltzmanngasse 3, A-1090 Vienna
Putz, F.	Österreichische Studiengesellschaft für Atomenergie G.m.b.H., Lenaugasse 10, A-1082 Vienna
Viehböck, F.P.	Institut für Allgemeine Physik, Technische Universität, Karlsplatz 13, A-1040 Vienna

BELGIUM

Bhatnagar, V.P.	Laboratoire de physique des plasmas, Ecole royale militaire, 30 Avenue de la Renaissance, B-1040 Brussels
Bosia, G.	Laboratoire de physique des plasmas, Ecole royale militaire, 30 Avenue de la Renaissance, B-1040 Brussels
Faulconer, D.W.	Laboratoire de physique des plasmas, Ecole royale militaire, 30 Avenue de la Renaissance, B-1040 Brussels
Gillon, L.P.	Université catholique de Louvain, 2 Chemin du Cyclotron, B-1348 Louvain la Neuve
Messiaen, A.M.A.	Laboratoire de physique des plasmas, Ecole royale militaire, 30 Avenue de la Renaissance, B-1040 Brussels
Vandenplas, P.E.M.	Laboratoire de physique des plasmas, Ecole royale militaire, 30 Avenue de la Renaissance, B-1040 Brussels
Weynants, R.R.R.	Laboratoire de physique des plasmas, Ecole royale militaire, 30 Avenue de la Renaissance, B-1040 Brussels

BRASIL

Sakanaka, P.H.	Universidade Estadual de Campinas, Commissão Nacional de Energia Nuclear, Instituto de Fisica, Campinas, SP

CANADA

Alcock, A.J.	National Research Council of Canada, Division of Physics, Montreal Road, Ottawa K1A 0R6
Hoffmann, C.R.J.	Atomic Energy of Canada Limited, Chalk River Nuclear Laboratories, Chalk River, Ontario
Johnston, T.W.	INRS-Energie, Université du Québec, C.P. 1020, Varennes, Quebec
Meyer, J.	Department of Physics, The University of British Columbia, Vancouver, B.C. V6T 1W5
Skarsgard, H.M.	Physics Department, University of Saskatchewan, Saskatoon, Saskatchewan S7N 0W0
Van Andel, H.W.H.	Université de Montréal, Département de physique, C.P. 6128, Montreal 101, Quebec

CZECHOSLOVAKIA

Hron, M.	Institute of Nuclear Research, 250 68 Řež
Sunka, P.	Institute of Plasma Physics, Czechoslovak Academy of Sciences, Nademlýnská 600, 180 69 Prague 9

DENMARK

Chang, C.T. — Research Establishment Risø, DK-4000 Roskilde

Jensen, V.O. — Research Establishment Risø, DK-4000 Roskilde

Nielsen, P. — Research Establishment Risø, DK-4000 Roskilde

FINLAND

Karttunen, S.J. — Technical Research Centre of Finland, Lönrotinkatu 37, Helsinki

FRANCE

Adam, J.A. — Association Euratom-CEA, B.P. No.6, F-92260 Fontenay-aux-Roses

Bamière, C.G. — SGDN, 51 Bd. de Latour Maubourg, F-75700 Paris

Bernard, A.M. — Commissariat à l'énergie atomique, Centre d'études de Limeil, B.P. No. 27, F-94190 Villeneuve-Saint-Georges

Bussac, M.N. — Ecole polytechnique, Plateau de Palaiseu, F-91120 Palaiseau

Cabé, J.F. — Commissariat à l'énergie atomique, Centre d'études de Valduc, B.P. No.14, F-21120 Is-sur-Tille

Canobbio, E. — Association Euratom-CEA, CEN Grenoble, F-38041 Grenoble

Consoli, T. — Département fusion contrôlée, Centre d'études nucléaires, F-38041 Grenoble Cedex

Dautray, R. — Commissariat à l'énergie atomique, 29 Rue de la Fédération, Paris 15

Dei-Cas, R. — Commissariat à l'énergie atomique, CEA, Centre d'études nucléaires, B.P. No. 6, F-92260 Fontenay-aux-Roses

Delcroix, J.L. — Université Paris-Sud, F-91405 Orsay

Delobeau, F.L. — Commissariat à l'énergie atomique, Centre d'études de Limeil, B.P. No. 27, F-94190 Villeneuve-Saint-Georges

Dolique, J.M. — Laboratoire de physique des plasmas, Université de Grenoble I, Domaine Universitaire, B.P. No. 53, F-38041 Grenoble-Cedex

Fabre, E.L. — Laboratoire PMI, Ecole polytechnique, Plateau de Palaiseau, F-91120 Palaiseau

FRANCE (cont.)

Frey, J.J.M.	Commissariat à l'énergie atomique, 29 Rue de la Fédération, Paris 15
Gourdon, C.	Commissariat à l'énergie atomique, Centre d'études nucléaires, B.P. No. 6, F-92260 Fontenay-aux-Roses
Jablon, C.J.	Laboratoire de physique des plasmas, Faculté des sciences, F-91405 Orsay
Koechlin, F.R.	Commissariat à l'énergie atomique, Département de physique du plasma et de la fusion contrôlée, B.P. No.6, F-92260 Fontenay-aux-Roses
Lecoustey, P.	Commissariat à l'énergie atomique, Centre de recherche nucléaire, B.P. No. 6, F-92260 Fontenay-aux-Roses
Parlange, F.J.M.	Commissariat à l'énergie atomique, Centre d'études nucléaires de Grenoble, Service fusion, F-38041 Grenoble Cedex
Prevot, F.G.	Commissariat à l'énergie atomique, Centre d'études nucléaires, B.P. No.6, F-92260 Fontenay-aux-Roses
Rioux, Ch.P.	Laboratoire de physique des plasmas, Université de Paris XI, F-91405 Orsay
Rioux-Damidau, F.Th.	Laboratoire de physique des plasmas, Université de Paris XI, F-91405 Orsay
Rolland, P.	Commissariat à l'énergie atomique, Centre d'études nucléaires de Grenoble, DPH-PFC/SIG CEA 85x, F-38041 Grenoble Cedex
Samain, A.J.	DPH/PFC, Département de physique du plasma et de la fusion contrôlée, P.B. No. 6, F-92260 Fontenay-aux-Roses
Soulé, J.L.	Commissariat à l'énergie atomique, DPH-PFC-CENFAR, B.P. No. 6, F-92260 Fontenay-aux-Roses
Valckx, F.P.G.	Commissariat à l'énergie atomique, Département de physique du plasma et de la fusion contrôlée, B.P. No. 6, F-92260 Fontenay-aux-Roses
Virmont, J.A.	Laboratoire PMI, Ecole polytechnique, Plateau de Palaiseau, F-91120 Palaiseau
Watteau, J.P.H.	Commissariat à l'énergie atomique, Centre d'études de Limeil, B.P. No. 27, F-94190 Villeneuve-Saint-Georges
Werkoff, F.	Commissariat à l'énergie atomique, Département de la fusion, B.P. No. 6, F-92260 Fontenay-aux-Roses

GERMAN DEMOCRATIC REPUBLIC

Alexander, K.F.	Akademie der Wissenschaften der DDR, Zentralinstitut für Elektronenphysik, Mohrenstr. 40/41, DDR-108 Berlin,

GERMANY, FEDERAL REPUBLIC OF

Becker, G.	Max-Planck-Institut für Plasmaphysik, D-8046 Garching
Biskamp, D.	Max-Planck-Institut für Plasmaphysik, D-8046 Garching
Bogen, P.	Institut für Plasmaphysik der Kernforschungsanlage Jülich, Postfach 1913, D-517 Jülich
Borrass, K.	Max-Planck-Institut für Plasmaphysik, D-8046 Garching
Bruhns, H.	Institut für Angewandte Physik II, Universität Heidelberg, Albert-Überle-Strasse 3–5, D-6900 Heidelberg 1
Conrads, J.P.F.	Institut für Plasmaphysik der Kernforschungsanlage Jülich, Postfach 1913, D-5170 Jülich
Derfler, H.	Max-Planck-Institut für Plasmaphysik, D-8046 Garching
Düchs, D.F.	Max-Planck-Institut für Plasmaphysik, D-8046 Garching
Duesing, G.	Max-Planck-Institut für Plasmaphysik, D-8046 Garching
Dum, C.T.	Max-Planck-Institut für Plasmaphysik, D-8046 Garching
Ebberink, J.	Interatom, Bensberg, Köln
Eberhagen, A.	Max-Planck-Institut für Plasmaphysik, D-8046 Garching
Eidmann, K.	Max-Planck-Institut für Plasmaphysik, D-8046 Garching
Engelhardt, W.W.	Max-Planck-Institut für Plasmaphysik, D-8046 Garching
Feneberg, W.	Max-Planck-Institut für Plasmaphysik, D-8046 Garching
Fünfer, E.	Max-Planck-Institut für Plasmaphysik, D-8046 Garching
von Gierke, G.O.	Max-Planck-Institut für Plasmaphysik, D-8046 Garching
Glock, E.	Max-Planck-Institut für Plasmaphysik, D-8046 Garching
Grieger, G.	Europäische Atomgemeinschaft Brüssel (EURATOM), Rue de la Loi 200, B-1040 Brussels, Belgium

GERMANY, FEDERAL REPUBLIC OF (cont.)

Gruber, O.	Max-Planck-Institut für Plasmaphysik, D-8046 Garching
Haas, G.	Max-Planck-Institut für Plasmaphysik, D-8046 Garching
Hashmi, M.	Max-Planck-Institut für Plasmaphysik, D-8046 Garching
Henkes, W.	Gesellschaft für Kernforschung, Institut für Kernverfahrenstechnik, Postfach 3640, D-7500 Karlsruhe 1
Herold, H.	Max-Planck-Institut für Plasmaphysik, D-8046 Garching
Herrnegger, F.	Max-Planck-Institut für Plasmaphysik, D-8046 Garching
Hintz, E.A.K.	Institut für Plasmaphysik der Kernforschungsanlage Jülich, Postfach 1913, D-5170 Jülich
Höthker, K.	Institut für Plasmaphysik der Kernforschungsanlage Jülich, Postfach 365, D-5170 Jülich
Hübenthal, K.	Bundesministerium für Forschung und Technologie, Postfach 12 03 70, Stresemannstr. 2, D-5300 Bonn
Hübner, K.	Institut für Angewandte Physik II, Universität Heidelberg, Albert-Überle-Straße 3–5, D-6900 Heidelberg 1
Kaeppeler, H.	Institut für Plasmaphysik der Universität Stuttgart, Pfaffenwaldring 31, D-7000 Stuttgart
Karger, F.H.	Max-Planck-Institut für Plasmaphysik, D-8046 Garching
Kaufmann, M.	Max-Planck-Institut für Plasmaphysik, D-8046 Garching
Keilhacker, M.M.K.	Max-Planck-Institut für Plasmaphysik, D-8046 Garching
Kever, H.	Kernforschungsanlage Jülich, Postfach 365, D-517 Jülich
Klingelhöfer, R.	Institut für Kernverfahrenstechnik, Kernforschungszentrum Karlsruhe, Postfach 3640, D-7500 Karlsruhe
Klüber, O.	Max-Planck-Institut für Plasmaphysik, D-8046 Garching
Kluge, W.G.	Institut für Plasmaforschung, Universität Stuttgart, Pfaffenwaldring 31, D-7000 Stuttgart
Knobloch, A.F.	Max-Planck-Institut für Plasmaphysik, D-8046 Garching

GERMANY, FEDERAL REPUBLIC OF (cont.)

Köppendörfer, W.	Max-Planck-Institut für Plasmaphysik, D-8046 Garching
Krause, H.	Max-Planck-Institut für Plasmaphysik, D-8046 Garching
Krompholz, H.	Institut für Angewandte Physik der Technischen Hochschule Darmstadt, Hochschulstraße 2, D-6100 Darmstadt
Kunze, H.-H.	Ruhr-Universität, Universitätsstraße, D-4630 Bochum
Lackner, K.	Max-Planck-Institut für Plasmaphysik, D-8046 Garching
Lang, R.S.	Max-Planck-Institut für Plasmaphysik, D-8046 Garching
Leischner, E.	Fa. Nukem, D-645 Hanau
Lengyel, L.L.	Max-Planck-Institut für Plasmaphysik, D-8046 Garching
Lisitano, G.	Max-Planck-Institut für Plasmaphysik, D-8046 Garching
Lortz, D.	Max-Planck-Institut für Plasmaphysik, D-8046 Garching
McCormick, K.	Max-Planck-Institut für Plasmaphysik, D-8046 Garching
Mayer, H.M.	Max-Planck-Institut für Plasmaphysik, D-8046 Garching
Meisel, D.	Max-Planck-Institut für Plasmaphysik, D-8046 Garching
Merkel, P.K.	Max-Planck-Institut für Plasmaphysik, D-8046 Garching
Michel, L.	Institut für Angewandte Physik der Technischen Hochschule Darmstadt, Hochschulstraße 2, D-6100 Darmstadt
Morandi, P.	Max-Planck-Institut für Plasmaphysik, D-8046 Garching
Müller, G.	Max-Planck-Institut für Plasmaphysik, D-8046 Garching
Müller, Günter	Institut für Plasmaforschung der Universität Stuttgart, Pfaffenwaldring 31, D-7000 Stuttgart
Mulser, P.	Max-Planck-Institut für Plasmaphysik, D-8046 Garching

GERMANY, FEDERAL REPUBLIC OF (cont.)

Murmann, H.-D.	Max-Planck-Institut für Plasmaphysik, D-8046 Garching
El-Nadi, A.	Institut für theoretische Physik, Ruhr-Universität Bochum, D-4630 Bochum
Neuhauser, J.	Max-Planck-Institut für Plasmaphysik, D-8046 Garching
Nührenberg, J.	Max-Planck-Institut für Plasmaphysik, D-8046 Garching
Ott, W.	Max-Planck-Institut für Plasmaphysik, D-8046 Garching
Pacher, G.W.	Max-Planck-Institut für Plasmaphysik, D-8046 Garching
Pfirsch, D.	Max-Planck-Institut für Plasmaphysik, D-8046 Garching
Porkolab, M.	Max-Planck-Institut für Plasmaphysik, D-8046 Garching
Raeder, J.	Max-Planck-Institut für Plasmaphysik, D-8046 Garching
Rapp, H.	Max-Planck-Institut für Plasmaphysik, D-8046 Garching
Rau, F.	Max-Planck-Institut für Plasmaphysik, D-8046 Garching
Räuchle, E.	Institut für Plasmaforschung der Universität Stuttgart, Pfaffenwaldring 31, D-7000 Stuttgart
Rebhan, E.	Max-Planck-Institut für Plasmaphysik, D-8046 Garching
Renner, E.	Max-Planck-Institut für Plasmaphysik, D-8046 Garching
Ringler, H.	Max-Planck-Institut für Plasmaphysik, D-8046 Garching
Rogister, A.L.	Association Euratom, Kernforschungsanlage Jülich, Postfach 365, D-517 Jülich
Röhr, H.	Max-Planck-Institut für Plasmaphysik, D-8046 Garching
Salat, A.	Max-Planck-Institut für Plasmaphysik, D-8046 Garching
Sardei, F.	Max-Planck-Institut für Plasmaphysik, D-8046 Garching
Schlüter, A.	Max-Planck-Institut für Plasmaphysik, D-8046 Garching

GERMANY, FEDERAL REPUBLIC OF (cont.)

Schlüter J.	Institut für Plasmaphysik der Kernforschungsanlage Jülich, Postfach 365, D-517 Jülich
Schmidt, H.	Institut für Plasmaforschung der Universität Stuttgart, Pfaffenwaldring 31, D-7000 Stuttgart
Schmitter, K.	Max-Planck-Institut für Plasmaphysik, D-8046 Garching
Sesnic, S.	Max-Planck-Institut für Plasmaphysik, D-8046 Garching
Sigel, R.	Max-Planck-Institut für Plasmaphysik, D-8046 Garching
Smeulders, P.	Max-Planck-Institut für Plasmaphysik, D-8046 Garching
Söldner, F.	Max-Planck-Institut für Plasmaphysik, D-8046 Garching
Speth, E.	Max-Planck-Institut für Plasmaphysik, D-8046 Garching
Srivastava, K.	Institut für theoretische Physik, Ruhr-Universität Bochum, D-4630 Bochum
Stäbler, A.	Max-Planck-Institut für Plasmaphysik, D-8046 Garching
Steuer, K.H.	Max-Planck-Institut für Plasmaphysik, D-8046 Garching
Streibl, B.	Max-Planck-Institut für Plasmaphysik, D-8046 Garching
Tasso, H.	Max-Planck-Institut für Plasmaphysik, D-8046 Garching
Waelbroeck, F.	Kernforschungsanlage Jülich, Postfach 365, D-517 Jülich
Wagner, F.	Max-Planck-Institut für Plasmaphysik, D-8046 Garching
Wagner, S.R.	Physikalische-Technische Bundesanstalt, Bundesallee 100, D-3300 Braunschweig
Waidmann, G.	Institut für Plasmaphysik der Kernforschungsanlage Jülich, Postfach 365, D-517 Jülich
Wegrowe, J.G.	Max-Planck-Institut für Plasmaphysik, D-8046 Garching
Wienecke, R.	Max-Planck-Institut für Plasmaphysik, D-8046 Garching

GERMANY, FEDERAL REPUBLIC OF (cont.)

Wilhelm, R.	Max-Planck-Institut für Plasmaphysik, D-8046 Garching
Wimmel, H.K.	Max-Planck-Institut für Plasmaphysik, D-8046 Garching
Witkowski, S.	Max-Planck-Institut für Plasmaphysik, D-8046 Garching
Wobig, H.	Max-Planck-Institut für Plasmaphysik, D-8046 Garching
Wolf, G.	Kernforschungsanlage Jülich, Postfach 365, D-517 Jülich
Zehrfeld, P.	Max-Planck-Institut für Plasmaphysik, D-8046 Garching
Zwicker, H.	Institut für Plasmaforschung der Universität Stuttgart, Pfaffenwaldring 31, D-7000 Stuttgart

HUNGARY

Ag, A.	Central Research Institute for Physics, P.O. Box 49, H-1525 Budapest
Hrehuss, G.	Central Research Institute for Physics, P.O. Box 49, H-1525 Budapest
Kostka, P.	Central Research Institute for Physics, P.O. Box 49, H-1525 Budapest
Pócs, L.	Central Research Institute for Physics, P.O. Box 49, H-1525 Budapest

IRAN

Katzenstein, J.	P.O.B. 3327,Teheran
Naraghi, M.	Atomic Energy Organization of Iran, Nuclear Research Center, P.O.B. 3327, Teheran

IRELAND

Moore-Lewy, G.	Geological Survey of Ireland, 14 Hume Street, Dublin 2

ISRAEL

Cupermann, S.	Department of Physics and Astronomy, Tel-Aviv University, Ramat-Aviv, Tel-Aviv

Owen, D.A.	Ben-Gurion University of the Negev, Department of Physics, Beer Sheva
Shvarts, D.	Nuclear Research Center-Negev, P.O. Box 9001, Beer Sheva

ITALY

Cenacchi, G.	Comitato Nazionale, Energia Nucleare, CNEN – Centro di Calcolo, Via Mazzini, I-240138 Bologna
Cicconi, R.	Facoltà 01, Ingegneria-Università, Viale Cambiaso 6, I-16145 Genoa
Galanti, M.	Associazione Euratom-CNEN sulla Fusione, Centro Gas Ionizzati, C.P. 65, I-00044 Frascati – Rome
Lampis, G.	Laboratorio di Fisica del Plasma del CNR, Via Celoria 16, I-20123 Milan
Maisonnier, C.	Associazione Euratom-CNEN sulla Fusione, Centro Gas Ionizzati, C.P. 65, I-00044 Frascati – Rome
Malesani, G.	Centro di Studio sui Gas Ionizzati, Consiglio Nazionale delle Recerche, ed Università di Padova, Associazione Euratom-CNR, Via Gradenigo 6/a, Padua
Nalesso, G.F.	Centro di Studio sui Gas Ionizzati, Consiglio Nazionale delle Recerche, ed Università di Padova, Associazione Euratom-CNR, Via Gradenigo 6/a, Padua
Nardi, V.	Istituto Elettrotecnico Nazionale Galileo Ferraris, Corso Massimo d'Azeglio 42, I-10125 Turin
Ortolani, S.	Centro di Studio sui Gas Ionizzati, Consiglio Nazionale delle Ricerche, ed Università di Padova, Associazione Euratom-CNR, Via Gradenigo 6/a, Padua
Pieroni, L.	Associazione Euratom-CNEN sulla Fusione, Centro Gas Ionizzati, C.P. 65, I-00044 Frascati – Rome
Sand, F.J.	Associazione Euratom-CNEN, C.P. 65, I-00044 Frascati – Rome
Toschi, R.	Associazione Euratom-CNEN, C.P. 65, I-00044 Frascati – Rome

JAPAN

Dodo, T.	Central Research Laboratory, Hitachi Ltd., Kokubunji, Tokyo 185
Hirano, K.	Institute of Plasma Physics, Nagoya University, Furo-cho, Chikusa-ku, Nagoya 464
Husimi, K.	Japan Atomic Energy Commission, 2-2-1-Kasumigaseki, Chiyoda-ku, Tokyo
Ikuta, K.	Institute of Plasma Physics, Nagoya University, Furo-cho, Chikusa-ku, Nagoya 464
Inoue, K.	Atomic Energy Research Laboratory, Hitachi Ltd. Ozenji, Tama-ku, Kawasaki-shi 215
Itatani, R.	Department of Electronics, Faculty of Engineering, Kyoto University, Yoshida-Honmachi, Sakyo-ku, Kyoto
Itô, H.	Plasma Physics Laboratory, Faculty of Engineering, Osaka University, Yamada-kami, Suita, Osaka 565
Itoh, S.	Institute of Plasma Physics, Nagoya University, Furo-cho, Chikusa-ku, Nagoya 464
Katsurai, M.	Department of Electronic Engineering, Faculty of Engineering, University of Tokyo, Hongo, Bunkyo-ku, Tokyo (Code 113)
Kitsunezaki, A.	Japan Atomic Energy Research Institute, Tokai-mura, Naka-gun, Ibaraki-ken 319-11
Maeda, H.	Japan Atomic Energy Research Institute, Tokai-mura, Naka-gun, Ibaraki-ken 319-11
Maejima, Y.	Tanashi Branch, Electrotechnical Laboratory, 5-4-1, Mukodai, Tanashi, Tokyo
Miyamoto, K.	Institute of Plasma Physics, Nagoya University, Furo-cho, Chikusa-ku, Nagoya 464
Mohri, A.	Institute of Plasma Physics, Nagoya University, Furo-cho, Chikusa-ku, Nagoya 464
Mori, S.	Japan Atomic Energy Research Institute, Tokai-mura, Naka-gun, Ibaraki-ken 319-11
Morimoto, S.	Plasma Physics Laboratory, Kyoto University, Gokasho, Uji
Muraoka, K.	Research Institute for Applied Mechanics, Kyushu University, Hakozaki, Fukuoka 812
Nakai, S.	Institute of Laser Engineering, Osaka University, Yamada-kami, Suita, Osaka 565

JAPAN (cont.)

Nakamura, K.	Faculty of Engineering, Niyazaki University, 1-1-1 Kirishima-cho, Miyazaki-shi
Ogawa, K.	Tanashi Branch, Electrotechnical Laboratory, 5-4-1- Mukodai, Tanashi, Tokyo
Sato, T.	Institute of Plasma Physics, Nagoya University, Furo-cho, Chikusa-ku, Nagoya 464
Sekiguchi, T.	University of Tokyo, Department of Electrical Engineering, Hongo, Bunkyo, Tokyo (Code 113)
Shibata, T.	Research Reactor Institute, Kyoto University, Kumatori, Osaka
Suzuki, Y.	Japan Atomic Energy Research Institute, Tokai-mura, Naka-gun, Ibaraki-ken 319-11
Takayama, K.	Institute of Plasma Physics, Nagoya University, Furo-cho, Chikusa-ku, Nagoya-464
Tamaru, T.	Electrotechnical Laboratory, Agency of Industrial Science and Technology, Ministry of Trade and Industry, 5-4-1 Tanashi-shi, Tokyo
Tanaka, M.	Japan Atomic Energy Research Institute, Tokai-mura, Ibaraki-ken 319-11
Terashima, Y.	Institute of Plasma Physics, Nagoya University, Nagoya 464
Todoroki, J.	Department of Physics, College of Science and Technology, Nihon University, Kanda-Surugadai 1-8, Chiyoda-ku, Tokyo
Tone, T.	Japan Atomic Energy Research Institute, Tokai-mura, Naka-gun, Ibaraki-ken 319-11
Toyama, H.	Department of Physics, Faculty of Science, University of Tokyo, Bunkyo-ku, Tokyo 113
Tsukishima, T.	Faculty of Engineering, Nagoya University, Furo-cho, Chikusa-ku, Nagoya 464
Uchida, T.	Department of Nuclear Engineering, University of Tokyo, 3-1 Hongo, 7-Chome, Bunkyo-ku, Tokyo 113
Uo, K.	Plasma Physics Laboratory, Kyoto University, Gokasho, Uji
Uyama, T.	Plasma Physics Laboratory, Faculty of Engineering, Osaka University, Yamada-kami, Suita, Osaka 565
Yamamoto, K.	Japan Atomic Energy Research Institute, 1-1 Shinbashi, Minato-ku, Tokyo 105

JAPAN (cont.)

Yamanaka, C. — Institute of Laser Engineering, Osaka University, Yamada-kami, Suita, Osaka 565

Yamazaki, K. — Department of Nuclear Engineering, Faculty of Engineering, University of Tokyo, 3-1 Hongo, 7-Chome, Bunkyo-ku, Tokyo 113

Yokoyama, K. — Department of Physics and Atomic Energy Research Institute, College of Science and Technology, Nihon University, Kanda-Surugadai, Chiyoda-ku, Tokyo

MEXICO

Melendez-Lugo, L. — Instituto Nacional de Energía Nuclear, Insurgentes Sur 1079, Mexico 18, D.F.

Vazquez-Reyna, M. — Instituto Nacional de Energía Nuclear, Insurgentes Sur 1079, Mexico 18, D.F.

NETHERLANDS

Barbian, E.P. — Association Euratom-FOM, FOM-Instituut voor Plasmafysica, Rijnhuizen, Jutphaas, P.O.B. 7

Bobeldijk, C. — FOM-Instituut voor Plasmafysica, Rijnhuizen, Jutphaas, P.O.B. 7

Braams, C.M. — FOM-Instituut voor Plasmafysica, Rijnhuizen, Jutphaas, P.O.B. 7

D'Ippolito, D.A. — FOM-Instituut voor Plasmafysica, Overeindseweg 2, Jutphaas, P.O.B. 7

Engelmann, F. — FOM-Instituut voor Plasmafysica, Overeindseweg 2, Jutphaas, P.O.B. 7

Hoekzema, J.A. — FOM-Instituut voor Plasmafysica, Rijnhuizen, Jutphaas, P.O.B. 7

Kistemaker, J. — FOM-Institute for Atomic and Molecular Physics, Kruislaan 407, Amsterdam

Mugge, J. — FOM-Institute voor Plasmafysica, Rijnhuizen, Jutphaas, P.O.B. 7

Nocentini, A. — FOM-Instituut voor Plasmafysica, Overeindseweg 2, Jutphaas, P.O.B. 7

Ornstein, L.Th.M. — FOM-Instituut voor Plasmafysica, Rijnhuizen, Jutphaas, P.O.B. 7

Piekaar, H.W. — FOM-Instituut voor Plasmafysica, Rijnhuizen, Jutphaas, P.O.B. 7

NETHERLANDS (cont.)

Pots, B.F.M.	FOM-Instituut voor Plasmafysica, Rijnhuizen, Jutphaas, P.O.B. 7
Rem, J.	FOM-Instituut voor Plasmafysica, Overeindseweg 2, Jutphaas, P.O.B. 7
Rietjens, L.H.Th.	Eindhoven University of Technology, Eindhoven
Schep, T.J.	FOM-Instituut voor Plasmafysica, Overeindseweg 2, Jutphaas, P.O.B. 7
Schram, D.C.	Eindhoven University of Technology, Eindhoven
Schüller, F.C.	FOM-Instituut voor Plasmafysica, Rijnhuizen, Jutphaas, P.O.B. 7

NORWAY

Berge, G.	Department of Applied Mathematics, University of Bergen, 5014 Bergen
Kildal, A.	Institute of Physics, University of Oslo, B.P. 1048, Oslo 3

PAKISTAN

Ahmad, M.	Nuclear Physics Division, Institute for Nuclear Science and Technology, Pinstech, P.O. Nilore, Rawalpindi

POLAND

Byszewski, W.W.	Institute of Fundamental Technological Research, Polish Academy of Sciences, u. Swietokrzyska 21, PL-00-049 Warsaw
Denus, S.	Institute of Plasma Physics and Laser Microfusion, PL-00-908 Warsaw 49, Bemowo, skr. poczt 49
Farny, J.	Institute of Plasma Physics and Laser Microfusion, PL-00-908 Warsaw 49, Bemowo, skr. poczt 49
Gryzinski, M.W.	Institute of Nuclear Research, Świerk k. Otwocka

SPAIN

Barrero, A.	Escuela Técnica Superior de Ingenieros Aeronáuticos, Pl. Cardenal Cisneros 3, Ciudad Universitaria, Madrid-3
Cordero-Lopez, F.	Junta de Energía Nuclear, Av. Complutense 22, Madrid-3

SPAIN (cont.)

Manero-Amoros, F.	Junta de Energía Nuclear, Av. Complutense 22, Madrid-3
Perea-Folgueras, A.	Junta de Energía Nuclear, Av. Complutense 22, Madrid-3
Velarde, G.	Junta de Energía Nuclear, Av. Complutense 22, Madrid-3
Verdaguer, F.	Junta de Energía Nuclear, Av. Complutense 22, Madrid-3

SWEDEN

Anderson, D.	Institute for Electromagnetic Field Theory and Plasma Physics, Chalmers University of Technology, S-40220 Gothenburg
Bergström, A.	National Defence Research Institute, FOA 214, S-104 50 Stockholm
Bonnedal, D.M.	Institute for Electromagnetic Field Theory and Plasma Physics, Chalmers University of Technology, S-40220 Gothenburg
Hellsten, T.A.K.	Department of Plasma Physics and Fusion Research, Royal Institute of Technology, S-10044 Stockholm 70
Lehnert, B.P.	Department of Plasma Physics and Fusion Research, Royal Institute of Technology, S-10044 Stockholm 70
Pauli, R.	The Swedish Atomic Energy Company, Fack, S-611 01 Nyköping 1
Rey, L.H.	Swedish National Board for Energy Source Development, Box 21048, S-10031 Stockholm 21
Svenningson, P.J.	Swedish National Board for Energy Source Development, Box 21048, S-10031 Stockholm 21

SWITZERLAND

Balmer, J.	Institute of Applied Physics, University of Berne, Sidlerstrasse 5, CH-3012 Berne
Bernard, L.C.	Centre de recherches en physique des plasmas, Ecole polytechnique fédérale de Lausanne, 21 Avenue des Bains, CH-1007 Lausanne
Bighel, L.	Centre de recherches en physique des plasmas, Ecole polytechnique fédérale de Lausanne, 21 Avenue des Bains, CH-1007 Lausanne

SWITZERLAND (cont.)

Donaldson, T.P.	Institute of Applied Physics, University of Berne, Sidlerstrasse 5, CH-3012 Berne
Hoegger, B.A.	Institut de physique, Université de Fribourg, CH-1700 Fribourg
Hofmann, F.	Centre de recherches en physique des plasmas, Ecole polytechnique fédérale de Lausanne, 21 Avenue des Bains, CH-1007 Lausanne
Nägele, H.P.	Nuclear AG, Technisches Büro Basel, Wiesestr. 14, CH-4000 Basel
Troyon, F.	Centre de recherches en physique des plasmas, Ecole polytechnique fédérale de Lausanne, 21 Avenue des Bains, CH-1007 Lausanne
Veprek, S.	Institute of Inorganic Chemistry, University of Zurich, Rämistr. 76, CH-8001 Zurich
Wägli, P.	Institute of Applied Physics, University of Berne, Sidlerstr. 5, CH-3012 Berne
Zimmermann, J.A.	Institute of Applied Physics, University of Berne, Sidlerstr. 5, CH-3012 Berne

TURKEY

Sinman, A.	Turkish Atomic Energy Commission, Ankara Nuclear Research Center, Beşevler-Ankara
Sinman, S.	Turkish Atomic Energy Commission, Middle East Technical University, Electrical Engineering Department, Ankara

UNITED KINGDOM

Bodin, H.A.B.	UKAEA, Culham Laboratory, Abingdon OX 14 3DB
Connor, J.W.	UKAEA, Culham Laboratory, Abingdon OX 14 3DB
Cordey, J.G.	UKAEA, Culham Laboratory, Abingdon OX 14 3DB
Deuchars, W.M.	Department of Physics, University of Strathclyde, John Anderson Building, 107 Rottenrow, Glasgow G4 0NG, Scotland
Dymoke-Bradshaw, A.K.L.	Imperial College, London SW7

UNITED KINGDOM (cont.)

Gill, R.D.	UKAEA, Culham Laboratory, Abingdon OX 14 3DB
Gray, D.R.	Blackett Laboratory, Imperial College, London SW7
Haines, M.G.	Imperial College, London SW 7
Hancox, R.	UKAEA, Culham Laboratory, Abingdon OX 14 1HB
Irving, J.	Department of Physics, University of Strathclyde, John Anderson Building, 107 Rottenrow, Glasgow G4 0NG, Scotland
Jukes, J.D.	UKAEA, Culham Laboratory, Abingdon OX 14 3DB
Lees, D.J.	UKAEA, Culham Laboratory, Abingdon OX 11 8DB
Morgan, F.	AWRE, Building N78, Aldermaston, Berkshire
Motz, H.	Department of Engineering Science, University of Oxford, Parks Road, Oxford
Paul, J.W.	UKAEA, Culham Laboratory, Abingdon OX 14 3DB
Peacock, N.J.	UKAEA, Culham Laboratory, Abingdon OX 14 3DB
Pease, R.S.	UKAEA, Culham Laboratory, Abingdon OX 14 3DB
Riviere, A.C.	UKAEA, Culham Laboratory, Abingdon OX 14 3DB
Roberts, K.V.	UKAEA, Culham Laboratory, Abingdon OX 14 3DB
Robinson, D.Ch.	UKAEA, Culham Laboratory, Abingdon OX 14 3DB
Sharp, L.E.	UKAEA, Culham Laboratory, Abingdon OX 14 3DB
Spalding, I.J.	UKAEA, Culham Laboratory, Abingdon OX 14 3DB
Sweetman, D.R.	UKAEA, Culham Laboratory, Abingdon OX 14 3DB
Taylor, J.B.	UKAEA, Culham Laboratory, Abingdon OX 14 3DB

UNITED KINGDOM (cont.)

Webb, S.J.	Blackett Laboratory, Plasma Group, Imperial College, London SW 7
Wooding, E.	Royal Holloway College, University of London, Egham Hill, Edham, Surrey TW 200EX

USSR

Buchelnikova, V.M.	Institute of Nuclear Physics, Novosibirsk, 90
Dimov, G.I.	Institute of Nuclear Physics, Novosibirsk, 90
Kadomtsev, B.B.	I.V. Kurchatov Institute of Atomic Energy, Moscow, D-182
Kolesnichenko, Ya.	Institute of Nuclear Research of the Ukrainian SSR Academy of Sciences, Kiev
Krokhin, O.	Lebedev Institute, Academy of Sciences, Leninskij pr. 53, Moscow
Krugliakov, E.	Institute of Nuclear Physics, Novosibirsk, 90
Kuznetsov, V.	Institute of Technical Physics, Leningrad
Kuznetsov, E.	I.V. Kurchatov Institute of Atomic Energy, Moscow, D-182
Nanobashvili, S.I.	Institute of Physics, Academy of Sciences, Tiflis
Rabinovich, M.S.	Lebedev Institute, Academy of Sciences, Leninskij pr. 53, Moscow
Savinkov, A.M.	I.V. Kurchatov Institute of Atomic Energy, Moscow, D-182
Shafranov, V.D.	I.V. Kurchatov Institute of Atomic Energy, Moscow, D-182
Smirnov, V.P.	I.V. Kurchatov Institute of Atomic Energy, Moscow, D-182
Strelkov, V.S.L.	I.V. Kurchatov Institute of Atomic Energy, Moscow, D-182
Suprunenko, V.A.	Physico-Technical Institute, Kharkov
Vil'dzhyunas, M.I.	Ioffe Physical-Technical Institute, Leningrad

USA

Alexeff, I.	Electrical Engineering Department, University of Tennessee, Knoxville, Tennessee 37916
Baker, D.A.	Los Alamos Scientific Laboratory, University of California, P.O. Box 1663, Los Alamos, New Mexico 87545
Bardwell, S.J.	Fusion Energy Foundation, Box 1943, G.P.O. New York, New York 10001
Barker, R.J.	Stanford Institute for Plasma Research, Via Crespi, Stanford University, Stanford, California 94305
Beal, J.W.	USERDA, Division of Magnetic Fusion Energy, Washington, D.C. 20545
Benford, J.N.	Physics International Company, 2700 Mercer St., San Leandro, California 94577
Berk, H.L.	Lawrence Livermore Laboratory, University of California, P.O. Box 808, Livermore, California 94550
Berman, Ph.G.	Department of Defense, Washington, D.C. 20301
Berry, L.A.	Thermonuclear Division, Oak Ridge National Laboratory, P.O. Box, Oak Ridge, Tennessee 37830
Bodner, S.E.	US Naval Research Laboratory, Code 7730, Washington, D.C. 20375
Book, D.L.	US Naval Research Laboratory, Plasma Dynamics Branch, Washington, D.C. 20375
Bostick, W.H.	Physics Department, Stevens Institute of Technology, Hoboken, New Jersey 07030
Boyd, D.A.	Department of Physics and Astronomy, University of Maryland, College Park, Maryland 20742
Brackbill, J.U.	Los Alamos Scientific Laboratory, Group CTR-6, MS 642, University of California, P.O. Box 1663, Los Alamos, New Mexico 8754
Callen, J.D.	Oak Ridge National Laboratory, Thermonuclear Division, P.O. Box Y, Oak Ridge, Tennessee 37830
Cantrell, E.L.	Los Alamos Scientific Laboratory, Group CTR-3, MS 638, University of California, Los Alamos, New Mexico 87545
Chen, F.F.	University of California, Los Angeles, California 90024
Clarke, J.F.	Oak Ridge National Laboratory, Union Carbide Corporation, Nuclear Division, P.O. Box Y, Bldg. 9201-2, Oak Ridge, Tennessee 37830

USA (cont.)

Coensgen, F.H.	Lawrence Livermore Laboratory, University of California, P.O. Box 808, Livermore, California 94550
Colchin, R.J.	Oak Ridge National Laboratory, P.O. Box Y, Building 9201-2, Oak Ridge, Tennessee 37830
Conant, K.J.	510th Ordnance Co., Prinz-Eugen-Kaserne, D-8870 Günzburg, Federal Republic of Germany
Conn, R.W.	Nuclear Engineering Department, University of Wisconsin, 1500 Johnson Drive, Madison, Wisconsin 53706
Coppi, B.	M.I.T., 77 Massachusetts Avenue, Cambridge, Massachusetts 02139
Davidson, R.C.	Department of Physics and Astronomy, University of Maryland, College Park, Maryland 20742
Dean, S.O.	USERDA, Administration, Mail Station G-234, Washington, D.C. 20545
Doggett, W.O.	North Carolina State University, P.O. Box 5342, Raleigh, North Carolina 27607
Drake, J.R.	Department of Physics, University of Wisconsin, 1150 University Avenue, Madison, Wisconsin 53706
Dreicer, H.	Los Alamos Scientific Laboratory, University of California, P.O. Box 1663, Los Alamos, New Mexico 87544
Emmert, G.A.	Nuclear Engineering Department, Engineering Research Building, University of Wisconsin, Madison, Wisconsin 53706 Present address: Max-Planck-Institut für Plasmaphysik, D-8046 Garching, Federal Republic of Germany
England, A.C.	Oak Ridge National Laboratory, P.O. Box Y, Oak Ridge, Tennessee 37830
Fleischmann, H.H.	Department of Applied Physics, Cornell University, Ithaca, New York 14853
Forman, P.R.	Los Alamos Scientific Laboratory, CTR-8, MS 639, P.O. Box 1663, Los Alamos, New Mexico 87544 Present address: Max-Planck-Institut für Plasmaphysik, D-8046 Garching, Federal Republic of Germany
Forsen, H.K.	Exxon Nuclear Co., 777 106th St. NE, Bellevue, Washington 98004
Fowler, T.K.	Lawrence Livermore Laboratory, University of California, P.O. Box 808, Livermore, California 94550
Frieman, E.A.	Plasma Physics Laboratory, Princeton University, James Forrestal Campus, P.O. Box 451, Princeton, New Jersey 08540

USA (cont.)

Furth, H.P.	Plasma Physics Laboratory, Princeton University, P.O. Box 451, Princeton, New Jersey 08540
Gale, A.J.	Ion Optics, Inc., 36 Montvale Avenue, Stoneham, Massachusetts 02180
Goldman, L.M.	Laboratory for Laser Energetics, University of Rochester, River Campus, Hope 110, Rochester, New York 14627
Gondhalekar, A.M.	Francis Bitter National Magnet. Laboratory, NW 14-2128, Massachusetts Institute of Technology, 170 Albany Street, Cambridge, Massachusetts 02139
Gottlieb, M.B.	Plasma Physics Laboratory, Princeton University, P.O. Box 451, Princeton, New Jersey 08540
Gould, R.W.	California Institute of Technology, MS 116-81, Pasadena, California 91125
Grad, H.	Courant Institute of Mathematical Sciences, New York University, 251 Mercer Street, New York, New York 10012
Grafstein, D.	Exxon Research and Engineering Co., P.O. Box 8, Linden, New Jersey 07036
Griem, H.R.	Department of Physics and Astronomy, University of Maryland, College Park, Maryland 20742
Gross, R.A.	School of Engineering and Applied Science, Columbia University, New York, New York 10027
Guest, G.E.	General Atomic Company, P.O. Box 81608, San Diego, California 92138
Haught, A.F.	United Technologies Research Center, Silver Lane, East Hartford, Connecticut
Hedrick, C.L.	Oak Ridge National Laboratory, Thermonuclear Division, P.O. Box Y, Oak Ridge, Tennessee 37830
Horton, C.W.	Department of Physics, University of Texas and Austin, Fusion Research Center, RLM 11.320, Austin, Texas 78712
Jassby, D.L.	Plasma Physics Laboratory, Princeton University, P.O. Box 451, Princeton, New Jersey 08540
Johnson, J.L.	Plasma Physics Division, Princeton University, P.O. Box 451, Princeton, New Jersey 08540,
Kapetanakos, C.A.	Naval Research Laboratory, Code 7760, Washington D.C.
Killeen, J.	National CTR Computer Center, Lawrence Livermore Laboratory, University of California, P.O. Box 808, L-318, Livermore, California 94550

USA (cont.)

Kindel, J.M.	Los Alamos Scientific Laboratory, University of California, Theoretical Division, T-6, MS-531, Los Alamos, New Mexico 8754
Kintner, E.E.	USERDA, Division of Magnetic Fusion Energy, Washington, D.C. 20545
Koloc, P.M.	Department of Physics and Astronomy, University of Maryland, College Park, Maryland 20742
Krakowski, R.A.	Los Alamos Scientific Laboratory, CTR-DOT, MS-641, P.O. Box 1663, Los Alamos, New Mexico 87545
Krall, N.A.	Science Application Inc., 1200 Prospect Street, La Jolla, California 92037
Kristiansen, M.	Department of Electrical Engineering, Texas Technical University, Lubbock, Texas 79409
Kuswa, G.W.	USERDA, Division of Laser Fusion, M/S, A 401, Washington, D.C. 20545
Liewer, P.C.	Department of Physics and Astronomy, University of Maryland, College Park, Maryland 20742
Lindl, J.D.	Lawrence Livermore Laboratory, Livermore, California 94550
Lister, G.G.	Plasma Physics Laboratory, Princeton University, P.O. Box 451, Princeton, New Jersey 08540
Luce, J.S.	Lawrence Livermore Laboratory, Box 808, L-71, Livermore, California 94551
McAlees, D.G.	Exxon Nuclear Co., 777 106th NE, Bellevue, Washington 98004
McCall, G.H.	Los Alamos Scientific Laboratory, P.O. Box 1663, Los Alamos, New Mexico 87544
McNamara, B.	Lawrence Livermore Laboratory, University of California, P.O. Box 808, Livermore, California 94551
Machalek, M.D.	Los Alamos Scientific Laboratory, University of California, P.O. Box 1663, Los Alamos, New Mexico 87545
Mayer, F.J.	KMS Fusion Inc., 3941 Research Park Drive, Ann Arbor, Michigan 48106
Mazzucato, E.	Plasma Physics Laboratory, Princeton University, P.O. Box 451, Princeton, New Jersey 08540
Meade, D.M.	Plasma Physics Laboratory, Princeton University, P.O. Box 451, Princeton, New Jersey 08540
Moir, R.W.	Lawrence Livermore Laboratory, P.O. Box 808, Livermore, California 94550

USA (cont.)

Ohkawa, T.	General Atomic Co., P.O. Box 81608, San Diego, California 92138
Papadopoulos, K.	US Naval Research Laboratory, Code 7759, Washington, D.C. 20375
Post, R.F.	Lawrence Livermore Laboratory, University of California, P.O. Box 808, Livermore, California 94595
Post, R.S.	USERDA, Department of Nuclear Engineering, University of Wisconsin, 1500 Johnson Dr., Madison, Wisconsin 53711
Ribe, F.L.	Los Alamos Scientific Laboratory, University of California, P.O. Box 1663, Los Alamos, New Mexico 81545
Robson, A.E.	Naval Research Laboratory, Code 7708, Washington, D.C. 20375
Rosenbluth, M.N.	Institute for Advanced Study, University of Princeton, Princeton, New Jersey 08540
Rostoker, N.	Department of Physics, University of California, Irvine, California 92717
Rutherford, P.H.	Plasma Physics Laboratory, Princeton University, Forrestal Campus, P.O. Box 451, Princeton, New Jersey 08540
Scott, F.R.	Electric Power Research Institute, 3412 Hillview Drive, Palo Alto, California 94304
Shohet, J.L.	Department of Electrical and Computer Engineering, The University of Wisconsin, Madison, Wisconsin 53706
Simon, A.	M.A.S. Department, University of Rochester, Rochester, New York 14627
Stacey, W.M.	Argonne National Laboratory, Bldg. 208, 9700 South Cass Avenue, Argonne, Illinois 60439
Stamper, J.A.	US Naval Research Laboratory, Washington, D.C. 20375
Stewart, L.D.	Oak Ridge National Laboratory, Bldg. 9201-2, P.O. Box Y, Oak Ridge, Tennessee 37830
Stodiek, W.	Plasma Physics Laboratory, Princeton University, P.O. Box 451, Princeton, New Jersey 08540
Sudan, R.N.	Laboratory of Plasma Studies, Cornell University, 308 Upson Hall, Ithaca, New York 14853
Tahsiri, H.	National University, 621 Sadi Avenue, Teheran, Iran
Tamano, T.	General Atomic Co., P.O. Box 81608, San Diego, California 92138

USA (cont.)

Tang, W.M.	Plasma Physics Laboratory, Princeton University, P.O. Box 451, Princeton, New Jersey 08540
Tataronis, J.A.	Courant Institute, New York University, 251 Mercer Street, New York, New York 10012
Taylor, R.J.	UCLA, Los Angeles, California 90024
Thomassen, K.	Los Alamos Scientific Laboratory, University of California, P.O. Box 1663, Los Alamos, New Mexico 87545
Toepfer, A.J.	Sandia Laboratories, Albuquerque, New Mexico 87115
Trivelpiece, A.W.	Maxwell Laboratories, Inc., 9244 Balboa Ave., San Diego, California 92123
Uckan, N.A.	Oak Ridge National Laboratory, Thermonuclear Division, P.O. Box Y, Oak Ridge, Tennessee 37830
Valeo, E.J.	Lawrence Livermore Laboratory, University of California, L-545, P.O. Box 808, Livermore, California 94550
Waniek, R.W.	Advanced Kinetics, Inc., 1231 Victoria Street, Costa Mesa, California 92627
Winske, D.	Los Alamos Scientific Laboratory, P.O. Box 1663, Los Alamos, New Mexico 87544
Winsor, N.K.	US Naval Research Laboratory, Code 7752, Washington, D.C. 20375
Wu, C.S.	University of Maryland, College Park, Maryland 20742
Yaakobi, B.	Laboratory for Laser Energetics, University of Rochester, River Campus, Hopeman Building, Rochester, New York 14627
Yonas, G.	Sandia Laboratories, Albuquerque, New Mexico 87115
Young, F.C.	US Naval Research Laboratory, Washington, D.C. 20375

ORGANIZATIONS

CEC

Böckhoff, K.H.	Euratom, Central Bureau for Nuclear Measurements, Steenweg naar Retie, 2440 Geel, Belgium
Casini, G.	Joint Research Center of the Commission of the European Communities, Ispra, Italy
Eckhartt, D.	Jet Design Group, Culham Laboratory, Abingdon OX 14 3DB, United Kingdom

Gibson, A.	Jet Design Group, Culham Laboratory, Abingdon OX 14 3DB, United Kingdom
Green, B.J.	Jet Design Group, Culham Laboratory, Abingdon OX 14 3DB, United Kingdom
Knoepfel, H.E.	Centro Gas Ionizzati, C.P. 65, I-00044 Frascati, Italy
Minardi, E.	Jet Design Group, Culham Laboratory, Abingdon OX 14 3DB, United Kingdom
Palumbo, D.	Euratom, CCE, 200 Rue de la Loi, Brussels, Belgium
Poffé, J.P.	Jet Design Group, Culham Laboratory, Abingdon OX 14 3DB, United Kingdom
Rebut, P.H.	Jet Design Group, Culham Laboratory, Abingdon OX 14 3DB, United Kingdom

ECE

Bishop, A.	EDE, United Nations, Palais des Nations, Geneva, Switzerland

IAEA

Twersky, D.	International Atomic Energy Agency, Nuclear Fusion Journal, Kärntner Ring 11, P.O. Box 590, A-1011 Vienna, Austria

UNESCO

Berkovsky, B.M.	UNESCO, 7, Place de Fontenoy, F-75700 Paris, France

AUTHOR INDEX

Roman numerals are volume numbers.
Italic numerals refer to the first page of a paper by the author concerned.
Upright numerals denote comments and questions in discussions.
Literature references are not indexed.

Abramov, V.A.: II *237*
Adam, J.C.: II 143, *489*; III 47, 75
Adati, K.: III *427*
Adcock, S.J.: I *317*
Aizawa, T.: I *503*
Akulina, D.K.: II *115*
Alcock, M.W.: II *305*
Alexeff, I.: II 565
Alikhanov, S.G.: III *517*
Allen, A.W.: I *511*
Amagishi, Y.: III *11*
Anderson, D.V.: III *161*
Anderson, O.A.: III *293*
Andryukhina, Eh.D.: II *115*
Anno, K.: II *289*
Apgar, E.: I *247*
Arai, T.: II *289*
Armandillo, E.: II *589*
Aronstein, R.: III *203*
Arunasalam, V.: I *21*
Asami, N.: III *239*
Ashby, D.E.T.F.: II *305*
Atkinson, D.W.: II *71*
Axon, K.B.: II *269*
Bagdasarov, A.A.: I *3*
Bailey, V.: II *543*
Baker, C.C.: III *255*
Baker, D.A.: I *419*, 427, 445
Baker, W.R.: III *293*
Bakhtin, V.P.: III *517*
Bakshaev, Yu.L.: I *185*
Baldwin, D.E.: III *147*
Baranchikov, E.I.: I *185*
Barber, G.S.: III *293*
Bardes, J.: I *99*
Bardet, R.: II *259*
Bariaud, A.: III *303*
Barnes, D.C.: II *203*
Barr, W.L.: III *223*
Bartsch, R.R.: II *193*
Basu, B.: II *455*
Baur, J.F.: I *317*
Becherer, R.: III *303*
Becker, G.: II *401*
Bekiarian, A.: I *99*
Bender, D.J.: III *223*
Benford, J.: II *543*, 565; III 403
Berezhetskij, M.S.: II *115*
Berge, G.: I 551
Berger, D.: II *411*
Bergeron, K.D.: I *167*
Berk, H.L.: II 111, 385; III *147*, 159
Berkner, K.H.: III *293*
Berlizov, A.B.: I *3*
Bernard, A.: III *471*
Bernard, L.C.: II *411*
Bernard, M.: II *259*
Berry, L.A.: I *49*, 95
Betancourt, O.: II *203*
Bezzerides, B.: I *123*
Bhatnagar, V.P.: I *359*
Bighel, L.: I *305*
Bird, W.L., Jr.: III *317*
Birdsall, D.H.: III *293*
Biskamp, D.: I *579*, 605
Blanc, P.: III *49*
Blaumoser, M.: II *81*
Blokh, M.A.: II *115*
Blythe, P.: II *613*
Bobeldijk, C.: I *493*, 501
Bobrovskij, G.A.: I *3*
Bodin, H.A.B.: I 427, *429*, 445, 461, 477, 501; II 201
Bodner, S.: I *217*, 225

Bogen, P.: I 539
Bogolyubskij, S.L.: I *177*
Bol, K.: I *21*
Bonnal, J.F.: III *303*
Book, D.L.: III *415, 507*
Boom, R.W.: III *203*
Bosia, G.: I *359*
Bostick, W.H.: I 567, 613; III 111, 495, *497*
Bowles, A.: III *203*
Box, S.J.C.: II *627*
Boyd, D.A.: I *21, 397*
Boyd, J.K.: III *161*
Boyer, W.B.: I *167*
Braams, C.M.: III 221, 545
Brackbill, J.U.: II *203,* 213
Bradley, J.: II *71*
Bretz, N.: I *21*
Briffod, G.: II *259*
Brooks, N.H.: I *317*
Brossier, P.: I *409*
Brusati, M.: I *21*
Brusnikin, V.M.: III *517*
Bruzzone, H.: III *483, 491*
Buchenauer, C.J.: II *193*
Buffa, A.: I *447*
Burgess, M.D.J.: III *405*
Burkhardt, L.C.: I *419*
Burleigh, R.J.: III *223*
Burt, J.: II *269*
Bush, C.E.: I *49*
Bussac, M.N.: I *607*
Buttram, M.T.: I *167*
Buzankin, V.V.: III *61*
Byers, J.A.: III *161*
Byszewski, W.W.: II *627*
Callen, J.D.: I *49*, 613; II 67, *369*, 385, 386, *489*
Campbell, P.M.: I *227*
Cannici, B.: I *259, 267*
Canobbio, E.: II 111; III *19*, 29
Cantrell, E.L.: II *193*
Carlson, G.A.: III *223*
Casini, G.: III 279
Cattanei, G.: II *81*
Catto, P.J.: II *489*
Cavallo, A.: II *81*
Celata, C.M.: I *397*
Chance, M.S.: II *395*
Chang, J.: I *167*
Chebotaev, P.Z.: III *535*
Chen, F.F.: II 649; III 189, 325
Cheng, C.Z.: II *467*
Chicherov, V.M.: III *327*
Chiyoda, K.: II *499*
Chu, C.K.: I *511*
Chu, K.R.: II *543*
Chu, M.S.: II *387*
Cima, G.: I *335*
Clark, R.: II *543*
Clarke, J.F.: II 257, *369*
Clauser, J.F.: III *135*
Clauser, M.J.: I *167*
Clement, M.: II *259*
Clemmer, R.G.: III *203*
Cobble, J.A.: II *145*
Coensgen, F.H.: III *135*, 145
Cohen, B.I.: II *489*
Cohen, R.: III *161*
Cohen, S.: I *21*
Colchin, R.J.: I *49;* III 59, 413
Colombant, D.: I *217*
Conn, R.W.: II 287, 421, 451, 509; III *203,* 221, 222, 237
Conrads, H.: I 163
Conrads, J.P.F.: II 649; III 221
Consoli, T.: II 153; III 75
Cooper, A.L.: III *507*
Cooper, R.: II *543*
Cooper, W.S.: III *293*
Cooperstein, G.: III *415*
Coppi, B.: I *247,* 265, 277, 301, 385, 415, 605; II 27, 93, 321, 385, *455,* 465, 509
Cordey, J.G.: I 95; II *305, 423,* 451; III 367
Correll, D.L.: III *135, 293*
Costa, S.: I *447*
Costley, A.E.: I *409*
Coudeville, A.: III *471*
Craig, A.D.: II *269*
Cummins, W.F.: III *135*
Cutler, T.A.: III *147, 161*
Dagazian, R.V.: II *203*
Dagenhart, W.K.: III *293*
Dakin, D.: II *543*
Dandl, R.A.: II *145*
Dangor, A.E.: II *555, 613*
Danilkin, I.S.: II *115*
Danilov, A.F.: I *591*
Dautray, R.: I *99*, 107
Davidson, R.C.: I *399;* III 101, *113,* 121, 131, 159

Davis, H.A.: III *385*
Davis, J.: III *203*
Davis, R.C.: III *293*
De Boo, J.C.: I *317*
Decker, G.: III *441*
Decoste, R.: I *217*
De Haan, P.: II *527*
De Jagher, P.C.: II *527*
Delellis, R.: III *491*
Delettrez, J.: I *109*
Dellis, A.N.: II *71*
Delobeau, F.: I *99*
De Mascureau, J.: III *471*
Demirkhanov, R.A.: III *31*
Derfler, H.: I 289; II 111
Devoto, R.S.: III *223*
Di Capua, M.: II *543*
Dikij, A.G.: II *129*
Di Marco, J.N.: I *419*
Dimock, D.: I *21*
Dimov, G.I.: III *177*, 189
D'Ippolito, D.A.: I *523*
Dnestrovskij, Yu.N.: I *3*, *591*
Dobrott, D.R.: II *387*
Dodo, T.: II *345*
Doggett, J.N.: III *223*
Dolotov, S.K.: III *327*
Donaldson, T.P.: II *589*
Dorst, D.: II *81*
Dory, R.A.: II *145*, *369*
Doschek, G.: I *217*
Downing, J.N.: II *193*
Drake, J.R.: II *333*
Dreike, P.: III *415*
Dremin, M.M.: II *169*
Driga, M.D.: III *317*
Drobot, A.T.: III *415*
Druaux, J.: III *303*
DuBois, D.F.: I *123*
Düchs, D.F.: II *43*
Dunlap, J.L.: I *49*
Dylla, F.: I *21*
Dymoke-Bradshaw, A.K.L.: II *555*
Eames, D.: I *21*
Eason, H.O.: II *145*
Ecker, B.: II *543*
Edery, D.: I *607*
Edlington, T.: II *305*
Edmonds, P.H.: I *49*
Ehlers, K.W.: III *293*
Ejima, S.: II *333*
Ekdahl, C.: II *543*
Elfimov, A.G.: III *31*
El-Nadi, A.: II 331
Elsner, A.: II *81*
Emmert, G.A.: II 201, 301; III *203*
Engelhardt, W.: I *259*, *267*
Engelmann, F.: II *19*, 27, 465; III 367
England, A.C.: I *49*
Equipe TFR: I *35*, *69*, *279*; III *39*
Erents, S.K.: II *269*
Estabrook, K.: I *133*
Eto, F.: III *239*
Eubank, H.: I *21*
Evstigneev, S.A.: III *327*
Fabre, E.: II *597*
Farnsworth, A.V., Jr.: I *167*
Fedyanin, O.I.: II *115*
Feldman, U.: I *217*
Ferch, R.L.: III *415*
Fielding, S.J.: II *269*
Fink, J.H.: III *223*
Fisher, R.K.: I *317*
Fleischmann, H.H.: I 415, 567; III *385*, 403
Fletcher, W.H.W.: II *305*
Ford, R.: III *507*
Forrest, M.J.: II *635*
Forslund, D.W.: I *123*
Foster, C.A.: I *49*
Fowler, T.K.: III 189
Fraenkel, B.: I *21*
Frank, R.: II *259*
Freemann, B.L.: II *193*
Freeman, J.R.: I *167*
Freeman, R.L.: I *317*
Freese, K.B.: II *193*
Freidberg, J.P.: I *523*; II *203*; III *123*
Friedman, A.: III *415*
Frieman, E.A.: II *489*
Fujisawa, N.: II *289*
Fujita, J.: II *95*
Fujiwara, M.: II *95*
Fumelli, M.: III *303*
Funahashi, A.: II *289*
Furth, H.P.: I 277, 301, 397, 567, 613; II 127, 321; III 175
Fussmann, G.: I *259*, *267*
Galanti, M.: III *447*
Garban, C.: II *597*
Garçonnet, J.P.: III *471*
Gauthier, A.: II *259*

Gegechkory, N.M.: I *3*
Gerasimov, B.P.: I *177*
Gerber, K.A.: II *543*; III *507*
Gernhardt, J.: I *259, 267*
Gerwin, R.A.: III *123*
Gesso, H.: II *215*
Ghose, S.: III *203*
Giannella, R.: I *447*
Gibson, A.: I 19, 95, 257, 301; II 421, 479; III 47, 59, 221
Gierke, G. von: I 19
Gill, R.D.: II *71, 269*
Girard, J.: I *21*
Gladd, N.T.: III *113*
Glock, E.: I *259, 267*
Glushkov, I.S.: III *517*
Goedbloed, J.P.: I *523*
Goeler, S. von: I *21*
Gohar, Y.: III *203*
Golden, J.: III *415*
Goldenbaum, G.C.: I *511*
Goldman, E.B.: I *109*, 121
Goldman, L.M.: I *109*
Goldman, M.V.: II *635*
Goldstein, S.A.: I *167;* III *415*
Goldston, R.J.: I *371*
Gondhalekar, A.: I *247*, 257
Goodall, D.H.J.: II *269*
Gorbunov, E.P.: I *3*
Gordeev, A.V.: I *185*
Gormezano, C.: III *135*
Gotô, S.: III *103*
Gottlieb, M.B.: III 335
Gourlan, C.: III *447*
Gowers, C.W.: I *429*
Grad, H.: II 153, *355*, 367, 421
Graffmann, E.: I *351*
Gratton, F.: III *483, 489*
Gratton, J.: III *483*
Gratton, R.: III *491*
Gray, D.R.: II *613*, 649
Grebenshchikov, S.E.: II *115*
Green, B.J.: I 265, 301, 537; II *3*, 17, 257
Greene, J.M.: II *359*
Greenspan, M.: II *543*
Gregoire, M.: II *259*
Grelot, P.: II *259*
Gribble, R.F.: II *193*
Grieger, G.: I 33, 257; II 79, *81*, 111, 179
Griem, H.R.: I 121, 265; II 17, 191, 267; III 101, 111, 131
Grimm, R.C.: II *395*
Grisham, L.R.: III *293*
Groening, D.E.: I *267*
Gross, R.A.: I *511*, 521
Grossmann, W.: I *511*
Grove, D.: I *21*
Gruber, O.: I *311*
Gruber, R.: II *411*
Gruber, S.: II *259*
Guest, G.E.: II *387*, 421
Guillaneux, P.: I *99*
Gureev, K.G.: III *455*
Guss, W.C.: I *317*
Haas, F.A.: II *423*
Haber, I.: II *455*
Haberstich, A.: I *419*
Hacker, H.: II *81*
Hadley, G.R.: I *167*
Hagenson, R.L.: I *419;* III *281*
Haines, M.G.: I 107, 225; III 131
Halama, H.: III *293*
Hall, L.S.: III *161*
Hamada, Y.: II *95*
Hamasaki, S.: III *113*
Hamberger, S.M.: II *71*
Hamilton, G.W.: III *223*
Hammer, D.A.: II *543;* III *507*
Hammerling, P.: I *227*
Hanatani, K.: II *103*
Hancox, R.: III *193*, 221, 335
Harris, E.G.: II *145*
Harris, J.H.: I *49*
Hasegawa, K.: II *289*
Haselton, H.H.: III *293*
Haste, G.R.: II *145*
Hatori, T.: II *345;* III *427*
Haughian, J.M.: III *293*
Hawryluk, R.: I *21*
Hayase, K.: I *471*
Hedrick, C.L.: II *145*, 153
Helava, H.: I *247*
Helton, F.J.: I *317;* II *387*
Hemsworth, R.S.: II *269*
Henins, I.: II *193*
Henkes, W.: III 145, 315
Herrnegger, F.: II *183*, 191, 201; III 131
Hess, W.: III *49*
Hesse, M.: II *259*
Hewett, D.W.: III *123*
Hidekuma, S.: III *427*
Hinnov, E.: I *21*

Hintz, E.: I *539*
Hirano, K.: I *503*
Hirano, Y.: I *463*
Hiratsuka, H.: II *289*
Hirayama, T.: II *289*
Hiroe, S.: III *427*
Hirose, A.: III *11*
Hobby, M.: II *269*
Hoekzema, J.A.: I *493*
Hoenen, F.: I *351*
Hoffman, A.L.: III *281*
Hofmann, F.: I *305*
Holmes, J.A.: II *369*
Hooper, E.B., Jr.: III *293*
Hoose, J.: I *109*
Hopkins, D.B.: III *293*
Hopman, H.J.: II *527*
Horton, R.: I *21*
Horton, W., Jr.: II 321, *467,* 479
Hosea, J.: I *21*
Hoshino, K.: III *3*
Höthker, K.: I *539,* 551; II 201; III 121
Howe, H.C.: I *49*
Howell, R.B.: I *419*
Hsieh, C.L.: I *317*
Hsuan, H.: I *21*
Hu, P.N.: II *355*
Huba, J.: III *113*
Hugill, J.: II *269*
Hui, B.: II *455*
Hui, B.H.: III *113*
Hull, D.: II *613*
Humphries, S.: III *415*
Hutchinson, I.H.: II *227*
Ichimura, M.: III *3*
Ichtchenko, G.: III *49*
Ide, T.: III *239*
Igitkhanov, Yu.L.: III *359*
Ignat, D.: I *21*
Iida, H.: III *239*
Iiyoshi, A.: II *103*
Ikegami, H.: II *145*
Ikuta, K.: III *395*
Il'inskij, S.E.: III *31*
Imasaki, K.: I *207*
Inoue, N.: III *3*
Inoue, S.: I *323*
Ioki, K.: III *239*
Isaka, M.: II *289*
Isler, R.C.: I *49*
Itô, H.: III *103,* 111
Itoh, K.: I *323*
Itoh, S.: II *95,* 101
Ivanov, A.A.: II *513*
Ivanov, N.V.: III *61*
Ivanovskij, M.A.: II *115*
Iwahashi, A.: I *323*
Izawa, Y.: I *147*
Izvozchikov, A.B.: I *3*
Jäckel, H.: II *81*
Jackel, S.: I *109*
Jacobson, A.R.: II *193*
Jaeger, E.F.: II *145*
Jaenicke, R.: II *81*
Jahns, G.L.: I *49*
Jahoda, F.C.: II *193*
Jarboe, T.R.: II *193*
Jardin, S.C.: II *395*
Jassby, D.L.: II *435*
Javel, P.: III *49*
Jenkins, D.J.: III *507*
Jensen, T.H.: I *317;* II *387*
Jobes, F.: I *21*
John, P.K.: II *627*
Johnson, D.: I *21*
Johnson, D.L.: I *167*
Johnson, J.L.: I 257; II 93, 385, *395*
Johnson, R.R.: I *227*
Johnston, T.W.: II 649
Jolas, A.: III *471*
Jones, E.M.: II *305*
Jukes, J.D.: I *479,* 489
Jungwirth, K.: II *535*
Junker, J.: II *81*
Jurgens, B.: II *527*
Kachen, G.I.: II *589*
Kadomtsev, B.B.: I 301, *555,* 567; II 525; III 335
Kadota, K.: II *95*
Kaeppeler, H.J.: III *437*
Kaganskij, M.G.: I *387*
Kaleck, A.: I *351*
Kalinichenko, S.S.: II *129*
Kalmykov, S.G.: I *387*
Kaneko, H.: I *323*
Kapetanakos, C.A.: III *415*
Karger, F.: I *259, 267,* 277, 301
Karr, H.J.: I *419*
Kasai, S.: II *289*
Kato, Y.: I *147*
Katsurai, M.: II *567;* III *337*
Kaufmann, M.: II *183;* III 121

Kawahata, K.: II *95*
Kawakami, T.: II *289*
Kawasaki, S.: III *427*
Kazawa, M.: II *289*
Keilhacker, M.M.K.: II 93, 287, 301
Kelly, H.: III *483*, 491
Kerner, W.: II *395*
Kerst, D.W.: II *333*
Kesner, J.: III *203*
Ketterer, H.E.: I *49*
Khol'nov, Yu.V.: II *115*
Kilkenny, J.D.: II *555*, *613*
Killeen, J.: II *435*
Kim, J.: III *293*
Kimura, H.: II *289*
Kindel, J.M.: I *123*, 131, 205
King, P.W.: I *49*
Kirov, A.G.: III *31*
Kishinevskij, M.E.: III *177*
Kistemaker, J.: II *527*
Kita, Y.: I *503*
Kitagawa, S.: I *503*
Kitagawa, Y.: I *147*
Klüber, O.: I *259*, *267*
Knobloch, A.F.: III *221*
Knoepfel, H.: III 403
Koba, Yu.V.: I *185*
Kodama, K.: II *289*
Koechlin, F.: I 33
Kogoshi, S.: II *567*
Kolesnichenko, Ya.I.: III *347*, 367
Komm, D.S.: I *247*, *409*
Kondo, K.: II *103*
Könen, L.: I *351*
Konoshima, S.: II *289*
Köppendörfer, W.: I 489, 551; III *79*, 101, 121
Korolev, V.D.: I *185*
Korzhavin, V.M.: III *455*
Kostomarov, D.P.: I *591*
Kováč, I.: II *535*
Kovan, I.A.: III *61*
Koyama, K.: II *605*
Krakowski, R.A.: III *281*
Krall, N.A.: III *113*
Krasheninnikov, S.I.: II *513*
Krause, H.: I *311*
Kristal, R.: II *193*
Kristiansen, M.: III 47
Krokhin, O.N.: III *563*
Krommes, J.A.: II *489*
Kruer, W.: I *133*
Kruglyakov, E.P.: III 545
Krupin, V.A.: III *61*
Kubis, J.J.: I *227*
Kukushkin, A.S.: I *615*
Kulcinski, G.L.: III *203*
Kulsrud, R.M.: II *435*
Kulygin, V.M.: I *85*
Kumagai, K.: II *289*
Kumazawa, R.: III *427*
Kunieda, S.: II *289*
Kunkel, W.B.: III *293*
Kunze, R.-C.: II *81*
Kuo, S.: III *203*
Kuo, Y.Y.: II *467*
Kuriki, K.: II *635*
Kurilko, P.I.: II *129*
Kuroda, T.: II *95*
Kurtmullaev, R.Kh.: III *517*
Kuznetsov, Yu.K.: II *129*
Lackner, K.: I *267*, 369, 605; II *401*
LaHaye, R.: II *333*
Lallia, P.: III *49*
Lampis, G.: I 19
Langdon, B.: I *133*
Larsen, E.: III *203*
Lasinski, B.: I *133*
Lazar, N.H.: II *145*
Lebedev, S.V.: I *387*
Lecoustey, P.: I 47
Lee, J.D.: III *223*
Lee, K.: I *123*
Lee, R.: III *415*
Lee, W.W.: II *467*
Lees, D.J.: II *71*, 79
Lehnert, B.P.: I 257, 289; II 27, 343; III 383
Lengyel, L.L.: II *577*
Leonov, V.M.: I *85*
Leppelmeier, G.W.: I *109*
Leuterer, F.: II *81*
Lewis, H.R.: III *123*
Lietzke, A.F.: I *317*
Liewer, P.C.: III *113*
Liksonov, V.I.: I *177*
Lindman, E.L.: I *123*
Lisitano, G.: I *259*, *267*
Lister, J.B.: II *71*
Liu, C.S.: I *399*; III *113*
Lodestro, L.L.: III *147*
Logan, B.G.: III *135*

Lohr, J.M.: I *317*
Lortz, D.: II 179, *183*, 191
Lovelace, R.V.: III *415*
Lozovskij, S.N.: III *31*
Lubin, M.J.: I *109*
Luce, J.S.: I 205
Luckhardt, S.C.: III *385*
Ludwig, G.: III *415*
Lui, H.C.: I *511*
Lukyanov, S.Yu.: I *3;* III *327*
Lunin, A.L.: III *517*
Luxon, J.L.: II *387*
Lyon, J.F.: I *49*
Lysenko, S.E.: I *3*
Lysojvan, A.I.: II *129*
Maeda, H.: II *289*, 301
Maejima, Y.: I *463*
Maeno, M.: II *289*
Mahdavi, M.A.: I *317*
Mahn, C.: III *49*
Maisonnier, C.: III *447*
Maki, K.: III *239*
Makishima, K.: I *323*
Maksimov, Yu.S.: I *3*
Malein, A.: II *71*
Malesani, G.: I *447*, 461
Malmberg, J.: II *305*
Manheimer, W.: III *415*
Manickam, J.: II *395*
Marcus, F.B.: II *369*
Mark, E.V.: II *81*
Marlier, S.: II *81*
Maron, N.: III *147*
Marsh, S.J.: III *415*
Martin, F.: I *247*
Martin, T.H.: I *167*
Martynenko, Yu.V.: III *327*
Marx, K.D.: II *435*
Mast, F.: I *311*
Masuzaki, M.: III *395*
Matoba, M.: I *147*
Matoba, T.: II *289*
Matsuda, K.: I *317*
Matsuda, S.: III *239*
Matsuda, Y.: II *467*
Matsumoto, Y.: II *605*
Matsuoka, K.: II *95*
Matsuura, K.: II *95*
Matsuzaki, Y.: II *289*
Max, C.: I *133*
Mayer, F.J.: I *227*, 243
Mayer, H.M.: I *259*, *267*
Maynard, C.W.: III *203*
Mazzucato, E.: I *21*, *371*, 385
McAlees, D.G.: II *145*, *369*
McCormick, K.: I *259*
McCoy, M.G.: II *435*
McCracken, G.M.: II *269*
McDaniel, D.H.: I *167*
McKay, W.: II *71*
McLean, E.: I *217*
McMahon, J.: I *217*
McNamara, B.: III *161*, 175
McNeill, D.H.: II *145*
Meger, R.A.: III *385*
Meisel, D.: I *259*, 265, *267*
Mendel, C.W., Jr.: I *167*
Mercier, C.: II *29*
Merezhkin, V.G.: I *85*
Meservey, E.: I *21*
Messiaen, A.M.: I *359*
Michaelis, M.: III *405*
Mihalczo, J.T.: I *49*
Mikhajlov, A.P.: I *177*
Milanese, M.: III *491*
Millar, W.: II *71*
Miller, G.: II *193*
Miller, P.A.: I *167*
Miller, R.L.: II *387;* III *281*
Mimura, M.: I *493*
Mirin, A.A.: II *435*
Mirnov, S.V.: I *291*
Mirnov, V.V.: III *535*
Mitchell, J.T.D.: III *193*
Mix, L.P.: I *167*
Miyahara, A.: II *95;* III *427*
Miyake, S.: III *427*
Miyamoto, K.: II 79, 93, *95*, 179, 351
Mizui, J.: I *147*
Mochizuki, T.: I *147*
Moeller, C.P.: I *317;* II *333*
Mohri, A.: III *395*, 403
Moir, R.W.: III *223*, 237, 301
Mok, Y.C.: I *399*
Mole, C.J.: III *317*
Molvig, K.: II *455*
Molvik, A.W.: III *135*
Mondt, J.P.: III *113*
Montgomery, B.: I *247*
Monticello, D.A.: I *569*
Moore, J.R.: II *369*
Morandi, P.: I *259*, *267*

Morgan, P.D.: II *635;* III *447*
Morikawa, J.: III *3*
Morimoto, S.: II *103*
Mosher, D.: III *415*
Motojima, O.: II *103*
Motz, H.: III *405,* 413
Mrowka, S.: II *71*
Mukhovatov, V.S.: I *85*
Müller, G.: II *81*
Münich, M.: III *79*
Murakami, M.: I *49*
Mutoh, T.: II *103*
Muzychenko, A.D.: III *417*
Nagami, M.: II *289*
Nagel, D.: I *217*
Nahrath, B.: III *441*
Nakai, S.: I *147, 207*
Nakasuga, M.: II *103*
Nalesso, G.F.: I *447*
Nardi, V.: III *497*
Narihara, K.: III *395*
Navratil, G.A.: II *333*
Nazet, C.: III *471*
Neau, G.L.: I *167*
Nechaev, Yu.I.: II *115*
Nee, A.: I *109*
Neidigh, R.V.: I *49*
Neilson, G.H.: I *49*
Nekrasov, F.M.: III *31*
Nelson, D.B.: II *145, 369*
Neuhauser, J.: II *183,* 213
Nexsen, W.E.: III *135*
Nguyen, T.K.: III *49*
Nielson, C.W.: III *123*
Nihei, H.: III *3*
Nishikawa, K.I.: II *345*
Nocentini, A.: II *19*
Noda, N.: I *503*
Nogi, Y.: II *215*
Notkin, G.E.: I *3*
Novikov, V.P.: III *417*
Nührenberg, J.: II 179, *183*
Obayashi, H.: III *427*
Oberson, R.: III *303*
Obiki, T.: II *103*
Ochiai, I.: I *323*
Odazima, K.: II *289*
Oepts, D.: I *493*
Offenberger, A.A.: II *635*
Ogawa, K.: I *463*
Ogden, J.M.: III *113*
Ohkawa, T.: I *317;* II 321, *333, 387*
Ohkubo, K.: II *95*
Ohlendorf, W.: III *49*
Ohtake, I.: II *103*
Ohtsuka, H.: II *289*
Ohwadano, Y.: II *567*
Ohyabu, N.: I *317*
Okada, O.: II *345*
Okada, S.: II *567*
Okuda, H.: II *467*
Olson, C.L.: I *167*
Onishchenko, V.V.: III *31*
Oomens, A.A.M.: I *493*
Oordt, A.v.: II *81*
Oppenländer, T.: III *441*
Ortolani, S.: I *447,* 477
Osanai, Y.: I *503;* II *215*
Ott, E.: III *415*
Overskei, D.: I *247*
Owen, L.W.: II *145*
Owren, H.M.: III *293*
Pacher, G.W.: III *49,* 59
Pacher, H.D.: III *49*
Paithankar, A.S.: I *359*
Palmadesso, P.: II *455*
Panasenkov, A.A.: I *85*
Papadopoulos, K.: I 95; II *455,* 525, 565
Pappas, D.: I *247*
Pare, V.K.: I *49*
Parker, R.: I *247*
Parlange, F.: II *259,* 267
Pashnev, V.K.: II *129*
Patou, C.: I *99*
Paul, J.W.M.: II *269,* 287
Peacock, N.J.: II *635,* 649
Pearlstein, L.D.: III *147*
Pease, R.S.: I 95, 427, 461, 521, 567; II 127, 153; III *549*
Pegoraro, F.: II *455*
Peiry, J.M.: I *305*
Pelah, I.: I *109*
Pellat, R.: I *607*
Peng, Y.-K.M.: II *369*
Pen'kina, V.S.: I *185*
Perkins, F.W.: II *435*
Perry, F.C.: I *167*
Petersen, P.I.: II *333*
Petrov, M.P.: I *3*
Pfirsch, D.: II 385
Pichugin, V.V.: III *517*
Piekaar, H.W.: III *11*

Piffl, V.: II *535*
Pinet, D.: II *259*
Piret, C.: I *359*
Pistunovich, V.I.: I *615;* II *513*
Pittenger, L.C.: III *293*
Pogutse, O.P.: II *237*
Ponte, N.S.: III *293*
Popkov, G.N.: I *3*
Popov, A.M.: I *591*
Popov, I.A.: III *61*
Popov, S.N.: II *115*
Popov, Yu.P.: I *167*
Popovics, C.: II *597*
Poquerusse, A.: II *597*
Porkolab, M.: III 37
Porrot, E.: II *259*
Pospieszczyk, A.: I *539;* II *269*
Post, R.F.: III *161,* 301, 315
Post, R.S.: II *333,* 343
Poukey, J.W.: I *167*
Pouzo, J.: III *491*
Powell, B.A.: II *71; 269*
Prager, S.C.: I *317*
Prater, R.: II *333*
Prelec, K.: III *293*
Prentice, R.: II *269*
Prestwich, K.R.: I *167*
Prior, W.: III *497*
Pritchard, B.A.: III *293*
Prono, D.S.: III *293*
Pross, G.: III *441*
Putnam, S.: II *543*
Putvinskij, S.V.: I *615*
Pyle, R.V.: III *293*
Quimby, D.C.: III *281*
Quinn, W.E.: II *193*
Quintenz, J.P.: I *167*
Rabinovich, M.S.: II *115,* 127, 179; III 403, 413
Rager, J.P.: III *447*
Raimbault, P.A.: III *303*
Ramirez, J.J.: I *167*
Ramponi, G.: I *409*
Rau, F.: II *81*
Rawls, J.M.: I *317;* II *387*
Razumova, K.A.: I *3*
Rebut, P.H.: II *3*
Rehker, S.: II *81*
Reid, G.W.: II *269*
Reisse, J.M.: I *99*
Rem, J.: I *523,* 537
Renner, H.: II *81*
Rensink, M.E.: II *435;* III *161, 223*
Reusch, M.: I *511*
Reuss, J.: II *55*
Rewoldt, G.: II *489*
Rey, G.: II *259*
Reznik, S.N.: III *347*
Ribe, F.L.: I 461, 551; II 191, *193,* 201, 223; III *317*
Ringler, H.: II *81*
Rioux, C.: III *527*
Ripin, B.: I *217*
Riviere, A.C.: II *305*
Roberts, K.V.: III 121
Roberts, M.: III *255*
Robinson, D.C.: I *335,* 369, *429,* 501
Robson, A.E.: II 603; III *507*
Rogers, J.D.: III *317*
Rognlien, T.D.: III *147*
Rohwein, G.J.: I *167*
Rolland, P.: II *55*
Rose, P.H.: III *281*
Rosenbluth, M.N.: I *569;* II *489;* III *555*
Ross, D.W.: II *489*
Rückle, B.: III *441*
Rudakov, L.I.: I *167, 185*
Rudolph, T.: II *635*
Rumsby, P.T.: III *405*
Rutgers, W.R.: I *399*
Rutherford, P.H.: I 95; II *489*
Ryan, P.M.: III *293*
Rylander, H.G.: III *317*
Ryutov, D.D.: III *535*
Saffert, J.: II *81*
Saison, R.: II *481*
Saito, H.: III *337*
Saito, K.: II *215*
Sako, K.: III *239*
Samain, A.: I 289, 385, 605; II 479; III 189
Samarskij, A.A.: I *177*
Sandel, F.: I *511*
Sapper, J.: II *81*
Sardei, F.: II *43*
Sasaki, A.: II *103*
Sasaki, R.: I *147*
Sato, K.: I *503*
Sato, K.N.: II *567*
Sato, M.: II *103*
Sato, T.: III *427*
Satomi, N.: III *103*

Sauthoff, N.: I *21*
Sayer, R.O.: II *369*
Sbitnikova, I.S.: II *115*
Scharer, J.: III *203*
Schechter, D.E.: III *293*
Schilling, G.: III *293*
Schivell, J.: I *21*
Schlüter, J.: I *351*
Schmidt, G.: I *21*
Schmidt, H.: III *441*
Schmitter, K.-H.: III *571*
Schneider, W.: II *183, 203*
Schofield, A.E.: I *419*
Schramm, G.: II *183*
Schrijver, H.: II *19*
Schultz, K.R.: III *223*
Seki, Y.: III *239*
Sekiguchi, T.: II *567;* III *337*
Semashko, N.N.: I *85*
Semenov, I.B.: I *291;* III *61*
Semenov, V.N.: III *517*
Sengoku, S.: II *289*
Sesnic, S.: I *259, 267*
Sethian, J.: II *543*
Sgro, A.G.: III *123*
Shaeffer, D.L.: I *49*
Shafranov, V.D.: II *155,* 179, 257
Shakhatre, M.: III *441*
Shakhovets, K.G.: I *387*
Sharp, L.E.: II *71*
Shatford, P.A.: II *71*
Shcheglov, D.A.: I *3*
Sherwood, A.R.: II *193*
Shibata, T.: II *289*
Shiho, M.: II *289*
Shiina, S.: II *215*
Shiina, T.: II *289*
Shimada, M.: II *289*
Shimada, T.: I *463*
Shimomura, Y.: II *289*
Shinohara, S.: I *323*
Shipuk, I.Ya.: III *517*
Shohet, J.L.: II 111, 143
Shoji, A.: II *289*
Shoji, T.: III *427*
Shpigel', I.S.: II *115*
Shvets, O.M.: II *129*
Siemon, R.E.: II *193*
Sigmar, D.J.: II *369*
Simik, A.: I *305*
Simonen, T.C.: III *135*
Sinitsyna, L.D.: I *85*
Skarsgard, H.M.: III *11*
Slater, D.C.: I *227*
Slushet, R.E.: I *371*
Sluyters, T.: III *293*
Smeulders, P.: I 257, 415; II *81*
Smirnov, V.P.: I *177, 185,* 205
Smith, R.: I *21*
Smolkin, G.E.: III *517*
Soboleva, T.K.: II *513*
Sokolov, Yu.A.: III *61*
Söldner, F.: III *89,* 131
Solntsev, A.M.: II *169*
Sommer, J.: III *79*
Soule, J.L.: I *607*
Spalding, I.J.: II *589,* 649; III 413
Spong, D.A.: II *145*
Stacey, W.M., Jr.: III *255,* 279
Stallard, B.W.: III *135*
Stamper, J.: I *217*
Start, D.F.H.: II *305*
Stauffer, F.J.: I *21, 399*
Stearns, J.W.: III *293*
Stefanovskij, A.M.: II *169*
Steinhauer, L.C.: III *281*
Stenz, C.: II *597*
Stephanakis, S.J.: III *415*
Steuer, K.-H.: III *89,* 101
Stevens, D.C.: II *355*
Stewart, J.J.: III *147*
Stewart, L.D.: III *293,* 301
Stillwagon, R.E.: III *317*
Stirling, W.L.: III *293*
Stöckel, J.: II *535*
Stodiek, W.: I *21,* 33, 605; II 79
Stott, P.E.: II *269*
Strachan, J.: I *21*
Streikov, V.S.: I *3,* 19, 33
Strickler, D.J.: II *369*
Suckewer, S.: I *21*
Sudan, R.N.: II 386, 565; III 159, 403, *415*
Sudo, S.: II *567*
Sugie, T.: II *289*
Sugimoto, H.: II *499*
Sugisaki, K.: I *471*
Sugiura, M.: II *605*
Sukhov, A.D.: I *185*
Summers, D.D.R.: II *269*
Sunaoshi, H.: II *289*
Šunka, P.: II *535*

Suprunenko, V.A.: II *129*, 143; III *37*
Surko, C.M.: I *371*
Suzuki, N.: II *289*
Suzuki, T.: III *239*
Suzuki, Y.: I *323*
Sviatoslavsky, I.: III *203*
Swain, D.W.: I *49*
Swannack, C.E.: III *317*
Sweeney, M.A.: I *167*
Sweetman, D.R.: II *305*, 321, 343; III 145, 175
Sykes, A.: I *429*
Sze, D.K.: III *203*
Takahashi, K.: II *289*
Takamura, S.: III *49*
Takayama, K.: III *427*
Takeuchi, H.: II *289*
Tamano, T.: I *317*; III 59
Tamaru, T.: I *471*, 477
Tamor, S.: I *409*
Tanahashi, S.: II *95*
Tanaka, H.: II *567*
Tanaka, M.: II *289*
Tang, W.M.-W.: II 465, *489*, 509
Tani, T.: II *289*
Tanimoto, M.: II *605*
Taquet, B.: II *259*
Tarasenko, V.F.: II *129*
Tarumov, Eh.Z.: I *185*
Tasso, H.: III *371*, 383
Tataronis, J.A.: I *511*
Taussig, R.T.: III *281*
Taylor, C.E.: III *223*
Taylor, R.J.: I 33, 47, 265, 277, 369; II 17, 67, 101, 267, *323*, 331, 351, 367, 451
Terashima, Y.: II *95*, *345*, 351
Thode, L.: II *543*
Thomas, C.L.: I *335*
Thomas, K.S.: II *193*
Thomassen, K.I.: III 279, *317*, 325
Thomson, J.: I *133*
Thorsos, E.: I *109*
Tilinin, G.N.: I *85*
Todoroki, J.: II *215*, 223
Toepfer, A.J.: I *167*, 243
Toi, K.: II *95*
Tokar', M.Z.: III *359*
Tokutake, T.: II *289*
Tolk, K.M.: III *317*
Tolok, V.T.: II *129*
Tone, T.: III *239*, 279
Tonon, G.: III *49*
Toyama, H.: I *323*
Toyoshima, N.: II *289*
Trivelpiece, A.W.: I *399*, 415
Troyon, F.: II *411*
Trubnikov, B.A.: III *455*
True, M.: II *467*
Trunk, M.: III *441*
Tsai, C.C.: III *293*
Tsang, K.T.: II *369*, *489*
Tsuji, H.: II *567*, III *337*
Tsuzuki, T.: III *395*
Tull, C.G.: II *435*
Turchi, P.J.: III *415*; *507*
Turkel, E.: II *355*
Turner, L.: III *123*
Turner, W.C.: III *135*
Tutter, M.: II *81*
Uchida, T.: III *3*
Uckan, N.A.: II *145*, *369*
Ueda, N.: II *289*
Ullschmied, J.: II *535*
Uo, K.: II *103*, 111
Utyugov, E.G.: III *517*
Uyana, T.: III *103*
Valckx, F.P.G.: III *303*, 315
Valeo, E.J.: I 131, *133*
Vandenplas, P.E.M.: I 289, *359*
Vandevender, J.P.: I *167*
Vanek, V.: I *317*
Vargas, M.: III *483*, *489*
Vasin, N.L.: I *3*
Vekshtejn, G.E.: III *535*
Veprek, S.: II 267
Verhage, A.J.L.: I *429*
Vershkov, V.A.: III *61*
Vertiporokh, A.N.: I *3*
Vikhrev, V.V.: II *237*; III *455*
Vil'dzhyunas, M.I.: I 397
Vinogradov, V.P.: I *3*
Vinogradova, N.D.: I *3*
Virmont, J.: II *597*
Vlasenkov, V.S.: I *85*
Vlases, G.C.: III *281*
Vogel, H.F.: III *317*
Vogelsang, W.F.: III *203*
Volkov, T.F.: III *359*
Voronov, G.S.: II *115*
Waddell, B.V.: I *569*
Waelbroeck, F.G.: I 47, 369; II 17

Wagner, C.E.: III *113*
Wagner, F.: I *259, 267*
Wakatani, M.: I *503*
Walker, A.C.: II *589*
Wang, T.S.: I *317;* II *387*
Ward, S.: II *589*
Watanabe, K.: III *103*
Watanabe, N.: III *427*
Watanabe, T.: III *427*
Watari, T.: III *427*
Watson, D.C.: III *147*
Watteau, J.P.: I *99*
Watts, M.R.C.: I *429*
Webb, D.R.A.: II *71*
Webb, S.J.: II *245*
Wegrowe, J.G.: III *49*
Weimer, K.E.: II *395*
Weiss, J.: II *259*
Weldon, D.M.: III *317*
Weldon, W.F.: III *317*
Weller, A.: II *81*
Welter, H.: I *579*
Werkoff, F.: II *29,* 67; III 29
Werner, R.W.: III *223*
Wesley, J.C.: II *387*
Wesson, J.A.: I *429*
Weynants, R.R.: I *359*
Wharton, C.: II *543*
Whealton, J.H.: III *293*
White, M.S.: II *613*
White, R.B.: I *569*
Whitlock, R.: I *217*
Widner, M.M.: I *167*
Wilgen, J.B.: I *49*
Wilhelm, R.: I *311*
Willenberg, H.J.: III *281*
Wilson, C.M.: II *269*
Wimmel, H.K.: II *481,* 509
Wing, W.R.: I *49*
Winske, D.: III *123,* 131
Winsor, N.: I *217;* II 153, *455;* III 159
Witkowski, S.: I 121, 163
Wobig, H.: II *81,* 93, 127, 153
Wolf, G.H.: I 537; II 287; III 121, 279
Wong, K.L.: I *511*
Wong, S.K.: II *333*
Woodall, D.: I *109*
Woodruff, G.L.: III *281*
Woodson, H.H.: III *317*
Wootton, A.J.: I *335*
Wright, R.E.: III *293*
Wright, T.P.: I *167*
Wu, C.S.: III *113*
Würsching, E.: II *81*
Yaakobi, B.: I *109,* 225
Yagi, I.: II *215*
Yamada, S.: I *503*
Yamaguchi, N.: I *147*
Yamaguchi, S.: I *503*
Yamamoto, S.: II *289*
Yamamoto, T.: II *289*
Yamanaka, C.: I 107, *147,* 163, *207*
Yamanaka, K.: III *395*
Yamanaka, T.: I *147*
Yamato, H.: III *239*
Yamauchi, T.: II *289*
Yamazaki, K.: III *3*
Yang, T.F.: III *203*
Yokokura, K.: II *289*
Yokoyama, K.: II *215*
Yokoyama, M.: I *147*
Yonas, G.: I *167*
Yoshida, K.: I *147*
Yoshikawa, S.: I *323*
Yoshimura, H.: II *215*
Yoshioka, S.: II *103*
Young, F.: I *217*
Young, K.: I *21*
Young, T.S.T.: II *543*
Young, W.D.: III *203*
Yushmanov, P.N.: II *513*
Zakajdakov, V.V.: III *177*
Zakharov, L.E.: II *155*
Zaveryaev, V.S.: I *3*
Zehrfeld, H.P.: I *267*
Zhdanov, S.K.: III *455*
Zippe, M.: II *81*
Zverev, N.M.: II *115*
Zweben, S.J.: I *49*

The following conversion table is provided for the convenience of readers and to encourage the use of SI units.

FACTORS FOR CONVERTING UNITS TO SI SYSTEM EQUIVALENTS *

SI base units are the metre (m), kilogram (kg), second (s), ampere (A), kelvin (K), candela (cd) and mole (mol).
[For further information, see International Standards ISO 1000 (1973), and ISO 31/0 (1974) and its several parts]

Multiply		*by*	*to obtain*
Mass			
pound mass (avoirdupois)	1 lbm	= 4.536×10^{-1}	kg
ounce mass (avoirdupois)	1 ozm	= 2.835×10^{1}	g
ton (long) (= 2240 lbm)	1 ton	= 1.016×10^{3}	kg
ton (short) (= 2000 lbm)	1 short ton	= 9.072×10^{2}	kg
tonne (= metric ton)	1 t	= 1.00×10^{3}	kg
Length			
statute mile	1 mile	= 1.609×10^{0}	km
yard	1 yd	= 9.144×10^{-1}	m
foot	1 ft	= 3.048×10^{-1}	m
inch	1 in	= 2.54×10^{-2}	m
mil (= 10^{-3} in)	1 mil	= 2.54×10^{-2}	mm
Area			
hectare	1 ha	= 1.00×10^{4}	m^2
(statute mile)^2	1 mile^2	= 2.590×10^{0}	km^2
acre	1 acre	= 4.047×10^{3}	m^2
yard^2	1 yd^2	= 8.361×10^{-1}	m^2
foot^2	1 ft^2	= 9.290×10^{-2}	m^2
inch^2	1 in^2	= 6.452×10^{2}	mm^2
Volume			
yard^3	1 yd^3	= 7.646×10^{-1}	m^3
foot^3	1 ft^3	= 2.832×10^{-2}	m^3
inch^3	1 in^3	= 1.639×10^{4}	mm^3
gallon (Brit. or Imp.)	1 gal (Brit)	= 4.546×10^{-3}	m^3
gallon (US liquid)	1 gal (US)	= 3.785×10^{-3}	m^3
litre	1 l	= 1.00×10^{-3}	m^3
Force			
dyne	1 dyn	= 1.00×10^{-5}	N
kilogram force	1 kgf	= 9.807×10^{0}	N
poundal	1 pdl	= 1.383×10^{-1}	N
pound force (avoirdupois)	1 lbf	= 4.448×10^{0}	N
ounce force (avoirdupois)	1 ozf	= 2.780×10^{-1}	N
Power			
British thermal unit/second	1 Btu/s	= 1.054×10^{3}	W
calorie/second	1 cal/s	= 4.184×10^{0}	W
foot-pound force/second	1 ft·lbf/s	= 1.356×10^{0}	W
horsepower (electric)	1 hp	= 7.46×10^{2}	W
horsepower (metric) (= ps)	1 ps	= 7.355×10^{2}	W
horsepower (550 ft·lbf/s)	1 hp	= 7.457×10^{2}	W

* Factors are given exactly or to a maximum of 4 significant figures

Multiply		*by*	*to obtain*
Density			
pound mass/inch^3	1 lbm/in^3	= 2.768×10^4	kg/m^3
pound mass/foot^3	1 lbm/ft^3	= 1.602×10^1	kg/m^3
Energy			
British thermal unit	1 Btu	= 1.054×10^3	J
calorie	1 cal	= 4.184×10^0	J
electron-volt	1 eV	≃ 1.602×10^{-19}	J
erg	1 erg	= 1.00×10^{-7}	J
foot-pound force	1 ft·lbf	= 1.356×10^0	J
kilowatt-hour	1 kW·h	= 3.60×10^6	J
Pressure			
newtons/metre^2	1 N/m^2	= 1.00	Pa
atmosphere[a]	1 atm	= 1.013×10^5	Pa
bar	1 bar	= 1.00×10^5	Pa
centimetres of mercury (0°C)	1 cmHg	= 1.333×10^3	Pa
dyne/centimetre^2	1 dyn/cm^2	= 1.00×10^{-1}	Pa
feet of water (4°C)	1 ftH_2O	= 2.989×10^3	Pa
inches of mercury (0°C)	1 inHg	= 3.386×10^3	Pa
inches of water (4°C)	1 inH_2O	= 2.491×10^2	Pa
kilogram force/centimetre^2	1 kgf/cm^2	= 9.807×10^4	Pa
pound force/foot^2	1 lbf/ft^2	= 4.788×10^1	Pa
pound force/inch^2 (= psi)[b]	1 lbf/in^2	= 6.895×10^3	Pa
torr (0°C) (= mmHg)	1 torr	= 1.333×10^2	Pa
Velocity, acceleration			
inch/second	1 in/s	= 2.54×10^1	mm/s
foot/second (= fps)	1 ft/s	= 3.048×10^{-1}	m/s
foot/minute	1 ft/min	= 5.08×10^{-3}	m/s
mile/hour (= mph)	1 mile/h	= 4.470×10^{-1} m/s; 1.609×10^0 km/h	
knot	1 knot	= 1.852×10^0	km/h
free fall, standard (= g)		= 9.807×10^0	m/s^2
foot/second^2	1 ft/s^2	= 3.048×10^{-1}	m/s^2
Temperature, thermal conductivity, energy/area·time			
Fahrenheit, degrees − 32	°F − 32	$\frac{5}{9}$	°C
Rankine	°R	$\frac{5}{9}$	K
1 Btu·in/ft^2·s·°F		= 5.189×10^2	W/m·K
1 Btu/ft·s·°F		= 6.226×10^1	W/m·K
1 cal/cm·s·°C		= 4.184×10^2	W/m·K
1 Btu/ft^2·s		= 1.135×10^4	W/m^2
1 cal/cm^2·min		= 6.973×10^2	W/m^2
Miscellaneous			
foot^3/second	1 ft^3/s	= 2.832×10^{-2}	m^3/s
foot^3/minute	1 ft^3/min	= 4.719×10^{-4}	m^3/s
rad	rad	= 1.00×10^{-2}	J/kg
roentgen	R	= 2.580×10^{-4}	C/kg
curie	Ci	= 3.70×10^{10}	disintegration/s

[a] atm abs: atmospheres absolute; atm (g): atmospheres gauge.

[b] lbf/in^2 (g) (= psig): gauge pressure; lbf/in^2 abs (= psia): absolute pressure.

HOW TO ORDER IAEA PUBLICATIONS

An exclusive sales agent for IAEA publications, to whom all orders and inquiries should be addressed, has been appointed in the following country:

UNITED STATES OF AMERICA — UNIPUB, P.O. Box 433, Murray Hill Station, New York, N.Y. 10016

In the following countries IAEA publications may be purchased from the sales agents or booksellers listed or through your major local booksellers. Payment can be made in local currency or with UNESCO coupons.

ARGENTINA	Comisión Nacional de Energía Atómica, Avenida del Libertador 8250, Buenos Aires
AUSTRALIA	Hunter Publications, 58 A Gipps Street, Collingwood, Victoria 3066
BELGIUM	Service du Courrier de l'UNESCO, 112, Rue du Trône, B-1050 Brussels
CANADA	Information Canada, 171 Slater Street, Ottawa, Ont. K1A 0S9
C.S.S.R.	S.N.T.L., Spálená 51, CS-110 00 Prague Alfa, Publishers, Hurbanovo námestie 6, CS-800 00 Bratislava
FRANCE	Office International de Documentation et Librairie, 48, rue Gay-Lussac, F-75005 Paris
HUNGARY	Kultura, Hungarian Trading Company for Books and Newspapers, P.O. Box 149, H-1011 Budapest 62
INDIA	Oxford Book and Stationery Comp., 17, Park Street, Calcutta 16; Oxford Book and Stationery Comp., Scindia House, New Delhi-110001
ISRAEL	Heiliger and Co., 3, Nathan Strauss Str., Jerusalem
ITALY	Libreria Scientifica, Dott. de Biasio Lucio "aeiou", Via Meravigli 16, I-20123 Milan
JAPAN	Maruzen Company, Ltd., P.O.Box 5050, 100-31 Tokyo International
NETHERLANDS	Marinus Nijhoff N.V., Lange Voorhout 9-11, P.O. Box 269, The Hague
PAKISTAN	Mirza Book Agency, 65, The Mall, P.O.Box 729, Lahore-3
POLAND	Ars Polona, Centrala Handlu Zagranicznego, Krakowskie Przedmiescie 7, Warsaw
ROMANIA	Cartimex, 3-5 13 Decembrie Street, P.O.Box 134-135, Bucarest
SOUTH AFRICA	Van Schaik's Bookstore, P.O.Box 724, Pretoria Universitas Books (Pty) Ltd., P.O.Box 1557, Pretoria
SPAIN	Diaz de Santos, Lagasca 95, Madrid-6 Calle Francisco Navacerrada, 8, Madrid-28
SWEDEN	C.E. Fritzes Kungl. Hovbokhandel, Fredsgatan 2, S-103 07 Stockholm
UNITED KINGDOM	Her Majesty's Stationery Office, P.O. Box 569, London SE1 9NH
U.S.S.R.	Mezhdunarodnaya Kniga, Smolenskaya-Sennaya 32-34, Moscow G-200
YUGOSLAVIA	Jugoslovenska Knjiga, Terazije 27, YU-11000 Belgrade

---

Orders from countries where sales agents have not yet been appointed and requests for information should be addressed directly to:



Division of Publications
International Atomic Energy Agency
Kärntner Ring 11, P.O.Box 590, A-1011 Vienna, Austria

77-04318

INTERNATIONAL
ATOMIC ENERGY AGENCY
VIENNA, 1977

SUBJECT GROUP: III
Physics/Plasma Physics, Fusion
PRICE: US $43.00